Experimental and theoretical studies of mononuclear high-valent nitrido-iron and oxo-iron complexes

Dissertation

zur

Erlangung des Doktorgrades (Dr.rer.nat.)

der

Mathematisch-Naturwissenschaftlichen Fakultät

der

Rheinischen Friedrich-Wilhelms-Universität Bonn

vorgelegt von

Oliver Moritz Krahe

aus Bonn

Bonn 2015

Angefertigt mit Genehmigung der Mathematisch-Naturwissenschaftlichen Fakultät der Rheinischen Friedrich-Wilhelms-Universität Bonn

1. Gutachter: Prof. Dr. Frank Neese

2. Gutachter: Prof. Dr. Robert Glaum

Tag der Promotion: 5. April 2016

Erscheinungsjahr: 2016

Abstract

Nitrido-iron and oxo-iron complexes are important species in manifold biological and industrial processes. While nitrido-iron complexes are intermediates in biological and industrial nitrogen fixation, oxo-iron complexes are known to be active species in biological oxidation reactions. Therefore, in the work presented herein, mononuclear nitrido-iron(V) complexes are studied as well as a novel oxo-iron species that shows distinct differences when compared to other complexes reported so far. The aim of studying the (spectroscopic) properties of those well-defined model systems is to benefit from their understanding when more complex systems are investigated, whose exact structures are not known in detail. Spectroscopic and theoretical methods are applied that individually provide valuable information, but the combination of both facilitates the interpretation of data and permits an even more detailed understanding of the systems. Proposed species can be further confirmed or ruled out by comparison of their calculated spectroscopic properties with experimental results.

Azido-iron(III) complexes that serve as precursors for the photolytic formation of nitrido-iron(V) complexes are studied in Chapter 4. Absorption bands are assigned to various LMCT-transitions by TD-DFT calculations, and bands observed in the visible region are confirmed to originate from azide ligand to metal transitions by resonance Raman spectroscopy. It has been assumed that excitation into these bands results in the elimination of N_2, thereby yielding high-valent nitrido-iron(V) complexes, while photolysis with UV-light results in the reductive elimination of an azide radical giving ferrous complexes. However, photolysis experiments with visible (470 nm) and UV-light (304 nm) on frozen solution Mössbauer samples of $[Fe^{III}(N_3)$cyc-ac$]PF_6$ have shown that both wavelengths result in the corresponding nitrido-iron(V) complex, whereas time-resolved IR measurements on fluid solution samples performed after photolysis with UV-light (266 nm) have revealed the formation of a ferrous species and an azide radical. Upon allowing the frozen solution sample of $[Fe^{V}$(N)cyc-ac$]PF_6$ to thaw it immediately decays. Interestingly, the analog complex $[Fe^{V}$(N)TMC-ac$]PF_6$ with methylated cyclam ligand obtained by photolysis of frozen solution samples of the parent azido-iron(III) complex $[Fe^{III}(N_3)$TMC-ac$]PF_6$ was shown to be stable in liquid solution. However, photolysis of the $[Fe^{III}(N_3)$TMC-ac$]PF_6$ complex in liquid solution did not yield the iron(V) complex. The chemoselectivity of photolysis is, therefore, found to be more complex than a simple wavelength dependence, with the collated data indicating that the state of aggregation determines which photoproducts are observed.

Previously reported iron(V) complexes and one new tetragonal nitrido-iron(V) species are studied in detail in Chapter 5. The first nitrido-iron(V) species reported were five coordinate porphyrin complexes, for which an *S*=3/2 ground state was assumed. The same ground state spin was deduced for the first non-heme iron(V) complex $[Fe^{V}(N)(N_3)cyc]^{+}$. However, combining the previously published spectroscopic data with state of the art calculations led to revised *S*=1/2 ground state assignment.

High-level multiconfigurational *ab initio* calculations have demonstrated, that even though the used ligand systems are not genuinely symmetric, the nitrido-iron(V) species exhibit a nearly degenerate $^2B_2[(d_{xy})^2(\pi_y^*/d_{yz})^1]$ ground state separated by only very few hundred wavenumbers from the $^2B_1[(d_{xy})^2(\pi_x^*/d_{xz})^1]$ excited state.

In certain transition metal complexes the strong nitrido π-ligand raises the energy of the d_{xz}/d_{yz}-orbitals above the $d_{x^2-y^2}$-orbital. However, for the studied tetragonal nitrido-iron(V) complexes this is not the case, as demonstrated by the calculations that result in a $^2B_2[(d_{xy})^2(\pi_y^*/d_{yz})^1]$ ground state and not the alternative $^2A_1[(d_{xy})^2(d_{x^2-y^2})^1]$ state. This is in line with the fully consistent interpretation of the spectroscopic data assuming a $^2B_2[(d_{xy})^2(\pi_y^*/d_{yz})^1]$ ground state.

EPR spectra for a series of tetragonal nitrido-iron(V) complexes ($g_3<g_2\approx g_1<g_e$) are reported here for the first time and show unexpectedly small g-values. Spin-Hamiltonian equations are derived for the g-values, taking into account the near degeneracy and the high degree of covalency in the studied systems. These provide a detailed explanation for the experimental results and demonstrate the large impact of low-lying excited states upon the g-values observed. Interestingly, comparison of the expected g-values for analogous nitrido- and oxo-iron(V) complexes showed only minor differences.

The fleeting nature of tetragonal nitrido-iron(V) complexes rendered their reactivity very challenging to study. However, it was shown that the tetragonal nitrido-iron(V) complexes $[Fe^{V}(N)cyc\text{-}ac]^+$ and $[Fe^{V}(N)(N_3)cyc]^+$ decay via a reductive nitrogen coupling mechanism yielding ferrous complexes an dinitrogen, which is the microscopic reverse of the Haber-Bosch process.

A novel oxo-iron(IV) complex $[Fe^{IV}(O)(NHC)_4(EtCN)]^{2+}$ was computationally studied and compared to previously published oxo-iron(IV) complexes in Chapter 6. While all previously studied tetragonal oxo-iron(IV) complexes and most other tetragonal oxo-transition metal complexes show the "classical" $d_{xy}<d_{xz},d_{yz}<d_{x^2-y^2}<d_{z^2}$ d-orbital splitting, a $d_{xy}<d_{xz},d_{yz}<d_{z^2}<d_{x^2-y^2}$ arrangement is found for the aforementioned species. The new complex $[Fe^{IV}(O)(NHC)_4(EtCN)]^{2+}$ and the complex $[Fe^{IV}(O)(TMC)(MeCN)]^{2+}$, which is the most widely studied "classical" system, show a $^3A_2[(d_{xy})^2(d_{xz},d_{yz})^2]$ doublet ground state, however, the excited quintet state was shown to be involved in CH-activation reactions by oxo-iron(IV) complexes. Notably, the distinct d-orbital splitting results in an $^5B_1[(d_{xy})^1(d_{xz},d_{yz})^2(d_{z^2})^1]$ excited quintet state for the new complex and $^5A_1[(d_{xy})^1(d_{xz},d_{yz})^2(d_{x^2-y^2})^1]$ excited quintet state for the complex $[Fe^{IV}(O)(TMC)(MeCN)]^{2+}$.

A computational study of hydrogen abstraction reactivity for the complexes $[Fe^{IV}(O)(NHC)_4(EtCN)]^{2+}$ and $[Fe^{IV}(O)(TMC)(MeCN)]^{2+}$ demonstrated significant differences between the two. While for the complex $[Fe^{IV}(O)(TMC)(MeCN)]^{2+}$ and all other existing oxo-iron(IV) complexes the well-established concept of two-state reactivity successfully describes the electronic structure in the underlying mechanism, this is not the case for $[Fe^{IV}(O)(NHC)_4(EtCN)]^{2+}$. More specifically, due to its distinct electronic structure of the latter complex in the quintet state, the usual lowest energy $^5\sigma$-pathway for hydrogen abstraction reaction is not accessible. Instead, for the $[Fe^{IV}(O)(NHC)_4(EtCN)]^{2+}$ complex it was shown that the reaction barrier is lowest in the triplet ground state.

Acknowledgements

During my PhD years I had the opportunity to work with many different people. I had the pleasure to learn from and to discuss with them various aspects of my research and they all supported me in various ways.

First and foremost, I want to thank Prof. Dr. Frank Neese for entrusting me with an interesting and challenging topic. Within the scope of the project I greatly enjoyed acquiring great interdisciplinary skills in spectroscopy, synthesis and cutting edge computational chemistry.

Dr. Eckhard Bill taught me to run my own EPR-measurements and enabled me to perform and to discuss many Mössbauer measurements, which greatly contributed to my work. I am also indebted to Bernd Mienert also deserves many thanks for running Mössbauer measurements and for helpful discussions about sample preparation and photolysis.

I am very grateful to Dr. Jason England for many stimulating discussions. Sharing with me his knowledge about high-valent iron chemistry was highly supportive in conducting my own research.

I also greatly benefited from very helpful discussions on my computational studies and the underlying chemistry with Dr. Tobias Krämer.

Dr. Igor Shapiro deserves thanks for discussions about the challenging field of computational photochemistry and for supporting me in my computational approach on the photochemistry of azido-iron complexes.

I am grateful to Dr. Jason England, Dr. Tobias Krämer and Dr. Igor Schapiro also for proof reading parts of the thesis.

In performing resonance Raman measurements, and in particular performing accompanying calculations I had the pleasure to discuss many aspects with Dr. Taras Petrenko. I am also grateful to Dr. Maurice van Gastel for helpful discussions about resonance Raman and EPR spectroscopy, from which I learned a lot. I enjoyed discussing the reactivity of oxo-iron(IV) complexes with Dr. Shengfa Ye who shared with me his great expertise in this field.

I also want to thank those people I had the pleasure to collaborate with:
Dr. Steffen Meyer and Prof. Dr. Franc Meyer for a very fruitful collaboration on various iron complexes.
Prof. Dr. Peter Vöhringer and his group for performing the time resolved IR measurements.
Dr. Marianne Engeser for performing and discussing with me numerous mass spectrometry measurements.
Prof. Dr. Alexander Filippou for providing me lab space during my time in Bonn.

I finally want to thank the university of Bonn and the Max-Planck society for financial support.

Prior Publications and Presentations

Portions of this dissertation have been previously published and/or presented publically.

Publications:

1) *The photochemistry of $[Fe^{III}N_3(cyclam\text{-}ac)]PF_6$ at 266 nm*
J. Torres-Alacan, O. Krahe, A. C. Filippou, F. Neese, D. Schwarzer, P. Vöhringer
Chem. Eur. J. **2012**, *18*, 3043.

2) *Ultrafast primary processes of an iron-(iii) azido complex in solution induced with 266 nm light*
H. Vennekate, D. Schwarzer, J. Torres-Alacan, O. Krahe, A. C. Filippou, F. Neese, P. Vöhringer
Phys. Chem. Chem. Phys. **2012**, *18*, 6165.

3) *Iron azides with cyclam derived ligands: precursors for high valent iron nitrides in the gas phase?*
O. Krahe, F. Neese, M. Engeser
Chem. Plus. Chem. **2013**, *9*, 1053.

4) *Decay of Fe^V nitride complexes via a N-N bond coupling reaction in solution: A combined spectroscopic and theoretical analysis*
O. Krahe, E. Bill, F. Neese
Angew. Chem. Int. Ed. **2014**, *53*, 8727. Selected as Very Important Paper

5) *A trans-1,2 end-on disulfide-bridged iron-tetracarbene dimer and its electronic structure*
S. Meyer, O. Krahe, C. Kupper, I. Klawitter, S. Demeshko, E. Bill, F. Neese, F. Meyer
Inorg. Chem. **2015**, *54*, 9770.

Publications by the Author not related to the Thesis:

1) *The Quest for Ring-Opening of Oxaphosphirane Complexes: A Coupled Cluster and Density Functional Study of CH_3PO Isomers and Their $Cr(CO)_5$ Complexes*
O. Krahe, F. Neese, R. Streubel
Chem. Eur. J. **2009**, *15*, 2594.

Oral Presentations:

1) *Interplay of theory and spectroscopy: Study of an nitrido-Fe^{V} complex and its formation*
Molecular Modelling Workshop, Erlangen, March 2012
Award for best Lecture

2) *Interplay of theory and spectroscopy: Study of an nitrido-Fe^{V} complex, its formation and its decay*
Princeton University, Groupseminar Prof. Dr. P. Chirik and others, Princeton/USA, May 2012

3) *Interplay of theory and spectroscopy: Study of an nitrido-Fe^{V} complex and its formation*
CECAM Workshop, Zaragoza/Spain, September 2012

4) *Interplay of theory and spectroscopy: Study of an nitrido-Fe^{V} complex and its formation*
Junges Chemiesymposium Ruhr, Dortmund, September 2012

5) *Interplay of theory and spectroscopy: Study of nitrido-Fe^{V} complexes and their formation*
Young Modelers Forum, London/GB, November 2012
Invited by the Molecular Graphics and Modelling Society

6) *Interplay of theory and spectroscopy in the study of nitrido-Fe^{V} complexes, their formation and their decay*
Anorganisch Chemisches Kolloquium, Universität Erlangen, January 2013
Invited by Prof. Dr. K. Meyer

7) *Interplay of theory and spectroscopy in the study of Fe^{V}-nitrides*
Koordinationschemie Treffen, Universität Bayreuth, February 2013

Poster Presentations:

1) *Photochemical formation of Fe^{V} spin centers and their electronic structure*
Molecular Modelling Conference, Heidelberg, October 2011

2) *Photochemical formation of FeV spin centers and their electronic structure: Resonance Raman-, EPR-, Mößbauer and theoretical Spectroscopy*
498. Seminar der Heraeus-Stiftung, Bad Honnef, February 2012
Award for best Poster

3) *Interplay of theory and spectroscopy: Study of an nitrido-Fe^{V} complex and its formation*
Bioinorganic Training Workshop, Penn State University/USA, May 2012

Contents

Nomenclature

cyc, Cyclam	1,4,8,11-tetraazacyclotetradecane
cyc-ac, Cyclam-ac	1,4,8,11-tetraazacyclotetradecane-1-acetate
TMC	1,4,8,11-tetra methyl-1,4,8,11-tetraazacyclotetradecane
TMC-ac	4,8,11-tri methyl-1,4,8,11-tetraazacyclotetradecane-1- acetate
TAML	tetraamide macrocyclic ligand: 3,3,6,6,9,9-hexamethyl-3,4,8,9-tetrahydro-1H-1,4,8,11-benzotetraazacyclotridecine-2,5,7,10(6H,11H)-tetraone
TPP	5,10,15,20-Tetraphenylporphyrin
TMP	5,10,15,20-Tetramesitylporphyrin
OEP	2,3,7,8,12,13,17,18-Octaethylporphyrin
^{t}BuIm	1-tert-butylimidazole
MeCN	Acetonitrile
PrCN	Butyronitrile
DCM	Dichlormethane
NHC	N-Heterocyclic carbene
SOMO	Singly occupied molecular orbital
DOMO	doubly occupied molecular orbital
HOMO	highest occupied molecular orbital
DFT	Density Functional Theory
TD-DFT	Time-Dependent Density Functional Theory
COSMO	Conductor like screening model
VDW	Van der Waals
ZPE	Zero point energy
BS	Broken Symmetry
BO	Born Oppenheimer
SOC	Spin-Orbit Coupling
CASSCF	Complete Active Space Self-Consistent Field
NEVPT2	N-electron valence state perturbation theory
δ	Mössbauer isomer shift in mm s^{-1}
ΔE_Q	Mössbauer quadrupole splitting in mm s^{-1}
g_e	g-Value of the free electron, g_e=2.0023
SH	Spin-Hamiltonian
LFT	Ligand Field Theory
EPR	Electron Paramagnetic Resonance
rR	Resonance Raman

List of Figures

List of Schemes

List of Tables

1. Introduction

Iron is by its mass the most common element on earth.[1] Besides its typical use as steel, in alloys and numerous other everyday life applications, it is a very important metal in biology as the effective site in metallo-enzymes.[1-2] Iron compounds do exist in a wide range of oxidation states, from –II to +VI, whereas the most common oxidation states are +II and +III.[1] Oxidation states +IV and higher are usually considered as high-valent. The scope of this thesis is to study mono nuclear nitrido-iron and oxo-iron complexes that appear exclusively in oxidation states +IV or higher and that belong therefore to the class of high-valent iron complexes.

Before in particular the chemistry of nitrido-iron and oxo-iron complexes is briefly reviewed (Chapter 1.2 and Chapter 1.3), some general properties of transition metal compounds with monoatomic ligands relevant for the present study will be discussed. This allows to examine the (electronic-) structure and properties of specific iron complexes studied here in a more general chemical context.

1.1. Transition Metal Complexes with Monoatomic Ligands

While metal-ligand multiple bonding is a common feature of early transition metal chemistry in high oxidation states, late transition metal complexes with multiple bonds tend to be highly reactive.[3-5] The most common multiple bonded monoatomic ligands are the oxo- and nitrido-groups.[4] Since the present thesis mainly addresses tetragonal complexes, trigonal species will not be discussed here in detail.

Nitrido- and oxo-ligands can be formally considered as closed-shell N^{3-} and O^{2-} groups. This implies that their p-orbitals are filled which makes them strong σ- and π-donor ligands. Multiple bonding to the metal is possible by overlap of orbitals with appropriate symmetry. Provided that the d-orbitals are not fully occupied, which implies that the metal adopts a higher oxidation state, π-bonding between the ligand p_x/p_y-orbitals and the d_{xz}/d_{yz}-orbitals of the metal as well as σ-bonding between the p_z-orbital and the d_{z^2}-orbital is possible. The classical example from which the d-orbital splitting of tetragonal complexes with strongly donating monoatomic-ligands was derived by Ballhausen and Gray is the vanadyl ion $[V^{IV}(O)(H_2O)_5]^{2+}$.[6] The classical 1+2+1+1 d-orbital splitting is outlined in Scheme 1.1. Typically, the frontier orbitals b_2, e*, b_1*, a_1* have mainly d-orbital character (d_{xy}, d_{xz}/d_{yz}, $d_{x^2-y^2}$, d_{z^2}) while the lower-lying a_1 and e orbitals in Scheme 1.1 have mainly ligand p-orbital character (p_z, p_x/p_y). Due to the higher charge, higher polarizability and lower effective nuclear charge (lower electronegativity) the nitrido-complexes are usually more covalent than the oxo-species.[4,7] The non-bonding b_2-orbital in Scheme 1.1 has mainly d_{xy}-character, while the b_1*-orbital is mainly derived from the metal $d_{x^2-y^2}$-orbital and is σ*-anti bonding with respect to the equatorial ligands.

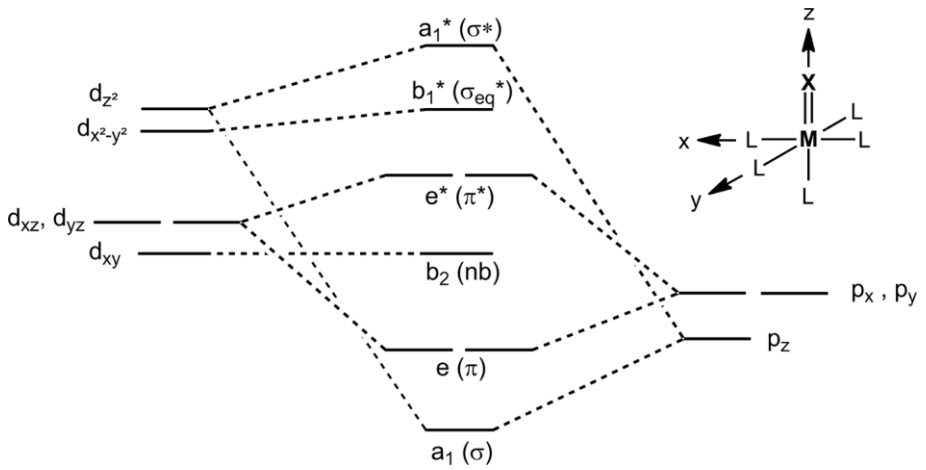

Scheme 1.1: Qualitative MO-diagram for oxo- and nitrido-complexes in C_{4v}-symmetry (X=O,N in the inset).[4]

This classical description for complexes with mono-atomic ligands is valid for the vast majority of reported complexes. However, there do exist some remarkable exceptions.

For a series of nitrido-manganese and nitrido-chromium complexes is was shown by Wieghardt *et al.* that the e*(d_{xz},d_{yz}) level is at similar energy as the b*$_1$($d_{x^2-y^2}$) level and the orbital splitting might be better described as 1+3+1.[8-10] Bendix *et al*. have further shown that in the complexes $[Cr^{V}(N)Cl_4]^{2-}$, $[Cr^{V}(N)(NCS)_4]^{2-}$, $[Cr^{V}(N)(N_3)_4]^{2-}$ and two $Cr^{V}N$-species with bidentate 1,3-diphenylpropane-1,3-dionate and pyrrolidinedithiocarbamate ligands the $^2B_1[b_2(d_{xy})\rightarrow b_1^*(d_{x^2-y^2})]$ transition appears at lower energy than the $^2E[b_2(d_{xy})\rightarrow e^*(d_{xz}/d_{yz})]$ transition.[11-13] Hence, due to the strongly donating nitrido-ligand the d_{xz}- and d_{yz}-orbitals are higher in energy than the b*$_1$($d_{x^2-y^2}$)-orbital. Appearance of the b*$_1$($d_{x^2-y^2}$)-orbital below the e*(d_{xz}-/d_{yz})-orbitals is further facilitated by weak equatorial ligands.[11-13] How the contrasting order of d-orbitals can be attributed to the nitrido-ligand is seen in a comparison of the analog complexes $[Cr(N)Cl_4]^{2-}$ and $[Cr(O)Cl_4]^{-}$.[11,14-15] While the lowest energy transition in the nitrido-species at 12887 cm^{-1} was assigned to the $^2B_1[b_2(d_{xy})\rightarrow b_1^*(d_{x^2-y^2})]$ excited state, the lowest energy band for the oxo-complex was observed at 13100 cm^{-1} and assigned to the $^2E[b_2(d_{xy})\rightarrow e^*(d_{xz}/d_{yz})]$ excited state. Hence, the oxo-complex is consistent with the d-orbital splitting derived by Ballhausen and Gray, while in contrast the nitrido-species does not fit into this “classical” picture.

Various nitrido- and oxo-complexes will be studied in this work and the discussed differences between nitrido- and oxo-ligands can have impact on their electronic structure. It will be further shown for oxo-iron complexes that by choosing an appropriate equatorial ligand, the energetic order of the $d_{x^2-y^2}$ and d_{z^2}-orbitals can be reversed compared to the “classical” energetic order, which will have notable effects on the chemical properties of these complexes.

1.2. High-Valent Nitrido-Iron Complexes

Nitrido-iron complexes have attracted attention since these species are assumed to play important roles in biological or industrial processes.[16-17] These include nitrogen transfer reactions,[18] synthesis of ammonia in biology by the enzyme nitrogenase[19-22] or in its industrial counterpart, the Haber-Bosch process.[23-24] Motivated by the complexity of these systems, various low molecular weight model compounds have been synthesized during the last decades. The aim is to study their (spectroscopic) properties in detail and to benefit from understanding these well-defined compounds when more complex systems are investigated whose exact structures are not known in detail. Several mononuclear complexes[16-17,25-28] and few dinuclear-complexes[29-31] as well as polynuclear[32-34] nitrido-iron species have been reported so far.

A variety of ligands were explored for mononuclear nitrido-complexes with four-, five-, or six-coordination on the iron centers resulting in trigonal/tetrahedral,[35-39] square-pyramidal,[40] and octahedral coordination geometries.[29,41-45] The most common way to obtain iron-nitrides is by photolysis of the parent azido-complex, which oxidizes the metal by two units and is accompanied by the elimination of dinitrogen (Scheme 1.2, right).[29,35-36,43,46-47] These photolytic reactions were usually performed with light in the visible region.

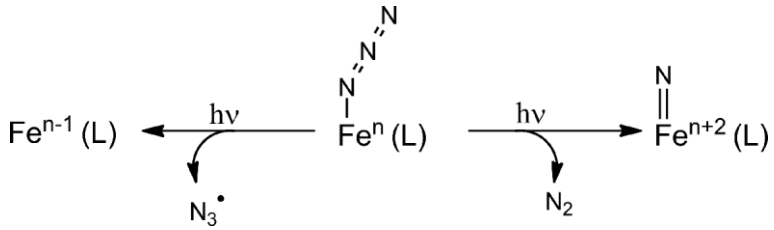

Scheme 1.2: Oxidative formation of nitrido-iron complexes and reductive formation of iron-complexes via photolysis of azido-iron precursors, n denotes the formal oxidation state (n=2, 3, 4).

However, in some cases where light of shorter wavelength was used in the photolysis of azido-iron(III) complexes, the formation of iron(II) was observed. This was assumed to result from homolytic Fe-N_3 bond cleavage in the azido-iron(III) precursor, resulting in iron(II) complexes by elimination of an azide radical (Scheme 1.2, left).[29,43]

By photolysis of the parent azido-iron(III) porphyrin complexes at 30K, Nakamoto and Wagner obtained a series of nitrido-iron(V) porphyrin complexes in 1988 (see Scheme 1.3, left).[40,46] However, the complexes were characterized only by resonance Raman spectroscopy. By comparison with other nitrido porphyrin complexes they assumed that the complexes show an *S*=3/2 ground state and the unpaired electrons are, in contrast to analogue oxo-complexes, located on the metal center only.

It took another decade (until 1999) until in the group of Karl Wieghardt the first non-heme nitrido-iron(V) complex *trans*-$[Fe^{V}(N)(N_3)cyc]^+$ (cyc=cyclam; 1,4,8,11-tetraazacyclotetradecane) was prepared by photolysis of a bis-azido iron(III) complex *trans*-$[Fe^{III}(N_3)_2cyc]^+$ at cryogenic temperature (see Scheme 1.3, center)[1].[29] Just one year later the same group published the characterization of an nitrido-iron(V) complex $[Fe^{V}(N)cyc\text{-}ac]^+$ (see Scheme 1.3, right) with a cyclam-derived ligand

[1] It should be noted that both isomers *trans*-$[Fe^{III}(N_3)_2cyc]^+$ and *cis*-$[Fe^{III}(N_3)_2cyc]^+$ were described previously,[29] however, in the present work only the *trans*-species is studied and the prefix *trans* is omitted in the following.

(cyc-ac=1,4,8,11-tetraazacyclotetradecane-1-acetate).[43] For both complexes initially an *S*=3/2 ground state was postulated based on magnetic Mössbauer measurements. However, in a later study it was shown that the correct spin ground state of the $[Fe^{V}(N)cyc\text{-}ac]^{+}$ complex is *S*=1/2.[41,45]

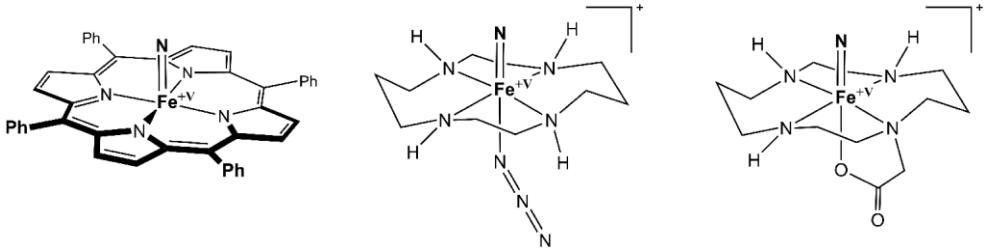

Nakamoto 1988[46] Wieghardt 1999[29] Wieghardt 2000[43]

Scheme 1.3: Structure of the nitrido-iron(V) complexes $[Fe^{V}(N)TPP]$, $[Fe^{V}(N)(N_3)cyc]^{+}$ and $[Fe^{V}(N)cyc\text{-}ac]^{+}$.

By photolysis of the azido-iron(IV)-complex $[Fe^{IV}(N_3)TMC\text{-}ac]^{2+}$ (TMC-ac=1-acetate-4,8,11-trimethyl -1,4,8,11-tetraazacyclotetradecane) it was even possible to obtain the first iron(VI) complex[48] $[Fe^{VI}(N)TMC\text{-}ac]^{2+}$ besides the ferrate ion $[Fe^{VI}O_4]^{2-}$ (see Scheme 1.4, left).[49]

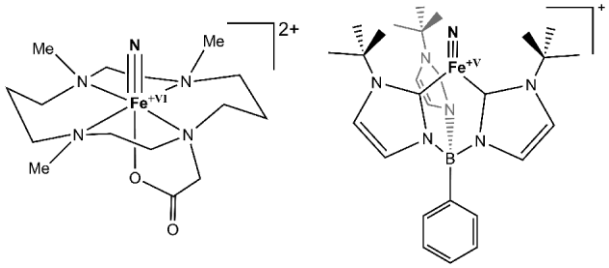

Wieghardt 2006[47] Smith, Meyer 2011[35]

Scheme 1.4: Structure of the tetragonal nitrido-iron(VI) complex $[Fe^{VI}(N)TMC\text{-}ac]^{2+}$ (left) and the trigonal nitrido-iron(V) complex $[Fe^{V}(N)(^{t}BuIm)_3BPh]^{+}$ that was characterized crystallographically.

The first pseudo-tetrahedral nitrido-iron(V) complex was synthesized in 2011 (see Scheme 1.4, right). This is the only nitrido-iron(V) compound reported so far for which it has been possible to determine the crystal structure.[35] Other examples of tetragonal nitrido-iron(V)-complexes are only stable in a frozen solvent matrix at cryogenic temperatures.[29,41,43-44]

All mononuclear nitrido-iron complexes show formal oxidation states between +IV and +VI. Lower oxidation states would result in population of orbitals that are anti-bonding with respect to the strongly donating nitrido-ligand and are therefore less stable. The nitrido-iron(IV) complexes reported so far are of threefold symmetry, diamagnetic, and several of these species were characterized crystallographically.[35-37,50] Inspection of the qualitative frontier orbital splitting reveals that in these d^4-complexes in trigonal symmetry only non-bonding orbitals are occupied ($e(d_{x^2-y^2},d_{xy})$) level in Scheme 1.5 left).[16,25,27] In contrast, tetragonal coordination (Scheme 1.5 right) would necessitate the occupation of anti-bonding orbitals with at least two electrons which has prevented the synthesis of tetragonal iron(IV)-complexes up to now.[2]

[2] It should be noted that in the present chapter mainly the simplified d-orbital labels are used (d_{xy}, d_{xz}, d_{yz}, $d_{x^2-y^2}$, d_{z^2}), even in nitrido-iron complexes it is possible that the frontier π^* and σ^* orbitals are mainly derived from nitrido 2p-orbitals. This will be discussed in detail in Chapter 5.5.2.

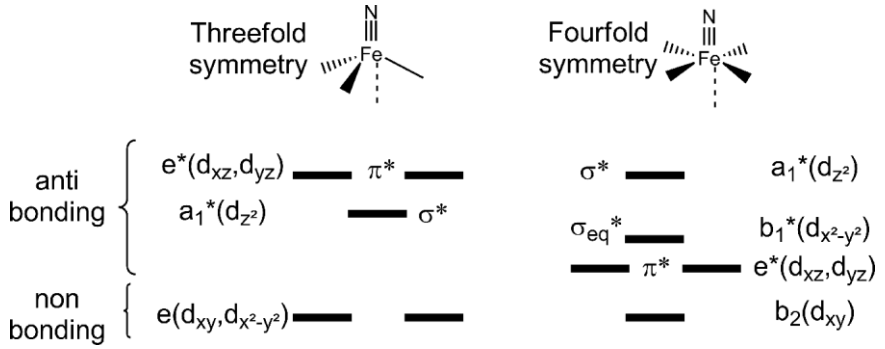

Scheme 1.5: Typical trigonal (left) and tetragonal (right) ligand fields of nitrido-iron complexes.[16]

For all tetragonal nitrido-iron(V) complexes (d^3) initially a *S*=3/2 ground state was proposed. For the $[Fe^{V}(N)cyc\text{-}ac]^{+}$ complex this was later corrected based on further spectroscopic data that revealed a *S*=1/2 spin ground state.[41]

Considering both possible spin states and the aforementioned circumstance that the $b^*_1(d_{x^2-y^2})$ orbital may be shifted below the $e^*(d_{xz}/d_{yz})$ set of orbitals due to the strong nitrido-ligand gives rise to four conceivable electronic ground states for tetragonal iron(V) complexes as outlined in Scheme 1.6.

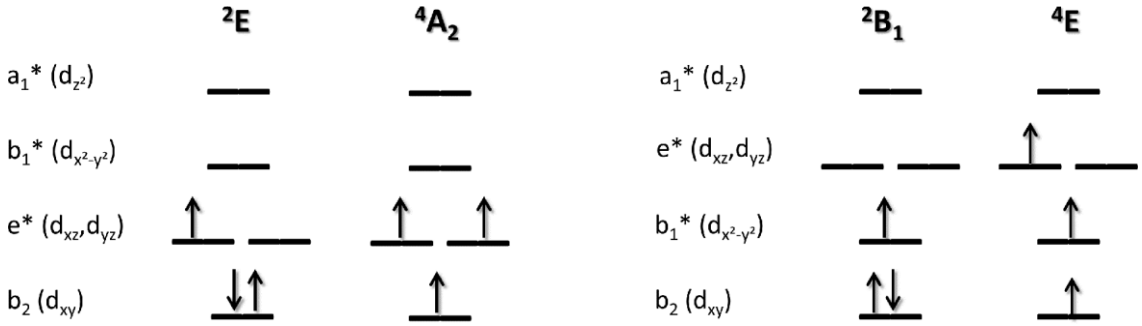

Scheme 1.6: Possible electronic configurations and ground states for a d^3-system in C_{4v} symmetry.

The different ground states then of course result in different properties (reactivity, spectroscopy) for these complexes. One goal of this thesis will be to determine the electronic structure and ground state of various tetragonal nitrido-iron(V) complexes by a combination of spectroscopic and theoretical methods.

The reactivity of trigonal nitrido-iron(IV) complexes was investigated for a number of transformations.[25,38,51] It was further shown that one species decays via formation of a Fe^{I}-NN-Fe^{I} dimer.[37,52] For the only trigonal nitrido-iron(V) species (Scheme 1.4 right) the formation of ammonia from water was reported.[35] Due to the fleeting nature of tetragonal nitrido-iron(V) complexes (these species are only stable in a frozen solvent matrix at cryogenic temperatures) their chemistry is less well understood.[29,40-41,43-44,46] The reactivity of the $[Fe^{V}(N)cyc\text{-}ac]^{+}$ complex towards CH-activations was studied in gas phase, but no reactivity was observed.[53] For the $[Fe^{V}(N)cyc\text{-}ac]^{+}$ and $[Fe^{V}(N)(N_3)cyc]^{+}$ complexes the reaction with phosphine in solution was investigated by time resolved IR-spectroscopy on a very short time scale.[54-56]

1.3. High-Valent Oxo-Iron Complexes

Another class of high-valent iron complexes that was investigated in much more detail than the nitrido-species are oxo-iron complexes. Oxo-iron(IV) complexes and formally oxo-iron(V) complexes have been identified in various enzymatic reactions as important intermediates.[57-66] They can be divided into heme-systems with porphyrin ligands and non-heme systems. Various reactions including halogenation, desaturation, cyclization, epoxidation and decarboxylation are known to involve oxo-iron complexes.[57,59] However, in most cases where oxo-iron complexes are involved, inert CH-bonds are activated by insertion of an oxygen atom resulting in hydroxo species.[57-66]

Cytochrome P450 that catalyzes the hydroxylation of alkane C-H bonds is a prototypical example for a heme-system that was extensively studied experimentally and theoretically.[67-68] Likewise mononuclear non-heme iron centers are found in a group of enzymes that also carry out oxidative transformations.[69-70] Non-heme oxo-iron(IV) intermediates have been characterized, e.g. for *TauD*, a prototypical α-ketoglutarate-dependent enzyme.[71-73]

To understand these complex biological reactions, considerable effort has been put towards the synthesis of low molecular weight model complexes during the last decades.[16,74] The first high-valent oxo-iron complex was synthesized by Groves *et al.* via oxidation of $[Fe^{III}(Cl)(TMP)]$ (TMP=tetramesityl porphyrin) in 1981.[64] This approach resulted in a formally oxo-iron(V) species $[Fe^{V}(O)(TMP)]$, however, detailed spectroscopic characterization has shown that the complex is better described as iron(IV) with a radical on the porphyrin ligand, $[Fe^{IV}(O)(TMP^{+\bullet})]$. The high-spin iron center (S_{Fe}=2) is antiferromagnetically coupled to the ligand radical resulting in an overall quartet ground state (S=3/2). Since then, a large number of heme oxo-iron complexes have been synthesized, characterized and their reactivity explored.[59,62-63]

The first non-heme oxo-iron(IV) complex $[Fe^{IV}(O)cyc\text{-}ac]^{+}$ was reported in 2000 by Wieghardt *et al*. (see Scheme 1.7, left).[43] In 2003 Rohde *et al.* reported the X-ray crystal structure for the $[Fe^{IV}(O)(TMC)(MeCN)]^{2+}$ complex, which represents the first crystal structure for an oxo-iron(IV) complex (see Scheme 1.7, right).[75] Many non-heme oxo-iron(IV) complexes have been reported in the following decade with tetragonal and trigonal coordination modes that were reviewed recently.[74]

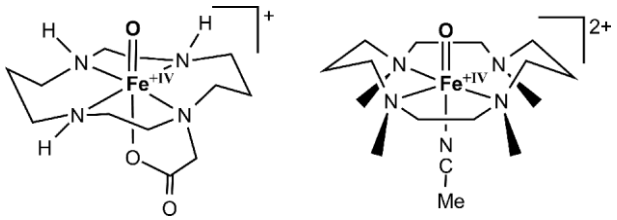

Scheme 1.7: The oxo-iron(IV) complexes $[Fe^{IV}(O)cyc\text{-}ac]^{+}$ (left) and $[Fe^{IV}(O)(TMC)(MeCN)]^{2+}$ (right).

Using a tetraamido macrocyclic ligand (TAML), Tiago de Oliveira *et al.* succeeded in synthesizing a well-defined non-heme oxo-iron(V) complex in 2007 (see Scheme 1.8, left).[76] Another complex that can be described as non-heme oxo-iron(V) has been synthesized recently in the Que group (see Scheme 1.8, right).[77] However, its electronic structure is complicated, possibly including a ligand radical. The spectroscopic properties notably differ from the TAML-system.[77]

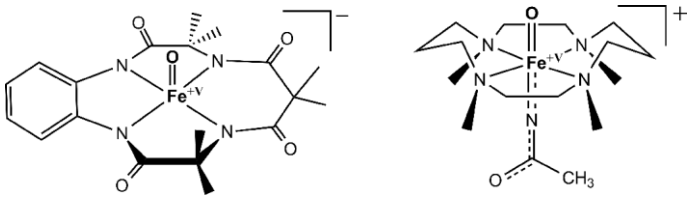

Scheme 1.8: The oxo-iron(V) complexes $[Fe^{V}(O)TAML]^{-}$ (left) and $[Fe^{V}(O)(TMC)(NC(O)Me)]^{+}$ (right).

The typical d-orbital splitting for oxo-iron complexes is shown in Scheme 1.9. Trigonal non-heme oxo-iron complexes usually show a *S*=2 ground state, while those in tetragonal coordination show a *S*=1 ground state ($[Fe^{IV}(O)(H_2O)_5]^{2+}$ is the only exception with *S*=2).[74]

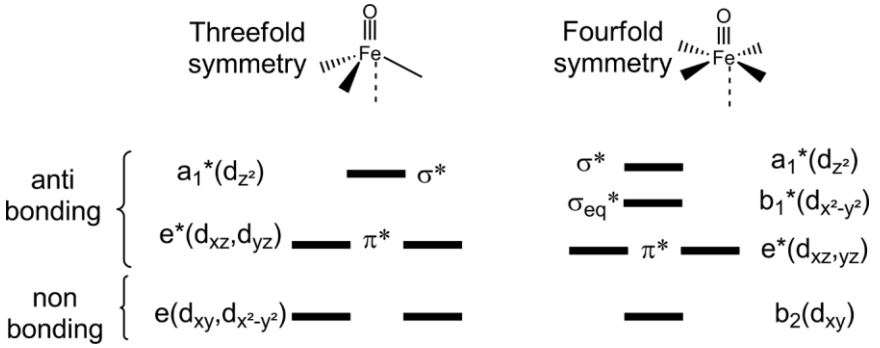

Scheme 1.9: Typical trigonal (left) and tetragonal (right) ligand fields of oxo-iron complexes.[16]

Sterically demanding ligands enforce the trigonal bipyramidal 5-fold coordination where the $e(d_{xy},d_{x^2-x^2})$-orbitals are non-bonding. In tetragonal symmetry only the $b_2(d_{xy})$-orbital is non-bonding while the degenerate $e(d_{xz},d_{yz})$-orbitals are anti-bonding. This enforces an intermediate-spin *S*=1 ground state and the qualitative ligand field splitting outlined in Scheme 1.9 follows the one derived by Ballhausen and Gray for the $[V^{IV}(O)(H_2O)_5]^{2+}$ complex.[6]

It should be noted here, while a large number of tetragonal oxo-iron(IV) complexes were synthesized in the last decade that are stable in solution for spectroscopic and kinetic measurements and several X-ray structures were determined, tetragonal nitrido-iron(IV) complexes remain elusive so far.[16,74] The reason can be found in the moderately covalent Fe-O bond while the Fe-N bond is very strong and covalent. Therefore, in the nitrido-species the $\pi^*(d_{xz}/d_{yz})$-orbitals are pushed up in energy compared to oxo-complexes which prevents occupation of these orbitals with electrons. This leads to the general conclusion that the formation of nitrido-complexes requires higher oxidation states on the metal center than it is necessary for the formation of oxo-complexes.

1.3.1. CH-Activation by Non-Heme Oxo-Iron(IV) Complexes

One of the key roles for oxo-iron(IV) complexes in biology is the oxidation of CH-bonds, yielding alcohols and an iron(II) moiety.[16,57,62,78] It was shown in experimental and theoretical studies for the heme-system Cpd I that the reaction is initiated by a rate-determining hydrogen abstraction, followed by rebound of the organic radical with the hydroxo-group which results in formation of an alcohol (see Scheme 1.10).[67,79-81] Further evidence was found, that non-heme oxo-iron(IV) species undergo the same reaction mechanism.[57,78,82-84]

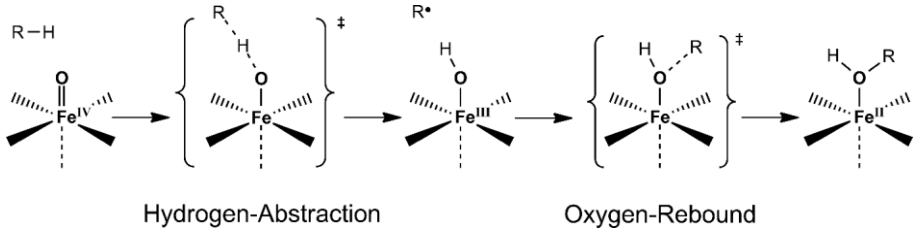

Scheme 1.10: Proposed reaction mechanism for CH-bond oxidation by oxo-iron(IV) complexes.

The hydrogen-abstraction and oxygen-rebound mechanism was also investigated in detail computationally and these studies further confirm the hydrogen-abstraction as the rate determining step.[67-68,84-95]

Some theoretical aspects of the hydrogen abstraction by tetragonal non-heme oxo-iron(IV) complexes will be briefly reviewed here to facilitate the association of results from the present work with previous results.

One of the fundamental outcomes from computational studies on the hydrogen abstraction by tetragonal oxo-iron(IV) complexes was that the barrier for hydrogen abstraction is lowest in the quintet state (S=2), while all investigated model complexes show a triplet ground state (S=1).[88] That states of different multiplicity than the starting molecules can be involved in chemical reactions was already proposed by Shaik and Schwarz in their pioneering work on gas-phase reactions between bare FeO^+ and H_2.[96-97] Since hydrogen abstraction by oxo-iron(IV) complexes were found to proceed via crossing of potential energy surfaces of different multiplicity (S=1 and S=2) this principle was termed "two-state-reactivity".[86,89,91,97]

However, besides different spin states there is another level of complexity. The iron center is reduced from iron(IV) to iron(III) by transfer of an hydrogen atom which can follow a so called σ-pathway or alternatively a π-pathway.[91,93] The different possibilities are best described by electron-shift-diagrams as outline in Scheme 1.11.[86,89,91,93,98-100]

In the π-pathway a spin-down electron is transferred from the substrate CH-bond (σ_{CH}) into the π*-orbital of the FeO-moiety.[86,91,101] The π*-orbital is anti-bonding between a metal d_{xz}/d_{yz}-orbital and a $2p_x/p_y$-orbital of the oxo-ligand (π* orbitals in Scheme 1.1). This results in a σ_{OH}-bond formed by an oxygen p_x/p_y-orbital and the hydrogen s-orbital which is accompanied by decrease of the formal Fe-O bond order. An unpaired spin-up electron remains on the substrate and one π*-orbital (d_{xz}/d_{yz}) is doubly occupied following electron transfer, since in the triplet and quintet state of the oxo-iron(IV) complex these orbitals are already singly occupied (see Scheme 1.11).[86,88-89,98-100,102-104]

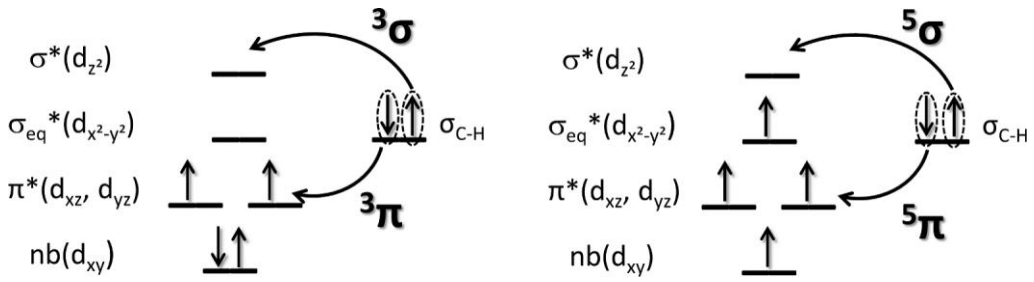

Scheme 1.11: Electron-shift-diagram for σ- and π-pathways in the triplet (left) and quintet (right) state.

In the σ-pathway, a spin-up electron is shifted from the CH-bond (σ_{CH}) to the metal σ*-orbital that is mainly derived from the d_{z^2}-orbital which forms an anti-bonding orbital with the oxygen p_z-orbital (σ* in Scheme 1.1). In this case a spin-up electron is transferred from the substrate into the vacant d_{z^2}-orbital, resulting in a spin-down electron on the substrate.[86,88-89,98-100,102-104]

Closer inspection of the involved orbitals explains some details of the geometric structures of the σ- and π-transition states. In the π-pathway, a sideways approach of the substrate to the metal results in best overlap between the σ_{CH}- and π*(d_{xz}/d_{yz})-orbitals (Scheme 1.12 left). However, due to steric effects the Fe-O-H bond angle is usually found to be slightly above 90°. For the σ-pathway maximum overlap between the σ_{CH}- and σ*(d_{z^2})- orbitals is achieved by adopting a linear Fe-O-H-angle (Scheme 1.12 right).[86,88-89,98-100,102-104]

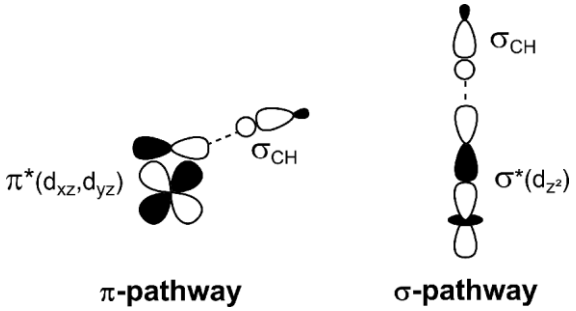

Scheme 1.12: Schematic overlap of substrate and FeO orbitals on the π- and σ-pathway.

For all non-heme oxo-iron(IV) complexes studied computationally so far, the ^{5}σ-pathway was found to be lowest in energy, despite the fact that nearly all synthetic model complexes show a triplet ground state.[86,88-89,100,104] This high-spin pathway is described as exchange enhanced.[104] Exchange interactions are related to Hund's rule in the sense that a state is lowest in energy for which the number of unpaired electrons reaches its maximum.[105] As can be seen in Scheme 1.11, the largest number of unpaired electrons can be found for the ^{5}σ-pathway in agreement with computational results, which have indeed identified this possibility as the lowest energy pathway.[86,88-89,98-100,102-104]

While in earlier computational studies only the ^{5}σ- and ^{3}π-pathways were investigated,[86,88-89,100,106-107] in few more recent studies reaction channels via the ^{3}σ- and ^{5}π-pathways were also explored.[87,91,93] These studies show that in general the reactivity for all viable pathways is:[87,91,93]

$$^5\sigma > {}^3\pi \approx {}^5\pi > {}^3\sigma$$

2. Physical Methods

A variety of physical methods is applied in the present thesis work, including EPR-, Mössbauer-, resonance Raman, IR- and Absorption-spectroscopy that are well described in various text books. For EPR-[108-111], Mössbauer[112-114] and resonance Raman-spectroscopy[114-116] a brief introduction is given here which is meant to make the interpretation of presented spectroscopic data more comprehensible.

2.1. Electron Paramagnetic Resonance Spectroscopy (EPR)

Electron Paramagnetic Resonance spectroscopy (EPR-spectroscopy) probes the absorption of microwave radiation by a paramagnetic species in an applied magnetic field.

Different energy states for paramagnetic species arise from the interaction of the unpaired electron spin moment with the magnetic field. This so called electronic Zeeman-effect is illustrated in Figure 2.1 for an S=1/2 system, in the simplest case this might be a free electron. The m_s=±1/2 levels that are degenerate without applied magnetic field are often described as α and β. Application of a magnetic field lifts the degeneracy and the splitting can be described by the electronic Zeeman Hamiltonian that depends on the magnetic field strength (B), the electron Bohr magneton (β), the electron spin operator ($\hat{S}$) and the g-value (g):

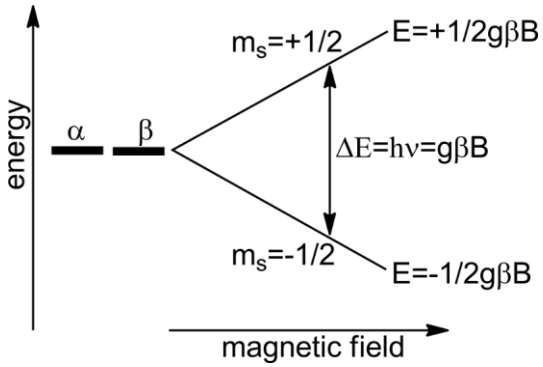

Figure 2.1: Splitting of the m_s=±1/2 levels by application of a magnetic field.

$$\hat{H} = g\beta \boldsymbol{B} \hat{S} \qquad 2.1$$

The g-value or spectroscopic splitting factor for a free electron (g_e) is 2.0023, however, for electrons in a molecule or ion it can strongly deviate from this value. The energy separation between the two states that arise by application of a magnetic field as indicated in Figure 2.1 is:

$$\Delta E = g\beta \boldsymbol{B} \qquad 2.2$$

EPR-experiments are usually carried out at fixed microwave frequency while the magnetic field is varied. Microwave absorption is observed, when the resonance condition given by Equation 2.2 is fulfilled.

Absorption of microwave radiation by paramagnetic species can strongly depend on the orientation of the complex in the magnetic field and the g-value is therefore anisotropic. Detailed information about the electronic structure can be obtained from the g-value, and further information can be gained from hyperfine coupling, which results from interactions of the electron spins with the nuclear spin of one or several atoms. In the following sections a brief review about the Spin-Hamiltonian for calculating the g-value will be given, which will be applied in detail in Chapter 5.6.

2.1.1. The Spin-Hamiltonian

One of the most important tools in analyzing and understanding spectroscopic data, e.g. from EPR-spectroscopy is the concept of spin-Hamiltonian. Originally it was developed by M. H. L. Pryce *"for a problem in paramagnetism"*,[117-118] more precisely for explaining the g-values and the temperature-independent paramagnetism of ions in a crystal. However, it was extended and can be used in various other spectroscopic methods e.g. nuclear magnetic resonance (NMR) and nuclear quadrupole resonance (NQR) spectroscopy. The spin-Hamiltonian allows to parameterize the experimental results in a simple, unified way without any explicit reference to the geometric and electronic structure of the studied system.[119-120] Spin-Hamiltonian expressions (sometimes with solely empirical relations) are used to fit experimental spectra to obtain for example g-values, hyperfine-, zero-field- or quadrupole-splitting. However, these data can be interpreted in detail with an appropriate theoretical model.[119-120] The spin-Hamiltonian is a special case of an effective-Hamiltonian, it only contains spin degrees of freedom besides some numerical parameters that can be obtained from the experimental data.

The spin-Hamiltonian that describes the interaction of various magnetic dipole moments (that result from the spin of an electron or nucleus) with the external magnetic field and between each other can be written as:[119-120]

$$\hat{H}_{spin} = \beta \boldsymbol{B} \boldsymbol{g} \hat{S} + \hat{S} \boldsymbol{D} \hat{S} + \sum_A \widehat{\boldsymbol{S}} \boldsymbol{A}^{(A)} \hat{I}^{(A)} - \beta_N g_N^{(A)} \hat{I}^{(A)} \boldsymbol{B} \qquad 2.3$$

The first term describes the electronic Zeeman-effect, the interaction of the electron spin with the external magnetic field. The second term describes the zero-field splitting (ZFS) which occurs only for systems with $S > ½$. It result from magnetic interaction of unpaired electrons and can be observed without the application of a magnetic field. The magnetic moments of the electrons can interact with the nuclear spin magnetic moment (which results in the hyperfine coupling in EPR spectra) and is considered by the third term. The interaction of the nuclear spin magnetic moment with the external magnetic field is considered in the fourth term. The interaction of the nuclear spins (which can be observed in NMR spectroscopy) as well as the nuclear quadrupole interaction are neglected here due to their limited relevance in EPR-spectroscopy.

Since in this work only the g-values of systems with on unpaired electron are studied in detail, it will be focused on the g-values in this brief introduction that is based on various text books and publications.[108,119-124]

2.1.2. The g-Value

In most paramagnetic compounds, the g-values deviate from the g-value of the free electron (g_e=2.0023). This occurs to varying degree due to the coupling of the electronic spin to the orbital momentum. General spin-Hamiltonian equations for the g-values are derived here and will be refined for the systems studied in this work.

The g-tensor contains four main contributions and can be written as ($\mu, \nu = x, y, z$):[119-120]

$$g_{\mu\nu} = g_{\mu\nu}^{(SB)} + g_{\mu\nu}^{(RCM)} + g_{\mu\nu}^{(GC)} + g_{\mu\nu}^{(OZ\,/\,SOC)} \approx \delta_{\mu\nu} g_e + g_{\mu\nu}^{(OZ/SOC)} \qquad 2.4$$

The first two terms result from the product of the spin magnetic moment and the magnetic field, the first one is the spin-Zeeman term and it can be shown that $g_{\mu\nu}^{(SB)} = \delta_{\mu\nu} g_e$ where g_e is the g-value of the free electron.[119-120] The second contribution is the relativistic mass correction which is usually small and can be neglected. [119-120] The third term $g_{\mu\nu}^{(GC)}$ arises from the gauge correction to the spin-orbit coupling. It is of the same order and most times of opposite sign of the $g_{\mu\nu}^{(RCM)}$ term and can be, therefore, neglected. The most important terms that affect the deviation of the g-value from g_e are the orbital Zeeman and spin-orbit coupling (SOC) terms, summarized in $g_{\mu\nu}^{(OZ\,/\,SOC)}$.

The effective operator for the SOC is usually written as[119-120]

$$\hat{H}_{SO} = \sum_A \sum_i \xi(r_{iA}) \boldsymbol{l_i^A s_i} \qquad 2.5$$

where the function $\xi(r_{iA})$ is

$$\xi(r_{iA}) = \frac{\alpha^2 Z_{eff}^A}{2\, r_{iA}^3} \qquad 2.6$$

Here, A runs over all nuclei, i over all electrons and r_{iA} is the distance between electron i and nuclei A. The effective nuclear charges Z_{eff}^A are semi-empirical parameters that need to be determined from experimental results or calculations.

The orbital Zeeman-effect can be described by the effective Hamiltonian

$$\hat{H}_{OZ} = \sum_i \boldsymbol{B l_i} \qquad 2.7$$

It shall be mentioned here, that this is not the actual Zeeman-operator which is

$$\hat{H}_{Ze} = \beta \boldsymbol{B} \sum_i (\boldsymbol{l_i} + g_e \boldsymbol{s_i}) \qquad 2.8$$

Following McWeeny[125-127] it is possible to express the spin-Hamiltonian on a way that it contains the effect of the magnetic perturbations and the interaction of the ground state magnetic sublevels with the excited states up to second order.[119-120] If then further Equation 2.5 and 2.7 are used, it is possible to express the g-value as:

$$g_{\mu\nu}^{(OZ\,/\,SOC)} = -\frac{1}{S}\sum_{b\,(S_b=S)} \Delta_b^{-1}\Big\{< 0SS|\ \sum_i l_{i\mu}\ |bSS >< bSS|\ \sum_{i,A}\xi(r_{iA}) l_{i\nu}^{A} s_{iz}\ |\ 0SS > \\ +< 0SS|\sum_{i,A}\xi(r_{iA}) l_{i\mu}^{A} s_{iz}\ |bSS >< bSS|\sum_i l_{i\nu}\ |\ 0SS >\Big\} \qquad 2.9$$

Here, *S* is the total spin of the ground state and Δ_b is the excitation energy into state b. In deriving this equation, it can be seen that only excited states of the ground state multiplicity have to be considered (which is different e.g. in analogue equations for the ZFS).[119-120] To evaluate this term the states $|bSS>$ with $M = S$ have to be known and the matrix elements of the angular momentum and the SOC operator between the ground and excited states have to be calculated. In principle, the sum runs over an infinite number of excited states but usually only very few excited states have to be considered.

It is assumed here, that the ground state with total spin *S* can be described by a single normalized Slater determinant with n doubly and m singly occupied MOs. This can be written as (a bar over the orbital indicates that it is occupied by a spin down electron, without a bar it is occupied by a spin-up electron)

$$|OSS> = |\psi_1\bar{\psi}_1\psi_2\bar{\psi}_2 \ldots \psi_n\bar{\psi}_n\psi_{O_1}\ldots\psi_{O_m}| \qquad 2.10$$

Analog to that, excited states will be represented by many electron wave functions of single configuration type. The excitation of an electron from a doubly occupied orbital (DOMO) into one of the singly occupied orbitals (SOMO) will result in the many electron wave function:

$$|I_i^{O_j} SS> = |\psi_1\bar{\psi}_1 \ldots \psi_i\bar{\psi}_{O_j}\ldots\psi_n\bar{\psi}_n\psi_{O_1}\ldots\ \psi_{O_m}| \qquad 2.11$$

And the excitation from a singly occupied orbital (O_i) into an empty orbital (a) results in:

$$|II_{O_i}^{a} SS> = |\psi_1\bar{\psi}_1 \ldots \psi_n\bar{\psi}_n\psi_{O_1}\ldots\psi_a\ldots\psi_{O_m}| \qquad 2.12$$

Other excitations, e.g. from a doubly occupied orbital into an empty orbital do not affect the g-value and will not be considered here.[119-120]

Making use of the Wigner-Eckart theorem[119,128] gives for the SOC matrix elements of DOMO to SOMO excitations

$$< 0SS|\ \sum_{i,A}\xi(r_{iA}) l_{i\nu}^{A} s_{0,i}\ |I_i^{O_j} SS> = -\frac{1}{2}\ <\psi_i|\sum_i \xi(r_A) l_\nu^A\ |\psi_{O_j}\ > \qquad 2.13$$

and for SOMO to empty orbital excitations

$$< 0SS|\ \sum_{i,A}\xi(r_{iA}) l_{i,\mu}^{A} s_0\ |II_{O_i}^{a} SS> = +\frac{1}{2}\ <\psi_{O_i}|\sum_i \xi(r_A) l_\mu^A\ |\psi_a\ > \qquad 2.14$$

It shall be noted here, that the two classes of excitations result in different signs of the spin-orbit coupling matrix elements due to rules, that were first formulated by Slater.[129-130] Inserting Equations 2.13 and 2.14 in Equation 2.9 then results in

$$g_{\mu\nu}^{(OZ\,/\,SOC)} = +\frac{1}{2S}\sum_{i\,(doubly)}\sum_{O_j\,(singly)} \Delta_{I_i^{Oj}}^{-1}\{L_{2\mu}^{i\,Oj}L_{1\nu}^{i\,Oj} + L_{1\mu}^{i\,Oj}L_{2\nu}^{i\,Oj}\} - \frac{1}{2S}\sum_{a\,(empty)}\sum_{O_j\,(singly)} \Delta_{II_{Oj}^{a}}^{-1}\{L_{2\mu}^{Oj\,a}L_{1\nu}^{Oj\,a} + L_{1\mu}^{Oj\,a}L_{2\nu}^{Oj\,a}\} \quad 2.15$$

Or with Equation 2.4, the g-values can be calculated by

$$g_{\mu\nu} = \delta_{\mu\nu}g_e + \frac{1}{2S}\sum_{i\,(doubly)}\sum_{O_j\,(singly)} \Delta_{I_i^{Oj}}^{-1}\{L_{2\mu}^{i\,Oj}L_{1\nu}^{i\,Oj} + L_{1\mu}^{i\,Oj}L_{2\nu}^{i\,Oj}\} - \frac{1}{2S}\sum_{a\,(empty)}\sum_{O_j\,(singly)} \Delta_{II_{Oj}^{a}}^{-1}\{L_{2\mu}^{Oj\,a}L_{1\nu}^{Oj\,a} + L_{1\mu}^{Oj\,a}L_{2\nu}^{Oj\,a}\} \quad 2.16$$

where the integrals of the reduced SOC-operator are written

$$L_{1\,\mu}^{i\,j} = <\psi_i \mid \sum_A \xi(r_A)\, l_\mu^A \mid \psi_j> \quad 2.17$$

and the orbital-Zeeman integrals

$$L_{2\,p}^{i\,j} = <\psi_i \mid l_p^A \mid \psi_j> \quad 2.18$$

To calculate the g-values with the help of Equation 2.16, knowledge about the excitation energies (Δ_n) is needed. These can be obtained e.g. from absorption spectroscopy. Furthermore, it is necessary to compute orbital Zeeman and SOC-matrix elements between molecular orbitals (MOs) which can be quite complicated. Within the framework of ligand field theory the orbitals are expressed by a linear combination of metal d- and ligand orbitals.

$$|\psi_i> = \alpha_i\,|d_i> + \beta_i\,|L_i> = \alpha_i\,|d_i> + \sqrt{1-\alpha_i^2}\,|L_i> \quad 2.19$$

Where d_i is a metal d-orbital, L_i are ligand orbitals of appropriate symmetry to overlap with the metal orbital and α_i and β_i are MO-coefficients of the metal and ligand orbitals, respectively.

Different approximations can be made in the evaluation of spin-orbit-coupling and orbital Zeeman matrix elements when molecular orbitals are used as briefly outlined on the following pages.

Spin-orbit coupling matrix elements

Calculation of the reduced SOC matrix elements (operator 2.17) between molecular orbitals (Equation 2.19) results in

$$\begin{aligned} L^{i\,j}_{1\,\mu} &\approx < \psi_i | \sum_A \xi(r_A)\, l^A_\mu \,| \psi_j > \\ &= \alpha_i\alpha_j < d_i | \sum_A \xi(r_A)\, l^A_\mu \,| d_j > + \alpha_i\beta_j < d_i | \sum_A \xi(r_A)\, l^A_\mu \,| L_j > \\ &\quad + \alpha_j\beta_i < L_i | \sum_A \xi(r_A)\, l^A_\mu \,| d_j > + \beta_i\beta_j < L_i | \sum_A \xi(r_A)\, l^A_\mu \,| L_j > \end{aligned} \qquad 2.20$$

Several approximations can be made to simplify this term. Equation 2.6 shows, that the SOC-operator $\xi(r_M)$ is depending on r_M^{-3}. Therefore, those terms that include ligand and metal orbitals (multi center terms) can be neglected. If then the SOC by only one specific ligand atom (L) is considered, and in the last step multi center terms are neglected again one obtains:

$$\begin{aligned} L^{i\,j}_{1\,\mu} &\approx < \psi_i | \sum_A \xi(r_A)\, l^A_\mu \,| \psi_j > \\ &\approx \alpha_i\alpha_j < d_i \big| \textstyle\sum_A \xi(r_A)\, l^A_\mu \big| d_j > + \beta_i\beta_j < L_i \big| \sum_A \xi(r_A)\, l^A_\mu \big| L_j > \\ &= \alpha_i\alpha_j < d_i | \xi(r_M)\, l^M_\mu + \xi(r_L)\, l^L_\mu | d_j > + \beta_i\beta_j < L_i | \xi(r_M)\, l^M_\mu + \xi(r_L)\, l^L_\mu | L_j > \\ &\approx \alpha_i\alpha_j < d_i | \xi(r_M)\, l^M_\mu | d_j > + \beta_i\beta_j < L_i | \xi(r_L)\, l^L_\mu | L_j > \end{aligned} \qquad 2.21$$

Most times, the ligand SOC is much smaller than for the metal. Therefore, the last term in Equation 2.21 can be neglected, unless heavier ligands (e.g. sulfur or bromine) are present.

$$L^{i\,j}_{1\,\mu} \approx < \psi_i \,\big|\, \xi(r_M)\, l^M_\mu \big| \psi_j > \approx \alpha_i\alpha_j\, \zeta_{i\,j} < d_i \big|\, l^M_\mu \big| d_j > \qquad 2.22$$

Where the radial integral over the operator $\xi(r_M)$ is:

$$\zeta_{i\,j} = < d_i | \xi(r_M) | d_j > \qquad 2.23$$

If it is assumed, that all metal d-orbitals have the same radial function, the radial integration becomes independent of *i* and *j* and it is obtained $\zeta_{ij} = \bar{\zeta}$. A collection of values for ζ can be found in the literature from Bendix *et al.*[131] and the values for iron are summarized in Table 2.1.

Table 2.1: Empirically determined SOC constants for Iron in cm^{-1} taken from Bendix *et al.*[131]

oxidation state	+II	+III	+IV	+V	+VI
ζ for iron	427	464	505	578	649

Very important is the factor $\alpha_i\alpha_j$ in Equation 2.22 which determines the metal-ligand covalency. The spin-orbit coupling constant is sometimes expressed as an effective SOC- constant $\zeta_{eff} = \zeta\alpha_i\alpha_j$ and given that $\alpha_i\alpha_j \leq 1$ it is described as a covalently reduced constant.

The remaining term that has to be calculated in Equation 2.22 is $< d_i \big|\, l^M_\mu \big| d_j >$. With the help of Table 2.2, which can be found in various text books, this is easily done.[108,111]

Table 2.2: Operation of l-operators on real p- and d-orbitals.

	l_x	l_y	l_z
$\|p_x>$	0	-i $\|p_z>$	i $\|p_y>$
$\|p_y>$	i $\|p_z>$	0	-i $\|p_x>$
$\|p_z>$	-i $\|p_y>$	i $\|p_x>$	0
$\|d_{x^2-y^2}>$	-i $\|d_{yz}>$	-i $\|d_{xz}>$	2i $\|d_{xy}>$
$\|d_{xy}>$	i $\|d_{xz}>$	-i $\|d_{yz}>$	-2i $\|d_{x^2-y^2}>$
$\|d_{yz}>$	i $\|d_{x^2-y^2}>$ + i $\sqrt{3}\|d_{z^2}>$	i $\|d_{xy}>$	-i $\|d_{xz}>$
$\|d_{xz}>$	-i $\|d_{xy}>$	i $\|d_{x^2-y^2}>$ - i $\sqrt{3}\|d_{z^2}>$	i $\|d_{yz}>$
$\|d_{z^2}>$	-i $\sqrt{3}\|d_{yz}>$	i $\sqrt{3}\|d_{xz}>$	0

Orbital Zeeman matrix elements

Much more difficult than the SOC-matrix elements is the evaluation of orbital Zeeman matrix elements. The operator does not contain any factor r^{-3} which would justify neglecting multi center terms.

$$\begin{aligned} L_{2\,p}^{i\,j} &\approx <\psi_i \,|\, l_\mu^M |\psi_j> \\ &= \alpha_i\alpha_j <d_i|l_\mu^M|d_j> + \alpha_i\beta_j <d_i|l_\mu^M|L_j> \\ &\quad + \alpha_j\beta_i <L_i|l_\mu^M|d_j> + \beta_i\beta_j <L_i|l_\mu^M|L_j> \end{aligned} \qquad 2.24$$

The first term is easy to evaluate, as it was for the SOC-matrix element. The second, third and fourth terms include contributions from the ligand and are sometimes neglected.[108,110] However, especially the last term can contribute significantly to the g-value.[132-134] In its calculation, it has to be considered that the metal of mono nuclear complexes is usually chosen to lie in the origin. Therefore the angular momentum operator l_μ^M, which refers to the metal, has to be shifted to the origin of the ligand orbitals. The x-, y- and z-component of the angular momentum operator can be written as shown in Equation 2.25.[135]

$$l_x = -i\hbar\left(y\frac{\partial}{\partial z} - z\frac{\partial}{\partial y}\right) \qquad 2.25a$$

$$l_y = -i\hbar\left(z\frac{\partial}{\partial x} - x\frac{\partial}{\partial y}\right) \qquad 2.25b$$

$$l_z = -i\hbar\left(x\frac{\partial}{\partial y} - y\frac{\partial}{\partial x}\right) \qquad 2.25c$$

Transformation of l_μ^M centered on the metal to another point in the coordinate system (e.g. the origin of the ligand orbitals) then leads to[109]

$$l_x^M = l_x^L - i\hbar\left(R_y\frac{\partial}{\partial z} - R_z\frac{\partial}{\partial y}\right) \qquad 2.26a$$

$$l_y^M = l_y^L - i\hbar\left(R_z\frac{\partial}{\partial x} - R_x\frac{\partial}{\partial y}\right) \qquad 2.26b$$

$$l_z^M = l_z^L - i\hbar\left(R_x\frac{\partial}{\partial y} - R_y\frac{\partial}{\partial x}\right) \qquad 2.26c$$

where l_μ^L is the angular momentum operator located at the ligand. R_x, R_y and R_z are the replacements along the x-, y- and z-axis, respectively. This can be negative and in Equations 2.26a-c it is further assumed, that the x-, y- and z-axis for the metal orbitals and ligand orbitals are parallel. If this would not be the case, also the angel between the ligands have to be considered.[109]

However, in the tetragonal systems that are studied here, this assumption can be made (e.g. for tetrahedral complexes this would not be possible). In the present complexes, covalency of one mono-atomic ligand (nitrido or oxo) is important (at X_6 in Figure 2.2). Inspection of the coordinate system (see Figure 2.2) allows to simplify Equations 2.26 further, since for the ligand on the z-axis R_x=R_y=0 and therefore some of the terms in Equation 2.26 vanish.

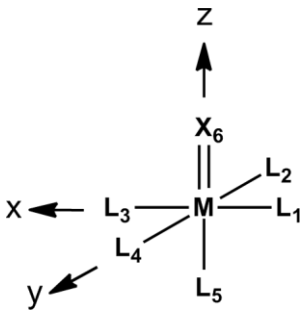

Figure 2.2: Axis system for the studied tetragonal systems.

It is seen that the z-component of the angular momentum operator is the same as long as it is only displaced along the z-axis:

$$l_x^M = l_x^L + i\hbar R_z \frac{\partial}{\partial y} \qquad 2.27a$$

$$l_y^M = l_y^L - i\hbar R_z \frac{\partial}{\partial x} \qquad 2.27b$$

$$l_z^M = l_z^L \qquad 2.27c$$

Neglecting the second and third term in Equation 2.24 and making use of the transformation of the angular momentum operator (Equations2.27) results in

$$L_{2\,p}^{i\,j} \approx < \psi_i \mid l_\mu^M \mid \psi_j > \\ = \alpha_i\alpha_j < d_i \mid l_\mu^M \mid d_j > + \beta_i\beta_j < L_i \mid l_\mu^L \mid L_j > - \beta_i\beta_j < L_i \mid i\hbar R_{LM}\nabla \mid L_j > \qquad 2.28$$

where the shift of the operator is written in a general form as $R_{\mathrm{LM}}\nabla$.

2.2. Mössbauer Spectroscopy

One of the most useful methods to study iron containing materials is Mössbauer spectroscopy. The underlying principal, *nuclear gamma resonance absorption*, was discovered by R. L. Mössbauer in 1958[136-138] and he was awarded the Nobel Prize for it in 1961.

There exists numerous text books and review articles that discuss the underlying principles and application of Mössbauer spectroscopy in detail.[113,139-142] Based upon these texts, a brief introduction shall be given here.

The Mössbauer effect requires a nucleus with a low-lying excited state which is observed for 43 elements. Still, it is mainly applied for ^{57}Fe (natural abundance 2.2%) due to its most favorable physical properties among the family of Mössbauer isotopes, and iron complexes are of high interest in the field of bioinorganic chemistry. The ^{57}Fe isotope possesses a nuclear ground state with nuclear spin I_g=1/2 and a nuclear excited state at 14.4 KeV with I_e=3/2. ^{57}Co is used as a source for γ-photons of the required energy to induce the excitation from the nuclear ground state into the nuclear excited state in the ^{57}Fe center. The loss of nuclear energy due to recoil imparted to the nucleus during emission and absorption prevents the observation of γ-resonance. However, R. L. Mössbauer has shown, that for a small fraction of nuclei, photon emission and absorption in solids is not affected by recoil energy loss. Therefore, solution samples have to be frozen or powder samples have to be used.

A further problem is, that the ^{57}Co γ-ray source only emits at certain energies. But as in every spectroscopic method, it is desired to scan through a certain energy range for recording the full absorption spectrum of a Mössbauer absorber (the sample). The energy of the photons have to be varied to detect the absorption as a function of the photon energy. In Mössbauer spectroscopy this is achieved by making use of the Doppler-effect. Moving the γ-source during the measurements towards and apart from the sample adds or subtracts energy to the photons. Doppler velocities required to observe usual splitting in ^{57}Fe Mössbauer spectroscopy are normally not higher than ±10 mm s^{-1}. In a standard Mössbauer setup, the transmission of γ-photons is detected and plotted as dependence on Doppler velocity.

Information about the geometric and electronic structure of iron containing samples is obtained, since the absorption is influenced by the chemical environment of the ^{57}Fe nucleus. The position and possible splitting of the Mössbauer signals depend on electric monopole (isomer shift) and quadrupole interactions (quadrupole splitting), magnetic hyperfine interaction, zero-field splitting, electronic Zeeman interaction and exchange coupling for multi nuclear systems.

The nuclear levels (ground and excited state) are shifted in energy due to electric monopole interactions, which is described as the isomer shift δ (see Scheme 2.1). If the coordination environment of the nucleus is lower than spherical, cubic or tetrahedral (which is in many complexes the case) the degeneracy of the excited state is partially lifted by quadrupole interaction and a splitting of the Mössbauer signal is observed (quadrupole splitting ΔE_Q, see Scheme 2.1, middle).

On the right hand side in Scheme 2.1 the effect of an applied magnetic field on the nuclear levels is indicated. Magnetic dipole interaction can completely lift the degeneracy of ground and excited states. Due to the selection rules Δm=0,±1, only six transitions are seen for the iron nuclei (Scheme 2.1).

Further effects like zero-field splitting or electronic Zeeman interaction can appear for paramagnetic species, however, these effects will not be discussed here in detail.

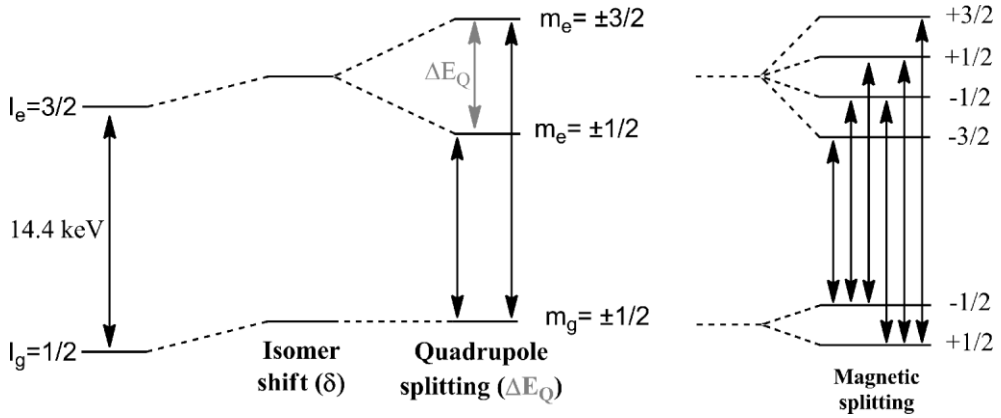

Scheme 2.1: Overview of ^{57}Fe hyperfine interactions.

Isomer shift (δ) and quadrupole splitting (ΔE_Q) are those parameters that are mainly discussed since they are easily obtained from Mössbauer measurements without the application of an external magnetic field. Both parameters are illustrated in the Mössbauer spectrum in Figure 2.3.

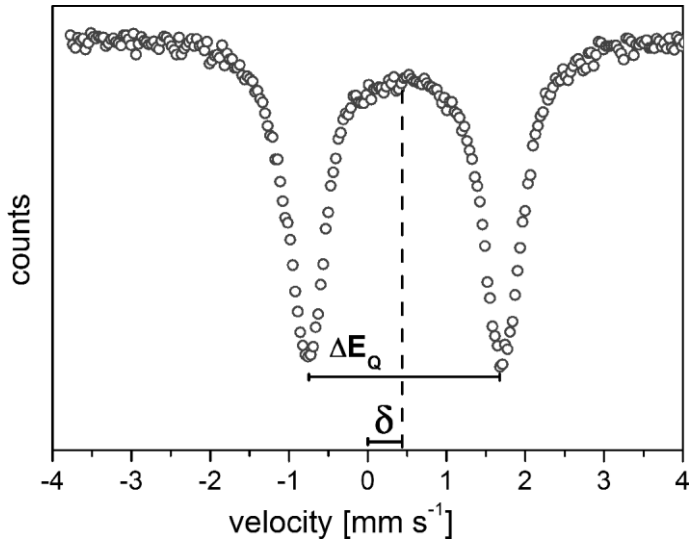

Figure 2.3: Illustrative Mössbauer spectrum with the isomer shift δ and quadrupole splitting ΔE_Q.

The isomer shift

The isomer shift (δ) is proportional to the electron density $e|\psi(0)|^2$ at the Mössbauer nucleus. This can be expressed by

$$\delta = \alpha\{|\psi(0)|^2 - C\}$$

where $\psi(0)$ is the radial part of the electron wave function at r=0, the constant C summarizes the properties of the source material and α is an isomer shift calibration constant which depends on various physical constants (e.g. the speed of light) and the nuclear transition energy.[139] The electron density at the nucleus mainly results from s-electrons, since p- and d-orbitals have nodes at r=0.

Based on basic shielding arguments, a correlation can be found between the oxidation state and the isomer shift. However, it was also shown that the isomer shift significantly depends on the iron-ligand bond distance and the 4s-contribution to $|\psi(0)|^2$.[143] All these effects result from the electronic structure of the considered complexes.

The following general trends can be often observed for the isomer shift:[140]

- A lower coordination number results in shorter bond lengths and lower isomer shifts.
- Longer bond distances in high-spin complexes than in low-spin complexes results in higher isomer shift values.
- Higher oxidation states result in shorter bond distances and lower isomer shifts.

The electron density at the iron nucleus can be easily calculated by DFT and a linear correlation is found that can be described by the equation

$$\delta = \alpha(\rho - C) + \beta$$

where ρ is the calculated electron density at the nucleus and the constants α, β and C are determined by linear regression analysis of experimental isomer shifts versus theoretically calculated electron densities for a series of compounds. These constants depend on the basis-set and DFT functional used, but a compilation for different methods is available in the literature.[143-144]

In the present thesis the B3LYP functional with a CP(PPP) basis set for iron was used to calculate the Mössbauer parameters which results in the following correlation between the isomer shift and the calculated electron density at the nucleus:[144]

$$\delta = -0.366(\rho - 11810) + 2.852$$

The quadrupole splitting

As mentioned before and shown in Scheme 2.1, the first excited state of the ^{57}Fe nucleus can be split due to the quadrupole moment into two doublets with the magnetic quantum numbers m_I=±1/2 and m_I=±3/2. Only nuclei with I>1/2 show a nuclear quadrupole moment, hence, the ground state is not affected. The electric quadrupole interaction depends on the orientation of the nuclei in the electric field generated by an antisymmetric charge distribution of the surrounding electrons. The hyperfine coupling energy (degree of splitting of the two levels in the excited state, which is observed as ΔE_Q) depends on the electric field gradient (efg, a 3x3 tensor) generated by the electrons and the nuclear quadrupole moment. Usually, a principal axes system is used where the V_{zz}-component is the so-called main component of the traceless tensor. By convention, the principal axes system is chosen in a way that $|V_{zz}| \geq |V_{yy}| \geq |V_{xx}|$. The symmetry parameter η is defined as

$$\eta = \frac{V_{xx} - V_{yy}}{V_{zz}} \qquad \text{for which } 1 \geq \eta \geq 0 \qquad 2.29$$

For axial symmetry $V_{xx} = V_{yy}$ and it follows that $\eta = 0$. The sign of V_{zz} depends on the symmetry of the electric charge distribution that causes the efg. Axial elongation along the z-axis will cause a negative V_{zz} and axial compression a positive V_{zz}. This will affect the sign of the ^{57}Fe quadrupole splitting which is given by

$$\Delta E_Q = \frac{eQV_{zz}}{2}\sqrt{1 + \frac{\eta^2}{3}} \qquad 2.30$$

where e is the proton charge and Q the quadrupole moment of the nucleus.

In DFT calculations the efg tensor is computed, from which η is obtained via Equation 2.29 and ΔE_Q via Equation 2.30.

2.3. Resonance Raman Spectroscopy

The physical principles of resonance Raman spectroscopy and vibrational spectroscopy in general are discussed in detail in the literature.[114,142] Here, based on common text books[114,142] and review papers[115-116] a brief review of the underlying principles is given that will be used in the present work.

Transitions to vibrationally excited states can be accessed by direct absorption of light in the infrared region (IR spectroscopy), since molecular vibrational frequencies lay in the IR region of the electromagnetic spectrum. Vibrational transitions can be also observed via a scattering technique, based on the Raman-effect.

The Raman-effect is observed when a sample is irradiated by a laser in a transparent region of the molecular spectrum. Hence, long wavelength lasers are used that do not coincide with allowed electronic transitions. A small fraction of the light is scattered by the sample molecules in all directions. Some of these collisions are inelastic resulting in a shift of the frequency of the scattered light with respect to the frequency of the incident light.

IR absorptions require the change of the dipole moment while Raman scattering requires a change in the molecular polarizability, as a result of the vibrational motions. In Raman scattering the intensity $\mathbf{I}_R$ varies directly with the square of the induced dipole-moment (**P**), that depends on the perturbing electric field component of the radiation (**E**) and the degree of electronic polarization (α). The polarizability of the molecule (α) is closely related to the molecular structure.[114,142]

$$\mathbf{I}_R \propto \mathbf{P}^2 = (\alpha\, \mathbf{E})^2 \qquad \text{with} \quad \alpha = \left(\frac{\partial \alpha\prime}{\partial Q_i}\right)_0 Q_i$$

Here, $\left(\frac{\partial \alpha\prime}{\partial Q_i}\right)_0$ is the change of the polarizability due to a normal mode vibration with the vibrational coordinate Q_i. Symmetric bond stretching vibrations, which produce large polarizability changes therefore usually dominate the Raman spectra.

In contrast to conventional (off-resonance) Raman-spectroscopy, in resonance Raman spectroscopy a laser is chosen with a wavelength that coincides with an allowed electronic transition. This causes a strong enhancement of certain modes in the resonance Raman spectrum (10^3-10^6 times more intense) compared to off-resonance measurements. The reason is that the polarizability and its dependence on the molecular motions (vibrations) is strongly enhanced via the electronic transition. As a result, not all Raman modes are enhanced but those that mimic the deformation of the molecule upon electronic excitation. Therefore, dd-transitions usually result in only small enhancements of the Raman lines given that the deformation of the molecular structure in an excited state from a dd-transition is usually small. Charge-transfer (CT) transitions generally result in strongly enhanced metal-ligand and intra ligand modes. Resonance Raman spectroscopy is therefore also much more selective than IR-spectroscopy since Raman modes are enhanced that are associated with the excited-state distortion and valuable information about the processes induced by irradiation can be obtained.

The underlying processes are outlined in Scheme 2.2 for Raman (green) and resonance Raman (red) scattering. Electronic states are indicated by black curves and vibrational levels are indicated by blue horizontal lines.

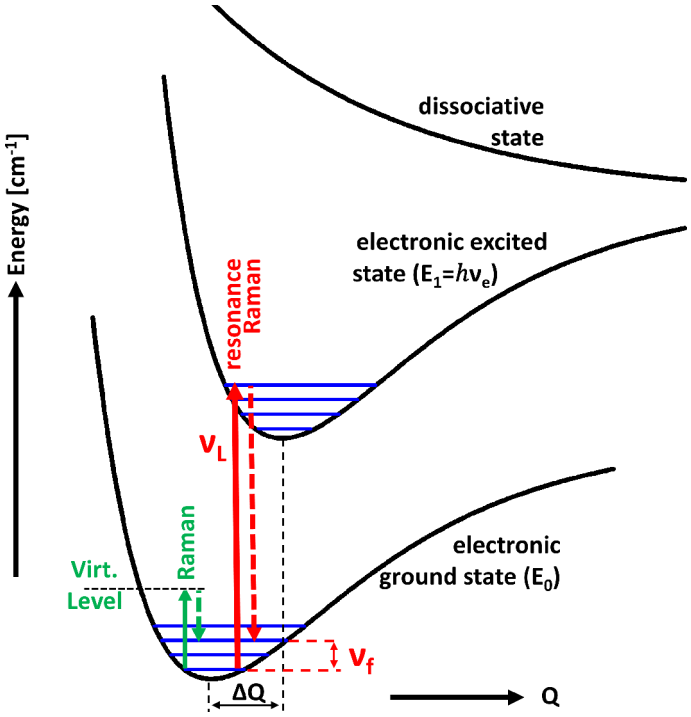

Scheme 2.2: Underlying processes of Raman and resonance Raman spectroscopy

In resonance Raman spectroscopy the sample is irradiated by a laser with wavelength ν_L which transfers the molecule into an electronic excited state with the energy $E_1=h\nu_e$. The molecule then falls back to the electronic ground state, but on a higher vibrational level (ν_f) which is often depicted as the final-state. Hence, the molecule did absorb the energy $h\nu_f$ and a signal will be observed in the resonance Raman spectrum at ν_f. In principal it is possible that the electronically excited state is a dissociative state. But as outlined in Scheme 2.2, there are no well-defined vibrational levels for the dissociative state. Therefore, it will be difficult to obtain useful resonance Raman data for such states, and the recorded signals might result also from the dissociated product.

Enhancement Mechanisms

By the application of second-order perturbation theory, the polarizability (α) can be written in terms of a sum-over-states form. This results in the Kramers-Heisenberg dispersion equation.[114,142,145]

$$\alpha_{\rho\sigma}(\omega) = \frac{1}{\hbar}\sum_{e}\left(\frac{<f|\mu_\rho|e><e|\mu_\sigma|g>}{\nu_e-\nu_g-\nu_L+i\Gamma_e}+\frac{<f|\mu_\sigma|e><e|\mu_\rho|g>}{\nu_e-\nu_f+\nu_L+i\Gamma_e}\right) \qquad 2.31$$

The subscripts ρ and σ are Cartesian directions (x,y,z) of the polarizability tensor α and the dipole moment operator μ. g, e and f are the ground, the electronic excited and final state (electronic ground state, vibrationally excited), respectively. The excitation energy in wavenumbers into the electronic excited state is then $\nu_e-\nu_g$ and the signal in the spectrum will be observed at $\nu_f-\nu_g$, the difference between the final state and the ground state. The laser frequency is ν_L and Γ_e is a damping constant corresponding to the half-bandwidth of the electronic excited state. It should be noted here, that ν_e is not only the energy difference between the electronic ground state and the electronic excited state. It is the difference between the electronic ground state on a specific vibrational level (most times a

low-lying vibrational level, but this also depends on the temperature) and a higher vibrational level on the electronic excited state. As already mentioned, well-defined vibrational levels on the excited state surface have to be accessible to gain proper resonance Raman signals, which might not be the case for dissociative states.

The denominator in the first term in Equation 2.31 decreases rapidly when the laser frequency (ν_L) approaches the energy for the excitation from the electronic ground in the excited state $\nu_{eg} = \nu_e - \nu_g$. Therefore it is the much more dominant term and the reason for the resonance enhancement.

Dropping the second term in Equation 2.31, and making use of the adiabatic Born-Oppenheimer approximation (separation of electronic and vibrational wave functions) results in[114]

$$\alpha_{\rho\sigma}(\omega) = \frac{1}{h}\sum_{n} \frac{\mu_\rho^{el}\mu_\sigma^{el} < j||n >< n||i >}{\nu_{ni} - \nu_L + i\Gamma_n} \qquad 2.32$$

Where *n* are vibrational levels of the electronic excited state with the band width Γ_n, ν_{ni} is the transition frequency from the ground vibrational level *i* to the level *n*; $|j>$, $|n>$ and $|i>$ are vibrational states (*j*,*i* electronic ground state; *n* electronic excited state) and the sum runs over all vibrational levels in the electronic excited state *n*. The pure electronic transition dipole moments are $\mu_\rho^{el} =< g|\mu_\rho^{el}|e >$ and $\mu_\sigma^{el} =< e|\mu_\sigma^{el}|g >$. The integrals $< j||n >$ and $< n||i >$ are Franck-Condon factors (overlap integrals) between the vibrational wave functions of the initial (i) and final (j) vibrational levels of the ground state with the intermediate vibrational level (n) of the electronic excited state. They are zero, unless there is a shift in the excited state along the vibrational coordinate (Q_k in Scheme 2.2). The dependence of μ^{el} on the coordinate Q_k can be expanded in a Taylor-series:[142]

$$\mu^{el} = \mu_0^{el} + \sum_k \mu_1^e Q_k + \ . \ . \ . \qquad 2.33$$

where $\mu_1^{el} = \left(\frac{\partial \mu_0^{el}}{\partial Q_k}\right)_0$. When the excited state |e> can gain absorption strength from other excited states by vibronic coupling via coordinate Q_k, μ_1^{el} can even exceed μ_0^{el}. The vibronic coupling can be written in Herzberg-Teller formalism as[142]

$$\mu_1^{el} = \frac{\mu_s^{el} < s|(\partial H_e/\partial Q_k)_0|e >}{\nu_s - \nu_e} \qquad 2.34$$

where |s> is another excited state that can mix with |e> by Q_k. ν_s and μ_s^e are the frequency and transition dipole moments of the mixing electronic state |s> and $(\partial H_e/\partial Q_k)_0$ is the vibronic coupling operator with H_e being the Hamiltonian for the total electronic energy of the molecule. Insertion of Equation 2.33 and 2.34 in Equation 2.32 yields a lengthy expression with various terms. The first three terms are called A-, B- and C- terms and are dominant in resonance Raman scattering.

$$\alpha_{\rho\sigma}(\omega) = A + B + C + \ . \ . \ . \qquad 2.35$$

The individual contributions are[114,116]

$$A = \frac{(\mu_0^{el})^2}{h} \sum_n \frac{< j||n >< n||i >}{\nu_{ni} - \nu_L + i\Gamma_n} \quad 2.36$$

$$B = \frac{\mu_0^{el}\mu_1^{el}}{h} \sum_n \frac{< j|Q_k|n >< n||i > + < j||n >< n|Q_k|i >}{\nu_{ni} - \nu_L + i\Gamma_n} \quad 2.37$$

$$C = \frac{(\mu_1^{el})^2}{h} \sum_n \frac{< j|Q_k|n >< n|Q_k|i >}{\nu_{ni} - \nu_L + i\Gamma_n} \quad 2.38$$

Two conditions must be fulfilled for an A-term contribution; i) The transition dipole moment μ_0^{el} must be non-zero ii) The Franck-Condon factors $< j||n >$ and $< n||i >$ must be non-zero.[116]

The first condition is fulfilled for electronic transitions that are electric-dipole-allowed. This is especially the case for charge transfer (CT) transitions. To get non-zero Franck-Condon factors, the vibrational wave functions have to be non-orthogonal. The most important contribution arises here due to the shift in the excited state potential along the vibrational coordinate, $\Delta_k^e = Q_k^e - Q_k^g$. The larger Δ_k^e (dimensionless normal coordinate displacement) the more intense is the resonance Raman signal.

Contributions by the B-term arise from vibronic coupling of the resonant state to other excited states (see Equation 2.34 which appears in 2.37).[116] The B-term is usually much smaller than the A-term, since it depends on the vibronic coupling contribution which is usually small. However, if the A-term contribution is small (e.g. due to small displacements Δ_k^e) the contributions from the B-term might be significant.

The C-term is usually much smaller than the B-term and can be therefore neglected most times. Only overtones are enhanced by the C-term.[116]

Resonance Raman intensity not only depends on the normal coordinate displacement, it is further depending on the excitation energy for the considered electronic transition. For a single electronic transition from the electronic ground state g_0, where g_l is a vibrational excited level in the electronic ground state and e is the electronic excited state the relation

$$I_{e,g_0 \to g_l} = \nu_l^2 \Delta_{\mathrm{e,l}}^2 \quad 2.39$$

is known as the Savin formula.[115,146-148]

Resonance Raman spectra were calculated by DFT within the independent mode displaced harmonic oscillator (IMDHO) model using the normal mode gradient technique for calculating the dimensionless displacements (Δ) for each normal mode.[149-151] Normal modes are obtained with the B3LYP functional in conjunction with the def2-TZVP basis set for the ground state. Excited state gradients are obtained from TD-DFT calculations with 20 roots on the same level of theory. The orca_asa program is used to simulate resonance Raman spectra for first order vibrational transitions.[150-151]

3. Computational Methods

During the last decades, the popularity of theoretical methods in chemical research has been steadily growing.[152-153] Computer hardware is constantly improving which makes the necessary resources available for a reasonable cost. Parallel to that, various quantum chemistry programs were developed which provides the necessary functionality in a user-friendly manner. Therefore, a lot of experimental work is nowadays accompanied by calculations that provide additional insight in the investigated systems. Postulated molecular structures and reaction mechanisms (reaction energies and barriers) can be easily supported by calculations. In addition, the calculation of (spectroscopic) molecular properties provides another level in supporting experimental results by theoretical methods.

The great variety of computational methods is reviewed in many text books[125,154-156] and publications[149,157-159] and based on these, the applied methods shall be briefly reviewed.

3.1. Density Functional Theory

The most popular computational method is density functional theory (DFT).[157,160-162] W. Kohn[163] was rewarded with the Nobel Prize in chemistry for its development together with J. Pople[164] for making it available to the chemical community.

The general non-relativistic molecular Hamiltonian operator that describes the interactions between *N* electrons and *M* nuclei in atomic units reads as:[154,156]

$$\begin{aligned}\widehat{H}_{BO} &= T_e + V_{eN} + V_{ee} + V_{NN} \\ &= -\frac{1}{2}\sum_{i=1}^{N}\nabla_i^2 - \sum_{i=1}^{N}\sum_{A=1}^{N}\frac{Z_A}{|\boldsymbol{r}_i - \boldsymbol{R}_A|} + \frac{1}{2}\sum_{i=1}^{N}\sum_{\substack{j=1\\ j\neq i}}^{N}\frac{1}{|\boldsymbol{r}_i - \boldsymbol{r}_j|} + \frac{1}{2}\sum_{A=1}^{M}\sum_{\substack{B=1\\ A\neq B}}^{M}\frac{Z_A Z_B}{|\boldsymbol{R}_A - \boldsymbol{R}_B|}\end{aligned} \qquad 3.1$$

A, *B* sum over all nuclei at positions $\mathbf{R}_A$ with nuclear charges Z_A and *i*, *j* sum over all electrons at positions $\mathbf{r}_i$. The terms on the right hand side describe the kinetic energy of the electrons, the potential of the electron-nuclei interaction, the potential of the electron-electron interaction and the potential energy of the nuclei. The Born-Oppenheimer (BO) approximation is used where the nuclear positions are considered as fixed since they are much heavier than electrons and move much more slowly. In the BO-Hamiltonian the kinetic energy term of the nuclei is therefore neglected.

The time-independent N-electron Schrödinger equation is associated with the N-electron Hamiltonian (Equation 3.1)

$$\widehat{H}_{BO}\Psi(\boldsymbol{x}_1,\ldots,\boldsymbol{x}_N|\boldsymbol{R}_1,\ldots,\boldsymbol{R}_M) = E\Psi(\boldsymbol{x}_1,\ldots,\boldsymbol{x}_N|\boldsymbol{R}_1,\ldots,\boldsymbol{R}_M) \quad 3.2$$

where $\mathbf{x}_i$ denotes the spatial ($\mathbf{r}_i$) and spin-degree of freedom ($\boldsymbol{\sigma}_i$) for the *i*-th electron. However, solving the 3N-dimensional antisymmetric wave function for a system with *N* electrons is quite challenging. Since the many-electron wave functions contain far more information than it is necessary in order to calculate the properties of a chemical system, it is desired to find solutions for Equation 3.2 without calculating the whole wave function.

In 1964 Hohenberg and Kohn formulated theorems that form the basis for DFT.[165] In the first Hohenberg-Kohn theorem they have shown that it should be possible to construct a functional $E[\rho]$, where $\rho(\boldsymbol{r})$ is the electron density at the point $\boldsymbol{r}$, that provides the exact energy, given the exact density is known. One can therefore write the total energy as a functional of the electron density, separated into different contributions (compare Equation 3.1)

$$\begin{aligned} E[\rho] &= V_{NN} + V_{eN}[\rho] + T[\rho] + V_{ee}[\rho] \\ &= V_{NN} + V_{eN}[\rho] + T[\rho] + J[\rho] + E'_{XC}[\rho] \end{aligned} \quad 3.3$$

where the electron-electron interaction consists of the Coulomb term of electron-electron repulsion ($J[\rho]$) and an exchange-correlation term for the electron-electron repulsion ($E'_{XC}[\rho]$), as it is the case in Hartree-Fock theory.[155] The kinetic energy functional $T[\rho]$ and the exchange-correlation functional $E'_{XC}[\rho]$ are unknown, but the second Hohenberg-Kohn theorem provides the necessary recipe to obtain the exact energy presuming that these functionals are known.[157,165] It states that $E[\rho]$ follows the variational principle and for any trial density $\tilde{\rho}$, minimization of $E[\rho]$ over the allowed range for $\tilde{\rho}$ would yield the exact ground state energy which can be expressed by

$$E[\rho] \leq E[\tilde{\rho}] \quad 3.4$$

where the equality holds if $\tilde{\rho}$ matches the exact density ρ.

One of the challenges in DFT is to express the kinetic energy of the electrons as a function of the electron density, $T[\rho]$. Walter Kohn and Lu Jeu Sham expressed the electron density as a function of the (Kohn-Sham-) orbitals

$$\rho(\boldsymbol{r}) = \sum_i |\psi_i(\boldsymbol{x})|^2 ds \quad 3.5$$

and considered a fictitious system of non-interacting electrons (as in Hartree-Fock theory) which is described by a single Stater determinant:[166]

$$\Psi_{KS}(\boldsymbol{x}) = |\psi_i \ldots \psi_N| \quad 3.6$$

The non-interacting kinetic energy is then calculated from the Kohn-Sham orbitals, where this term is only indirectly a function of the electron density, since the Kohn-Sham orbitals are a function of the electron density:

$$T_s[\rho] = -\frac{1}{2}\sum_i < \psi_i|\nabla^2|\psi_i > \quad 3.7$$

Equation 3.3 is now reformulated as

$$E[\rho] = V_{NN} + V_{eN}[\rho] + T_s[\rho] + J[\rho] + E_{XC}[\rho] \quad 3.8$$

where the exchange correlation functional is redefined as

$$E_{XC}[\rho] = E'_{XC}[\rho] + T[\rho] - T_s[\rho] \quad 3.9$$

and now contains the part of the kinetic energy that is not covered by $T_s[\rho]$.

The 2nd Hohenberg-Kohn theorem can be applied now to obtain the single-particle Kohn-Sham equation by variation of the electron density, using the Lagrange method of undetermined multipliers:[154,156-157]

$$h_{KS}\psi_i = \left\{-\frac{1}{2}\nabla^2 + v_{eff}(\boldsymbol{r})\right\}\psi_i = \varepsilon_i\psi_i \quad 3.10$$

$$v_{eff}(\boldsymbol{r}) = -\sum_A Z_A|\boldsymbol{r} - \boldsymbol{R_A}|^{-1} + \int \rho(\boldsymbol{r'})|\boldsymbol{r} - \boldsymbol{r'}|^{-1}d\boldsymbol{r'} + V_{XC}(\boldsymbol{r}) \quad 3.11$$

The effective potential seen by the electrons ($v_{eff}(\boldsymbol{r})$) contains the nuclear contributions, the electronic Coulomb repulsion and the exchange-correlation potential, which is the derivative of the exchange-correlation energy (Equation 3.9) with respect to the density: [154,156-157]

$$V_{XC}(\boldsymbol{r}) = \frac{\delta E_{XC}[\rho]}{\delta\rho(\boldsymbol{r})} \quad 3.12$$

The Kohn-Sham equations are at this point very similar to the Hartree-Fock equations, the only difference is that the exchange term is replaced by the local exchange-correlation potential. The big challenge in DFT is to derive approximate expressions for $E_{XC}[\rho]$.

The Kohn-Sham orbitals are expanded in terms of a set of basis functions (Equation 3.13) and inserting these in the Kohn-Sham equation (Equation 3.10) results in a matrix pseudo-eigenvalue equation (Equation 3.14)

$$\psi_i(\boldsymbol{x}) = \sum_\mu c_{\mu i}\varphi_\mu(\boldsymbol{x}) \quad 3.13$$

$$\boldsymbol{F}(\boldsymbol{c})\boldsymbol{c}_i = \varepsilon_i\boldsymbol{S}\boldsymbol{c}_i \quad 3.14$$

where $\boldsymbol{F}$ is the Kohn-Sham Matrix, $\boldsymbol{c}_i$ is a vector with the elements $c_{\mu i}$ and $\boldsymbol{S}$ is the overlap matrix with elements $S_{\mu\nu} = <\varphi_\mu|\varphi_\nu>$.[154,156-157]

In a special case where a fraction c_{HF} of Hartree-Fock exchange is added to Kohn-Sham theory the Kohn-Sham matrix reads

$$F_{\mu\nu} = h_{\mu\nu} + J_{\mu\nu}(P) - c_{HF}K_{\mu\nu}(P) + c_{DF}V_{\mu\nu}^{XC}[\rho] \quad 3.15$$

where h is the one-electron matrix, **P** the density matrix and $\mathbf{V^{XC}}$ the exchange-correlation matrix. The most difficult contribution is the exchange-correlation term and various approximations were developed for its calculation.

The first approximation made to derive a formula for the exchange functional is the local density approximation (LDA), or for the unrestricted case the local spin approximation (LSD). [154,156] In this approach, a uniform electron gas is assumed for which expressions for the exchange energy are

obtained. Even this is a strong simplification since the electron density in molecules is not homogeneous, it significantly improves the results. Various parametrizations were proposed and the most popular ones are from Vosko, Wilks and Nusair[167] or Perdew and Wang.[168]

In the generalized gradient approximation (GGA) further terms are taken into account to consider the inhomogeneity of the electron density. These terms include the gradient of the electron density $\nabla\rho(\boldsymbol{r})$. Popular GGA functionals are BP86 by Perdew and Wang[169-171] or PBE by Perdew, Burke and Ernzerhof.[172-173]

Becke suggested in 1993 to include a fraction of the non-local Hartree-Fock exchange and the resulting functionals are described as hybrid functionals. The most popular hybrid functional is B3LYP which consists of the exchange part B88 by Becke,[171,174] a correlation part by Perdew,[169-170] as well as an exchange contribution from Hartree-Fock theory. This exchange functional can be written as

$$E_{XC}^{B3LYP} = aE_X^{HF} + (1-a)E_X^{LSD} + bE_X^{B88} + E_C^{LSD} + c(E_C^{LYP} - E_C^{LSD}) \qquad 3.16$$

where a, b and c are empirically derived constants with the values 0.20, 0.72 and 0.81.

3.1.1. Computational Setup for DFT Calculations

All calculations were performed with the ORCA program, developed by Frank Neese.[175]

Within the scope of the present work, molecular structures were optimized with the GGA-functional BP86, and in certain cases with the B3LYP functional. Bühl *et al.* have shown that the BP86 functional results in very good geometries for transition metal complexes.[176-177] In all calculations with the BP86 functional the resolution of the identity (RI) approximation[178] was applied. The triple-ζ basis set def2-TZVP developed by Weigend *et al.*[179-180] was used in conjunction with the def2-TZV/J auxiliary basis set for the RI approximation. Solvent effects were taken into account implicitly, within the conductor like screening model (COSMO).[181-182] Structures from geometry optimizations were confirmed as minima (transition states) on the potential energy surface by numerical frequency calculation that did result only in positive (one negative) normal modes. In some cases, dispersion correction was included in the DFT calculations.[183-185]

IR-frequencies were also calculated by the BP86 functional, but without COSMO. For increased accuracy, 10^{-9}Eh was used as the convergence criterion for the energy change in the SCF procedure and the size of the DFT integration grid was set to 434 angular points. Molecular structures were considered to be converged in the optimization when the root mean square (RMS) of the gradient was below $3x10^{-5}$ Eh/bohr, the RMS of the displacements was below $6x10^{-4}$ bohr, and the energy change compared to the previous optimization step was below 10^{-6} Eh (verytightscf, grid5, tightopt). Vibrational frequency calculations were performed through two-sided numerical differentiation of the analytical gradient. 6N displacements were calculated (N is the number of atoms) with a numerical increment of 0.005 bohr. Calculated harmonic frequencies were scaled by the factor 0.9914. A calibration study has shown that the root-mean-square deviation between experimental and calculated frequencies with this setup is about 41 cm^{-1}.[186]

Energies and properties were calculated with the same setup as used for geometry optimization but the BP86 functional was replaced by the B3LYP functional[169-171,174] and the RIJCOSX[187] approximation was used.

For resonance Raman spectra,[150-151,188-189] the geometries were optimized with the B3LYP functional, the def2-TZVP basis set and the corresponding def2-TZV/J auxiliary basis set for the RIJCOSX approximation. To increase the accuracy for the obtained vibrations, tight conversion criteria and integration grids were employed (verytightscf, grid5, gridx9). Calculated modes were scaled by the factor 0.9614 for comparison with the experimental fundamentals.[186] Excited states were calculated by TD-DFT within the Tamm-Dancoff approximation on the same level of theory.[190-192]

To calculate Mössbauer parameters, a previously published calibration study was used which correlates the calculated electron density at the iron nucleus with the experimental isomer shift.[144] In these calculations, for iron the integration grid was increased (grid7), the CP(PPP) basis set[143] was used and for all other atoms the def2-TZVP basis set was employed. The RIJCOSX approximation was not used in these calculations.

Exchange coupling constants were calculated within the broken symmetry approach.[193-194]

3.2. Complete Active Space Self-Consistent Field Method

In certain cases, the electronic structure of chemical compounds cannot be properly described by methods that are based on one Stater determinant only. More flexibility in the wave function is necessary e.g. to describe near degenerate states, the situation of weak, nearly broken bonds or excited states that have to be represented by mixtures of single- and double-excitations.[149,158-159,195] The resulting effects can be taken into account by a multi configurational self-consistent field method (MCSCF). In this case, the total electronic wave function $\Psi(\boldsymbol{x})$ is formed as a linear combination of many-electron wave functions (Φ_I) that are Slater determinants or linear combinations of Slater determinants, so called configuration-state functions (CSFs). The Ansatz for the N-electron wave function is then:[158]

$$\Psi(\boldsymbol{x_1}, \dots, \boldsymbol{x_N}) = \sum_J c_J \Phi_\mathrm{J}(\boldsymbol{x_1}, \dots, \boldsymbol{x_N}) \qquad 3.17$$

This can result in a large number of configurations which can be applied only to very small molecules or light atoms. However, the number of determinants/CSFs can be drastically reduced by only treating a certain range of electrons and orbital by this approach. The chosen number of electrons is then allowed to distribute in the chosen orbital range in every possible manner, which corresponds to Full-CI. Orbitals are therefore divided in three subsets. The inactive orbitals are all doubly occupied in each CSF and represent a "SCF sea" in which the active electrons move.[158] The external orbitals are all unoccupied in all CSFs. Between the inactive and external orbitals are the active space orbitals with occupation numbers between 0 and 2. The multi configurational character is then introduced by a Full-CI within the active space.[149] This method is known as complete active space self-consistent field method for which the notation CASSCF(*n*,*m*) is used to denote the size of the active space (*n*: active electrons, *m*: active orbitals). While in a Hartree-Fock calculation the MO-coefficients are varied in order to minimize the energy, during a CASSCF calculations the MO-coefficients as well as the CI-coefficients (c_J in Equation 3.17) are varied. This procedure is stable for the ground state but certain problems can arise for the optimization of the excited state wave function. To overcome this, usually state average CASSCF (SA-CASSCF) calculations are performed over a specific number of roots, where a single set of orbitals minimizes the average energy. Hence, the resulting wave function is an average of the roots included in the calculation.

By adding more flexibility to the wave function as described above, the CASSCF method takes static correlation into account and is able to describe the electronic structure of complexes that show significant multi-configurational character, e.g. due to (nearly) degenerate states. However, dynamic correlation, which is the correlation of the movements of electrons, is not covered. Based on a CASSCF wave-function it is possible to take dynamic correlation into account e.g. by multi-configurational second-order perturbation theory (CASPT2)[159] or N-electron valence state second-order perturbation theory (NEVPT2)[196-199]. Both methods are based on multireference perturbation theory applied on top of a CASSCF wave function. However, the more recently developed NEVPT2 method shows certain advantages over CASPT2, e.g. it is intruder state free.[196-199] A strongly contracted version of NEVPT2 is implemented in ORCA and used to calculate excited state energies.[198-199]

Calculation of Spin-Orbit Coupling and g-Values

The starting point for taking spin-orbit coupling (SOC) into account is a multi-configurational wave function $\Psi_{\mathrm{I}}^{S,M}$ where the superscript S denotes the total spin and M its spin-projection quantum number ($M = +S, S-1, \ldots, -S$). The subscript I runs over the number of roots considered in the calculation and the wave function is obtained e.g. from a CASSCF calculation. SOC Effects are treated through quasi-degenerate perturbation theory (QDPT)[200] which amounts to the diagonalization of the Born-Oppenheimer ($\widehat{H}_{BO}$) and SOC-operator ($\widehat{H}_{SOC}$) in the basis of the states $\{\Psi_{\mathrm{I}}^{S,M}\}$. The matrix elements are obtained by

$$< \Psi_{\mathrm{I}}^{S,M} \left| \widehat{H}_{BO} + \widehat{H}_{SOC} \right| \Psi_{\mathrm{I}'}^{S',M'} >= \delta_{IJ}\delta_{SS'}\delta_{MM'}E_I + < \Psi_{\mathrm{I}}^{S,M} \left| \widehat{H}_{SOC} \right| \Psi_{\mathrm{I}'}^{S',M'} > \qquad 3.18$$

The spin-orbit coupling operator can be approximated by an effective one-electron spin-orbit mean-field (SOMF) operator.[200-201] SOC-Matrix elements are calculated between all state-averaged CASSCF wave functions and only diagonal elements are replaced by NEVPT2 energies that contain dynamic correlation. Diagonalization of the SOC matrix results in eigenvalues and eigenfunctions where for odd *S* the doubly degenerate pairs of eigenvalues represent Kramers pairs Φ and $\overline{\Phi}$. These are used as a basis for the Zeeman operator and elements of the g-matrix are obtained by[202-204]

$$\begin{aligned} g_{kx} &= 2Real < \Phi | \mathrm{L_k} + g_e S_k | \overline{\Phi} > \\ g_{ky} &= -2Imaginary < \Phi | \mathrm{L_k} + g_e S_k | \overline{\Phi} > \\ g_{kz} &= 2Real < \Phi | \mathrm{L_k} + g_e S_k | \Phi > \end{aligned} \qquad \mathrm{k = x, y, z} \qquad 3.19$$

and the true G tensor is built from the g-matrix $G = gg^T$. The square roots of the eigenvalues from a further diagonalization of G results in the principal g-values

$$g_{xx} = \sqrt{G_{xx}} \qquad g_{yy} = \sqrt{G_{yy}} \qquad g_{zz} = \sqrt{G_{zz}} \qquad 3.20$$

Even a multi-configurational approach to calculate g-values in the above described manner gives good results for transition metal complexes, there are some exceptions. The electronic structure of systems with a (nearly) degenerate ground state are properly described by CASSCF/NEVPT2, however, the g-values are strongly affected by low lying excited states (the splitting of a nearly degenerate state).[205] Only minor changes in the lowest excited state can result in notable changes of the calculated g-values. This is the case in some of the studied systems as will be discussed in Chapter 5.6.

3.2.1. Computational Setup for CASSCF Calculations

CASSCF calculations were performed as single point calculations on DFT-optimized geometries or structures that were determined by X-ray diffraction. Most crucial is the selection of orbitals that are included in the active space, for which no general rules exist.[159,195,206] The only constant factor is that the reference wave function should include all important nondynamic correlation effects.[195] For transition metal complexes, dd-transitions can be low in energy which results in multiconfigurational character and all d-orbitals should be included in the active-space. If the complex is purely ionic, metal d- and ligand-orbitals are energetically well separated. Given that they do not interact (overlap/mix) it is not necessary to include ligand orbitals into the active space. However, the more covalent the ligand-metal bonds become the larger is their contribution to nondynamic correlation effects. Then not only the metal d-orbitals (that most times represent anti-bonding orbitals) should be included in the active space but also the corresponding bonding-orbitals that are most times derived from ligand p- or s-orbitals.[195]

In the present work, the studied iron(V) complexes feature a very covalent bonding between the metal and the nitrido- or oxo-ligand, respectively. Therefore, all bonding (π_x, π_y, σ) and anti-bonding orbitals (π_x^*, π_y^*, σ^*) are included in the active space. Details about the chosen orbitals will be given in the corresponding chapters.

Quasi restricted orbitals from DFT calculations were chosen as initial guess for the CASSCF calculations after orbitals were rotated in the desired order. Where the aim was to study the ground state electronic structure, state average CASSCF (SA-CASSCF) calculations were performed over the smallest possible number of roots, which still results in a converged wave function.

To calculate the g-values of azido-iron(III) complexes or iron(V) complexes, SA-CASSCF calculations were performed over 20-roots. Test calculations with more roots resulted in nearly identical results.

All CASSCF as well as the NEVPT2 calculations were performed with the def2-TZVP basis set and the corresponding def2-TZV/C auxiliary basis set for the RI approximation.

4. Azido-Iron(III) Complexes

Nitrido-iron(V) complexes studied in the present thesis are obtained by photolysis of their parent azido-iron(III) complexes. Besides the dinitrogen elimination resulting in nitrido-iron(V) species, the reductive elimination of azide radicals yielding ferrous complexes and the redox neutral elimination of azide anions are conceivable reaction pathways of the studied azido-iron(III) complexes.[29,43,47,56]

The complexes $[Fe^{III}(N_3)cyc\text{-}ac]^+$,[41,43] $[Fe^{III}(N_3)_2cyc]^+$[29] and $[Fe^{III}(N_3)TMC\text{-}ac]^+$[42,48] were previously studied by Mössbauer-, EPR-, UV-*vis* and IR-spectroscopy and their crystal structures were determined. In the present chapter, additional spectroscopic data on these species is collected and combined with quantum chemical calculations. This will allow a deeper understanding of their spectroscopic properties and provides insight in their photochemical properties and reactions the azido-iron(III) complexes can undergo.

4.1. Synthesis of Azido-Iron(III) Complexes

The complexes $[Fe^{III}(N_3)_2cyc]ClO_4$,[9] $[Fe^{III}(N_3)TMC\text{-}ac]PF_6$,[42] and $[Fe^{III}(N_3)TPP]$[30] were synthesized as published previously.

Substantial amounts of the $[Fe^{III}(N_3)cyc\text{-}ac]PF_6$ complex were necessary which was not possible to obtain with the previously published synthesis.[43,292-293] As a consequence, a new synthetic route was worked out. The ligand cyc-ac•4HCl (cyc-ac=cyc-ac=1,4,8,11-tetraazacyclotetradecane-1-acetate) was synthesized as published previously[294-295] and was found to contain 1.5 equivalents of water.

Unless otherwise specified, commercially available solvents and starting materials were used.

4.1.1. $[Fe^{III}(Cl)cyc\text{-}ac]PF_6$

To a suspension of cyc-ac•4HCl•1.5H_2O (500 mg, 1.16 mmol) in absolute ethanol (15 mL) under inert argon atmosphere, triethylamine (0.8 mL, 5.8 mmol) was added. A clear, colorless solution was obtained after 5 minutes of stirring at room temperature. This solution was transferred under argon to a Schlenk tube containing anhydrous $FeCl_3$ (188 mg, 1.16 mmol) and after further 5 minutes of stirring a clear brown-orange solution was obtained. For 2h the reaction mixture was heated at 50°C. After cooling the solution to room temperature, a solution of NH_4PF_6 (378 mg, 2.32 mmol) in absolute ethanol (5 mL) was added. The reaction mixture was stored for 12 h at 5°C and the red precipitate obtained was separated from the solvent by filtration. The solid was washed with absolute ethanol (3x3 mL), diethyl ether (2x3 mL) and dried under vacuum for 2h.

Yield: 501 mg (1.01 mmol, 87%)

IR (in KBr) [cm^{-1}]: 3432(m, br), 3261 (s), 3202 (m), 2981 (m), 2961 (m), 2934 (m), 2905 (m), 2879 (m), 1683 (vs, sh, ν(C=O)) 1669 (vs, ν (C=O)), 1466 (m), 1431 (m), 1385 (w), 1345 (m), 1323 (m), 1297 (s), 1243 (w), 1137 (w), 1103 (m, sh), 1096 (m), 1072 (sh), 1064 (m), 1040 (sh), 1031 (s), 969 (w), 937 (m), 929 (m), 911 (w), 881 (s), 841 (vs, (PF_6)), 814 (s), 743 (w), 558 (s, PF_6), 539 (w), 522 (w), 490 (m), 428 (m), 410 (w);

MS (ESI positive, acetonitrile): m/z: 348.1 $[M\text{-}PF_6]^+$, 312.1 $[M\text{-}PF_6\text{-}HCl]^+$
MS (ESI negative, acetonitrile): m/z: 145.0 $[PF_6]^-$

Elemental analysis for $C_{12}H_{25}ClF_6FeN_4O_2P$ (493.61 g mol^{-1})
calculated (%): C 29.20, H 5.10, N 11.35, Cl 7.18
found (%): C 29.06, H 4.89, N 11.65, Cl 7.67

4.1.2. $[Fe^{III}(N_3)cyc\text{-}ac]PF_6$

NaN_3 (410 mg, 6.31 mmol) and $[Fe(Cl)cyc\text{-}ac]PF_6$ (1.046 g, 2.12 mmol) were suspended in acetonitrile (80 mL) and stirred at room temperature for 2 h. The red-brown solution was filtered, and the filtrate was evaporate under reduced pressure. The remaining solid was cooled with an ice bath (~0°C) and washed with methanol (3x1 mL) and diethyl ether (3x3 mL). After drying in vacuum for 1h a brown solid was obtained.

Yield: 830 mg (1.66 mmol, 78%)

IR (in KBr) [cm^{-1}]: 3433 (m, br), 3262 (m), 3231 (m), 3209 (m), 2962 (m), 2932 (m), 2882 (m), 2051 (vs, n(N3)), 1682 (vs,sh, ν(C=O)) 1663 (vs, ν(C=O)), 1470 (m), 1458 (m), 1435 (m), 1384 (w), 1341 (m), 1328 (m), 1299 (m,sh), 1284 (s), 1256 (m,sh), 1135 (w), 1106 (m,sh), 1095 (s), 1073 (sh), 1064 (m), 1042 (m), 1032 (s), 969 (w), 937 (m), 929 (m), 910 (w), 881 (s), 838 (vs, ν (PF_6)), 812 (s), 740 (m), 559 (s,PF_6), 538 (w), 522 (w), 489 (m), 429 (m), 408 (w)

MS (ESI positive,acetonitrile): m/z: 355.2 $[M\text{-}PF_6]^+$, 327.2 $[M\text{-}PF_6\text{-}N_2]^+$, 312.2 $[M\text{-}PF_6\text{-}HN_3]^+$

Elemental analysis for $C_{12}H_{25}F_6FeN_7O_2P$ (500.18 g mol^{-1})
calculated (%): C 28.82, H 5.04, N 19.60
found (%): C 28.95, 5.00, N 19.53.

4.1.3. $^{57}FeCl_3$-Precursor

Isotope ^{57}Fe enriched material was synthesized for the Mössbauer measurements. A small wire of pure ^{57}Fe (12 mg) was dissolved by heating in concentrated hydrochloric acid (5 mL) for 1h under air at 90°C. The hydrochloric acid was evaporated under reduced pressure, the residue was dissolved in hydrochloric acid (5 mL) and the solution was again heated at 90°C for 1h under air. After cooling down to room-temperature, the hydrochloric acid was evaporated under reduced pressure. For the synthesis of the complex $[^{57}Fe^{III}(Cl)cyc\text{-}ac]PF_6$, the $^{57}FeCl_3$ obtained was dissolved in absolute ethanol and transferred under argon via a filter-cannula to a Schlenk tube containing the ligand cyc-ac•4HCl•1.5H_2O. The Synthesis of $[^{57}Fe^{III}(Cl)cyc\text{-}ac]PF_6$ and $[^{57}Fe^{III}(N_3)cyc\text{-}ac]PF_6$ it was following the procedures described above.

4.2. Electronic Structure Calculations on Azido-Iron(III) Complexes

The structures of the complexes $[Fe^{III}(N_3)cyc\text{-}ac]^+$, $[Fe^{III}(N_3)_2cyc]^+$ and $[Fe^{III}(N_3)TMC\text{-}ac]^+$ are optimized by DFT (BP86/def2-TZVP/RI/COSMO(acetonitrile)). Selected bond-lengths and angles are provided in Table 4.1 and good agreement is found between the computed structures and those determined by X-ray crystallography.

Table 4.1: Selected experimental and calculated bond lengths and angles of azido-iron(III) complexes.

	$[Fe(N_3)cyc\text{-}ac]^+$		$[Fe(N_3)_2cyc]^+$				$[Fe(N_3)TMC\text{-}ac]^+$		
bond distance [Å]	calc.	exp.[43]	calc.		exp.[29]		calc. *S*=1/2	calc. *S*=5/2	exp.[42]
Fe-N_3	1.93	1.931	1.947	1.947	1.937	1.937	1.917	1.933	1.953
FeN-N_2	1.208	1.209	1.208	1.208	1.180	1.180	1.202	1.198	1.202
FeN_2-N	1.163	1.156	1.164	1.164	1.145	1.145	1.116	1.163	1.16
Fe-O/N	1.907	1.889	-	-	-	-	1.929	2.070	1.953
Fe-N_{eq}	2.053	2.028	2.036		2.004		2.067	2.193	2.129
Fe-N_{eq}	2.029	2.001	2.035		1.998		2.121	2.227	2.162
Fe-N_{eq}	2.03	2.007	2.036		2.004		2.078	2.174	2.129
Fe-N_{eq}	2.036	2.002	2.035		1.998		2.119	2.251	2.162
bond angle [°]									
N/O-Fe-N_3	175.48	172.74	180.00		180.0		174.82	176.09	180.00
Fe-N-N_2	134.61	131.80	131.85	131.85	129.5	129.5	140.77	173.37	147.78
N_3	175.36	175.7	175.62	175.62	176.4	176.4	175.12	179.66	177.98

Geometries of the complex $[Fe^{III}(N_3)TMC\text{-}ac]^+$ were optimized in the high-spin and low-spin state, since it has been reported previously that this complex undergoes a (partial) spin crossover at low temperature.[42,48] Comparison of the calculated geometric parameters for both considered spin states reveals that for both structures, agreement with the X-ray structure is inferior than it was found for the complexes $[Fe^{III}(N_3)cyc\text{-}ac]^+$ and $[Fe^{III}(N_3)_2cyc]^+$ (see Table 4.1). Besides the ambiguous spin state, the reason might also be the low quality XRD-data. Only disordered crystals were obtained and the crystal structure was solved in the space group $P2_1/n$ which results in a center of inversion in the iron atom. This of course introduces higher symmetry into the structure than possible, since the axial ligands are different and a center of inversion is not feasible. For this reason, identical Fe-O and Fe-N_3 bond distances were obtained experimentally, which is not necessarily true.

The low-spin state for $[Fe^{III}(N_3)TMC\text{-}ac]^+$ is calculated to be 22 kJ mol^{-1} higher in energy than the high-spin state. This relatively small splitting is very reasonable, since spin crossing behavior was observed for this complex experimentally.[42,48] The intermediate-spin state was calculated to be 29 kJ mol^{-1} higher in energy than the high-spin state (B3LYP/def2-TZVP/RIJCOSX/ COSMO(acetonitrile)).

Furthermore, the calculated Mössbauer parameters (B3LYP/def2-TZVP/Fe:CP(PPP)) are in good agreement with the previously published experimental data, and the data that was re-recorded for the $[Fe^{III}(N_3)cyc\text{-}ac]^+$ complex in this thesis work (see Table 4.2).

Table 4.2: Experimental and calculated Mössbauer parameters for iron(III) complexes.

Compound	*S*	calculated			experimental			Exp. Ref.
		δ [mm s^{-1}]	ΔE_Q [mm s^{-1}]	η	δ [mm s^{-1}]	ΔE_Q [mm s^{-1}]	η	
$[Fe^{III}(N_3)cyc\text{-}ac]^+$	1/2	0.26	-2.36	0.27	0.27	-2.53	0.40	[43]
					0.27	(-)2.30		[41]
					0.30[a]	-2.70[a]	0.42[a]	this work
$[Fe^{III}(N_3)_2cyc]^+$	1/2	0.27	-2.09	0.30	0.29	(-)2.26		[29]
$[Fe^{III}(N_3)TMC\text{-}ac]^+$	1/2	0.34	-2.07	0.28	0.33	(-)2.21		[42]
					0.34[a]	-2.43[a]	0.3[a]	[42]
	3/2	0.49	1.45	0.12				
	5/2	0.48	-1.10	0.58	0.35	(-)0.84		[42]
					0.42[a]	-0.32[a]	0[a]	[42]

a: Measurements at 4.2 K with applied magnetic field

Besides the DFT calculations, higher level complete active space self-consistent field (CASSCF) calculations were performed. Qualitatively, this gave similar results on the electronic structure as obtained from the DFT calculations. However, the CASSCF calculations in combination with n-electron valence perturbation theory (NEVPT2) allows to calculate the EPR g-values with much better accuracy (especially for transition metal complexes) than by DFT.[207] Furthermore, electronic excitations can be calculated much more accurate than within the framework of density functional theory.

In the active space for in the CASSCF calculations, all d-orbitals were included, four doubly occupied π-orbitals from the azide ligand(s) and two vacant π*-orbitals of the azide ligand(s). This results in an active space of 13 electrons in 11 orbitals. A plot of the active space orbitals is shown in Figure 4.1. Those π-orbitals of the azide ligand that lie perpendicular to the plane of the cyclam-ligand are labeled $\pi_\perp$ and can form an σ-bond e.g. with the d_{z^2}-orbital. Those π-orbitals that lie parallel to the cyclam plane are labeled $\pi_\perp$ and can form π-bonds e.g. with the d_{xz}- and d_{yz}-orbitals.

All three complexes show a $(d_{xy})^2(d_{yz})^2(d_{xz})^1$ electronic ground state configuration ($^2B_1$ state within C_{2v}-symmetry).[1] This electronic configuration is typical for low-spin iron(III) complexes in pseudo octahedral coordination with axial elongation, that moves the d_{xy}-orbital below the d_{xz}- and d_{yz}-orbitals and further rhombic distortion lifts the degeneracy of the d_{xz}- and d_{yz}-orbitals.

[1] The $(d_{xy})^2(d_{xz})^2(d_{yz})^1$ electronic configuration is of course equivalent to that, it is obtained by interchanging the x- and y-axis.

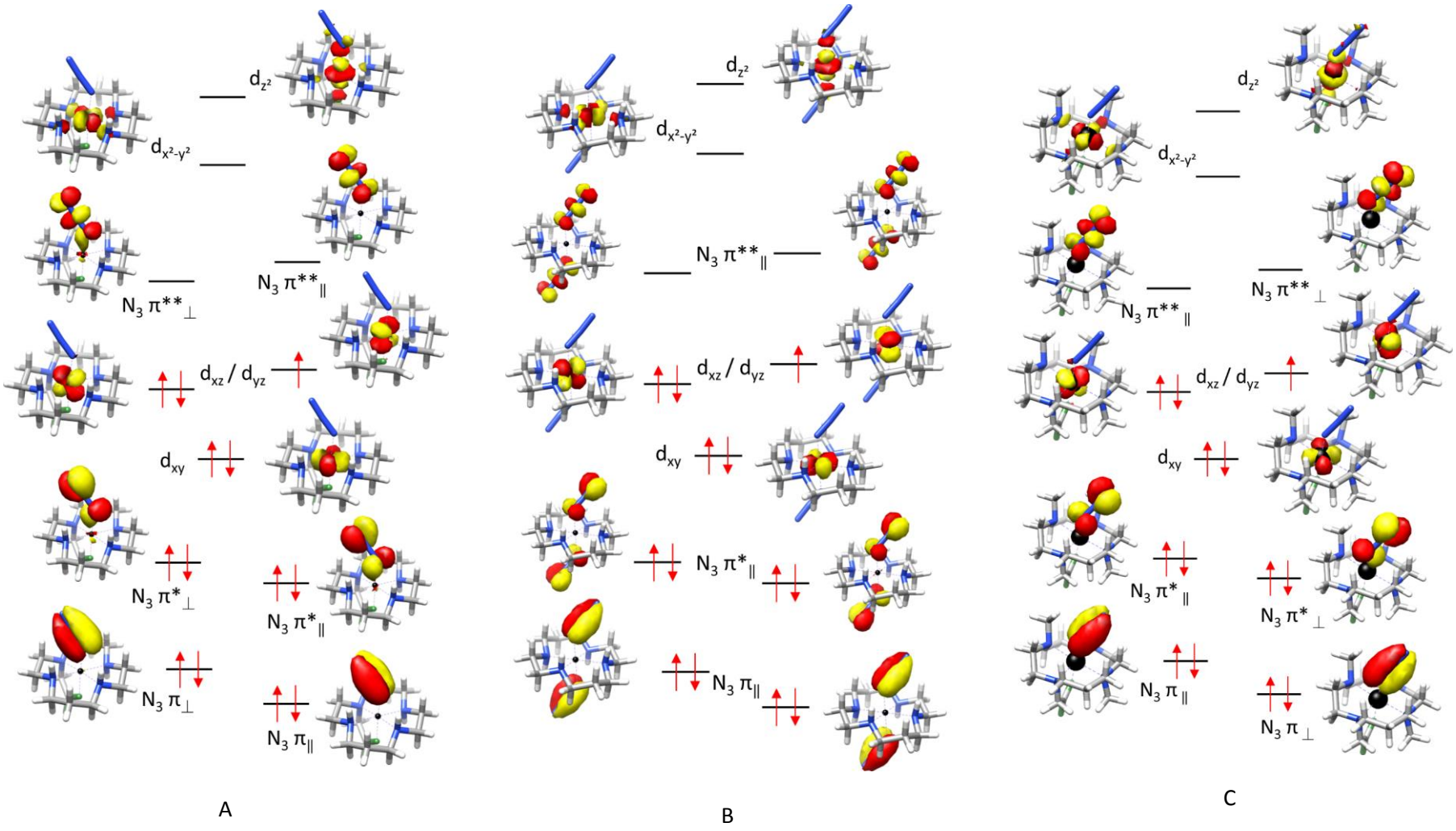

Figure 4.1: Active space orbitals from CASSCF(13,11) calculations on $[Fe^{III}(N_3)cyc\text{-}ac]^+$ (A), $[Fe^{III}(N_3)_2cyc]^+$ (B) and $[Fe^{III}(N_3)TMC\text{-}ac]^+$ (C) with outlined ground state configuration.

The lowest excited state was calculated to be $^2B_2[d_{yz} \rightarrow d_{xz}]$ resulting from a transition of a β-electron from the d_{yz}- into the d_{xz}-orbital and the second excited state $^2A_2[d_{xy} \rightarrow d_{xz}]$ results from elevating a β-electron from the d_{xy}-orbital into the singly-occupied d_{xz}-orbital (see Table 4.3). In perfect O_h-symmetry these complexes would exhibit a triply degenerated $^2T_{2g}$ ground-state.

EPR-spectra of the complexes $[Fe^{III}(N_3)cyc\text{-}ac]^+$, $[Fe^{III}(N_3)_2cyc]^+$ and $[Fe^{III}(N_3)TMC\text{-}ac]^+$ will be discussed in Chapter 5.4. In anticipating these results, the g-values are provided in Table 4.3 together with those obtained from the CASSCF/NEVPT2 calculations. The calculated g-values are in very good agreement to the experimental ones.

Table 4.3: CASSCF(13,11)/NEVPT2 calculated lowest excited states and g-values for Fe^{III} low-spin complexes

	$^2B_2$ $(d_{xy})^2(d_{xz})^2(d_{yz})^1$ [cm^{-1}]	$^2A_2$ $(d_{yz})^2(d_{xz})^2(d_{xy})^1$ [cm^{-1}]	calculated			experimental		
			g_1	g_2	g_3	g_1	g_2	g_3
$[Fe^{III}(N_3)cyc\text{-}ac]^+$	2158	4471	1.83	2.22	2.67	1.81	2.29	2.60
$[Fe^{III}(N_3)_2cyc]^+$	2230	4092	1.85	2.24	2.65	1.85	2.31	2.54
$[Fe^{III}(N_3)TMC\text{-}ac]^+$	1355	4270	1.68	2.10	3.20	1.78[a]	2.26[a]	2.70[a]

a: Experimental g-values taken from Berry, Bill, Bothe, Neese, Wieghardt, *J. Am. Chem. Soc.* **2006**, *128*, 13515.

Experimental structures, g-values and Mössbauer parameters of the azido-iron(III) complexes are very well reproduced by the quantum chemical calculations. These experimental spectroscopic parameters have been studied previously, but the calculations performed here demonstrates the predictive power of the used theoretical methods. New spectroscopic data will be presented in the following chapters, accompanied with calculations that will provide further insight and a deeper understanding of experimental results.

4.3. Absorption Spectra of Azido-Iron(III) Complexes at Room Temperature

The photolysis of azido-iron(III) complexes is studied in the present work and therefore the absorption spectra are of special relevance, since they provide insight in electronic transitions that can be induced by irradiation. Assignment of observed bands will be supported by TD-DFT calculations. Attempts were further made to calculate the absorption spectra with the CASSCF/NEVPT2 method. However, reasonable prediction of the LMCT-states was not possible, which is known to be a potential problem in CASSCF calculations.[195]

Room temperature spectra are discussed here and the UV-*vis* spectra obtained at low temperature from frozen solutions as well as the photolysis of these samples will be discussed in the next chapter (Chapter 4.4).

4.3.1. The Complex $[Fe^{III}(N_3)cyc\text{-}ac]^+$

Room temperature absorption spectra were recorded from 1mM acetonitrile solutions in 1mm quartz cells and the acetonitrile background was subtracted from the resulting spectra. In Figure 4.2, results for the complex $[Fe^{III}(N_3)cyc\text{-}ac]PF_6$ are shown. The spectrum was decomposed into Gaussian bands (in blue, sum of the Gaussian functions in red) and the result of this decomposition is summarized in Table 4.4. Arrows in Figure 4.2 indicate wavelengths that will be used for resonance Raman measurements (514 nm) and photolysis experiments (470 nm, 304 nm, 266 nm) in the present work.

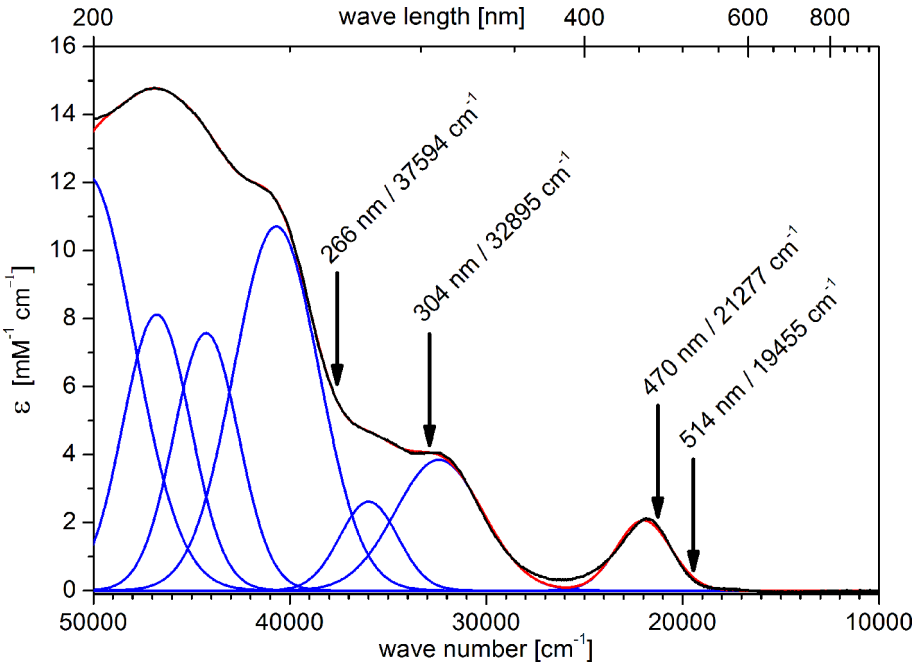

Figure 4.2: Room temperature UV-*vis* spectrum of $[Fe^{III}(N_3)cyc\text{-}ac]PF_6$ in acetonitrile solution (black) and decomposition in single Gaussian bands (blue; in red: sum of the Gaussian functions). Arrows indicate wavelengths used for resonance Raman measurements (514 nm) and photolysis experiments (470 nm, 304 nm, 266 nm).

Table 4.4: Result from Gaussian deconvolution of the UV-*vis* spectrum of $[Fe^{III}(N_3)cyc\text{-}ac]PF_6$.

Excitation	ε	f_{osc}	FWHM
[cm^{-1}]	[M^{-1} cm^{-1}]		[cm^{-1}]
21895	2120	0.0304	3220
32108	3960	0.0869	5042
35861	4640	0.0491	3695
40598	11320	0.2504	5072
44227	13560	0.1349	3850
46730	14780	0.1537	4018
50221	13900	0.3094	5528

The complex $[Fe^{III}(N_3)cyc\text{-}ac]^+$ shows an isolated absorption at 21895 cm^{-1} (458 nm, ε=2120 M^{-1} cm^{-1}), as seen in Figure 4.2 and previously reported in the literature.[43] Even higher molar absorptions are usually expected for LMCT-transitions (ε>10 $mM^{-1}cm^{-1}$),[208] this band presumably results from an transition from the azide ligand to the iron center. This will be verified by resonance Raman measurements in Chapter 4.5.1. Further signals were observed at higher energy and decomposed in Gaussian bands at 32108 cm^{-1}, 35861 cm^{-1} and 40698 cm^{-1}, respectively. However, bands from 40000 cm^{-1} on strongly overlap and a decomposition in Gaussian functions is difficult. Attempts were also made to measure the UV-*vis* spectrum of the $[Fe^{III}(Cl)cyc\text{-}ac]PF_6$ precursor under identical conditions. This would allow to identify the LMCT-bands that result from the azide ligand since LMCT-bands from the chloride ligand are expected to appear at much higher energy. However, strong concentration dependence was observed in the UV-*vis* spectra which is a clear sign that the complex is not stable in solution. Similar behavior was observed when it was tried to measure the EPR-spectrum of $[Fe^{III}(Cl)cyc\text{-}ac]PF_6$ in solution. Presumably, the chloride ligand is more labile than the azido ligand and undergoes a substitution reaction with solvent molecules in solution.

TD-DFT calculations were performed to gain insight into the nature of the observed bands. In Table 4.5 difference density plots are provided and in Figure 4.3 the experimental spectrum is shown together with the calculated oscillator strengths indicated by blue bars. In very good agreement with the experimentally observed band at 21824 cm^{-1}, an intense band was calculated to appear at 22533 cm^{-1}. The difference density plot for this transition (see Table 4.5) identifies it as a LMCT-transition from the azide ligand π-system to the metal. The donating π-orbital lies parallel to the plane of the equatorial cyclam ligand and is therefore labeled by $\pi_{\parallel}$ as it was done in Figure 4.1, the singly occupied orbital (SOMO) d_{xz} is the accepting orbital for this LMCT-transition.

The experimental band at 32108 cm^{-1} does, referring to the TD-DFT calculations, result from a $\pi_{\perp}(N_3) \rightarrow d_{z^2}$ transition that was calculated to appear at 30389 cm^{-1}. At 34319 cm^{-1} a LMCT-transition from the carboxylate group to the iron-center was calculated that might be assigned to the experimental band observed at 35861 cm^{-1}.

Table 4.5: Difference density plots from TD-DFT calculations on the complex $[Fe^{III}(N_3)cyc\text{-}ac]^+$ (red:negative, yellow:positive), calculated transition energies, oscillator strengths (f_{osc}) and description of the electronic transition.

	calculated transition (f_{osc})	main character
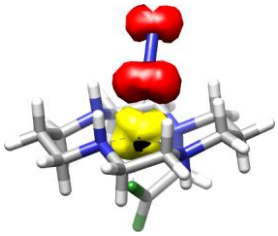	23140 cm^{-1} (0.0294) exp.: 21895 cm^{-1} (0.0304)	$\pi_{\parallel}(N_3) \rightarrow d_{xz/yz}$ (SOMO)
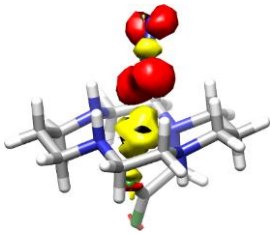	30389 cm^{-1} (0.0107) exp.: 32108 cm^{-1} (0.0869)	$\pi_{\perp}(N_3) \rightarrow d_{z^2}$
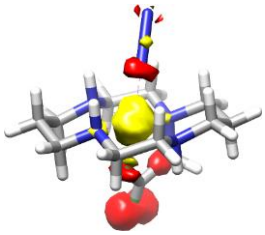	34319 cm^{-1} (0.0177) exp: 35861 cm^{-1} (0.0491)	$\pi(\text{-}CO_2) \rightarrow d_{x^2-y^2} + d_{z^2}$
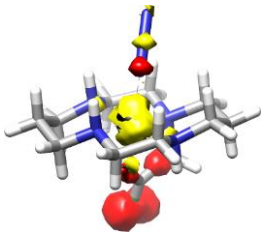	37427 cm^{-1} (0.0476)	$\pi(\text{-}CO_2) \rightarrow d_{z^2}$
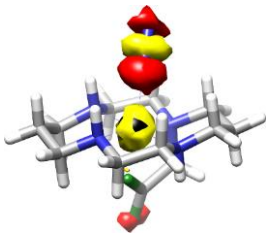	38958 cm^{-1} (0.0352)	$\pi_{\perp}(N_3) \rightarrow \pi^*(N_3) + d_{z^2}$
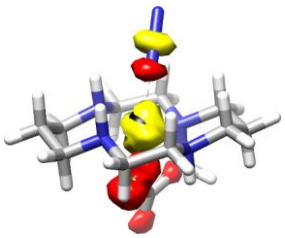	41401 cm^{-1} (0.0624)	$\pi(\text{-}CO_2) \rightarrow d_{z^2}$
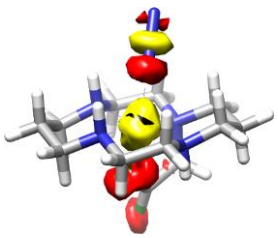	41828 cm^{-1} (0.0486)	$\pi(\text{-}CO_2) \rightarrow d_{z^2}$

The assignment of experimentally observed bands above 40000 cm^{-1} is difficult since several bands seem to overlap in this region. A band with high intensity was included in the fit at 40598 cm^{-1}, however, this absorption might be a superposition of two or more bands. Several transitions were also calculated to appear in the 35000 cm^{-1}-45000 cm^{-1} region. A LMCT transitions from the carboxylate group to the metal $\pi(CO_2)\rightarrow d_{z^2}$ was calculated to appear at 37427 cm^{-1} and a mixture of LMCT $\pi_{\perp}(N_3)\rightarrow d_{z^2}$ and intra-ligand-transition $\pi_{\perp}(N_3)\rightarrow\pi^*(N_3)$ was calculated to appear at 38958 cm^{-1}, respectively (see Table 4.5). At 41401 cm^{-1} and 41828 cm^{-1}, two very similar transitions from the carboxylate-group to the metal d_{z^2}-orbital were calculated. However, the experimental spectrum was decomposed in one Gaussian function at 40598 cm^{-1} for this region.

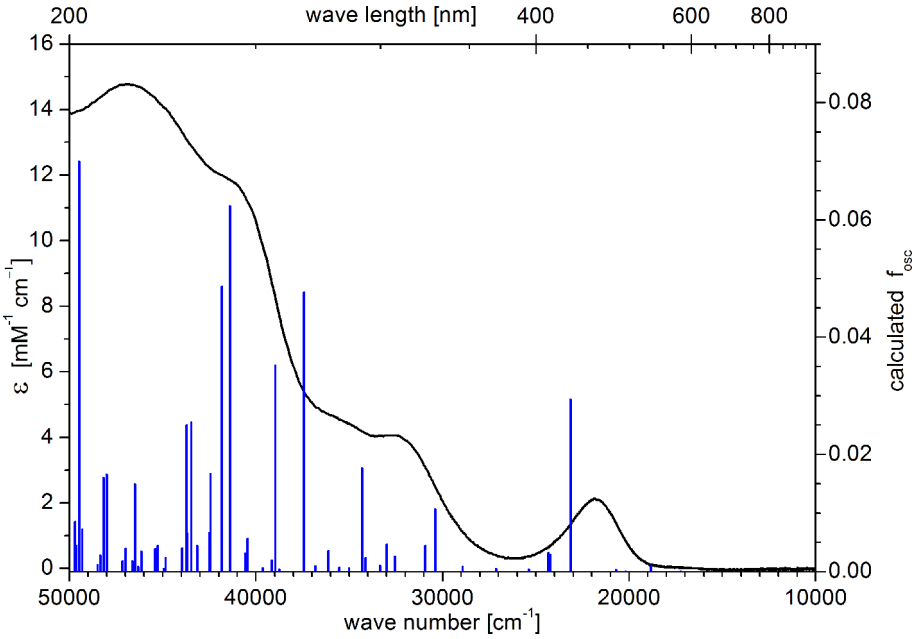

Figure 4.3: Experimental absorption spectrum of $[Fe^{III}(N_3)cyc\text{-}ac]PF_6$ in acetonitrile at room temperature (black) and calculated (B3LYP/def2-TZVP/RIJCOSX) oscillator strengths (blue).

The calculations clearly support the assignment of the experimentally observed band at 21895 cm^{-1} to a LMCT-band from the azide ligand to the metal center. This will be further verified by resonance Raman measurements in Chapter 4.5.1. TD-DFT calculations further reveal, that transitions at higher energy result from additional azide ligand to metal transitions, but carboxylate to metal transitions also play an important role in the explanation of the experimental spectrum.

In the photolysis experiments, light with 470 nm wavelength will be used. The discussed TD-DFT results suggest that 470 nm (21277 cm^{-1}) encounters the LMCT-transition from the $\pi_{\parallel}(N_3)$-orbital to metal the $d_{xz/yz}$-orbital. In the photolysis experiment with 304 nm (32895 cm^{-1}) light, presumably a transition from the $\pi_{\perp}(N_3)$-orbital into the metal d_{z^2}-orbital is induced which was calculated by TD-DFT to appear at 30389 cm^{-1}. 266 nm light used in the time resolved IR measurements (see Chapter 4.5.3) lies between the bands at 35861 cm^{-1} (279 nm) and 40598 cm^{-1} (246 nm) that resulted from a Gaussian decomposition of the experimental spectrum. The performed calculations suggest that the observed transition at 35861 cm^{-1} results from a LMCT-transition from the carboxylate group to the metal. Assignment of the band at 40598 cm^{-1} is more difficult. It might also result from a carboxylate to metal transition, or a transition from the azide ligand to the metal and partially to a ligand π^*-orbital. Hence, the nature of the electronic transitions induced by a 266 nm laser is unfortunately not known, besides the fact that it is a LMCT transition.

4.3.2. The Complex $[Fe^{III}(N_3)_2cyc]^+$

Under the same conditions as discussed above for the complex $[Fe^{III}(N_3)cyc\text{-}ac]PF_6$ (room temperature, acetonitrile solution), the UV-*vis* absorption spectrum for the bis-azido complex $[Fe^{III}(N_3)_2cyc]ClO_4$ was recorded. The spectrum and the decomposition into Gaussian functions is shown in Figure 4.4, results of the decomposition are provided in Table 4.6. Arrows in Figure 4.4 indicate wavelengths that are used for resonance Raman measurements (514 nm) and photolysis experiments (470 nm).

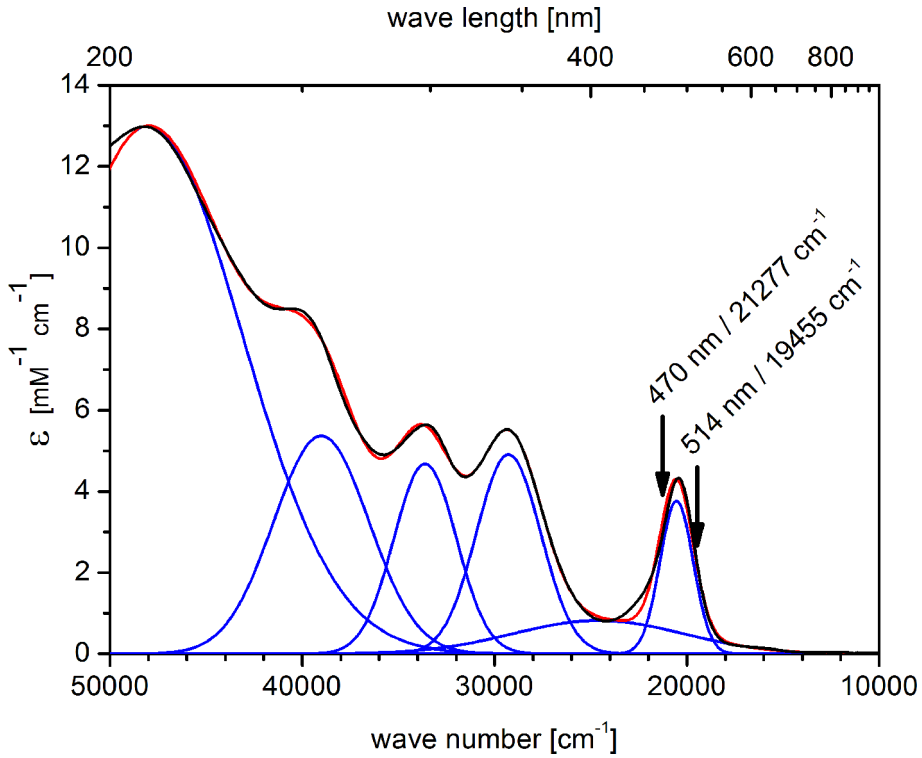

Figure 4.4: Room temperature UV-*vis* spectrum of $[Fe^{III}(N_3)_2cyc]ClO_4$ in acetonitrile (black) and decomposition in Gaussian bands (red: sum of the Gaussian functions). Arrows indicate wavelengths used for resonance Raman measurements (514 nm) and photolysis experiments (470 nm).

Table 4.6: Result from Gaussian deconvolution of the UV-*vis* spectrum of $[Fe^{III}(N_3)_2cyc]ClO_4$ (Figure 4.4.)

Excitation [cm^{-1}]	ε [M^{-1} cm^{-1}]	fosc	FWHM [cm^{-1}]
20499	4310	0.0352	2037
23784	840	0.0389	10576
29182	5497	0.0889	3948
33533	5640	0.0822	3825
38849	7660	0.1443	5857
47507	12890	0.6860	11539

Again, an isolated band in the visible region is observed (20499 cm^{-1}/488 nm) as reported previously,[29] only slightly lower in energy than for the mono-azido complex $[Fe^{III}(N_3)cyc\text{-}ac]PF_6$ (21895 cm^{-1}). This band presumably results from a LMCT-transition from the azide ligand to the metal. A very broad band with low intensity had to be included at 23784 cm^{-1} for a reasonable fit of the spectrum but it is not clear if this results from the sample or is a problem e.g. from the subtracted background. The bands on the higher energy side again overlap, however, they are more separated from each other than in the complex $[Fe^{III}(N_3)cyc\text{-}ac]^+$, which facilitates the decomposition into Gaussian functions. Bands of similar intensity were observed at 29182 cm^{-1}, 33533 cm^{-1} and 38849 cm^{-1}.

The experimental results are again combined with TD-DFT calculations (B3LYP/def2-TZVP/RIJCOSX/COSMO) to support the assignment of observed bands. Calculated oscillator strengths together with the experimental spectrum are shown in Figure 4.5. Difference density plots for the four most intense calculated transitions are provided in Table 4.7.

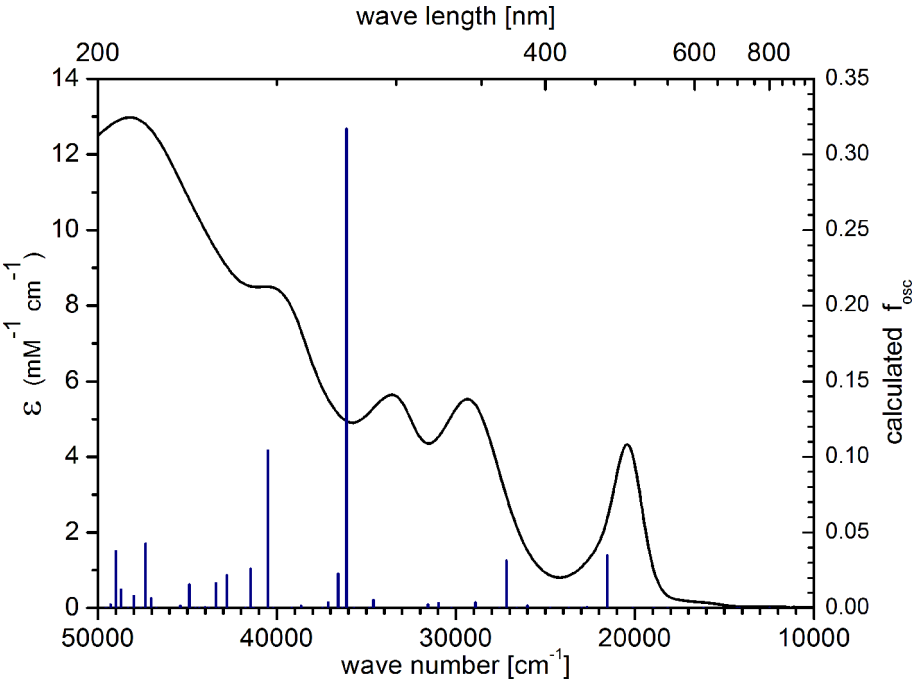

Figure 4.5: Experimental (black) and calculated (blue bars, oscillator strength) absorption spectrum of $[Fe^{III}(N_3)_2cyc]ClO_4$

A transition with significant intensity is calculated to appear at 21537 cm^{-1}, in good agreement with the experimentally observed band at 20499 cm^{-1}. As also predicted by the TD-DFT calculations for the mono azido complex $[Fe^{III}(N_3)cyc\text{-}ac]PF_6$, this band results from a LMCT-transition from the azido $\pi_{\parallel}$-orbital to the singly occupied d_{xz}-metal orbital (see Table 4.7).

A transition from the azide ligand ($\pi_{\perp}$-orbital) into the metal d_{z^2}-orbital was calculated to appear at 27185 cm^{-1}, which is in reasonable agreement with the band observed at 29182 cm^{-1} in the experimental spectrum. A band of very similar nature was calculated to appear at 36103 cm^{-1} (see Table 4.7). The calculated oscillator strength is very high, however, the position is in reasonable agreement with the experimentally observed band at 33533 cm^{-1}. Presumably, in the calculations the oscillator strength for this transition is strongly overestimated. Analog transitions ($\pi_{\perp} \rightarrow d_{z^2}$) were calculated for the mono-azido complex $[Fe^{III}(N_3)cyc\text{-}ac]^+$ at slightly lower energy, 30389 cm^{-1} and 38958 cm^{-1}, respectively.

An azido intra-ligand transition ($\pi \rightarrow \pi^*$) was calculated to be at 40510 cm^{-1}, which is in good agreement with the experimentally observed band at 38849 cm^{-1}. In the mono-azido complex $[Fe^{III}(N_3)cyc\text{-}ac]^+$, a similar band was calculated to appear at almost identical energy, 38958 cm^{-1}. Intra ligand $\pi \rightarrow \pi^*$ transitions in the 30000 cm^{-1} – 40000 cm^{-1} range have also been reported for various azido-manganese and -chromium complexes previously.[9-10]

Table 4.7: Difference density plots from TD-DFT calculations on the complex $[Fe^{III}(N_3)_2cyc]^+$ (red:negative, yellow:positive), calculated transition energies, oscillator strengths (f_{osc}) and description of the transition.

	calculated transition (f_{osc})	main character
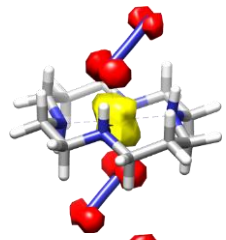	21537 cm^{-1} (0.0346) exp.: 20499 cm^{-1} (0.0352)	$\pi_{\parallel}(N_3) \rightarrow d_{xz/yz}$ (SOMO)
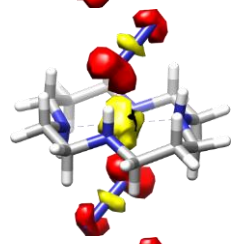	27185 cm^{-1} (0.0314) exp.: 29182 cm^{-1} (0.0889)	$\pi_{\perp}(N_3) \rightarrow d_{z^2}$
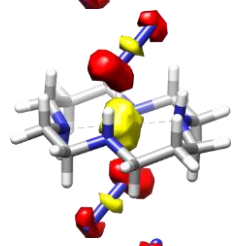	36103 cm^{-1} (0.3171) exp.: 33533 cm^{-1} (0.0822)	$\pi_{\perp}(N_3) \rightarrow d_{z^2}$
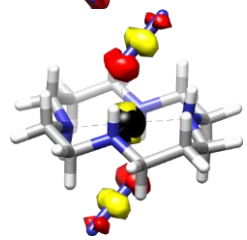	40510 cm^{-1} (0.1040) exp.: 38849 cm^{-1} (0.1443)	$\pi_{\parallel}(N_3) \rightarrow \pi^*(N_3)$

Individual band positions for the mono-azido-complex $[Fe^{III}(N_3)cyc\text{-}ac]PF_6$ and the bis-azido-complex $[Fe^{III}(N_3)cyc]ClO_4$ differ, however, strong analogy can be found in the absorption spectra. Most striking is the isolated band in the visible region that, based on the TD-DFT calculations, can be assigned to a LMCT-transition from the azide ligand to the singly occupied metal d-orbital. For both complexes it has been reported before, that irradiation into this band leads to elimination of N_2 and formation of an nitrido-iron(V) species.[29,43] To get further insight in the processes that are initiated by light that coincides with this band, resonance Raman measurements are performed and will be discussed in Chapter 4.5.

At higher energy, for both complexes LMCT-transitions from the azide ligand to the metal d_{z^2}-orbital are predicted by TD-DFT and bands at the corresponding positions can be found in the experimental spectra. Furthermore, azido intra-ligand transitions ($\pi \rightarrow \pi^*$) were calculated and LMCT-transitions from the carboxylate-group to the metal center for the complex $[Fe^{III}(N_3)cyc\text{-}ac]PF_6$.

In particular for the complex $[Fe^{III}(N_3)cyc\text{-}ac]PF_6$ understanding the nature of transitions at higher energy is crucial, since for this complex photolysis experiments with a wavelength of 304 nm and 266 nm were performed (see Chapter 4.5.3 and Chapter 4.6.2). The assignment of these bands allows therefore a deeper understanding of the processes that take place upon photolysis with light in this region.

4.4. Absorption Spectra and Photolysis of Azido-Iron(III) Complexes at Low Temperature

UV-*vis* spectra were also recorded at low temperature on frozen solution samples. In certain cases, this allows to observe vibronic coupling, the coupling between electronic transitions and vibrational motions. Further, it is possible to photolyze the sample and to record absorption spectra of the resulting species. It will be shown by Mössbauer spectroscopy (Chapter 4.6.1), EPR-spectroscopy (Chapter 5.4) and has been reported in the literature[41,43,45] that photolysis of frozen solution samples with 470 nm light results in the nitrido-iron(V) complex $[Fe^{V}(N)cyc\text{-}ac]^{+}$.

To get a transparent sample, solvents had to be used that form a glass upon freezing. In the present case, samples of ~1mM concentration were prepared in a 1:9 mixture of ethanol and methanol. The solution was prepared in a glove box under inert N_2-atmosphere and degassed by freezing the solution with liquid nitrogen, applying vacuum on the frozen solution, and allowing the solution to thaw again. This "freeze-and-pump" procedure was repeated two times. The solution was then transferred in a 1mm UV-*vis* cell and immediately frozen with liquid nitrogen outside the glove-box. Measurements were performed by placing the sample in an Oxford-Instruments cryostat cooled by liquid nitrogen and equipped with quartz glass windows. The photolysis was performed with a 560mW LED lamp emitting light of 470 nm while the sample was kept in the cryostat. Correction of the recorded data for the effect of scattering did not significantly improve the results. Therefore, the raw data is presented here which allows a good qualitative analysis.

4.4.1. The Complex $[Fe^{III}(N_3)cyc\text{-}ac]PF_6$

The UV-*vis* spectrum of the complex $[Fe^{III}(N_3)cyc\text{-}ac]PF_6$ recorded at 80K is shown in Figure 4.6 (black trace). No significant differences between the low temperature and room temperature spectra are observed (compare Figure 4.2), no effects of vibronic coupling are present. After photolysis of the sample in the cryostat with 470 nm light for 30 min, the band in the visible region (21895 cm^{-1}) completely disappeared. This is in line with the expectations since it is assumed to result from an LMCT-transition of the azide ligand to the metal and the azide ligand is expected to be transformed into a nitrido-group by release of dinitrogen. Absorption bands observed at higher energy (30000 cm^{-1} – 40000 cm^{-1}) also disappeared after the photolysis process. This can be partially explained by the elimination of the azide ligand. However, the band at 40598 cm^{-1} for the azido-complex was assumed to result from a transition from the carboxylate-group to the metal and given that the carboxylate group is not affected in the photolysis,[41,45] LMCT-bands from the carboxylate-group to the metal center might be expected.

dd-transitions calculated by the CASSCF/NEVPT2 method for the resulting complex $[Fe^{V}(N)cyc\text{-}ac]^{+}$ will be discussed in detail in Chapter 5.5.2, page 131. It will be shown that the $^2A_2[a_1(d_{xy})\rightarrow b_2(\pi_y^*)]$ transition is expected at 19358 cm^{-1} and the $^2A_1[b_2(\pi_y^*)\rightarrow a_1(d_{z^2})]$ transition at 16959 cm^{-1}. Due to

covalency these transitions are expected to show the highest intensity among the dd-transitions. However, it was not possible to identify any bands in this region in the experimental spectrum.

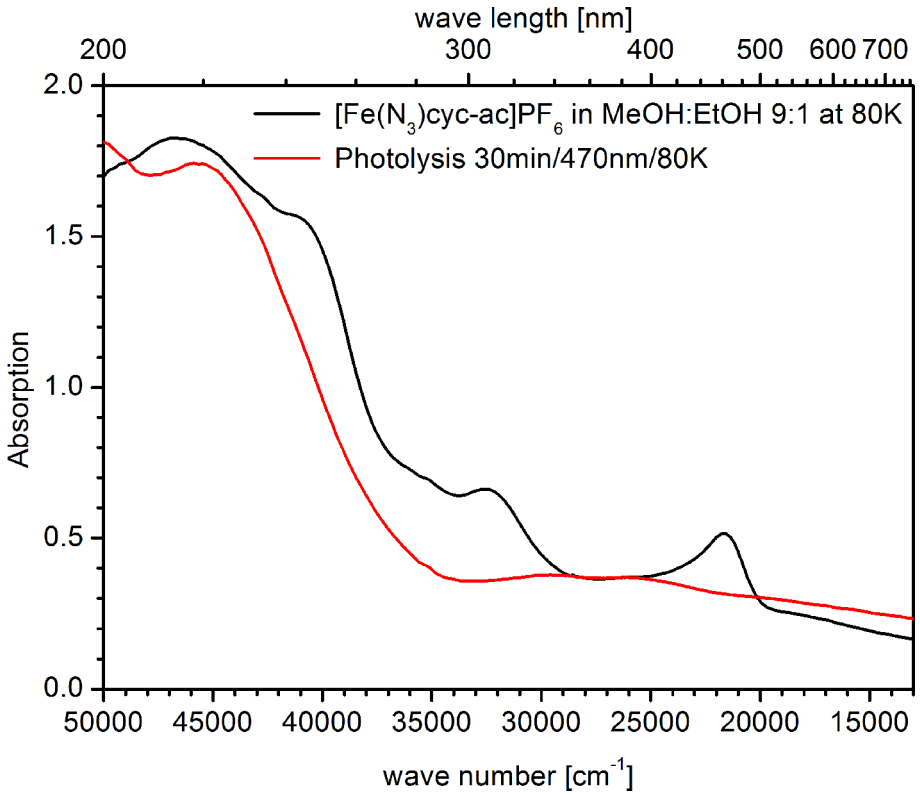

Figure 4.6: UV-*vis* spectrum of $[Fe^{III}(N_3)cyc\text{-}ac]PF_6$ in ~1mM in MeOH:EtOH solution at 80K before (black) and after (red) photolysis with 470nm light.

The absence of significant bands for the nitrido-iron(V) complex is still in agree with the qualitative observation during the photolysis of EPR-, Mössbauer- or the UV-*vis* samples. The initially slightly yellow frozen solution samples are completely bleached during the photolysis and a white sample is obtained after the photolysis has been completed. Therefore, resonance Raman measurements on the nitrido-iron(V) complex will be difficult, if not impossible, since there are no absorption bands that can be used for laser excitation.

4.4.2. The Complex $[Fe^{III}(N_3)_2cyc]ClO_4$

The absorption spectrum for the complex $[Fe^{III}(N_3)_2cyc]ClO_4$ recorded in Methanol:Ethanol 9:1 at 80K is shown in Figure 4.7 (black curve). Again, the spectrum is nearly identical to the one obtained at room temperature in acetonitrile solution (see Figure 4.4). No vibronic coupling is observed. After photolysis with 470 nm light for 60 min the bands observed for the azido-iron(III)-complex completely vanish (red curve in Figure 4.7) as it was also the case for the $[Fe^{III}(N_3)cyc\text{-}ac]PF_6$ complex.

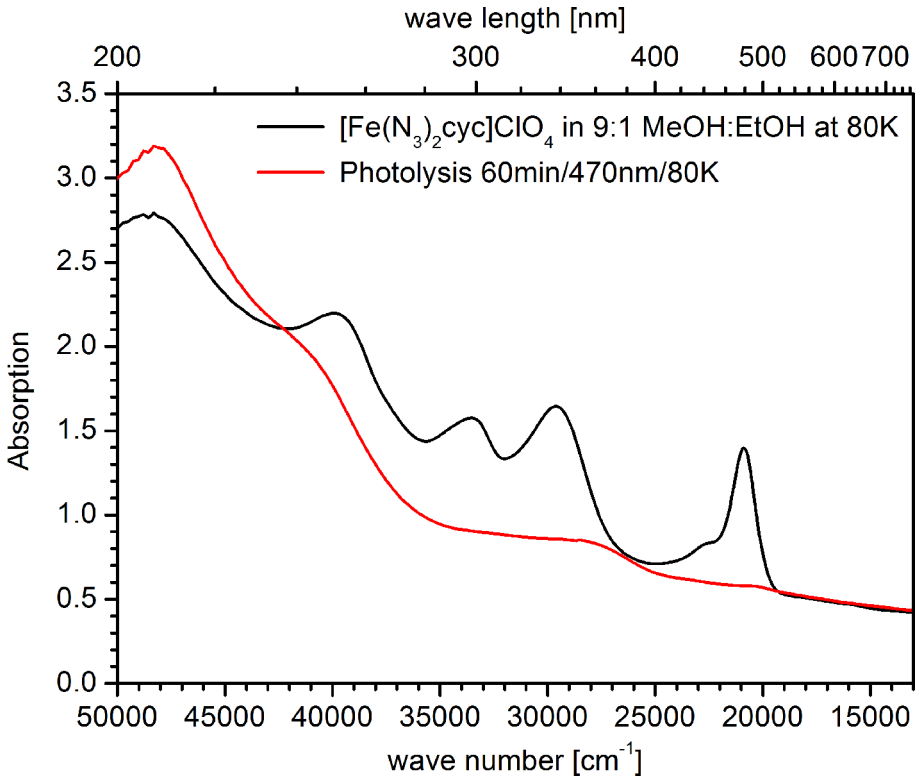

Figure 4.7: UV-*vis* spectrum of $[Fe^{III}(N_3)_2cyc]ClO_4$ 1mM in MeOH:EtOH solution at 80K before (black) and after (red) photolysis with 470nm light.

In anticipating results from CASSCF/NEVPT2 calculations on the complex $[Fe^{V}(N)(N_3)cyc]^+$ (Chapter 5.5.2, page 131), it is noted that the most intense dd-transitions $^2A_2[a_1(d_{xy})\rightarrow b_2(\pi_y^*)]$ and $^2A_1[b_2(\pi_y^*)\rightarrow a_1(d_{z^2})]$ were calculated to be 19949 cm^{-1} and 17567 cm^{-1}, respectively. However, no significant bands are observed in this region experimentally.

This again agrees with the qualitative observations made during the preparation of EPR- and UV-*vis*-samples that turned completely white after the photolysis has been completed, while the initial azido-iron(III) complex in frozen solution is slightly yellow/orange. However, the absence of any absorption bands again prevents the measurement of resonance Raman spectra on the nitrido-iron(V) complex $[Fe^{V}(N)(N_3)cyc]^+$.

4.5. Vibrational Spectroscopy on Azido-Iron(III) Complexes

Azide ligands show several characteristic bands in their IR spectrum and further vibrations can be identified by (resonance) Raman spectroscopy. While IR spectroscopy on the complexes $[Fe^{III}(N_3)cyc\text{-}ac]PF_6$ and $[Fe^{III}(N_3)_2cyc]ClO_4$ provides basic information on the structure of these species, more insight in the processes that proceed upon photo excitation is obtained by resonance Raman spectroscopy.

High-valent nitrido-iron(V) species studied in the present work are obtained by photolysis of azido-iron(III) complexes and resonance Raman spectroscopy on the iron(III) precursors can provide valuable information about the underlying processes. The azido-iron(III) complexes are transformed into nitrido-iron(V) complexes by photolysis with 470 nm light, as will be shown in more detail in Chapter 4.6.1, Chapter 5.4 and has been reported previously.[29,41,43,45]

The complexes $[Fe^{III}(N_3)cyc\text{-}ac]PF_6$ and $[Fe^{III}(N_3)cyc]ClO_4$ show absorption bands at 458 nm (21895 cm^{-1}) and 488 nm (20499 cm^{-1}), respectively (see Chapter 4.3). TD-DFT calculations discussed in Chapter 4.3 suggested that these bands result from LMCT-transitions from the azide ligand(s) to the metal center. In the initial studies on these systems[29,43] it was assumed that irradiation into these bands induces the elimination of N_2 and the formation of high-valent nitrido species.

As outlined in the introductory Chapter 2.3, high intensity is found in resonance Raman measurements for modes that mimic the deformation of the molecule upon electronic excitation,[114,116] and therefore intense signals are expected upon irradiation into these bands that originate from azide modes. However, if the electronic excited state is of dissociative nature (e.g. with respect to N_2-elimination), detection of resonance Raman signals can be difficult, as outlined in the introduction (Chapter 2.3).

Given that azido-iron(III) complexes are photo labile, the excitation wavelength for the resonance Raman experiments was chosen in a way that it does not hit the maximum of the visible absorption of interest, but the tail of the absorption band on the lower energy side at 514 nm (so called pre-resonance Raman spectroscopy). This way it was tried to avoid irradiation damage of the samples during the measurements.

Experimental results will be combined with DFT calculations to support the assignment of experimentally observed signals. Frequency and TD-DFT calculations in this chapter were performed with the B3LYP functional, the def2-TZVP basis set and the corresponding auxiliary basis set for the RIJCOSX approximation. In Chapter 4.3 it was already shown for both complexes considered here, that an intense signal in the visible region is very well reproduced by TD-DFT calculations, which is required to calculate resonance Raman spectra properly. A scaling factor of 0.9614 was applied on the calculated harmonic modes to compare them with the experimental fundamentals.[186]

4.5.1. IR and Resonance Raman Spectroscopy on the Complex $[Fe^{III}(N_3)cyc\text{-}ac]PF_6$

Azide anions show 3N-5 = 4 normal modes. One antisymmetric ($\nu_{as}(N_3)$) and one symmetric stretching mode ($\nu_s(N_3)$) as well as two degenerate bending modes. When the azide anion is coordinated to a metal in an end-on and bent fashion, these two bending modes are described as in plane $\delta_{ip}(N_3)$ and out-of-plane $\delta_{op}(N_3)$ modes. The four azido normal modes will also be present in azides that are bond to a transition metal. Coordination of the azide anion to the metal gives rise to further stretching and bending modes between the metal and ligand ($\nu(Fe\text{-}N_3)$ and $\delta(Fe\text{-}N_3)$). For the O-Fe-N_3 fragment, 3N-6=9 normal modes are expected, that are spanned by 7A'+2A'' in C_s symmetry for the complex $[Fe^{III}(N_3)cyc\text{-}ac]^+$, that does not show any symmetry element besides a mirror plane.[209] Both, A' and A'' vibrations are IR- and Raman active, respectively.

IR Spectroscopy

IR samples were prepared as KBr disks from ~200 mg KBr (stored at 110°C prior usage for drying) and ~2 mg of the sample. Recorded spectra were baseline corrected and manually normalized to show the same intensity for the natural- and ^{15}N-isotope samples. Resulting IR spectra of $[Fe^{III}(N_3)cyc\text{-}ac]PF_6$ and $[Fe^{III}(^{15}NN_2)cyc\text{-}ac]PF_6$ are shown in Figure 4.8. Peaks at 835 cm^{-1} and 560 cm^{-1} originate from the PF_6^- counter anion and are indicated by asterisks.[210]

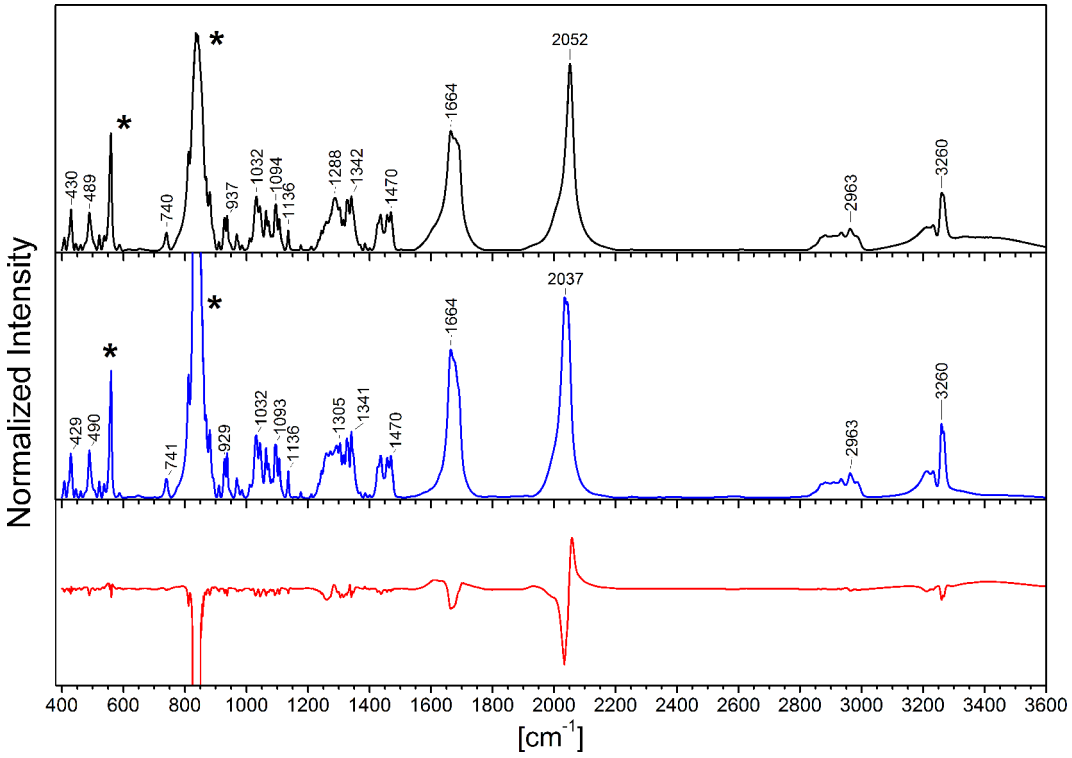

Figure 4.8: IR spectrum of $[Fe^{III}(N_3)cyc\text{-}ac]PF_6$ in black, $[Fe^{III}(^{15}NN_2)cyc\text{-}ac]PF_6$ in blue and the difference spectrum in red.

The signals at 3260 cm^{-1} and around 3230 cm^{-1} are typical for the N-H stretching vibrations of amine ligands,[211] signals between 2850 cm^{-1} and 3000 cm^{-1} are characteristic for C-H stretching vibrations.[211] Both can be assigned to the organic ligand. The intense signal at 2052 cm^{-1} shows an isotope shift (from

2052 cm^{-1} to 2037 cm^{-1}) and results from the antisymmetric stretching vibration of the azide and the band at 1664 cm^{-1} can be assigned to the C=O stretching vibration of the carboxylate group.

Given that many peaks overlap at lower energy (shown in more detail in Figure 4.9), assigning signals in this region is difficult. As discussed before (*vide supra*), the azide ligand features a symmetric stretching vibration $\nu_s(N_3)$ that is expected in this area, as reported for a series of high-spin azido iron(III) porphyrins in the 1318 cm^{-1} – 1324 cm^{-1} range,[209] or at 1210 cm^{-1} in a non-heme high-spin bis-azido iron(III) complex.[212] However, the C-O stretching mode (between carbon and the iron bond oxygen) of the carboxylate is also expected in this region, which was previously assigned to a signal at 1285 cm^{-1} for the present complex.[43] When the natural isotope sample and the ^{15}N-isotope labeled material are compared (Figure 4.9), only minor, not very well resolved, differences can be observed in the 1220 cm^{-1}-1350 cm^{-1} area and identification of the $\nu_s(N_3)$ signal is difficult.

In Figure 4.10, the IR spectra of the complexes $[Fe^{III}(N_3)cyc\text{-}ac]PF_6$, $[Fe^{III}(^{15}NN_2)cyc\text{-}ac]PF_6$, and their chloride precursor $[Fe^{III}(Cl)cyc\text{-}ac]PF_6$ are compared. Most features of the three spectra are identical, besides some minor variations in the 1220 cm^{-1}-1350 cm^{-1} region where the chlorine complex shows less signals. This agrees with the expectation that the azido complexes should show signals for the symmetric stretching vibration $\nu_s(N_3)$ in this region. The chloride complex $[Fe^{III}(Cl)cyc\text{-}ac]PF_6$ shows a clear signal at 1296 cm^{-1} which presumably represents the C-O vibration of the carboxylate group, as mentioned before. However, due to the number of signals that overlap in this region it is not possible to clearly identify the symmetric stretching vibration $\nu_s(N_3)$. C-H Wagging (bending) modes usually appear in the same region as the $\nu_s(N_3)$ mode[211] and might overlap with the signal of the $\nu_s(N_3)$ mode.

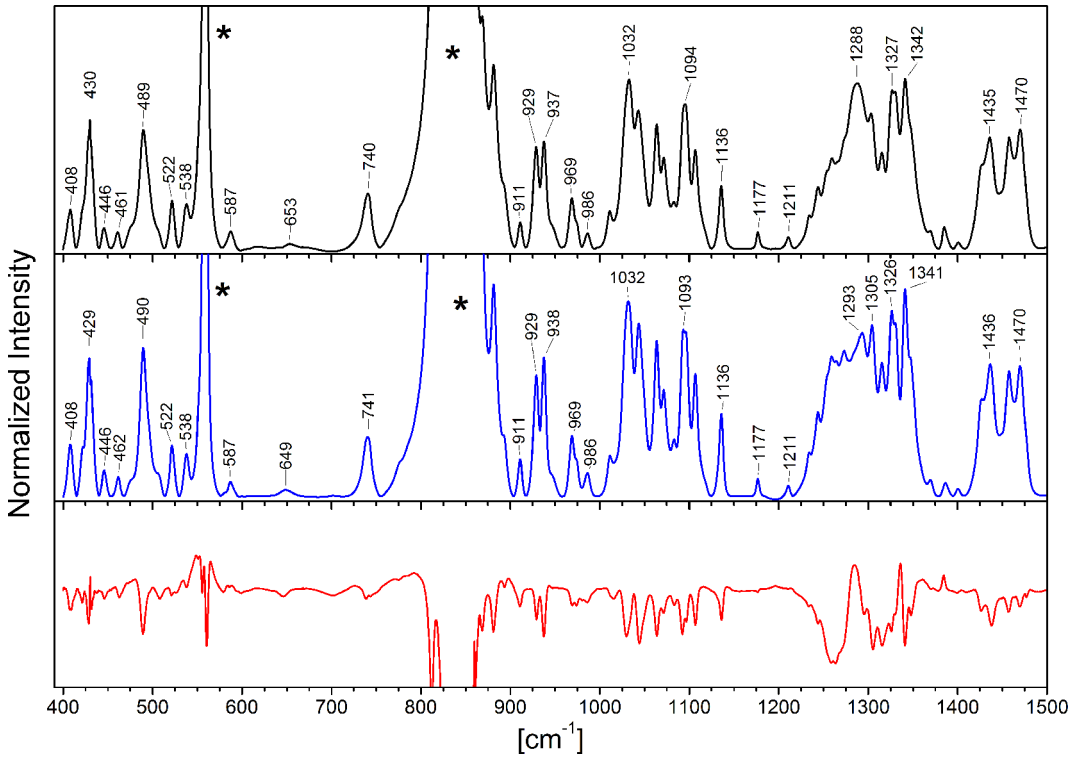

Figure 4.9: 390 cm^{-1} – 1500 cm^{-1} region of the IR spectra for the $[Fe^{III}(N_3)cyc\text{-}ac]PF_6$ complex in black, $[Fe^{III}(^{15}NN_2)cyc\text{-}ac]PF_6$ in blue and the difference spectrum in red.

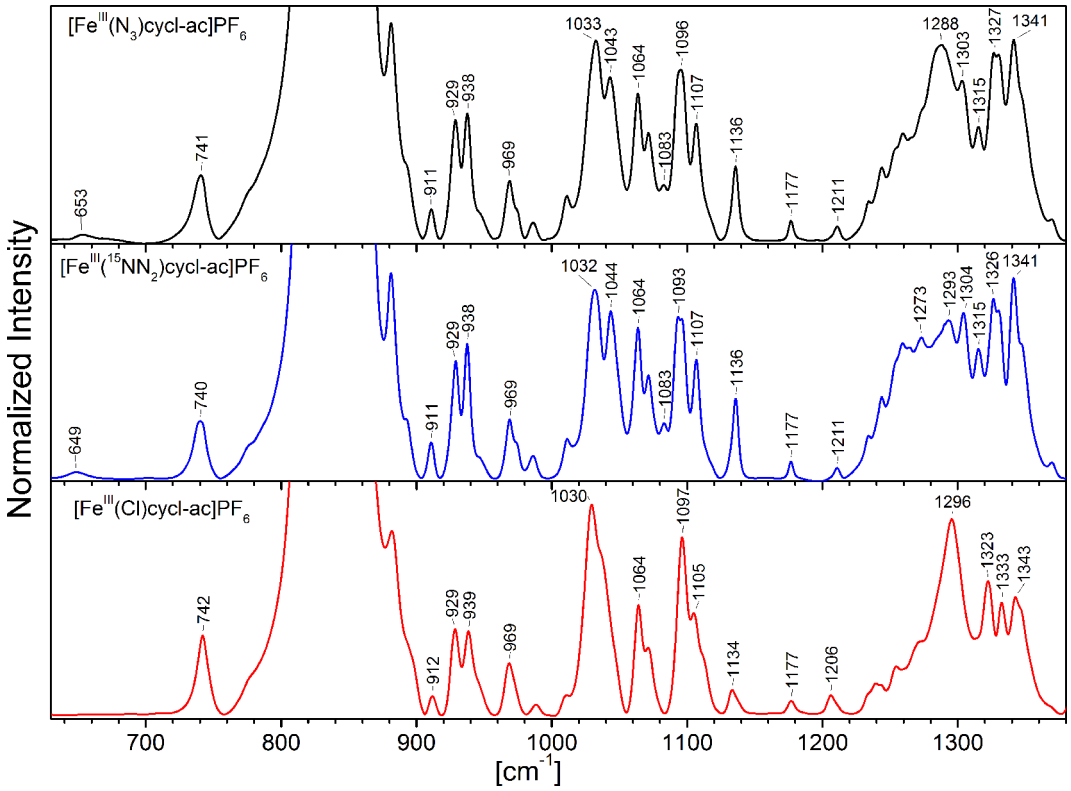

Figure 4.10: Comparison of the IR-spectra from $[Fe^{III}(N_3)cyc\text{-}ac]PF_6$ (black), $[Fe^{III}(^{15}NN_2)cyc\text{-}ac]PF_6$ (blue) and $[Fe^{III}(Cl)cyc\text{-}ac]PF_6$ (red) in the 630 cm^{-1} – 1380 cm^{-1} region.

A small signal is observed at 653 cm^{-1}, which is not present in the chloride complex and shows an isotope effect of -4 cm^{-1} (see Figure 4.10). This presumably results from a bending mode between iron and the azide ligand, as will be also shown in the resonance Raman spectra and the DFT calculations (*vide infra*).

To support the assignment of observed IR bands, spectra were calculated by DFT including isotope labeling effects. In the experiments, samples with isotopes in their natural abundance and ^{15}N-isotope labeled azide was used. It has to be adhered to the fact, that in commercially available sodium-azide which was used in the synthesis (see Chapter 4.1), only one of the terminal nitrogen-atoms is ^{15}N-labeled. Therefore, a mixture of azido-iron complexes is obtained with the terminal azido-nitrogen atom ^{15}N-labeled (Fe-NN^{15}N, in the following denoted as γ-^{15}N) and with a ^{15}N-labeled nitrogen atom bond to iron (Fe-^{15}NNN, denoted as α-^{15}N). However, the differences between the two ^{15}N-isomers were not resolved in the obtained vibrational spectra but have to be considered in the DFT calculations. Some cases are reported in the literature where a splitting of azide vibrations was observed in measurements at 20 K due to the presence of two different ^{15}N-isomeres.[40,46,209] Calculated modes (mainly resulting from the O-Fe-N_3 fragment) that are affected by ^{15}N-isotope labeling are provided in Table 4.8. The calculations predict largest isotope effects for the symmetric and antisymmetric stretching vibrations of the azide ligand. Table 4.8 further reveals that the isotope shift significantly depends on which N-atom is ^{15}N-substituted (α-^{15}N or γ-^{15}N). In the following discussion the average calculated isotope effect for the two ^{15}N-isomers will be used that is also provided in Table 4.8.

Table 4.8: Calculated modes with significant iron/azide contribution and possible isotope ^{15}N-patterns.

mode / character	Fe-NNN	α-^{15}N (Fe-^{15}NNN)		γ-^{15}N (Fe-NN^{15}N)		^{15}N-average	
	[cm^{-1}]	[cm^{-1}]	Δ	[cm^{-1}]	Δ	[cm^{-1}]	Δ
$\nu_{as}(N_3)$ / A'	2078	2074	-4	2057	-21	2066	-12
$\nu_{s}(N_3)$ / A'	1301	1274	-27	1286	-15	1277	-21
$\delta_{ip}(N_3)$ / A'	663	656	-7	661	-2	658	-5
$\delta_{op}(N_3)$ / A''	596	593	-3	592	-3	592	-4
ν_{as}(O-Fe-N_3) / A'	471	471	0	471	0	471	0
ν_{s}(O-Fe-N_3) / A'	352	350	-1	351	0	351	-1
δ_{ip}(O-Fe-N_3) / A'	191	190	-1	191	-1	191	-1
δ_{op}(O-Fe-N_3) / A''	173	171	-1	173	-1	172	-1
δ(Fe-N_3) / A'	96	96	0	94	-2	95	-1

In Figure 4.11 the calculated spectra in the 600cm^{-1}-1500cm^{-1} region are shown. C-H bending modes of "scissoring" type are visible in the 1400 cm^{-1} - 1450 cm^{-1} range and probably correspond to the experimentally observed signals between 1400 cm^{-1} and 1500 cm^{-1} (see Figure 4.9). Signals that are calculated to appear at 1063 cm^{-1} and 1028 cm^{-1} (see Figure 4.11) refer to C-N stretching modes and those at 992 cm^{-1} to N-H bending/wagging modes of the ligand. These can be assigned to the experimentally observed signals at 969 cm^{-1}, 938 cm^{-1} and 929 cm^{-1}, respectively (see Figure 4.10).

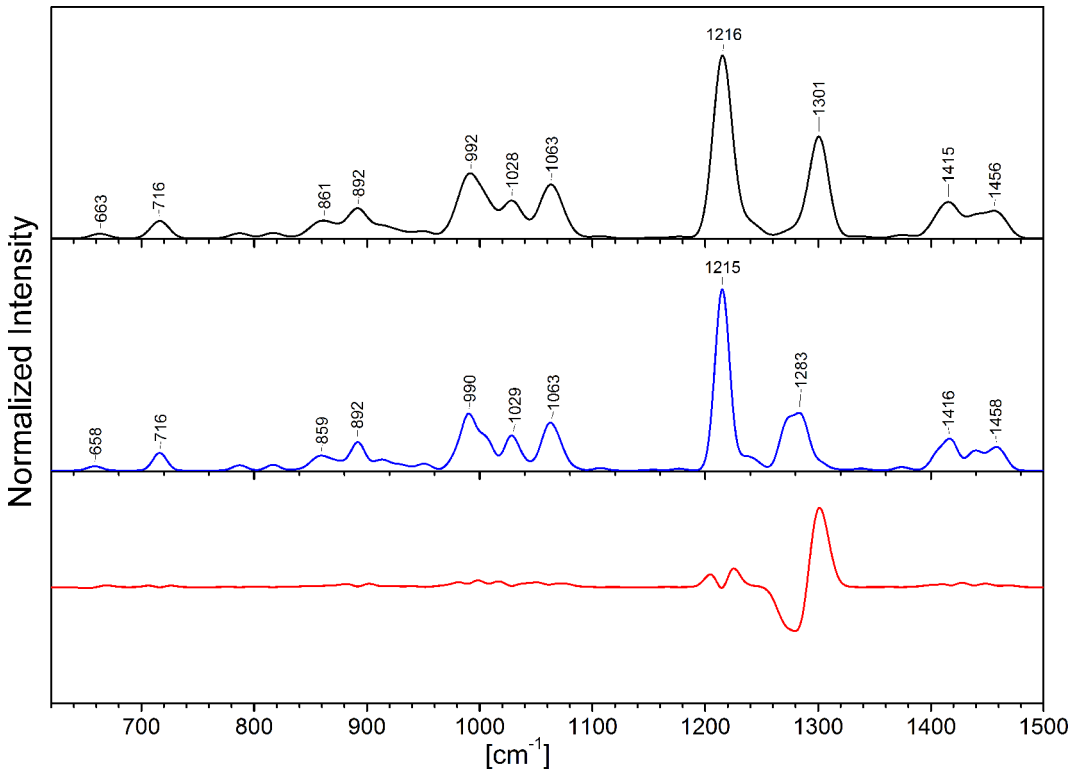

Figure 4.11: Calculated IR spectra for the [Fe^{III}(N_3)cyc-ac]$^+$ complex (black), a 50:50 mixture of the [Fe^{III}(^{15}NNN)cyc-ac]$^+$ and [Fe^{III}(NN^{15}N)cyc-ac]$^+$ isotope labeled material (blue) and a differential spectrum of the two calculations. Line shapes were generated using a Gaussian function with 15 cm^{-1} line width.

DFT calculations predict the symmetric stretching vibration of the azide ligand to appear at 1301 cm^{-1} and the C-O stretching vibration at 1216 cm^{-1}. For the symmetric stretching vibration $\nu_s(N_3)$ further an average isotope effect of -21 cm^{-1} was calculated (see Table 4.8). However, as already discussed (*vide supra*) it is not possible to clearly identify the signal of the symmetric stretching vibration in the

experimental IR spectra. Only minor variations, not very well defined, are observed in the corresponding spectral range which precludes to assign the $\nu_s(N_3)$ mode to a distinct experimentally observed peak.

The experimentally observed signal at 653 cm^{-1} (isotope shift -4 cm^{-1}) is in good agreement with the calculated down shift of a signal from 663 cm^{-1} to 658 cm^{-1}, respectively. It originates from the in-plane bending mode $\delta_{ip}(N_3)$ of the azide ligand. Even the signal is very small in the IR-measurements, this assignment is very reasonable as will be further shown in the following resonance Raman section.

Resonance Raman Spectroscopy

Resonance Raman samples were prepared from 6 mmol L^{-1} acetonitrile solutions in EPR quartz tubes. The measurements were performed at 77 K by placing the sample in a quartz glass finger dewar with liquid nitrogen. Separate measurements for the 100 cm^{-1}-1450 cm^{-1} and the 1320cm^{-1}-2500 cm^{-1} range were stitched together ensuring overlap that includes at least one peak for normalization. The instrument was calibrated to the signal of Na_2SO_4 and the acetonitrile solvent signals. To obtain reasonable spectra, 30 measurements, each one for 30 seconds, were accumulated to obtain the final spectrum. Solvent and quartz signals from the sample tube are omitted in the presented data on which the Savitsky−Golay smoothing algorithm has been applied, too.

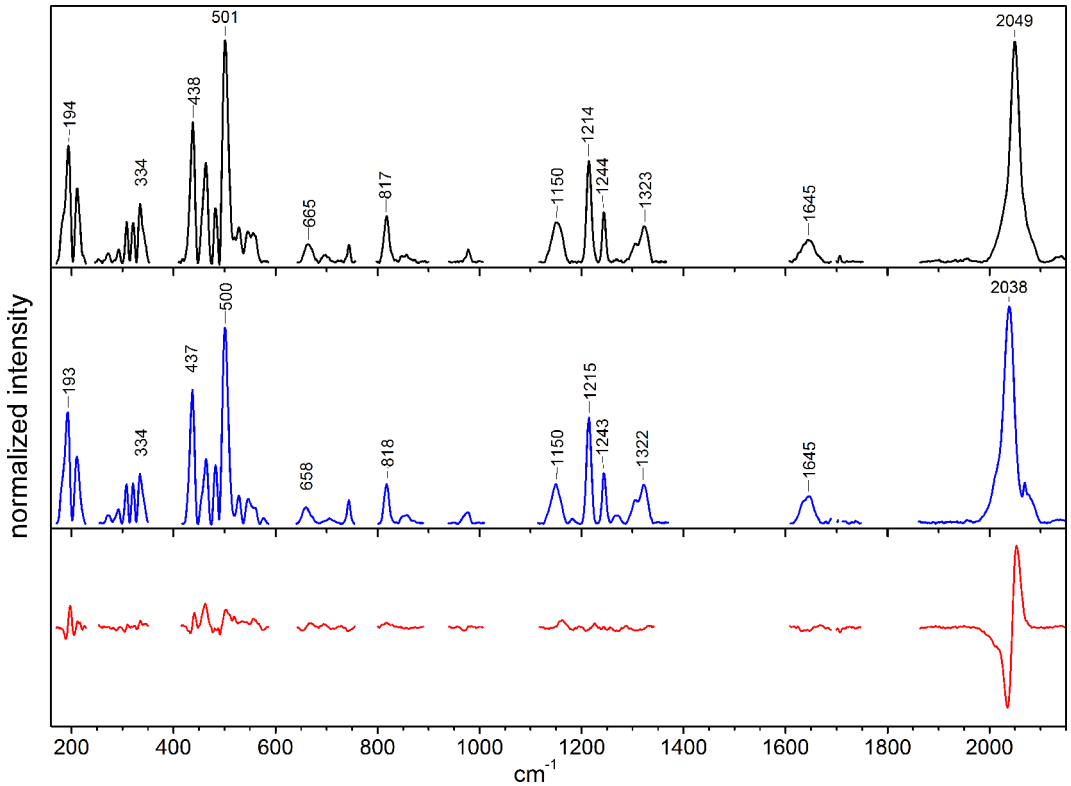

Figure 4.12: Resonance Raman spectra from $[Fe^{III}(N_3)$cyc-ac$]PF_6$ at 514 nm/220mW/77K in acetonitrile; Black: natural isotope, blue: ^{15}N-isotope labeling on the azide; red: difference spectrum. Spectra were normalized to the peak intensity at 2049 cm^{-1}/ 2038 cm^{-1}.

Figure 4.12 shows the resonance Raman spectra of $[Fe^{III}(N_3)cyc\text{-}ac]PF_6$ obtained from natural isotope and ^{15}N-labeled material. In contrast to published resonance Raman studies on azido iron(III)porphyrins at 20 K,[40,46,209] the difference between the two ^{15}N-isotope isomers (α-^{15}N vs γ-^{15}N) was not resolved in the present experiments.

Very clear is the intense signal for the antisymmetric azide stretching vibration at 2051 cm^{-1} (2041 cm^{-1} for ^{15}N-material), as it was present in the IR-spectra at 2052 cm^{-1} (2037 cm^{-1}). Figure 4.13 shows the 180 cm^{-1}-1350 cm^{-1} range of the spectra in more detail.

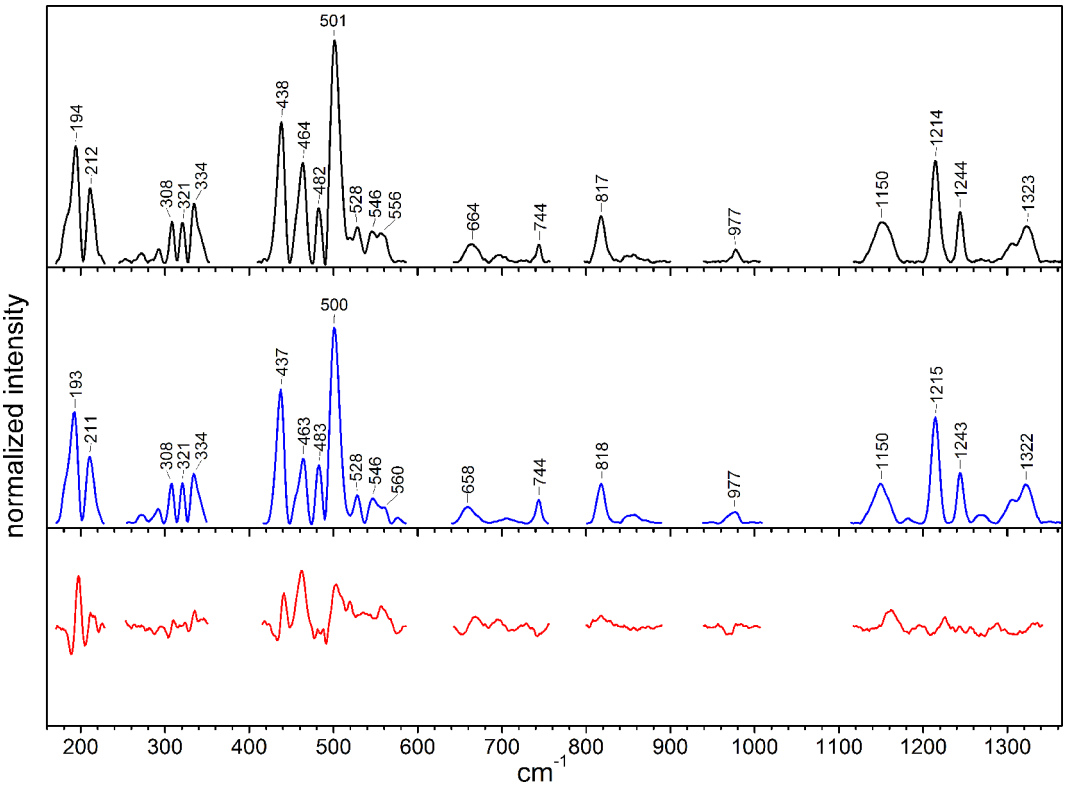

Figure 4.13: Zoom in the 180 cm^{-1} – 1350 cm^{-1} area of spectra in Figure 4.12.

In the range where the symmetric stretching vibration of the azide ligand is expected, signals at 1150 cm^{-1}, 1214 cm^{-1}, 1244 cm^{-1} and 1323 cm^{-1} were detected; however, none of these signals show a significant isotope shift. For the IR-spectra only minor intensity variations were observed but a clear identification of the $\nu_s(N_3)$ mode and its isotope-shift was impossible, too. However, in the IR-spectra it might be the case that the signal is hidden under additional peaks (see discussion in the previous section). The resonance Raman signals in the 1100 cm^{-1} – 1400 cm^{-1} range were decomposed into Gaussian peaks for a more detailed analysis (not shown here), however, this did not result in any further information. Possibly, the signal at 1305 cm^{-1} and/or at 1324 cm^{-1} correspond to the expected $\nu_s(N_3)$ signal, but this assignment is equivocally.

An isotope shift of -6 cm^{-1} was observed for the signal at 665 cm^{-1}, similar to the IR-spectra where a shift from 653 cm^{-1} to 649 cm^{-1} was detected. This signal can be therefore assigned to one of the $\delta(N_3)$ bending mode (in-plane or out-of-plane).

Resonance Raman spectra were calculated by DFT for the natural isotope and the ^{15}N-labeled complex to support band assignments, as shown in Figure 4.14. The excitation wavelength in the calculations was shifted, according to the deviation of the calculated UV-*vis* absorption from the experimentally observed band at 458 nm (21485 cm^{-1}). The calculated spectrum for the ^{15}N-labeled material was generated in a way that calculations were performed for the α-^{15}N and γ-^{15}N species separately and the shown spectrum is a 50:50 mixture of these two calculated spectra. The plot was generated using Gaussian functions with a linewidth of 10 cm^{-1} which results in a splitting of the signals 2078 cm^{-1} and 1301 cm^{-1} due to the two different ^{15}N-isotope isomers (α-^{15}N and γ-^{15}N). Calculated resonance Raman modes are summarized in Table 4.9 and the displacements are described graphically in Figure 4.16 (page 62). In Table 4.9 (page 61) also the calculated dimensionless normal coordinate displacements (Δ) are provided. Dimensionless normal coordinate displacements are of interest, since it is well established that they correlate with the resonance Raman intensity by $I_{rR} \propto \omega^2 \cdot \Delta^2$.[213-214]

Assignment of the calculated band at 2078 cm^{-1} to the antisymmetric stretching vibration in the experimental spectrum at 2049 cm^{-1} and the valence stretching vibration of the C=O group which was calculated to be 1714 cm^{-1} and found experimentally at 1645 cm^{-1} is straightforward and was already discussed (*vide supra*).

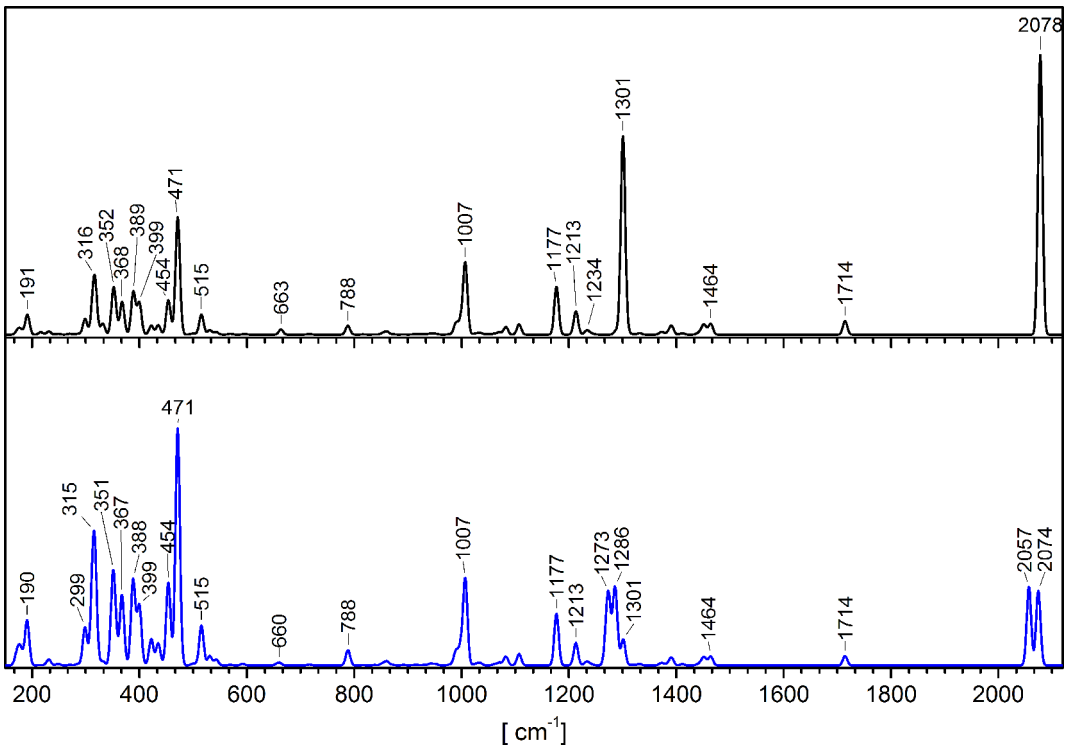

Figure 4.14: Calculated resonance Raman spectrum of [Fe^{III}(N$_3$)cyc-ac]$^+$. Black: natural isotope; blue: ^{15}N-labeled complex.

Calculated and experimental resonance Raman spectra in the 150 cm^{-1} – 1750 cm^{-1} range are compared in Figure 4.15. Even the intensity of several peaks differs, the overall pattern is reproduced reasonably well in the calculations.

Low intensity was calculated for two δ(C-H) scissoring modes and one δ(C-H) wagging mode at 1464 cm^{-1}, 1451 cm^{-1} and 1391 cm^{-1}, respectively. In the experimental spectrum they were not

detectable since many solvent peaks appear in this region. Therefore, a comparison to the experimental results is not possible for these modes.

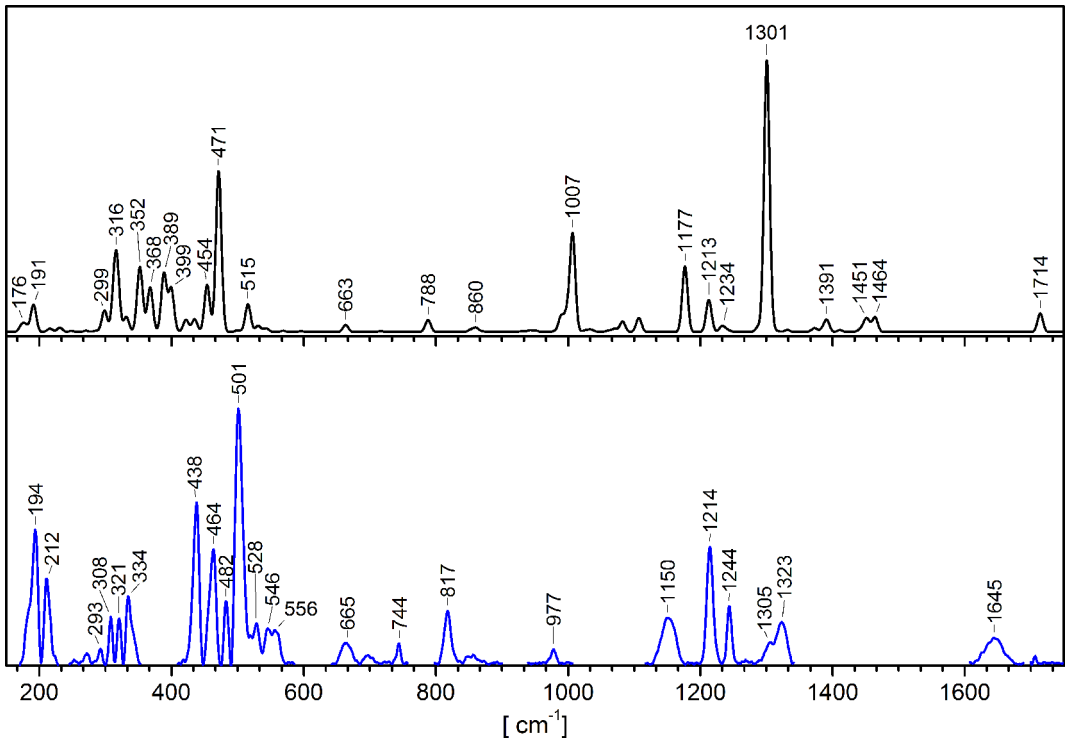

Figure 4.15: Calculated (black) and experimental (blue) resonance Raman spectra for $[Fe^{III}(N_3)cyc\text{-}ac]^+$ in the 150 cm^{-1} to 1750 cm^{-1} range.

As discussed above (*vide supra*), five vibrations are observed in the 1150 cm^{-1} – 1330 cm^{-1} range in the experimental spectrum (1323 cm^{-1}, 1305 cm^{-1}, 1244 cm^{-1}, 1214 cm^{-1}, 1150 cm^{-1}). This is in agreement with the calculations, since five signals are also predicted in this region by DFT, with two modes calculated to appear at the same position at 1301 cm^{-1}. The mode which is calculated to be 1301 cm^{-1} can be assigned to the symmetric stretching vibration of the azide (see Figure 4.16) and an average down shift of -21 cm^{-1} was calculated (see Table 4.8). The second mode that was also calculated to appear at 1301 cm^{-1} is a combination of δ(C-H) twisting modes (see Figure 4.16). Therefore, the mode at 1301 cm^{-1} splits up in three bands in the calculations for the ^{15}N-isotope labeled complex as it can be seen in Figure 4.14. The two coinciding signals at 1301 cm^{-1} might correspond to the modes observed at 1323 cm^{-1} and 1305 cm^{-1} in the experiment, however, it is not clear why the isotope effect is not detected experimentally.

In the experimental spectrum a signal was detected at 665 cm^{-1}, which was already assigned to a deformation mode $\delta(N_3)$ of the azide ligand due to the isotope shift from 665 cm^{-1} to 658 cm^{-1} (see as well the IR spectra in Figure 4.10). This is in good agreement with the mode that was calculated to be 663 cm^{-1}, which shows a down shift of -5 cm^{-1} upon ^{15}N-substitution. From the calculations it can be further seen, that the visible mode is the in-plane bending mode ($\delta_{ip}(N_3)$ at 663 cm^{-1}), as outlined in Figure 4.16. The corresponding out-of-plane bending mode ($\delta_{op}(N_3)$) was calculated to appear at 596 cm^{-1} without any significant resonance Raman intensity.

A possible assignment of the resonance Raman modes (experimental and calculated) is provided in Table 4.9 and the modes are outlined graphically in Figure 4.16.

Table 4.9: Calculated and experimental resonance Raman modes, their assignment, dimensionless normal coordinate displacements and calculated relative resonance Raman intensity.

exp. freq.	calc. freq.	Δ	calc. rel. intensity	mode description
[cm^{-1}]	[cm^{-1}]			
2049	2078	0.42	1.00	$\nu_{as}(N_3)$ / A’
1645	1714	-0.10	0.05	ν_s(C=O)
	1464	0.10	0.04	δ(C-H), scissoring modes
	1451	-0.09	0.03	δ(C-H), scissoring modes
	1391	0.10	0.03	δ(C-H), wagging modes
1323	1301	-0.41	0.52	$\nu_s(N_3)$ / A’
1305	1301	0.25	0.19	δ(C-H), twisting modes
1244	1234	0.07	0.01	δ(C-H), twisting modes
	1217	-0.03	0.00	ν_s(C-O)
1214	1213	-0.18	0.08	δ(C-H), twisting modes (mainly N-CH_2-COO)
1150	1177	-0.26	0.17	δ(N-H) (and δ(C-H), rocking modes)
	1107	-0.13	0.04	δ(N-H) and δ(C-H) twisting modes
	1082	-0.11	0.03	δ(N-H) and δ(C-H) twisting modes
977	1007	0.37	0.25	δ(N-H), wagging modes
817	860	-0.09	0.01	δ(C-H), rocking modes
744	788	0.19	0.03	δ(C-H), rocking modes / ν (N-CH_2COO)
665	663	0.10	0.02	$\delta_{ip}(N_3)$, in-plane bending / A’
	596	-0.07	0.00	$\delta_{op}(N_3)$, out-of-plane bending / A’’
528	515	-0.43	0.07	δ(CH_2), rocking modes
501	471	1.14	0.42	ν_{as}(O-Fe-N_3) / A’
	389	0.83	0.15	ν(Fe-N_{cyc})
	368	0.82	0.12	δ(O-Fe-N_3) / ν(Fe-N_{cyc})
482	454	-0.72	0.12	ν(Fe-N_{cyc})
438	399	-0.66	0.11	ν(Fe-N_{cyc})
334	352	-0.80	0.14	ν_s(O-Fe-N_3) / A’
321	316	1.10	0.16	ν(Fe-N_3)
308	299	-0.68	0.06	ν(Fe-N_{cyc})
212	191	-1.25	0.07	δ_{ip}(O-Fe-N_3) / A’
194	176	0.69	0.02	δ_{op}(O-Fe-N_3) / A’’
	96	1.78	0.03	δ(Fe-N_3) / A’

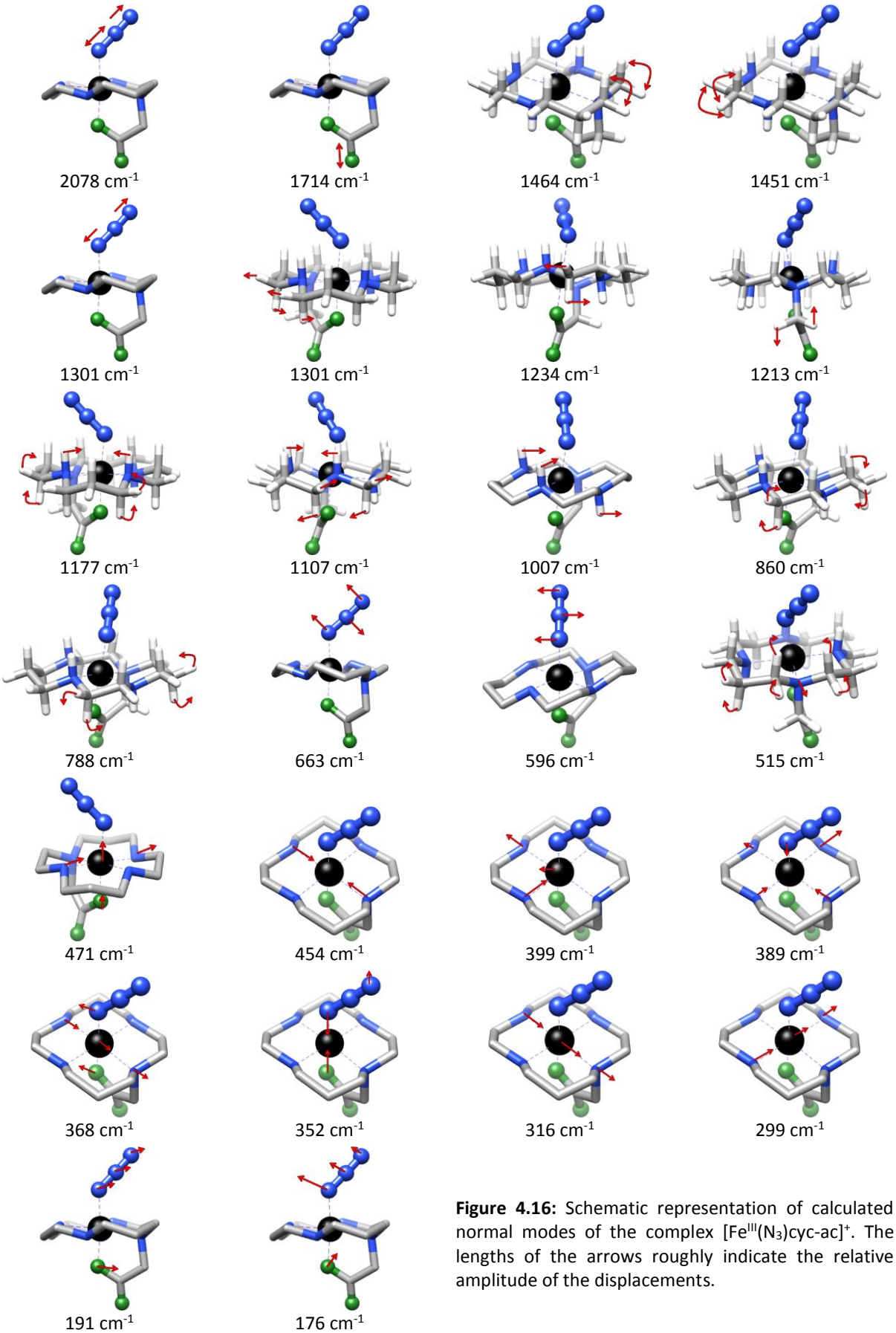

Figure 4.16: Schematic representation of calculated normal modes of the complex $[Fe^{III}(N_3)cyc\text{-}ac]^+$. The lengths of the arrows roughly indicate the relative amplitude of the displacements.

The area below 600 cm^{-1} was studied previously by nuclear resonance vibrational spectroscopy (NRVS).[45] Therefore, the experimental resonance Raman results are correlate to the published NRVS data where possible and provided in Table 4.10.[45] From the calculations as well as the experimental NRVS study, normal mode composition factors for iron (e_{Fe}^2) can be extracted, that correlate with the intensity which is also considered in the mode assignment. Several modes observed in the NRVS-study can be also found in the presented resonance Raman spectra.

Table 4.10: Comparison of the resonance Raman results with the data of a previously published NRVS study

	Present resonance Raman Study				NRVS Data from Literature[a]			
	rR exp.	calculated			experimental		calculated	
	freq. [cm^{-1}]	freq. [cm^{-1}]	Δ	e_{Fe}^2	freq. [cm^{-1}]	e_{Fe}^2	freq. [cm^{-1}]	e_{Fe}^2
ν_{as}(O-Fe-N_3)	501	471	1.14	0.29	512	0.29	480	0.33
ν(Fe-N_{cyc})	438	399	-0.66	0.23	432	0.28	411	0.28
ν(Fe-N_3)	321	316	1.10	0.15	323	0.15	320	0.13
ν(Fe-N_{cyc})	308	299	-0.68	0.23	307	0.19	299	0.21
δ_{ip}(O-Fe-N_3)	212	191	-1.25	0.02	-	-	-	-
ν(Fe-N_{cyc})	-	212	-0.09	0.03	207	0.02	189	0.01
δ_{op}(O-Fe-N_3)	194	176	-0.73	0.02	196	0.02	171	0.02

a: Petrenko *et al*. *J. Am. Chem. Soc.* **2007**, *129*, 11053.

Based on experimental and computational IR-, resonance Raman as well as previously published NRVS-spectroscopy data it was possible to assigne several bands in the vibrational spectra. For two bands ($\nu_{as}(N_3)$, $\delta_{ip}(N_3)$), the assignment is very clear based on the observed isotope shift. However, for the symmetric stretching vibration of the azide ligand no isotope effect was observed in the resonance Raman spectra, even it was clearly predicted in the calculations. In the IR-measurements only minor variations were observed in the corresponding spectral region which did not allow a distinct assignment of the symmetric azide stretching mode. Reasons might be a too low resolution of the experimental data or the isotope effect is overestimated in the calculations.

Broadening of the experimental spectra might be caused by the presence of more than one isomer. In Figure 4.17 the structure that coincides with the X-ray structure is shown, however, rotation of the azide ligand results in an additional isomer that is calculated to be only 2 kJ mol^{-1} higher in energy (B3LYP/RIJCOSX/def2-TZP/COSMO). A relaxed surface scan along the O-Fe-N-N dihedral angle (not shown here in detail) reveals that the barrier of this rotation is not more than 10 kJ mol^{-1}. Given that samples were prepared from solution and then frozen with liquid nitrogen, it is throughout possible that in the sample more than one conformation is present which results in broadening of the experimental signals. Calculated modes that significantly involve the azide ligand are provided in Table 4.11 for the two possible isomers shown in Figure 4.17 and different ^{15}N-isotope labeling isomers. The data reveals differences of up to 10 cm^{-1} between the *cis*- and *trans*-isomers.

Another potential problem in the resonance Raman measurements is irradiation damage, since azido iron(III) complexes can be photolyzed with light of similar wavelength as used in the measurements.

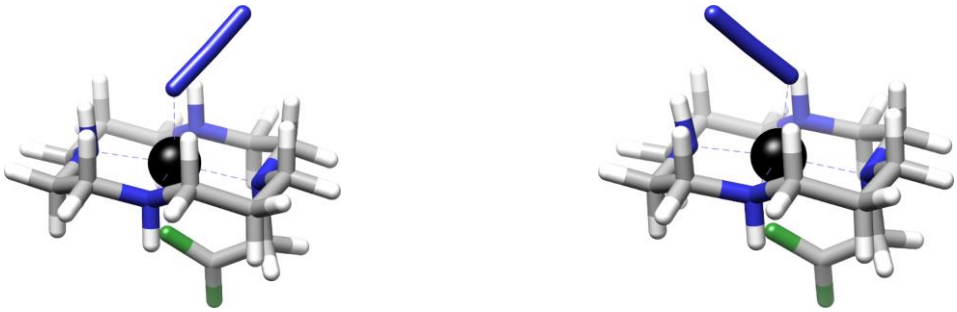

Figure 4.17: *Cis*-configuration of the $[Fe^{III}(N_3)cyc\text{-}ac]^+$ complex as found in the crystal structure[43] (left) and the corresponding *trans*-structure (right).

Table 4.11: Calculated modes with significant iron/azide contribution for both isomers and possible isotope ^{15}N-patterns. The differences between the *cis*-/*trans*- isomers is denoted as Δ.

mode / character	Fe-NNN			Fe-^{15}NNN			Fe-NN^{15}N		
	cis	*trans*	Δ	*cis*	*trans*	Δ	*cis*	*trans*	Δ
$\nu_{as}(N_3)$ / A’	2078	2075	3	2074	2071	3	2057	2053	4
$\nu_{s}(N_3)$ / A’	1301	1292	9	1274	1264	10	1286	1277	9
$\delta_{ip}(N_3)$ / A’	663	668	-5	656	661	-5	661	666	-5
$\delta_{op}(N_3)$ / A’’	596	601	-5	593	598	-5	592	598	-6
ν_{as}(O-Fe-N_3) / A’	471	476	-5	471	476	-5	471	476	-6
ν_{s}(O-Fe-N_3) / A’	352	349	3	350	348	2	351	349	2
δ_{ip}(O-Fe-N_3) / A’	191	195	-4	190	194	-4	191	195	-4
δ_{op}(O-Fe-N_3) / A’’	173	171	2	171	169	2	173	171	2
δ(Fe-N_3) / A’	96	91	5	96	91	5	94	90	4

As outlined at the beginning of this chapter, the aim of the resonance Raman measurements was to investigate the effect of irradiation into a visible absorption band of the complex $[Fe^{III}(N_3)cyc\text{-}ac]PF_6$. Experimentally observed peaks at 2049 cm^{-1} and 664 cm^{-1} can be clearly assigned to the azide ligand due to the presence of a significant isotope shift upon ^{15}N-isotope labeling. By far the highest intensity was observed for the antisymmetric stretching vibration of the azide ligand at 2049 cm^{-1}. It can, therefore, be concluded that the azide ligand is involved in the observed absorption at 458 nm (21845 cm^{-1}) in the UV-*vis* spectrum and the previous assumption that this represents a LMCT-transition is supported by the present resonance Raman study.

The observation of an intense band for the antisymmetric azide stretching vibration implies, that irradiation in the visible band induces an antisymmetric deformation of the azide ligand. This mimics the elimination of N_2 from the azido complex (see Figure 4.16, mode at 2078 cm^{-1}) and indicates that breaking the FeN-N_2 bond might be possible by photolysis with visible light. Unfortunately, attempts to measure off-resonance Raman spectra failed and comparison of Raman and resonance-Raman spectra, which would show in more detail which modes are enhanced due to resonance, is not possible. The difficulties in obtaining well resolved resonance Raman data might also result from the fact that the excited states are dissociative. However, in anticipating a result from Chapter 4.8.2 it should be noted, that TD-DFT calculations do not provide evidence that the corresponding excitation is dissociative with respect to the N_2-elimination. Still, the data discussed in this chapter shows clearly that the azide ligand is involved in the excited state accessed by photolysis with visible light and of course, this is necessary for the photolytic elimination of N_2 from the azido complex.

4.5.2. IR and Resonance Raman Spectroscopy on the Complex $[Fe^{III}(N_3)_2cyc]ClO_4$

Vibrational spectroscopy measurements were also performed on the *trans*-bis-azido complex $[Fe^{III}(N_3)_2cyc]ClO_4$, similar to those for the mono-azido complex $[Fe^{III}(N_3)cyc\text{-}ac]PF_6$. While the mono-azido complex $[Fe^{III}(N_3)cyc\text{-}ac]^+$ shows only C_s symmetry, the bis-azido complex $[Fe^{III}(N_3)_2cyc]^+$ is C_{2h}-symmetric (the crystal structure has been solved in the space group $P2_1/n$) which is expected to result in a lower number of active modes in the IR- and Raman-spectra, respectively. In a simplified treatment considering only the $Fe(N_3)_2$ fragment, 3N-6=15 normal mode vibrations are expected that are span by $5A_g$, $1B_g$, $3A_u$ and $6B_u$. The A_g and B_g modes are only Raman active while the A_u and B_u modes are only IR active. Therefore, the vibrations are either visible in the Raman- or in the IR-spectrum, but in contrast to the mono-azido complex, not in both.

IR Spectroscopy

Room temperature IR-measurements were performed on KBr-disks of ~200 mg dry KBr and ~2 mg of the sample. Recorded spectra were baseline corrected and manually normalized to show the same intensity for the ^{14}N- and ^{15}N-isotope sample. Peaks at 1093 cm^{-1} and 625 cm^{-1} result from the perchlorate counter-ion and are marked by asterisks. Basic IR-spectroscopy data was already published in literature.[29]

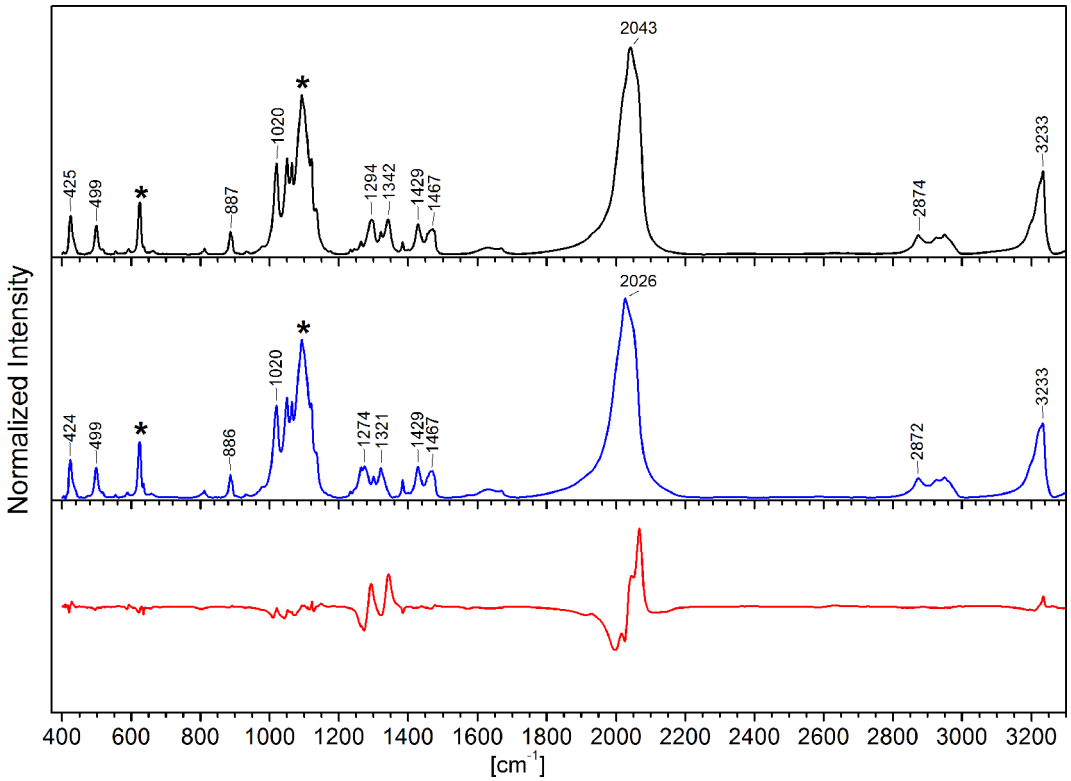

Figure 4.18: Room-temperature IR-spectra of $[Fe^{III}(^{14}N_3)_2cyc]^+$ (black), $[Fe^{III}(^{15}NN_2)_2cyc]^+$ (blue) and their difference spectrum (red).

The most intense peak is observed at 2043 cm^{-1} (2026 cm^{-1} for the ^{15}N-sample) which is typical for the antisymmetric stretching vibration of azide ligands.[215] This is further confirmed by the observed isotope shift of -17 cm^{-1} upon ^{15}N-substitution. On the higher energy side, the signal observed at 3233 cm^{-1} is typical for N-H stretching vibrations and results from the amine groups of the cyclam-ligand.[211] The signals in the 2800 cm^{-1} – 3000 cm^{-1} range are typical for C-H stretching vibrations that can be also assigned to the cyclam-ligand.[211]

The 400 cm^{-1}-1500 cm^{-1} region is shown in more detail in Figure 4.19. In comparison to the spectra of the complex $[Fe^{III}(N_3)cyc\text{-}ac]^+$ (see Chapter 4.5.1, page 53), less signals are found which can be explained by higher symmetry in the bis-azido complex $[Fe^{III}(N_3)_2cyc]^+$.

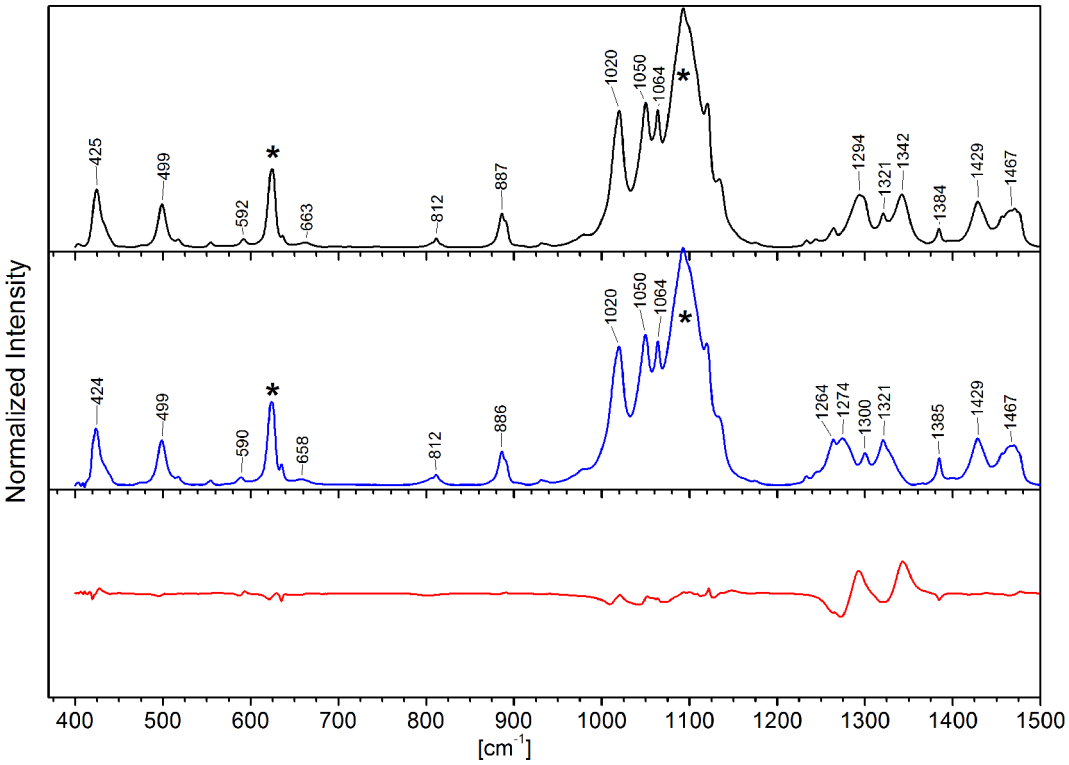

Figure 4.19: Zoom in the 400 cm^{-1}-1500 cm^{-1} region of the IR-spectra in Figure 4.18.

Signals were observed at 1471 cm^{-1} and 1429 cm^{-1} that are typical for cyclam $\delta(CH_2)$ and δ(N-H) bending modes, in agreement with a previous study on analog complexes (e.g. *trans*-$[CoCl_2cycl]ClO_4$).[216]

Comparing the ^{14}N- and ^{15}N-spectra reveals moderate changes in the 1250 cm^{-1}-1350 cm^{-1} region. Even these peaks seem to overlap with various other signals, the signals at 1342 cm^{-1} and 1294 cm^{-1} seems to be shifted to 1321 cm^{-1} and 1274 cm^{-1}, respectively, due to ^{15}N-isotope labeling. This region is typical for the symmetric stretching vibration of azide ligands[215] which agrees well with the observed isotope shift. However, in the IR spectrum only one peak for the in-phase coupling of the symmetric stretching vibrations from the two azide ligands should be present ($\nu_s(N_3)$), while in the recorded spectrum more than one band in this region is affected by ^{15}N-isotope labeling. Further difficulties arise since several signals overlap. A distinct assignment of the symmetric stretching vibration based on the recorded IR-spectra is therefore difficult, but presumably the 1342 cm^{-1} or the 1294 cm^{-1} signals result from the symmetric stretching vibration of the azide ligands.

Signals observed at 1020 cm^{-1} and 887 cm^{-1} can be assigned to N-H wagging modes and the signal at 812 cm^{-1} to CH_2-rocking modes, again based on a comparison with analog complexes that were studied previously.[216]

Even the signals are small, isotope effects are observed for the 663 cm^{-1} and 592 cm^{-1} signals that appear at 658 cm^{-1} and 590 cm^{-1} in the ^{15}N-labeled sample, respectively. For the mono-azido complex $[Fe^{III}(N_3)cyc\text{-}ac]^+$ one signal was observed at 653 cm^{-1} for the $\delta_{ip}(N_3)$ bending mode. For the bis-azido complex, out-of-phase combinations of the in-plane (B_u) and out-of-plane (A_u) bending modes are expected to show IR intensity. Therefore, the signals at 663 cm^{-1} and 592 cm^{-1} can be assigned to bending modes of the azide ligand.

To support the band assignment, vibrations were calculated by DFT. Those mode that originate mainly from the $Fe(N_3)_2$-fragment are expected to show an isotope shift upon ^{15}N-isotope labeling. It should be noted here, that for the bis-azido complex even three different ^{15}N-isomers are possible, depending on which nitrogen atom is ^{15}N-labeled (α,α-^{15}N, α,γ-^{15}N or γ,γ-^{15}N). The 15 normal modes that are mainly derived from the $Fe(N_3)_2$-fragment are summarized in Table 4.12, including the calculated isotope shift and if the mode is expected to be IR or Raman active resulting from the irreducible representation of the mode. In Figure 4.25 (page 73) the modes are sketched schematically. An average isotope shift is also provided in Table 4.12, which will be used in the following discussion.

Table 4.12: Calculated normal modes and ^{15}N-isotope effect for the $Fe(N_3)_2$ fragment of the $[Fe^{III}(N_3)_2cyc]^+$ complex. R stands for Raman active and IR for IR active.

mode	act.	^{14}N	α, α-^{15}N		α, γ-^{15}N		γ, γ- ^{15}N		^{15}N-average	
				Δ		Δ		Δ		Δ
		cm^{-1}	cm^{-1}	cm^{-1}	cm^{-1}	cm^{-1}	cm^{-1}	cm^{-1}	cm^{-1}	cm^{-1}
$\nu_{as}(N_3)$ / A_g	R	2077	2073	-4	2070	-6	2056	-21	2066	-10
$\nu_{as}(N_3)$ / B_u	IR	2069	2066	-3	2051	-18	2048	-21	2055	-14
$\nu_{s}(N_3)$ / A_g	R	1300	1271	-29	1283	-17	1285	-15	1279	-20
$\nu_{s}(N_3)$ / B_u	IR	1293	1265	-28	1267	-25	1279	-14	1271	-22
$\delta_{ip}(N_3)$ / B_u	IR	674	666	-8	669	-4	672	-2	669	-5
$\delta_{ip}(N_3)$ / A_g	R	663	656	-7	658	-5	661	-2	658	-5
$\delta_{op}(N_3)$ / A_u	IR	608	605	-3	605	-3	605	-3	605	-3
$\delta_{op}(N_3)$ / B_g	R	601	598	-3	598	-3	598	-3	598	-3
ν(Fe-N_3) / B_u	IR	390	389	-2	389	-1	390	0	389	-1
ν(Fe-N_3) / A_g	R	335	331	-4	332	-2	334	-1	332	-2
δ(Fe-N_3) / B_u	IR	197	195	-2	196	-1	196	-1	196	-1
δ(Fe-N_3) / A_u	IR	192	188	-3	190	-2	191	0	190	-2
δ(Fe-N_3) / A_g	R	178	176	-2	176	-1	176	-1	176	-1
$\delta(N_3)$ / B_u	IR	94	94	0	93	-1	93	-1	93	-1
$\delta(N_3)$ / A_u	IR	34	35	1	33	-1	33	-1	34	0

The largest isotope shift is predicted for the antisymmetric and the symmetric stretching mode of the azide ligands. It can be further seen, that the isotope shift strongly depends on the ^{15}N-substitution mode (terminal γ-^{15}N or iron bond α-^{15}N). Given that all three possibilities will be present in the ^{15}N-labeled sample, this might cause broadening in the experimental spectra.

In the IR-spectrum the antisymmetric stretching vibration is observed at 2043 cm^{-1} with an isotope shift of -17 cm^{-1} upon ^{15}N-labeling (2026 cm^{-1}) which is in good agreement with the calculated average shift of -14 cm^{-1} from 2069 cm^{-1} to 2055 cm^{-1} (see Table 4.12). A comparison of the experimental and calculated 300 cm^{-1} - 1500 cm^{-1} region is shown in Figure 4.20.

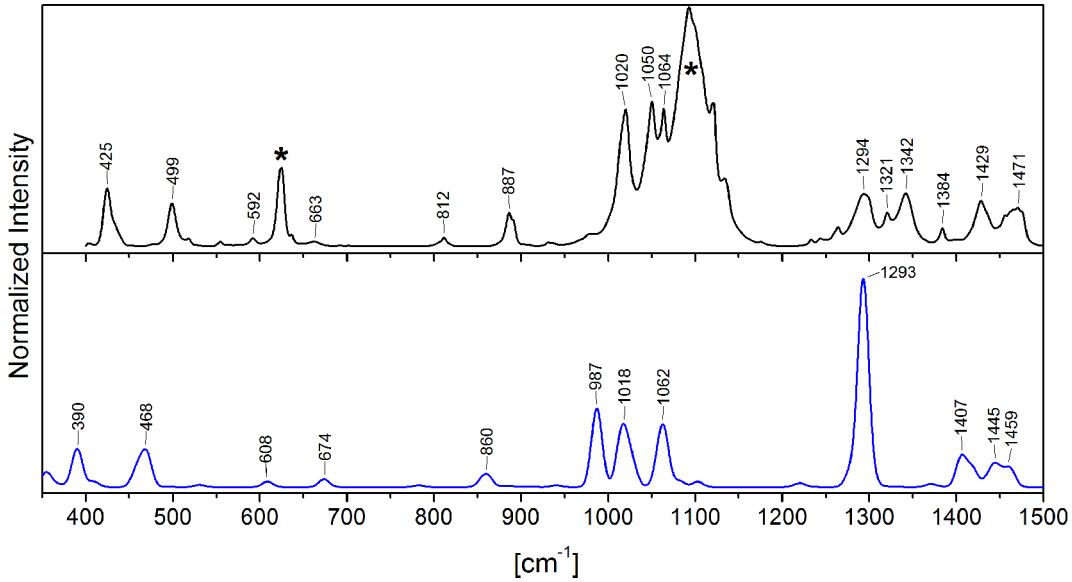

Figure 4.20: 400 cm^{-1} – 1500 cm^{-1} region of the Experimental (black) and calculated (blue) IR spectrum of $[Fe^{III}(N_3)_2cyc]^+$.

Reasonable agreement between the relatively small and broad experimental signals at 1471 cm^{-1} and 1429 cm^{-1} and the calculated spectrum is found. In the experimental spectrum, these were already assigned to $\delta(CH_2)$ and δ(N-H) bending modes (*vide supra*) that are calculated to be 1459 cm^{-1} and 1407 cm^{-1}.

The IR-active symmetric stretching vibration of the azide ligand is predicted to appear at 1293 cm^{-1} as one single peak, showing an average ^{15}N-shift of -22 cm^{-1}. However, several signals are observed experimentally in this region that are affected by ^{15}N-substitution and a clear identification of the isotope shift is not possible (*vide supra*). Even the isotope shift for the symmetric stretching vibration varies significantly depending on the ^{15}N-labeling isomer (-28 cm^{-1}, -25 cm^{-1}, -14 cm^{-1}, for $\alpha\alpha$-^{15}N, $\alpha\gamma$-^{15}N, $\gamma\gamma$-^{15}N, respectively), this cannot explain the observed isotope shift for more than one peak in this region.

A CH_2-rocking mode and a combination of various ν(C-C) stretching vibrations were calculated to be 1064 cm^{-1} and 1058 cm^{-1} that can be assigned to the experimental signals at 1064 cm^{-1} and 1050 cm^{-1}, respectively. A CH_2-rocking mode is further predicted to appear at 860 cm^{-1} by DFT and two NH-wagging modes at 987 cm^{-1} / 1018 cm^{-1}. This agrees well with the assignment of the experimental signal at 812 cm^{-1} to a CH_2-rocking mode and the signals at 987 cm^{-1}/1018 cm^{-1} to NH-wagging modes, based on comparison with previously studied analog complexes.[216]

The out-of-phase combinations of the in-plane / out-of-plane bending modes $\delta_{ip}(N_3)$/ $\delta_{ip}(N_3)$ of the azide ligands were calculated to be 674 cm^{-1} and 608 cm^{-1}, with isotope shifts of -5 cm^{-1} and -3 cm^{-1}, respectively. This agrees well with the experimentally observed bands at 663 cm^{-1} and 592 cm^{-1} that show isotope shifts of -5 cm^{-1} and -2 cm^{-1}, respectively.

Finally, the DFT calculations suggest to assign the signal at 499 cm^{-1} to a stretching mode between the iron atom and the equatorial cyclam nitrogen atoms which was calculated to be 468 cm^{-1} and the experimental peak at 425 cm^{-1} to a stretching mode between iron and the azide ligands calculated to be 390 cm^{-1}. For both, only a negligible isotope shift was calculated which agrees with the experimental results.

Resonance Raman Spectroscopy

Resonance Raman measurements were performed on samples prepared in EPR quartz tubes from acetonitrile solution and frozen with liquid nitrogen (77K). A laser with a wavelength of 514 nm was chosen for the excitation at a power of 10 mW. Separate measurements were performed for the 100 cm^{-1}-1450 cm^{-1} and the 1320 cm^{-1}-2500 cm^{-1} range that were stitched together ensuring overlap that includes at least one peak for normalization. The instrument was calibrated to the signals of Na_2SO_4 and the acetonitrile solvent peaks. To obtain reasonable spectra, 100 measurements, each one for 5 seconds, were accumulated to obtain the final spectrum. Solvent and quartz signals from the sample tube are omitted in the presented spectra.

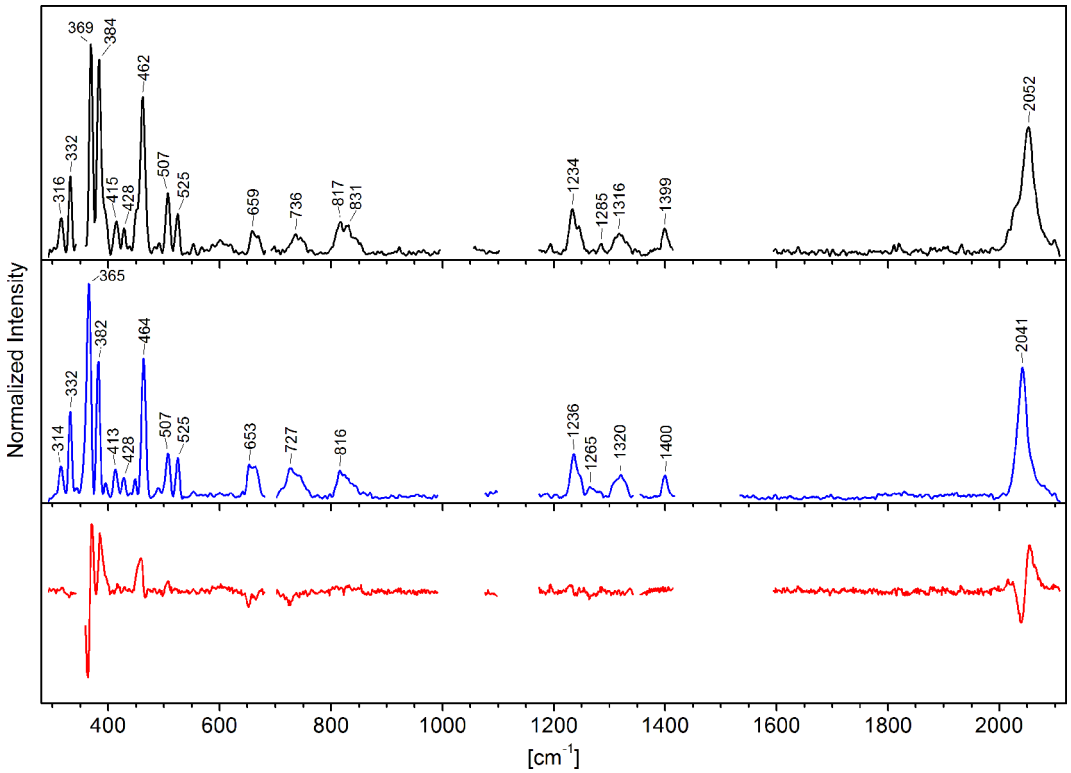

Figure 4.21: Resonance Raman measurements on $[Fe^{III}(N_3)_2cyc]ClO_4$ at 514 nm /10mW/77K in acetonitrile; Black: natural isotope, blue: ^{15}N-isotope labeling on the azide; red: difference spectrum. Spectra were normalized to the peak intensity at 2052 cm^{-1}/ 2041 cm^{-1}.

An intense signal was observed at 2052 cm^{-1} that shows an isotope shift of -11 cm^{-1} upon ^{15}N-substitution. This is typical for the antisymmetric stretching vibration of azide ligands. Given that in the resonance Raman measurements the in-phase combination of both azide ligands (of A_g symmetry) is observed while in the IR measurements the out-of-phase combination (B_u) was observed (2043 cm^{-1}),

it is throughout expected that the peaks in the IR and resonance Raman spectra appear at slightly different energies.

Unfortunately, the quality of the obtained data is very low and for less intense peaks it is even difficult to determine peak positions accurately. In Figure 4.22, the 300 cm^{-1} – 1450 cm^{-1} region of the resonance Raman spectra is shown in detail. As discussed in the previous section, the symmetric stretching vibration of azide ligands is expected around ~1300 cm^{-1} with a significant isotope shift upon ^{15}N-isotope substitution. However, this is not observed in the experimental spectra as it was also the case for the $[Fe^{III}(N_3)cyc\text{-}ac]^+$ complex. Presumably, one of the peaks at 1234 cm^{-1}, 1285 cm^{-1}, 1316 cm^{-1} or 1399 cm^{-1} result from the symmetric stretching vibration of the azide ligands.

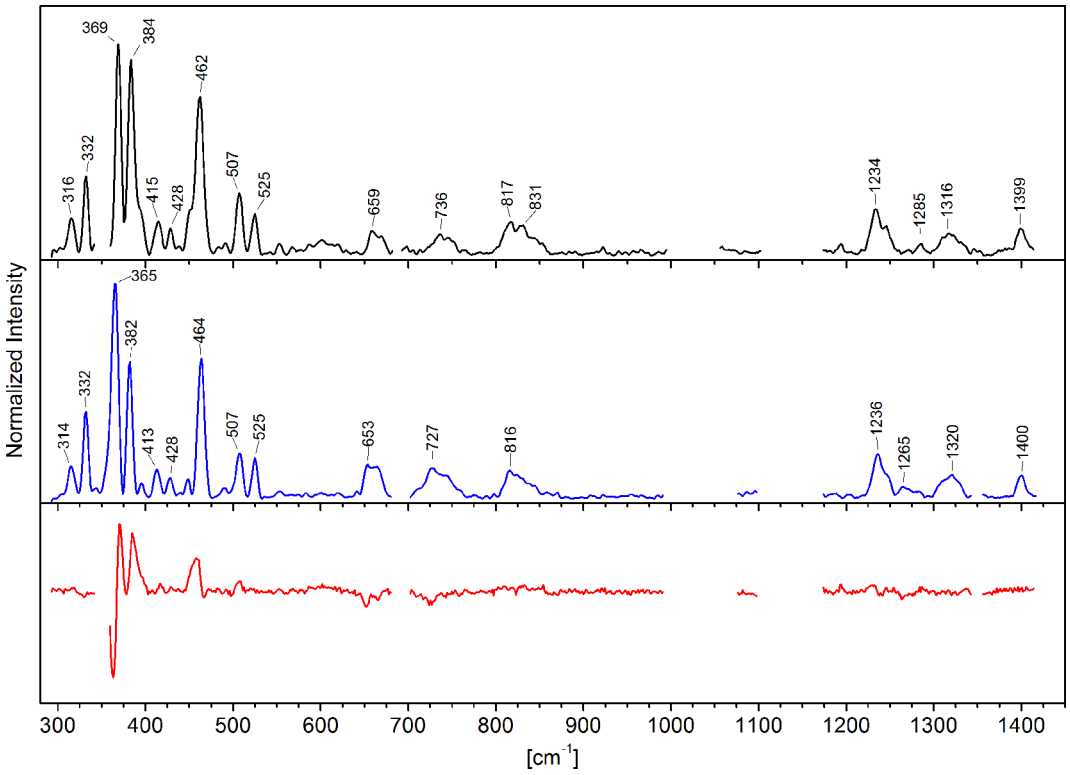

Figure 4.22: Zoom into the 300 cm^{-1} – 1450 cm^{-1} region of the spectra in Figure 4.21.

Three broad signals were recorded in the 650 cm^{-1}-840 cm^{-1} region. Due to the high noise level, it is not even possible to deduce the exact maximum of these peaks. Two signals are expected in this region for the in-phase combination of the $\delta_{ip}(N_3)$ and $\delta_{op}(N_3)$ bending modes that are expected to show an isotope effect.

Signals observedat 462 cm^{-1}, 384 cm^{-1} and 369 cm^{-1} show relatively high intensity in the experimental spectrum and a small shift upon ^{15}N-isotope labeling (2 cm^{-1}, -2 cm^{-1}, -4 cm^{-1}). However, due to the low quality of the data it is not clear if this is really an effect that can be attributed to an isotope shift or is just a result of the high noise-level.

Again, DFT-calculations are performed to support the assignment of the observed peaks. A comprehensive list, including a description of the modes and a possible assignment to experimentally observed peaks is provided in Table 4.13. Calculated spectra for the natural isotope and for the ^{15}N-

isotope labeled compound are provided in Figure 4.23. The antisymmetric stretching vibration is calculated to be 2076 cm^{-1} which is in reasonable agreement with the experimentally observed signal at 2052 cm^{-1}. An isotope shift of -11 cm^{-1} is observed experimentally which is in excellent agreement with the calculated average shift of -10 cm^{-1} (see Table 4.12).

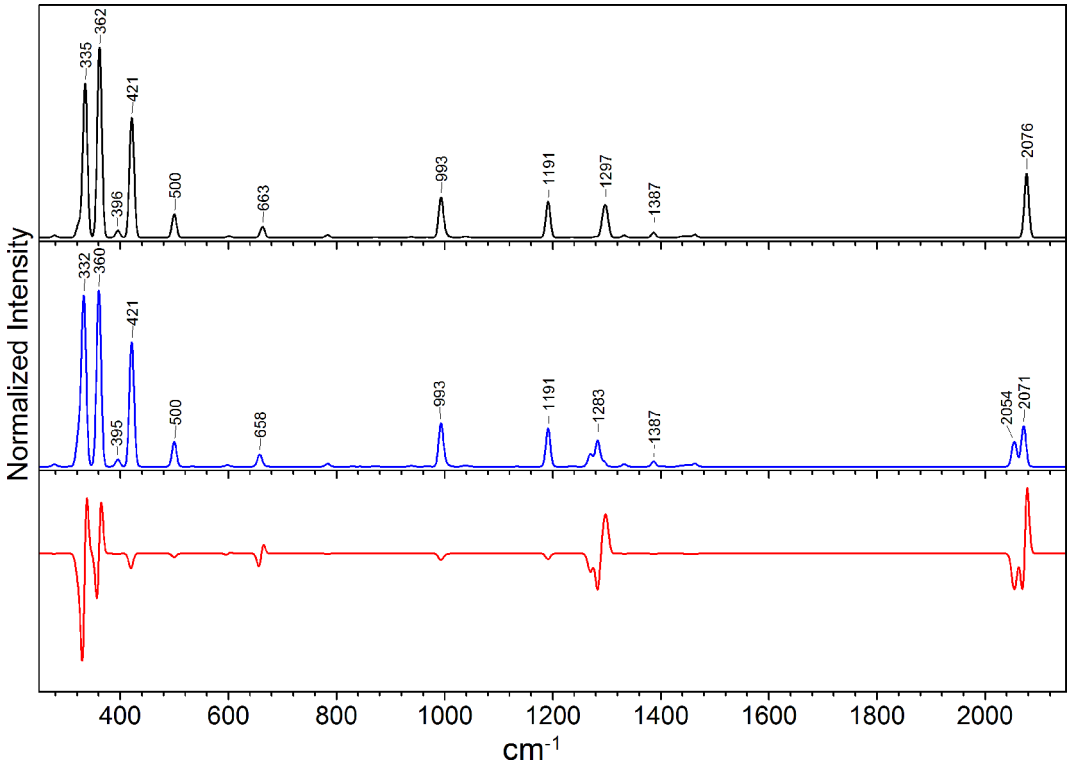

Figure 4.23: Calculated resonance Raman spectrum for $[Fe^{III}(N_3)_2cyc]^+$. Black: Natural isotope, Blue: mixture of the different ^{15}N-isotope labeling possibilities, red: Difference spectrum. Level of theory: B3LYP/RIJCOSX/def2-TZVP excitation wavelength 512 nm.

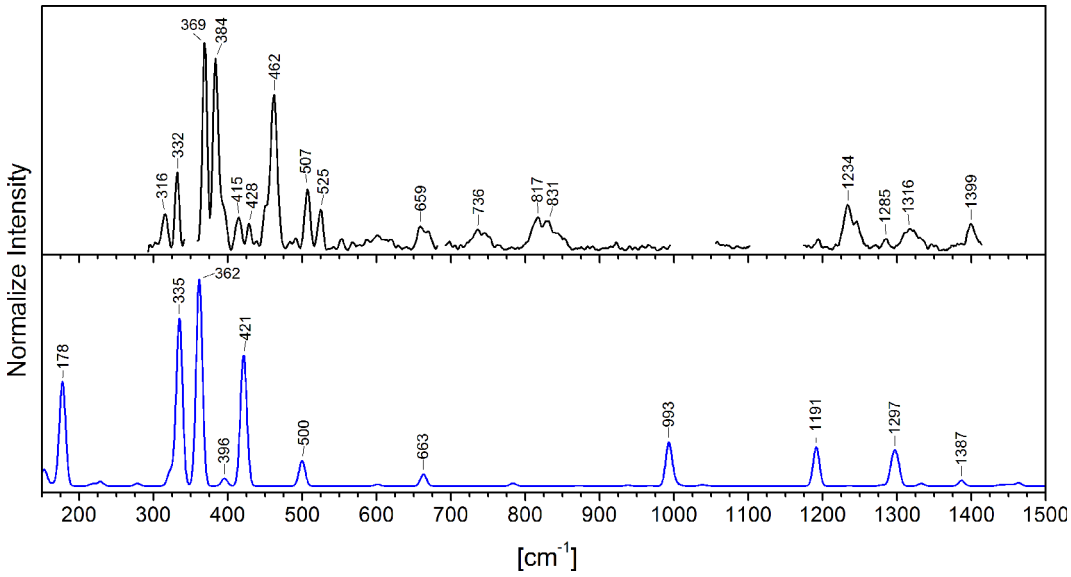

Figure 4.24: Experimental (black) and calculated (blue) resonance Raman spectrum for $[Fe^{III}(N_3)_2cyc]^+$.

The 150 cm^{-1} - 1500cm^{-1} area of the experimental and calculated spectra are compared in Figure 4.24. Assignment of the peaks in the 1200 cm^{-1} – 1400 cm^{-1} range is still very difficult due to the high noise level and the absence of any isotope effect in the experimental spectra. Still, a possible assignment is provided in Table 4.13, even it is vague. Calculated modes are illustrated in Figure 4.25.

The in phase combination of the $\delta_{ip}(N_3)$ bending modes is predicted by DFT to appear at 663 cm^{-1} with an isotope shift of -5 cm^{-1} upon ^{15}N-substitution and can be assigned to the experimentally observed signal at ~659 cm^{-1}. The Raman active $\delta_{op}(N_3)$ mode is predicted by DFT to appear at 601 cm^{-1}, but with negligible resonance Raman intensity. It is therefore not expected in the experimental spectrum.

Table 4.13: Calculated and experimental resonance Raman modes for $[Fe^{III}(N_3)_2cyc]^+$, suggested assignment based on the calculations, dimensionless normal coordinate displacements (Δ) for the LMCT transition and the calculated relative resonance Raman intensity.

exp. freq. [cm^{-1}]	calc. freq. [cm^{-1}]	calc. rel. int.	Δ	mode description
2052	2077	0.34	0.38	$\nu_{as}(N_3)$, in-phase combination / A_g
	2069			$\nu_s(N_3)$, out-of-phase combination / B_u
1399	1387	0.03	-0.13	$\delta(CH_2)$ wagging mode
1316	1300	0.11	-0.26	$\nu_s(N_3)$; in-phase combination / A_g.
	1297	0.11	-0.23	$\delta(CH_2)$ twisting mode
1285				
1234	1191	0.19	-0.29	δ(N-H) bending + $\delta(CH_2)$ rocking
	993	0.21	-0.27	δ(N-H) bending
831				
817				
736				
659	663	0.06	-0.50	$\delta_{ip}(N_3)$ / A_g
525	500	0.12	-0.23	$\delta(CH_2)$ rocking mode
507				
462	421	0.54	-0.38	ν(Fe-N_{Cyc})
428	396	0.04	0.05	ν(Fe-N_{Cyc})
415				
384	362	1.00	0.70	ν(Fe-N_{Cyc}) + ν(Fe-N_3)
369	335	0.81	0.24	ν(Fe-N_{Cyc}) + ν(Fe-N_3)
322	178 (?)	0.50	-2.12	δ(Fe-N_3)
316				

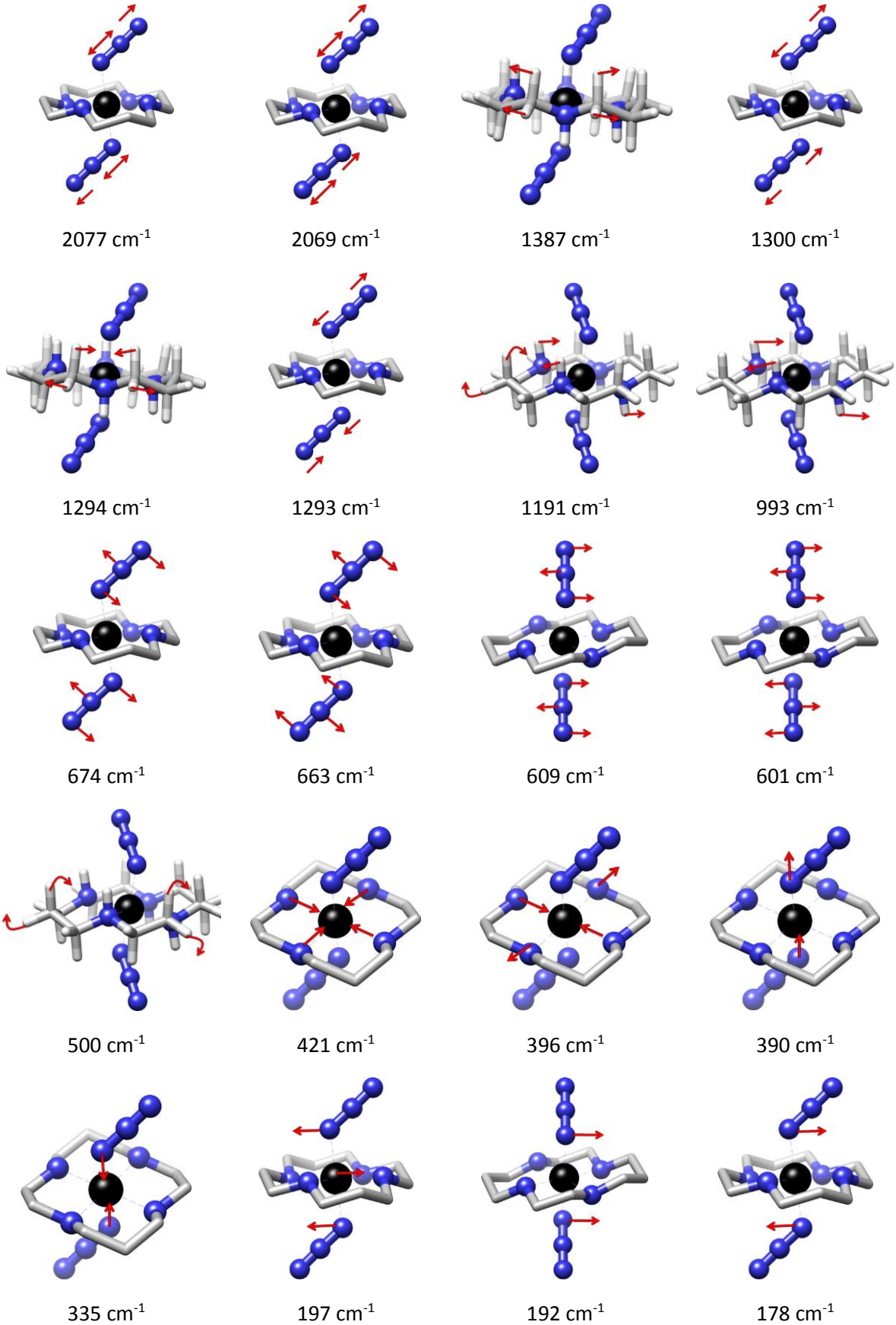

Figure 4.25: Schematic representations of calculated normal modes for the $[Fe^{III}(N_3)_2cyc]^+$ complex.

The experimental peak pattern in the 350 cm^{-1} – 500 cm^{-1} range is reasonably well reproduced in the calculations, even in the calculations these modes appear systematically at lower energy. At 421 cm^{-1} a ν(Fe-N_{Cyc}) stretching vibration between iron and the equatorial cyclam-nitrogen atoms was calculated which can be assigned to the experimental peak at 462 cm^{-1}. As discussed in Chapter 4.5.1, similar vibrations were identified for the $[Fe^{III}(N_3)cyc\text{-}ac]^+$ complex by resonance Raman spectroscopy and in previously published NRVS-measurements.[45] The intense signal calculated at 362 cm^{-1} results from a stretching vibration between iron and all iron bond atoms and shows a small isotope shift of -2 cm^{-1}. Due to the position and the high intensity in the experimental spectrum, this calculated mode can be assigned to the experimental peak at 384 cm^{-1} that also shows an isotope shift of -2 cm^{-1}. A similar vibration was calculated to appear at 335 cm^{-1} that shows an isotope shift of -3 cm^{-1}. It can, therefore, be assumed that the experimental signal observed at 369 cm^{-1}, that also shows a small isotope shift, results from this vibration.

A summary of the calculated and experimental resonance Raman modes is given in Table 4.13 together with a possible assignment. The modes are sketched schematically in Figure 4.25.

Even the quality of the obtained data is low, it was possible to assign few bands based on the experimentally observed isotope effect and DFT calculations. However, it remains difficult to identify the symmetric stretching vibration of the azide ligand, as it was also the case for the mono-azido complex $[Fe^{III}(N_3)cyc\text{-}ac]^+$. In the IR-spectrum, slight variations were observed in the corresponding region, however, several bands overlap in this spectral range. In the experimental resonance Raman spectra, no isotope shift was observed in the corresponding region at all.

A reason for the aforementioned difficulties might be the presence of several isomers for the ^{15}N-labeled species, since in the azide anions only one nitrogen atom is ^{15}N-substituted. It was shown by DFT-calculations that the isotope shift significantly depends on the ^{15}N-substitution pattern ($\alpha\alpha$-^{15}N, $\alpha\gamma$-^{15}N or $\gamma\gamma$-^{15}N). Given that the barrier of rotation for the azide ligand is expected to be small, several conformations for the azide ligand are possible as it was shown in more detail for the mono-azido complex (see page 64). The presence of further conformations besides the one characterized by X-ray crystallography will result in additional peaks and/or broadening of the signals. Further difficulties might result from irradiation damage given that photolysis of the azido-iron(III) complexes is possible with a similar wavelength alike the one used in the resonance Raman measurements.

Hence, there are several potential reasons for the limited quality of the obtained spectra. But still, the data provides valuable information. As already assumed from the intensity and position of the signal at 488 nm / 20499 cm^{-1} in the experimental absorption spectrum and corresponding TD-DFT calculations (Chapter 4.3.2), the resonance Raman data supports the assignment of this band to a LMCT-transition from the azide ligand to the metal. The antisymmetric-stretching mode of the azide ligand calculated to be 2077 cm^{-1}, for which an intense signal is obtained in the resonance Raman spectrum, indicates a non-symmetric deformation of the azide ligands upon irradiation in the LMCT band. This might results in the elimination of N_2 and formation of an nitrido-iron(V) complex.

4.5.3. Time Resolved IR Spectroscopy on the Complex $[Fe^{III}(N_3)cyc\text{-}ac]PF_6$ [2]

In collaboration with the group of Prof. Peter Vöhringer (University of Bonn) and the group of Prof. Dirk Schwarzer (Max-Planck-Institute for biophysical Chemistry, Göttingen) the photochemistry of the complex $[Fe^{III}(N_3)cyc\text{-}ac]PF_6$ was investigated by time-resolved IR measurements.[217-218] It shall be stated here explicitly that the time resolved IR spectra shown in this chapter were recorded by these groups and are not part of the thesis. Significant amounts of the sample were synthesized by the author of the present thesis and DFT calculations were performed to support the experimental results. Publications based on the results presented in this Chapter 4.5.3 (*Eur.J.Chem* **2012**, *18*, 3043 and *Phys.Chem.Chem.Phys.* **2012**, *14*, 6165) have been written together by all involved groups. The results will be discussed here briefly without going in details of the experimental work., the experimental results are only provided here for consistency.

Time resolved IR measurements allow to probe the photochemistry on a very short time scale. Therefore, detection of short living species is possible that cannot be studied by steady-state methods, i.e. Mössbauer or EPR-spectroscopy used in the present thesis. For these methods, the investigated compounds have to be stable at least for very few minutes (EPR) or several hours (Mössbauer).

Step-scan and rapid-scan time-resolved Fourier transform infrared spectroscopy allows to record IR-spectra immediately after the sample was excited by a 266 nm laser pulse. In the present study, picosecond (ps) to millisecond (ms) time resolutions were achieved, depending on the used experimental setup. The time resolved IR-spectra were measured from 0.6-2.0 mmol L^{-1} solutions of the complex $[Fe^{III}(N_3)cyc\text{-}ac]PF_6$ in argon purged acetonitrile. Vacant coordination sites that originate from photo-elimination of a ligand are assumed to be occupied immediately by a solvent acetonitrile molecule. It is well established that these processes take place within a few picoseconds.[219-220]

Detected IR modes are compared to those obtained from DFT calculations to support the assignment to the proposed photo products. For those complexes where the spin ground state is not known, calculations were performed for all conceivable multiplicities. Structures were optimized with the BP86/def2-TZVP/RI/COSMO level of theory and given energies are obtained from B3LYP/def2-TZVP/RIJCOSX/COSMO single point calculations on these geometries including ZPE correction from the BP86 frequency calculations. IR modes were calculated on the BP86/def2-TZVP/RI level of theory with tightened convergence criteria (see page 31 for details). The calculated and experimental vibrations are summarized in Table 4.14. It will be referred to these during the discussion of the results.

The absorption spectrum of the complex $[Fe^{III}(N_3)cyc\text{-}ac]PF_6$ in acetonitrile solution was already discussed in Chapter 4.3.1. The chosen laser wavelength of 266 nm (37594 cm^{-1}) lies between two transitions at 35861 cm^{-1} (279 nm) and 40598 cm^{-1} (246 nm), deduced from a Gaussian deconvolution of the experimental spectrum (see Chapter 4.3.1). The higher energy tail of the lower energy band and the lower energy tail of the higher energy band encounters with the laser wavelength and therefore several excited states might play a role in the observed photochemistry. TD-DFT calculations have

[2] This section is reprinted with permission from J.T. Alacan, O. Krahe, A.C. Filippou, F. Neese, D. Schwarzer, P. Vöhringer "The Photochemistry of $[Fe^{III}N_3(cyclam\text{-}ac)]PF_6$ at 266 nm", *Chem. Eur. J.* **2012**, *18*, 3043. Copyright 2014 John Wiley & Sons, Inc and Reproduced from Ref.[217] with permission from the PCCP Owner Societies.

shown that several LMCT transitions appear in the corresponding region, however, a clear assignment is difficult (see discussion on page 45). Therefore, the nature of the excited state that might be reached upon excitation with a 266 nm laser is unfortunately not known in detail, besides the fact that it must be a LMCT-state. Experimentally observed IR bands at 2051 cm^{-1} and 1698 cm^{-1} were already in Chapter 4.5.1 assigned to the antisymmetric stretching vibration of the azide ligand and the carboxylate stretching vibration, respectively.

Table 4.14: Calculated and experimental IR frequencies for observed and conceivable species For those species where the spin ground state is not known, calculated relative energies are provided.

	S	rel E [kJ mol^{-1}]	ν(C=O) Calc. [cm^{-1}]	ν(C=O) Exp. [cm^{-1}]	$\nu_{as}(N_3)$ Calc. [cm^{-1}]	$\nu_{as}(N_3)$ Exp. [cm^{-1}]
$[Fe^{III}(N_3)cyc\text{-}ac]^+$	1/2		1702	1689	2053	2051
$[Fe^{II}(N_3)cyc\text{-}ac]^+$	0		1651	1635	2063	2051
$[Fe^{III}(MeCN)cyc\text{-}ac]^{2+}$	1/2	0	1733			
	3/2	19	1717			
	5/2	36	1711			
$[Fe^{II}(MeCN)cyc\text{-}ac]^+$	0		1687	1640		
$[Fe^{V}(N)cyc\text{-}ac]^+$	1/2		1643	1658 (from ref [56])		
$[Fe^{II}(CO)cyc\text{-}ac]^+$	0	0	1696[a] 1912[b]	1655[a] 1945[b]		
	1	69	1692[a] 1933[b]			
	2	64	1682[a] 1919[b]			
$[Fe^{III}(NCO)cyc\text{-}ac]^+$	1/2	0	1706[a] 2210[c]			
	3/2	29	1692[a] 2211[c]			
	5/2	26	1682[a] 2187[c]			
$[Fe^{II}(O_2)cyc\text{-}ac]^+$	0	70	1698	1677		
	1	0	1706			
	2	52	1700			
N_3^-	0				2035	2006
$N_3^\bullet$	1/2				1705	1660
$N_6^{\bullet-}$	1/2				1901	

[a] acetato CO, [b] carbon monoxide ligand, [c] isocyanato ligand

Difference spectra recorded 104 ms and 11 s after excitation with a 266 nm laser are shown in Figure 4.26, left. Bleaching of the antisymmetric azide stretching vibration at 2051 cm^{-1} is observed after irradiation with a 266 nm laser pulse. The carbonyl stretching vibration at 1689 cm^{-1} is shifted about 49 cm^{-1}, resulting in a signal at 1640 cm^{-1}. It was proposed previously by Grapperhaus *et al.*[43] that photolysis in solution with UV light yields the low-spin ferrous complex $[Fe^{II}(MeCN)cyc\text{-}ac]^+$ via reductive elimination of an azide radical ($N_3^\bullet$). The same photoreaction is assumed here upon photolysis with 266 nm light. As shown in Table 4.14, even the shift of the carbonyl stretching vibration is underestimated by the DFT-calculations, reasonable agreement between theory and experiment is found when the calculated modes for the azido-iron(III) complex and the formed iron(II) complex

$[Fe^{II}(MeCN)cyc\text{-}ac]^+$ are compared to the experimental results. Hence, the species formed upon irradiation with a 266 nm laser can be assigned to the ferrous low-spin complex[3] $[Fe^{II}(MeCN)cyc\text{-}ac]^+$.

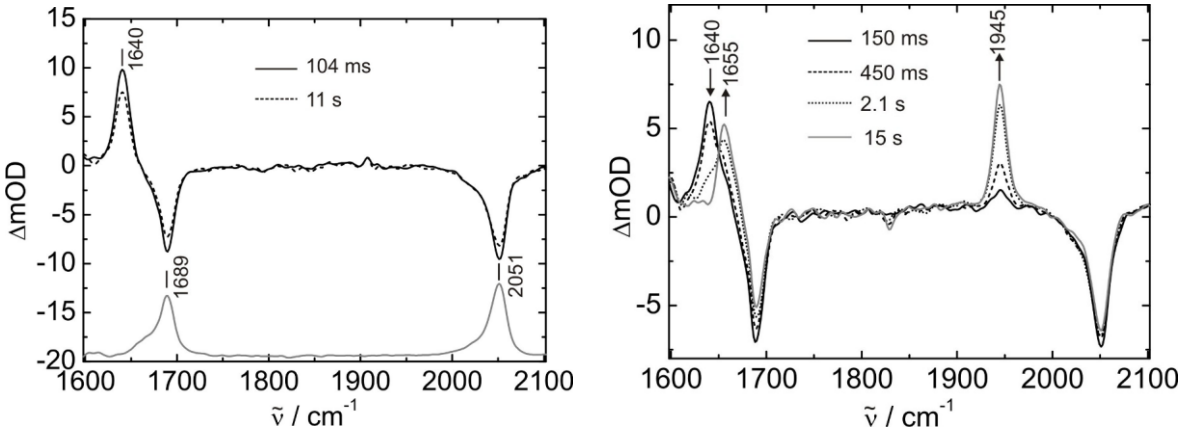

Figure 4.26: FTIR-Spectra of $[Fe^{III}(N_3)cyc\text{-}ac]PF_6$ in acetonitrile after 266 nm laser excitation. Left: Difference spectra 104 ms and 11 s after irradiation, grey curve represents the stationary FTIR spectrum. Right: FTIR difference spectra in CO purged acetonitrile 150 ms, 450 ms, 2.1 s and 15 s after laser excitation.

Further experiments were performed to prove the formation of the complex $[Fe^{II}(MeCN)cyc\text{-}ac]^+$, and to rule out the formation of the nitrido-iron(V) complex $[Fe^{V}(N)cyc\text{-}ac]^+$ via the elimination of N_2. Therefore, time resolved IR-measurements were performed on an identical sample that was purged this time with carbon monoxide prior excitation with a 266 nm laser. If the $[Fe^{II}(MeCN)cyc\text{-}ac]^+$ complex is formed it is expected to react with CO resulting in the complex $[Fe^{II}(CO)cyc\text{-}ac]^+$ since CO is a much better ligand than the acetonitrile solvent molecules. For the formed carbon-monoxide complex a new characteristic band is expected from the CO ligand in the range between 1800 cm^{-1} and 2100 cm^{-1}.[215,221] On the other hand, if the nitrido-iron(V) species is formed, it can react with CO resulting in an isocyanato complex $[Fe^{III}(NCO)cyc\text{-}ac]^+$. For the isocyanato complex a characteristic new IR band is expected around 2200 cm^{-1}.[215,222-223] The possible reactions are shown in Scheme 4.1.

For both complexes (NCO and CO) the low-spin state is predicted to be the ground state by DFT. The stretching vibration of the CO ligand in the $[Fe^{II}(CO)cyc\text{-}ac]^+$ complex is calculated to appear at 1912 cm^{-1} and the carbonyl stretching vibration of the carboxylate group at 1696 cm^{-1}, respectively. For the isocyanato complex a new band is expected at 2210 cm^{-1} while the carbonyl stretching vibration of the carboxylate group is expected at 1706 cm^{-1}. Hence, a small down shift of the carboxylate mode is expected for the CO-complex while a small shift to higher energy is expected for the isocyanato complex. Therefore, it is possible to distinguish the two potentially formed species based on their characteristic IR-mode for the new ligand.

[3] The nature of the formed complex will be investigated in detail in Chapter 4.6. It will be shown that electrochemical reduction of $[Fe^{III}(N_3)cyc\text{-}ac]PF_6$ results in the low-spin ferrous complex $[Fe^{II}(MeCN)cyc\text{-}ac]PF_6$ that shows a carboxylate stretching vibration at 1688 cm^{-1}, in agreement with the mode observed for the species that is formed here upon photolysis with a 266 nm laser.

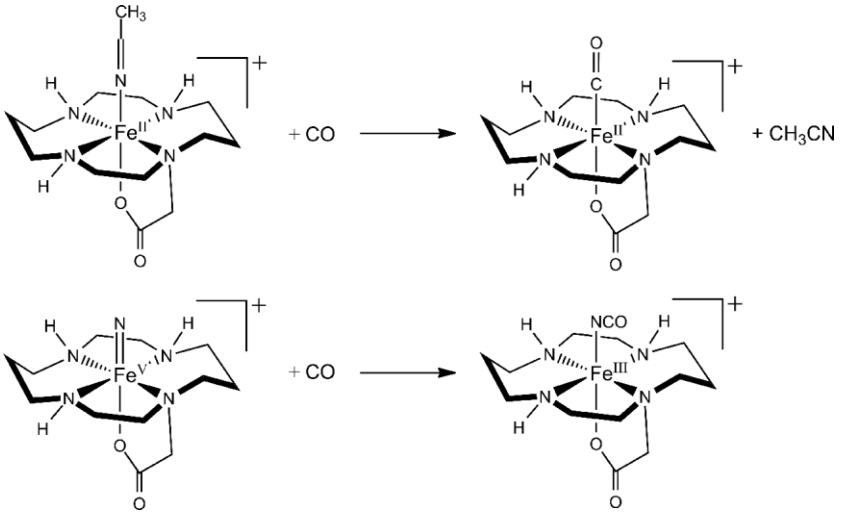

Scheme 4.1: Plausible reactions of the generated iron complexes upon photolysis in the presence of CO.

The resulting spectrum after photolysis of the $[Fe^{III}(N_3)cyc\text{-}ac]^+$ complex in the presence of CO is shown in Figure 4.26, right. Spectra recorded 150 ms and 450 ms after laser-excitation are nearly identical to those spectra obtained without CO. The azido mode at 2051 cm^{-1} is bleached while the carbonyl stretching vibration is shifted to 1640 cm^{-1}. However, spectra recorded after 2.1 s and 15 s show a shift of the 1640 cm^{-1} feature to 1655 cm^{-1}. Simultaneously a new signal evolves at 1945 cm^{-1}. This is completely consistent with the calculated modes for the carbon monoxide complex $[Fe^{II}(CO)cyc\text{-}ac]^+$. The experimentally observed mode at 1945 cm^{-1} is in good agreement with the calculated mode for the CO-ligand (1912 cm^{-1}). For the carboxylate CO-band a downshift of 34 cm^{-1} is observed while the DFT calculations predict a down shift of only 6 cm^{-1}. However, this is still within the accuracy of the DFT calculations. A signal at about 2210 cm^{-1}, which is the calculated IR-mode for the isocyanato complex, was not observed. Therefore it is clearly shown by a combination of experiments and DFT calculations that upon laser excitation with 266 nm in solution, the low-spin ferrous complex $[Fe^{II}(MeCN)cyc\text{-}ac]^+$ is formed, that can be trapped with carbon monoxide.

To explore in more detail the sub-millisecond processes following the 266 nm photolysis, step-scan FTIR difference absorption spectra were recorded with a time resolution of 500 ns for time delays of up to 800 µs. The resulting spectra are shown in Figure 4.27.

Again, the signal of the azido antisymmetric stretching vibration at 2051 cm^{-1} disappears. However, a small new feature evolves at 2006 cm^{-1} that disappears after 80 µs while the signal of the azido mode partially recovers with a delay of 800 µs. In the region of the carbonyl-stretching mode, a rather broad feature in the range from 1630 cm^{-1} to 1670 cm^{-1} appears in the 500 ns spectrum. After 80 µs the signal at ~1638 cm^{-1} has slightly increased. Notably, while the signal at 2051 cm^{-1} partially recovers, this is not seen for the 1689 cm^{-1} signal of the initial $[Fe^{III}(N_3)Cyc\text{-}ac]^+$ complex. Hence, the recovery of the 2051 cm^{-1} signal in the spectrum recorded 80 µs after photolysis cannot be explained by reformation of the initial $[Fe^{III}(N_3)Cyc\text{-}ac]^+$ complex. In the difference spectrum recorded 800 µs after laser excitation, the signal at 1660 cm^{-1} completely decayed, whereas an absorption at 1640 cm^{-1} remains and continues to persist for at least 10 s, as it was the case in the spectra shown in Figure 4.26, left. Furthermore, the band at 1689 cm^{-1}, which was assigned to the carboxylate group of the initial complex $[Fe^{III}(N_3)cyc]^+$,is partially recovered.

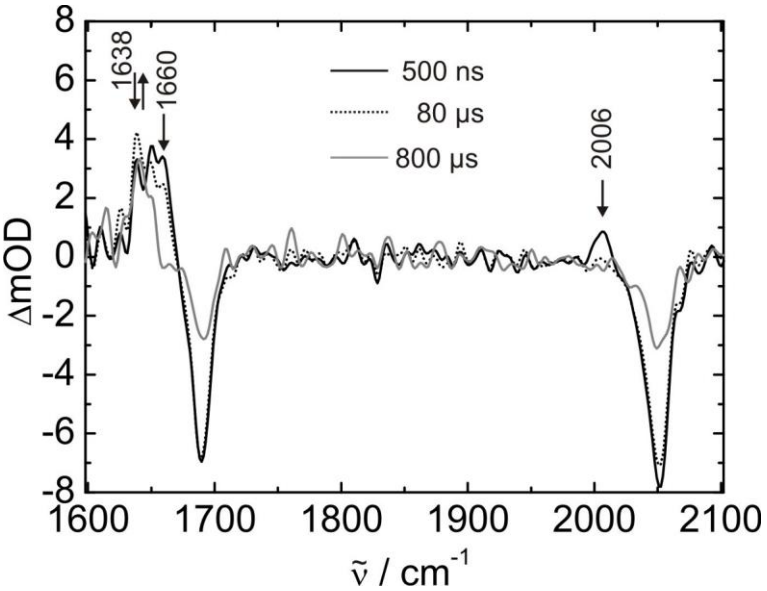

Figure 4.27: Difference FTIR spectra recorded 500 ns, 80 µs and 800 µs after excitation with a 266 nm laser.

It is obvious from the measurements shown in Figure 4.27 that further processes take place on a shorter time scale, in addition to those observed in the rapid-scan measurements (Figure 4.26).

The signal at 1660 cm^{-1} decays within 800 µs and was therefore not visible in the measurements with a millisecond resolution shown in Figure 4.26, left. It was discussed that the just shown formation of the $[Fe^{II}(MeCN)cyc\text{-}ac]^+$ complex proceeds via elimination of an azide radical. However, the azide radical itself was not observed in the measurements with millisecond resolution. This very reactive species was observed up to now only at cryogenic temperatures in a nitrogen matrix with an antisymmetric stretching vibration at 1658 cm^{-1}.[224-225] Therefore, it is very likely that the signal observed at 1660 cm^{-1} after 80 µs results from the azide radical whose antisymmetric stretching vibration was calculated to be 1705 cm^{-1}.

Interesting is the transient observation of a signal at 2006 cm^{-1}, since this coincides with the signal that can be observed for the free azide anion in acetonitrile solution (see Figure 4.35, page 91 for the IR spectrum of tetrabutylammonium azide in acetonitrile). The antisymmetric stretching vibration of the azide anion is further calculated to appear at 2035 cm^{-1}, which is in reasonable agreement with the measured signal at 2006 cm^{-1}. Further kinetic analysis[218] (not shown here in detail) reveals that the decay of the signal at 2006 cm^{-1} is correlated with the rise of the 1638 cm^{-1} band which indicates that the 1638 cm^{-1} signal is formed through a reaction that consumes azide anions. As mentioned before, this reaction cannot be the recovery of the initial $[Fe^{III}(N_3)Cyc\text{-}ac]^+$ complex since the characteristic signal of the carboxylate group at 1689 cm^{-1} does not recover parallel to that within the first 80 µs.

The formation of an azide anion can be easily explained by redox-neutral dissociation of this ligand from the parent $[Fe^{III}(N_3)cyc\text{-}ac]^+$ complex, which is shown in Scheme 4.2 as pathway b. As discussed before, occupation of the vacant coordination site by an acetonitrile solvent molecule is expected to be fast. Still, it is not clear which species is responsible for the signal observed at 1638 cm^{-1}, which is coupled with the consumption of azide anions. A possibility would be the adduct formation with azide radicals. This radical-anion species $N_6^{\bullet-}$ was observed earlier, its characteristic IR vibration is calculated here by DFT to appear at 1901 cm^{-1} and was observed experimentally at 1842 cm^{-1}.[226]

Hence, this species would be expected at much higher energy in the IR spectrum than the observed 1638 cm^{-1} signal. The only remaining reaction partner for the azide anions resulting in a new species that shows a signal at 1938 cm^{-1} is the iron(II) complex $[Fe^{II}(MeCN)cyc\text{-}ac]^+$. This is indicated in Scheme 4.2 as pathway c.

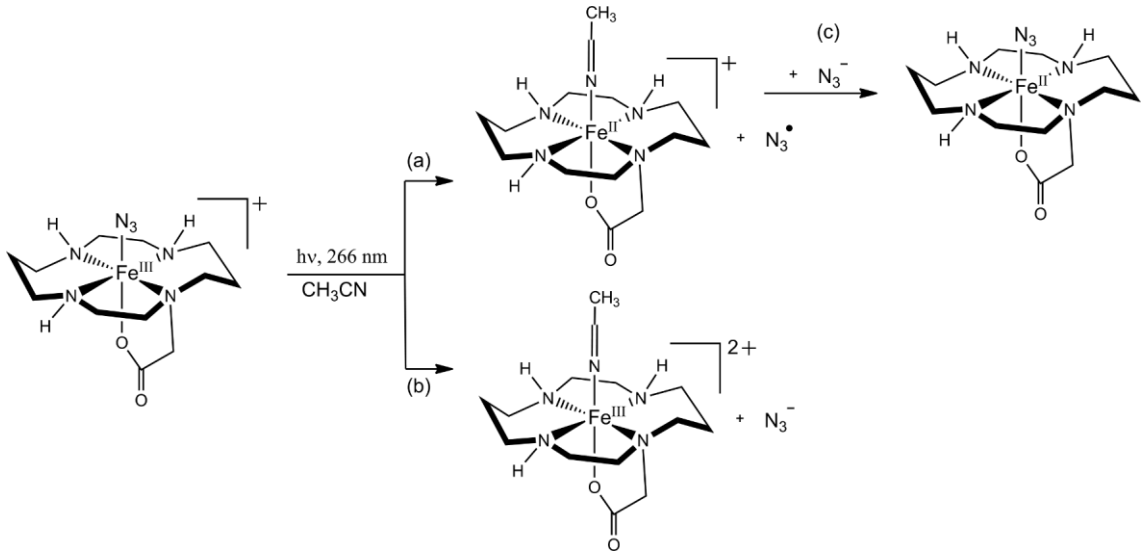

Scheme 4.2: Possible photo-dissociative pathways and subsequent reactions.

The iron(II) complex formed via azide radical elimination reacts with azide anions that are present in the solution due to redox-neutral dissociation of the azide anion from the initial $[Fe^{III}(N_3)cyc\text{-}ac]^+$ complex. This can be supported again by DFT calculations. For the neutral ferrous complex $[Fe^{II}(N_3)cyc\text{-}ac]$ the antisymmetric stretching vibration of the azide ligand was calculated to appear at 2063 cm^{-1}, hence, upshifted about 10 cm^{-1} when compared to the calculations for the iron(III) analogue. Experimentally, the antisymmetric stretching mode is observed at 2051 cm^{-1} for the putative iron(II) complex $[Fe^{II}(N_3)cyc\text{-}ac]$ as well as for the analogue iron(III) complex $[Fe^{III}(N_3)cyc\text{-}ac]^+$. Even a different of 10 cm^{-1} was calculated for this vibration by DFT, this is still in good agreement with the experiment and might not be resolved in the measurements due to the line width of the signal. The carbonyl stretching vibration for the azido-iron(II) complex is predicted to be 1651 cm^{-1} and therefore 51 cm^{-1} below the calculated mode for the azido-iron(III) complex. This is in nearly perfect agreement with the experimentally observed down shift of 54 cm^{-1}. It was further probed computationally if the proposed reaction is thermodynamically feasible and it turned out that the substitution of a coordinated solvent molecule in $[Fe^{II}(MeCN)cyc\text{-}ac]^+$ by an azide anion resulting in the complex $[Fe^{II}(N_3)cyc\text{-}ac]$ (pathway c in Scheme 4.2) is exothermic about -18 kJ mol^{-1}. This proposed reaction was further verified by additional kinetic analysis where the photolysis was performed in the presence of a large excess of azide anions.[218]

Further measurements were performed with a femtosecond time resolution by the group of Prof. Dirk Schwarzer.[217] This allows to study even faster processes than those that were discussed above. In these experiments, also a 266 nm laser was used for the photo excitation and the dynamics were studied by time-resolved IR spectroscopy.

In agreement with the just discussed results, a bleaching of the signal at 2051 cm^{-1} was initiated upon excitation with the 266 nm laser. Furthermore, a shift of the carbonyl stretching vibration to higher energy was observed (see Figure 4.28). The signal at ~1650 cm^{-1} was analyzed in detail and a

deconvolution of the spectrum recorded 80 ps after the excitation results in two peaks at 1659 cm^{-1} and 1643 cm^{-1} which reveals that the signal must result from two different species (see Figure 4.28, left). In analogy to the signal observed at 1660 cm^{-1} in the measurements with a ns resolution (see Figure 4.27), the 1659 cm^{-1} peak is assigned to the azide radical formed by reductive elimination from the parent $[Fe^{III}(N_3)cyc\text{-}ac]^+$ complex. This is also in reasonable agreement with the calculated antisymmetric stretching vibration for the azide radical at 1705 cm^{-1}. Again, the signal at 1643 cm^{-1} can be assigned to the ferrous low-spin complex $[Fe^{II}(MeCN)cyc\text{-}ac]^+$ that results from the elimination of the azide radical and whose carbonyl stretching vibration was calculated to be 1687 cm^{-1}.

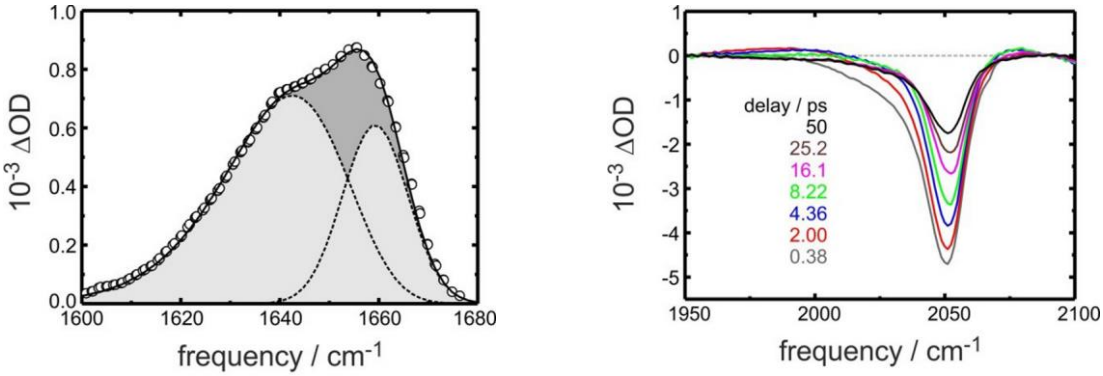

Figure 4.28: Gaussian decomposition of the ~1650 cm-1 band observed 80 ps after photolysis with a 266 nm laser (left) and difference spectra of azido stretching region after different time delays (right).

Detailed inspection of the spectra in the ~2050 cm^{-1} region (see Figure 4.28, right) shows further interesting results about the azide ligand. The signal at 2051 cm^{-1} is bleached immediately after photo excitation within very few picoseconds (i.e. at a delay of 0.38 ps in Figure 4.28, right). However, at such early delays no induced absorption is observed for the excited molecule.

A possible explanation would be the formation of a species that does not show a characteristic IR-band. For the azide radical ($N_3^{\bullet}$) it was reported earlier that it can form a cyclic isomer,[227-230] that was previously studied computationally. Calculations at the CASSCF(15,12)/cc-pVTZ level of theory revealed that the cyclic isomer represents a minimum structure that is 126 kJ mol^{-1} higher in energy than the linear isomer.[228,230] The antisymmetric stretching vibration for the linear isomer was calculated to appear at 1659 cm^{-1} in this study and the breathing mode of the cyclic species at 1632 cm^{-1}. However, the infrared activity of the cyclic isomer turned out to be two orders of magnitude lower than for the linear isomer, which can be easily explained by symmetry reasons.[227]

Therefore, in the present work it is investigated computationally if the formation of such a cyclic azide isomer is also feasible for the $[Fe^{III}(N_3)cyc\text{-}ac]^+$ complex. On the B3LYP/def2-TZVP/RIJCOSX level of theory it was indeed possible to locate a minimum structure with a cyclic azide coordinated to the iron complex via one nitrogen atom, as shown in Figure 4.29. By DFT this isomer in the doublet state was calculated to be 235 kJ mol^{-1} higher in energy than the parent $[Fe^{III}(N_3)cyc\text{-}ac]^+$ complex with a linear azide ligand (the quartet state is 38 kJ mol^{-1} and the sextet state is 46 kJ mol^{-1} higher in energy than the doublet state, respectively). CASSCF/NEVPT2 calculations were used to calculate the energy difference of these two isomers in the doublet state with higher accuracy. The chosen active space consisted of 7 electrons (five d-electrons of Fe(III) and two electrons from an azide ligand π-orbital) in 7 orbitals (five d-orbitals, one doubly occupied and one virtual azido-π-orbital). For both isomers the same active space was chosen and state average calculations over 10 roots were performed. The

resulting NEVPT2 energy difference between the ground state structure with a linear azide ligand and the isomer with a cyclic azide ligand is 256 kJ mol^{-1}.

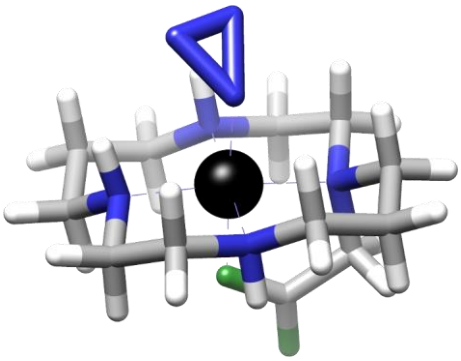

Figure 4.29: Structure of the [Fe^{III}(N$_3$)cyc-ac]$^+$ complex with a cyclic azide isomer coordinated at iron.

DFT frequency calculations (B3LYP/def2-TZVP/RIJCOSX, scaling factor 0.9614[186]) result in a stretching (breathing) mode for the cyclic azide at 1779 cm^{-1} with an intensity ~200 times lower than that for the acetato-CO-stretching vibration. Hence, the DFT calculations support the assumption that a species with a cyclic isomer of the azide ligand will be formed within the first picoseconds that does not show any signal for the azide ligand in the IR spectrum. Furthermore, the energy of a 266 nm photon inducing the photolysis corresponds to 450 kJ mol^{-1} which shows that the cyclic isomer might be accessible in the photochemical reaction, even it was calculated to be high in energy (256 kJ mol^{-1}).

Time-resolved IR measurements in combination with DFT calculations provided valuable information about the photochemistry of the complex [Fe^{III}(N$_3$)cyc-ac]$^+$ in solution upon excitation with a 266 nm laser. It was possible to detect the ferrous [Fe^{III}(MeCN)cyc-ac]$^+$ complex that was further trapped with CO. Further, a signal observed at 1660 cm^{-1} on a μs time scale presumably results from the azide radical which is in agreement with the initially assumed reductive elimination reaction upon photolysis with light in the UV-region.[43]

However, it should be mentioned here that in a very recent study Vöhringer *et al.* have shown that formation of the nitrido-iron(V) complex [Fe^{V}(N)cyc-ac]$^+$ can also be observed as a product from the photolysis of the parent azido-iron(III) complex with a 266 nm laser.[56]

In Chapter 4.6.3, photolysis experiments on frozen and liquid solution Mössbauer samples will be performed. These will reveal differences and similarities to the just discussed fluid solution room temperature measurements.

4.6. Mössbauer Experiments and Photolysis of the Complex $[Fe^{III}(N_3)cyc\text{-}ac]PF_6$ [4]

One of the most useful methods to investigate iron complexes is ^{57}Fe-Mössbauer spectroscopy. Mössbauer spectroscopy provides valuable information about the iron center in the compounds of interest, as outlined in the introduction (Chapter 2.2). Mössbauer experiments on the $[Fe^{III}(N_3)cyc\text{-}ac]PF_6$ complex and its photolysis products were performed previously.[43] However, the variable wavelength photolysis experiments were conducted using different conditions which makes it difficult to draw any conclusions about wavelength dependence. Therefore, photolysis experiments on Mössbauer samples were performed under identical conditions, where only the wavelength of the light source used was varied, or the same light source was used for different samples (liquid solution or frozen solution).

Samples were prepared from 1 mM solutions of the $[^{57}Fe^{III}(N_3)cyc\text{-}ac]PF_6$ complex in dry acetonitrile or butyronitrile, respectively. The compound was synthesized from 100% ^{57}Fe enriched material. ~0.7 mL of the solution was transferred in a Mössbauer cup under an inert atmosphere of argon and frozen using liquid nitrogen.

Mössbauer measurements were performed on a conventional spectrometer with alternating constant acceleration of the γ-source (1.8 GBq, 57Co/Rh), which was kept at room temperature. The Sample was placed in an Oxford Instruments Variox cryostat at 80 K. Magnetic Mössbauer measurements were performed in an Oxford Instruments Mössbauer-Spectromag 2000 cryostat where the sample was cooled down by Helium to 4.2 K. The magnetic field in the setup used is oriented perpendicular to the γ-beam and the magnetic field is stabilized at 1.0 T or 7.0 T. Calibration was performed with metallic iron and isomer shifts are quoted relative to the center of the magnetic spectrum of α-iron.

[4] This section is reprinted/adapted with permission from O. Krahe, E. Bill, F. Neese "Decay of Iron(V) Nitride Complexes By a N-N Bond-Coupling Reaction in Solution: A Combined Spectroscopic and Theoretical Analysis", *Angew. Chem. Int. Ed.* **2014**, *53*, 8727. Copyright 2014 John Wiley & Sons, Inc

4.6.1. Photolysis of Frozen Solution Samples with 470 nm Light

It was reported before, that photolysis of a frozen solution of $[Fe^{III}(N_3)cyc\text{-}ac]PF_6$ with light in the visible region results in the formation of nitrido-iron(V) complex $[Fe^{V}(N)cyc\text{-}ac]PF_6$.[43] In the present study, a blue LED lamp was used that mainly emits light with a wavelength of 470 nm (in the previous studies 420 nm light was used). As discussed in Chapter 4.3.1, 470 nm light coincides with an absorption of the complex that is assigned to a LMCT transition from the azide ligand to the metal ($\pi_{||}(N_3)\rightarrow d_{xz}/d_{yz}$).The sample was kept in a Dewar with liquid nitrogen during the photolysis process. After 6h of photolysis, the sample was transferred into a cryostat for the Mössbauer measurements while keeping the sample frozen by cooling with liquid nitrogen at all time. The Mössbauer spectra obtained before (top) and after (bottom) the photolysis are shown in Figure 4.30.

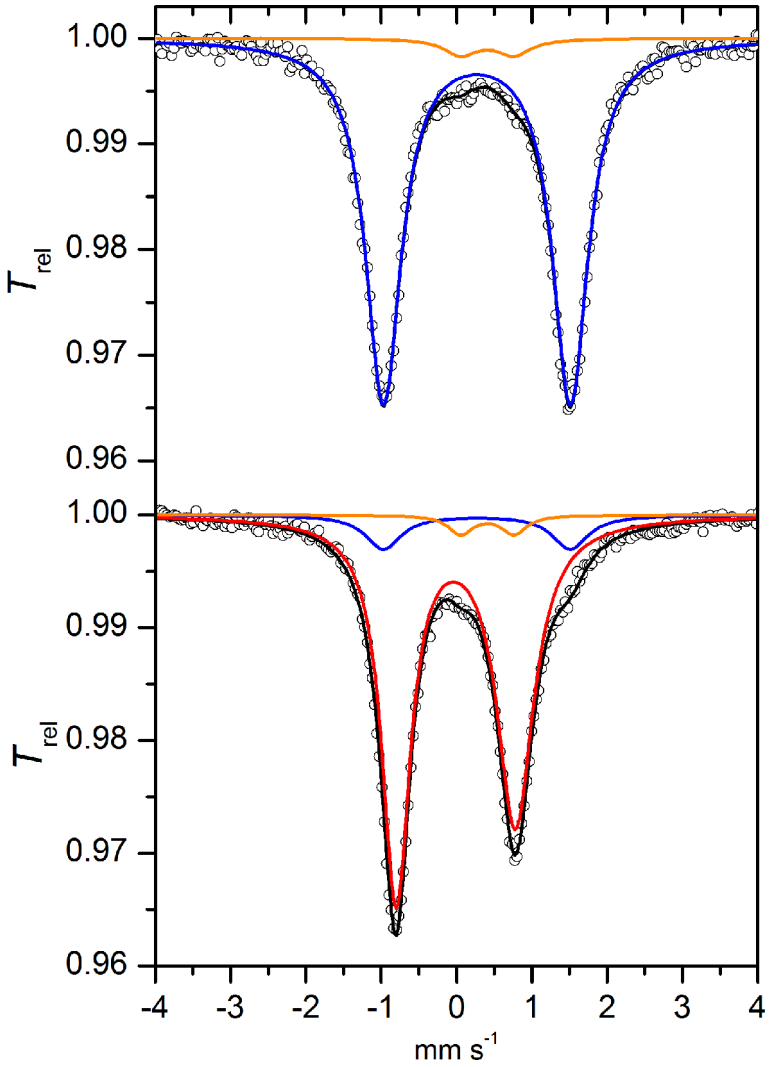

Figure 4.30: ^{57}Fe-Mössbauer spectra of a 1 mM solution of $[Fe^{III}(N_3)cyc\text{-}ac]PF_6$ in acetonitrile before (top) and after (bottom) photolysis at 77K with 470 nm light.

The spectrum of the iron(III) starting material (Figure 4.30, top, blue curve) was simulated with the Mössbauer parameters δ=0.27 mm s^{-1} and ΔE_Q=2.48 mm s^{-1} that account for ~96% of the spectrum. An impurity of 4% (orange trace, presumably ferric low-spin) was simulated with Mössbauer parameters δ=0.41 mm s^{-1} and ΔE_Q=0.71 mm s^{-1}. The sum of the simulations is indicated by the black curve in Figure

4.30. These Mössbauer-parameters are in good agreement with the previously published results and the calculated values shown in Table 4.15.[41,43]

After 6h photolysis with 470 nm light the Mössbauer spectrum changed significantly (Figure 4.30, bottom). The small impurity of ~4% remained, but most of the iron(III) starting material disappeared and a new signal with smaller isomer shift and smaller quadrupole splitting evolved. This new feature accounts for 87% of the spectrum and was simulated with the Mössbauer parameters δ=-0.01 mm s^{-1} and ΔE_Q=1.58 mm s^{-1} (red trace in Figure 4.30, bottom). This is once again in good agreement with previously published results for the nitrido-iron(V) complex.[41,43] DFT calculations (B3LYP/def2-TZVP/Fe: CP(PPP)/COSMO) were performed on the nitrido-iron(V) complex[5] and the predicted Mössbauer parameters are in good agreement with the experimental result. These results are summarized in Table 4.15.

Table 4.15: Experimental and calculated Mössbauer parameters for the $[Fe^{III}(N_3)cyc\text{-}ac]PF_6$ and $[Fe^{V}(N)cyc\text{-}ac]PF_6$ complexes.

	experimental			calculated		
	δ [mm s^{-1}]	ΔE_Q [mm s^{-1}]	η	δ [mm s^{-1}]	ΔE_Q [mm s^{-1}]	η
$[Fe^{III}(N_3)cyc\text{-}ac]PF_6$	0.27	-2.48	0.42	0.26	-2.36	0.27
$[Fe^{V}(N)cyc\text{-}ac]PF_6$	-0.01	1.58		-0.11	-1.89	0.61

η and the sign of ΔE_Q are obtained from measurements with applied magnetic field, see Chapter 5.8

It is, therefore, confirmed that the azido-iron(III) complex is oxidized during photolysis which is evident in a decrease of the isomer shift.

[5] Mössbauer parameters for the complexes $[Fe^{III}(N_3)cyc\text{-}ac]^+$ and $[Fe^{V}(N)cyc\text{-}ac]^+$ were calculated by DFT previously and are reported in Ref.[41]

4.6.2. Photolysis of Frozen Solution Samples with 304 nm Light

In the initial work by Grapperhaus *et al.* photolysis with UV-light at 300 nm was performed on solution samples at -35°C.[43] After photolyzing the sample, a new species with the Mössbauer parameters δ= 0.56 mm s^{-1} and ΔE_Q= 0.54 mm s^{-1} was detected and assigned to an low-spin iron(II) complex. From these results it was concluded that the photolysis with 300 nm light occurs primarily via homolytic cleavage of the Fe-N_3 bond, resulting in an iron(II) complex. Given that the photolysis experiments with visible and UV light were not performed under identical conditions (frozen vs. solution), the photolysis was repeated here with 304 nm light under the same conditions as just described for the experiment with 470 nm light. As discussed in Chapter 4.3.1, with 304 nm light other electronic excitations are expected than with 470 nm light which might result in different photochemical reactions.

An identical sample (1mM [^{57}Fe(N_3)cyc-ac]PF_6 in acetonitrile) was prepared and cooled down with liquid nitrogen. The sample was then photolyzed for 11h with light of 304 nm while the sample was kept in a Dewar cooled with liquid nitrogen. A HBO 100 mercury arc lamp equipped with a monochromator was used as the light source. The resulting Mössbauer-spectrum is shown in Figure 4.31 (the initial spectrum before photolysis was identical to that in Figure 4.30).

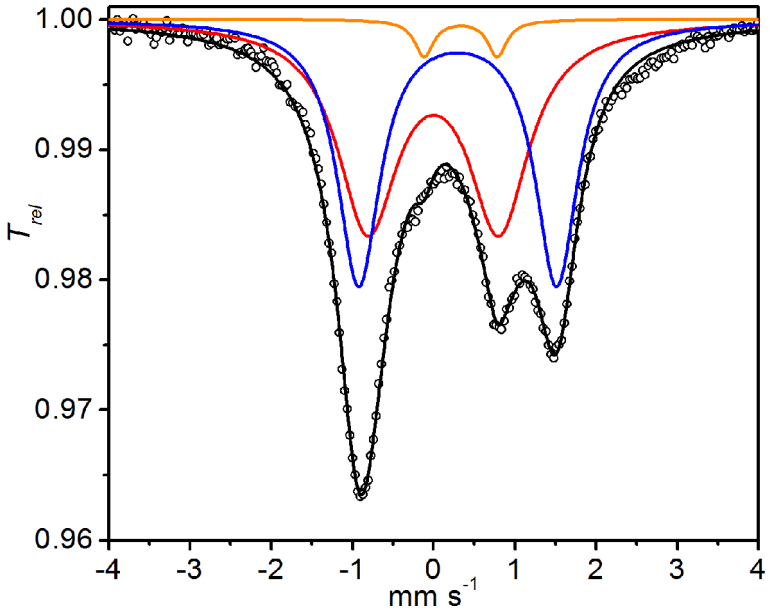

Figure 4.31: Mössbauer spectrum of 1mM [$^{57}Fe^{III}$(N_3)cyc-ac]PF_6 in acetonitrile after photolysis with 304 nm light for 11h.

Clearly, the photolysis is incomplete and iron(III) starting material partially remains (47%, blue line). But a new species was formed (red line 50%), simulated with the Mössbauer parameters δ= -0.01 mm s^{-1} and ΔE_Q= 1.58 mm s^{-1}. Hence, the isomer shift is reduced and did not increase as it would be expected for a reduction of the iron center. The Mössbauer parameters of the new species are completely identical to those obtained after photolysis with 470 nm light (*vide supra*). It can, therefore, be concluded that the nitrido-iron(V) complex [Fe^V(N)cyc-ac]PF_6 is formed independent of the wavelength used for photolysis and no iron(II) is formed on frozen solution samples. The initial conclusion of wavelength dependence for photolysis on Mössbauer samples[43] can be, therefore, not confirmed here. It should be mentioned again, that in the present experiments completely identical photolysis conditions were chosen, only the wavelength for the photolysis was varied.

4.6.3. Photolysis in Liquid Solution with 470 nm Light

Further photolysis experiments were performed on a Mössbauer sample with 470 nm light. Again a sample of 1mM [^{57}Fe(N_3)cyc-ac]PF_6 was prepared but this time butyronitrile was used as the solvent. The low melting point of butyronitrile (m.p. -112°C) allows the sample to be cooled down significantly, without yielding a solid frozen solution sample. The solution was prepared in a glove box and filled in a 1 mL Mössbauer cup containing a miniature stirring bar. The sample was then placed carefully in a Schlenk tube, taken out of the glove box but kept under argon at all times. While continuously stirring the solution with a magnetic stirring plate it was cooled with a cooling bath of dry ice / acetone. During the whole process, including the photolysis with 470 nm light for 1h, the cooling bath was kept below -65°C. After the photolysis was complete, the stirring bar was removed with a magnet and the sample was frozen with liquid nitrogen for Mössbauer measurements, the result of which are shown in Figure 4.32.

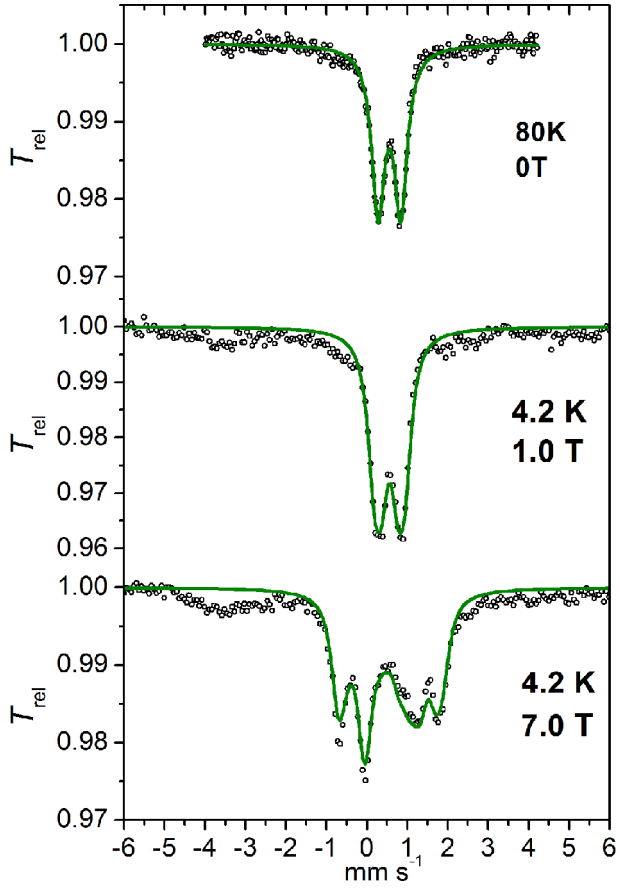

Figure 4.32: Mössbauer spectrum of 1mM [$^{57}Fe^{III}$(N_3)cyc-ac]PF_6 in butyronitrile after photolysis with 470 nm light for 1h at -65°C, without (top), with 1.0T (middle) and with 7.0T (bottom) applied magnetic fields.

The initial [Fe^{III}(N_3)cyc-ac]PF_6 complex is quantitatively converted into a new species with a relatively small quadrupole splitting ΔE_Q= 0.57 mm s^{-1}, an isomer shift of δ= 0.57 mm s^{-1} and the symmetry parameter η=0.31. Given that this combination of isomer shift and quadrupole splitting could result either from a high-spin ferric or low-spin ferrous complex, measurements were performed with applied magnetic field (Figure 4.32, middle and bottom). The species was found to be diamagnetic,

hence, it has to be a low-spin ferrous complex. Based upon close agreement with the parameters previously reported by Grapperhaus *et al.* (δ= 0.56 mm s^{-1} / ΔE_Q= 0.54 mm s^{-1}) for the photolysis in solution with 300 nm light[43] it can be assumed that the ferrous species $[Fe^{II}(PrCN)cyc\text{-}ac]^+$ is formed, where the sixth coordination site is occupied by a butyronitrile solvent molecule. To verify this assumption further, DFT calculations were performed on this species (B3LYP/def2-TZVP/Fe: CP(PPP)/COSMO) that yielded the Mössbauer parameters δ= 0.54 mm s^{-1}, ΔE_Q= +0.42 mm s^{-1} and η=0.31, in very good agreement with the experimental results. Hence, whereas by photolysis in liquid solution with visible light (470 nm) the ferrous low-spin complex $[Fe^{II}(PrCN)cyc\text{-}ac]^+$ is formed, photolysis of frozen samples yields iron(V) $[Fe^{V}(N)cyc\text{-}ac]^+$.

From the presented Mössbauer study of photolyzed samples of the complex $[Fe^{III}(N_3)cyc\text{-}ac]PF_6$ the following conclusions can be drawn.

I) The initially proposed wavelength dependence is not observed in the present experiments on frozen solution samples. Beyond use of different wavelengths (304 nm or 470 nm) the photolysis was performed under identical conditions (frozen solution). Even different electronic transitions are expected to be induced by the significantly different wavelengths used (see discussion in Chapter 4.3.1), photolysis on frozen solution samples only yield the nitrido-iron(V) complex $[Fe^{V}(N)cyc\text{-}ac]^+$.

II) It was further shown, that the photolysis of $[Fe^{III}(N_3)cyc\text{-}ac]PF_6$ in liquid butyronitrile solution with 470 nm light results in the low-spin ferrous complex $[Fe^{II}(PrCN)cyc\text{-}ac]PF_6$. Higher-energy light from the UV region is not necessary.

It should be noted here, that it is of course only possible to detect species that are stable during/after the photolysis. Hence, it might be the case that when the photolysis is performed in fluid solution, the primary photo product immediately undergoes further reactions and the complexes detected in the Mössbauer measurements are not the actual direct product of the photolysis. This will be discussed in more detail in Chapter 5.9 where the decay of nitrido-iron(V) complexes is studied. It will be shown that the ferrous complex $[Fe^{II}(PrCN)cyc\text{-}ac]PF_6$ is also obtained via the decay of the $[Fe^{V}(N)cyc\text{-}ac]PF_6$ complex. It is, therefore, possible that during the photolysis of the $[Fe^{III}(N_3)cyc\text{-}ac]PF_6$ complex in butyronitrile solution the nitrido-iron(V) complex is formed and then decays immediately to the iron(II) complex $[Fe^{II}(PrCN)cyc\text{-}ac]PF_6$. However, in Chapter 4.5.3 evidence was provided for direct formation of the iron(II) complex $[Fe^{II}(MeCN)cyc\text{-}ac]PF_6$ and an azide radical by photolysis in solution with a 266 nm laser.

In a very recent time resolved IR-study, Vöhringer *et al.*[56] proposed the formation of the iron(III) complex $[Fe^{III}(MeCN)cyc\text{-}ac]^{2+}$ upon photolysis with a 450 nm laser. However, in the just discussed Mössbauer results this species was neither observed in the frozen solution, nor in the liquid solution photolysis experiments with 470 nm light.

4.6.4. Electrochemical Formation of Iron(II) Complexes

In the initial work on the azido iron(III) complexes $[Fe^{III}(N_3)cyc\text{-}ac]PF_6$ and $[Fe^{III}(N_3)_2cyc]ClO_4$, Mössbauer data of electrochemically reduced species derived from the parent iron(III) complexes were reported and these species were formulated as $[Fe^{II}(N_3)cyc\text{-}ac]PF_6$ and $[Fe^{II}(N_3)_2cyc]ClO_4$.[29,43] Surprisingly, the reported values are identical to those Mössbauer parameters obtained for the iron(II) complexes that result from the photolysis of the azido-iron(III) complexes in solution, which were formulated as $[Fe^{II}(MeCN)cyc\text{-}ac]PF_6$ and $[Fe^{II}(MeCN)(N_3)cyc]ClO_4$. The values are summarized in Table 4.16, together with the data recorded within this thesis for the $[Fe^{II}(MeCN)cyc\text{-}ac]PF_6$ complex (see Chapter 4.6.3 and Chapter 5.9), and DFT calculations on the proposed iron(II) species.

Table 4.16: Experimental and calculated Mössbauer data for various iron(II) complexes.

	Experimental		Calculated	
	δ [mm s^{-1}]	ΔE_Q [mm s^{-1}]	δ [mm s^{-1}]	ΔE_Q [mm s^{-1}]
$[Fe^{II}(MeCN)cyc\text{-}ac]^+$	0.56[a]	0.56[a]	0.54	+0.42
"$[Fe^{II}(N_3)cyc\text{-}ac]$"	0.56[a]	0.56[a]	0.64	+0.66
$[Fe^{II}(MeCN)(N_3)cyc]^+$	0.55[b]	0.72[b]	0.55	+0.66
"$[Fe^{II}(N_3)_2cyc]$"	0.55[b]	0.72[b]	0.65	+0.84

[a] Experimental data for electrochemically reduced complexes taken from Ref.[43] [b] taken from Ref.[29]

It would be expected that the Mössbauer parameters of the ferrous complexes differ depending upon the identity of the axial ligand, which could be either a neutral acetonitrile solvent molecule or an anionic azide ligand. This is shown as well in the calculated Mössbauer parameters, where the iron(II) complexes in which the azide ligand is replaced by a solvent molecule show a slightly larger isomer shift and quadrupole splitting than those where the reduction is assumed to proceed without replacement of an azide ligand with a solvent molecule (see Table 4.16). The calculated Mössbauer parameters for those species, where the apical azide ligand is replaced by a solvent molecule are further in better agreement with the experimental results than those calculated for the complexes where the azide ligand is not replaced.

It shall be shown here by electrochemical experiments combined with IR spectroscopy, that the complexes obtained by electrochemical reduction indeed are the species $[Fe^{II}(MeCN)cyc\text{-}ac]PF_6$ and $[Fe^{II}(MeCN)(N_3)cyc]ClO_4$ and not, as previously assumed the complexes $[Fe^{II}(N_3)cyc\text{-}ac]$ and $[Fe^{II}(N_3)_2cyc]$.

The IR spectrum for the $[Fe^{III}(N_3)cyc\text{-}ac]PF_6$ complex shows a characteristic signal at 2053 cm^{-1} for the antisymmetric stretching vibration of the azide ligand and at 1688 cm^{-1} for the carbonyl stretching mode (see Figure 4.33). This is in agreement with the IR spectra discussed in Chapter 4.5.1 and the time resolved IR measurements discussed in Chapter 4.5.3. Upon electrochemical one electron reduction the azide vibration nearly completely vanishes and a new feature evolves at 2006 cm^{-1}. In parallel, the carbonyl stretching vibration is shifted from 1688 cm^{-1} to 1636 cm^{-1}.

Interestingly, upon reduction of the bis-azido complex $[Fe^{III}(N_3)_2cyc]ClO_4$ the signal of the antisymmetric stretching vibration is only reduced by about ~50% while again a signal evolves at 2006 cm^{-1} (Figure 4.34).

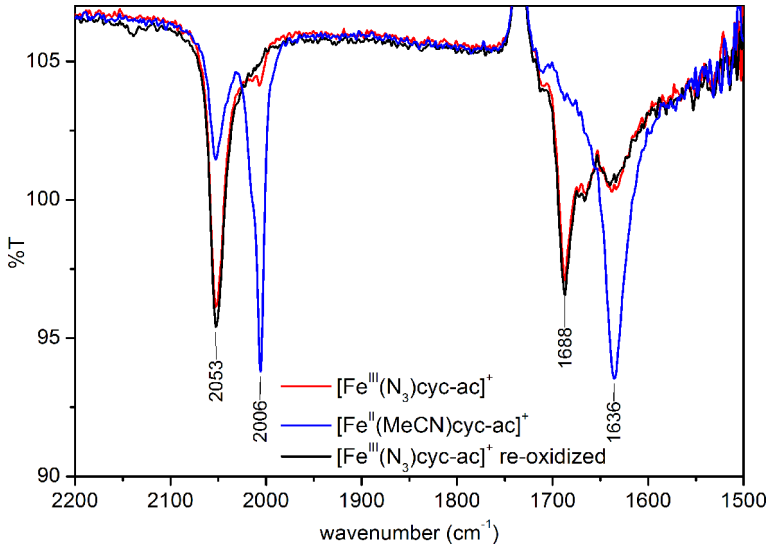

Figure 4.33: IR spectra of $[Fe^{III}(N_3)cyc\text{-}ac]PF_6$ (1.5 mM) before (red) and after (blue) electrochemical one-electron reduction in acetonitrile solution with 0.5 M tetrabutylammonium hexafluorophosphate as the electrolyte. The black trace shows the recovery of the initial IR signals after re-oxidation.

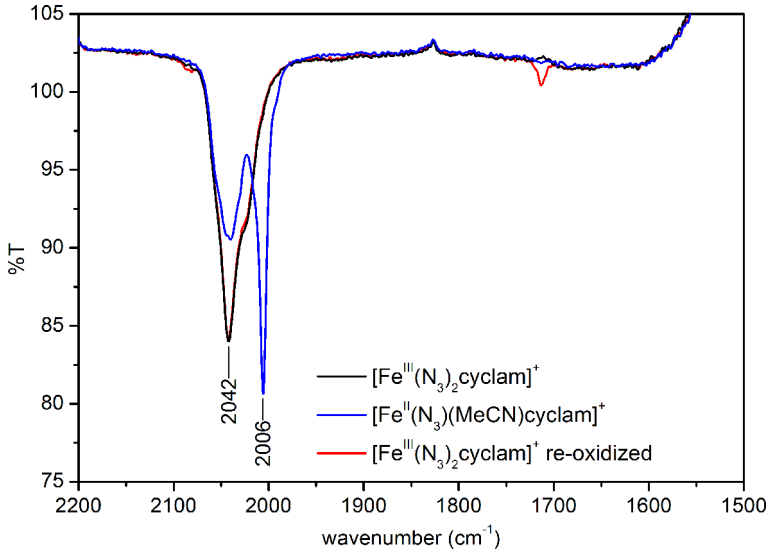

Figure 4.34: IR spectra of $[Fe^{III}(N_3)_2cyc]ClO_4$ (1.5 mM) before (red) and after (blue) electrochemical one-electron reduction in acetonitrile solution with 0.5 M tetrabutylammonium hexafluorophosphate as the electrolyte. The black trace shows the recovery of the initial IR signals after re-oxidation.

In Figure 4.35, the IR spectrum of tetrabutylammonium azide in acetonitrile (20 mM) is shown and it turns out that the antisymmetric stretching mode of a free azide anion appears at 2006 cm^{-1}. This is at exactly the same position as the new signal that evolves upon one-electron reduction of the complexes $[Fe^{III}(N_3)cyc\text{-}ac]PF_6$ and $[Fe^{III}(N_3)_2cyc]ClO_4$. It can, therefore, be concluded that during the reversible one-electron reduction of the azido-iron(III) complexes, an azide ligand is replaced by a solvent molecule (acetonitrile) and free azide anions are present in the solution. This substitution is reversible and when the complexes are electro-chemically re-oxidized the azido-iron(III) starting complexes are recovered.

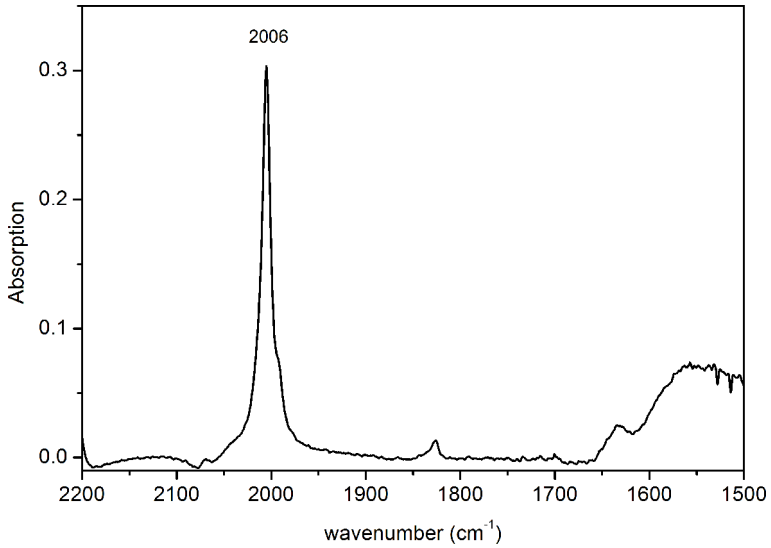

Figure 4.35: IR spectra of tetrabutylammonium azide (20 mM) in acetonitrile solution.

This interpretation of the IR data is in good agreement with the results of the time dependent IR measurements and DFT calculations on the complex $[Fe^{III}(N_3)cyc\text{-}ac]PF_6$ that were discussed in Chapter 4.5.3. The antisymmetric stretching vibration for the azido-iron(III) complex is predicted by DFT (BP86/def2-tzvp/RI) to be 2053 cm^{-1} (exp.: 2053 cm^{-1}) and the carbonyl stretching vibration to be 1702 cm^{-1} (exp.: 1688 cm^{-1}). For the hypothetical $[Fe^{II}(N_3)cyc\text{-}ac]$ complex an upshift of the azide stretching vibration about 10 cm^{-1} is predicted by DFT (2063 cm^{-1}) and a significant down shift of the carbonyl vibration about 52 cm^{-1} (1651 cm^{-1}). Hence, the calculated downshift of the carbonyl vibration might be in agreement with the experimental results, however, for the azide stretching vibration a significant down shift was observed experimentally which does not agree with the calculations on the $[Fe^{II}(N_3)cyc\text{-}ac]$ complex. In good agreement with the experimental findings, a downshift of the carbonyl-stretching vibration from 1702 cm^{-1} to 1687 cm^{-1} is predicted by DFT for the formation of the complex $[Fe^{II}(MeCN)cyc\text{-}ac]^+$ where upon reduction the azide ligand is replaced by a solvent molecule.

DFT calculations of the bis-azido complex also support formulation of the electrochemically formed iron(II) complex as $[Fe^{II}(MeCN)(N_3)cyc]^+$. The antisymmetric stretching vibration for the complex $[Fe^{III}(N_3)_2cyc]^+$ is predicted by DFT to be 2052 cm^{-1} (exp.: 2042 cm^{-1}). For the iron(II) complex $[Fe^{II}(N_3)_2cyc]$ it is predicted to appear at nearly the same position (2053 cm^{-1}) but the band is calculated to be about 22% more intense which does not agree with the experimental results. For the $[Fe^{II}(MeCN)(N_3)cyc]^+$ complex, the antisymmetric stretching vibration is calculated to be 2062 cm^{-1}, which is 10 cm^{-1} higher in energy compared to the azido-iron(III) species. Furthermore it is predicted to be 39% less intense than for the parent Fe(III) complex, which is in good agreement with the experimental findings. The predicted shift of 10 cm^{-1} upon reduction of the $[Fe^{III}(N_3)_2cyc]^+$ complex and formation of the $[Fe^{II}(MeCN)(N_3)cyc]^+$ species is not observed in the experiments. However, this is probably just not resolved due to the experimental bandwidth of ~20 cm^{-1}.

Thus, the Mössbauer, IR and DFT data show that the iron(II) species obtained by electrochemical reduction are the well-defined complexes $[Fe^{II}(MeCN)cyc\text{-}ac]^+$ and $[Fe^{II}(MeCN)(N_3)cyc]^+$, identical to those complexes obtained by photolysis of the parent azido-iron(III) complexes in solution. The complexes $[Fe^{II}(N_3)cyc\text{-}ac]$ and $[Fe^{II}(N_3)_2cyc]$ are not obtained under the conditions of the electrochemical experiments.

4.7. Mass Spectrometry on Azido-Iron(III) Complexes[6]

In collaboration with Dr. Marianne Engeser (University of Bonn) azido-iron(III) complexes were studied in the gas phase.[231] The results were published in *ChemPlusChem* **2013**, *78*, 1053-1057. Samples were synthesized by the author of this thesis, the measurements were performed by Dr. Marianne Engeser at the University of Bonn and the publication was written together. The shown spectra in this Chapter 4.7 were not recorded by the author of this thesis, however, a brief summary of the results shall be presented here.

Due to the fleeting nature of tetragonal nitrido-iron (V) complexes, they have been studied mainly at cryogenic temperatures.[29,40-41,43,45-46] However, Schröder *et al.* also observed the formation of these high-valent species in the gas phase where the reactivity was probed and the decay mechanism investigated for the azido-iron(III) complex $[Fe^{III}(N_3)cyc\text{-}ac]PF_6$ (**1**), which is studied in this thesis by various spectroscopic and theoretical methods.[53,232]

Mass spectrometry measurements were performed on the complexes $[Fe^{III}(N_3)cyc\text{-}ac]PF_6$ (**1**·PF_6), $[Fe^{III}(N_3)_2cyc]ClO_4$ (**2**·ClO_4) and $[Fe^{III}(N_3)TMC\text{-}ac]PF_6$ (**3**·PF_6) (see Scheme 4.3) with special attention paid to the formation of high-valent nitrido-species.

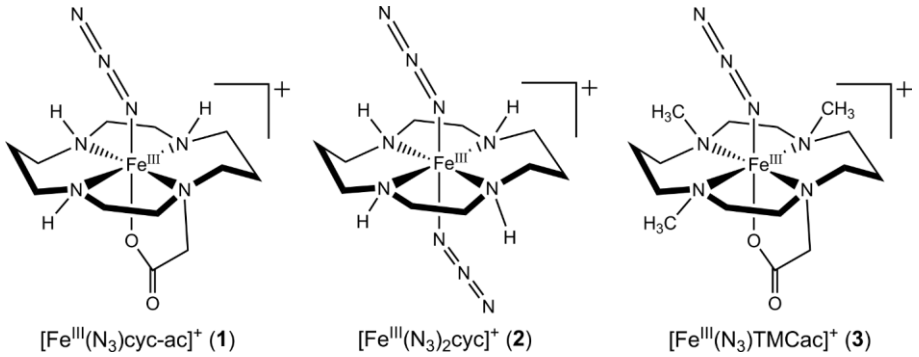

Scheme 4.3: Complexes investigated in the gas phase.

The results from measurements on the $[Fe^{III}(N_3)cyc\text{-}ac]^+$ complex (**1**) are shown in Figure 4.36 and confirm the results from the study performed by Schröder *et al*.[53] Not only is the azide-cation (m/z=355.2) seen in the ESI-MS spectrum, but also the fragment $[\mathbf{1}\text{-}N_2]^+$ at m/z=327 resulting from the nitrido-iron(V) complex $[Fe^{V}(N)cyc\text{-}ac]^+$, which was confirmed by ^{15}N-isotope labeling. In addition, the $[\mathbf{1}\text{-}HN_3]^+$ fragment at m/z= 312 resulting from elimination of the azide anion and deprotonation of one cyclam amine group was detected. The ratio of these two fragments can be varied by changing the ionization parameters in collision-induced dissociation (CID) spectra of mass-selected $[Fe^{III}(N_3)cyc\text{-}ac]^+$ (see Figure 4.36 b+c). Interestingly, the loss of an azide radical ($N_3^{\bullet}$), as proposed in the initial work on the $[Fe^{III}(N_3)cyc\text{-}ac]PF_6$ from photolysis in solution[43] or in more recent time-resolved IR studies,[217-218] is not seen in the gas phase.

[6] This section is reprinted with permission from O. Krahe, F. Neese, M. Engeser "Iron Azides with Cyclam-Derived Ligands: Are They Precursors for High-Valent Iron Nitrides in the Gas Phase?" *ChemPlusChem* **2013**, *78*, 1053. Copyright 2013 John Wiley & Sons, Inc

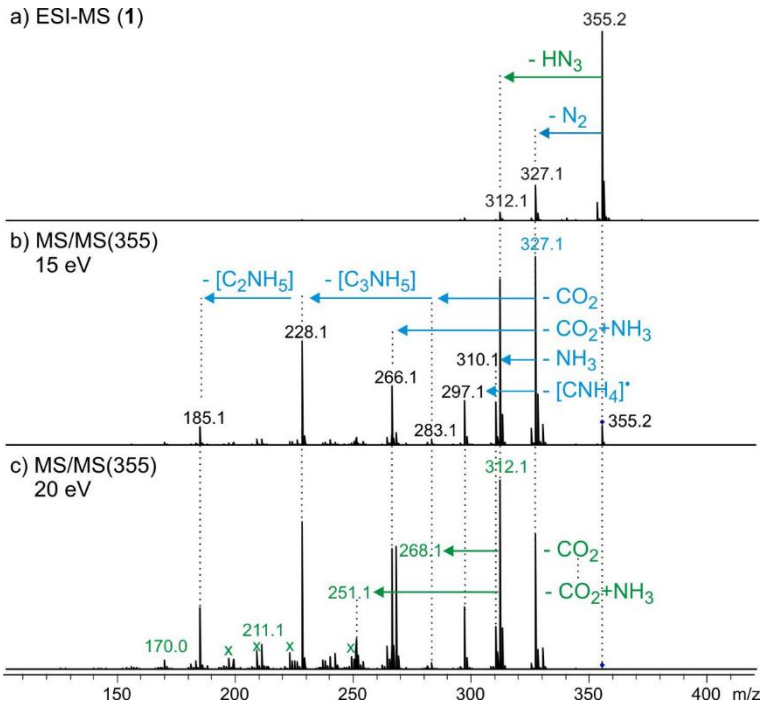

Figure 4.36: ESI-MS spectrum of $[Fe^{III}(N_3)cyc\text{-}ac]PF_6$ (**1**) (a) and CID spectra of mass-selected **1** (m/z=355) at varied collision energy (b,c). Fragments stemming from initial loss of NH_3 are marked in green.

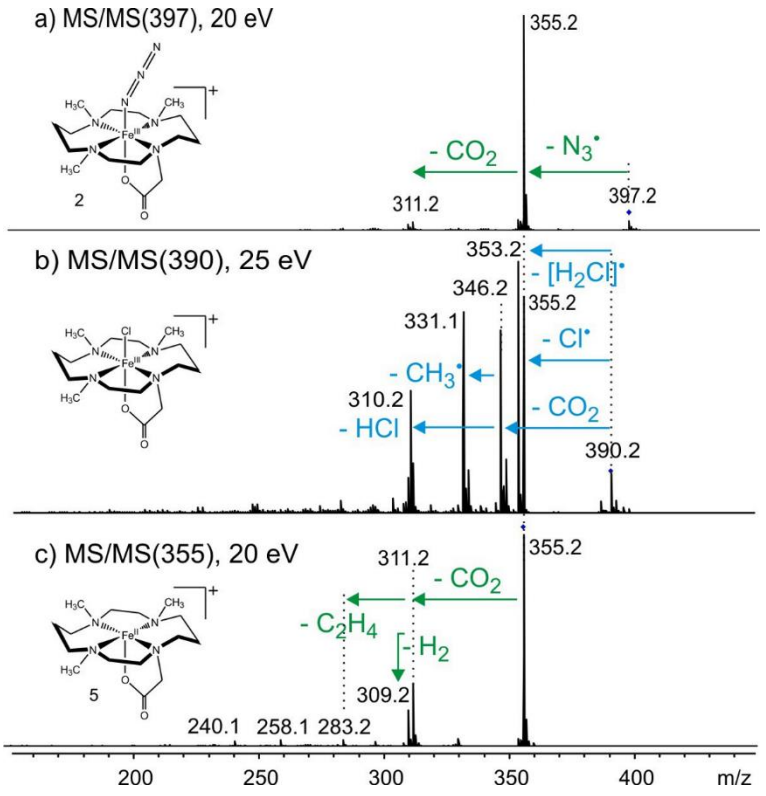

Figure 4.37: CID MS/MS spectra of $[Fe^{III}(N_3)TMC\text{-}ac]^+$ (**3**, m/z=397.2) (a), the respective chloride complex m/z=390.2 (b) and the $[Fe^{II}TMC\text{-}ac]^+$ fragmentation product (m/z=355.2).

Interesting differences are observed for the analogue complex of **1**, where the cyclam amino groups are methylated. The resulting spectra for thecomplex $[Fe^{III}(N_3)TMC\text{-}ac]^+$ (**3**) and the corresponding chloride complex $[Fe^{III}(Cl)TMC\text{-}ac]^+$ are shown in Figure 4.37. Loss of hydrazoic acid (HN_3) is not possible since the N-H protons of the cyclam-amine groups are replaced by methyl-groups. However, the expulsion of N_2 and formation of the nitrido-iron(V) complex is not observed neither. Instead, the loss of an azide radical ($N_3^{\bullet}$) is observed, which results in the ferrous species $[Fe^{II}TMC\text{-}ac]^+$ (m/z=355.2). Formation of this complex was proposed earlier during the photolysis of the corresponding azido-iron(III) complex **3**.[47] However, it will be shown in Chapter 5.4.2 that photolysis of the $[Fe^{III}(N_3)TMC\text{-}ac]^+$ (**3**) complex can also result in the iron(V) complex $[Fe^{V}(N)TMC\text{-}ac]^+$, which is not observed in the gas phase. The iron(II) species further degrades via CO_2 expulsion followed by the fragmentation of the cyclam ligand by ethylene elimination (see MS/MS spectrum Figure 4.37 c). Similar fragmentation is observed for the iron(III) chloride complex $[Fe^{III}(Cl)TMC\text{-}ac]^+$ (Figure 4.37 b), with direct loss of CO_2 also observed for this species.

Further measurements were performed on the bis-azido complex $[Fe^{III}(N_3)_2cyc]^+$ (**2**) that are shown in Figure 4.38. In contrast to the aforementioned complexes, the primary fragmentation reaction observed is the expulsion of HN_3 resulting in the coordinatively unsaturated iron(III) mono-azido complex $[Fe^{III}(N_3)cyc\text{-}H]^+$ at m/z=297 (see Scheme 4.4 for the molecular structure). Minor amounts of the high-valent species $[Fe^{V}(N)(N_3)cyc]^+$ are only observed after carefully fine-tuning of the collision energies. For the analogue cyclam-acetate complex $[Fe^{III}(N_3)cyc\text{-}ac]^+$ (**1**) a nitrido-iron(V) species was the main fragmentation product at low collision energies. As it was not observed for the mono-azido complex **1**, loss of an azide radical is not observed for **2**, either. However, for the azido complex with the methylated cyclam ligand (**3**) loss of an azide radical was observed.

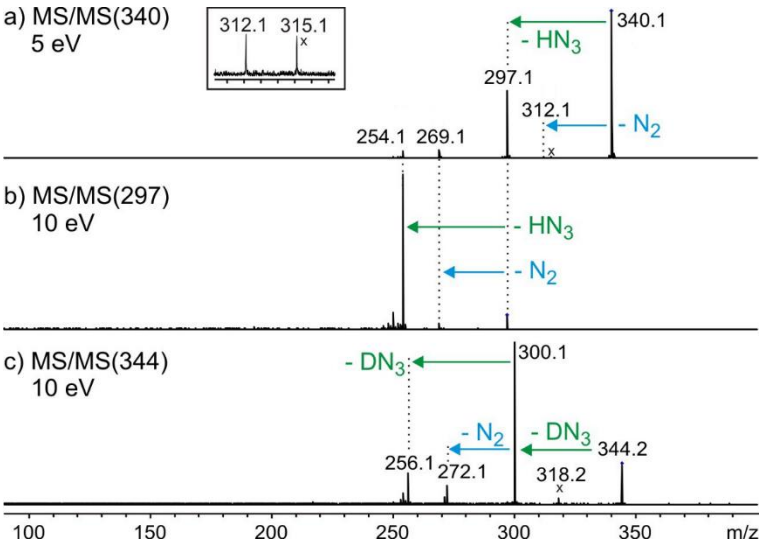

Figure 4.38: CID MS/MS spectra of (a) $[Fe^{III}(N_3)_2cyc]^+$ (**2**, m/z=340.1), (b) the primary fragmentation product $[Fe^{III}(N_3)cyc\text{-}H]^+$ m/z=297.1, (c) the deuterated analogue of $[Fe^{III}(N_3)_2cyc]^+$ (D_4-**2**, m/z=344.2).

Consecutive fragmentation of the $[Fe^{III}(N_3)cyc\text{-}H]^+$ ([**2**-HN_3]$^+$) species at higher energies (see MS/MS spectrum for m/z= 297, Figure 4.38 b) leads to the iron(III) complex with two fold deprotonated cyclam ligand ($[Fe^{III}(cyc\text{-}2H)]^+$, [**2**-$2N_3$]$^+$, m/z=254) via expulsion of a second molecule HN_3 (see Scheme 4.4 for the molecular structure). This was further confirmed by measurements on material where the amine groups of the cyclam ligand were deuterated (see Figure 4.38 c).

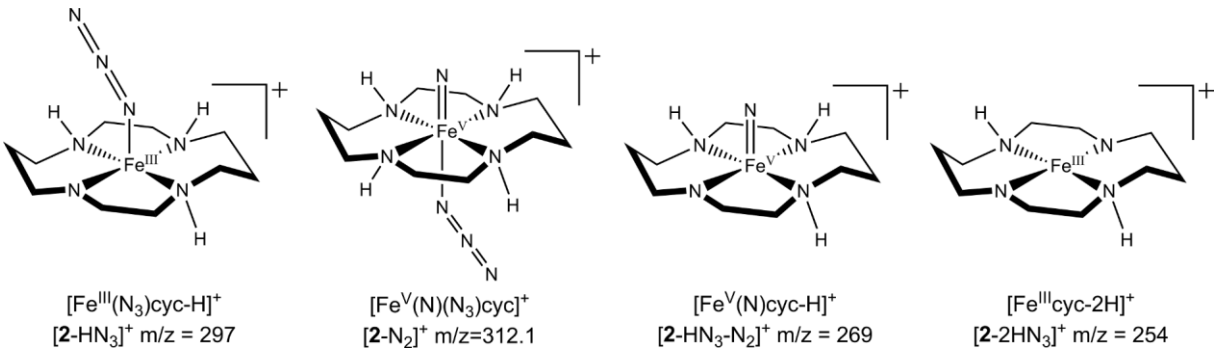

Scheme 4.4: Major fragmentation products observed in CID mass spectra of $[Fe^{III}(N_3)cyc]^+$ (**2**)

Interestingly, it was also possible to detect small amounts of the five coordinate nitrido-iron(V) complex $[Fe^{V}(N)cyc\text{-}H]^+$ (m/z=269) that results from HN_3 expulsion followed by loss of N_2 (spectrum in Figure 4.38 b, structure in Scheme 4.4). This species was detected alongside fragmentation products for the deuterated complex (m/z= 272.1, Figure 4.38 b). The presence of the iron(V) complexes $[Fe^{V}(N)(N_3)cyc]^+$ as well as $[Fe^{V}(N)cyc\text{-}H]^+$ in the gas phase, even in small amounts, is very interesting. By the initial Mössbauer measurements performed by Meyer *et al.*[29] it was not possible to say what exactly the coordination number of iron is, and if the azide ligand in *trans*-position to the nitride is still intact. However, clear evidence for an azide ligand in *trans*-position to the nitride will be provided from low-temperature IR measurements (see Chapter 5.2) and from DFT calculations of the Mössbauer parameters (see Chapter 5.1) on the nitrido-iron(V) complexes derived from the bis-azido complex $[Fe^{III}(N_3)_2cyc]^+$ (**2**).

The gas phase measurements provide an interesting additional perspective to the investigations on azido iron(III) complexes in the condensed phase (solution / frozen solution). Analog to the Mössbauer photolysis experiments on frozen solution samples (Chapter 4.6.1 and 4.6.2), the formation of the nitrido-iron(V) complex was observed in the gas phase for the complex $[Fe^{III}(N_3)cyc\text{-}ac]^+$. On the other hand, the azide radical elimination that was observed in the condensed phase (time resolved IR study Chapter 4.5.3), was not observed in the mass spectrometry measurements, while in the gas phase HN_3 expulsion was detected, which was not seen for photolysis experiments performed in the condensed phase.

For the methylated complex $[Fe^{III}(N_3)TMC\text{-}ac]^+$ only the elimination of an azide radical was observed, in agreement with previous studies on frozen solution samples. Regardless, in Chapter 5.4.2 it will be shown that the formation of the iron(V) complex $[Fe^{V}(N)TMC\text{-}ac]^+$ in frozen solution is also possible.

Major differences are found for the bis-azido complex $[Fe^{III}(N_3)_2cyc]^+$ when its behavior in the gas phase is compared to the photolysis experiments in frozen solution. Only minor amounts of the $[Fe^{V}(N)(N_3)cyc]^+$ complex were detected in the MS-experiments, while this is the main product of photolysis in frozen solution, as was shown in a previous Mössbauer study[29] and is confirmed by EPR-measurements discussed in Chapter 5.4.1 of this thesis. The main fragmentation reaction observed in the gas phase is the loss of hydrazoic acid (HN_3), which was not observed in the condensed phase.

4.8. DFT Calculations on the Elimination of N_2, N_3^- and $N_3^\bullet$ from Azido Iron(III) Complexes

Azido-iron(III) complexes were investigated in the antecedent chapters by various spectroscopic techniques in combination with calculations. Before the nitrido-iron(V) species will be studied in detail in the following sections, possible reactions for the azido-iron(III) complexes shall be explored also by DFT calculations. These provide insight in the energetics of competing reactions and the role of excited states will be probed by TD-DFT.

Possible reactions induced thermally or photo-chemically are the reductive elimination of an azide radical ($N_3^\bullet$) yielding an iron(II) complex, the oxidative elimination of N_2 yielding a nitrido-iron(V) complex or the redox-neutral elimination an azide anion (N_3^-). These reactions are outlined in Scheme 4.5 for the $[Fe^{III}(N_3)cyc\text{-}ac]^+$ complex. The formation of iron(II) and iron(V) was already discussed in conjunction with Mössbauer measurements in Chapter 4.6. The redox neutral elimination of an azide anion was observed in the time resolved IR experiments (Chapter 4.5.3) and also proposed in a recently published study.[56]

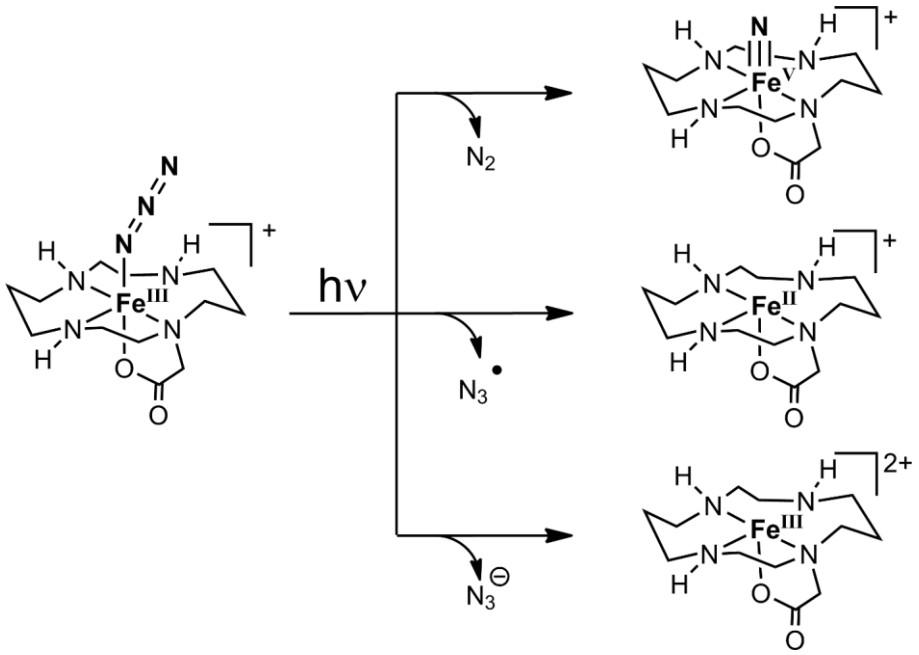

Scheme 4.5: Possible N_2 -, $N_3^\bullet$- and $N_3^\ominus$-elimination reactions for the $[Fe^{III}(N_3)cyc\text{-}ac]^+$ complex.

The Energetics of the reactions outlined in Scheme 4.5 are investigated by DFT calculations for the complexes $[Fe^{III}(N_3)cyc\text{-}ac]^+$ and $[Fe^{III}(N_3)TMC\text{-}ac]^+$. The photochemical elimination of N_2 and the N_3^--anion from the complex $[Fe^{III}(N_3)cyc\text{-}ac]^+$ will be explored in Chapter 4.8.2 within the framework of time-dependent density functional theory (TD-DFT).

Structures were optimized using the BP86 functional, the def2-TZVP basis set and the corresponding def2-TZVP/J auxiliary basis-set for the RI approximation. Solvent effects were taken into account within the conductor like screening model approach assuming acetonitrile as the solvent and van der Waals correction (D3ZERO) was employed. Final energies are calculated for these optimized geometries using the B3LYP functional in conjunction with the RIJCOSX approximation and thermal corrections were obtained from the frequency calculation with the BP86 functional. Azido-nitrogen atoms are labeled by α, β and γ in the following discussion, starting with the iron bond nitrogen atom ($Fe\text{-}N_\alpha\text{–}N_\beta\text{–}N_\gamma$).

4.8.1. Thermal Reactions of the Complex $[Fe^{III}(N_3)cyc\text{-}ac]^+$

As a first step, relaxed surface scans were performed for the complex $[Fe^{III}(N_3)cyc\text{-}ac]^+$ in the doublet spin ground state as well as the excited quartet- and sextet-states. In these calculations the Fe-N_3 and FeN-N_2 distances were stepwise increased and frozen, while all the remaining bonding parameters were energy minimized. Results from these calculations are shown in Figure 4.39. The energy is given relative to the energy of the equilibrium geometry in the doublet ground state and the energy is plotted against the bond distance of the constrained bond.

The graph in Figure 4.39 clearly shows for all conceivable spin states a maximum energy when the FeN-N_2 bond was elongated about ~0.5 Å, followed by a decay of the relative energy. This indicates, that in this region a transition state should be located. When the Fe-N_3 bond was elongated, only a significant rise of the relative energy was observed without passing through a maximum which prevents the location of a transition state.

Furthermore, it is interesting to follow the Loewdin spin-population on selected atoms during the performed scans since this reveals if a closed-shell or radical moiety is eliminated from the iron complex (see Figure 4.39). For the scan along the nitrogen-nitrogen bond (FeN-N_2) it is seen that part of the spin-population is transferred from iron to the α-nitrogen atom that is bond to iron. This is expected, due to the strong covalency in the formed iron-nitride where the unpaired electron is located in an anti-bonding Fe-N π-bond (see Chapter 5.5 for a detailed discussion of the electronic structure of nitrido-iron(V) complexes).

The spin-population during the scan along the iron-azido bond (Fe-N_3) is very interesting, since it reveals if an iron(III) complex and an azide anion is formed or an iron(II) complex and an azide radical, respectively. From the corresponding graph (Figure 4.39, right) it is clear, that the unpaired electron(s) remain exclusively on iron for all spin states. No spin-population was calculated for the azide nitrogen atoms. This is in agreement with the expectations, based on experimental redox-potentials. The $N_3^-/N_3^\bullet$ redox couple shows a very high redox potential (+1.33 V in acetonitrile vs. NHE[233]) while the potential for the Fe^{III}/Fe^{II} redox couple is much lower (+0.69 V, see Chapter 4.6.4) for the complex $[Fe^{III}(N_3)cyc\text{-}ac]^+$. This indicates, that the iron(II) complex in the presence of an azide radical under electrochemical conditions is not expected to be stable. The iron(III) complex and an azide anion would be formed immediately.

As mentioned before, the relaxed surface scan along the iron-nitrogen bond reveals that a transition state for the cleavage of the iron-nitrogen bond cannot be located. However, Gibbs free energies for the elimination of an azide radical and an azide anion were calculated and are shown in Scheme 4.6. The given energies are relative to the complex $[Fe^{III}(N_3)cyc\text{-}ac]^+$ in its doublet ground-state. Furthermore, calculations were performed where the axial coordination site was saturated by an acetonitrile molecule which was used as solvent in the experiments. From the data in Scheme 4.6 it is clear that all considered reactions are highly endergonic. For the azide anion this can be rationalized by the charge separation that is necessary to form an anionic azide and a cationic iron fragment (charge 2+).

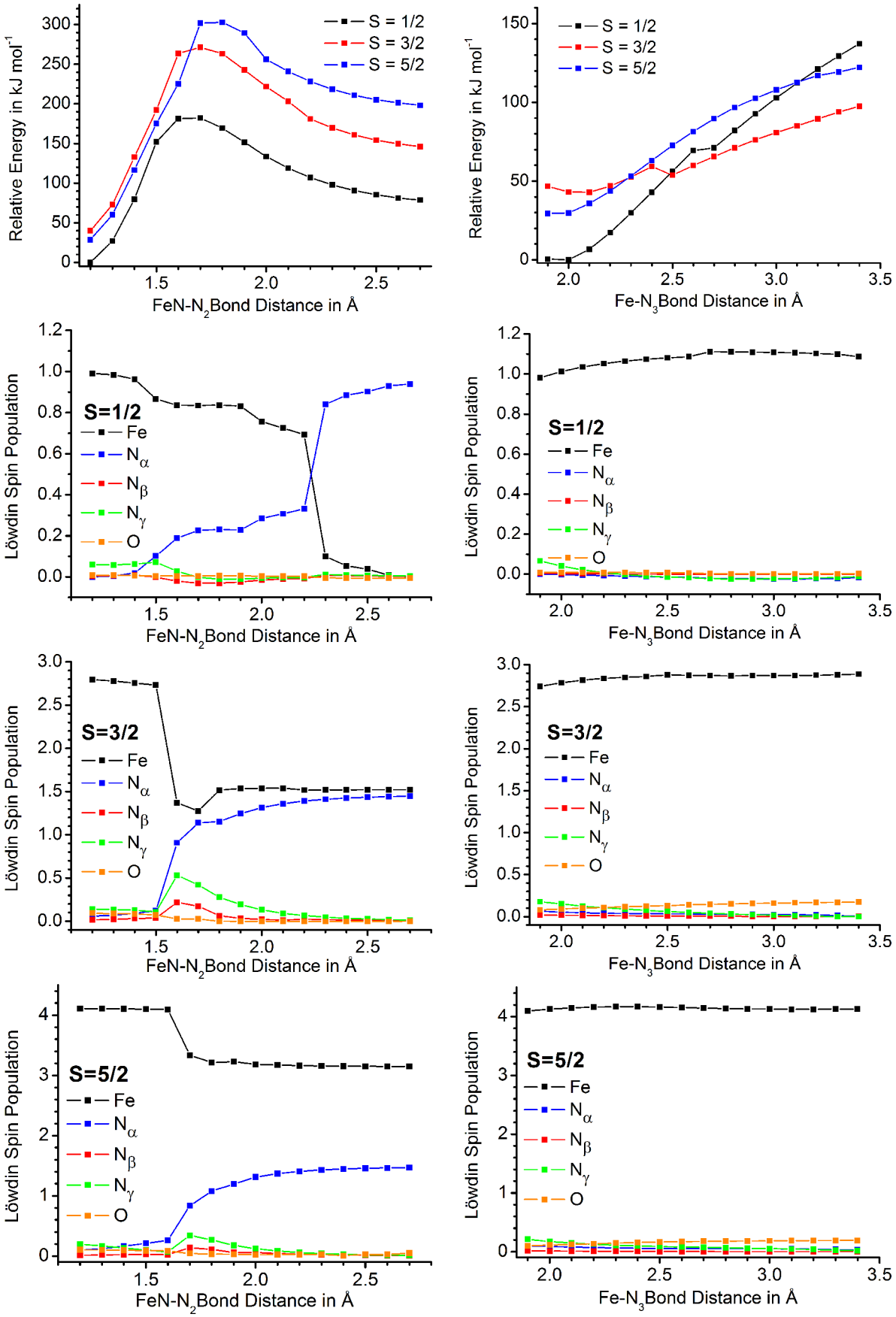

Figure 4.39: Results from relaxed surface scan along the FeN-N_2 (left) and Fe-N_3 bond (right). Top: Energies relative to the lowest energy structure/spin state, column 2-4, Löwdin spin population on iron, the iron bond (N_α), the central (N_β) and the terminal azido nitrogen atom (N_γ) for spin states *S*=1/2, 3/2, 5/2.

Further, the calculations demonstrate that the spin state preference depends on the coordination number. For the five coordinate complexes $[Fe^{III}(cyc\text{-}ac)]^{2+}$ and $[Fe^{II}(cyc\text{-}ac)]^{+}$, the intermediate-spin configuration is preferred for the former and the high-spin state for the latter. If the sixth coordination site that results from removal of the azide ligand is saturated with an acetonitrile molecule, for the $[Fe^{III}(MeCN)(cyc\text{-}ac)]^{2+}$ complex low-spin is lowest in energy. For the $[Fe^{II}(MeCN)(cyc\text{-}ac)]^{+}$ complex the high-spin state was calculated to be 11 kJ mol^{-1} lower in energy than the low-spin state. However, there is strong experimental evidence (see Chapter 4.6.3) that the complex $[Fe^{II}(MeCN)(cyc\text{-}ac)]^{+}$ is a diamagnetic low-spin species. Presumably DFT fails here to predict the correct spin state, which is known to be difficult when the energy difference is as small as in the present case.[234]

$[Fe^{III}(N_3)cyc\text{-}ac]^{+} \longrightarrow [Fe^{II}cyc\text{-}ac]^{+} + N_3^{\bullet}$	S_{Fe}=0	180 kJ mol^{-1}
	S_{Fe}=1	135 kJ mol^{-1}
	S_{Fe}=2	107 kJ mol^{-1}
$[Fe^{III}(N_3)cyc\text{-}ac]^{+} + MeCN \longrightarrow [Fe^{II}(MeCN)cyc\text{-}ac]^{+} + N_3^{\bullet}$	S_{Fe}=0	140 kJ mol^{-1}
	S_{Fe}=1	179 kJ mol^{-1}
	S_{Fe}=2	129 kJ mol^{-1}
$[Fe^{III}(N_3)cyc\text{-}ac]^{+} \longrightarrow [Fe^{III}cyc\text{-}ac]^{2+} + N_3^{-}$	S_{Fe}=1/2	158 kJ mol^{-1}
	S_{Fe}=3/2	111 kJ mol^{-1}
	S_{Fe}=5/2	130 kJ mol^{-1}
$[Fe^{III}(N_3)cyc\text{-}ac]^{+} + MeCN \longrightarrow [Fe^{III}(MeCN)cyc\text{-}ac]^{2+} + N_3^{-}$	S_{Fe}=1/2	89 kJ mol^{-1}
	S_{Fe}=3/2	114 kJ mol^{-1}
	S_{Fe}=5/2	115 kJ mol^{-1}

Scheme 4.6: Gibbs free energy (ΔG) for azide-elimination from $[Fe^{III}(N_3)cyc\text{-}ac]^{+}$, S_{Fe} refers to the spin on iron in the products (BP86/def2-TZVP/RI/COSMO/D3ZERO //B3LYP/def2-TZVP/RIJCOSX/COSMO/D3ZERO)

The transition states and reaction enthalpies for the N_2-elimination were calculated for the $[Fe^{III}(N_3)cyc\text{-}ac]^{+}$ complex, as shown in Scheme 4.7.

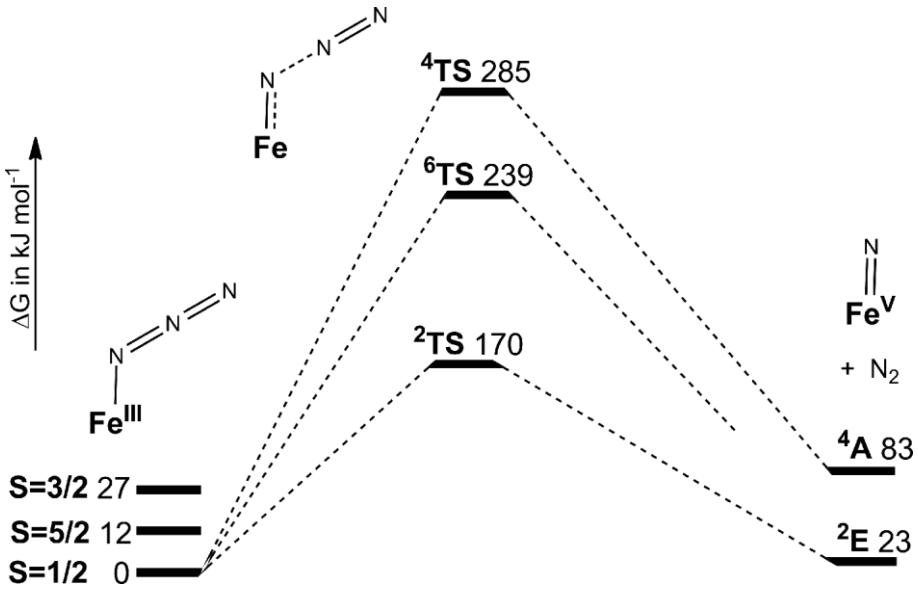

Scheme 4.7: Gibbs free energy (ΔG) the N_2-elimination from $[Fe^{III}(N_3)cyc\text{-}ac]^{+}$, energies in kJ mol^{-1}. BP86/def2-TZVP/RI/COSMO(Acetonitrile)/D3ZERO // B3LYP/def2-TZVP/RIJCOSX/COSMO(Acetonitrile)/D3ZERO

The reaction barrier for elimination of N_2 is calculated to be lowest in the doublet state, however, the calculated barrier of 170 kJ mol^{-1} is still very high. To overcome such a barrier in a thermal reaction is rather unlikely, but a photochemical elimination can still be possible. On the other hand, mass

spectrometry measurements discussed in Chapter 4.7 have revealed that the nitrido-iron(V) complex is also formed in the gas phase without photo excitation. Formation of the iron(V) species in the doublet state is calculated to be endergonic about 23 kJ mol^{-1}. The calculations demonstrate that the N_2-elimination is expected to proceed on the doublet state surface, since transition states in the sextet or quartet state are 69 kJ mol^{-1} and 115 kJ mol^{-1} higher in energy, respectively.

Besides the separate relaxed scans for the iron-nitrogen and nitrogen-nitrogen bonds, further calculations were performed where both bond distances were constrained simultaneously. The iron-nitrogen bond was varied between 1.5 Å and 3.2 Å and at the same time the bond distance between the iron bond azide nitrogen atom and the central-azide nitrogen atom was varied from 0.9 Å to 2.8 Å. The results of these calculations are shown as a three-dimensional potential energy surface plot in Figure 4.40. As expected, the iron(III)-azido structure represents a minimum on the energy surface (local minimum on the upper left in Figure 4.40). Elongation of the nitrogen-nitrogen bond leads to an increase in energy and at a bond-distance of ~1.7 Å (Fe-N ~1.8 Å) a maximum is reached from where the energy decreases again. On this way, another minimum in the calculated area is found for the nitrido-iron(V) structure at an iron-nitrogen bond length of 1.6 Å (on the lower left hand side in Figure 4.40). On the other hand, upon lengthening the iron-nitrogen bond distance the energy was found to only constantly increase. No maximum is passed within the range of the calculations. It should be noted here again, that elongation of the iron azide bond (Fe-N_3) results in an iron(III) complex and an azide anion, not in an azide radical.

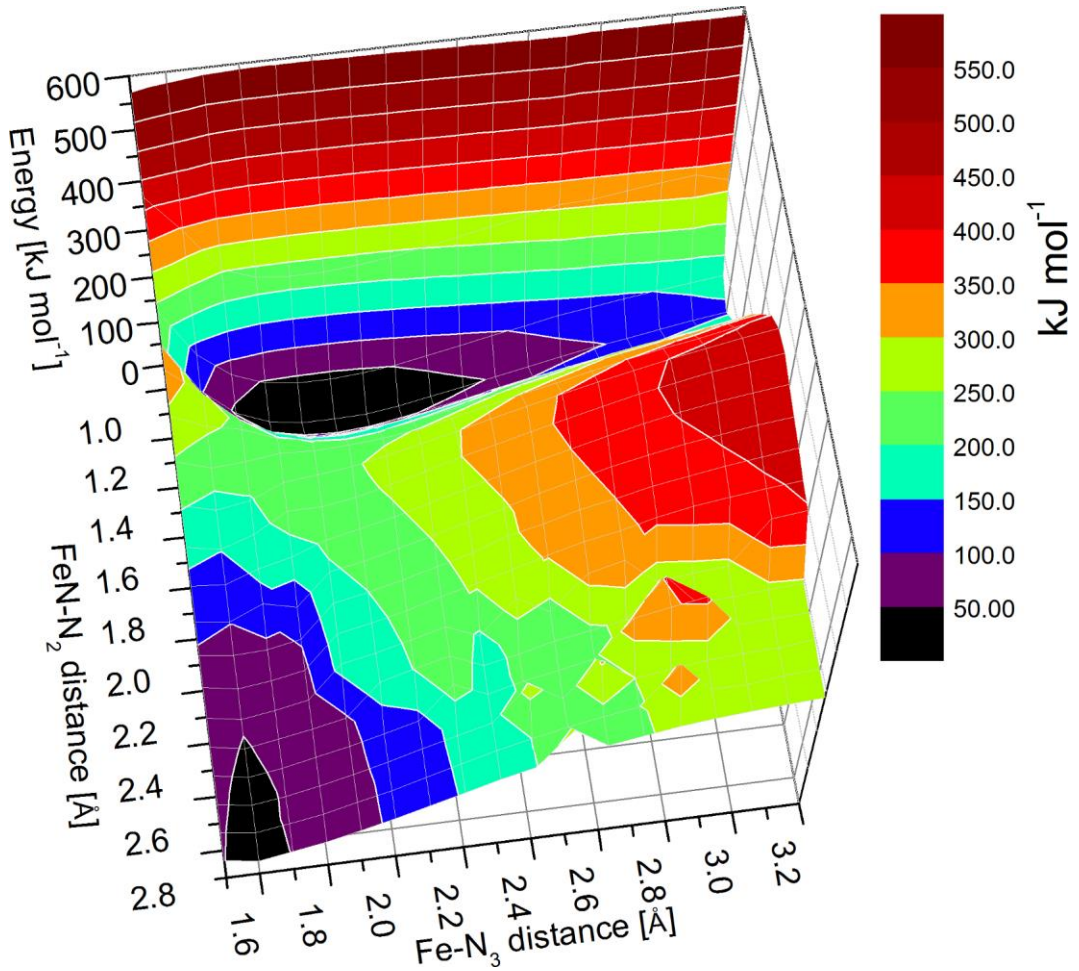

Figure 4.40: Three-dimensional potential energy surface scan on the complex $[Fe^{III}(N_3)cyc\text{-}ac]^+$ that leads to $Fe^{V}N + N_2$ in one direction and $Fe^{III} + N_3^-$ in the other direction.

The present calculations show that a very high barrier have to be overcome to form an nitrido-iron(V) complex from the corresponding azido-iron(III)-complex via N_2-eliminations. However, the calculated barrier of 170 kJ mol^{-1} is lower than the photon energy of 470 nm light that was used in the photolysis (see e.g. Chapter 4.6.1) and photons of 470 nm (255 kJ mol^{-1}) might deliver enough energy to overcome a that high barrier. For the elimination of the azide ligand from the iron(III)-complex it was not possible to locate a transition state. The calculations revealed that by elongation of the iron-azide bond an azide anion and an iron(III) complex is obtained, for all conceivable spin states. The results clearly demonstrate, that the formation of an iron(II)-complex and an azide radical cannot proceed on the electronic ground-state surface. This reaction, which was observed experimentally, has to proceed in an electronically excited state, which might open further reaction channels for the azide radical elimination.[41,43,217-218]

4.8.2. Computational Studies on the Photolysis of the Complex $[Fe^{III}(N_3)cyc\text{-}ac]^+$

Thermal reactions of the azido-iron(III) complex $[Fe^{III}(N_3)cyc\text{-}ac]^+$ were explored in the antecedent chapter by DFT calculations without considering electronically excited states. Here, it will be tried to investigate the photochemistry, hence, the electronic excited states during these reactions. The reactions discussed in the present work are mainly initiated by irradiation with light of well-defined wavelengths. Hence, specific electronically excited states will be populated that might initiate the elimination of N_2, N_3^- or $N_3^\bullet$. The absorption spectrum of the azido-iron(III) complex was already discussed in Chapter 4.3.1 where observed transitions were assigned to specific electronic transitions with the help of TD-DFT calculations.

A comprehensive theoretical study of the photochemistry of the present azido-iron(III) complexes or transition metal complexes in general is computationally demanding and challenging[235-237] due to the size of the complexes but also due to its complex photochemistry. The latter originates from a large number of energetically close lying states which is in particular the case for transition metal complexes with only partially filled d-shells. It can be foreseen that a high density of excited electronic states would lead to many (near)-degeneracies or crossing points such as conical intersections (CI) and inter system crossings (ISC).[238] The proper treatment of such degeneracies requires the calculation of non-adiabatic couplings (NACs) between the corresponding states. These NACs are necessary to evaluate probabilities of state transitions in order to map the path from the excited state to the ground state.[236] An appropriate method for the qualitatively correct description requires a multiconfigurational ansatz. For this purpose CASSCF is commonly used in the computational photochemistry. Due to the size of the azido-iron(III) complexes such a treatment is too expensive and as mentioned in Chapter 4.1, it was not possible to calculate the LMCT transition in the visible region properly by CASSCF/NEVPT2. Hence, in this case one is constrained to less expensive methods such as TD-DFT. Although TD-DFT is useful to calculate excitation energies (e.g. to reproduce experimental UV-*vis* spectra as done in Chapter 4.3) it has a serious drawback in the calculation of photochemical reactions. Todd Martinez and coworkers have shown that the dimensionality of a degeneracy, such as a conical intersection, is not correctly

described at the TD-DFT level of theory.[239] In consequence of this incorrect description TD-DFT can lead to a wrong path and unphysical dwell on excited states.

Further complication arises from the choice of the simulation technique. It was shown that even for a small organic molecule such as ethylene the static calculations, i.e. a minimum energy path, yields unrealistic crossing points.[240] These crossing points differ from those determined from molecular dynamics simulations where the kinetic energy is explicitly considered. Given that a large number of crossings is expected for the close lying excited states in azido-iron(III)-complexes with half-filled 3d-shell, its correct description and location is crucial.

Due to the size of the system an attempt to describe the initial excited state relaxation until an early encounter of a crossing of the excited states is made using TD-DFT. The aim is to see whether the excitation is leading directly to a dissociative state or a more complex path involving multiple crossings and the consequent change of the excited state character is required.

Excited state gradients calculated by TD-DFT

The gradients for selected excited states are calculated at the ground state geometry. Calculations were performed on the B3LYP/def2-TZVP/RIJCOSX level of theory with a total of 40 roots (the same method was used to calculate the absorption spectrum discussed in Chapter 4.3.1). For visualization, the gradients are scaled by a factor 50 and they are indicated by yellow vectors in Figure 4.41 for the excited states that were already described in Table 4.5 (page 44). The length of the vectors is direct proportional to the size of the gradient.

First it is followed the initial assumption that irradiation into the LMCT-band observed at 21895 cm^{-1} (calculated $\pi_{\parallel}(N_3) \rightarrow d_{xz/yz}$ / 23140 cm^{-1}) induces the elimination of dinitrogen, resulting in the nitrido-iron(V)-complex.[43] However, from the gradient shown in Figure 4.41 for this transition it seems to be unlikely that this excitation will directly result in a cleavage of the FeN-N_2 bond. The gradient at the azide ligand does not indicate a shortening of the Fe-N_3 bond, much more it is an elongation of the Fe-N_3 bond and a shortening of the nitrogen-nitrogen bond between the iron bond nitrogen atom and the central nitrogen atom in the azide ligand (FeN-N_2). Given that this nitrogen-nitrogen bond is calculated to be about 0.07 Å longer than the bond between the central and terminal nitrogen atoms, the calculated gradient rather suggests the elimination of an azide anion or –radical, since for these species a totally symmetric N_3-group would be expected with equivalent nitrogen-nitrogen bond-lengths. Further, the gradients indicate a shortening of the Fe-O bond which is in contradiction to an EXAFS study[41] and DFT-calculations (see Chapter 5.5 and in the literature[41,45]) which have shown that the Fe-O bond in the nitrido-iron(V) complex is longer than in the azido-iron(III) complex.

Very similar gradients are calculated for the $\pi_{\perp}(N_3) \rightarrow d_{z^2}$ transition that is predicted to appear at 30389 cm^{-1}. However, the Fe-O bond distance might be elongated when following the gradient. This can be understood easily, since the d_{z^2}-orbital, which is the electron acceptor for this transition, is anti-bonding with respect to the axial ligands.

The next two transitions that were calculated to be 34319 cm^{-1} and 37427 cm^{-1} are LMCT-transitions from the carboxylate group to the metal center. Therefore the gradient is largest for the carboxylate-group atoms.

At 38958 cm^{-1} an azido intra-ligand excitation ($\pi_{\perp}(N_3) \rightarrow \pi^*(N_3) + d_{z^2}$) is predicted by TD-DFT which corresponds very well with the gradient at the azide ligand. This gradient again rather suggests the elimination of an azide anion or –radical than of dinitrogen.

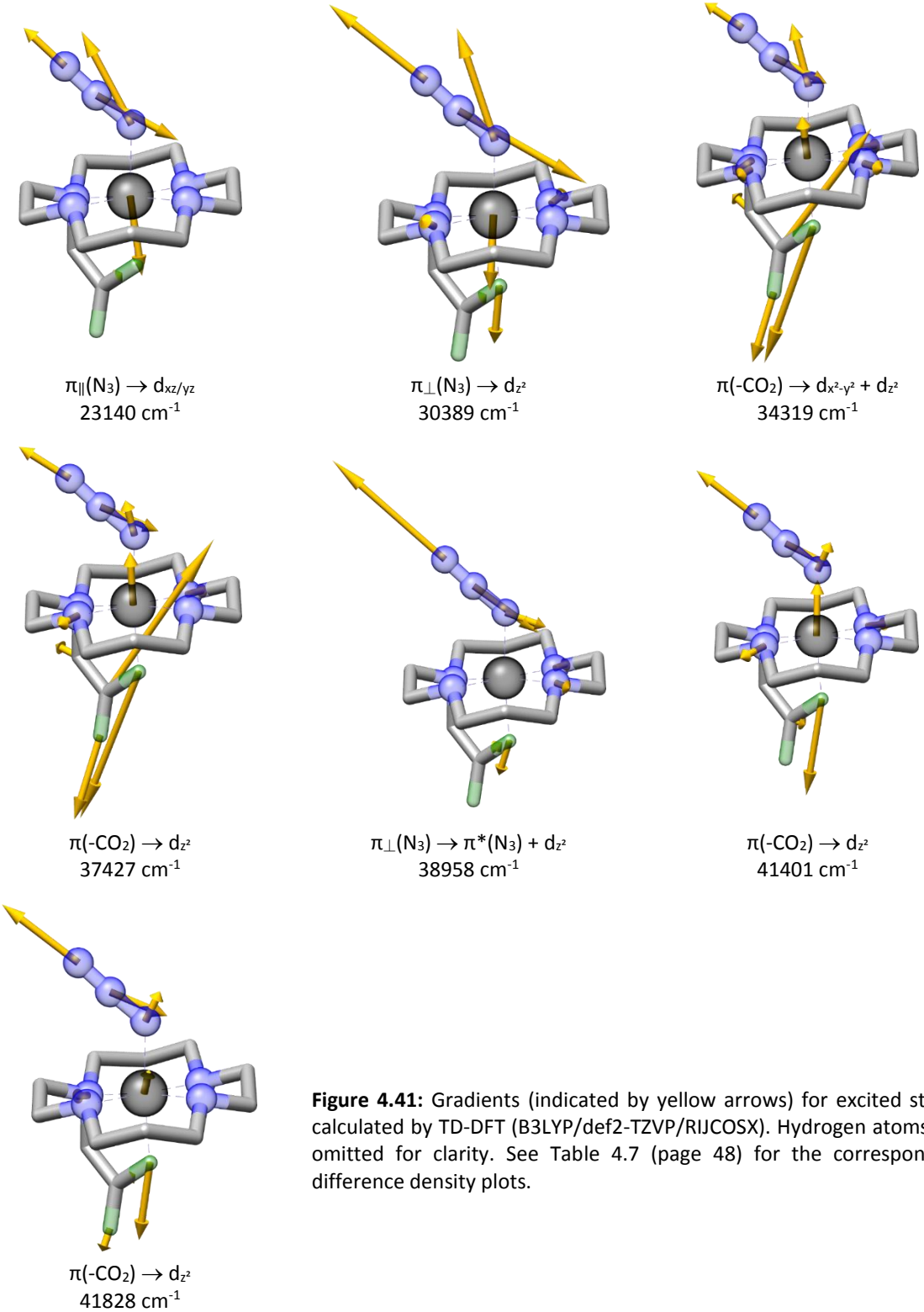

Figure 4.41: Gradients (indicated by yellow arrows) for excited states calculated by TD-DFT (B3LYP/def2-TZVP/RIJCOSX). Hydrogen atoms are omitted for clarity. See Table 4.7 (page 48) for the corresponding difference density plots.

The remaining two excitations that show significant intensity were calculated to be carboxylate to metal LMCT-transitions at 41401 cm^{-1} and 41828 cm^{-1}, respectively. However the gradients show significant magnitude not only for the carboxylate group but also for the azido nitrogen atoms. Notably, the gradient for the $\pi(\text{-}CO_2) \rightarrow d_{z^2}$ transition calculated to appear at 41401 cm^{-1} is the only one where a shortening of the iron-nitrogen bond might be concluded from. This would be expected for the formation of the nitrido-iron(V) species. However, for all considered excited states, the overall gradients calculated for the azide ligand do rather imply the formation of an isolated N_3-group (anion or radical) with equivalent nitrogen-nitrogen bond-distances. Hence, from the static calculation of the gradients, it cannot be concluded that an excited state can lead directly to the elimination of dinitrogen.

TD-DFT calculations on the N_2-elimination

The calculated gradients of course only provide a static picture on possible photochemical reactions initiated in a specific excited state. To gain some basic insight in the excited states during the elimination of dinitrogen another approach was chosen here:

A relaxed surface scan calculation was performed on the $[Fe^{III}(N_3)cyc\text{-}ac]^+$ complex, where the distance between the iron-bond nitrogen atom and the central nitrogen atom of the azide ($FeN\text{-}N_2$) was varied which leads to the elimination of N_2. This results in molecular structures along the pathway of dinitrogen elimination in the electronic ground state. Results of these calculations were already discussed in Chapter 4.8.1. Similar calculations are performed in this context, however, excited states were calculated by TD-DFT on the optimized structures. This presents a rough approximation because the relaxation of the molecular structure in the excited states is not considered. However, it might allow a qualitative inspection of excited states for dissociative character that might induce the elimination of dinitrogen.

Structures were minimized using the BP86/def2-TZVP/RI/COSMO(Acetonitrile) level of theory. The considered bond was varied in 0.02 Å steps. TD-DFT calculations were performed for 40 roots (states) on these structures at the same level, the BP86 functional was only replaced by the B3LYP functional and the RIJCOSX approximation was used.

In Figure 4.42 result for the scan along the nitrogen-nitrogen bond is shown. The lowest black trace represents the electronic ground state (root 0) and is therefore analogue to the plot in Figure 4.39. On the very left (the Franck Condon region), at a constrained nitrogen-nitrogen bond distance of 1.2 Å the result corresponds to the TD-DFT results discussed in Chapter 4.3.1 and the character of these transitions is indicated on the left hand side.

For the $\pi_{\|}(N_3) \rightarrow d_{xz/yz}$ transition that was initially assumed to induce the elimination of N_2, it was possible to follow the excited state in a limited range where it is relatively well separated from other states and inspection of the difference densities confirm that the points on the potential energy surface that are shaded light yellow correspond to this state. However, at a bond distance of 1.4 Å crossing with other states occur and it is not clear anymore which point on the PES corresponds to this excited state. The character of this excitation changed to a degree that it cannot be identified anymore by inspection of the difference-density plots. Figure 4.2 still reveals for the range where the

$\pi_{\parallel}(N_3)\rightarrow d_{xz/yz}$ excited state is not crossing any other states that the energy of this state significantly rises, while it would be expected to decrease for a dissociative state. By visual inspection of the graph, the started path is continued following a minimum energy pathway, connecting states that are close in energy (see cyan shaded pathway in Figure 4.42). This is of course relatively arbitrary, since NAC, the probability to move from one excited state surface to another, is completely neglected. However, following the indicated path from its beginning in the Franck-Condon region, crossing of a high barrier on the excited state surface (about 11770 cm^{-1}=141 kJ mol^{-1} high) is necessary at a FeN-N_2 distance of 1.44 Å which appears to be rather unlikely. The TD-DFT calculations, therefore, do not provide evidence that the excited LMCT state $\pi_{\parallel}(N_3)\rightarrow d_{xz/yz}$ is dissociative with respect to the FeN-N_2 bond.

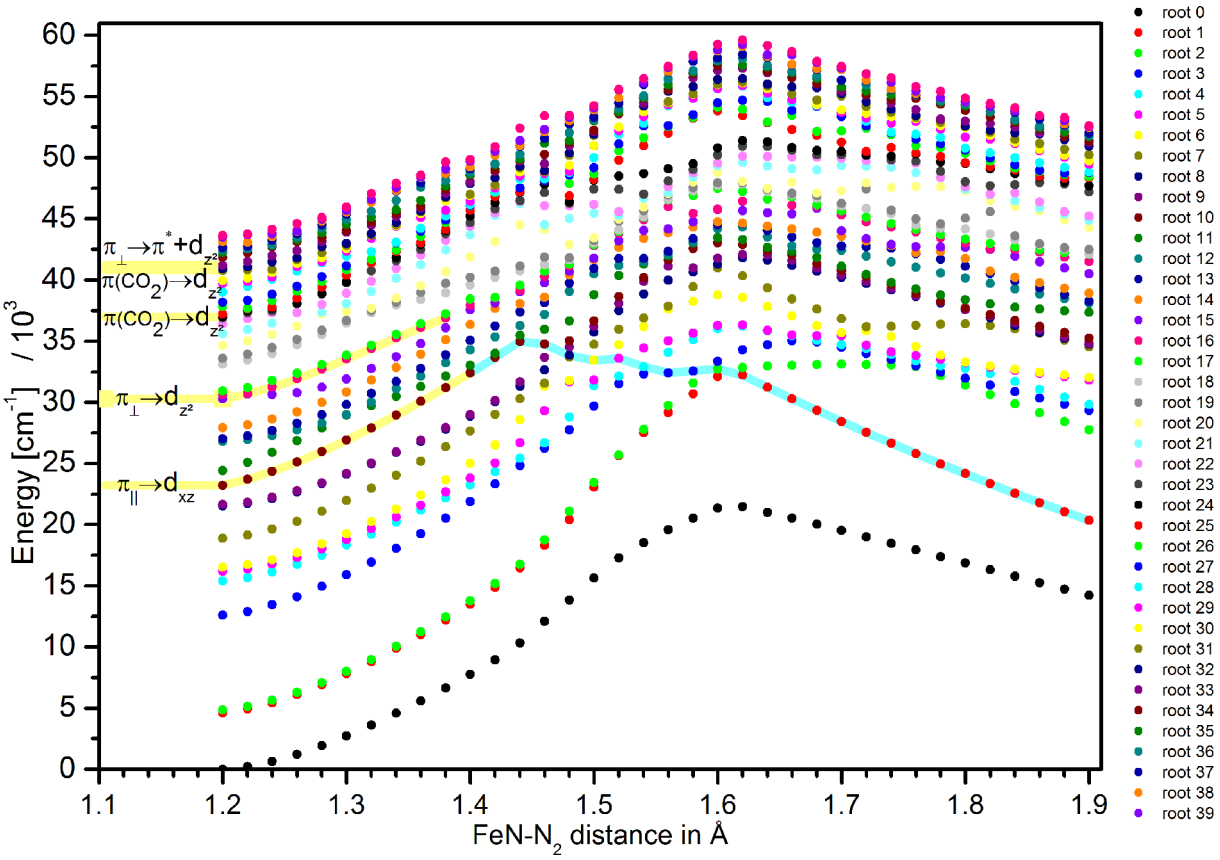

Figure 4.42: Excited state energies for a relaxed surface scan along the FeN-N_2 bond.

Similar conclusions as just discussed can be drawn for the $\pi_{\perp}(N_3)\rightarrow d_{z^2}$ transition. It was partially possible to follow this excited state during the scan (see light yellow underlined trace in Figure 4.42 starting at ~30000 cm^{-1}) and it is seen that the energy of this state also increases. Hence, the $\pi_{\perp}(N_3)\rightarrow d_{z^2}$ excited state is not found to be dissociative in the TD-DFT calculations. Nonetheless, crossing with other states occurs at an early stage for this state which might allow reactions to proceed on another potential energy surface. However, by visual inspection of the plot no pathway is found starting with the $\pi_{\perp}(N_3)\rightarrow d_{z^2}$ excited state where the energy is significantly decreasing.

It should be also noted that the $\pi_{\perp}(N_3)\rightarrow d_{z^2}$ excitation appears at higher energy (calculated 30389 cm^{-1}, assigned to the experimentally observed band at 32108 cm^{-1}, see Chapter 4.3.1) than the energy of 470 nm (21277 cm^{-1}) light which was used in the photolysis experiments. In these experiments with 470 nm light that exclusively yielded the nitrido-iron(V) complex (see Chapter 4.6.1), population of the $\pi_{\perp}(N_3)\rightarrow d_{z^2}$ excited states is therefore not possible.

For excited states even higher in energy, it is much more difficult to follow them during the scan along the FeN-N_2 bond distance. Many states close in energy are calculated which makes it difficult to follow possible reaction pathways.

The TD-DFT results do not provide evidence that the $\pi_{||}(N_3)\rightarrow d_{xz/yz}$ LMCT-transition observed in the visible region at 21895 cm^{-1} (calculated 23140 cm^{-1}) results in a state that is dissociative with respect to the FeN-N_2 bond. Given the assumption and the constraints of the TD-DFT calculation it can be only excluded that the N_2-elimination process is not directly initiated. Hence, it rather points towards a more complicated cleavage of the nitrogen-nitrogen bond.

One possibility might be that other spin states play a role in the N_2-elimination reaction that were not taken into account in the present TD-DFT study. However, it was shown in Chapter 4.8.1 that the reaction barrier (in the electronic ground state) is significantly higher in energy for the quartet (239 kJ mol^{-1}) and sextet (285 kJ mol^{-1}) state when compared to the transition state in the doublet spin ground-state (170 kJ mol^{-1}, see Scheme 4.7). Still, a photon of 470 nm (=21277 cm^{-1} = 255 kJ mol^{-1}) delivers enough energy to overcome the very high barrier for the (thermal) N_2-elimination in the doublet state.

As mentioned before, one might also consider more complicated mechanisms for the N_2-elimination. Based on time resolved IR-measurements, an intermediate was proposed with a cyclic azide species coordinated to iron (see Chapter 4.5.3 page 82) which might also play a role in the N_2-elimination. However, this species was calculated to be 234 kJ mol^{-1} (B3LYP/def2-TZVP) or 255 kJ mol^{-1} (CASSCF(7,7)/NEVPT2/def2-TZVP) higher in energy than the ground state azido-iron(III) complex. Hence, this species is even higher in energy than the calculated transition state for the thermal N_2-elimination (170 kJ mol^{-1}). Furthermore, it should be mentioned that in the experiments where this species was proposed a laser of 266 nm wave length was used. Hence, light of much higher energy than the 470 nm light source used for the formation of the nitrido-iron(V) complex in Chapter 4.6.1.

A satisfactory computationally explanation of the underlying photochemical mechanism for the N_2-elimination cannot be provided here. An excited state that is dissociative with respect to the elimination of N_2, or a pathway that shows a low barrier for the elimination of N_2 on the excited state surface was not found within the chosen approach.

TD-DFT calculations on the N_3-elimination

In analogy to the TD-DFT calculations on the N_2-elimination discussed above, calculations on the N_3-elimination were performed. The bond distance between iron and the azido-nitrogen atom bond to iron was varied from 1.92 Å to 2.6 Å in 0.02 Å steps (in the full optimization a Fe-N_3 distance of 1.93 was calculated, see Table 4.1). Structures were optimized at the BP86/def2-TZVP/RI/COSMO(Acetonitrile) level of theory and for the excited states the B3LYP functional was used in conjunction with the RIJCOSX approximation. The results are shown in Figure 4.43.

For the electronic ground state (root 0) the same curve was obtained as already shown in Figure 4.39. The energy increases without reaching any maximum and it should be noted again, that in the performed scan in the ground state an iron(III) complex and an azide anion are obtained, not an iron(II) complex and an azide radical. However, LMCT transitions from the azide ligand to the iron center can result in an azide radical and an iron(II) complex.

Remarkable differences are found when the plot is compared to the results for the FeN-N_2-scan (Figure 4.42). While in the scan along the FeN-N_2 bond the energy for all states rises during lengthening the selected bond, in the present case the energy decreases for certain states when the Fe-N_3 bond is elongated. The LMCT-transition from the azide ligand into the SOMO ($\pi_{\parallel}(N_3)\rightarrow d_{xz/yz}$) is underlined light yellow and it is possible to follow it by inspection of the difference densities during the whole scan. Its energy decreases until an iron-azide distance of 2.14 Å is reached (at 21477 cm^{-1}, it should be noted that at this point the state did already cross with another state). Then it increases again, reaching 25002 cm^{-1} which is even above the energy at the starting point of the scan in the Franck Condon region. However, it is possible that the reaction proceeds via non-adiabatic transitions between multiple electronic states that are crossing. In the present case a transition to another state at a bond distance of 2.16 Å is conceivable and a possible minimum energy pathway is shaded orange in Figure 4.3. Even the energy does not decrease much further on this pathway, it is a possible reaction pathway for the elimination of an azide.

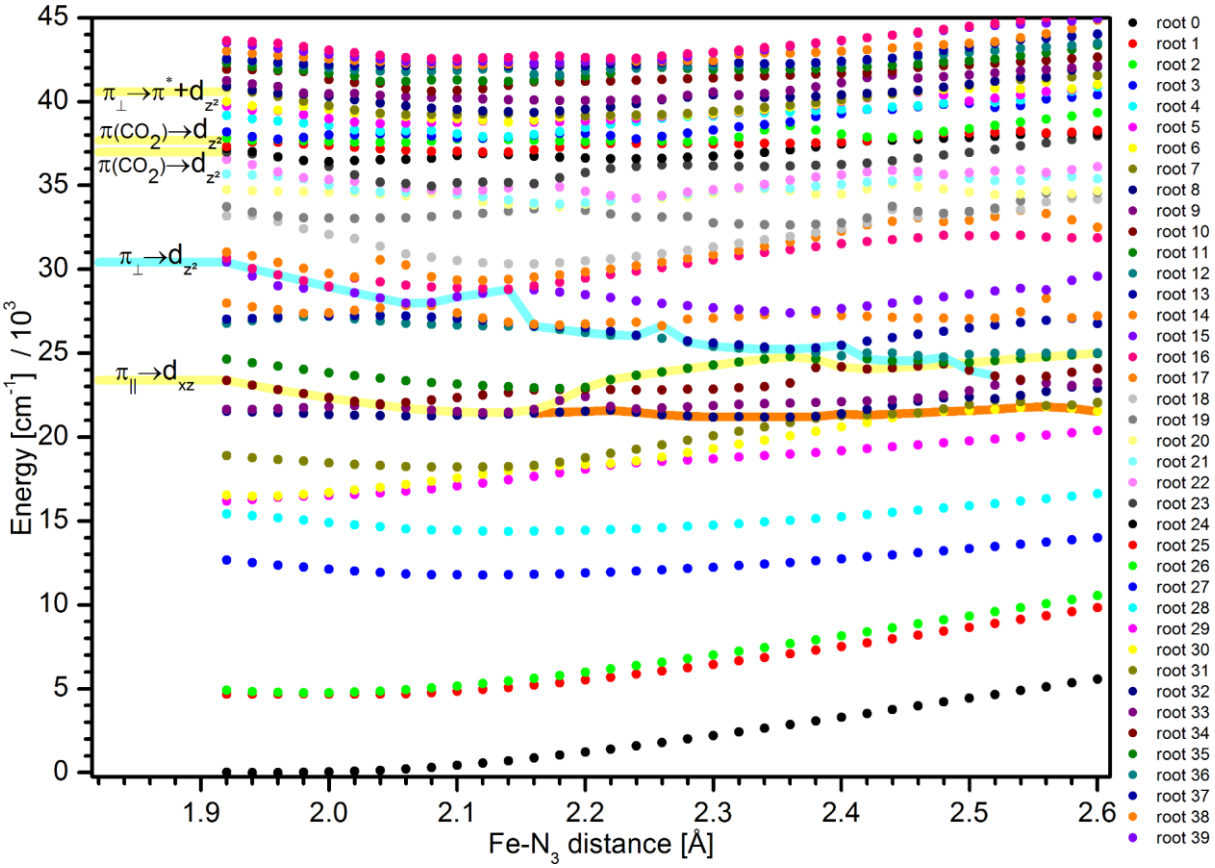

Figure 4.43: Excited state energies for a relaxed surface scan along the Fe-N_3 bond.

The transition from the azide ligand to the metal d_{z^2}-orbital ($\pi_{\perp}(N_3)\rightarrow d_{z^2}$) also decreases in energy, even more significantly than the $\pi_{\parallel}(N_3)\rightarrow d_{xz/yz}$ transition. It was possible to follow this transition by inspection of the difference density plots until an iron-azide distance of 2.52 Å is reached (see cyan

shaded pathway in Figure 4.43). The curve evolves rather irregular between 2.08 Å and 2.16 Å where the energy is first increasing and then decreasing again. This is indicating a strong interaction with neighboring excited states. However, the transition to another excited state at this point is possible, allowing to follow a pathway on which the energy is further decreasing. The $\pi_{\perp}(N_3) \rightarrow d_{z^2}$ excitation that was calculated to be 30389 cm^{-1} and assigned to the experimentally observed band at 32108 cm^{-1} might therefore also open a reaction channel that is dissociative with respect to the Fe-N_3 bond.

It is again not possible to follow higher excited states on the potential energy surface. There are too many excited states very close in energy.

The shown PES (Figure 4.43) correlates well with the calculated excited state gradients (shown in Figure 4.41). Most excited state gradients suggested the elimination of an azido-group which is in agreement with the fact that these states (as far as it was possible to identify them on the PES) decrease in energy when the Fe-N_3 bond is elongated.

The finding that some LMCT-transitions decrease in energy for the Fe-N_3 scan can be understood from the removal of one axial ligand. Removing an axial ligand will lower the energy especially for the d_{z^2}-orbital that is antibonding with respect to these ligands. Hence, LMCT-transitions where the d_{z^2}-orbital is the accepting orbital will appear at lower energy. This explains the dissociative nature of the $\pi_{\perp}(N_3) \rightarrow d_{z^2}$ transition. On the other hand, the elimination of dinitrogen will result in a nitrido-iron complex where the monoatomic nitrido ligand is a very strong donor ligand. It will therefore rise the energy of the d-orbitals as well as the energy of the LMCT-transitions.

The chosen approach includes some strong approximations, but by TD-DFT it was tried to gain some insight into the photochemical reactions of the $[Fe^{III}(N_3)cyc\text{-}ac]^+$ complex. It was not possible to identify any dissociative states during the FeN-N_2 bond cleavage. As discussed, this might indicate that the N_2-elimination process is more complicated than it was considered here. The reason might be as well, that the chosen approach is a too drastic simplification and more subtle effects have to be considered, e.g. relaxation of the molecular structure in electronically excited states. Dissociative states were only found for the cleavage of the Fe-N_3 bond.

4.8.3. Thermal Reactions of the Complex $[Fe^{III}(N_3)TMC\text{-}ac]^+$

The dinitrogen, azide anion and azide radical elimination reactions were further investigated computationally for the complex $[Fe^{III}(N_3)TMC\text{-}ac]^+$. Considering all possible spin states is of special relevance here, because the azido-iron(III) complex shows spin crossover behavior at low temperature[42,48] and it is not clear in which spin state the reactions proceed. Gibbs free energies for the azide anion and azide radical elimination from $[Fe^{III}(N_3)TMC\text{-}ac]^+$ in the quintet state, which is calculated to be the ground state, are summarized in Scheme 4.8.

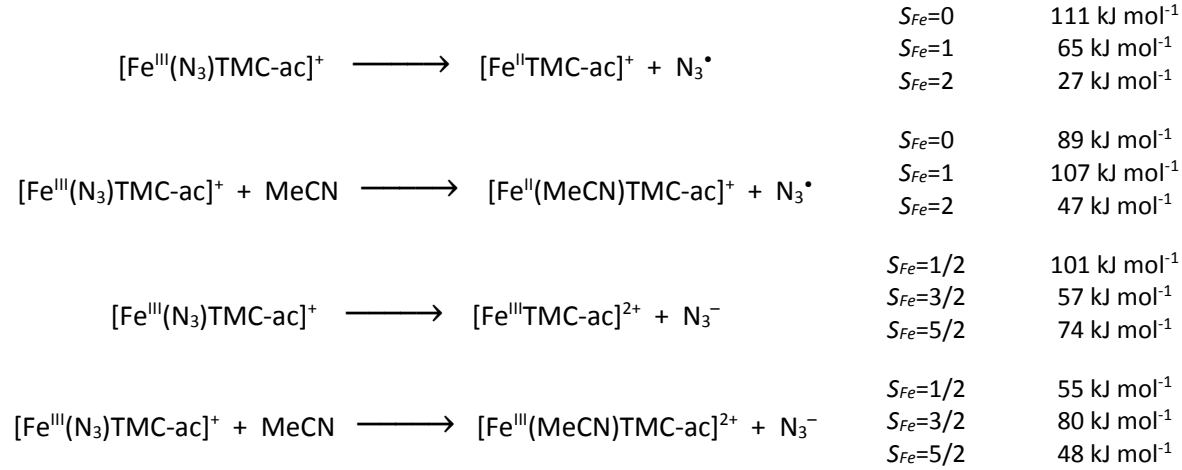

Scheme 4.8: Gibbs free energy (ΔG) for N_3-elimination from $[Fe^{III}(N_3)(TMC\text{-}ac)]^+$, S_{Fe} refers to the spin on iron in the products (BP86/def2-TZVP/RI/COSMO/D3ZERO//B3LYP/def2-TZVP/RIJCOSX/COSMO/D3ZERO).

For the complexes $[Fe^{II}(TMC\text{-}ac)]^+$, $[Fe^{II}(MeCN)(TMC\text{-}ac)]^+$ and $[Fe^{III}(MeCN)(TMC\text{-}ac)]^{2+}$ the S=5/2 spin state is calculated to be lowest in energy. For the complex $[Fe^{III}(TMC\text{-}ac)]^{2+}$ a S=3/2 ground state is predicted. This indicates, that with the methylated ligand system TMC-ac$^-$, the additional axial solvent molecule has less influence on the spin states than for the complex with the non-methylated ligand system cyc-ac (see Scheme 4.8). As already concluded in a previous study from the spin crossover behavior of the $[Fe^{III}(N_3)(TMC\text{-}ac)]^+$ complex, the methylation of the cyclam acetato ligand leads to a system with lower ligand field strength.[42] Possible impacts on the electronic structure of nitrido-iron(V) complexes due to the weaker ligand will be discussed in Chapter 5.5.

In general, the reactions are calculated to be less endergonic than for the complex $[Fe^{III}(N_3)cyc\text{-}ac]^+$, especially the elimination of an azide radical is only endergonic about 27 kJ mol^{-1}. This is in line with the mass spectrometry measurements where azide radical elimination was observed as the mayor fragmentation product for the $[Fe^{III}(N_3)(TMC\text{-}ac)]^+$ complex (see Chapter 4.7).

Similar to the calculations performed on the $[Fe^{III}(N_3)(cyc\text{-}ac)]^+$ complex in the antecedent section, the N_2-elimination reaction from $[Fe^{III}(N_3)(TMC\text{-}ac)]^+$ was calculated for various spin states. Energies are given relative to the azido-iron(III) complex in the S=5/2 state, which was calculated to be the spin ground state (see Scheme 4.9).

The lowest energy transition state is the one in the doublet state, as shown in Scheme 4.9. Transition states in the sextet and quartet state are 67 kJ mol^{-1} and 93 kJ mol^{-1} higher in energy, respectively. Hence, if the lowest energy pathway is followed in the thermal elimination of N_2, a change from high-spin for the azido-iron(III) complex to low-spin is necessary.

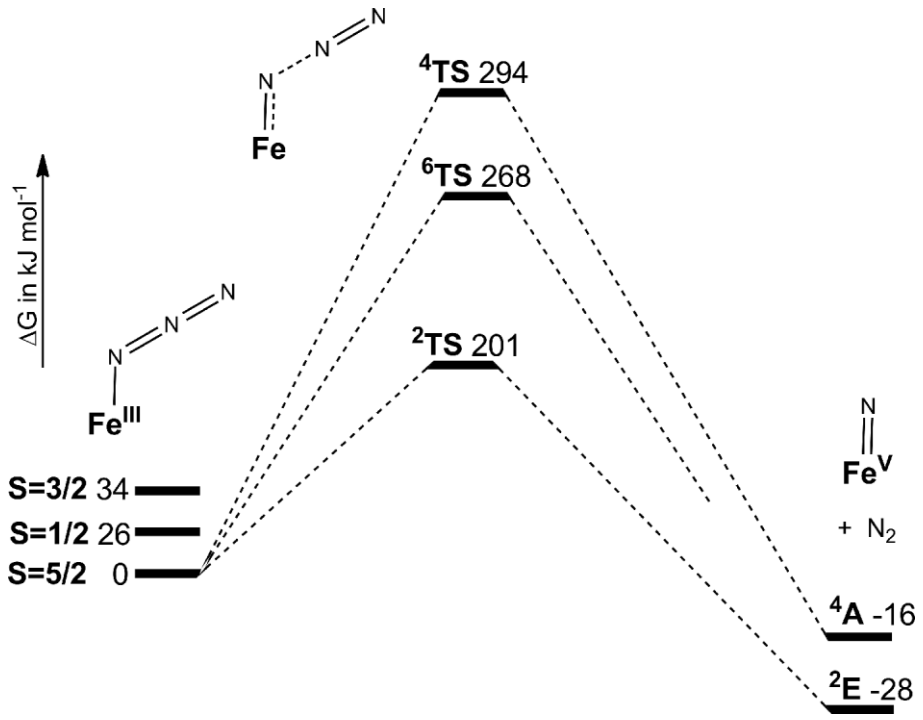

Scheme 4.9: Gibbs free energy (ΔG) for N_2-elimination from $[Fe^{V}(N)(TMC\text{-}ac)]^{+}$, Energies in kJ mol^{-1}. BP86/def2-TZVP/RI/COSMO(Acetonitrile)/D3ZERO //B3LYP/def2-TZVP/RIJCOSX/COSMO(Acetonitrile)/D3ZERO

For the resulting nitrido-iron(V) complex $[Fe^{V}(N)(TMC\text{-}ac)]^{+}$ the doublet state is calculated to be slightly lower in energy than the quartet state (about 12 kJ mol^{-1}). It is further interesting to see, that the formation of the $[Fe^{V}(N)(TMC\text{-}ac)]^{+}$ species in is calculated to be exergonic about -28 kJ mol^{-1}, while the formation of the $[Fe^{V}(N)(cyc\text{-}ac)]^{+}$ complex is endergonic about +23 kJ mol^{-1}). However, the barrier for the TMC-ac complex is calculated to be 31 kJ mol^{-1} higher in energy than for the cyc-ac complex.

Given that the calculated reaction barrier for the complex $[Fe^{III}(N_3)TMC\text{-}ac]^{+}$ is even higher in energy than for the non-methylated $[Fe^{III}(N_3)(cyc\text{-}ac)]^{+}$-complex, a thermal reaction seems to be even less realistic. However, it should be noted that the calculated barrier of 201 kJ mol^{-1} is still below the energy of 470 nm photons (255 kJ mol^{-1}). Light of 470 nm is used in Chapter 5.4.2 to irradiate EPR-samples of the $[Fe^{III}(N_3)TMC\text{-}ac]^{+}$ complex which results in the nitrido-iron(V) species $[Fe^{V}(N)TMC\text{-}ac]^{+}$.

4.9. Discussion and Conclusions

In the present chapter, azido-iron(III) complexes were studied by various experimental and theoretical methods and possible (photochemical) reactions were explored. These reactions are the elimination of N_2 yielding nitrido-iron(V) complexes, the $N_3^{\bullet}$-radical elimination yielding iron(II) complexes, and the redox-neutral N_3^--anion elimination.

The complexes $[Fe^{III}(N_3)cyc\text{-}ac]PF_6$ and $[Fe^{III}(N_3)_2cyc]ClO_4$ show absorption bands in the visible region at 21895 cm^{-1} (458 nm) and 20499 cm^{-1} (488 nm), respectively, and light that coincides with these characteristic bands was used in their photolysis. TD-DFT calculations and resonance Raman measurements have shown that these absorptions originate from azido-to-metal LMCT-transitions. An intense antisymmetric stretch vibration of the azide ligand was observed in the resonance Raman spectra, which indicates that irradiation into the visible band induces an antisymmetric distortion of the azide ligand, as would be expected in the elimination of N_2.

Photolysis of frozen solution Mössbauer samples of the complex $[Fe^{III}(N_3)cyc\text{-}ac]PF_6$ with 470 nm or 304 nm light, both resulted exclusively in formation of the nitrido-iron(V) complex $[Fe^{V}(N)cyc\text{-}ac]PF_6$. This demonstrates, that even when very different electronic transitions are induced by irradiation, photolysis of frozen solution samples results in identical nitrido-iron(V) species. In other words, a wavelength dependence is not observed. In contrast, 470 nm photolysis of liquid solution samples yielded the low-spin ferrous complex $[Fe^{II}(MeCN)cyc\text{-}ac]PF_6$. However, from steady-state Mössbauer measurements it is not possible to definitively conclude if this is the primary photo product or a decay product of the species initially formed in liquid solution. This question will be addressed in more detail in Chapter 5.9.1, where elucidation of the decay mechanism of nitrido-iron(V) complexes in solution is provided. In addition, the effect of the state of aggregation upon the product of photolysis of the complex $[Fe^{III}(N_3)TMC\text{-}ac]PF_6$ is discussed in Chapter 5.4.2.

Time-resolved IR measurements were performed for the complex $[Fe^{III}(N_3)cyc\text{-}ac]^+$ in order to investigate the primary photochemical events observed in solution upon irradiation with a 266 nm laser. The data revealed the formation of the ferrous complex $[Fe^{II}(MeCN)cyc\text{-}ac]^+$ via reductive elimination of an azide radical ($N_3^{\bullet}$). In contrast, in the gas phase (without any photoexcitation) the N_2-elimination and formation of the nitrido-iron(V) complex was found to be the lowest-energy dissociation pathway for $[Fe^{III}(N_3)cyc\text{-}ac]PF_6$ (see Chapter 4.7 as well as Ref.[53]). Elimination of a neutral azide radical was not observed even at higher collision energies. On the other hand, for the analogous complex of the methylated cyclam ligand, $[Fe^{III}(N_3)TMC\text{-}ac]PF_6$, loss of an azide radical was detected as the main fragmentation product in the gas phase and the nitrido-iron(V) complex was not observed at all.

DFT calculations were performed to gain insight in the energetics of the potential reactions and the photochemistry of the complex $[Fe^{III}(N_3)cyc\text{-}ac]PF_6$. The reaction barrier for N_2-elimination from the complex $[Fe^{III}(N_3)cyc\text{-}ac]^+$ in the doublet state is calculated to be 170 kJ mol^{-1} high, and even higher in energy for the quartet (285 kJ mol^{-1}) and sextet state (239 kJ mol^{-1}). Therefore, the barrier appears to be too high for a thermal reaction. However, light of 470 nm that was used in the photolysis experiments corresponds to a photon energy of 255 kJ mol^{-1}, which is sufficient energy to overcome the high barrier and the reaction is assumed to be initiated by an electronic excitation. In response,

the role of excited states during the N_2-elimination reaction was explored using TD-DFT calculations. However, within the chosen approach, it was not possible to identify any excited state that shows significant dissociative character with respect to the FeN-N_2 bond. Calculations further revealed that upon elongation of the Fe-N_3 bond an azide anion and iron(III) complex is obtained, and not an azide radical and iron(II) complex. This clearly shows that the elimination of an azide radical, yielding an iron(II) complex, is not possible on the electronic ground state surface. Photoexcitation is required to reduce the metal and oxidize the ligand.

In summary it can be concluded, that the photochemical reactions of the azido-iron(III) complexes considered are far more complex than the previously assumed wavelength dependence. There seem to be further effects that dictate whether the oxidative ($Fe^{V}N$), reductive (Fe^{II}) or redox-neutral (Fe^{III}) pathway is chosen. The state of aggregation (liquid solution vs. frozen solution) appears to have a strong influence on the outcome of the reaction. A possible explanation for this is that the photochemical azide radical and/or anion elimination might be reversible, whilst the oxidative formation of a nitrido-iron(V) complex is expected to be irreversible due to the expulsion of a highly inert N_2 molecule. Given that the rigid solid environment in frozen solution is likely to suppress the extensive nuclear reorganization required for successful loss of azide,[241] prolonged irradiation under these conditions would then yield the high-valent species exclusively. This supposition is in line with relaxed surface scans demonstrating that after passing an energetic maximum at which the FeN-N_2 bond is elongated by about only 0.5 Å a new energy minimum is accessible, whereas upon lengthening the Fe-N_3 bond by about 1.5 Å (resulting in an azide anion) the energy was found to only constantly increase.

The discussed results provide new insight into the photolysis of azido-iron(III) complexes and are, therefore, relevant for planning photochemical routes to new nitrido-iron(V) complexes. These can serve as model systems for the plethora of biological and industrial processes that potentially involve iron nitrides. The nitrido-iron(V) complexes whose formation was studied in the present chapter, plus other examples, will be investigated in detail in Chapter 5.

5. Nitrido- and Oxo-Iron(V) Complexes

Only a few iron(V) complexes of tetragonal symmetry (square pyramidal or octahedral) are known, as outlined in the introduction (Chapter 1.2 and 1.3). The photolysis of azido-iron(III) complexes and the formation of nitrido-iron(V) complexes was already investigated by Mössbauer-, absorption-, (time resolved) IR spectroscopy and quantum chemical calculations in the antecedent chapters. In the present chapter, previously reported and one new nitrido-iron(V) complex are studied by spectroscopic and theoretical methods in detail. This provides new insight into their electronic structure and a detailed understanding of observed spectroscopic parameters. As outlined in the introduction (Chapter 1), nitrido- and oxo-iron(V) species can serve as model complexes for more complex industrial or biological systems. Hence, an in-depth understanding of these species is crucial to allow a transfer of the results to more complex systems.

The spin state of the previously reported nitrido-iron(V) complexes $[Fe^{V}(N)(N_3)cyc]^{+}$, $[Fe^{V}(N)TPP]$, $[Fe^{V}(N)OEP]$ and $[Fe^{V}(N)TMP]$ is still under dispute. A simple computational approach for determining the correct spin state would be to calculate the relative spine state energies. However, beyond that the calculation of experimentally observable parameters for different spin states provides further evidence for the correct spin state, as will be shown in Chapter 5.1 and Chapter 5.3. Further information about the structure and spin state of the iron(V) complex $[Fe^{V}(N)(N_3)cyc]^{+}$ will be obtained from low temperature IR-spectroscopy and photolysis experiments in Chapter 5.2.

EPR-spectra for tetragonal nitrido-iron(V) complexes have not been reported in the literature so far.[1] Therefore, spectra recorded for a series of tetragonal nitrido-iron(V) complexes will be discussed in detail in Chapter 5.4 and the g-values will be analyzed in detail, supported by extended quantum chemical calculations.

Furthermore, the decay pathway of tetragonal nitrido-iron(V) complexes will be studied and the underlying mechanism is revealed in a combination of experimental and computational methods (Chapter 5.9).

[1] EPR-data was presented in Ref.[242] which was assumed to result from the species $[Fe^{V}(N)(N_3)cyc]ClO_4$. However, the low quality of the data was already noted in this work. In the following chapters it will be shown that the observed spectrum did not result from the complex $[Fe^{V}(N)(N_3)cyc]ClO_4$.

5.1. Vibrational Spectroscopy Calculations and the Spin-State of Nitrido-Iron(V) Porphyrin Complexes[2]

Nakamoto *et al.* reported the first nitrido-iron(V) complexes in 1989.[40,46] These porphyrin complexes were obtained by photolyzing resonance Raman samples of the parent azido-iron(III) porphyrinato complexes. Based on a comparison with analog transition metal oxo- and nitrido porphyrin complexes a quartet ground state was assumed. Key vibrational modes further indicated that the complexes do not undergo ligand oxidation, as known for several analog oxo-porphyrin complexes that are best described as iron(IV) species with a ligand centered radical, [Fe^{IV}(O)($POR^{\bullet+}$)].[40,46,62,92,244-246] However, further spectroscopic data besides the resonance Raman study is not available.

The characteristic iron-nitrido stretching vibration ν(Fe-N) was identified as such in the resonance Raman experiments by ^{15}N-isotope labeling. Given that the formal bond-order of the nitrido-iron bond is affected by the spin state (this will be discussed in Chapter 5.5.2), also the nitrido stretching vibration is expected to be highly sensitive to the spin state. Therefore, ν(Fe-N) modes were calculated by DFT (BP86/def2-TZVP/RI, modes scaled by 0.9914) for both conceivable spin states for the series of porphyrin complexes reported by Nakamoto *et al.*[40,46] Attempts were also made to find a broken-symmetry solution including a ligand radical, but all calculations converged to solutions with a closed-shell ligand. Calculated modes and relative spin state energies (B3LYP/def2-TZVP/RIJCOSX) are provided in Table 5.1.

Table 5.1: Experimental and calculated ν(FeN) modes for the doublet and quartet state and calculated doublet-quartet gap ($\Delta E_{d\text{-}q}$) for three Fe^{V}N porphyrin complexes.

	ν(FeN) exp.[a] [cm^{-1}]	*S*	ν(FeN) calc. [cm^{-1}]	$\Delta E_{d\text{-}q}$ [kJ mol^{-1}]
[Fe^{V}(N)TPP]	876	1/2	956	0
		3/2	713	76
[Fe^{V}(N)OEP]	876	1/2	969	0
		3/2	686	74
[Fe^{V}(N)TMP]	873	1/2	960	0
		3/2	719	81

a: Experimental data taken from Ref. [46] and Ref.[40]

Best agreement between experimental and calculated modes is found for the doublet state, and the doublet state is also calculated to be lower in energy. The relatively large deviation between experimental and calculated modes can be attributed to the nearly degenerate ground state for the nitrido-iron(V) complexes (see detailed discussion in Chapter 5.5) which is difficult to describe properly by the single configurational DFT method.

The results provide strong evidence that the considered complexes possess a doublet ground state and not a quartet state as initially assumed. The calculations further confirm that the ligand is closed shell.

[2] It should be noted here, that DFT calculations on a nitrido-iron(V) porphyrin complex have been performed previously by Ghosh *et al.,*[243] however, the *S*=1/2 ground state was not considered in this work and calculated vibrational modes were not reported.

5.2. Low Temperature IR-Spectroscopy on the Complexes $[Fe^{III}(N_3)_2cyc]ClO_4$ and $[Fe^{V}(N)(N_3)cyc]ClO_4$

The complex *trans*-$[Fe^{III}(N_3)_2cyc]^+$ features two potentially photo-labile azide ligands. Azide ligands in general show an intense antisymmetric stretching vibration ($\nu_{as}(N_3)$) in the IR-spectra, as discussed in Chapter 4.5.2. These modes are therefore a good IR-probe for the structure of complexes that feature azide ligands. To evaluate if only one, or possibly both azide ligands in the $[Fe^{III}(N_3)_2cyc]^+$ complex are photolyzed, low temperature IR-measurements and photolysis experiments were performed.

Samples were prepared as KBr disks from approximately 200 mg of dry KBr and 2 mg of the complex under inert atmosphere in the glove box. The powder was transferred in the pressing tool and pressed until a transparent sample disk was obtained. The disk was directly transferred in a high vacuum cell which was cooled with helium down to 8 K. The windows of the vacuum cell allow measurement of IR-spectra and the photolysis of the sample with visible light. For the photolysis, the same LED lamp with a dominant wavelength of 470 nm was used as for the photolysis of EPR-samples (see Chapter 5.4.1) and a similar wavelength (419 nm) has been used in the photolysis of Mössbauer samples previously.[29] IR-spectra were recorded before, after 60 min photolysis and after 120 min photolysis (see Figure 5.1). The spectrum recorded before the photolysis (black trace in Figure 5.1) is identical to the one recorded at room temperature (Figure 4.18).

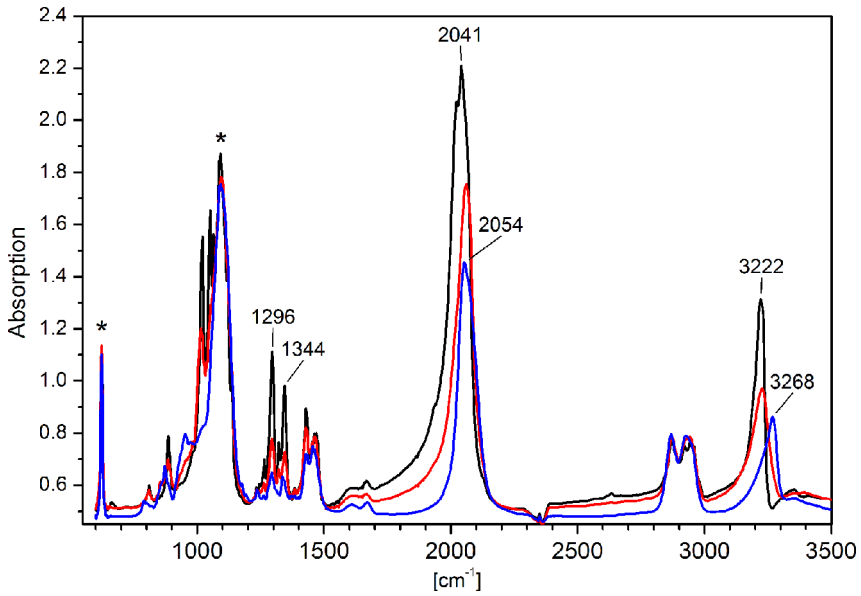

Figure 5.1: Low temperature IR spectrum of the $[Fe^{III}(N_3)_2cyc]ClO_4$ complex before (black) and after irradiation with 470nm light at 8K for 60 min (red) and for 120 min (blue).

The most pronounced feature is the antisymmetric azide stretching vibration at 2041 cm^{-1}. The vibration at 3222 cm^{-1} can be assigned to the N-H vibrations and the symmetric azide stretching vibration is expected in the region around 1320 cm^{-1}. Possibly the peaks at 1296 cm^{-1} and/or 1344 cm^{-1} result from the symmetric stretching vibration of the azide ligand, peaks at 1294 cm^{-1} and 1342cm^{-1} have been also observed in the room temperature IR-spectra (Chapter 4.5.2, page 53). However, for the symmetric complex *trans*-$[Fe^{III}(N_3)_2cyc]^+$ only one IR-active symmetric stretching mode for the azide ligands is expected (see discussion in Chapter 4.5.2).

During the photolysis the $\nu_{as}(N_3)$ mode loses intensity and is shifted from 2041 cm^{-1} to 2054 cm^{-1}. The loss of intensity in the region around ~1320 cm^{-1} can be attributed to the symmetric stretching vibration. Interestingly, both bands at 1296 cm^{-1} and 1344 cm^{-1} nearly vanish completely. This indicates that both signals are related to the azide ligands and possibly they result from different isomers as discussed in Chapter 4.5.2. The shift of the N-H vibrations from 3222 cm^{-1} to 3268 cm^{-1} can be explained by the large influence of the metal center to which the amino groups are directly bond. A shift to higher energy shows that the N-H bond is weakened upon oxidation of the iron center from iron(III) to Iron(V).

It was reported recently from time-resolved IR-measurements in solution, that the azide vibration is shifted about 20 cm^{-1} from 2041 cm^{-1} to 2061 cm^{-1} upon formation of the nitrido-iron(V) complex $[Fe^{V}(N)(N_3)cyc]^{+}$ from the parent iron(III) complex $[Fe^{III}(N_3)_2cyc]^{+}$.[54] Considering the significantly different sample preparations (solid sample at 8K vs. solution at room temperature) this is in good agreement with the results presented here.

Reductive elimination of an azide ligand might be also conceivable, however, in all studies the photolysis of solid samples with visible light resulted in the nitrido-iron(V) moiety.[29] Further, an azide radical should appear in the IR-spectrum around 1660 cm^{-1} (see Chapter 4.5.3 and Ref.[218]), which is not the case here. The elimination of an azide anion can be ruled out, since this should in a $\nu_{as}(N_3)$ band for the azide anion in the 2006 cm^{-1} region, as shown in Figure 4.35 from solution measurements.

DFT calculations were performed to supports the band assignment (BP86/def2-TZVP/RI, modes scaled by 0.9914). The antisymmetric stretching vibration of the bis-azide $[Fe^{III}(N_3)_2cyc]^{+}$ is calculated to appear at 2053 cm^{-1}. For the $[Fe^{V}(N)(N_3)cyc]^{+}$ complex the spin state is still under dispute, and initially a quartet state was assumed.[29] Therefore, vibrations were calculated for both spin states. For the antisymmetric stretching vibration of the remaining azide ligand in the complex $[Fe^{V}(N)(N_3)cyc]^{+}$ in the doublet state, an upshift about 25 cm^{-1} from 2053 cm^{-1} to 2078 cm^{-1} is calculated. For the quartet state a downshift about 14 cm^{-1} to 2039 cm^{-1} is calculated, when compared with the bis-azido iron(III) complex (see Table 5.2). For the doublet state, this is in good agreement with the experimental finding of a 13 cm^{-1} shift upon formation of the nitrido-iron(V) species. For the quartet state, the calculated down shift of the antisymmetric stretching vibration is in contradiction to the experimental finding.

Table 5.2: Experimental and calculated $\nu_{as}(N_3)$ modes for $[Fe^{III}(N_3)_2cyc]^{+}$ and $[Fe^{V}(N)(N_3)cyc]^{+}$.

	$\nu_{as}(N_3)$ exp [cm^{-1}]	*S*	$\nu_{as}(N_3)$ calc [cm^{-1}]
$[Fe^{III}(N_3)_2cyc]^{+}$	2041	1/2	2053
$[Fe^{V}(N)(N_3)cyc]^{+}$	2054 / 2061[a]	1/2	2078
		3/2	2039

a: The $\nu_{as}(N_3)$ mode was reported to be 2061 cm^{-1} at room temperature in solution in Ref.[54]

This leads to the conclusion, that the formed complex is best described as $[Fe^{V}(N)(N_3)cyc]^{+}$, with an azide ligand still bound to iron. The results further provide strong evidence, that the formed nitrido-iron(V) complex shows a doublet ground state. Mössbauer parameters will be calculated in the following chapter which will support the revised *S*=1/2 ground state assignment.

5.3. Mössbauer Parameter Calculations and the Spin-State of the Complex $[Fe^{V}(N)(N_3)cyc]^{+}$

The first non-heme nitrido-iron(V) complex was obtained by photolysis of the *trans*-$[Fe^{III}(N_3)_2cyc]ClO_4$ complex. From Mössbauer measurements with applied magnetic field it was concluded, that the formed $[Fe^{V}(N)(N_3)cyc]ClO_4$ complex possesses a quartet state (S=3/2)[29] and the same spin state was initially assumed for the complex $[Fe^{V}(N)cyc\text{-}ac]^{+}$ only few years later.[43] However, magnetic measurements, Mössbauer spectroscopy and DFT-calculations for the complex $[Fe^{V}(N)cyc\text{-}ac]^{+}$ led to a revised S=1/2 ground state assignment in 2005.[41] This study demonstrated that Mössbauer parameters for different spin states can be calculated accurately by DFT, and comparison with experimental results allows to deduce the correct spin state.

Mössbauer parameters calculated here for the $[Fe^{V}(N)(N_3)cyc]^{+}$ complex in the doublet and quartet state are provided in Table 5.3. Calculated Mössbauer parameters for the parent azido-iron(III) complex were already provided in Chapter 4.1, page 39.

Table 5.3: Experimental[a] and calculated Mössbauer parameters for iron(V) complexes derived from $[Fe^{III}(N_3)_2cyc]ClO_4$ for different spin states (B3LYP/def2-TZVP, Fe:CP(PPP)/COSMO).

	S	calculated		
		δ mm s^{-1}	ΔE_Q mm s^{-1}	relative Energy
$[Fe^{V}(N)(N_3)cyc]^{+}$	1/2	-0.10	-1.90	0
	3/2	0.06	-4.22	57 kJ mol^{-1}
Experimental[a]		-0.04	-1.90	

a: From K. Meyer, E. Bill, B. Mienert, T. Weyhermüller, K. Wieghardt, *J.Am.Chem.* **1999**, *121*, 4859-4876.

It is evident from Table 5.3 that the calculated isomer shift (δ) for both spin states is in agreement with the experimental results, within the error range of the calculations.[143-144] Still, slightly better agreement is found for the doublet state. The calculated quadrupole splitting are less ambiguous and better agreement between the calculated and experimental value is found for the doublet state than for the quartet state. The quadrupole splitting calculated for the quartet state is impressively large; for a pseudo octahedral complex with half-filled t_{2g} shell a very small value would be expected.[139] This shows the large influence of the strong nitrido-ligand that causes strong anisotropy in the electric field gradient.

The doublet state is further calculated to be 57 kJ mol^{-1} lower in energy than the quartet state (Table 5.3). Therefore, it is concluded, that the investigated species $[Fe^{V}(N)(N_3)cyc]^{+}$ exhibits a doublet state, and not as initially assumed, a quartet state.[29] This is completely consistent with the assumptions made based on low-temperature IR measurements and calculations discussed in the antecedent Chapter 5.2.

The electronic structure of the nitrido-iron(V)-complex will be discussed in detail in Chapter 5.5.

5.4. EPR Spectroscopy on Iron(V) Complexes and their Iron(III) Precursors

Due to the paramagnetic nature of nitrido-iron(V) and their parent azido-iron(III) complexes, investigations by EPR-spectroscopy are eligible. EPR measurements on the tetragonal nitrido-iron(V) complexes will provide new insight in their spectroscopic properties, since these species have not been investigated by EPR-spectroscopy before.[3]

The EPR-spectra of the azido-iron(III) complexes $[Fe^{III}(N_3)cyc\text{-}ac]PF_6$,[43] $[Fe^{III}(N_3)_2cyc]ClO_4$,[29] $[Fe^{III}(N_3)TMC\text{-}ac]PF_6$[48] and $[Fe^{III}(N_3)TPP]$[245] were reported in the literature before. These iron(III) complexes have been further characterized by various other spectroscopic methods that are EPR-, Mössbauer-, UV-*vis*- and IR-spectroscopy and their X-ray structures were determined. Further results from spectroscopy and calculations were presented in Chapter 4.

EPR-data for iron(V) complexes only exist for the pseudo tetrahedral nitrido-iron(V) complex $[Fe^{V}(N)(^{t}BuIm)_3BPh]^{+}$[35,247] and the tetragonal oxo-iron(V) complexes $[Fe^{V}(O)TAML]^{-}$ [76] and $[Fe^{V}(O)(TMC)(NC(O)Me)]^{+}$.[77]

EPR-Sample preparation

The sample preparation turned out to be very crucial, since different ways of preparing the sample yields spectra of significantly different quality. By using acetonitrile as solvent (1 mmol L^{-1} concentration), only a broad signal was obtained for the iron(III) starting compounds $[Fe^{III}(N_3)cyc\text{-}ac]PF_6$ and $[Fe^{III}(N_3)_2cyc]ClO_4$, which makes it difficult to compare their spectra with those obtained after photolysis. Adding a large excess of inert salt (100 mmol L^{-1} Bu_4NClO_4) results in a better resolution, but signals for two very similar species (possibly different conformations) were obtained. A mixture of 1:10 methanol:acetonitrile resulted in spectra with three very well resolved g-values. Further improvement, especially an increase in intensity, was obtained by a 1:10 solvent mixture of methanol:butyronitrile.

Samples of the complex $[Fe^{III}(N_3)TMC\text{-}ac]PF_6$ were prepared from 1 mmol L^{-1} solutions in 1:5 methanol:butyronitrile. Samples of the complex $[Fe^{III}(N_3)TPP]$ were prepared from 1 mmol L^{-1} solutions in 1:9 DCM:toluene.

Quartz glass EPR tubes were used, filled in a glove box under inert argon atmosphere with ~0.2 mL of the sample solution and melt-sealed. Samples were photolyzed with an LED lamp that exhibit a dominant wave length at 470 nm, the same light source was used to photolyze UV-*vis*- (Chapter 4.4), Mössbauer (Chapter 4.6) and IR-samples (Chapter 5.2).

Continuous wave (cw) X-Band EPR spectra were recorded on a Bruker E500 ELEXSYS EPR spectrometer equipped with an Oxford flow-cryostat CF 935.

[3] EPR-data was presented in Ref.[242] that was assumed to result from the species $[Fe^{V}(N)(N_3)cyc]ClO_4$. However, the low quality of the data was already noted in this work. In the following chapters it will be shown that the signal observed in this work did not result from the complex $[Fe^{V}(N)(N_3)cyc]ClO_4$.

5.4.1. The Complexes $[Fe^{III}(N_3)cyc\text{-}ac]PF_6$ / $[Fe^{V}(N)cyc\text{-}ac]PF_6$ and $[Fe^{III}(N_3)_2cyc]ClO_4$ / $[Fe^{V}(N)(N_3)cyc]ClO_4$

Well resolved rhombic EPR-spectra for the complexes $[Fe^{III}(N_3)cyc\text{-}ac]PF_6$ and $[Fe^{III}(N_3)_2cyc]ClO_4$ were obtained that show typical low-spin iron(III) g-values; one smaller than g_e (the g-value of a free electron, g_e=2.0023) and two g-values larger than g_e (see Figure 5.2 and Figure 5.5). Spectra simulation yielded the g-values g_1 = 1.81, g_2 = 2.29 and g_3 = 2.60 for $[Fe^{III}(N_3)cyc\text{-}ac]PF_6$ and g_1 = 1.85, g_2 = 2.31 and g_3 = 2.54 for $[Fe^{III}(N_3)_2cyc]ClO_4$ (see Figure 5.3 and Figure 5.6). These g-values are in very good agreement with those calculated by CASSCF/NEVPT2 with deviations below ~0.1 (see Chapter 4, Table 4.3 page 41) and the experimental ones reported previously.[29,43]

After measuring the initial EPR-spectrum of the iron(III) complexes, the samples were transferred into a finger dewar with liquid nitrogen, keeping the sample frozen at all times. Each sample was photolyzed with 470 nm light at 80 K for 30 minutes. In Chapter 4.6.1 it was shown for the complex $[Fe^{III}(N_3)cyc\text{-}ac]PF_6$ and in the literature for both complexes previously,[29,43] that these photolysis conditions yield nitrido-iron(V) complexes. EPR-measurements after photolysis show, that the initial signals completely vanished and a new and broad signal evolved at higher magnetic field (see Figure 5.2 and Figure 5.5).

Given that the identical samples were used for measurements before and after photolysis, the intensity of the samples from double integration can be compared. However, the accuracy of this method is limited, but a roughly quantitative estimate can be made to verify that the new species is the main product and not an impurity or side product. Double integration reveals that the sample of the iron(V) species $[Fe^{V}(N)cyc\text{-}ac]^+$ possesses 85% of the intensity that the parent iron(III) sample has shown prior photolysis. For the iron(V) sample of the complex $[Fe^{V}(N)(N_3)cyc]ClO_4$ obtained by photolysis of $[Fe^{III}(N_3)_2cyc]ClO_4$, a remaining intensity of 119% was calculated. This clearly shows the limitations of the method, but it still indicates that the lower height of the signals in both photolyzed samples results from broadening and not a loss of total intensity by formation of EPR-silent species (e.g. Fe^{II} low-spin). Hence, most (if not all) of the iron(III) species is converted into nitrido-iron(V) complexes. Accordingly, Mössbauer measurements under comparable conditions have shown, that only iron(V) is formed by photolyzing frozen solution samples of the parent azido-iron(III) complex (see literature[29,41,43] or Mössbauer measurements on $[Fe^{V}(N)cyc\text{-}ac]^+$ in Figure 4.30, page 84).

The new spectra obtained by photolysis are nearly axial, only with a slight rhombic distortion. They were simulated with the g-values g_1 = 1.036, g_2 = 1.629 and g_3 = 1.746 for $[Fe^{V}(N)cyc\text{-}ac]^+$ and g_1 = 0.985, g_2 = 1.626 and g_3 = 1.748 for $[Fe^{V}(N)(N_3)cyc]^+$, as shown in Figure 5.4 and Figure 5.7, respectively.

The sealed samples were allowed to thaw and immediately frozen again, after they were liquid. In EPR-measurements performed after this procedure, no signal was detected anymore. This is in line with the results that will be discussed in Chapter 5.8, where it will be shown that in fluid solution the nitrido-iron(V) species immediately form EPR-silent low-spin iron(II) complexes.

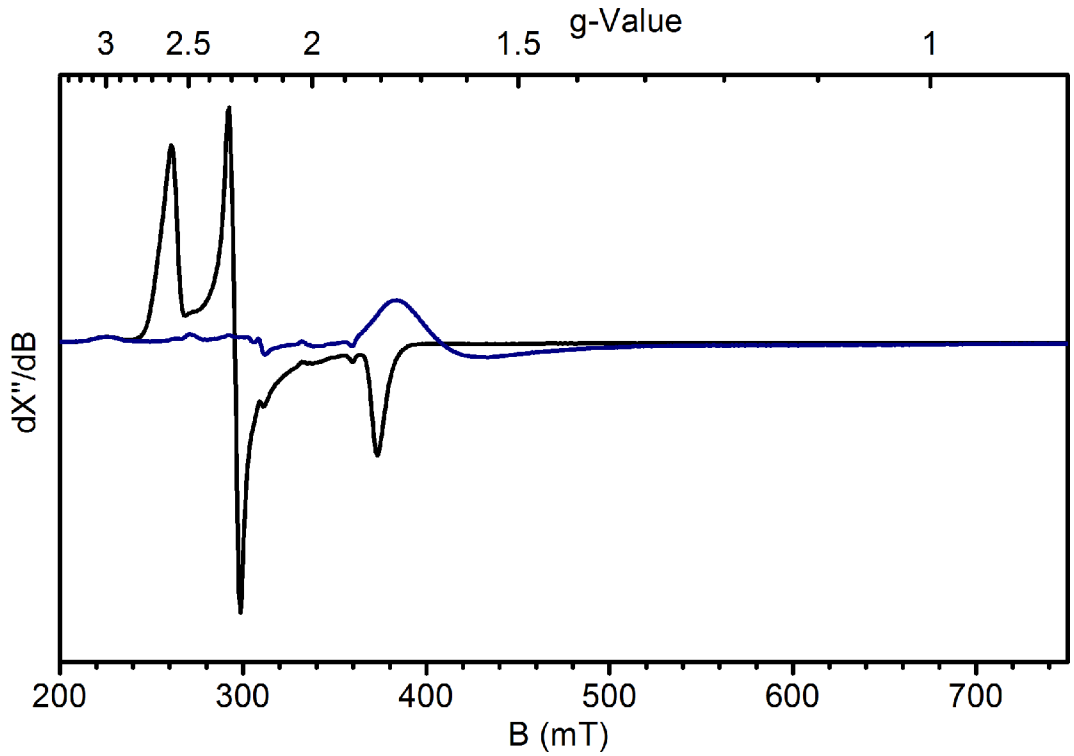

Figure 5.2: EPR spectrum of the complex $[Fe^{III}(N_3)cyc\text{-}ac]PF_6$ before (black) and after (blue) photolysis. X-Band measurements at 10 K, 10 mW, 15 G, 1 mmol L^{-1} in 1:10 MeOH:PrCN

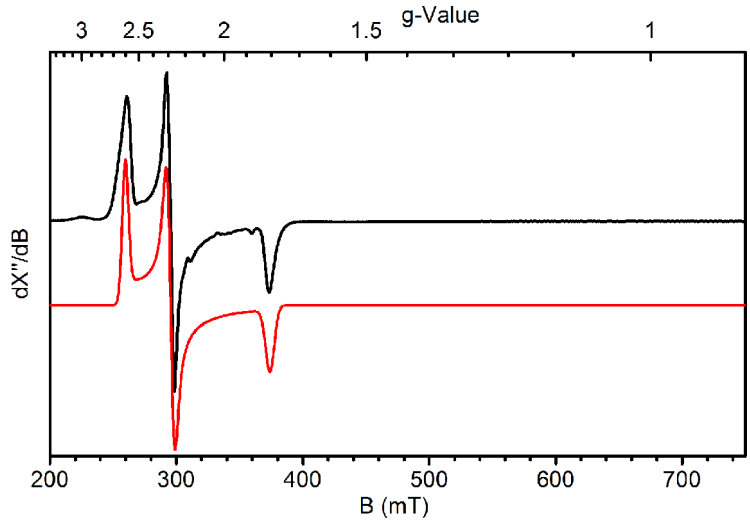

Figure 5.3: Experimental (black) and simulated (red) EPR-spectrum of the complex $[Fe^{III}(N_3)cyc\text{-}ac]PF_6$.

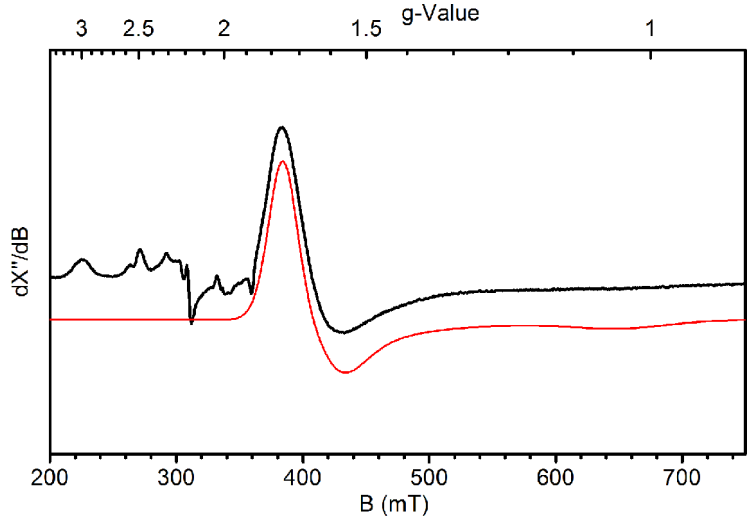

Figure 5.4: Experimental (black) and simulated (red) EPR-spectrum of the complex $[Fe^{V}(N)cyc\text{-}ac]PF_6$, obtained by photolysis of $[Fe^{III}(N_3)cyc\text{-}ac]PF_6$ (y-axis scaled up).

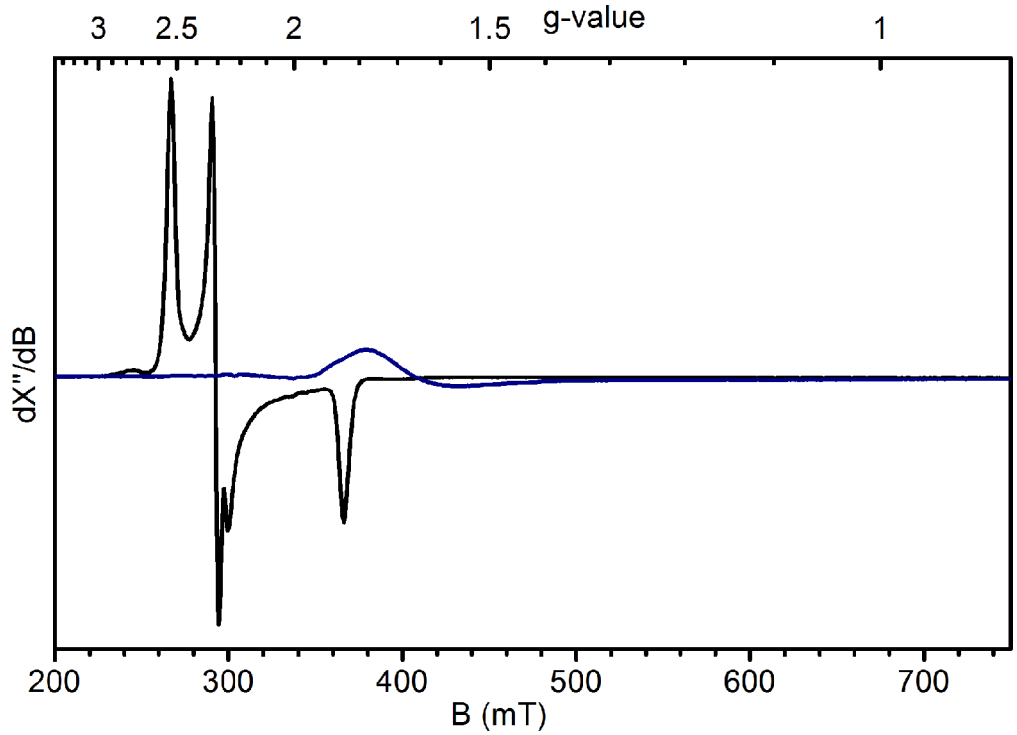

Figure 5.5: EPR spectrum of the complex $[Fe^{III}(N_3)_2cyc]ClO_4$ before (black) and after (blue) photolysis. X-Band measurements at 10 K, 10 mW, 15 G, 1 mmol L^{-1} in 1:10 MeOH:PrCN

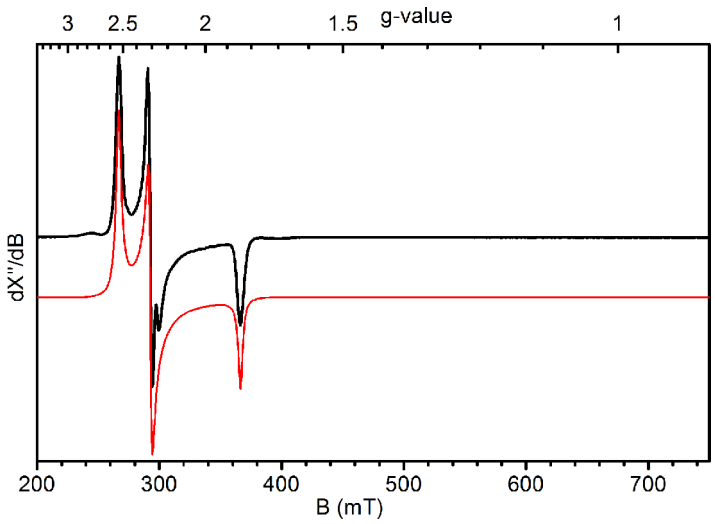

Figure 5.6: Experimental (black) and simulated (red) EPR-spectrum of the complex $[Fe^{III}(N_3)_2cyc]ClO_4$.

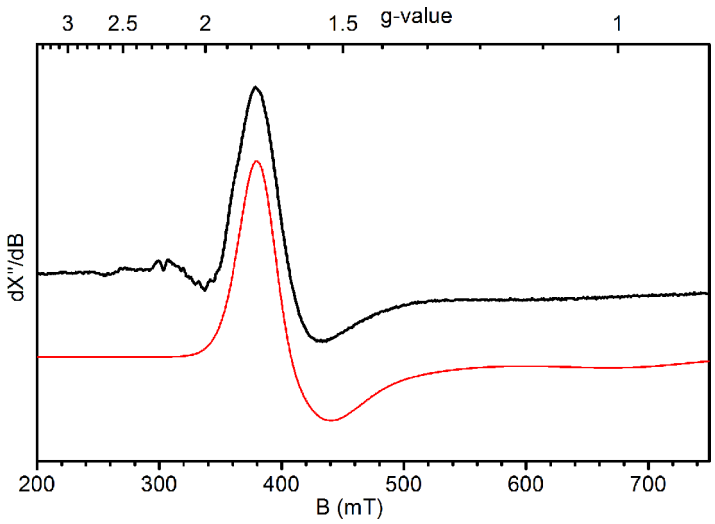

Figure 5.7: Experimental (black) and simulated (red) EPR-spectrum of the complex $[Fe^{V}(N)(N_3)cyc]ClO_4$ obtained by photolysis of $[Fe^{III}(N_3)_2cyc]ClO_4$ (y-axis scaled up).

5.4.2. The Complexes $[Fe^{III}(N_3)TMC\text{-}ac]PF_6$ and $[Fe^{V}(N)TMC\text{-}ac]PF_6$

One more azido iron(III) complex that was used for photolysis experiments previously is the complex $[Fe^{III}(N_3)TMC\text{-}ac]PF_6$.[47] It also obeys a cyclam derived ligand, but the amine groups were methylated. Earlier studies have revealed that due to steric reasons the TMC-ac ligand causes a weaker ligand field than its non-methylated analogue in the $[Fe^{III}(N_3)cyc\text{-}ac]PF_6$ complex.[48] The EPR-spectrum for the complex $[Fe^{III}(N_3)TMC\text{-}ac]PF_6$ shows several peaks that can be explained by the presence of high- and low-spin species (see Figure 5.9). This was discussed in detail in the literature before and combined with magnetic measurements it was shown, that the complex undergoes a (incomplete) spin crossover at low temperature.[42,48] Hence, the high- and low-spin species in the EPR-spectrum presumably belongs to the same species (elemental analysis and mass spectrometry revealed high purity of the sample). After measuring the EPR-spectrum of the iron(III) starting material the sample was photolyzed for 4 hours at 80 K with 470 nm light.

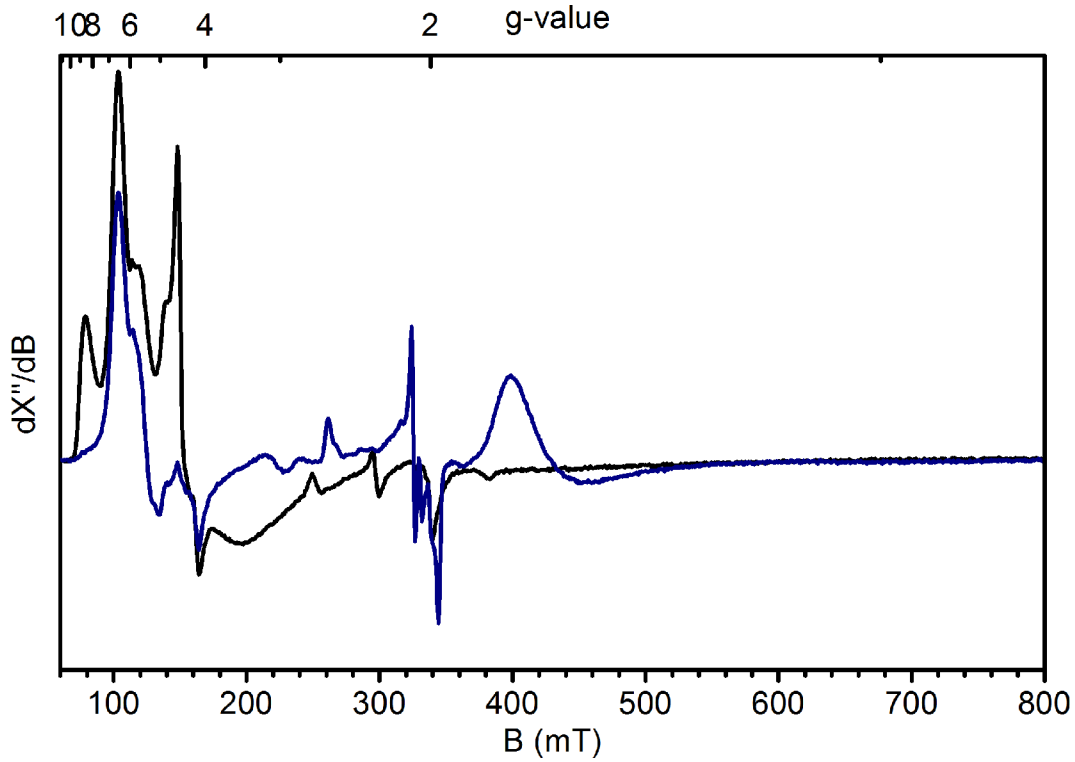

Figure 5.8: EPR spectrum of complex $[Fe^{III}(N_3)TMC\text{-}ac]PF_6$ before (black) and after (blue) photolysis. X-Band measurements at 10 K, 1 mW, 20 G, 1 mmol L^{-1} in 1:5 MeOH:PrCN

Significant changes can be observed in the EPR-spectrum after photolysis (see Figure 5.8). The intensity of the iron(III) species decreases, a minor new species (probably low-spin iron(III)) is formed, and a dominant new signal evolved at higher magnetic field (see Figure 5.8). The line shape of the new feature is very similar to the EPR-spectra obtained for the nitrido-iron(V) complexes $[Fe^{V}(N)cyc\text{-}ac]PF_6$ and $[Fe^{V}(N)(N_3)cyc]ClO_4$. Simulation of the spectrum (see Figure 5.9) results in g-values $g_1 = 0.919$, $g_2 = 1.547$ and $g_3 = 1.677$, very similar to the aforementioned complexes $[Fe^{V}(N)cyc\text{-}ac]^+$ and $[Fe^{V}(N)(N_3)cyc]^+$ (Chapter 5.4.1). It is concluded therefore, that also the complex $[Fe^{III}(N_3)TMC\text{-}ac]PF_6$ undergoes, at least partially, an oxidative N_2-elimination and forms the nitrido-iron(V) complex $[Fe^{V}(N)TMC\text{-}ac]PF_6$. It cannot be shown if iron(II) is also formed by the present EPR measurements. For the detection of an high-spin iron(II) species measurements in parallel-mode would be necessary and low-spin iron(II) species are EPR-silent.

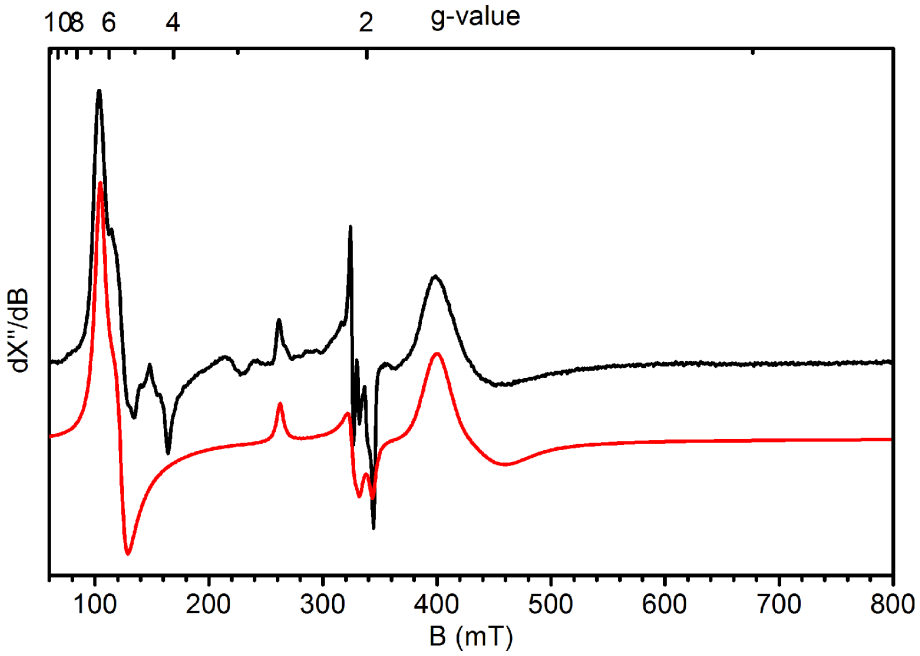

Figure 5.9: Experimental (black) and simulated (red) EPR-spectrum of $[Fe^{V}(N)TMC\text{-}ac]PF_6$ obtained by photolysis of $[Fe^{III}(N_3)TMC\text{-}ac]PF_6$ (y-axis scaled up).

As mentioned before, the nitrido-iron(V) complexes $[Fe^{V}(N)cyc\text{-}ac]^+$ and $[Fe^{V}(N)(N_3)cyc]^+$ immediately decay upon allowing the samples to thaw (see detailed discussion in Chapter 5.8). In these complexes the nitrido ligand is easily accessible for reactions, since it is not shielded by the ligand. In contrast to the $[Fe^{V}(N)cyc\text{-}ac]^+$ complex, the $[Fe^{V}(N)TMC\text{-}ac]PF_6$ compound features methyl-groups that might introduce some degree of sterical protection for the nitride. By storing a EPR-sample that shows the iron(V) signal at -80° C where the solvent (1:5 MeOH:PrCN) is liquid, its stability was probed. Indeed, after 13 h at -80°C the nitrido-iron(V) signal is still present. It does not even vanish when the same sample is stored for further 18 h at -24° C (see Figure 5.10). Hence, the $[Fe^{V}(N)TMC\text{-}ac]^+$ species is stable in liquid solution at low temperature.

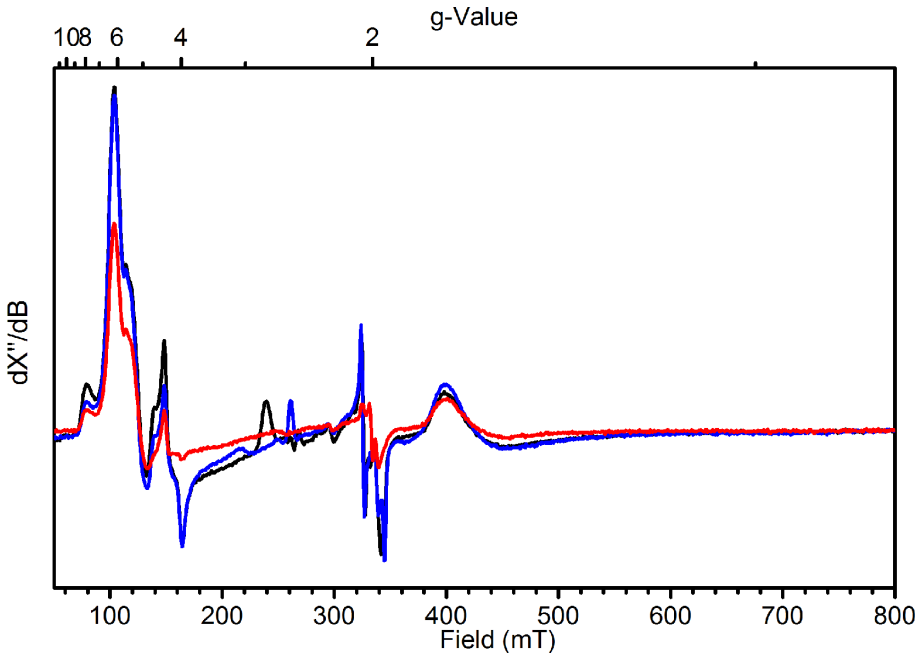

Figure 5.10: EPR spectrum of $[Fe^{V}(N)TMC\text{-}ac]PF_6$ obtained by photolysis (black) and after storing for 13 h at -80° C (red) and 18h at -24° C (blue) X-Band at 10 K, 1 mW, 20 G, 1 mmol L^{-1} in 1:5 MeOH:PrCN

A complete photolytic conversion of the azido-iron(III) complex $[Fe^{III}(N_3)TMC\text{-}ac]^+$ into the corresponding nitrido-iron(V) species in frozen solution was not successful. Given that the complex $[Fe^{V}(N)TMC\text{-}ac]^+$ is stable in liquid solution, the question arises whether it is possible to photolyze the parent azido-iron(III) complex in liquid solution to obtain the nitrido-iron(V) species. This experiment is very interesting with respect to the photolysis conditions and how these affect the selectivity of light induced reactions (formation of iron(II) vs. iron(V)). This is a matter of discussion for the $[Fe^{III}(N_3)cyc\text{-}ac]PF_6$ complex, where different products are observed depending on the photolysis conditions (frozen solution vs. liquid solution; formation of iron(II) vs. formation of iron(V), see discussion in Chapter 4.6 and Chapter 4.9).[43,54,217-218]

An identical sample was prepared and result in the same Fe(III) EPR-spectrum as shown before (see Figure 5.11). The sample was then placed in a finger dewar with a mixture of methanol and liquid nitrogen, which results in a temperature of approximately -95°C. This is above the melting point of the butyronitrile (m.p. -112 °C) - methanol (m.p. -97°C) solvent mixture (ratio 10:1) which was used as solvent. The sample was then photolyzed with 470 nm light for 2 minutes, after which already a significant bleaching of the initially yellow sample was observed. The EPR-spectrum recorded thereafter revealed a loss of intensity, especially for the high-spin species in the initial spectrum, while no nitrido-iron(V) signal evolved (Figure 5.11). The photolysis was continued for 5 minutes but no further significant changes were observed in the spectrum. Interestingly, the changes in the EPR-spectra in the low-field region (50-150 mT) are nearly identical to those observed when the sample was photolyzed in frozen solution. However, formation of iron(V) was not observed.

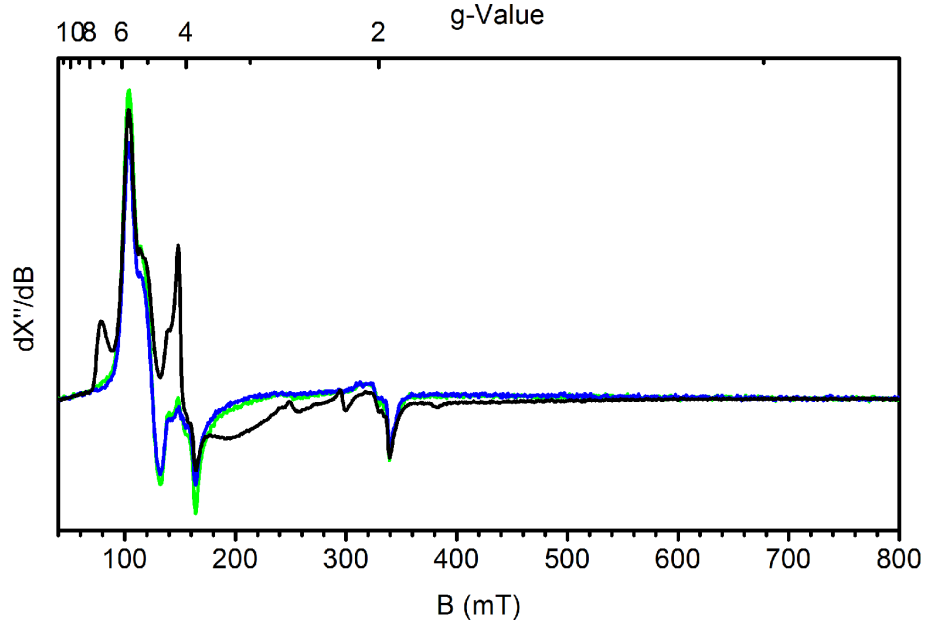

Figure 5.11: EPR spectrum of $[Fe^{III}(N_3)TMC\text{-}ac]PF_6$ (black), after 2 min 470 nm photolysis at -95° C (green) and further 5 min photolysis under the same conditions (blue). X-Band measurements at 10K/0.2mW/20G.

It can, therefore, be concluded that the state of aggregation is crucial for the photolysis of the $[Fe^{III}(N_3)TMC\text{-}ac]PF_6$ complex. Photolyzing a frozen sample at 80 K yields the nitrido-iron(V) species, while photolysis at -95°C in liquid solution does not result in the nitrido-iron(V) complex. Since the nitrido-iron(V) complex $[Fe^{V}(N)TMC\text{-}ac]^+$ was shown to be stable in solution at this temperature (and even at higher temperature) it should be detectable in subsequent EPR-measurements if it is formed as the primary photoproduct. The loss of intensity in the spectrum after photolysis can be presumably explained by the formation of an EPR-silent iron(II) species.

5.4.3. The Complexes [$Fe^{III}(N_3)TPP$] and [$Fe^{V}(N)TPP$]

The first nitrido-iron(V) species were reported in 1988 by Nakamoto *et al.*,[40,46] and in Chapter 5.1 it was shown that these complexes exhibit a doublet ground state. However, further spectroscopic characterization beside the resonance Raman measurements are elusive. It was therefore tried here to record EPR-spectra of the [$Fe^{V}(N)TPP$] species formed by photolysis of the parent azido-iron(III) porphyrin complex.

Simulation of the X-band EPR spectrum of the [$Fe^{III}(N_3)TPP$] complex results in g-values g_1=6.00, g_2=5.95 and g_3=2.00, that are typical for porphyrin high-spin iron(III) complexes (see Figure 5.12).[245]

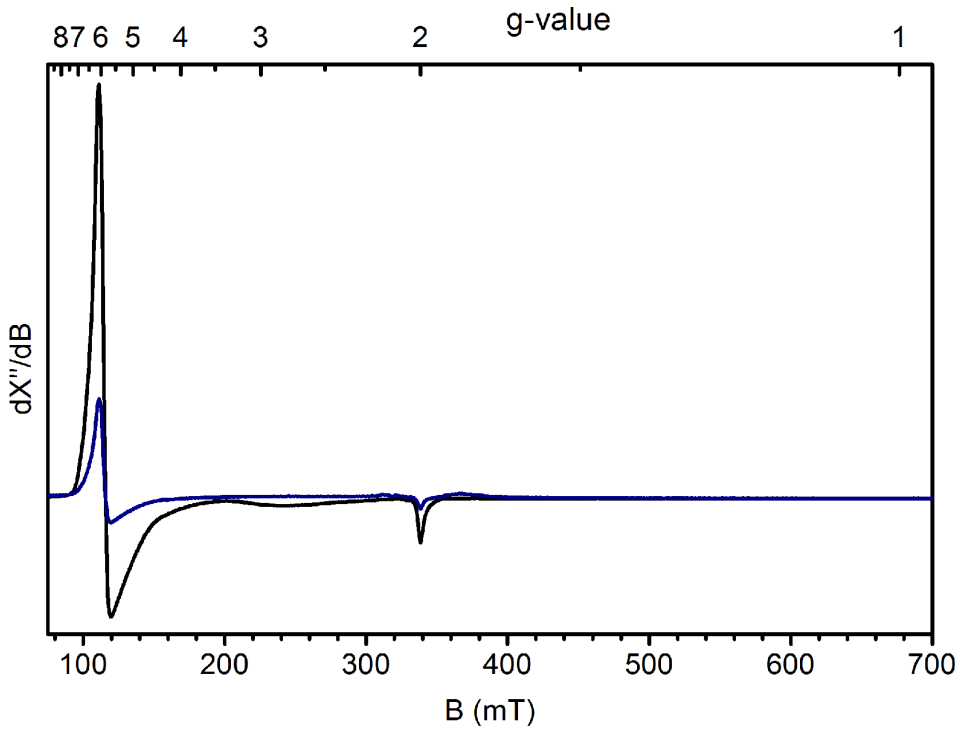

Figure 5.12: EPR spectrum of the complex [$Fe^{III}(N_3)TPP$] before (black) and after (blue) photolysis.X-Band measurements at 10 K, 0.2 mW, 20 G, 1 mmol L^{-1} in 1:9 DCM:Toluene

The EPR-sample was then placed in an Oxford Instruments cryostat with a house designed sample holder and kept at 80K with liquid nitrogen. It was photolyzed for 18 hours with 470 nm light.

EPR-measurements after photolysis show that the iron(III) signal has decreased and a small new feature appeared at higher magnetic field (see blue trace in Figure 5.12). The new feature becomes more obvious in a spectrum measured at 2 mW microwave power (instead of 0.2 mW which was used for the initial measurements on the iron(III) complex in Figure 5.12). The result is shown in Figure 5.13 together with the simulation, which results for the new species in g-values g_3=1.80, g_2=1.54 and the smallest g-value had to be fixed at g_1=1.00, since otherwise a simulation was not possible. The new compound represents 11% of the overall intensity. By numerical integration of the spectrum the absorption shape spectrum is obtained where the feature at higher magnetic fields becomes more obvious (Figure 5.14).

The simulated g-values are again similar to those of the nitrido-iron(V) complexes discussed in Chapter 5.4.1 and Chapter 5.4.2 and the peak shows a similar band shape. Therefore, it is concluded that (even

in low yield) the nitrido-iron(V) complex is formed which was previously only detected in resonance Raman measurements.[40,46] The large g-shift further provides evidence that the nitrido-iron(V) complex is a “real” iron(V) species without oxidized ligand, as it was previously proposed,[40,46].

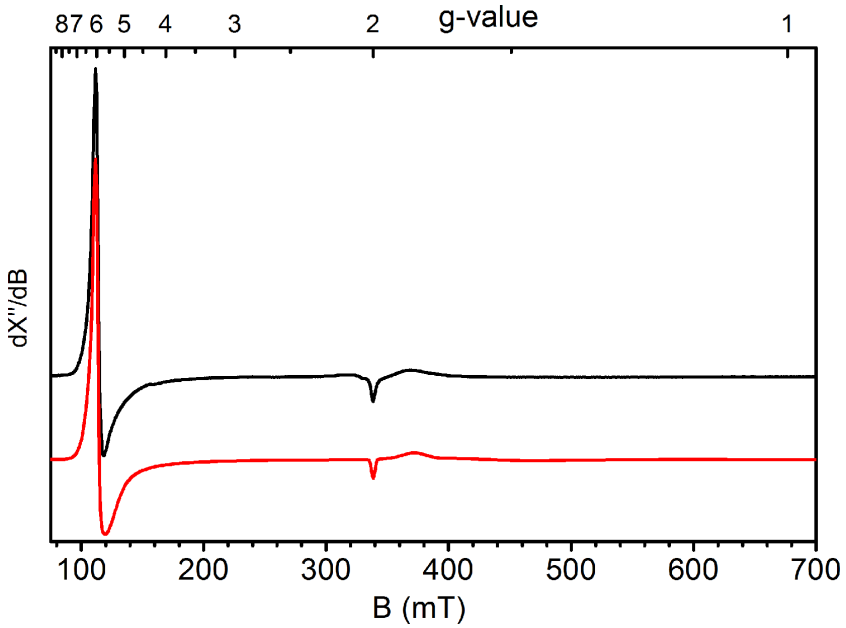

Figure 5.13: Experimental EPR-spectrum of photolyzed [$Fe^{III}(N_3)TPP$] measured at 2mW/20G (black) and simulation (red).

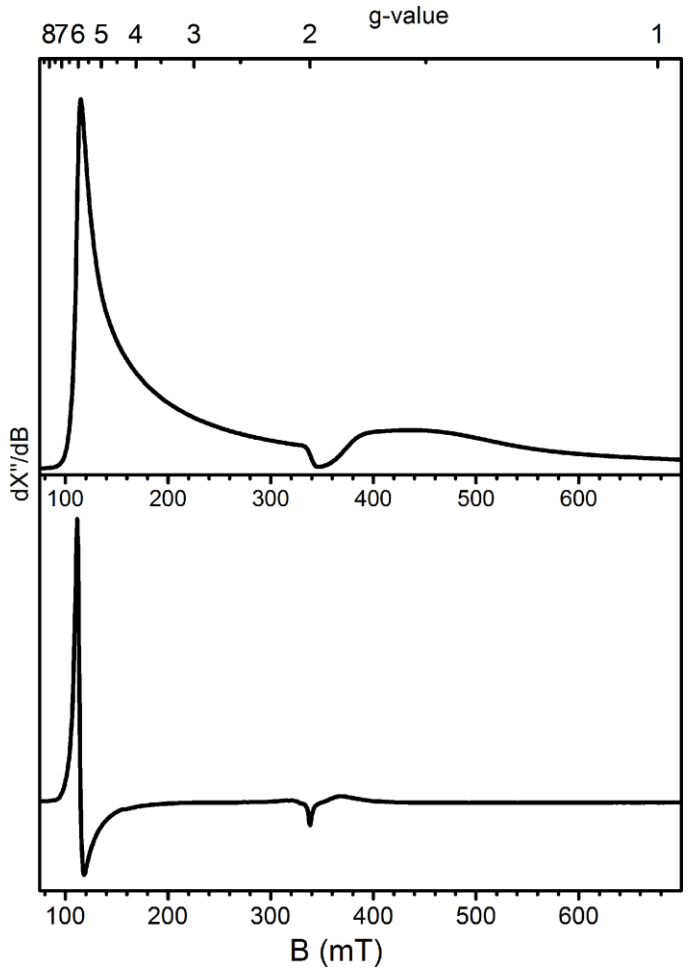

Figure 5.14: Numerical integration for the EPR spectrum of [$Fe^{V}(N)TPP$] measured at 2mW/20G/10K (top) and the measured spectrum (bottom).

5.4.4. Comparison of Nitrido-Iron(V) EPR-Spectra

The spectra presented in Chapter 5.4.1, 5.4.2 and 5.4.3 are the first EPR-spectra of tetragonal nitrido-iron(V) complexes and to the best of our knowledge there are no other low-spin first-row transition metal d^3 complexes in tetragonal coordination reported in the literature so far. A summary of the measured g-values is given in Table 5.4 and a comparison of all four measured iron(V) EPR-spectra is shown in Figure 5.15, zoomed in on the characteristic iron(V) feature.

Table 5.4: g-Values from X-band EPR measurements on nitrido-iron(V) complexes.

	g_1	g_2	g_3
$[Fe^{V}(N)cyc\text{-}ac]^{+}$	1.036	1.629	1.746
$[Fe^{V}(N)(N_3)cyc]^{+}$	0.985	1.626	1.748
$[Fe^{V}(N)TMC\text{-}ac]^{+}$	0.919	1.547	1.677
$[Fe^{V}(N)TPP]$	(1)*	1.539	1.802

* g-value had to be fixed to one for the simulation

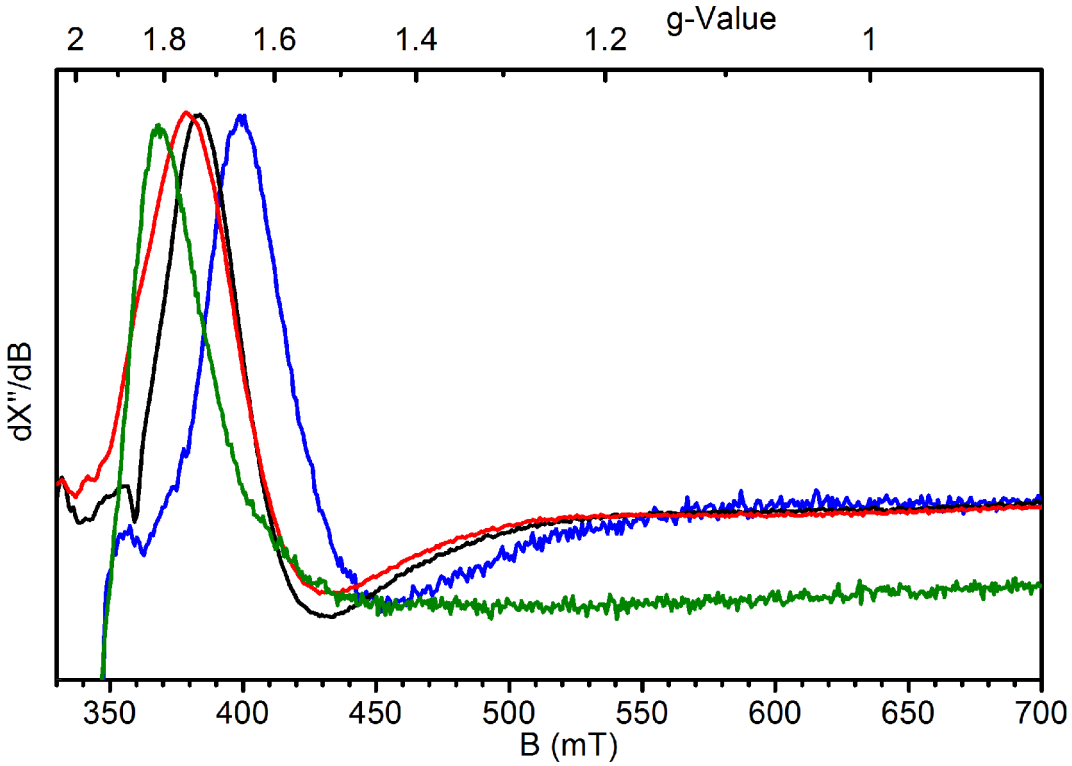

Figure 5.15: $Fe^{V}N$ EPR spectra of $[Fe^{V}(N)TPP]$ (green), $[Fe^{V}N(N_3)cyc]^{+}$ (red), $[Fe^{V}N(cyc\text{-}ac)]^{+}$ (black) and $[Fe^{V}(N)TMC\text{-}ac]^{+}$ (blue).

The plot reveals a very similar band shape for all four complexes. The dominant signal at ~1.7 of the complexes $[Fe^{V}(N)cyc\text{-}ac)]^{+}$ and $[Fe^{V}N(N_3)cyc]^{+}$ are nearly identical, while the signal of the $[Fe^{V}(N)TPP]$ complex is slightly shifted to lower magnetic field and the signal of the $[Fe^{V}(N)TMC\text{-}ac]^{+}$ complex is slightly shifted to higher magnetic field.

The measured g-values will be discussed in detail in Chapter 5.6 in combination with quantum chemical calculations and spin-Hamiltonian equations derived for the g-values.

5.5. Computational Study of Tetragonal Iron(V) Complexes

Density functional theory calculations have been performed on the nitrido-iron(V) complexes $[Fe^{V}(N)cyc\text{-}ac]^{+}$ and $[Fe^{V}(N)POR]$ previously.[41,243] However, for the porphyrin complex only the quartet state was considered which is not the correct ground state, as demonstrated in Chapter 5.4.3. More detailed calculations on a higher level of theory are presented here for these and other nitrido-iron(V) complexes that were investigated by EPR-spectroscopy in Chapter 5.1.

Furthermore, calculations on the oxo-iron(V) complex $[Fe^{V}O(TAML)]^{-}$ are performed that was studied previously by various spectroscopic methods and DFT-calculations.[76] High level CASSCF/NEVPT2 calculations are performed here, that will result in a detailed understanding of the electronic structure and g-values.

Unfortunately, there is no ligand system for which the nitrido- as well as the oxo-iron(V) complex exist. It was therefore not yet possible to study experimentally the differences between a mono-atomic nitrido- and oxo-ligand on iron(V) complexes and the same holds for iron(IV) complexes.[16] Therefore, the hypothetical complex $[Fe^{V}(O)cyc\text{-}ac]^{2+}$ is included in the theoretical study, whose nitrido-analogue $[Fe^{V}(N)cyc\text{-}ac]^{+}$ is also investigated experimentally in the present work.[41,43]

The analysis of the electronic structure presented in this chapter is based on complete active space self-consistent field calculations. DFT calculations on various spectroscopic parameters were already discussed in Chapter 4, 5.1 and 5.3 for iron(II), iron(III) and iron(V) complexes, respectively.

Results from quantum chemical calculations and EPR-spectroscopy (Chapter 5.4) will be brought together in Chapter 5.6. Spin Hamiltonian equations for the g-values are derived that allows a detailed analysis and interpretations of the experimental results.

Calculations were also performed on the tetragonal oxo-iron(V) complex $[Fe^{V}(O)(TMC)(NC(O)CH_3]^{+}$ that was synthesized in the group of Lawrence Que and published in 2012.[77] Since this complex significantly differs from all other tetragonal iron(V) complexes it will be discussed separately in Chapter 5.7.

5.5.1. The Molecular Structure of Tetragonal Iron(V) Complexes

Molecular structures of the iron(V) complexes were optimized with the BP86 functional, a triple zeta def2-TZVP basis-set, the resolution of the identity approximation (RI) and the appropriate auxiliary basis-set. Solvent effects were taken into account by COSMO considering acetonitrile as solvent.

For the nitrido-iron(V) complexes $[Fe^{V}(N)TPP]$,[40,46,209] $[Fe^{V}(N)cyc\text{-}ac]^{+}$[43] and $[Fe^{V}(N)(N_3)cyc]^{+}$[29] initially a triplet ground state (S=3/2) was assumed. This was corrected later for the $[Fe^{V}(N)cyc\text{-}ac]^{+}$ complex, for which a doublet state (S=1/2) was assigned based on magnetic measurements and DFT calculations.[41] For the $[Fe^{V}(N)(N_3)cyc]^{+}$ and $[Fe^{V}(N)TPP]$ complexes it was shown in a combination of previously published spectroscopic data and new DFT calculations that these complexes exhibit a doublet ground state (see Chapter 5.1, 5.2 and 5.3). To get further insight in the spin state energetics, the complexes were optimized by DFT in the doublet- and quartet-state and relative energies were calculated by CASSCF/NEVPT2 on these structures (details of the CASSCF calculations will be discussed in the following chapter). The complex $[Fe^{V}(O)TAML]^{-}$ was not included in the spin state calculations, since its S=1/2 spin state was clearly assigned based on the reported spectroscopic data.[76]

Table 5.5: Selected bond length and angles for iron(V) complexes in the doublet-/quartet state and relative spin state energies calculated by CASSCF/NEVPT2 (optimized at BP86/def2-TZVP/COSMO). X_{ax} is the ligand *trans* to the nitrido-/oxo-ligand and N_{eq} are the nitrogen atoms in the equatorial plane.

	S	$\Delta E_{D\text{-}Q}$	Fe-N/O	Fe-X_{ax}	Fe-N_{eq}				N-Fe-X	N_{eq}-Fe-N_{eq}	
		[kJmol^{-1}]	[Å]	[Å]	[Å]	[Å]	[Å]	[Å]	[°]	[°]	[°]
$[Fe^{V}(N)cyc\text{-}ac]^{+}$	1/2	0	1.597	2.066	2.051	2.035	2.038	2.069	176.51	168.41	174.86
	3/2	+89	1.718	2.071	2.046	2.034	2.032	2.064	178.40	173.40	177.93
$[Fe^{V}(O)cyc\text{-}ac]^{2+}$	1/2	0	1.597	1.902	2.060	2.023	2.041	2.104	173.12	167.68	176.61
	3/2	+83	1.666	1.927	2.061	2.058	2.049	2.071	177.71	172.72	177.18
$[Fe^{V}(N)(N_3)cyc]^{+}$	1/2	0	1.595	2.160	2.050	2.049	2.032	2.025	175.90	173.30	172.05
	3/2	+87	1.718	2.157	2.043	2.040	2.031	2.032	175.33	176.49	176.62
$[Fe^{V}(N)TMC\text{-}ac]^{+}$	1/2	0	1.594	2.054	2.125	2.092	2.115	2.080	173.77	172.69	174.59
	3/2	+52	1.610	2.021	2.261	2.176	2.207	2.151	173.12	171.77	173.79
$[Fe^{V}(N)TPP]$	1/2	0	1.580	-	1.988	2.013	1.989	2.015	-	166.02	157.39
	3/2	+111	1.705	-	1.967	1.974	1.968	1.976		167.88	167.76
$[Fe^{V}(O)TAML]^{-}$	1/2		1.609	-	1.866	1.909	1.861	1.922	-	153.38	141.69

The calculated spin state energies show clear preference for the doublet state in all nitrido-iron(V) complexes. Separation of the doublet and quartet states for the complexes $[Fe^{V}(N)cyc\text{-}ac]^{+}$, $[Fe^{V}(O)cyc\text{-}ac]^{2+}$ and $[Fe^{V}(N)(N_3)cyc]^{+}$ is calculated to be very similar (89 kJ mol^{-1}, 83 kJ mol^{-1} and 87 kJ mol^{-1}, respectively) while it is significantly lower for the $[Fe^{V}(N)TMC\text{-}ac]^{+}$ complex (52 kJ mol^{-1}). The largest energy difference is calculated for the porphyrin complex $[Fe^{V}(N)TPP]$ where the quartet state is 111 kJ mol^{-1} higher in energy than the doublet state.

Interestingly, the oxo-iron and nitrido-iron bond-lengths are very similar for all complexes. For the $[Fe^{V}(N)cyc\text{-}ac]^{+}$ complex the Fe-N distance was previously determined in EXAFS measurements to be 1.61 Å which is in good agreement with the calculations (1.597 Å).[41] The most significant difference

between the analogue iron(V)-complexes $[Fe^{V}(N)cyc\text{-}ac]^{+}$ and $[Fe^{V}(O)cyc\text{-}ac]^{2+}$ is found for the iron-carboxylate oxygen distance, which is much longer in the nitrido-species (2.066 Å vs. 1.902 Å). This reflects the strong trans-influence of the nitrido-group as it was shown previously for smaller model systems.[7] The nitrido-complex $[Fe^{V}(N)(N_3)cyc]^{+}$ that features an azide ligand in *trans*-position to the nitrido group shows a nitrido-iron bond-length that is nearly identical to the nitrido-/oxo-iron bond of the two just discussed species.

The iron(V) complex with tris-methylated cyclam-acetato ligand $[Fe^{V}(N)TMC\text{-}ac]^{+}$ shows slightly longer equatorial metal-ligand bond lengths when compared with the complexes with non-methylated cyclam derived ligands ($[Fe^{V}(N)cyc\text{-}ac]^{+}$ and $[Fe^{V}(O)cyc\text{-}ac]^{2+}$). It has been shown in a previous study that this can be attributed to steric effects of the methyl groups.[48]

In the five-coordinate nitrido-iron(V) porphyrin complex the iron atom is much further located above the equatorial ligand plane than in the non-heme, cyclam based systems. This is seen from the angle between the equatorial nitrogen ligand atom, the iron center and the nitrogen atom in *trans* position. These angles are smaller for the porphyrin complex than for the other tetragonal nitrido-iron(V) complexes (see Table 5.5).

For the $[Fe^{V}(O)TAML]^{-}$ complex that was synthesized in the group of Collins,[76] an iron-oxo bond-distance of 1.609 Å was calculated. This is in excellent agreement with the published EXAFS data (1.60 Å) and previous DFT-calculations (1.60 Å).[76] The bond-distances calculated for iron and the TAML nitrogen-atoms was determined to be 1.87 Å on average in the EXAFS measurements,[76] which is also in good agreement with the calculations performed here (see Table 5.5).

For most complexes, the nitrido-iron or oxo-iron bond-length is longer for the quartet-state than for the doublet state. This can be explained by the occupation of an additional anti-bonding π*-orbital between iron and the nitrido-/oxo-ligand, as will be discussed in detail in the following section.

5.5.2. The Electronic Structure of Tetragonal Iron(V) Complexes

Complete active space self-consistent field (CASSCF) calculations were performed on the DFT optimized structures. The chosen active space consists of all iron 3d-orbitals, the 2p-orbitals of the nitrido/oxo ligand and the bonding combination of the $d_{x^2-y^2}$-orbital with the equatorial lone-pairs of the nitrogen ligand atoms. This results in an active space of 11 electrons in 9 orbitals. State-average CASSCF calculations over 3 roots were performed and on top of this wave function dynamic correlation was taken into account with the NEVPT2 method. Inclusion of dynamic correlation turned out to be crucial in the present systems, since the CASSCF-single point calculations resulted in the wrong ground state for some species. For labeling the orbitals/states C_{2v}-symmetry was assumed and orbitals are shown in increasing energetic order. In certain cases, the relative order of the orbitals differs, e.g. for the $[Fe^{V}(N)cyc\text{-}ac]^{+}$ complex $1a_1$ is the σ_{eq}- and $2a_1$ is the σ_z-orbital, while for $[Fe^{V}(O)cyc\text{-}ac]^{2+}$ $1a_1$ is the σ_z- and $2a_1$ is the σ_{eq}-orbital. To avoid any misconception, simplified σ/π-labels will be used in the following discussion that are also provided in the MO-figures.

A plot of the active space orbitals is given in Figure 5.16 for the complexes $[Fe^{V}(N)cyc\text{-}ac]^{+}$ and $[Fe^{V}(O)cyc\text{-}ac]^{2+}$ and in Figure 5.17 for the complexes $[Fe^{V}(N)(N_3)cyc]^{+}$ and $[Fe^{V}(N)TMC\text{-}ac]^{+}$, together with an outline of the electronic ground state configuration. For all complexes, the qualitative picture is very similar. As expected from simple LFT-considerations, the p_x- and p_y- orbitals of the monoatomic ligands form π-bonding orbitals of b_1- and b_2-symmetry (π_x, π_y) with the d_{xz}- and d_{yz}-orbitals, as well as the corresponding anti-bonding orbitals (π_x^*, π_y^*), respectively. A σ-bond and the corresponding anti-bonding σ*-orbital of a_1-symmetry is formed between the p_z-orbital of the ligand atom and the d_{z^2}-orbital of the metal. The none-bonding metal d_{xy}-orbital (a_2) is doubly occupied and the unpaired electron is located in the anti-bonding π_y^*-orbital ($2b_2$).[4]

[4] The coordinates were chosen in a way, that the d_{yz}-orbital is singly occupied. Of course, rotation of the coordinate system about 90° is possible resulting in a singly occupied d_{xz}-orbital. This would not change anything in the electronic structure or the experimentally observable spectroscopic parameters (e.g. for the g-values only g_{xx} and g_{yy} would be interchanged).

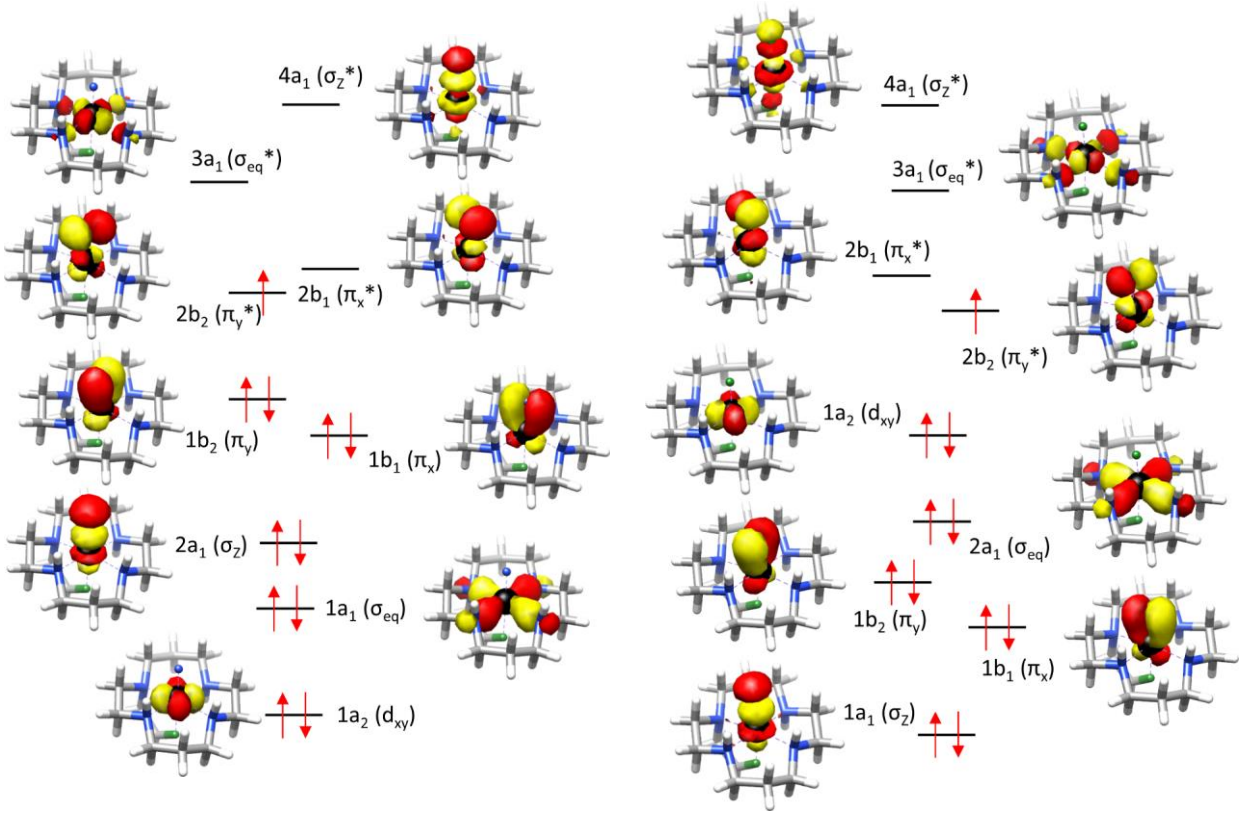

Figure 5.16: Active space orbitals from SA-CASSCF(11,9)/3 roots calculations on $[Fe^{V}(N)cyc\text{-}ac]^{+}$ (left) and $[Fe^{V}(O)cyc\text{-}ac]^{2+}$ (right) with outlined ground state configuration.

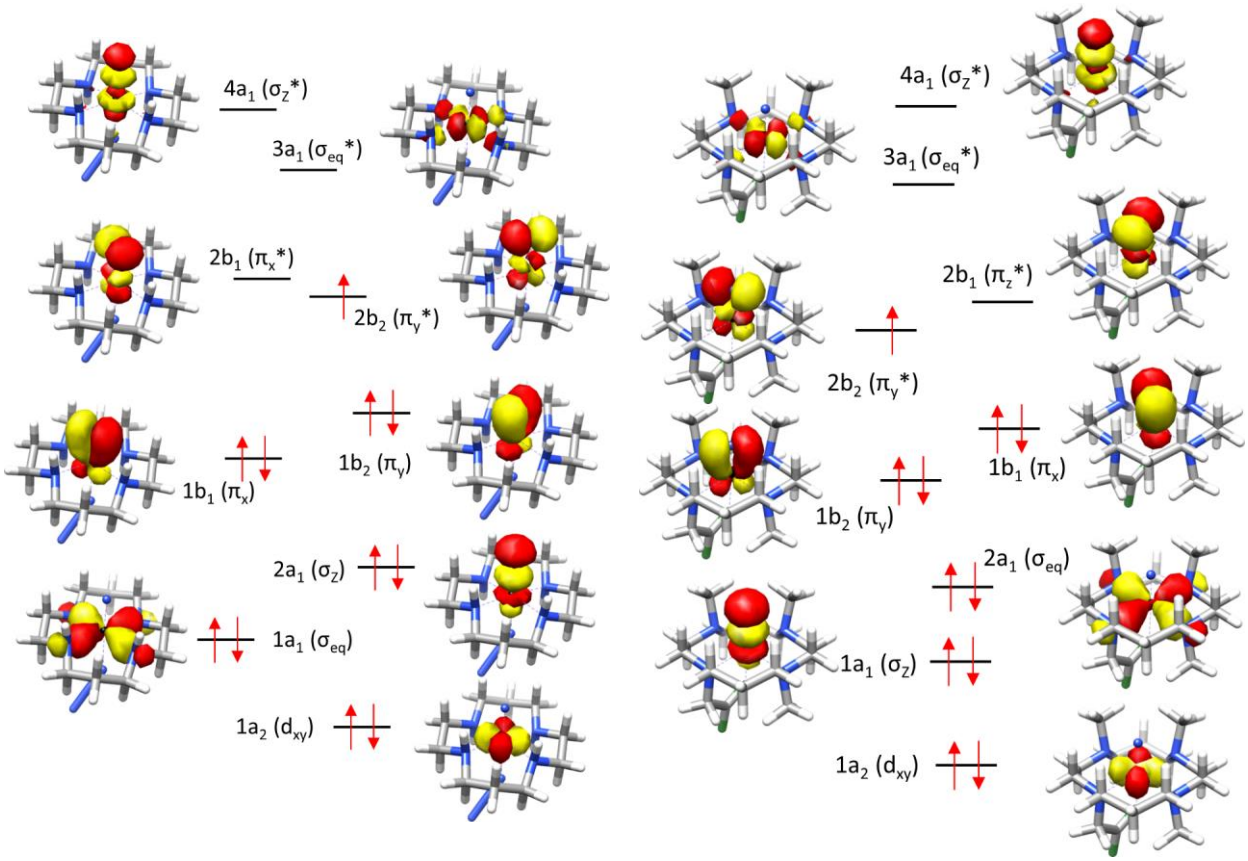

Figure 5.17: Active space orbitals from SA-CASSCF(11,9)/3 roots calculations on $[Fe^{V}(N)(N_3)cyc]^{+}$ (left) and $[Fe^{V}(N)TMC\text{-}ac]^{+}$ (right) with outlined ground state configuration.

Analogous calculations were also performed on the porphyrin complex [Fe^{V}(N)TPP] and the oxo-complex [Fe^{V}(O)TAML]$^{-}$. In Figure 5.18 the active space orbitals of the porphyrin complex are shown. As already mentioned in the previous section (Chapter 5.1, page 114), iron(V)-porphyrin complexes are known to form ligand centered radicals. Oxo-iron complexes, that are formally iron(V), are then better described as iron(IV)-complexes with an oxidized ligand, which results in an unpaired electron centered on the ligand, [Fe^{IV}(O)$POR^{+\bullet}$].[246] However, attempts to calculate the electronic structure by DFT including ligand centered radicals always converged to solutions with a closed shell ligand (see Chapter 5.1). Further, experimental evidence was provided in the initial study by Nakamoto *et al.*[40,46] that the nitrido-iron(V) porphyrin complexes do not undergo ligand oxidation. Therefore, the chosen active space should be sufficient and inclusion of further ligand orbitals is not necessary.

The qualitative electronic structure that can be derived from the molecular orbitals is very similar to the above discussed non-heme iron(V)-complexes. The unpaired electron is located in an anti-bonding π_y*-orbital ($2b_2$) and the non-bonding d_{xy}-orbital ($1a_2$) is doubly occupied (see Figure 5.18).

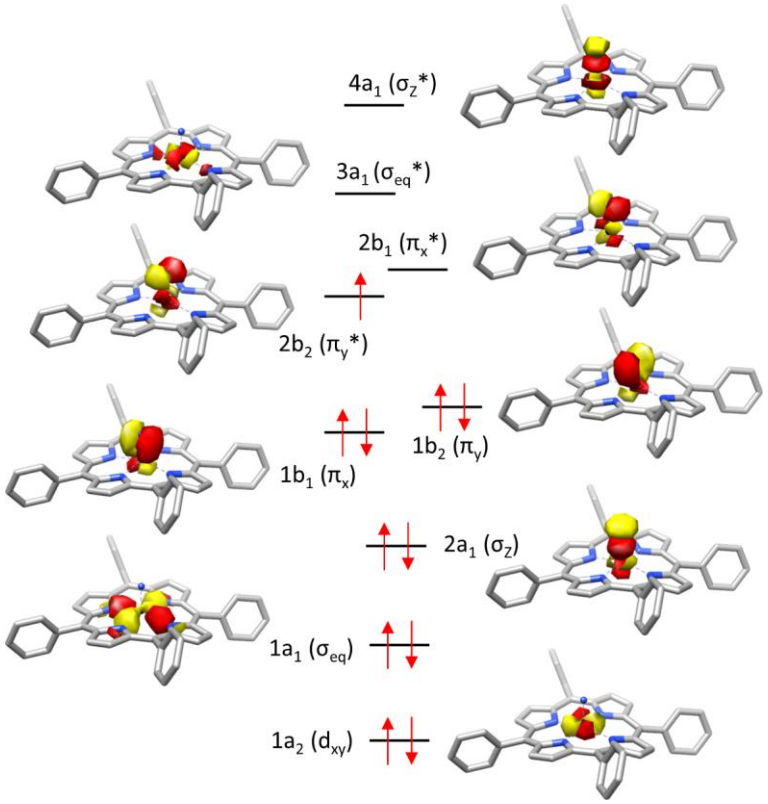

Figure 5.18: Active space orbitals from a CASSCF(11,9) calculation on the [Fe^{V}(N)TPP] complex and outlined ground state electronic configuration. Hydrogen atoms are omitted.

Active space orbitals for the oxo-iron(V) complex [Fe^{V}(O)TAML]$^{-}$ are shown in Figure 5.19 and the resulting qualitative picture is again analog to the above discussed iron(V)-complexes. The unpaired electron is located in the π*-orbital ($2b_2$) while the non-bonding d_{xy}-orbital ($1a_2$) is doubly occupied.

Hence, the calculations reveal a qualitative similar electronic structure for all tetragonal iron(V) complexes. The unpaired electron is located in the π_y*-orbital of b_2-symmetry, resulting in a $^2B_2$ [$(d_{xy})^2(\pi_y^*/d_{yz})^1$] ground state when assuming C_{2v}-symmetry. The formal bond-order for the nitrido-/oxo-iron Bond is 2.5.

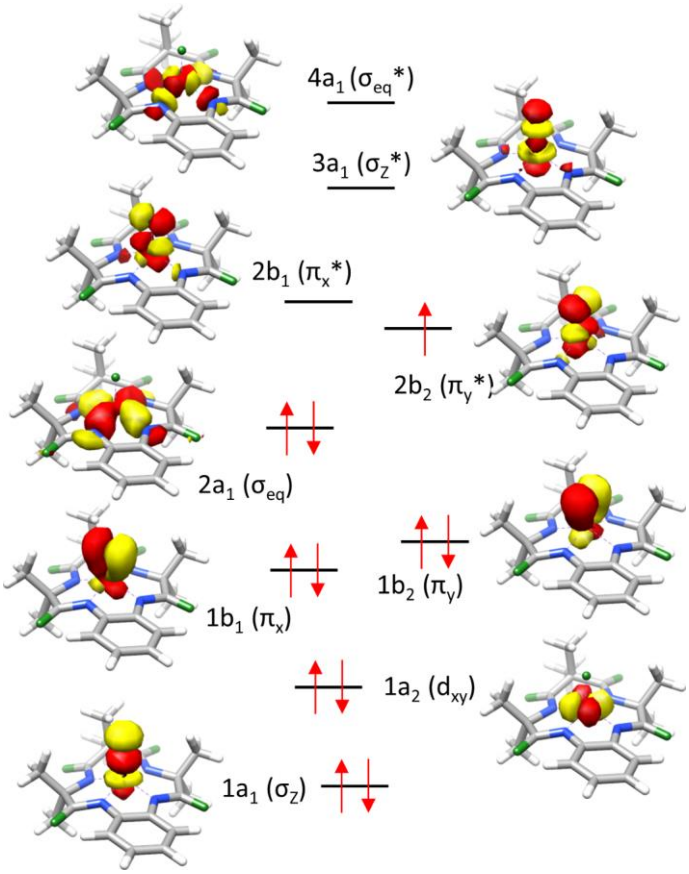

Figure 5.19: Active space orbitals from a SA-CASSCF(11,9)/3 roots calculation on the $[Fe^{V}(O)TAML]^{-}$ complex and outlined ground state electronic configuration.

Jesper Bendix *et al*. have shown that the strong axial nitrido ligand can significantly destabilize the d_{xz}/d_{yz}-orbitals, and provided the equatorial ligands are weak, they might be raised energetically even above the $d_{x^2-y^2}$-orbital (e.g. in $[Cr^{V}(N)Cl_4]^{2-}$, see also discussion in Chapter 1).[11] Therefore, a $d_{xy}<d_{x^2-y^2}<d_{xz}/d_{yz}<d_{z^2}$ ligand field splitting is sometimes discussed in the literature[248-249] as an potential alternative to the classical $d_{xy}< d_{xz}/d_{yz}< d_{x^2-y^2}<d_{z^2}$ orbital splitting derived by Ballhausen and Grey[6] for tetragonal transition metal complexes with multiply bonded monoatomic ligands (see Scheme 1.1, page 2). For a d^3-low-spin complex such as the present iron(V) species, a $^2A_1[(d_{xy})^2(d_{x^2-y^2})^1]$-ground state would be therefore throughout conceivable, but is not found for the investigated systems.

The discussed MO-schemes indicated that in the quartet state an additional π*-orbital might be occupied, resulting in a formal bond order of 1.5 for the Fe-N or Fe-O bond, respectively. This is indeed the case for the complexes $[Fe^{V}(N)cyc\text{-}ac]^{+}$, $[Fe^{V}(O)cyc\text{-}ac]^{2+}$ and $[Fe^{V}(N)(N_3)cyc]^{+}$ that show a $^4A_1[(d_{xy})^1(\pi_y^*/d_{yz})^1(\pi_x^*/d_{xz})^1]$ quartet state about 89 kJ mol^{-1}, 87 kJ mol^{-1} and 83 kJ mol^{-1} higher in energy than the doublet ground state, respectively. However, for the complex $[Fe^{V}(N)TMC\text{-}ac]^{+}$ the $^4B_1[(d_{xy})^1(\pi_y^*/d_{yz})^1(\sigma_{eq}^*/d_{x^2-y^2})^1]$ state was calculated to be the lowest energy quartet state, only 52 kJ mol^{-1} higher in energy than the doublet ground state. Hence, the additional unpaired electron is located in the $\sigma_{eq}^*(d_{x^2-y^2})$-orbital and not in the π_x^*-orbital, as found for all other tetragonal iron(V) complexes. The relatively small doublet-quartet gap for the TMC-ac complex and also different changes in the bond distances when the *S*=1/2 and *S*=3/2 structures are compared indicates its exceptional position in the series of iron(V) complexes studied here (see Table 5.5). While the nitrido-iron/oxo-iron bond distances in the complexes $[Fe^{V}(N)cyc\text{-}ac]^{+}$, $[Fe^{V}(O)cyc\text{-}ac]^{2+}$ and $[Fe^{V}(N)(N_3)cyc]^{+}$ is

significantly elongated in the *S*=3/2 structures when compared to the *S*=1/2 structure due to the occupation of an antibonding π_x*-orbital, this is not observed for the complex $[Fe^{V}(N)TMC\text{-}ac]^{+}$ (see Table 5.5). In contrast, for the $[Fe^{V}(N)TMC\text{-}ac]^{+}$ complex the equatorial Fe-N bonds distance are increased in the quartet state due to population of the σ_{eq}*($d_{x^2-y^2}$)-orbital that is antibonding with respect to the equatorial ligands. This demonstrates that the TMC-ac ligand in the complex $[Fe^{V}(N)TMC\text{-}ac]^{+}$ is the weakest equatorial ligand in the present series of iron(V) complexes, facilitating the occupation of the σ_{eq}*($d_{x^2-y^2}$)-orbital by one electron in the quartet state while only one π*-orbital of the Fe-N/Fe-O bond is occupied by one electron. The lower ligand field strength is also seen in the parent azido-iron(III) complexes. While the complex $[Fe^{III}(N_3)TMC\text{-}ac]^{+}$ is high-spin at room temperature,[42,48] the related six-coordinate non-heme complexes $[Fe^{III}(N_3)cyc\text{-}ac]^{+}$ and $[Fe^{III}(N_3)_2cyc]^{+}$ are low-spin. The calculations therefore reveal, that in the excited quartet state the complex $[Fe^{V}(N)TMC\text{-}ac]^{+}$ shows a d-orbital splitting as derived by Bendix *et al*. e.g. for the complex $[Cr^{V}(N)Cl_4]^{2-}$.[11]

The orbital plots in Figure 5.16, Figure 5.17, Figure 5.18 and Figure 5.19 show that the bonding (σ/π) and anti-bonding (σ*/π*) orbitals between the monoatomic ligand and the metal center are strongly delocalized, in particular for the nitrido-species. Hence, the bonds are very covalent as expected for mono-atomic nitrido- or oxo-ligands.[4] Higher covalency in the nitrides can be explained by the higher formal charge of the nitrido ligand (-3) and the lower effective nuclear charge (electronegativity) of nitrogen, when compared to the oxo-ligand. Therefore, the occupied nitrogen 2p-orbitals appear higher in energy than the oxo-orbitals, thus allowing π-donation from nitrogen to iron since the nitrogen orbitals will be better energetically matched with the valence d-orbitals on iron.[7]

Loewdin population analysis demonstrates this quantitatively (see Table 5.6). For the nitrido-iron(V) complexes the π*-orbitals (including the SOMO) are slightly more nitrogen- than metal centered while the corresponding π-orbitals are more metal- than nitrogen-centered. Therefore, the bonding situation in the nitrido-complexes can be described as inverted-bonding which was also concluded from DFT-calculations previously.[250] While formally the nitrido-complexes are iron(V)-species, they might be described as a resonance of the type $Fe^{V}(S_{Fe}=1/2)\ N^{3-} \leftrightarrow Fe^{II}(S_{Fe}=0)N^{\bullet}(S_N=1/2)$ as proposed previously for the $[Fe^{V}(N)cyc\text{-}ac]^{+}$-complex based on DFT-calculations.[41,250] In contrast, the oxo-iron(V) complexes are less covalent and can be still considered as pure iron(V) complexes where the π*-orbitals are mainly metal-derived (d_{xy}/d_{yz}) and the π-orbitals are mainly oxygen derived ($2p_x$, $2p_y$).

Table 5.6: Loewdin orbital composition for metal d- and ligand orbitals from CASSCF calculations on iron(V) complexes For σ_{eq} and σ_{eq}* the average percentage of the four equatorial ligand atoms is given.

	$\pi_x(d_{xz}+p_x)$ ($1b_1$)		$\pi_y(d_{yz}+p_y)$ ($1b_2$)		$\sigma_z(p_z)$ ($1a_1/2a_1$)		σ_{eq} ($2a_1/1a_1$)		d_{xy} (a_2)	π_x*(d_{xz}-p_x) ($2b_1$)		π_y*(d_{yz}-p_y) ($2b_2$)		σ_z*(d_{z^2}) ($4a_1/3a_1$)		σ_{eq}*($d_{x^2-y^2}$) ($3a_1/4a_1$)	
	Fe [%]	L [%]	Fe [%]	L [%]	Fe [%]	L [%]	Fe [%]	4xL [%]	Fe [%]	Fe [%]	L [%]	Fe [%]	L [%]	Fe [%]	L [%]	Fe [%]	4xL [%]
$[Fe^{V}(N)cyc\text{-}ac]^{+}$	56	42	56	42	43	56	25	14	98	48	50	49	49	59	35	84	3
$[Fe^{V}(O)cyc\text{-}ac]^{2+}$	38	59	44	53	36	60	42	10	98	61	36	60	38	64	25	67	6
$[Fe^{V}(N)(N_3)cyc]^{+}$	56	41	56	41	43	55	25	14	98	48	50	48	49	58	35	84	3
$[Fe^{V}(N)TMC\text{-}ac]^{+}$	57	41	57	40	43	56	23	14	98	47	50	47	50	59	35	85	3
$[Fe^{V}(N)TPP]$	55	43	57	41	47	52	26	14	98	47	51	49	49	56	40	85	3
$[Fe^{V}(O)TAML]^{-}$	35	63	37	61	37	60	43	11	97	64	32	66	28	64	27	69	6

MO-coefficients can be derived from the Loewdin orbital composition in Table 5.6. Those who will be relevant in the calculation of the g-values (see Chapter 5.6) are summarized in Table 5.7. Metal coefficients are denoted by α and ligand coefficients by β. Given that the composition of the π_x*- and π_y*-orbitals are close to identical (see Table 5.6) the coefficients are harmonized in one ligand and one metal coefficient $\alpha_\pi = \alpha_{xz} = \alpha_{yz}$ and $\beta_\pi = \beta_x = \beta_y$, respectively. The coefficients for the equatorial nitrogen-atoms that form an σ*-bond with the metal $d_{x^2-y^2}$-orbital are denoted by β_σ. Since the $a_2(d_{xy})$-orbital is purely metal centered (97%-98%) the corresponding coefficient α_{xy} is unity and not considered in the following discussion.

Table 5.7: MO coefficients derived from Loewdin orbital composition in Table 5.6.

	π_x* / π_y*		σ_z*/d_{z^2}		σ_{eq}*/$d_{x^2-y^2}$	
	α_π	β_π	α_{z^2}	β_z	$\alpha_{x^2-y^2}$	β_σ
$[Fe^V(N)cyc\text{-}ac]^+$	0.70	0.71	0.79	0.61	0.94	0.18
$[Fe^V(O)cyc\text{-}ac]^{2+}$	0.79	0.62	0.85	0.53	0.86	0.26
$[Fe^V(N)(N_3)cyc]^+$	0.70	0.71	0.79	0.61	0.94	0.18
$[Fe^V(N)TMC\text{-}ac]^+$	0.70	0.72	0.79	0.61	0.94	0.18
$[Fe^V(N)TPP]$	0.70	0.71	0.76	0.65	0.94	0.18
$[Fe^V(O)TAML]^-$	0.83	0.56	0.84	0.54	0.86	0.25

Calculated Excited states for tetragonal iron(V) complexes

Besides the electronic ground state, excited states and their relative order contain valuable information on the studied systems. On top of SA-CASSCF(11,9) calculations with 20 roots (same active space as in the above discussed calculations), NEVPT2 calculations were performed to obtain accurate excitation energies. Calculated one electron excitation energies are provided in Table 5.8.

Table 5.8: CASSCF(11,9)/NEVPT2 excitation energies for tetragonal Fe^V-complexes

State:	$^2B_1$ $[2b_2(\pi_y^*)\rightarrow 2b_1(\pi_x^*)]$ [cm^{-1}]	1^2A_1 $[2b_2(\pi_y^*)\rightarrow 3a_1(\sigma_{eq}^*)]$ [cm^{-1}]	$^2A_2$ $[1a_2(d_{xy})\rightarrow 2b_1(\pi_y^*)]$ [cm^{-1}]	2^2A_1 $[2b_2(\pi_y^*)\rightarrow 4a_1(\sigma_z^*)]$ [cm^{-1}]
$[Fe^V(N)cyc\text{-}ac]^+$	340	2653	19358	16959
$[Fe^V(O)cyc\text{-}ac]^{2+}$	627	23683	8764	23845
$[Fe^V(N)(N_3)cyc]^+$	431	5509	19949	17569
$[Fe^V(N)TMC\text{-}ac]^+$	567	2160	20323	16844
$[Fe^V(N)TPP]$	637	4195	23745	12108
$[Fe^V(O)TAML]^-$	2112	28752 (2^2A_1)*	12016	11642 (1^2A_1)*

*The excitation in the $d_{x^2-y^2}$- and d_{z^2}-orbital are swapped for the TAML complex.

Even the ligand systems are not genuine symmetric, all complexes show a very low lying $^2B_1[2b_2(\pi_y^*)\rightarrow 2b_1(\pi_x^*)]$ excited state implying nearly fourfold symmetry on the iron site. In C_{4v}-symmetry the ground state would be ^2E with a degenerate set of $\pi_y^*(d_{yz})$-and $\pi_x^*(d_{xz})$-orbitals. Only for the TAML-system the rhombic distortion is larger, resulting in a splitting of the ^2E-state by 2112 cm^{-1}. Deviation from C_{4v}-symmetry (which would result in a ^2E ground state) can be attributed to Jahn-Teller distortion, however, given that the used ligands are not genuinely symmetric it might also be a result of geometric constrains by the ligands systems.

The $1^2A_1[2b_2(\pi_y^*)\rightarrow 3a_1(\sigma_{eq}^*/d_{x^2-y^2})]$ excitation is important in the overall discussion of transition metal nitrido compounds since the $^2A_1[(d_{xy})^2(d_{x^2-y^2})^1]$ state is a throughout conceivable alternative to the $^2B_2[(d_{xy})^2(\pi_y^*/d_{yz})^1]$ ground state (*vide supra*).[248-249] However, for the complex $[Fe^V(N)TMC\text{-}ac]^+$ that features the weakest equatorial ligand in the studied complexes it is calculated to be separated from the $^2B_2$ ground state by 2160 cm^{-1} (26 kJ mol^{-1}), and for all other iron(V) complexes it was calculated to appear at even higher energies.

The excitation $^2A_2[1a_1(d_{xy})\rightarrow 2b_2(\pi_y^*/d_{yz})]$ is a measure for the covalency and strength of the Fe-N or Fe-O π-bond, respectively.[251] In this excited state an electron is transferred from the non-bonding $a_2(d_{xy})$-orbital into the π*-anti-bonding $2b_2(\pi_y^*/d_{yz})$-orbital. Given that π-bonding is stronger in the nitrido-complexes than in the oxo-complexes, the corresponding anti-bonding orbitals $2b_2(\pi_y^*/d_{yz})$ and $2b_1(\pi_x^*/d_{xz})$) are higher in energy for the former. Excitations where these are the accepting orbitals are, therefore, expected to appear at higher energy for the nitrido- than for the oxo-complexes. This explains why the $^2A_2[1a_1(d_{xy})\rightarrow 2b_2(\pi_y^*/d_{yz})]$ excited state is much higher in energy for the nitrido-complexes than for the oxo-complexes, which is best seen for the analogue complexes $[Fe^V(N)cyc\text{-}ac]^+$ (19258 cm^{-1}) and $[Fe^V(O)cyc\text{-}ac]^{2+}$ (8764 cm^{-1}).

The $^2A_2[1a_1(d_{xy})\rightarrow 2b_2(\pi_y^*/d_{yz})]$ excitation energy calculated for the heme-system $[Fe^V(N)TPP]$ is at the same order as found for the non-heme nitrido-complexes. Appearance of this transition at higher energy for the nitrido- than for the oxo-complexes might explain why the $[Fe^V(N)TPP]$ complex is a real iron(V) species, while analogue heme oxo-iron complexes are better described as iron(IV) with an oxidized ligand. Oxidation of the ligand would require electron transfer from the porphyrin π-system to a metal orbital, as outlined in Scheme 5.1 for an oxo-complex. However, the electron accepting π*-orbitals for this electron-transfer are much higher in energy for the nitrido- than for the oxo-complexes. Hence, ligand oxidation is possible for oxo-iron heme complexes but not for the analogue nitrido-species, as outlined in Scheme 5.1.

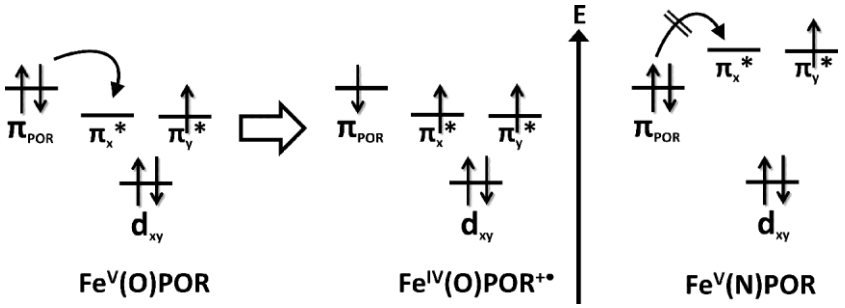

Scheme 5.1: Qualitative electronic structure and electron transfer in oxo-iron(V) porphyrin and oxo-iron(IV) porphyrin radical complexes, and the electronic structure of nitrido-iron(V) porphyrin complexes.

Further differences between the oxo- and nitrido species are indicated by the $1^2A_1[2b_2(\pi_y^*/d_{yz})\rightarrow 4a_1(\sigma_{eq}^*/d_{x^2-y^2})]$ excited state. When the $[Fe^V(N)cyc\text{-}ac]^+$ and $[Fe^V(O)cyc\text{-}ac]^{2+}$ complexes with identical equatorial ligands are compared, this excitation appears at much higher energy for the oxo-species. Given that the $d_{x^2-y^2}$-orbital is expected to be at similar energy in both systems it can be concluded that the anti-bonding $2b_2(\pi_y^*/d_{yz})$-orbital is at much higher energy (hence, more anti-bonding) for the nitrido-complex when compared to the analogue oxo-species. The $1^2A_1[2b_2(\pi_y^*/d_{yz})\rightarrow 3a_1(\sigma_{eq}^*/d_{x^2-y^2})]$ excitation is calculated to be highest in energy for the $[Fe^V(O)TAML]^-$-complex. Besides the oxo-ligand, this is further influenced by the strongly donating bis-

anionic TAML-ligand. It will rise the energy of the $d_{x^2-y^2}$-orbital even above the d_{z^2}-orbital. Therefore, the $2^2A_1[2b_2(\pi_y^*/d_{yz}) \rightarrow 4a_1(\sigma_{eq}^*/d_{x^2-y^2})]$ excited state appears at higher energy (28752 cm^{-1}) than the $1^2A_1[2b_2(\pi_y^*/d_{yz}) \rightarrow 3a_1(\sigma_z^* d_{z^2})]$ excited state (11642 cm^{-1}) for the TAML system.

Comparing the individual excitation energies results in the relative frontier orbital arrangement $d_{xy} < \pi_y^*(d_{yz}) \approx \pi_x^*(d_{xz}) < d_{x^2-y^2} < d_{z^2}$ for all complexes studied here, besides the $[Fe^V(O)TAML]^-$-complex where the $d_{x^2-y^2}$ and d_{z^2} orbitals are swapped resulting in $d_{xy} < \pi_y^*(d_{yz}) \approx \pi_x^*(d_{xz}) < d_{z^2} < d_{x^2-y^2}$. Scheme 5.2 shows a qualitative MO-diagram for a distorted octahedral nitrido complex in C_{2v}-symmetry (also the excitation energies were considered here and not only the calculated orbital energies).

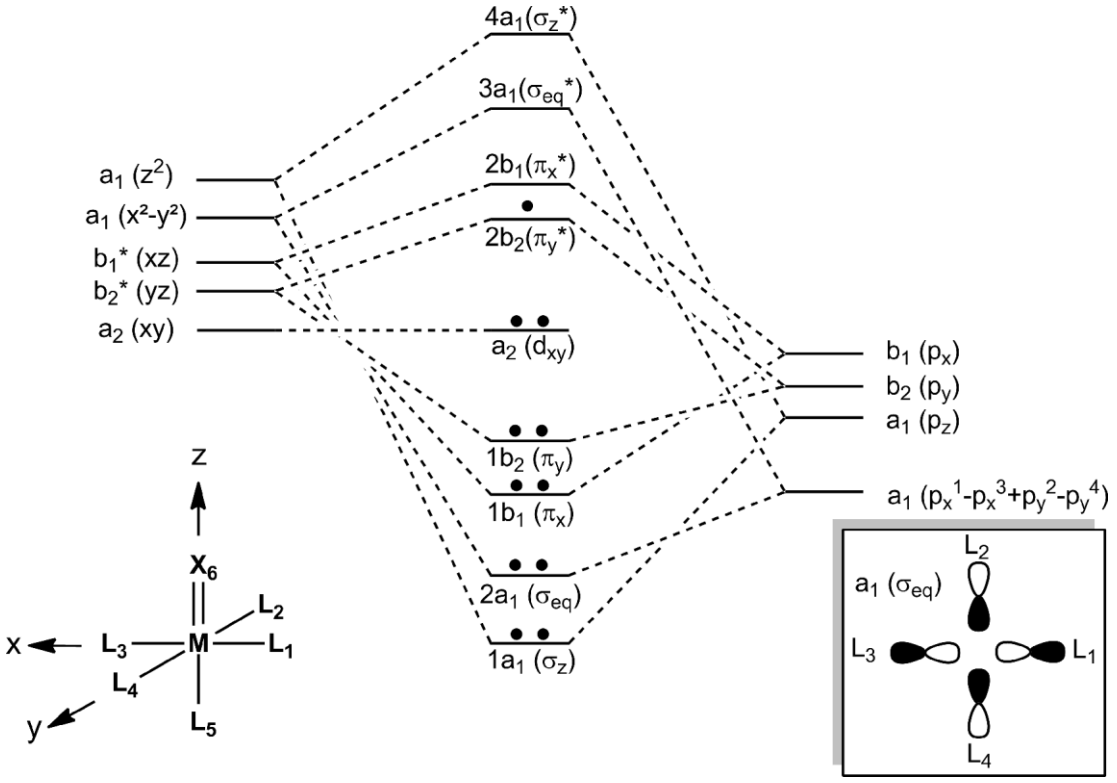

Scheme 5.2: MO-scheme for an nitrido-iron(V) complex in C_{2v} symmetry. The coordinate system is outlined on the lower left hand side and the box on the lower right hand side illustrates how the equatorial a_1-orbital is formed by p-orbitals of the equatorial ligand. Electrons that occupy orbitals are symbolized by black circles.

The calculations have shown that the nitrido-complexes are very covalent. Given that also the experimental g-values are very similar, the properties of these complexes seems to be strongly driven by the $\{Fe \equiv N\}^{2+}$-unit. However, the equatorial ligands still have significant impact on the electronic structure as seen in the $^2B_2[(d_{xy})^2(\pi_x^*/d_{xz})^1]$ ground state while a $1^2A_1[(d_{xy})^2(d_{x^2-y^2})^1]$ ground state would be possible with weak (or without) equatorial ligand. Hence, the present complexes cannot be considered as a $\{Fe \equiv N\}^{2+}$-unit with additional ligands, whereas it was shown by Bendix that e.g. tetragonal nitrido-chromium(V) complexes can be described as $\{Cr \equiv N\}^{2+}$-units with additional ligands instead of chromium complexes with a nitrido and further ligands.[11]

The large covalency effects in the discussed complexes will also affect numerous spectroscopic properties; e.g. EPR g-values (the g-shift),[108-110] Mössbauer quadrupole splitting/isomer shifts[7,139] as well as the intensity in X-Ray absorption spectroscopy.[7,252] Taking these effects into account, the g-values of the tetragonal iron(V) complexes will be discussed in detail in the following chapter.

5.6. Analysis of the g-Values in tetragonal Iron(V) complexes

Within the framework of ligand field theory, spin-Hamiltonian (SH) equations for the g-values can be derived (see introduction 2.1.1and 2.1.2). This will not only provide a qualitative understanding of the g-values, in an accurate treatment g-values can be reproduced nearly quantitatively. Results from the CASSCF/NEVPT2 calculations (excitation energies, MO-coefficients) discussed in Chapter 5.5.2 will be used in the derived equations.

One-particle wave functions (molecular orbitals, MOs) are defined using the coordinate system and ligand labels shown in Figure 2.2, page 18. Based on the calculations in Chapter 5.5.2 the MOs for the relevant frontier orbitals are defined as:

$1a_2$	$\psi_{xy} \approx \lvert d_{xy}\rangle$	5.1a
$2b_1$	$\psi_{xz} \approx \alpha_{xz}\lvert d_{xz}\rangle - \beta_x\lvert p_x^6\rangle$	5.1b
$2b_2$	$\psi_{yz} \approx \alpha_{yz}\lvert d_{yz}\rangle - \beta_y\lvert p_y^6\rangle$	5.1c
$3a_1$	$\psi_{x^2-y^2} \approx \alpha_{x^2-y^2}\lvert d_{x^2-y^2}\rangle + \beta_\sigma(\lvert p_x^3\rangle - \lvert p_x^1\rangle + \lvert p_y^2\rangle - \lvert p_y^4\rangle)$	5.1d
$4a_1$	$\psi_{z^2} \approx \alpha_{z^2}\lvert d_{z^2}\rangle - \beta_z\lvert p_z^6\rangle$	5.1e

For the shake of convenience frontier orbitals are labeled in the following as d-orbitals, even in the nitrido-complexes they show more ligand p-orbital than metal d-orbital character (see Chapter 5.5.2). One-electron excitation energies will be labeled by Δ_n where *n* is the accepting orbital and in cases where a spin-down electron is excited, it is the donating orbital, e.g. the excitation energy of the $^2B_1[2b_2(\pi_y^*/d_{yz})\rightarrow 2b_1(\pi_x^*/d_{xz})]$ transition is denoted by Δ_{xz}.

As outlined in the introduction (Chapter 2.1.2) and in various text books[108,111,124] the g-values for an *S*=1/2 system can be calculated by Equation 2.16.(page 15). For the d^3-iron(V) systems with the electronic ground state configuration $(d_{xy})^2(d_{yz})^1$ this results in the following equations:

$$g_{xx} = g_e - \frac{2\alpha_{x^2-y^2}^2\alpha_{yz}^2\zeta_{Fe}}{\Delta_{x^2-y^2}(1^2A_1)} - \frac{2\left[3\alpha_{yz}^2\alpha_z^2+\sqrt{3}\alpha_{yz}\alpha_{z^2}\beta_y\beta_z\right]\zeta_{Fe}}{\Delta_{z^2}(2^2A_1)} \quad 5.2$$

$$g_{yy} = g_e + \frac{2\alpha_{yz}^2\alpha_{xy}^2\,\zeta_{Fe}}{\Delta_{xy}(^2A_2)} \quad 5.3$$

$$g_{zz} = g_e - \frac{2\zeta_{Fe}(\alpha_{yz}^2\alpha_{xz}^2-2\beta_x\beta_y\alpha_{yz}\alpha_{xz})}{\Delta_{xz}(^2B_1)} \quad 5.4$$

It is directly seen, that Equation 5.2-5.4 would result in $g_{xx}<g_e$, $g_{zz}<g_e$ and $g_{yy}>g_e$ which is not in agreement with the experimental results, where all g-values are found to be smaller than g_e (see Table 5.4). However, the CASSCF/NEVPT2 calculations revealed a very low lying excited state only very few hundred wave numbers above the ground state. This is at the same order of magnitude as the spin-orbit coupling constant for iron(V) (ζ_{Fe^V} =580 cm^{-1}, in the following denoted as ζ_{Fe}).[131] Therefore, the usual approach based on non-degenerated perturbation theory is not valid here, and the near degeneracy has to be taken into account in deriving spin Hamiltonian expressions for the g-values.

5.6.1. Spin-Hamiltonian Equations for the g-Values in the Degenerate Case

In C_{4v}-symmetry the studied tetragonal iron(V) systems would show a degenerate $^2E[(d_{xy})^2(d_{yz},d_{xz})^1]$ state, however, rhombic distortion does split this degenerate state in the two close lying states $^2B_2[(d_{xy})^2(d_{yz})^1]$ and $^2B_1[(d_{xy})^2(d_{xz})^1]$ in C_{2v}-symmetry. The many particle wave functions ($|\Psi_n^{S,M}>$, *M*=+*S*, …,–*S*) for these close lying states are (only for *M*=+1/2 given here)

$$|\Psi_{yz}^{\frac{1}{2},+\frac{1}{2}}> = |\psi_{xy}\bar{\psi}_{xy}\psi_{yz}| \qquad ^2B_2 \text{ in } C_{2v} \qquad \text{(ground state)}$$

$$|\Psi_{xz}^{\frac{1}{2},+\frac{1}{2}}> = |\psi_{xy}\bar{\psi}_{xy}\psi_{xz}| \qquad ^2B_1$$

and for the remaining one-electron excited states that affect the g-value

$$|\Psi_{xy}^{\frac{1}{2},+\frac{1}{2}}> = |\psi_{xy}\psi_{yz}\bar{\psi}_{yz}| \qquad ^2A_2$$

$$|\Psi_{x^2-y^2}^{\frac{1}{2},+\frac{1}{2}}> = |\psi_{xy}\bar{\psi}_{xy}\psi_{x^2-y^2}| \qquad 1^2A_1$$

$$|\Psi_{z^2}^{\frac{1}{2},+\frac{1}{2}}> = |\psi_{xy}\bar{\psi}_{xy}\psi_{z^2}| \qquad 2^2A_1$$

Where ψ_n denotes an orbital occupied by a spin-up electron and $\bar{\psi}_n$ is an orbital occupied by a spin-down electron.

Quasi degenerate treatment of the lowest excitation

In the present case the effect by spin orbit coupling and the crystal field on the ground state are of very similar order and a successively treatment of these perturbations will lead to significant errors. It is possible to circumvent this problem by treating these two perturbations simultaneously within the framework of quasi degenerate perturbation theory.[124,253-255]

The spin-orbit coupling (SOC) and Born-Oppenheimer (BO) Hamiltonian is calculated in the basis $|\Psi_{yz,xz}^{\frac{1}{2},\pm\frac{1}{2}}>$. MO-coefficients for the π-bonds formed by d_{xz}+p_x and d_{yz}+p_y orbitals are harmonized in one ligand/metal coefficient $\alpha_\pi \approx \alpha_{xz} \approx \alpha_{yz}$ and $\beta_\pi \approx \beta_x \approx \beta_y$ as discussed in the antecedent chapter (see Table 5.19).

$$< \Psi_{yz,xz}^{\frac{1}{2},\pm\frac{1}{2}} | V_{rhomb} + \sum_{i=x,y,z} \zeta_{Fe} \boldsymbol{l}_i^{Fe} \boldsymbol{s}_i | \Psi_{yz,xz}^{\frac{1}{2},\pm\frac{1}{2}} > = \begin{pmatrix} 0 & \frac{i\alpha_\pi^2\zeta_{Fe}}{2} & 0 & 0 \\ -\frac{i\alpha_\pi^2\zeta_{Fe}}{2} & \Delta_{xz} & 0 & 0 \\ 0 & 0 & 0 & -\frac{i\alpha_\pi^2\zeta_{Fe}}{2} \\ 0 & 0 & \frac{i\alpha_\pi^2\zeta_{Fe}}{2} & \Delta_{xz} \end{pmatrix}$$

Equation 5.5

Columns and rows are in the order $\Psi_{yz}^{\frac{1}{2},+\frac{1}{2}}$, $\Psi_{xz}^{\frac{1}{2},+\frac{1}{2}}$, $\Psi_{yz}^{\frac{1}{2},-\frac{1}{2}}$, $\Psi_{xz}^{\frac{1}{2},-\frac{1}{2}}$ which results in a block matrix. The rhombic splitting of the ^{2}E ground state (in C_{4v} symmetry) is Δ_{xz}. For calculating the matrix elements, MOs defined in Equations 5.1a-e were used.

Eigenvalues and eigenfunctions are obtained by diagonalization of the secular determinant of Equation 5.5. This can be done separately for the upper left block ($\Psi_{yz}^{\frac{1}{2},+\frac{1}{2}}$, $\Psi_{xz}^{\frac{1}{2},+\frac{1}{2}}$) and the lower right block ($\Psi_{yz}^{\frac{1}{2},-\frac{1}{2}}$, $\Psi_{xz}^{\frac{1}{2},-\frac{1}{2}}$) of the resulting block matrix. It has to be considered, that some entities of the matrix are imaginary.[256]

The following eigenfunctions and corresponding eigenvalues are obtained for the basis $\Psi_{yz}^{\frac{1}{2},+\frac{1}{2}}$, $\Psi_{xz}^{\frac{1}{2},+\frac{1}{2}}$:

$$E_0 = \frac{1}{2}\left(\Delta_{xz} - \sqrt{\Delta_{xz}^2 + (\alpha_\pi^2\zeta_{Fe})^2}\right) \qquad |\Theta_0^{+\frac{1}{2}}> = \cos\theta\,|\Psi_{yz}^{\frac{1}{2},+\frac{1}{2}}> + i\sin\theta\,|\Psi_{xz}^{\frac{1}{2},+\frac{1}{2}}>$$

$$E_1 = \frac{1}{2}\left(\Delta_{xz} + \sqrt{\Delta_{xz}^2 + (\alpha_\pi^2\zeta_{Fe})^2}\right) \qquad |\Theta_1^{+\frac{1}{2}}> = \cos\theta\,|\Psi_{xz}^{\frac{1}{2},+\frac{1}{2}}> - i\sin\theta\,|\Psi_{yz}^{\frac{1}{2},+\frac{1}{2}}>$$

And for the matrix with the basis $\Psi_{yz}^{\frac{1}{2},-\frac{1}{2}}$, $\Psi_{xz}^{\frac{1}{2},-\frac{1}{2}}$:

$$E_0 = \frac{1}{2}\left(\Delta_{xz} - \sqrt{\Delta_{xz}^2 + (\alpha_\pi^2\zeta_{Fe})^2}\right) \qquad |\Theta_0^{-\frac{1}{2}}> = \cos\theta\;|\Psi_{yz}^{\frac{1}{2},-\frac{1}{2}}> - i\sin\theta\,|\Psi_{xz}^{\frac{1}{2},-\frac{1}{2}}>$$

$$E_1 = \frac{1}{2}\left(\Delta_{xz} + \sqrt{\Delta_{xz}^2 + (\alpha_\pi^2\zeta_{Fe})^2}\right) \qquad |\Theta_1^{-\frac{1}{2}}> = \cos\theta\,|\Psi_{xz}^{\frac{1}{2},-\frac{1}{2}}> + i\sin\theta\,|\Psi_{yz}^{\frac{1}{2},-\frac{1}{2}}>$$

The lower Kramers doublet is then:

$$|\Theta_0^{+\frac{1}{2}}> = \cos\theta\,|\Psi_{yz}^{\frac{1}{2},+\frac{1}{2}}> + i\sin\theta\,|\Psi_{xz}^{\frac{1}{2},+\frac{1}{2}}> \qquad 5.6a$$

$$|\Theta_0^{-\frac{1}{2}}> = \cos\theta\;|\Psi_{yz}^{\frac{1}{2},-\frac{1}{2}}> - i\sin\theta\,|\Psi_{xz}^{\frac{1}{2},-\frac{1}{2}}> \qquad 5.6b$$

With

$$cos^2\theta = \frac{1}{2} + \frac{1}{2}\left(1 + \left(\frac{\alpha_\pi^2\zeta_{Fe}}{\Delta_{xz}}\right)^2\right)^{-\frac{1}{2}} \qquad 5.7$$

$$sin^2\theta = \frac{1}{2} - \frac{1}{2}\left(1 + \left(\frac{\alpha_\pi^2\zeta_{Fe}}{\Delta_{xz}}\right)^2\right)^{-\frac{1}{2}} \qquad 5.8$$

$$tan\,\theta = -\frac{2\,\alpha_\pi^2\zeta_{Fe}}{\Delta_{xz}} \qquad 5.9$$

$\cos\theta$ and $\sin\theta$ in Equation 5.6a-b can be considered as coefficients that determine the contribution of the low lying state to the ground state with $\cos^2\theta + \sin^2\theta = 1$.

Perturbation of the lowest Kramers doublet with remaining excitations

The Kramers doublet in Equation 5.6 is perturbed with the remaining excitations which is done by second order perturbation theory. Spin-orbit coupling matrix elements are calculated here between states which results in the correct signs,[125,129-130,257] and not between orbitals as it is frequently done in the literature which would require to adjust the sign in the final equations.[108-109,111,124]

$$|\widetilde{\Psi}_0^{\frac{1}{2'},+\frac{1}{2}}> = cos\theta\,|\Psi_{yz}^{\frac{1}{2'},+\frac{1}{2}}> + i\,sin\theta\,|\Psi_{xz}^{\frac{1}{2'},+\frac{1}{2}}> - \sum_n \frac{<\Psi_n^{\frac{1}{2},\pm\frac{1}{2}}|\zeta_{Fe}\,\boldsymbol{l^{Fe}s}\,|\,\Theta_0^{\frac{1}{2}}>}{\Delta_n}|\Psi_n^{\frac{1}{2'},\pm\frac{1}{2}}>$$

$$\begin{aligned}
&= cos\theta\,|\Psi_{yz}^{\frac{1}{2'},+\frac{1}{2}}> + i\,sin\theta\,|\Psi_{xz}^{\frac{1}{2'},+\frac{1}{2}}> \\
&- \Delta_{x^2-y^2}^{-1}\left[cos\theta < \Psi_{x^2-y^2}^{\frac{1}{2'},-\frac{1}{2}}|\zeta_{Fe}\,\boldsymbol{l^{Fe}s}|\Psi_{yz}^{\frac{1}{2'},+\frac{1}{2}}> + i\,sin\theta < \Psi_{x^2-y^2}^{\frac{1}{2'},-\frac{1}{2}}|\zeta_{Fe}\,\boldsymbol{l^{Fe}s}|\Psi_{xz}^{\frac{1}{2'},+\frac{1}{2}}>\right]|\Psi_{x^2-y^2}^{\frac{1}{2'},-\frac{1}{2}}> \\
&- \Delta_{xy}^{-1}\left[cos\theta < \Psi_{xy}^{\frac{1}{2'},-\frac{1}{2}}|\zeta_{Fe}\,\boldsymbol{l^{Fe}s}|\Psi_{yz}^{\frac{1}{2'},+\frac{1}{2}}> + i\,sin\theta < \Psi_{xy}^{\frac{1}{2'},-\frac{1}{2}}|\zeta_{Fe}\,\boldsymbol{l^{Fe}s}|\Psi_{xz}^{\frac{1}{2'},+\frac{1}{2}}>\right]|\Psi_{xy}^{\frac{1}{2'},-\frac{1}{2}}> \\
&- \Delta_{z^2}^{-1}\left[cos\theta < \Psi_{z^2}^{\frac{1}{2'},-\frac{1}{2}}|\zeta_{Fe}\,\boldsymbol{l^{Fe}s}|\Psi_{yz}^{\frac{1}{2'},+\frac{1}{2}}> + i\,sin\theta < \Psi_{z^2}^{\frac{1}{2'},-\frac{1}{2}}|\zeta_{Fe}\,\boldsymbol{l^{Fe}s}|\Psi_{xz}^{\frac{1}{2'},+\frac{1}{2}}>\right]|\Psi_{z^2}^{\frac{1}{2'},-\frac{1}{2}}>
\end{aligned}$$

$$\begin{aligned}
|\widetilde{\Psi}_0^{\frac{1}{2'},+\frac{1}{2}}> \approx\ & cos\theta\,|\Psi_{yz}^{\frac{1}{2'},+\frac{1}{2}}> + i\,sin\theta\,|\Psi_{xz}^{\frac{1}{2'},+\frac{1}{2}}> - \frac{i\alpha_\pi\alpha_{x^2-y^2}\,\zeta_{Fe}}{2\Delta_{x^2-y^2}}\,[cos\theta - sin\theta]|\Psi_{x^2-y^2}^{\frac{1}{2'},-\frac{1}{2}}> \\
&+ \frac{\alpha_\pi\zeta_{Fe}}{2\Delta_{xy}}[sin\theta - cos\theta]|\Psi_{xy}^{\frac{1}{2'},-\frac{1}{2}}> - \frac{i\sqrt{3}\alpha_\pi\,\alpha_{z^2}\zeta_{Fe}}{2\Delta_{z^2}}[cos\theta + sin\theta]|\Psi_{z^2}^{\frac{1}{2'},-\frac{1}{2}}>
\end{aligned} \qquad 5.10$$

And analogously

$$\begin{aligned}
|\widetilde{\Psi}_0^{\frac{1}{2'},-\frac{1}{2}}> \approx\ & cos\theta\,|\Psi_{yz}^{\frac{1}{2'},-\frac{1}{2}}> - i\,sin\theta\,|\Psi_{xz}^{\frac{1}{2'},-\frac{1}{2}}> - \frac{i\alpha_\pi\alpha_{x^2-y^2}\,\zeta_{Fe}}{2\Delta_{x^2-y^2}}\,[cos\theta - sin\theta]|\Psi_{x^2-y^2}^{\frac{1}{2'},+\frac{1}{2}}> \\
&+ \frac{\alpha_\pi\zeta_{Fe}}{2\Delta_{xy}}[cos\theta - sin\theta]|\Psi_{xy}^{\frac{1}{2'},+\frac{1}{2}}> - \frac{i\sqrt{3}\alpha_\pi\,\alpha_{z^2}\zeta_{Fe}}{2\Delta_{z^2}}[cos\theta + sin\theta]|\Psi_{z^2}^{\frac{1}{2'},+\frac{1}{2}}>
\end{aligned} \qquad 5.11$$

Calculation of the Zeeman matrix

The Zeeman matrix is calculated in the basis of the Kramers doublet Equation 5.10 and 5.11 $|\widetilde{\Psi}_0^{\frac{1}{2'},\pm\frac{1}{2}}>$ with the operator:

$$H_{Ze} = \beta_e \sum_{i=x,y,z} \boldsymbol{B_i}(\boldsymbol{l_i} + g_e\boldsymbol{s_i}) = \beta_e \sum_{i=x,y,z} \boldsymbol{B_i}\boldsymbol{\mu_i} = \beta_e(\mu_x B_x + \mu_y B_y + \mu_z B_z) \qquad 5.12$$

The resulting terms $<\widetilde{\Psi}_0^{\frac{1}{2'},\pm\frac{1}{2}}|\boldsymbol{s}_i|\widetilde{\Psi}_0^{\frac{1}{2'},\pm\frac{1}{2}}>$ that give rise to the contributions $<\psi_n^{\pm\frac{1}{2}}|\boldsymbol{s}_i|\psi_m^{\pm\frac{1}{2}}>$ are easily calculated. More difficult to evaluate are the orbital Zeeman matrix elements $<\widetilde{\Psi}_0^{\frac{1}{2'},\pm\frac{1}{2}}|\boldsymbol{l}_i|\widetilde{\Psi}_0^{\frac{1}{2'},\pm\frac{1}{2}}>$ or $<\psi_n^{\pm\frac{1}{2}}|\boldsymbol{l}_i|\psi_m^{\pm\frac{1}{2}}>$, respectively, given that covalency cannot be neglected the same way as done for the spin-orbit coupling matrix elements (see Chapter 2.1.2, page 17). Calculation of the orbital Zeeman

matrix element $< \psi_{yz}|l_z^{Fe}|\psi_{xz} >$ will be outlined here, since it leads to interesting results that further simplify the calculations. The remaining orbital Zeeman matrix elements are provided in Appendix 7.1.1, page 205.

<u>matrix elements:</u> $< \psi_{yz}|l_z^{Fe}|\psi_{xz} >$ and $< \psi_{xz}|l_z^{Fe}|\psi_{yz} >$

$$< \psi_{yz}|l_z^{Fe}|\psi_{xz} > = - < \psi_{xz}|l_z^{Fe}|\psi_{yz} >$$
$$= \alpha_\pi^2 < d_{yz}|l_z^{Fe}|d_{xz} > + \beta_\pi^2 < p_y^{(6)}|l_z^{Fe}|p_x^{(6)} > - \alpha_\pi\beta_\pi[< d_{yz}|l_z^{Fe}|p_x^{(6)} > + < p_y^{(6)}|l_z^{Fe}|d_{xz} >]$$

here, $l_z^{Fe} = l_z^L$ (Equation 2.28c, page 18)

$$= + i\,\alpha_\pi^2 + \beta_\pi^2 < p_y^{(6)}|l_z^{L6}|p_x^{(6)} > - \alpha_\pi\beta_\pi < d_{yz}|l_z^{L6}|p_x^{(6)} > - \alpha_\pi\beta_\pi < p_y^{(6)}|l_z^{Fe}|d_{xz} >$$

$$= + i\,\alpha_\pi^2 + i\,\beta_\pi^2 - i\,\alpha_\pi\beta_\pi < d_{yz}|\,|p_y^{(6)} > - i\,\alpha_\pi\beta_\pi < p_y^{(6)}|\,|d_{yz} >$$

since $< d_{yz}|\,|p_y^{(6)} > = < p_y^{(6)}|\,|d_{yz} > = S_\pi$ and[5] $\alpha_\pi^2 + \beta_\pi^2 - 2\alpha_\pi\beta_\pi S_\pi = 1$

$$< \psi_{yz}|l_z^{Fe}|\psi_{xz} > = - < \psi_{xz}|l_z^{Fe}|\psi_{yz} > = + i \qquad 5.13$$

This result shows that covalency cancels out even without neglecting any term (e.g. p-d-overlap).[133,258] As will be shown shortly, the just evaluated matrix element is the only orbital Zeeman matrix element that goes into the formula for the g_{zz}-value. Therefore, the g_{zz}-value will be affected by covalency only through θ. In the studied systems, the error for the g_{zz}-value is about ~50% if ligand contributions would have been neglected here, since then covalency would not cancel out.

The calculated orbital Zeeman matrix elements are used to evaluate the individual contributions to the Zeeman matrix (the whole Zeeman matrix and all contributions, including terms quadratic order in energy (Δ_n^{-2}) are provided in the Appendix 7.1.2, page 208). Zeeman matrix elements relevant for calculating the g-values are (B_x, B_y, B_z and β_e omitted):

$$\langle \widetilde{\Psi}_0^{\frac{1}{2},+\frac{1}{2}} \left| \boldsymbol{l_z} + g_e \boldsymbol{s_z} \right| \widetilde{\Psi}_0^{\frac{1}{2},+\frac{1}{2}} \rangle = -\sin 2\theta$$

$$\langle \widetilde{\Psi}_0^{\frac{1}{2},+\frac{1}{2}} \left| \boldsymbol{l_x} + g_e \boldsymbol{s_x} \right| \widetilde{\Psi}_0^{\frac{1}{2},-\frac{1}{2}} \rangle = \frac{g_e \cos 2\theta}{2}$$
$$- \frac{\alpha_\pi^2 \alpha_{x^2-y^2}^2 \zeta_{Fe}(\cos^2\theta - \sin\theta\cos\theta)}{\Delta_{x^2-y^2}} - \frac{\left[3\alpha_\pi^2\alpha_{z^2}^2 + \sqrt{3}\alpha_\pi\alpha_{z^2}\beta_\pi\beta_z\right]\zeta_{Fe}(\cos^2\theta + \sin\theta\cos\theta)}{\Delta_{z^2}} - \frac{\alpha_\pi^2\zeta_{Fe}(\sin^2\theta - \sin\theta\cos\theta)}{\Delta_{xy}}$$

$$\langle \widetilde{\Psi}_0^{\frac{1}{2},+\frac{1}{2}} \left| \boldsymbol{l_y} + g_e \boldsymbol{s_y} \right| \widetilde{\Psi}_0^{\frac{1}{2},-\frac{1}{2}} \rangle = \frac{i\,g_e \cos 2\theta}{2} - \frac{i\,\alpha_\pi^2\,\zeta_{Fe}(\cos^2\theta - \cos\theta\sin\theta)}{\Delta_{xy}}$$
$$- \frac{i\,\alpha_\pi^2\alpha_{x^2-y^2}^2\,\zeta_{Fe}(\sin^2\theta - \cos\theta\sin\theta)}{\Delta_{x^2-y^2}} - \frac{i\,[3\alpha_\pi^2\alpha_{z^2}^2 + \sqrt{3}\alpha_\pi\alpha_{z^2}\beta_\pi\beta_z]\,\zeta_{Fe}(\sin^2\theta + \cos\theta\sin\theta)}{\Delta_{z^2}}$$

[5] It should be noted here, that the overlap-integral S_π is negative since ψ_{yz} and ψ_{xz} are anti-bonding orbitals (see their definition in Equation 5.1b and 5.1c, page 135).

Final expressions for the g-values

For obtaining expressions for the g-values, the Zeeman matrix is compared with the matrix of the general spin-Hamiltonian $H_{spin} = \zeta \sum_{i,j} g_{ij} s_i B_j$ in the basis of the Kramers doublet. The secular determinant must produce the same energy as the secular determinant of the Zeeman matrix.[109] By comparison of the matrix elements, the following relations are obtained:[6]

$$g_{xx} = 2 \cdot Real \left(\langle \widetilde{\Psi}_0^{\frac{1}{2},+\frac{1}{2}} \middle| \boldsymbol{l_x} + g_e \boldsymbol{s_x} \middle| \widetilde{\Psi}_0^{\frac{1}{2},-\frac{1}{2}} \rangle \right)$$

$$g_{yy} = 2\,i \cdot Imaginary \left(\langle \widetilde{\Psi}_0^{\frac{1}{2},+\frac{1}{2}} \middle| \boldsymbol{l_y} + g_e \boldsymbol{s_y} \middle| \widetilde{\Psi}_0^{\frac{1}{2},-\frac{1}{2}} \rangle \right)$$

$$g_{zz} = 2 \cdot Real \left(\langle \widetilde{\Psi}_0^{\frac{1}{2},+\frac{1}{2}} \middle| \boldsymbol{l_z} + g_e \boldsymbol{s_z} \middle| \widetilde{\Psi}_0^{\frac{1}{2},+\frac{1}{2}} \rangle \right)$$

This finally leads to the following expressions for the g-values:

$$g_{xx} = g_e \cos 2\theta - \frac{2\alpha_{x^2-y^2}^2 \alpha_\pi^2 \zeta_{Fe} (\cos^2\theta - \sin\theta\cos\theta)}{\Delta_{x^2-y^2}} \qquad 5.14$$

$$- \frac{2\left[3\alpha_\pi^2\alpha_\sigma^2 + \sqrt{3}\alpha_\pi\,\alpha_{z^2}\beta_\pi\beta_z\right]\zeta_{Fe}(\cos^2\theta + \sin\theta\cos\theta)}{\Delta_{z^2}} - \frac{2\alpha_\pi^2\zeta_{Fe}(\sin^2\theta - \sin\theta\cos\theta)}{\Delta_{xy}}$$

$$- \frac{g_e\alpha_\pi^2\zeta_{Fe}^2}{4}\left[\frac{\alpha_{x^2-y^2}^2(\cos\theta - \sin\theta)^2}{\left(\Delta_{x^2-y^2}\right)^2} - \frac{(\cos\theta - \sin\theta)^2}{(\Delta_{xy})^2} + \frac{3\alpha_{z^2}^2(\cos\theta + \sin\theta)^2}{(\Delta_{z^2})^2}\right]$$

$$g_{yy} = g_e \cos 2\theta + \frac{2\alpha_\pi^2\,\zeta_{Fe}(\cos^2\theta - \cos\theta\sin\theta)}{\Delta_{xy}} \qquad 5.15$$

$$+ \frac{2\alpha_{x^2-y^2}^2\alpha_\pi^2\,\zeta_{Fe}(\sin^2\theta - \cos\theta\sin\theta)}{\Delta_{x^2-y^2}} + \frac{2\,[3\alpha_\pi^2\alpha_{z^2}^2 + \sqrt{3}\alpha_\pi\,\alpha_{z^2}\beta_\pi\beta_z]\,\zeta_{Fe}(\sin^2\theta + \cos\theta\sin\theta)}{\Delta_{z^2}}$$

$$+ \frac{g_e\alpha_\pi^2\zeta_{Fe}^2}{4}\left[\frac{\alpha_{x^2-y^2}^2(\cos\theta - \sin\theta)^2}{\left(\Delta_{x^2-y^2}\right)^2} - \frac{(\cos\theta - \sin\theta)^2}{(\Delta_{xy})^2} + \frac{3\alpha_{z^2}^2(\cos\theta + \sin\theta)^2}{(\Delta_{z^2})^2}\right]$$

$$g_{zz} = g_e - 2\sin 2\theta \qquad 5.16$$

$$- \frac{\alpha_\pi^2\alpha_{x^2-y^2}^2\zeta_{Fe}^2[\cos\theta - \sin\theta]^2}{\Delta_{xy}\Delta_{x^2-y^2}} + g_e\left[\frac{\alpha_\pi^2\zeta_{Fe}^2[\cos\theta - \sin\theta]^2}{4\left(\Delta_{xy}\right)^2} - \frac{\alpha_\pi^2\alpha_{x^2-y^2}^2\zeta_{Fe}^2[\cos\theta - \sin\theta]^2}{4\left(\Delta_{x^2-y^2}\right)^2} - \frac{3\alpha_\pi^2\alpha_{z^2}^2\zeta_{Fe}^2[\cos\theta + \sin\theta]^2}{4\left(\Delta_{z^2}\right)^2}\right]$$

[6] An alternative way is to calculate the eigenvalues under the assumption of a magnetic field along the x-, y- or z-axis, resulting in the energy separation between the two levels, e.g. ΔE_x for $B_x \neq B_y = B_z = 0$. This has to coincide with the resonance condition $h\nu = g_{xx}\mu B = \Delta E_x$ from which the desired expression for g_{xx} is obtained.[108-109]

In the case that $\Delta_{xz} \gg \zeta$, the angle θ minimizes and the small-angle approximation can be applied for $\cos\theta$, $\sin\theta$ and $\tan\theta$ in Equations 5.7, 5.8 and 5.9. This way it is possible to show that the Equations 5.14, 5.15 and 5.16 turn in to the equations for the non-degenerate case (Equation 5.2, 5.3 and 5.4).

The fictitious angle θ can be computed from α_π and $\Delta_{xz}(^2B_1[2b_2(\pi_y^*)\rightarrow 2b_1(\pi_x^*)])$ that were obtained from the CASSCF/NEVPT2 calculations (see Equations 5.7-5.9, page 141) and will be denoted by θ_{calc} in the following. However, when terms of quadratic order in energy (Δ_n^{-2}) are neglected (it will be shown that these contributions are very small), Equation 5.16 allows to obtain θ directly from the experimental g_{zz}-value. In the following, the angle derived from the experimental g_{zz}-value will be denoted by θ_{exp}.

$$2\arcsin\left(\frac{g_e - g_{zz}}{2}\right) = \theta_{exp} \qquad 5.17$$

Using θ_{exp} derived from the experimental g_{zz}-value will avoid inaccuracies that might be introduced through the calculated excitation energy $\Delta_{xz}(^2B_1[2b_2(\pi_y^*)\rightarrow 2b_1(\pi_x^*)])$ and the MO-coefficient α_π when calculating the spin-orbit coupling matrix element between the close lying $^2B_1$ and $^2B_2$ states.

It is further seen in the formulas 5.14, 5.15 and 5.16 that not only g_{zz}-depends on the low-lying $^2B_1[2b_2(\pi_y^*)\rightarrow 2b_1(\pi_x^*)]$ excited state. The g_{xx}- and g_{yy}-values are also affected by this excitation via the fictitious angle θ, which is not the case in non-degenerate case (see Equations 5.2-5.4, page 139).

5.6.2. Resulting g-Values from Spin-Hamiltonian Expressions

The CASSCF/NEVPT2 calculated excitation energies (Table 5.8) and MO-coefficients derived from the Loewdin orbital composition (Table 5.7) are used to calculate g-values with the equations 5.14-5.16. Further, a spin-orbit coupling constant ζ_{Fe}=578 cm^{-1} is used for iron(V).[131] Contributions by terms of the order Δ_n^{-2} in equations 5.14-5.16 are small and therefore neglected in the following discussion (these are provided in Appendix 7.1.3, Table 7.1 and Table 7.2 page 209).

In agreement with the experimental results, all three g-values obtained with θ_{calc}, θ_{exp} and those calculated directly with the CASSCF/NEVPT2 method are smaller than g_e=2.0023 (see Table 5.9.).

Table 5.9: g-Values obtained with the derived Eq. 5.14- 5.16 calculated with θ_{calc} (CASSCF/NEVPT2) and θ_{exp} (obtained from experimental g_{zz}-values). Further, g-values calculated directly by CASSCF/NEVPT2 and experimental results are provided.

	LFT (θ_{calc})			LFT (θ_{exp})		NEVPT2/CASSCF			experimental		
	g_{xx}	g_{yy}	g_{zz}	g_{xx}	g_{yy}	g_2	g_3	g_1	g_2	g_3	g_1
$[Fe^V(N)cyc\text{-}ac]^+$	1.322	1.551	0.715	1.518	1.768	1.317	1.379	0.363	1.629	1.746	1.036
$[Fe^V(N)(N_3)cyc]^+$	1.513	1.703	0.900	1.564	1.755	1.460	1.492	0.339	1.626	1.748	0.985
$[Fe^V(N)TMC\text{-}ac]^+$	1.528	1.802	1.117	1.432	1.690	1.540	1.561	0.406	1.547	1.677	0.919
$[Fe^V(N)TPP]$	1.602	1.859	1.190	-	-	1.629	1.714	0.687	1.539	1.802	(1)
$[Fe^V(O)TAML]^-$	1.760	2.044	1.634	1.779	2.058	1.931	2.021	1.648	1.97[a]	1.99[a]	1.74[a]
$[Fe^V(O)cyc\text{-}ac]^{2+}$	1.639	1.816	1.009	-	-	1.507	1.556	0.621	-	-	-

a: g-values taken from literature[76], all other values are from own measurements (see Chapter 5.4).

General trends of the experimental g-values are reasonably well reproduced by the SH-equations with θ_{calc}, however, the g-values are systematically underestimated. g-Values obtained directly from the CASSCF/NEVPT2 calculations also reproduce the general trends of the experimental results, however, they are also systematically to low. Making use of θ_{exp} results in very good agreement between experimental and calculated g_{xx}-/g_{yy}-values (g_{zz} calculated with θ_{exp} is of course identical to the experimental g_{zz}-value).

Obviously the value used for θ has to be very accurate to obtain reasonable g-values with the SH-equations. It was shown previously for the AlO molecule[205] that accurate prediction of low-lying excited states is necessary to reproduce experimental g-values precisely. This indicates that due to the dependence of θ on $\Delta_{xz}(^2B_2)$ (see Equation 5.7/5.8, page 141), inaccurateness in this calculated low-lying excitation significantly affects the g-values. By making use of θ_{exp} (obtained from the experimental g_{zz}-values) in equations 5.14-5.16, excellent agreement with the experimental g-values is obtained.

The individual contributions from different terms in Equation 5.14-5.16 are listed in Table 5.10 obtained with θ_{calc} and in Table 5.11 with θ_{exp} obtained from the experimental g_{zz}-value. Contributions by terms of the order Δ_n^{-2} in equations 5.14-5.16 are provided in Appendix 7.1.3, Table 7.1 and Table 7.2 page 209. Since these contributions are small they are neglected in the following.

Table 5.10: Contributions to the g-values by different terms obtained with θ_{calc}.

				g_{xx}			g_{yy}			g_{zz}
	$\cos^2\theta_{calc}$	$\sin^2\theta_{calc}$	$g_e\cos 2\theta_{calc}$	$\Delta_{x^2-y^2}$ (1^2A_1)	Δ_{z^2} (2^2A_1)	Δ_{xy} ($^2A_2$)	$\Delta_{x^2-y^2}$ (1^2A_1)	Δ_{z^2} (2^2A_1)	Δ_{xy} ($^2A_2$)	$2\sin 2\theta_{calc}$
$[Fe^V(N)cyc\text{-}ac]^+$	0.883	0.117	1.533	-0.106	-0.111	0.006	-0.039	0.040	0.017	-1.287
$[Fe^V(N)(N_3)cyc]^+$	0.917	0.083	1.671	-0.058	-0.105	0.005	-0.017	0.032	0.018	-1.102
$[Fe^V(N)TMC\text{-}ac]+$	0.948	0.052	1.795	-0.165	-0.107	0.005	-0.039	0.025	0.020	-0.885
$[Fe^V(N)TPP]$	0.957	0.043	1.830	-0.089	-0.142	0.004	-0.019	0.030	0.018	-0.812
$[Fe^V(O)TAML]^-$	0.991	0.009	1.968	-0.018	-0.195	0.005	-0.002	0.018	0.059	-0.368
$[Fe^V(O)cyc\text{-}ac]^{2+}$	0.934	0.066	1.738	-0.015	-0.098	0.015	-0.004	0.026	0.056	-0.993

Table 5.11: Contributions to the g-values by different terms obtained with θ_{exp}.

				g_{xx}			g_{yy}			g_{zz}
	$\cos^2\theta_{exp}$	$\sin^2\theta_{exp}$	$g_e\cos 2\theta_{exp}$	$\Delta_{x^2-y^2}$ (1^2A_1)	Δ_{z^2} (2^2A_1)	Δ_{xy} ($^2A_2$)	$\Delta_{x^2-y^2}$ (1^2A_1)	Δ_{z^2} (2^2A_1)	Δ_{xy} ($^2A_2$)	$2\sin 2\theta_{exp}$
$[Fe^V(N)cyc\text{-}ac]^+$	0.938	0.062	1.753	-0.131	-0.109	0.005	-0.034	0.028	0.021	-0.966
$[Fe^V(N)(N_3)cyc]^+$	0.930	0.070	1.724	-0.061	-0.105	0.005	-0.017	0.029	0.019	-1.017
$[Fe^V(N)TMC\text{-}ac]+$	0.920	0.080	1.683	-0.148	-0.109	0.005	-0.043	0.032	0.018	-1.083
$[Fe^V(O)TAML]^-$	0.996	0.004	1.985	-0.019	-0.191	0.004	-0.001	0.013	0.061	-0.262

The values $\cos^2\theta$ and $\sin^2\theta$ indicate how much the low lying $^2B_2[2b_2(\pi_y^*)\rightarrow 2b_1(\pi_x^*)]$ excited state with the excitation energy Δ_{xz} affects the g-values. For the TAML complex, the largest Δ_{xz} is calculated in the series of compounds which is clearly reflected in the very low value of $\sin^2\theta$.

In the non-degenerate case, excitations of the unpaired electron into an empty orbital always cause a negative g-shift ($g_{nn}<g_e$) while excitations from a doubly occupied orbital into the singly occupied orbital cause a positive g shift ($g_{nn}>g_e$).[119-120] However, in a degenerate perturbation theory treatment as it is outlined here, this is not the case anymore. The term that arises from the perturbation sum which includes the excitation $\Delta_{z^2}[2b_2(\pi_y^*)\rightarrow 4a_1(\sigma_z^*/d_{z^2})]$ in the denominator causes a positive contribution to the g_{yy}-value (see Table 5.10 or Table 5.11), even it is an excitation from the SOMO to an empty orbital.

Dependence of the g-values on the low-lying $^2B_1[2b_2(\pi_y^*)\rightarrow 2b_1(\pi_x^*)]$ excited state

As seen in Equations 5.7-5.9, cos θ and sin θ are functions of the fraction $\alpha_\pi^2\zeta_{Fe}/\Delta_{xz}(^2B_1)$. The nominator results from the reduced spin-orbit coupling matrix element between the nearly degenerate states $^2B_2[(d_{xy})^2(\pi_y^*)^1]$ (ground state) and $^2B_1[(d_{xy})^2(\pi_x^*)^1]$ (first excited state), while the denominator is the energetic (rhombic) splitting of these two states. Given that both contributions are at the same order of magnitude (*vide supra*), small changes in the rhombic splitting can have notable effects on cos θ and sin θ, and therefore on the g-values. These changes can be caused by Jahn-Teller distortion or simply result from a non-symmetric coordination environment (the ligand system).

Understanding the influence of the low-lying $^2B_1[2b_2(\pi_y^*)\rightarrow 2b_1(\pi_x^*)]$ excited state on the g-values is important to interpret EPR-spectra of the present complexes properly and to transfer the findings on more complex biological or industrial systems for which the species studied here might serve as model complexes. Therefore, this effect will be explored in more detail for the $[Fe^V(N)cyc\text{-}ac]^+$ complex.

Analysis of the g-values as a function of the lowest excited state is easily done by varying the excitation energy $\Delta_{xz}(^2B_1)$ in Equations 5.14-5.16 while keeping all other parameters constant to the CASSCF/NEVPT2 calculated values for the remaining excitations. Further, in the CASSCF/NEVPT2 calculations the diagonal element of the spin-orbit coupling matrix for the $^2B_1(\Delta_{xz})$ excited state is varied stepwise in the range 300 cm^{-1}-5000 cm^{-1}. g-Values as a function of $^2B_1(\Delta_{xz})$ are shown in Figure 5.20, the experimental g-values are indicated by grey dashed lines. The upper x-axis ($\sin^2\theta$x100) indicates the contribution of the lowest excited state via spin orbit coupling on the ground state (cf. Equation 5.6).

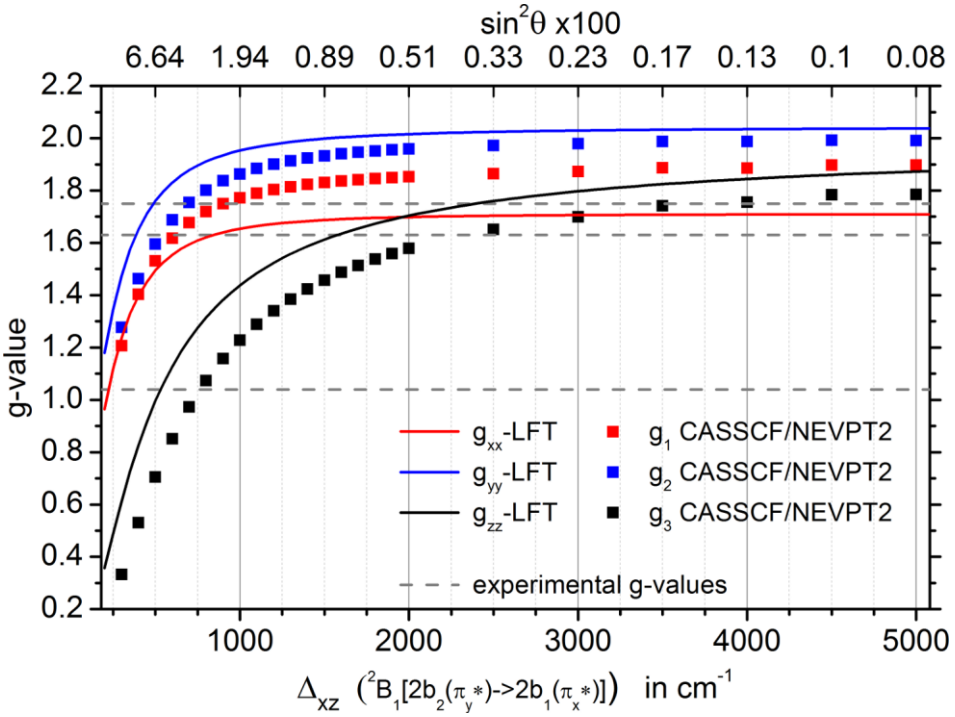

Figure 5.20: Dependence of the g-values on Δ_{xz} , obtained by SH-equations (solid lines) and CASSCF/NEVPT2 calculations (squares) for the $[Fe^V(N)cyc\text{-}ac]^+$ complex. Experimental g-values are indicated by grey dashed lines.

The plot in Figure 5.20 demonstrates a steep dependence of all three g-values on Δ_{xz} for small excitation energies ($\Delta_{xz}(^2B_1)$<1500 cm^{-1}). Traces for the SH-formulas 5.14-5.16 and the more sophisticated CASSCF/NEVPT2 calculations run very parallel and g_{zz}- and g_{yy}-values obtained from the CASSCF/NEVPT2 calculations are systematically smaller than those obtained from the SH-equations. The g_{xx}-values obtained from the CASSCF/NEVPT2 calculations are systematically larger than those obtained from the LFT-expressions and agreement between both approaches is generally slightly inferior than for the g_{yy}- and g_{zz}-values. This is probably a result of the much more accurate incorporation of covalency in the quantum chemical calculations. In deriving the SH-equations, several ligand-metal and ligand-ligand overlap integrals were neglected, in particular for the expressions for g_{xx} (this can be seen by detailed inspection of the calculated orbital Zeeman terms provided in Appendix 7.1.1, page 205 and the applied approximations).

The curve for the g_{zz}-value obtained by the CASSCF/NEVPT2 method reveals that at $\Delta_{xz} \approx$ 800 cm^{-1} best agreement between the experimental and calculated g_{zz}-value is found, hence, ~460 cm^{-1} above the calculated value of 340 cm^{-1} (see Table 5.8, page 136). For g_{xx} and g_{yy} best agreement is found at ~600 cm^{-1}/700 cm^{-1}, hence, 260 cm^{-1}/360 cm^{-1} above the calculated excitation energy, respectively. This demonstrates that the calculated $\Delta_{xz}(^2B_1)$ value is only few hundred wave numbers to low. Hence, the absolute deviation is a very small, beyond the accuracy of the CASSCF/NEVPT2 method, however, since the excitation energy itself is very small the relative deviation is large.

g-Values obtained directly from the CASSCF calculations as well as those obtained with the SH expressions and θ_{calc} are underestimated (see Table 5.9), which also indicates that the lowest excitation energy $\Delta_{xz}(^2B_1)$ calculated by CASSCF/NEVPT2 is underestimated by very few hundred wave numbers.

On the other hand, it should be also noted that minor changes in the calculated spin-orbit coupling matrix element between the low lying $^2B_2$ and $^2B_1$ states will have a similar effect on the g-values. Overestimating the spin-orbit coupling matrix element will result in smaller g-values. By determining θ_{exp} from the experimental g_{zz}-value, both potential sources of inaccuracy are circumvented.

Previously reported experimental g-values for the [Fe^V(O)TAML]$^-$ complex are significantly larger than those presented here for the tetragonal nitrido-iron(V) complexes (see Table 5.9).[76] This is completely in line with the just demonstrated dependence of the g-values on the low-lying $^2B_1[2b_2(\pi_y^*)\rightarrow 2b_1(\pi_x^*)]$ excitation. This excitation is calculated to be much higher in energy for the [Fe^V(N)TAML]$^-$ complex when compared to the nitrido-species (see Table 5.8), resulting in a smaller g-shift and larger g-values.

g-Values of oxo- versus nitrido-complexes

The electronic structure of nitrido-iron(V) and oxo-iron(V) complexes was studied computationally in Chapter 5.5.2. Given that analog oxo- and nitrido-complexes with identical ligand systems do not exist, the hypothetical species $[Fe^{V}(O)cyc\text{-}ac]^{2+}$ was included in the calculations, which is the oxo-analog of the experimentally studied complex $[Fe^{V}(N)cyc\text{-}ac]^{+}$. The CASSCF/NEVPT2 calculations have demonstrated stronger covalency in the nitrido complexes that further affects the excitation energies (see discussion in Chapter 5.5.2). g-Values for the nitrido-complex $[Fe^{V}(N)cyc\text{-}ac]^{+}$ were calculated as 1.317, 1.379 and 0.363 and for the oxo-complex $[Fe^{V}(O)cyc\text{-}ac]^{2+}$ as 1.507, 1.556 and 0.621, respectively. Hence, in the calculations the g-values for the oxo-iron(V) complex appear to be larger than for the nitrido-iron(V) complex. However, in the antecedent section it was shown that the g-values strongly depend on the lowest excited state $^{2}B_1[2b_2(\pi_y^*)\rightarrow 2b_1(\pi_x^*)]$ which was calculated to be 340 cm^{-1} for the nitrido and 627 cm^{-1} for the oxo-complex. This is in line with the analysis on the previous pages that has shown that a lower $\Delta_{xz}(^{2}B_1)$ excitation energy results in smaller g-values. In the antecedent section it was further demonstrated that the derived Equations 5.14-5.16 provide a good basis for analyzing the g-values. Differences in the g-values for the nitrido-iron(V) and oxo-iron(V) complexes, therefore, can be compared in terms of the derived equations. For the analog complexes $[Fe^{V}(N)cyc\text{-}ac]^{+}$ and $[Fe^{V}(O)cyc\text{-}ac]^{2+}$ g-values are plotted as a function of the lowest excitation Δ_{xz} in Figure 5.21, which allows to compare the resulting g-values independent of Δ_{xz}. All other parameters in Equations 5.14-5.16 were kept to the calculated values provided in Table 5.7 and Table 5.8. Selected points of the shown curves are provided in Table 5.12 and Table 5.13 for the nitrido- and oxo-complex, respectively, including the individual contributions by various terms in the Equations 5.14-5.16.

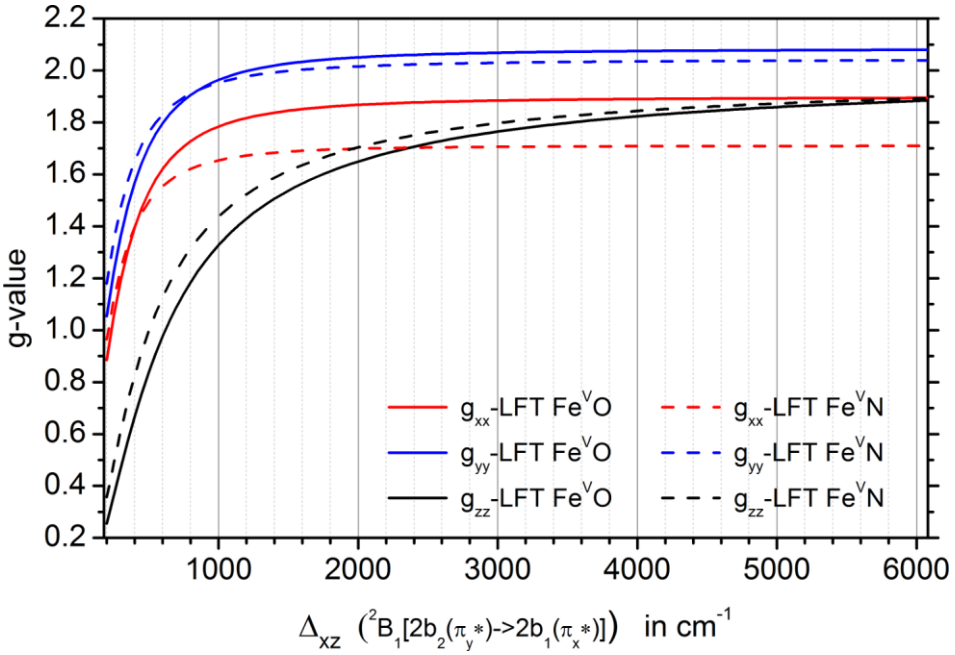

Figure 5.21: Dependence of the g-values for the $[Fe^{V}(N)cyc\text{-}ac]^{+}$ and $[Fe^{V}(O)cyc\text{-}ac]^{2+}$ complexes on the $^{2}B_1[2b_2(\pi_y^*)\rightarrow 2b_1(\pi_x^*)]$ excited state.

The g_{yy}-values for both complexes turn out to be very similar, which is rather unexpected. The g_{yy}-value significantly depends on the $\Delta_{xy}(^{2}A_2)$ excitation energy and contributions from the $\Delta_{z^2}(2^{2}A_1)$ and $\Delta_{x^2-y^2}(1^{2}A_1)$ excitations mainly cancel out (see Table 5.12 and Table 5.13). However, the $^{2}A_2[1a_2(d_{xy})\rightarrow 2b_2(\pi_y^*)]$ excited state was calculated to be much higher in energy for the nitrido- than

for the oxo-complexes (see Table 5.8). Therefore, a significantly larger g_{yy}-value would be expected for the nitrido-complex as it is seen in the Δ_{xy} contribution to g_{yy} in Table 5.12 and Table 5.13, respectively. However, this effect is cancelled out via the $g_e \cos 2\theta$ term which is larger for the nitrido-complex due to the higher degree of covalency, resulting in very similar g_{yy}-values for the oxo- and nitrido-complexes.

The most significant difference between the oxo- and nitrido-complexes can be seen in the g_{xx}-values in Figure 5.21, that are slightly smaller for the nitrido- than for the oxo-complex. This g-value is mainly affected by the $1^2A_1[2b_2(\pi_y^*)\rightarrow 3a_1(d_{x^2-y^2})]$ ($\Delta_{x^2-y^2}$) and $2^2A_1[2b_2(\pi_y^*)\rightarrow 4a_1(d_{z^2})]$ (Δ_{z^2}) excitations. The 2^2A_1 excited state was calculated to appear only slightly higher in energy for the oxo-complex (23845 cm^{-1}) when compared to the nitrido-complex (16959 cm^{-1}) while the 1^2A_1 excited state was calculated to appear at much higher energy for the oxo-complex (23683 cm^{-1}) than for the nitrido-complex (2653 cm^{-1}). As can be seen in Table 5.12 and Table 5.13, the negative g-shift caused by $1^2A_1(\Delta_{x^2-y^2})$ on g_{xx}, which is not compensated by the$g_e \cos 2\theta$ term that is larger for the nitride, results in a smaller g_{xx}-value for the nitrido-complex.

Table 5.12: Contributions for selected points from the curve shown in Figure 5.21 for $[Fe^V(N)cyc\text{-}ac]^+$.

		g_{xx}			g_{yy}			g_{zz}	resulting g-values:		
Δ_{xz} [cm^{-1}]	$g_e \cos 2\theta_{calc}$	$\Delta_{x^2-y^2}$ 1^2A_1)	Δ_{z^2} (2^2A_1)	Δ_{xy} ($^2A_2$)	$\Delta_{x^2-y^2}$ 1^2A_1)	Δ_{z^2} (2^2A_1)	Δ_{xy} ($^2A_2$)	$2 \sin 2\theta_{calc}$	g_{xx}	g_{yy}	g_{zz}
500	1.737	-0.130	-0.109	0.005	-0.035	0.029	0.020	-0.996	1.503	1.751	1.005
1000	1.925	-0.160	-0.103	0.004	-0.022	0.015	0.025	-0.552	1.665	1.942	1.448
1500	1.967	-0.170	-0.100	0.003	-0.016	0.010	0.027	-0.376	1.699	1.987	1.624
2000	1.982	-0.175	-0.098	0.002	-0.012	0.007	0.027	-0.284	1.711	2.004	1.716
2500	1.989	-0.178	-0.097	0.002	-0.010	0.006	0.028	-0.228	1.716	2.012	1.772
3000	1.993	-0.180	-0.097	0.001	-0.009	0.005	0.028	-0.190	1.718	2.017	1.809
3500	1.996	-0.181	-0.096	0.001	-0.007	0.004	0.028	-0.163	1.720	2.021	1.836
4000	1.997	-0.182	-0.096	0.001	-0.007	0.003	0.029	-0.143	1.720	2.023	1.857

Table 5.13: Contributions for selected points from the curve shown in Figure 5.21 for $[Fe^V(O)cyc\text{-}ac]^{2+}$.

		g_{xx}			g_{yy}			g_{zz}	resulting g-values:		
Δ_{xz} [cm^{-1}]	$g_e \cos 2\theta_{calc}$	$\Delta_{x^2-y^2}$ (1^2A_1)	Δ_{z^2} (2^2A_1)	Δ_{xy} ($^2A_2$)	$\Delta_{x^2-y^2}$ (1^2A_1)	Δ_{z^2} (2^2A_1)	Δ_{xy} ($^2A_2$)	$2 \sin 2\theta_{calc}$	g_{xx}	g_{yy}	g_{zz}
500	1.625	-0.014	-0.100	0.016	-0.004	0.032	0.050	-1.168	1.528	1.703	0.834
1000	1.884	-0.018	-0.095	0.011	-0.003	0.017	0.066	-0.677	1.782	1.963	1.325
1500	1.947	-0.019	-0.092	0.008	-0.002	0.011	0.071	-0.467	1.844	2.027	1.535
2000	1.971	-0.020	-0.090	0.007	-0.002	0.008	0.074	-0.354	1.867	2.051	1.647
2500	1.982	-0.021	-0.089	0.005	-0.001	0.006	0.076	-0.285	1.878	2.063	1.717
3000	1.988	-0.021	-0.088	0.005	-0.001	0.005	0.077	-0.238	1.883	2.069	1.763
3500	1.992	-0.021	-0.088	0.004	-0.001	0.004	0.078	-0.205	1.887	2.073	1.797
4000	1.994	-0.021	-0.087	0.004	-0.001	0.004	0.078	-0.179	1.889	2.075	1.822

The g_{zz}-value only depends on the $2 \sin 2\theta_{calc}$ term, that via θ only depends on the spin orbit coupling matrix element between the close lying states $^2B_2$ and $^2B_1$ and the excitation energy $\Delta_{xz}(^2B_1)$ as can be seen in Equation 5.8. Since covalency is larger in the nitrido-complex, the spin-orbit coupling matrix element between the two close lying states is smaller for the nitride resulting in a smaller $2 \sin 2\theta_{calc}$ term for the nitride when compared to the oxide (given that identical values for Δ_{xz} are used). For the same reason $g_e \cos 2\theta$ is larger for the nitrido-complex when compared to the oxo-complex (see Equation 5.7 and the resulting values in Table 5.12 and Table 5.13).

A recent study has shown that significant differences can be found in the reactivity of nitrido-iron(V) and oxo-iron(V) complexes.[250] However, as demonstrated in the present chapter, only small variations between these two species are found in their g-values, based on differences in the excitation energies and the covalency effects. These differences between the oxo- and nitrido-complexes cancel out to a large degree in the resulting g-values. Hence, distinguishing the oxo and nitrido species solely based on X-Band EPR measurements might be challenging as long as hyperfine coupling is not properly resolved. Within the present work attempts were also made to use more advanced EPR techniques (ENDOR, HYSCORE, ESEEM), however, these experiments were unfortunately not successful.

5.7. The Complex $[Fe^{V}(O)(TMC(NC(O)CH_3))]^{+}$

In 2012 the tetragonal oxo-iron(V) complex $[Fe^{V}(O)(TMC)(NC(O)CH_3)]^{+}$ was published by the group of Lawrence Que (see Scheme 5.3).[77] The complex features an acetylimido ligand that was formed upon oxidation of a coordinate acetonitrile solvent molecule in the $[Fe^{IV}(O)(TMC)(MeCN)]^{2+}$ species (this iron(IV) complex will be discussed in detail in Chapter 6).

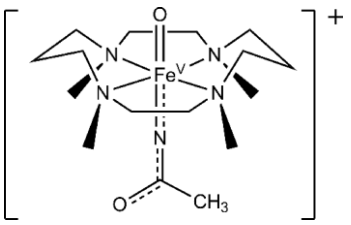

Scheme 5.3: $Fe^{V}O$ complex published by Que *et al*.[77]

Interestingly, the g-values 1.971, 2.010 and 2.053 for this complex significantly differ from those that were recorded for the tetragonal nitrido-iron(V) complexes (see Chapter 5.1) and the previously published $[Fe^{V}(O)TAML]^{-}$ complex. They do further not show the $g_1,g_2<g_e<g_3$ pattern expected for a $(xy)^2(yz)^1$ electronic configuration with Equation 5.2-5.4. In the present chapter, the electronic structure and resulting g-values will be analyzed and compared with tetragonal iron(V) complexes discussed in the previous chapters.

5.7.1. Electronic Structure Calculations

Previously published DFT-calculations on the $[Fe^{V}(O)(TMC)(NC(O)CH_3)]^{+}$ complex already revealed, that the electronic structure is more complex and delocalized than for other iron(V) complexes. The need of including an iron(IV) resonance structure with a ligand based radical for a balanced description of the electronic structure was also discussed.[77] Therefore, a large active space for the CASSCF calculations is chosen to consider as accurate as possible the delocalization and to calculate excited states and spectroscopic parameters properly.All iron 3d-orbitals, the 2p orbitals of the oxo-ligand, the nitrogen $2p_x$- and $2p_y$-orbitals of the acetylimido ligand and the bonding combination of the cyclam nitrogen lone-pairs in the equatorial plane (N_{eq}) with the iron $d_{x^2-y^2}$-orbital were included. This results in an active space of 15 electrons in 11 orbitals. Coordinates were used, that are provided in the literature from a structure optimized at the BP86/6-311G level of theory.[77] Active space orbitals from a SA-CASSCF(15,11) calculation over 3 roots are shown in Figure 5.22 and the Loewdin orbital composition is provided in Table 5.14.

The plot demonstrates strong covalency and incorporation of the acetylimido nitrogen 2p-orbitals in a delocalized π-system within the linear [O=Fe=N]-group. This results in a bonding combination without nodal plane (π_x, π_y), a linear-combination with one nodal plane (π_x*, π_y*) and a linear-combination with two nodal planes (π_x**/d_{xz}, π_y**/d_{yz}). All of these π-orbitals can be found in the orbital plot, even not all orbitals are equally delocalized over the N-, Fe- and O-atoms (see Figure 5.22 and Loewdin orbital composition in Table 5.14).

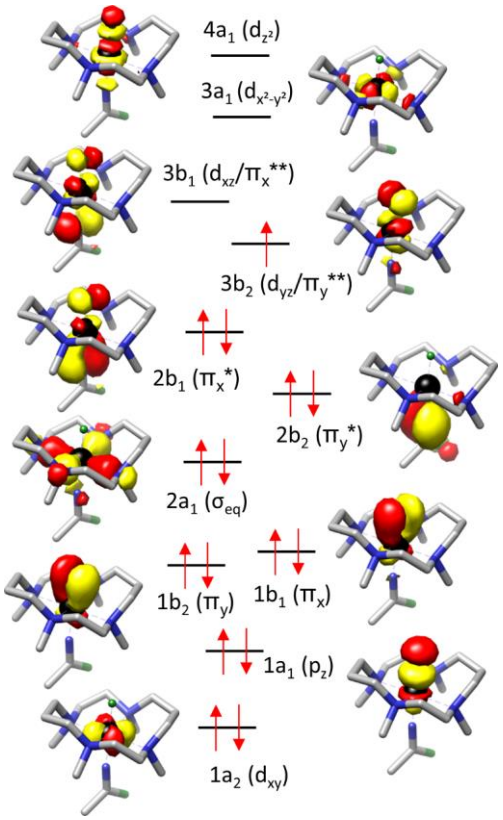

Figure 5.22: Active space orbitals from SA-CASSCF(15,11)/3 roots calculation on $[Fe^{V}(O)(TMC)(NC(O)CH_3)]^+$ and outlined ground state electronic configuration. Hydrogen atoms are omitted for clarity.

Table 5.14: Loewdin orbital composition from SA-CASSCF(15,11)/3 roots calculation and MO-coefficients.

	Loewdin orbital composition							MO-coefficients					
MO	Fe [%]	O [%]	N [%]	N_{eq} [%]	C [%]	O' [%]		Fe	O	N	N_{eq}	C	O'
$1a_1$ (σ_z/p_z)	31	65						0.57	0.82				
$1b_2$ (π_y)	32	65					$\alpha''_{yz}/\beta''^{O}_{y}$	0.57	0.82				
$1b_1$ (π_x)	35	59	1				$\alpha''_{xz}/\beta''^{O}_{x}$	0.61	0.78	0.12			
$1a_2$ (d_{xy})	98							1					
$2a_1$ (σ_{eq})	19			14				0.51			0.43		
$2b_2$ (π_y*)	7	0	63	0	13	8	$\alpha''_{yz}/\beta''^{O}_{y}/\beta''^{N}_{y}$	0.27		0.83		0.38	0.29
$2b_1$ (π_x*)	24	22	43		5		$\alpha'_{xz}/\beta'^{O}_{x}/\beta'^{N}_{x}$	0.50	0.48	0.68		0.23	
$3b_2$ (π_y**)	68	27	2				$\alpha_{yz}/\beta^{O}_{y}/\beta^{N}_{y}$	0.84	0.53	0.16			
$3b_1$ (π_x**)	46	12	34		4		$\alpha_{xz}/\beta^{O}_{x}/\beta^{N}_{x}$	0.69	0.35	0.59		0.20	
$3a_1$ ($d_{x^2-y^2}$)	88			2			$\alpha_{x^2-y^2}/\beta_{eq}$	0.96		0.15			
$4a_1$ (d_{z^2})	67	24	3				$\alpha_{z^2}/\beta^{O}_{z}$	0.86	0.51				

As it was the case for the already discussed oxo-iron(V) complexes (see Chapter 5.5), the singly occupied orbital is an iron-oxo π_y**-orbital of b_2-symmetry (in C_{2V}) which is mainly derived from the metal d_{yz}-orbital. The corresponding unoccupied π_x**-orbital ($3b_1$) is mainly derived from the metal d_{xz}-orbital but the acetylimido nitrogen p_x-orbital also contributes significantly (34%, see Table 5.14). The $2b_1(\pi_x*)$ and $2b_2(\pi_y*)$ orbitals are mainly derived from the acetylimido nitrogen atom, the $1b_1(\pi_x)$ and $1b_2(\pi_y)$ orbitals are mainly derived from the mono atomic oxo-ligand. Describing the metal center as iron(V), $(d_{xy})^2(d_{yz})^1$ with an bis-anionic acetylimido ligand is therefore fully consistent with the orbital picture provided in Figure 5.22 and the Loewdin orbital composition in Table 5.14, even the electronic structure is partially delocalized.

SA-CASSCF(15,11)/NEVPT2 calculations were also performed with 40 roots to obtain one-electron excitation energies. The results that are summarized in Table 5.15 reveal some clear differences when compared to the tetragonal oxo-iron(V) complexes $[Fe^{V}(O)TAML]^{-}$, $[Fe^{V}(O)cyc\text{-}ac]^{2+}$ or the nitrido-iron(V) complexes discussed in Chapter 5.5.2.

Table 5.15: Excitation energies from SA-CASSCF(15,11)/NEVPT2 calculation with 40 roots on the $[Fe^{V}(O)TMC(NC(O)CH_3]^{+}$ complex.

dd-transitions	1^2A_1 $[3b_2(d_{yz})\rightarrow 3a_1(d_{x^2-y^2})]$	1^2B_1 $[3b_2(d_{yz})\rightarrow 3b_1(d_{xz})]$	1^2A_2 $[1a_1(d_{xy})\rightarrow 3b_2(d_{yz})]$	2^2A_1 $[3b_2(d_{yz})\rightarrow 4a_1(d_{z^2})]$
	$[cm^{-1}]$	$[cm^{-1}]$	$[cm^{-1}]$	$[cm^{-1}]$
	6369	7573	18825	19224
LMCT-transitions	2^2B_1 $[2b_1(\pi_x^*)\rightarrow 3b_2(d_{yz})]$	1^2B_2 $[2b_2(\pi_y^*)\rightarrow 3b_2(d_{yz})]$	3^2B_1 $[1b_1(\pi_x)\rightarrow 3b_2(d_{yz})]$	2^2B_2 $[1b_2(\pi_y)\rightarrow 3b_2(d_{yz})]$
	$[cm^{-1}]$	$[cm^{-1}]$	$[cm^{-1}]$	$[cm^{-1}]$
	10966	15193	23852	23234

While for the iron(V) complexes discussed in Chapter 5.5 a very low lying $^2B_1[3b_2(d_{yz})\rightarrow 3b_1(d_{xz})]$ excited state was calculated, the lowest excited state for the complex $[Fe^{V}(O)TMC(NC(O)CH_3]^{+}$ is predicted to be the $1^2A_1[3b_2(d_{yz})\rightarrow 3a_1(d_{x^2-y^2})]$ state. This state is separated from the $^2B_2$ ground state by 6369 cm^{-1}, hence, the ground state is far off from being degenerate. The $^2B_1[3b_2(d_{yz})\rightarrow 3b_1(d_{xz})]$ state is calculated to be the second lowest excited state (7573 cm^{-1}), which was calculated to be the lowest excited state for the iron(V)-complexes discussed in Chapter 5.5.2. This demonstrates that the present complex is fare off from being C_4-symmetric which was already concluded by Que *et al.* based on the x/y anisotropy of the ^{57}Fe and ^{17}O A-tensor.[77] The $1^2A_2[1a_1(d_{xy})\rightarrow 3b_2(d_{yz})]$ excited state was calculated to be 18825 cm^{-1}, which is at the same order of magnitude as it was calculated for the nitrido-iron(V) complexes in Chapter 5.5.2 (see Table 5.8, page 136) and significant higher in energy when compared to the oxo-iron(V) complexes $[Fe^{V}(O)cyc\text{-}ac]^{2+}$ (8764 cm^{-1}) and $[Fe^{V}(O)TAML]^{-}$ (12016 cm^{-1}). It can, therefore, be concluded that the π(FeO)-bond in the $[Fe^{V}(O)TMC(NC(O)CH_3]^{+}$ complex is as strong as the π(FeN)-bond in the nitrido-iron(V) complexes, and stronger than in the oxo-iron(V) complexes $[Fe^{V}(O)TAML]^{-}$ and $[Fe^{V}(O)cyc\text{-}ac]^{2+}$ (see discussion in Chapter 5.5.2).

Another remarkable difference are low lying LMCT transitions from the π-orbitals of the [O-Fe-N] unit into the SOMO; $2^2B_1[2b_1(\pi_x^*)\rightarrow 3b_2(d_{yz})]$, $3^2B_1[1b_1(\pi_x)\rightarrow 3b_2(d_{yz})]$, $1^2B_2[2b_2(\pi_y^*)\rightarrow 3b_2(d_{yz})]$ and $2^2B_2[b_2(\pi_y)\rightarrow 3b_2(d_{yz})]$, respectively (see Table 5.15). As these are LMCT-transition, they are expected to show significantly higher intensity in the absorption spectrum than the d-d-transitions. Indeed, two absorption bands were observed in the experimental spectrum at 12821 cm^{-1} and 24390 cm^{-1} which is in reasonable agreement with the calculations (see Table 5.15).[77] Given that the LMCT-transitions 2^2B_1 and 3^2B_1 can couple with the $^2B_2$-ground state via spin-orbit coupling ($B_1\otimes A_2\otimes B_2=A_1$, where A_2 is the irreducible representation for a rotation with respect to the z-axis), they contribute to the shift of the g-value from g_e. Hence, they have to be taken into account in the interpretation of the g_{zz}-value as will be shown in the following section.

5.7.2. Interpretation of the g-Values

Quantum chemical calculation (*vide supra*) on the complex $[Fe^{V}(O)TMC(NC(O)CH_3]^+$ have revealed that not only the oxo-ligand, but also the acetylimido ligand is covalently bond to the iron center. This has to be considered in the definition of molecular orbitals used in Equation 2.16 to derive expressions for the g-values.

$$\psi_{xy} \approx |d_{xy}\rangle \quad \text{5.18a}$$

$$\psi_{xz} \approx \alpha_{xz}|d_{xz}\rangle - \beta_x^O|p_x^O\rangle + \beta_x^N|p_x^N\rangle \quad \text{5.18b}$$

$$\psi_{yz} \approx \alpha_{yz}|d_{yz}\rangle - \beta_y^O|p_y^O\rangle + \beta_y^N|p_y^N\rangle \quad \text{5.18c}$$

$$\psi_{x^2-y^2} \approx \alpha_{x^2-y^2}|d_{x^2-y^2}\rangle + \beta_\sigma\left(|p_x^3\rangle - |p_x^1\rangle + |p_y^2\rangle - |p_y^4\rangle\right) \quad \text{5.18d}$$

$$\psi_{z^2} \approx \alpha_{z^2}|d_{z^2}\rangle - \beta_z|p_z^O\rangle \quad \text{5.18e}$$

$$\psi_{\pi_x^*} \approx \alpha'_{xz}|d_{xz}\rangle - \beta'^{O}_{x}|p_x^O\rangle - \beta'^{N}_{x}|p_x^N\rangle \quad \text{5.18f}$$

$$\psi_{\pi_x} \approx \alpha''_{xz}|d_{xz}\rangle + \beta''^{O}_{x}|p_x^O\rangle - \beta''^{N}_{x}|p_x^N\rangle \quad \text{5.18g}$$

As mentioned in the discussion of the electronic structure, LMCT-transitions with the appropriate symmetry (here $2^2B_1[\pi_x^* \rightarrow d_{yz}]$ and $3^2B_1[\pi_x \rightarrow d_{yz}]$) contribute to the g-value, in the present case to g_{zz}. With Equation 2.16 and by taking into account LMCT-transitions, the following expressions are obtained for the g-values.

$$g_{xx} = g_e - \frac{2\zeta_{Fe}\alpha_{yz}^2\alpha_{x^2-y^2}^2}{\Delta_{x^2-y^2}(1^2A_1)} - \frac{2\zeta_{Fe}(3\alpha_{yz}^2\alpha_{z^2}^2+\sqrt{3}\beta_y^O\beta_z^O\alpha_{yz}\alpha_{z^2})}{\Delta_{z^2}(2^2A_1)} \quad \text{5.19a}$$

$$g_{yy} = g_e + \frac{2\zeta_{Fe}\alpha_{yz}^2}{\Delta_{xy}(1^2A_2)} \quad \text{5.19b}$$

$$g_{zz} = g_e - \frac{2\zeta_{Fe}(\alpha_{xz}^2\alpha_{yz}^2+\beta_x^O\beta_y^O\alpha_{xz}\alpha_{yz}+\beta_x^N\beta_y^N\alpha_{xz}\alpha_{yz})}{\Delta_{xz}(1^2B_1)} + \frac{2\zeta_{Fe}(\alpha'^2_{xz}\alpha_{yz}^2+\alpha'_{xz}\alpha_{yz}\beta'^{O}_{x}\beta_y^O-\alpha'_{xz}\alpha_{yz}\beta'^{N}_{x}\beta_y^N)}{\Delta_{\pi_x^*}(2^2B_1)} + \frac{2\zeta_{Fe}(\alpha'^2_{xz}\alpha_{yz}^2-\alpha'_{xz}\alpha_{yz}\beta'^{O}_{x}\beta_y^O-\alpha''_{xz}\alpha_{yz}\beta''^{N}_{x}\beta_y^N)}{\Delta_{\pi_x}(3^2B_1)} \quad \text{5.19c}$$

It should be noted for g_{zz} that the contributions from the LMCT-states 2^2B_1 and 3^2B_1 are of opposite sign than the contribution of the dd-excited state 1^2B_1.

g-Values obtained from Equations 5.19a-c with calculated MO-coefficients (Table 5.14) and excitation energies (Table 5.15) as well as those directly obtained from the CASSCF/NEVPT2 calculations are summarized in Table 5.16 together with the reported[77] experimental results.

Table 5.16: g-Values obtained from SH-equations, CASSCF/NEVPT2 calculations and experimental ones taken from literature.[77]

	g_{xx}	g_{yy}	g_{zz}
LFT (Eq. 5.19)	1.774	2.045	1.954 (1.926)[a]
CASSCF/NEVPT2	1.955	2.006	1.962
experimental[77]	1.971	2.053	2.010

a: Without LMCT-transitions

g-Values obtained from the CASSCF/NEVPT2 calculations are systematically underestimated but still in reasonable agreement with the experimental g-values. Equations 5.19a-c also underestimate the g-values, but general trends are reasonably well reproduced. Deviations, especially for g_{xx}, might result from the rather simple description of covalency in the SH-expressions. For g_{zz} a g-value of 1.954 is obtained while it is 1.926 if the LMCT-transitions are neglected (see Table 5.16). This reflects the positive g-shift for g_{zz} due to the low lying LMCT-transitions, even their effect is small within the chosen approach. The obtained value for g_{zz} is still smaller than g_e, however, qualitatively it is shown that the low-lying LMCT-transitions are presumably the reason why two g-values larger than g_e were observed for the $[Fe^{V}(O)TMC(NC(O)CH_3]^+$ complex.

Hence, due to the ground state that is fare of from being degenerate and the low lying LMCT-transitions, observed g-values for the $[Fe^{V}(O)TMC(NC(O)CH_3]^+$ complex differ significantly from the g-values observed for the tetragonal iron(V) species discussed in Chapter 5.6.

5.8. The Complex $[Fe^{V}(N)(^{t}BuIm)_3BPh]^{+}$ [7]

The first trigonal iron(V) complex $[Fe^{V}(N)(^{t}BuIm)_3PhB]^{+}$ was synthesized in 2011 in the group of Karsten Meyer, and it is the only iron(V) complex characterized by X-ray crystallography so fare.[35] DFT-calculations were performed earlier on this complex and additional CASSCF calculations performed here allow to compare this trigonal species with the tetragonal iron(V) complexes studied in this thesis. While the ligand systems for the tetragonal iron(V) complexes do not impose high symmetry, the tris-carbene ligand shows nearly perfect three-fold symmetry. However, due to Jahn-Teller distortion the symmetry is lower than C_{3v}.

As it was done for the tetragonal iron(V) complexes, all d-orbitals and nitrido 2p-orbitals were included in the active space. Furthermore, linear-combinations of the equatorial carbene lone-pairs were included that would span a degenerated e-level within C_{3v}-symmetry. In labeling the orbitals and excited states, lower symmetry of C_{2v}-was assumed which will be justified by the calculations. Active space orbitals from this CASSCF(13,10) calculation are shown in Figure 5.23.

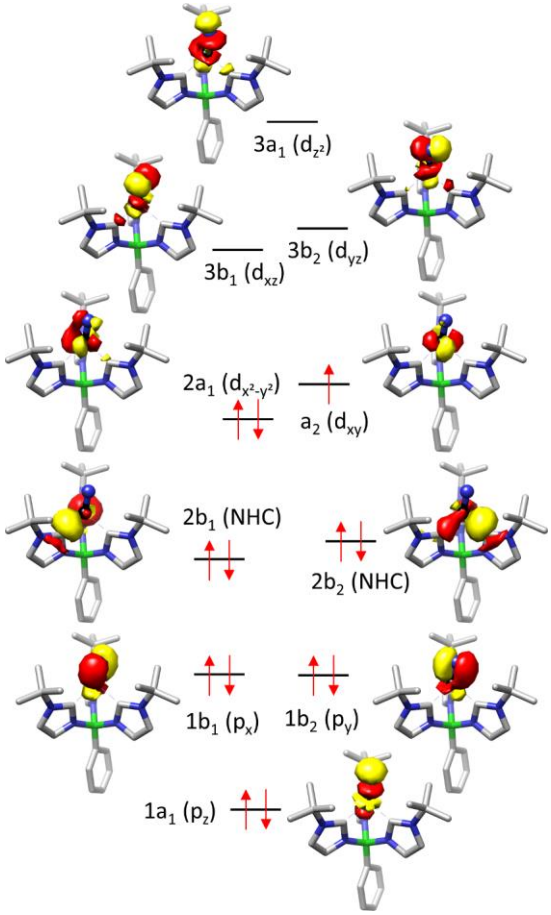

Figure 5.23: Active space orbitals from SA-CASSCF(13,10) calculations with 2-roots on the $[Fe^{V}(N)(^{t}BuIm)_3BPh]^{+}$ complex and outlined ground state electronic configuration.Hydrogen atoms are omitted.

The three d-electrons are located in the d_{xy}- and $d_{x^2-y^2}$-derived orbitals that are non-bonding with respect to the iron-nitrido bond. In contrast to the tetragonal iron(V)-complexes, the antibonding π- and σ-orbitals derived from the metal d_{xz}-, d_{yz}- and d_{z^2}-orbitals are vacant which explains the stability

[7] It should be noted here, that at the same time the complex was investigated by advanced EPR-techniques in combination with quantum mechanical calculations by Hoffman *et al.* and results were published very recent.[247]

of the trigonal iron(V) complex. As evident from the orbital plot and the Loewdin orbital composition provided in Table 5.17, the nitrido-iron bond is again strongly covalent.

Table 5.17: Loewdin orbital compositions for $[Fe^{V}(N)(^{t}BuIm)_3BPh]^{+}$ (SA-CASSCF(13,10)/2 roots)

	$1a_1$ (p_z)		$1b_2$ (p_y)		$1b_1$ (p_x)		$2b_1$ (NHC)			
	Fe	N	Fe	N	Fe	L	Fe	C	C	C
popul.	51	47	50	48	51	47	24	26	26	0

	$2b_2$ (NHC)				a_2 (d_{xy})		$2a_1$ ($d_{x^2-y^2}$)	$3b_1$ (d_{xz})		$3b_2$ (d_{yz})		$3a_1$ (d_{z^2})	
	Fe	C	C	C	Fe	N	Fe	Fe	N	Fe	L	Fe	L
popul.	27	38	8	8	85	8	91	55	37	54	38	53	42

Calculated one-electron excitation energies are provided in Table 5.18. In idealized C_{3v}-symmetry, the complex would exhibit a degenerate ^2E ground state. However, the calculations reveal a splitting of the lowest level about 4114 cm^{-1}, hence, much larger than found for the tetragonal nitrido-iron(V) complexes (see Chapter 5.5). The complex is therefore considered as C_{2v}-symmetric resulting in a $^2A_2[(d_{x^2-y^2})^2(d_{xy})^1]$ ground state, separated from the lowest $^2A_1$ excited state by 4114 cm^{-1}.

Table 5.18: Calculated excitations (NEVPT2/CASSCF(13,10)/20-roots) for the $[Fe^{V}(N)(^{t}BuIm)_3BPh]^{+}$ complex

	Calculations		Experimental[a]	
	energy [cm^{-1}]	f_{osc} ($x10^4$)	energy [cm^{-1}]	ε [M^{-1} cm^{-1}]
$^2A_1[2a_1(d_{x^2-y^2})\rightarrow 2a_2(d_{xy})]$	4114	0.1659		
$^2B_1[2a_2(d_{xy})\rightarrow 3b_1(d_{xz})]$	19681	3.0003		
$^2B_2[2a_2(d_{xy})\rightarrow 2b_2(d_{yz})]$	21063	5.9954	17762	1400
$2^2A_1[2a_2(d_{xy})\rightarrow 3a_1(d_{z^2})]$	22088	14.2601	22124	1500

a: Experimental data taken from Ref.[35]

Experimentally, absorption bands for the $[Fe^{V}(N)(^{t}BuIm)_3PhB]^{+}$ complex were observed at 17762 cm^{-1} and 22124 cm^{-1}. This is in reasonable agreement with the NEVPT2/CASSCF calculations that predict the largest oscillator strengths (f_{osc}) for the $^2B_2$, $^2B_1$ and 2^2A_1 excited states, respectively. The calculated excitation energies further indicate that the d_{z^2}-, d_{xz}- and d_{yz}-orbitals are close in energy.

g-Values were obtained from SA-CASSCF(13,10)/NEVPT2 calculations over 20 roots as 1.975, 1.976 and 2.424, and are in good agreement with the experimental results $g_{\perp}$=1.98 and $g_{||}$=2.30. Hoffman *et al.* have performed an in-depth analysis of these g-values including the effect of Jahn-Teller distortion[247] based on equations previously derived by Ammeter *et al*.[253,259-260]

Clearly, the g-shift (deviation of the g-values from g_e) for the trigonal nitrido-iron(V) complex is much smaller than for the tetragonal iron(V) species discussed in Chapter 5.6. This can be explained by the nearly degenerate ground state in the tetragonal complexes resulting in a large orbital momentum and a large g-shift, while Jahn-Teller distortion is large in the present trigonal nitrido-complex and therefore the ground state is significantly separated from other excited states. This results in a smaller orbital momentum and a smaller g-shift. Still, it was shown by Hoffman *et al.*, that the g-values of the tris-carbene complex are significantly affected by the lowest excited state,[247] as it was to a very large degree for the tetragonal iron(V) complexes as discussed in Chapter 5.6.

5.9. Decay of Tetragonal Nitrido-Iron(V) Complexes[8]

Even through there are a few nitrido-iron(V) complexes reported in the literature, little is known about their reactivity.[25] In contrast, various reactions have been performed with nitrido-iron(IV) complexes, all of which possess a pseudo-tetrahedral geometry. For example, the addition of phosphines to form the corresponding phosphoraniminato complexes,[37,39,261] and the reaction with iso-nitriles and carbon monoxide.[51] Furthermore, dimerization of nitrido-iron(IV) complexes has been observed, resulting in an Fe^{I}-NN-Fe^{I} dimer.[37,52] For the sole nitrido-iron(V) complex that has been crystallographically characterized (a pseudo tetrahedral complex with tripodal N-heterocyclic carbene ligand, NHC) formation of ammonia from water was reported.[35]

Studying the reactivity of tetragonal nitrido-iron(V) complexes is very challenging due to the fleeting nature of these species, which have been generated mainly at cryogenic temperatures in a solid solvent matrix. Reactivity towards C-H activation has been studied only in the gas phase, but no C-H activation was observed,[53] and evidence was found recently in room temperature time resolved IR measurements that these complexes react with phosphines.[54,262]

Attempts were made to trap the nitrido-iron(V) complex $[Fe^{V}(N)cyc\text{-}ac]^{+}$ chemically. EPR-samples were prepared including a large excess of potential trapping agents, and the samples were photolyzed to form the iron(V) complex as described in Chapter 5.4. By allowing the samples to thaw, reaction with the added reagent is expected. Chosen reagents were trimethylamine N-oxide (Me_3NO), N-tertiary-butyl nitrone (PBN) and triphenyl phosphane (PPh_3). For a nitrido-iridium(IV) complex it was shown previously that oxygen transfer from Me_3NO to the nitrido ligand yields the analog nitrosyl complex.[263] However, formation of the previously studied[264] nitrosyl complex $[Fe(NO)cyc\text{-}a]^{+}$ from the nitrido-iron(V) complex was not observed and the parent azido-iron(III) complex already undergoes not very well defined reactions with Me_3NO. Due to the radical character of the nitrido-ligand (see discussion in Chapter 5.5.2), reactivity towards the spin-trapping reagent PNB was tested. Formation of the nitrido-iron(V) species in the presence of PBN was possible, however, after allowing the sample to thaw no EPR-signal was detected anymore. It is, therefore, assumed that only EPR-silent species are formed, either by reaction with PBN or via the decay mechanism that will be described in the following chapter.

Finally, it was tried to react the nitrido-iron(V) complex with PPh_3 as it was previously done in time resolved IR measurements.[56] Photolysis of the azido-iron(III) complex at cryogenic temperature in the presence of PPh_3 resulted in the nitrido-iron(V) signal in the EPR-spectrum. After allowing the sample to thaw, various new signals were observed but the intensity of the spectrum was relatively low. The main feature might result from an high-spin iron(III) complex, however, due to the mixture of various species clear identification of the formed products was not possible.

Due to the difficulties in trapping the nitrido-iron(V) complex $[Fe^{V}(N)cyc\text{-}ac]^{+}$ chemically, only the self-decay process of nitrido-iron(V) complexes in tetragonal coordination will be studied here, by allowing a sample of cryogenically trapped iron(V) to thaw.

[8] This section is reprinted/adapted with permission from O. Krahe, E. Bill, F. Neese "Decay of Iron(V) Nitride Complexes By a N-N Bond-Coupling Reaction in Solution: A Combined Spectroscopic and Theoretical Analysis", *Angew. Chem. Int. Ed.* **2014**, *53*, 8727. Copyright 2014 John Wiley & Sons, Inc

5.9.1. The Decay of Nitrido-Iron(V) Complexes Investigated by Mössbauer Spectroscopy

In Chapter 4.5.3 (page 84) it was demonstrated by Mössbauer spectroscopy that the high-valent complex $[Fe^{V}(N)cyc\text{-}ac]PF_6$ can be obtained by preparative photolysis of the parent $[Fe^{III}(N_3)cyc\text{-}ac]PF_6$ complex. The Mössbauer sample, whose spectrum is shown in Figure 4.30, was prepared under an inert atmosphere of argon and was kept frozen with liquid nitrogen at all times. After the spectrum of the nitrido-iron(V) complex was recorded, the sample was again transferred to a Schlenk tube while keeping it frozen with liquid nitrogen. The sample was then again set under an inert atmosphere of argon and allowed to thaw. As soon as the sample was thoroughly melted, the sample was frozen once again with liquid nitrogen. The entire thaw/freeze process took about ~5 min. The Mössbauer spectra recorded after this thawing process are shown in Figure 5.24.

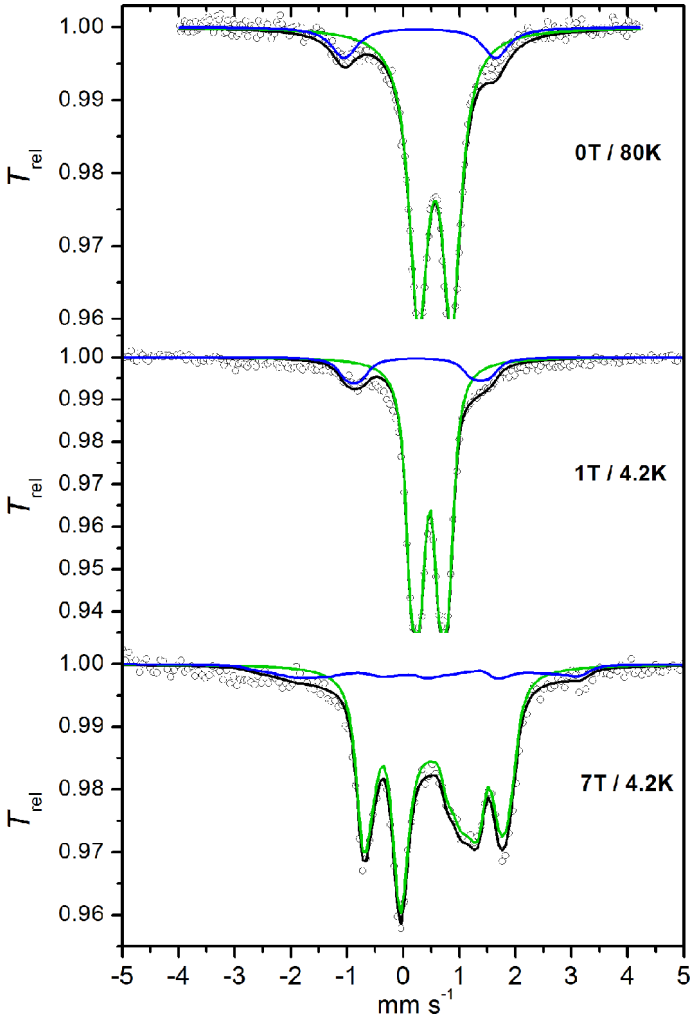

Figure 5.24: Mössbauer spectra of the decay product of the nitrido-iron(V) complex recorded at 80K (top), at 4.2K and 1T applied magnetic field (middle) and at 4.2K and 7T applied field (bottom). The solid green and blue lines represent spin-Hamiltonian simulations for the Fe^{II}-complex and the Fe^{III}-species, respectively.

The results of the fit are provided in Table 5.19 alongside the corresponding DFT calculated Mössbauer parameters (B3LYP/def2-TZVP/Fe:CP(PPP)). Clearly, the signal associated with the nitrido-iron(V) complex completely vanished and a new species with the Mössbauer parameters $\delta = 0.57$ mm s^{-1} and $\Delta E_Q = +0.59$ mm s^{-1} appears (compare spectra in Figure 5.24 with Figure 4.30).

Table 5.19: Mössbauer data from the simulation shown in Figure 5.24 and results from DFT calculations.

	$[Fe^{II}(MeCN)cyc\text{-}ac]PF_6$		$Fe^{III}(N_3)cyc\text{-}ac]PF_6$	
	exp (87%)	calc	exp (13%)	calc
δ [mm s^{-1}]	0.57	0.54	0.27	0.26
Δ [mm s^{-1}]	0.59	+0.42	-2.7	-2.36
η	0.42	0.41	0.40	0.27
g-matrix			1.91, 2.26, 2.55	
Euler angles (α,β,γ)			12, -144, 0	
A /$g_N\beta_N$ [T]			-41.17, 34.98, -6.32	

Remarkably, the fraction of residual $Fe^{III}N_3$ starting material remaining from incomplete photolysis (13%) was not affected by the thaw/freeze procedure. It can, therefore, be concluded that the nitrido-iron(V) complex does not oxidize the iron(III) precursor or undergo any other reaction with it. The moderate isomer shift and low quadrupole splitting of the new species are identical to the values obtained for the complex that did result from photolysis in solution (see Chapter 4.5.3, Figure 4.32). The performed Mössbauer measurements with applied magnetic field show once again, that the species is diamagnetic and must originate from low-spin iron(II), hence, the $[Fe^{II}(MeCN)cyc\text{-}ac]PF_6$ complex.

Mössbauer and DFT results demonstrate that the $[Fe^{V}(N)cyc\text{-}ac]^+$ complex decays differently in solution than in the gas phase. For the gas phase, only formation of iron(III) products have been detected in a study by Schröder *et al.* which was explained by intramolecular decomposition through ligand degradation.[53]

In polar solutions (1mM in acetonitrile) collisions of complex cations are more likely than in low-pressure gas atmosphere. Therefore, intermolecular reactions of the high-valent species might be favored over intramolecular decomposition. Then, the easiest conceivable way to transform the nitrido-iron(V) complexes to low-spin ferrous species is the direct coupling of two nitrides, which results in one equivalent of N_2 and two low-spin iron(II) complexes (see Scheme 5.4).

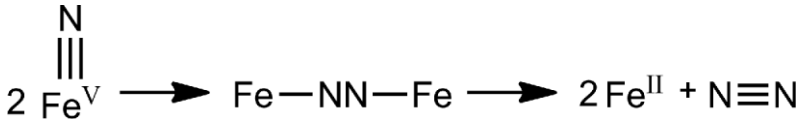

Scheme 5.4: Proposed decay pathway for tetragonal $Fe^{V}N$ complexes.

Interestingly, the formation of an low-spin iron(II) complex was observed previously, too, when the $[Fe^{V}(N)N_3cyc]ClO_4$ complex was allowed to thaw, however, the formation mechanism was not further investigated.[29] For this species the Mössbauer parameters δ= 0.55 mm s^{-1}, ΔE_Q= +0.72 mm s^{-1} were reported in the initial work by Meyer *et al*.[29] This species can be further confirmed to be the low-spin ferrous complex $[Fe^{II}(N_3)(MeCN)cyc]^+$ by DFT calculations, which yields Mössbauer parameters δ = 0.55 mm s^{-1}, ΔE_Q = +0.66 mm s^{-1}, in very good agreement with the previously reported experimental results.[29]

DFT calculations of the Mössbauer parameters were further performed for the dimeric complexes $(N_2)[Fe^{II}(cyc\text{-}ac)]_2^{2+}$ and $(N_2)[Fe^{II}(N_3)(cyc)]_2^{2+}$ which yielded δ = 0.44 mm s^{-1}, ΔE_Q= +0.78 mm s^{-1} and η = 0.41 for the former and δ= 0.39 mm s^{-1}, ΔE_Q = +0.73 mm s^{-1} η = 0.21 for the latter. Hence, the agreement between the experimental and the calculated parameters for the monomeric iron(II)

complexes is better than between the experimental and the calculated Mössbauer values for the dimeric iron(II) complexes. In the coordinating solvent, it can be assumed that the weakly bond dimer immediately dissociates and the vacant coordination site is filled with a solvent molecule. This further supports the formulation of the iron(II) complexes detected by Mössbauer spectroscopy as $[Fe^{II}(MeCN)cyc\text{-}ac]PF_6$ and $[Fe^{II}(MeCN)(N_3)cyc]ClO_4$.

Therefore, a similar decay process can be assumed for the nitrido-iron(V) complexes $[Fe^{V}(N)cyc\text{-}ac]PF_6$ and $[Fe^{V}(N)(N_3)cyc]ClO_4$, where the complex is reduced to iron(II) in an six-electron redox process and the nitrido-ligand is replaced by an acetonitrile solvent molecule.

5.9.2. Detection of the formed $^{15}N_2$ by EI-MS

Since it was shown by Mössbauer spectroscopy in combination with DFT calculations that the decay of the nitrido-iron(V) complexes $[Fe^{V}(N)cyc\text{-}ac]^+$ and $[Fe^{V}(N)(N_3)cyc]^+$ results in the low-spin ferrous complexes $[Fe^{II}(MeCN)cyc\text{-}ac]^+$ and $[Fe^{II}(MeCN)(N_3)cyc]^+$, it shall now be demonstrated what the underlying mechanism is. This can be proven by mass spectrometry via ^{15}N-isotope labeling of the azide ligand. The proposed mechanism is outlined in Scheme 5.5 including expected ^{15}N-isotope labeling.

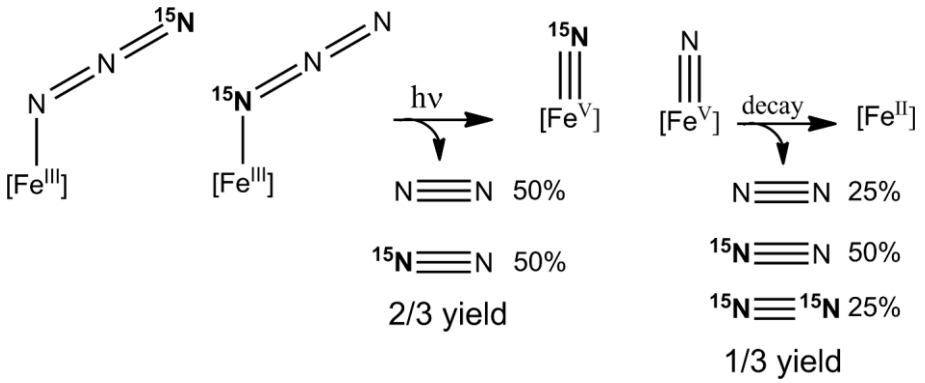

Scheme 5.5: Proposed decay pathway with ^{15}N isotope labeling.

In commercially available ^{15}N-sodium azide that was used in the synthesis of the complexes, only one of the terminal nitrogen atoms is ^{15}N-labeled. This results in an equal mixture of azido-iron(III) complexes where the terminal or the iron bond azido nitrogen atom is ^{15}N-isotope labeled (Scheme 5.5, left side). Photolysis then results in equal amounts of ^{15}N- and ^{14}N-nitrido-iron(V) as well as an equal mixture of $^{14}N_2$ and $^{14}N^{15}N$ (Scheme 5.5, middle). Subsequent nitride coupling and decay of the resulting $[Fe^{II}\text{-}NN\text{-}Fe^{II}]^{2+}$ intermediate during melting of the samples leads to the same N_2 isotopes, albeit in different yields. However, in addition, doubly labeled $^{15}N^{15}N$ is generate upon dimerization of two $Fe^{V}(^{15}N)$ groups. Of the overall formed N_2, 2/3 are obtained in the photolysis and 1/3 in the final decay of the $Fe^{V}(N)$-complexes (Scheme 5.5). The dimerization is the only possible means to form $^{15}N^{15}N$. The alternative pathway through $N_3^{\bullet}$ radical coupling ($2N_3^{\bullet} \rightarrow 3N_2$) is excluded as the absence of Fe^{II} photoproducts also rules out the formation of $N_3^{\bullet}$ by reductive $Fe^{III}\text{-}N_3$ cleavage, that is, the reaction $Fe^{III}N_3 \rightarrow Fe^{II} + N_3^{\bullet}$ is not observed (see Mössbauer spectrum Figure 4.30, page 84).

To detect the formed $^{15}N_2$ isotope electron ionization mass spectrometry measurements of the product gas phase were performed. In a glove box under argon atmosphere, 2 mM solutions of [Fe($^{15}NN_2$)cyc-ac]PF_6 and [Fe($^{15}NN_2$)$_2$cyc]ClO_4 in acetonitrile were prepared and ~1 mL of the solution was filled in glass sample cells that were sealed with a septum. The samples were frozen with liquid nitrogen and photolyzed for 6h with 470 nm light. It was made sure that the sample was covered with liquid nitrogen during this process and the septum kept out of the nitrogen to avoid nitrogen/air diffusion into the cells. The samples were then allowed to thaw and the gas phase above the sample was transferred into the spectrometer via a gas tight syringe. The results of the measurements, the calculated isotope ratio and the natural abundance are shown in Table 5.20, the full data is provided in the appendix, including background measurements (page 210).

Table 5.20: Relative amounts of dinitrogen isotopes obtained from melting photolyzed samples of [Fe($^{15}NN_2$)cyc-ac]PF_6 and [Fe($^{15}NN_2$)$_2$cyc]ClO_4.

	Natural abundance [%]	calculated [%]	observed for [Fe($^{15}NN_2$)cyc-ac]PF_6 [%]	observed for [Fe($^{15}NN_2$)$_2$cyc]ClO_4 [%]
$^{14}N^{14}N$	99.2813	41.7	73.9	82.2
$^{14}N^{15}N$	0.7174	50.0	22.2	15.4
$^{15}N^{15}N$	0.0013	8.3	3.9	2.5

Even it was not possible to purge the spectrometer completely from atmospheric N_2 which did result in a lower yield of ^{15}N-labeled material than calculated, the detected intensity of 3.9% $^{15}N_2$ for [Fe($^{15}NN_2$)cyc-ac]PF_6 and 2.5% for [Fe($^{15}NN_2$)$_2$cyc]ClO_4 is clearly above the natural abundance and above the detection limit. This demonstrates that N_2 is formed via nitrogen coupling of two nitrido-iron(V) complexes.

5.9.3. DFT calculations on the Mechanism

For a deeper understanding of the nitride-coupling pathway and its driving force, DFT calculations were performed. To show that the dimerization reaction is the energetically most favored pathway, conceivable reactions with the solvent (acetonitrile) were also investigated computationally.

Structures were optimized with the BP86 functional in conjunction with the resolution of the identity (RI) approximation, the def2-TZVP basis set and the corresponding def2-TZV/J auxiliary basis set. The conductor like screening model (COSMO) was used to take into account solvent effects considering acetonitrile as the solvent which was used in the experiments. Furthermore, empirical van der Waals correction was used in all calculations. Reported energies were obtained by B3LYP calculations with the RIJCOSX approximation on the BP86 optimized structures. Thermal corrections were used from the BP86 frequency calculations.

The results for the dimerization reactions are shown in Scheme 5.6. It is clear from the calculated Gibbs free energy that the dimerization is strongly exergonic. The newly formed N-N-bond in the dimeric intermediate shows a bond distance of 1.158 Å for [(cyc-ac)FeN-NFe(cyc-ac)]$^{2+}$ and 1.161 Å for

[(cyc)(N_3)FeN-NFe(N_3)(cyc)]$^{2+}$, respectively, which is slightly longer than the calculated bond length of 1.102 Å for the free N_2 molecule.

In the coordinating acetonitrile solvent this intermediate is expected to be unstable. This is seen in the final step in Scheme 5.6 where the substitution of the dinitrogen molecule by acetonitrile is calculated to be exergonic about -54 kJ mol^{-1} and -55 kJ mol^{-1}, respectively.

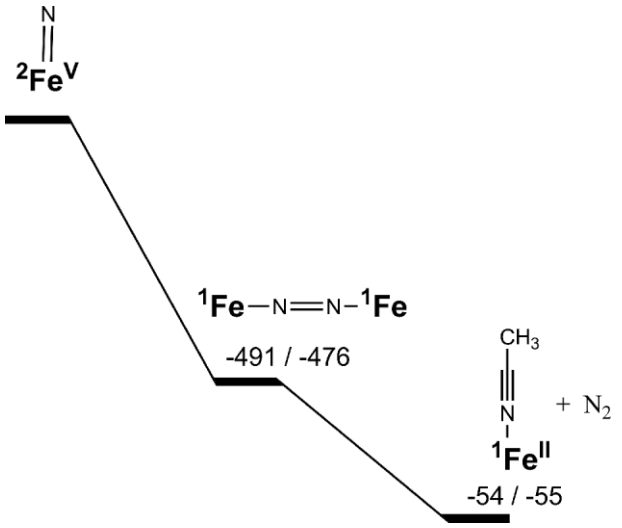

Scheme 5.6: Calculated dimerization pathway for [Fe^{V}(N)cyc-ac]$^{+}$ / [Fe^{V}(N)(N_3)cyc]$^{+}$, with the spin multiplicity of iron as ^{n}Fe superscript and energies in kJ mol^{-1}.

Due to the change of the multiplicity during the dimerization reaction from a triplet to a singlet ground state it was not possible to locate a transition state for this reaction. Relaxed surface scans were performed along the nitride-nitride distance during the coupling reaction as shown in Figure 5.25. It is clearly seen for the triplet and singlet state that while shortening the N-N-distance the relative energy strongly decreases without any discernible barrier which would be characteristic for a transition state.

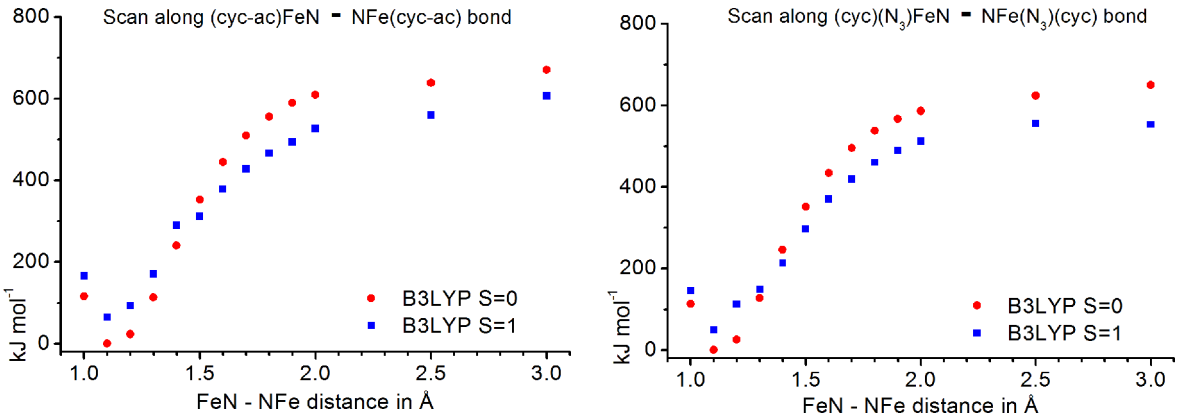

Figure 5.25: Relaxed surface scan along the incipient N-N-bond on the triplet (blue) and singlet (red) surface for [Fe^{V}(N)cyc-ac]$^{+}$ (left) and [Fe^{V}(N)(N_3)cyc]$^{+}$ (right).

The scans further reveal a change of the spin state from triplet, for the two Fe^{V}N-fragments separated about 3 Å, to singlet in the dimer structure. Optimization of the dimers in the triplet state showed that the triplet is 66 kJ mol^{-1} higher in energy for the (N_2)[Fe(cyc-ac)]$_2^{2+}$ dimer and 89 kJ mol^{-1} higher in energy for the (N_2)[Fe(N_3)(cyc)]$_2^{2+}$ dimer, relative to the corresponding singlet states.

As discussed in Chapter 5.5.2, the very covalent Fe-N bond in the nitrido-iron(V) complexes can be assumed to have the resonance forms $Fe^{V}(S_{Fe}=1/2)\ N^{3-} \leftrightarrow Fe^{II}(S_{Fe}=0)N^{\bullet}(S_{N}=1/2)$. Based upon the nitride-radical resonance structure, the dimerization can be regarded as a radical coupling reaction that proceeds in a barrier-free fashion. The stability of the dimeric intermediate is likely due to the strong driving force for formation of a triple bond in the resulting dinitrogen molecule. However, in acetonitrile solution dissociation of the dimer followed by saturation of the vacant coordination site by a solvent molecule is expected and this was further calculated to be exergonic about 54 kJ mol^{-1}/55 kJ mol^{-1}, respectively.

Since the described reaction appears to process barrier-free and is extremely exergonic, competing reactions are very unlikely. This notion is in good agreement with the very clean formation of the iron(II) species from the $[Fe^{V}(N)cyc\text{-}ac]PF_6$ complex observed in the Mössbauer measurements, which lacks any detectable side products (see Figure 5.24). To validate this assumption, DFT calculations were performed for possible reactions of the nitrido-iron(V) complex $[Fe^{V}(N)cyc\text{-}ac]^{+}$ with the acetonitrile solvent. Intramolecular reactions are not considered here, since these would result in iron(III) complexes as shown in a mass spectrometry study by Schröder *et al*.[53] But the Mössbauer measurements (see Figure 5.24) reveal that a low-spin ferrous species is formed exclusively.

The first considered reaction is the hydrogen-abstraction from an acetonitrile molecule resulting in an acetonitrile radical and an iron-imido complex. All possible spin states were considered in these reactions (Scheme 5.7). The transition state in the doublet spin state was calculated to be 133 kJ mol^{-1} higher in energy than the starting molecule, and 14 kJ mol^{-1} lower in energy than the transition state in the quartet spin state (147 kJ mol^{-1}). The calculated barrier of 133 kJ mol^{-1} seems to be too high to make H-abstraction feasible at room temperature. The overall reaction is further calculated to be endergonic about 48 kJ mol^{-1} for the imido-complex in its triplet ground state. All attempts to locate a transition state for a direct nitrogen insertion into the C-H-bond failed for all possible spin states. It can be concluded therefore that the H-abstraction from a solvent molecule is very unlikely.

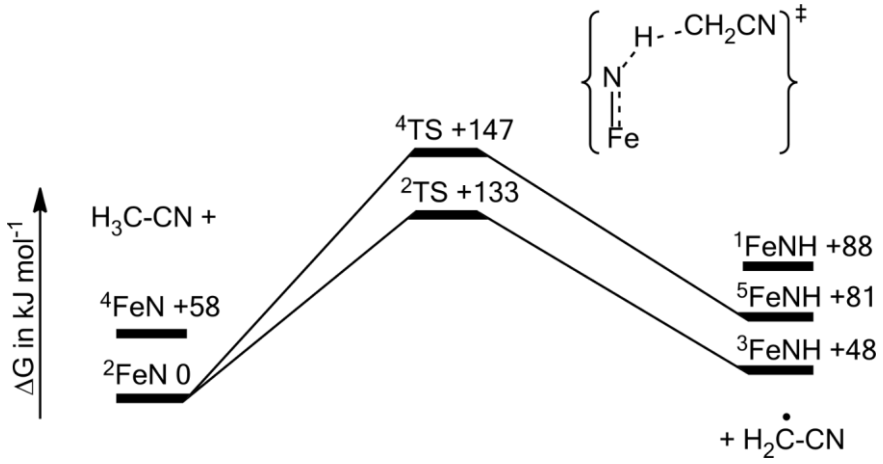

Scheme 5.7: Calculated C-H-activation pathway for $[Fe^{V}(N)cyc\text{-}ac]^{+}$ from acetonitrile, with the spin multiplicity of iron as ^{n}Fe superscript and energies in kJ mol^{-1}.

Another feasible reaction would be the attack of the acetonitrile nitrogen on the nitrido nitrogen (see Scheme 5.8). Even throughout the reaction is calculated to be slightly exergonic, about -5 kJ mol^{-1} for

the product in the doublet state, the barrier lowest in energy is calculated to be 102 kJ mol^{-1}. Again, this seems to be too high to allow this reaction thermally.

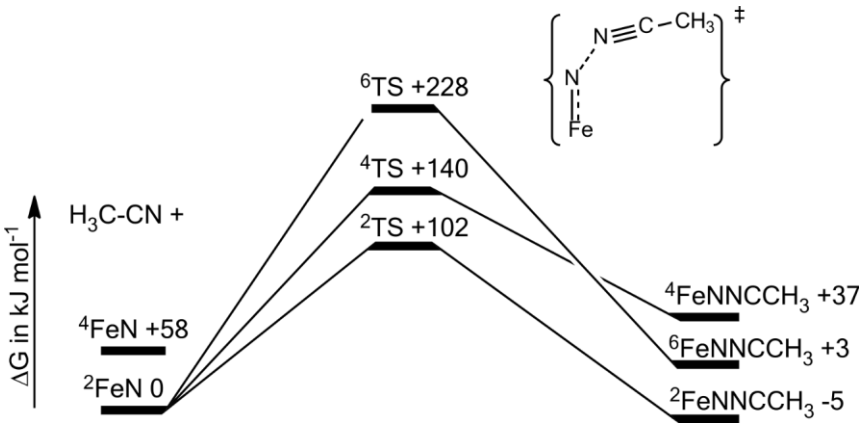

Scheme 5.8: Calculated coordination of acetonitrile on $[Fe^{V}(N)cyc\text{-}ac]^{+}$, with the spin multiplicity of iron as ^{n}Fe superscript and energies in kJ mol^{-1}.

In this chapter, it was shown by Mössbauer spectroscopy that the nitrido-iron(V) complexes exclusively form iron(II) low-spin complexes. By mass spectrometry and ^{15}N-isotope labeling it was verified that the underlying mechanism is a nitride coupling that results in the formation of dinitrogen. This was further supported by DFT-calculations of the proposed mechanism, and possible side reactions with the acetonitrile solvent which can be ruled out due to the very high reaction barriers calculated.

The dimerization, which could be described as an “inverse” of the Haber-Bosch reaction, is very fast and exergonic and the reaction equilibrium is strongly on the dinitrogen side. It will, therefore, be challenging to push it to the nitride side for possible ammonia formation or N-functionalization of substrates from dinitrogen. Still, the results provide interesting insight in the reactivity of tetragonal nitrido-iron(V) complexes.

It should be noted here as well, that the shown results also impact the understanding of the photolysis of the azido-iron(III) complexes in solution. It is clear now that upon photolysis of Mössbauer samples in solution, it will not be possible to detect the formation of nitrido-iron(V) complexes. They would decay immediately resulting in the discussed iron(II) species which are also obtained when the initial photochemical reaction involves homolytic cleavage of the Fe-N_3 bond. Hence, more sophisticated experimental techniques, such as the time resolved IR measurements discussed in Chapter 4.5.3, are necessary to investigate the formation of nitrido-iron(V) complexes in solution.

Furthermore, the data presented here as well as the results discussed in Chapter 4.5.3 reveal that the identical iron(II) complexes $[Fe^{II}(MeCN)cyc\text{-}ac]^{+}$ and $[Fe^{II}(MeCN)(N_3)cyc]^{+}$ can be formed in various ways. i) By photolysis in solution ii) by electrochemical one-electron reduction iii) via the decay of the related nitrido-iron(V) complexes. All of these transformations result in the same low-spin ferrous complexes.

5.10. Discussion and Conclusions

In this chapter, iron(V) complexes were investigated by means of experimental and computational methods. Besides the tetragonal nitrido-iron(V) complexes that were studied experimentally in the present thesis, the computational survey also included previously reported oxo-iron(V) complexes for comparison.

The combined results from previously published Mössbauer and resonance Raman experiments with DFT calculations unequivocally demonstrated that the complex $[Fe^{V}(N)(N_3)cyc]^{+}$ and a series of nitrido-iron(V) porphyrin complexes have a low-spin *S*=1/2 ground state, and not a *S*=3/2 ground state as initially assumed.[9,40,46] This result is highly crucial for the understanding of the electronic structure and spectroscopic parameters of these complexes.

For the previously described tetragonal nitrido-iron(V) complexes $[Fe^{V}(N)cyc\text{-}ac]^{+}$, $[Fe^{V}(N)(N_3)cyc]^{+}$, $[Fe^{V}(N)TPP]$ and the new complex $[Fe^{V}(N)TMC\text{-}ac]^{+}$ it was possible to record EPR-spectra for the first time. All four complexes show nearly axial spectra ($g_1<g_2\approx g_3<g_e$) with all g-values smaller than g_e. Given that one g-value larger than g_e is usually expected for these low-spin d^3-complexes with the electron configuration $(d_{xy})^2(d_{yz})^1$, at first sight the g-values appear to be counterintuitive. It was further shown by EPR-spectroscopy that the complex $[Fe^{V}(N)TMC\text{-}ac]^{+}$ obtained by photolysis of the parent azido-iron(III) complex in frozen solution is stable in fluid solution. However, photolysis of the azido-iron(III) complex directly in fluid solution did not yield the nitrido-iron(V) species which demonstrates the notable effect of the state of aggregation on the photochemical reactions.

Even the used ligand systems are not genuinely symmetric, CASSCF/NEVPT2 calculations have revealed that all tetragonal nitrido-iron(V) complexes exhibit a nearly degenerate $^2B_2[(d_{xy})^2(\pi_y^*/d_{yz})^1]$ ground state separated from the $^2B_1[(d_{xy})^2(\pi_x^*/d_{xz})^1]$ first excited state only by a few hundred wave numbers.

Within the framework of quasi degenerate perturbation theory (QDPT) spin-Hamiltonian equations were derived for the g-values, taking into account the near degeneracy and large covalency of the studied iron(V) complexes. These expressions show that the very low-lying excited state $^2B_1[2b_2(\pi_y^*)\rightarrow 2b_1(\pi_x^*)]$ gives rise to the experimentally observed small g-values ($g_x,g_y,g_z<g_e$) and further demonstrate the strong dependence of the g-values on this low-lying excited state. By inclusion of the hypothetical oxo-iron(V) complex $[Fe^{V}(O)cyc\text{-}ac]^{2+}$ in the calculations and the detailed spin-Hamiltonian analysis of the g-values, it was shown that there are only subtle variations in the g-values for analog oxo- and nitrido-complexes. These result from differences in the excitation energies and covalency effects.

The experimental g-values and calculated electronic structure for all tetragonal nitrido-iron(V) complexes are very similar, which indicates that the properties are strongly driven by the $\{Fe \equiv N\}^{2+}$ unit. Bendix *et al.* suggested e.g. for the $[Cr^{V}(N)Cl_4]^{2-}$complex that it might be regarded as an $\{Cr \equiv N\}^{2+}$ unit ligated by four chloride ligands rather than an Cr^{V}-center with nitrido- and chloride-ligands.[11] For the nitrido-chromium(V) complex $[Cr^{V}(N)Cl_4]^{2-}$ it was further shown that the $d_{x^2-y^2}$-orbital lies below the d_{xz}/d_{yz}-orbitals due to the very strong axial nitrido-ligand, which for the tetragonal nitrido-iron(V) complexes would result in an $^2A_1[(d_{xy})^2(d_{x^2-y^2})^1]$ ground state. However, CASSCF/NEVPT2 calculations have revealed that this state is well separated from the $^2B_2[(d_{xy})^2(\pi_y^*/d_{yz})^1]$ ground state for the tetragonal nitrido-iron(V) complexes. Hence, the equatorial ligands in the nitrido-iron(V)

complexes throughout affect the electronic structure. Considering the nitrido-iron(V) complexes as isolated $\{\mathrm{Fe} \equiv \mathrm{N}\}^{2+}$ units would underestimate the effect of the equatorial ligands and result in an $^2A_1[(d_{xy})^2(d_{x^2-y^2})^1]$ ground state. Good correlation between the experimental and calculated spectroscopic parameters have further demonstrated, that the electronic structure derived from the calculations properly describes the studied systems.

CASSCF/NEVPT2 calculations on the $[Fe^V(O)TMC(NC(O)CH_3]^+$ complex have shown that in contrast to other tetragonal iron(V) complexes the ground state is far off from being degenerate. Due to the increased separation of excited states from the ground state (>6000 cm^{-1}), the g-shift is significantly smaller resulting in g-values close to g_e for the complex $[Fe^V(O)TMC(NC(O)CH_3]^+$. Furthermore, contributions from LMCT-transitions partially cancel out the negative g-shift for the g_{zz}-value which results in $g_{zz} \approx g_e$, in agreement with the previously reported experimental results.[77]

Finally, it was demonstrated that the tetragonal nitrido-iron(V) complexes $[Fe^V(N)cyc\text{-}ac]^+$ and $[Fe^V(N)(N_3)cyc]^+$ undergo a reductive nitride coupling reaction yielding dinitrogen and ferrous complexes. This six electron transfer reaction can be considered as the reverse of the Haber-Bosch reaction. The reaction equilibrium is lying strongly on the dinitrogen side which will undoubtedly make it a challenging task to shift it to the nitride side for possible ammonia formation or N-functionalization of substrates from dinitrogen.

In summary, spectroscopy combined with calculations provided detailed insight in the electronic structure of nitrido- and oxo-iron(V) complexes. This allows for an in-depth understanding of spectroscopic parameters, as demonstrated in particular for the g-values of a series of tetragonal nitrido-iron(V) complexes. g-Values were shown to be strongly sensitive to the lowest-lying excited state and, therefore, changes in the coordination sphere are expected to have notable effects on the observed g-values. This result may also have relevance in more complex industrial or biological systems, for which the complexes investigated here can serve as model systems.

6. Oxo-Iron(IV) Complexes

The number of iron(V) complexes that have been synthesized and characterized is somewhat limited.[16,25] All of these complexes were discussed in the previous chapters. In contrast, a larger number of complexes does exist for another class of high-valent iron species, the oxo-iron(IV)-complexes.[74] Oxo-iron(IV) complexes are key intermediates in numerous heme and non-heme iron enzymes that are capable of oxidizing unactivated C-H bonds.[57,78] Therefore, much effort has been put into the synthesis and characterization of model oxo-iron(IV) complexes during the last decade.[74] Of special interest is the reactivity of these species which was studied by various experimental and computational methods, in the hope to gain a better understanding of the more complex biological systems, the present species can serve as model complexes for.[85-86,91,93,101,265] Interestingly, the first synthetic non-heme oxo-iron(IV) complex $[Fe^{IV}(O)cyc\text{-}ac]^{+}$ was synthesized in the group of Wieghardt,[43] which is the oxo-iron(IV) analogue of the nitrido-iron(V) complex $[Fe^{V}(N)cyc\text{-}ac]^{+}$ described in previous chapters.

Besides the penta-aquo complex $[Fe^{IV}(O)(H_2O)_5]^{+}$ all synthetic oxo-iron(IV) complexes reported in the literature are based on tetra- or pentadentate N-donor ligands.[74] However, in 2013 the Franc Meyer group succeeded in synthesizing an oxo-iron(IV) complex with tetradentate N-heterocyclic carbene (NHC) ligand (see Scheme 6.1).[266] Its electronic structure and reactivity is studied here computationally and related to the experimental results. The experimental results of this chapter were obtained in the group of Prof. Franc Meyer. They are not part of the thesis and are only shown here for completeness. To compare the properties of the new complex $[Fe^{IV}(O)(NHC)_4(EtCN)]^{2+}$ with the established systems based on N-donor ligands, analogue calculations were performed for the complex $[Fe^{IV}(O)(TMC)(MeCN)]^{2+}$ (see Scheme 6.1). The synthesis and analysis of $[Fe^{IV}(O)(TMC)(MeCN)]^{2+}$ including the crystal structure was published in 2003.[75] This was a great breakthrough in the chemistry of high-valent oxo-iron complexes since it was the first in detail characterization of such a species.[75]

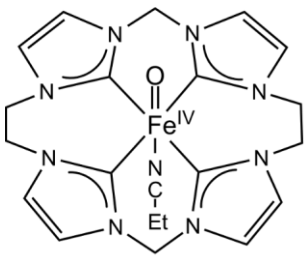

$[Fe^{IV}(O)(NHC)_4(EtCN)]^{2+}$

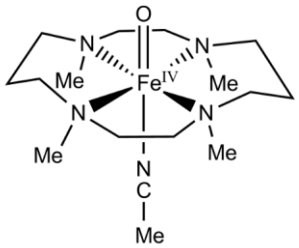

$[Fe^{IV}(O)(TMC)(MeCN)]^{2+}$

Scheme 6.1: Oxo-iron(IV) complexes studied in this work.

6.1. Determination of the Electronic Structure of Oxo-Iron(IV) Complexes

As a first step, the electronic structure of both oxo-iron(IV) complexes was studied by DFT and CASSCF/NEVPT2 calculations. Structures for the NHC-system $[Fe^{IV}(O)(NHC)_4(EtCN)]^{2+}$ and TMC-system $[Fe^{IV}(O)(TMC)(MeCN)]^{2+}$ were optimized for all conceivable spin states using the BP86 functional, the RI-approximation, the def2-TZVP(-f) basis set and the corresponding auxiliary basis set for the RI approximation. Solvent effects were taken into account by using COSMO with acetonitrile as solvent. Relative energies were calculated on these structures with the B3LYP functional, the def2-TZVP basis set and the corresponding def2-TZV/J auxiliary basis set for the RIJCOSX approximation. COSMO was used to incorporate solvent effects. Relative energies reported in this chapter take into account zero point energy corrections obtained from the BP86 frequency calculations. Mössbauer parameters were calculated with the same setup, the basis set for iron was replaced by the CP(PPP) basis set and the RIJCOSX approximation was not used.

In the active space for the CASSCF calculations, all metal 3d-orbitals and oxo 2p-orbitals were included. Further, the bonding combination of the equatorial ligand with the metal $d_{x^2-y^2}$-orbital was taken into account, which results in an active space of 12 electrons in 9 orbitals, CASSCF(12,9). CASSCF calculations were performed on structures that were optimized with DFT in the triplet and quintet state, respectively.

6.1.1. Electronic Structure of the Complex $[Fe^{IV}(O)(TMC)(MeCN)]^{2+}$

Table 6.1 summarizes key bond parameters, relative energies and Mössbauer parameters for the oxo-iron(IV) TMC complex. These are in good agreement with previously published studies.[92,106-107,251,267-268] Experimental data was obtained from the literature.[75]

Table 6.1: Calculated parameters for the complex $[Fe^{IV}(O)(TMC)(MeCN)]^{2+}$ and experimental[75] values.

S	rel. Energy		Mössbauer[c]			selected bond distances					
	B3LYP[a]	NEVPT2[b]	δ	ΔE_Q	η	Fe-O	Fe-N	Fe-N	Fe-N	Fe-N	Fe-N[d]
	[kJ mol^{-1}]		[mm s^{-1}]			[Å]	[Å]	[Å]	[Å]	[Å]	[Å]
0	134		0.07	-3.03	0.69	1.660	2.098	2.099	2.127	2.128	1.973
1	0	0	0.09	+0.85	0.16	1.650	2.095	2.096	2.135	2.137	2.014
2	4	22	0.13	-0.82	0.35	1.646	2.175	2.176	2.240	2.241	1.998
Exp.[75]	*S*=1		0.17	+1.24	0.5	1.646	2.067	2.069	2.109	2.117	2.058

a: B3LYP/def2-TZVP/RIJCOSX/COSMO(acetonitrile), BP86/def2-TZVP(-f)/RI/COSMO optimized + ZPE corr.
b: Active space orbitals see below, SA-CASSCF(12,9) over 5 roots, relative energies of NEVPT2 ground states
c: B3LYP/def2-TZVP/Fe:CP(PPP)/COSMO calculation on BP86 optimized geometries
d: Distance between iron and the axial coordinated acetonitrile molecule

The spin state was determined experimentally to be *S*=1. This is in agreement with the DFT-calculations which place the quintet and singlet state 4 kJ mol^{-1} and 134 kJ mol^{-1} higher in energy than the triplet state, respectively. Given that the quintet state is important for the discussion of the complexes reactivity (*vide infra*), the triplet-quintet gap was further calculated by the higher level CASSCF/NEVPT2 method (see next pages for a discussion of the active space orbitals). Again, the triplet state is predicted to be the ground state, 22 kJ mol^{-1} lower in energy than the quintet state. The calculated Mössbauer isomer shift is in reasonable agreement with the experimental value for all considered spin states. However, the calculated quadrupole splitting of +0.85 mm s^{-1} for the triplet state agrees best with the experimental value of +1.24 mm s^{-1}.

The calculated iron-oxygen bond distance for the *S*=1 as well as for the *S*=2 state is in good agreement with the crystallographically determined value, while for the *S*=0 state it is slightly overestimated. However, the equatorial iron-nitrogen bond distances for the quintet-state are predicted to be much longer than the experimental values while good agreement is found for the triplet and singlet state. Overall, the agreement between the experimental and computational results is best for the *S*=1 state (however, it does not differ much from the bond distances for the singlet state), which is consistent with the experimentally determined spin state.

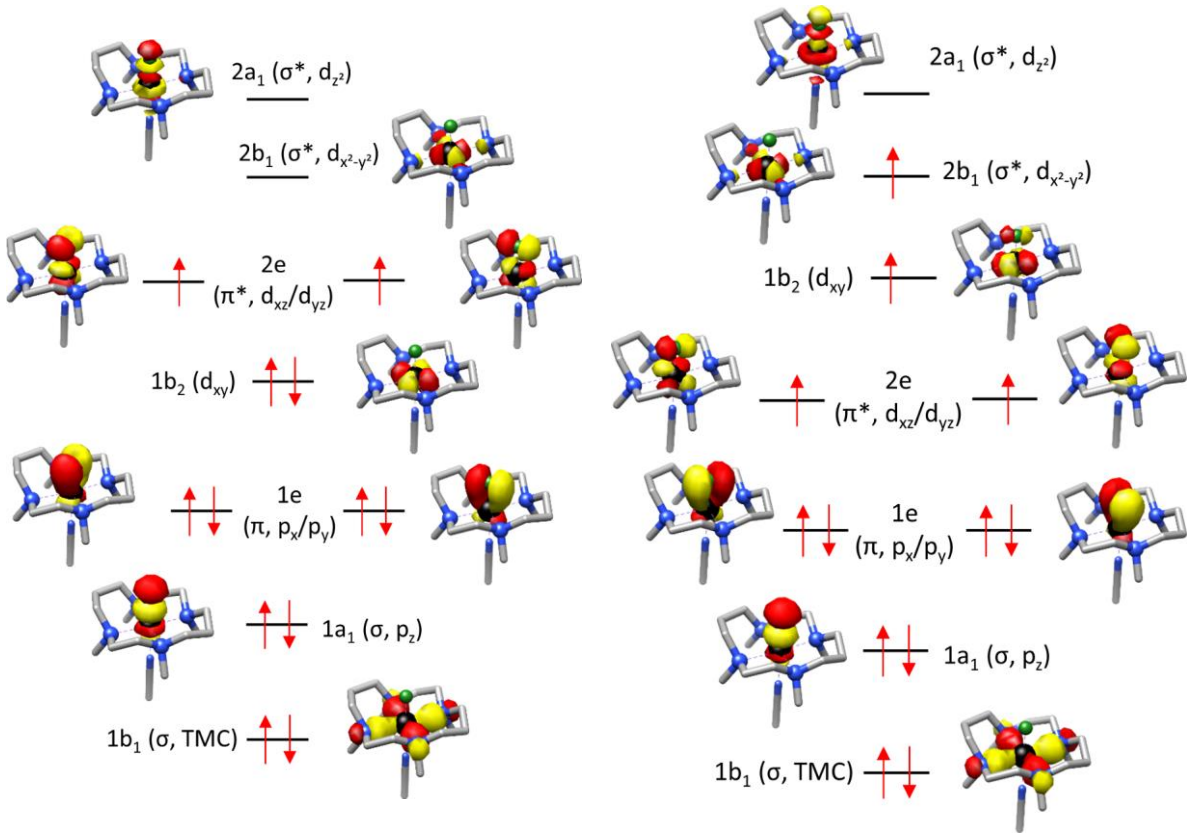

Figure 6.1: Active space orbitals from SA-CASSCF(12,9) calculations over 5 roots for $[Fe^{IV}(O)(TMC)(MeCN)]^{2+}$ in the triplet (left) and quintet state (right). Orbitals are sorted by increasing occupation number which in the present case coincides with the energetic order (hydrogen atoms omitted for clarity).

The active space orbitals from a SA-CASSCF(12,9) calculation are shown in Figure 6.1 for the *S*=1 and *S*=2 states. In the triplet ground state (see Figure 6.1 left) the none bonding d_{xy}-orbital ($1b_2$) is doubly occupied while the d_{xz}- and d_{yz}-orbitals (2e) are each singly occupied and form π*-bonds with the oxo-ligand. The vacant $d_{x^2-y^2}$-orbital ($2b_1$) is anti-bonding with respect to the equatorial TMC-ligand and an σ*-orbital is formed between the iron d_{z^2}-orbital and the oxygen p_z-orbital ($2a_1$). Singl occupation of the d_{xz}/d_{yz}-orbitals results in a $^3A_2$ ground state within approximate C_{4v}-symmetry.

In the quintet state (see Figure 6.1 right) in addition to the d_{xz}- and d_{yz}-orbitals, the d_{xy}- and $d_{x^2-y^2}$-orbitals are also singly occupied. This results in a $^5A_1$ ground state assuming C_{4V}-symmetry. Like in the case of the triplet state, the d_{z^2}-orbital is vacant and the bonding orbitals between the oxo-ligand and iron as well as the TMC-ligand and iron are identical.

A comparison of the electronic structure for the triplet and quintet state explains the geometrical changes in the DFT calculations when changing from *S*=1 to *S*=2 (see Table 6.1). Since adjustments in the population of Fe-O anti-bonding orbitals (d_{xz}, d_{yz}, d_{z^2}) is negligible, the modification of the Fe-O distance is only very small. Further, the formal bond order in the triplet as well as in the quintet state is 2. However, population of the $d_{x^2-y^2}$-orbital in the quintet state (anti-bonding with respect to the equatorial ligand) results in notable elongation in the equatorial Fe-N bonds compared to the triplet ground state.

6.1.2. Electronic Structure of the Complex $[Fe^{IV}(O)(NHC)_4(EtCN)]^{2+}$

Similar calculations as discussed above for the $[Fe^{IV}(O)(TMC)(MeCN)]^{2+}$ complex were performed for the novel tetra-carbene $[Fe^{IV}(O)(NHC)_4(EtCN)]^{2+}$ complex synthesized in the group of Franc Meyer.[266] Again, the triplet state was calculated to be the ground state by DFT and the quintet and singlet states are 69 kJ mol^{-1} and 120 kJ mol^{-1} higher in energy, respectively. Higher level CASSCF/NEVPT2 calculations result in an even larger triplet-quintet gap (245 kJ mol^{-1}). Hence, in agreement with the experimental findings the triplet state is calculated to be the ground state, however, the separation from the quintet state is significantly larger than for the TMC-complex.

Table 6.2: Calculated parameters for the $[Fe^{IV}(O)(NHC)_4(EtCN)]^{2+}$ complex and experimental[266] values.

S	rel. Energy		Mössbauer[c]			selected bond distances					
	B3LYP[a]	NEVPT2[b]	δ	ΔE_Q	η	Fe-O	Fe-C	Fe-C	Fe-C	Fe-C	Fe-N[d]
	[kJ mol^{-1}]		[mm s^{-1}]			[Å]	[Å]	[Å]	[Å]	[Å]	[Å]
0	120		-0.20	-4.03	0.37	1.680	1.967	2.034	2.035	2.035	
1	0	0	-0.18	+2.93	0.01	1.673	1.981	2.042	2.041	2.041	2.049
2	69	245	-0.16	-2.03	0.05	1.743	2.025	1.976	1.979	1.979	3.838
Exp.	*S*=1		-0.13	+3.08	0.27	1.661	1.979	2.037	2.045	1.980	2.105

a: B3LYP/def2-TZVP/RIJCOSX/COSMO(acetonitrile), BP86/def2-TZVP(-f)/RI/COSMO optimized + ZPE corr.
b: Active space orbitals see below, SA-CASSCF(12,9) over 5 roots, relative energies of NEVPT2 ground states
c: B3LYP/def2-TZVP/Fe:CP(PPP)/COSMO calculation on BP86 optimized geometries
d: Distance between iron and the axial coordinated propionitril molecule

Mössbauer parameters calculated by DFT for the triplet state are in good agreement with the experimental ones, while those calculated for the singlet and quintet state show larger deviations. Good agreement is further found for the bond lengths calculated in the triplet state when compared to the distances determined by X-ray diffraction. Interestingly, the iron-oxo bond increases significantly (0.07 Å) when going from the triplet to the quintet state. Furthermore, the propionitril solvent molecule is no longer bonded to the iron-center in the quintet state. This was not the case for the TMC-complex and indicates differences in the electronic structure.

The active space orbitals from a SA-CASSCF(12,9) calculation are shown in Figure 6.2 for *S*=1 and *S*=2. In the triplet state the occupied orbitals and SOMOS are identical to those of the TMC-system. This again results in a $^3A_2$ ground state assuming C_{4v}-symmetry. However, the vacant $d_{x^2-y^2}$-orbital turns out to be higher in energy than the d_{z^2}-orbital. To verify that these orbitals are indeed swapped when compared to the TMC-system excited states will be discussed in Chapter 6.1.3 (page 177).

For the quintet state the MO-scheme reveals (Figure 6.2 right) that the d_{xy}-, d_{xz}-, d_{yz}- and d_{z^2}-orbitals are occupied by one electron and the $d_{x^2-y^2}$-orbital remains vacant. Hence, while for the $[Fe^{IV}(O)(TMC)(MeCN)]^{2+}$ complex in the quintet state the $d_{x^2-y^2}$-orbital is singly occupied and the d_{z^2}-orbital is vacant, it is the other way around for the $[Fe^{IV}(O)(NHC)_4(EtCN)]^{2+}$ complex. Within C_{4v}-symmetry, this results in a $^5B_1[(d_{xy})^1(d_{xz},d_{yz})^2(d_{z^2})^1]$ state for the NHC-system and the TMC-complex obeys a $^5A_1[(d_{xy})^1(d_{xz},d_{yz})^2(d_{x^2-y^2})^1]$ state in the quintet state. For the $[Fe^{IV}(O)(NHC)_4(EtCN)]^{2+}$ complex, the $^5A_1[(d_{xy})^1(d_{xz},d_{yz})^2(d_{x^2-y^2})^1]$ state is calculated (CASSCF(12,9)/NEVPT2) to be separated from the lowest energy quintet state $^5B_1[(d_{xy})^1(d_{xz},d_{yz})^2(d_{z^2})^1]$ by 9033 cm^{-1} and for the $[Fe^{IV}(O)(TMC)(MeCN)]^{2+}$ complex the $^5B_1$ state is separated from the lowest energy quintet state $^5A_1$ by 20822 cm^{-1}, respectively.

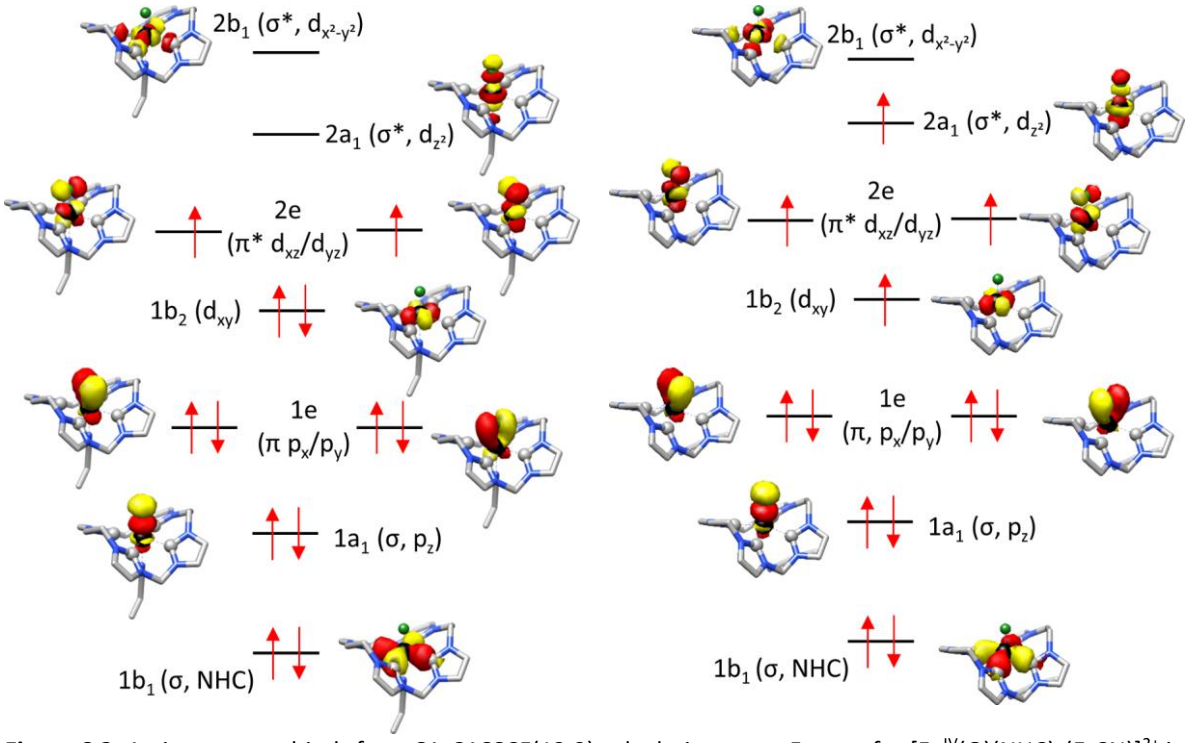

Figure 6.2: Active space orbitals from SA-CASSCF(12,9) calculations over 5 roots for $[Fe^{IV}(O)(NHC)_4(EtCN)]^{2+}$ in the triplet (left) and quintet (right) state. Orbitals are sorted by increasing occupation number which in the present case coincides with the energetic order (hydrogen atoms omitted for clarity).

These differences in the electronic structure also explain the significant elongation of the iron-oxygen bond in the NHC-complex when going from *S*=1 to *S*=2, which is not observed for the TMC-complex (see Table 6.2, page 175). Occupation of the d_{z^2}-orbital in the NHC-complex results in an elongation of the iron-oxo bond (~0.07 Å) since the d_{z^2}-orbital is σ* anti-bonding with respect to the oxo-ligand. For the TMC-complex in the quintet state the d_{z^2}-orbital remains vacant, while the $d_{x^2-y^2}$-orbital is occupied. Therefore, only the equatorial bonds are significantly elongated (~0.1 Å) related to the anti-bonding character between the $d_{x^2-y^2}$-orbital and the equatorial ligand. The differences in the electronic structure also results in different bond orders for the quintet state. While for the $[Fe^{IV}(O)(NHC)_4(EtCN)]^{2+}$ complex the formal Fe-O bond order in the quintet state is 1.5, it is 2.0 for the $[Fe^{IV}(O)(TMC)(MeCN)]^{2+}$ complex.

These differences seen for the two oxo-iron(IV) complexes can be explained by the nature of the equatorial ligand. While the TMC-ligand is only a moderate equatorial σ-donor ligand, the tetra carbene ligand is a strong σ-donor. Therefore, the $d_{x^2-y^2}$-orbital in the NHC-complex is energetically raised even above the d_{z^2}-orbital which itself forms a strongly anti-bonding σ*-orbital with the oxygen $2p_z$-orbital. On the other hand, for all tetragonal non-heme oxo-iron(IV) complexes that have been studied so far,[7,85-86,91-93,101,251,267-270] the same d-orbital splitting was found as described here for the $[Fe^{IV}(O)(TMC)(MeCN)]^{2+}$ complex. Hence, the NHC-complex is to date the first studied example that differs from these "classical" systems. Since the C-H activation by oxo-iron(IV) complexes proceeds via the excited quintet state, the changes in the novel carbene-complex are expected to affect its reactivity. This will be studied in detail in Chapter 6.2 (page 181) where the complexes reactivity will be compared with the TMC-complex as a representative of "classical" oxo-iron(IV) complexes.

6.1.3. Excited States and Ligand Field Splitting of the Complexes $[Fe^{IV}(O)(TMC)(MeCN)]^{2+}$ and $[Fe^{IV}(O)(NHC)_4(EtCN)]^{2+}$

The excited states for oxo-iron(IV) model complexes have been previously analyzed by means of computational methods.[269-270] For the $[Fe^{IV}(O)(TMC)(MeCN)]^{2+}$ complex absorption and MCD-data were published and analyzed with the help of TD-DFT calculations.[75,251,267,271] In this section, results are presented for the $[Fe^{IV}(O)(TMC)(MeCN)]^{2+}$ and $[Fe^{IV}(O)(NHC)_4(EtCN)]^{2+}$ complexes. The first 20 roots for the doublet state are calculated by the high level CASSCF/NEVPT method which will allow a detailed study and comparison of the excited states for both complexes.

Excitations for oxo-iron(IV) complexes in their $^3A_2$ ground state (assuming ideal C_{4v}-symmetry) result in a large number of possible excited states, possible dd-excitations are shown in Scheme 6.2.

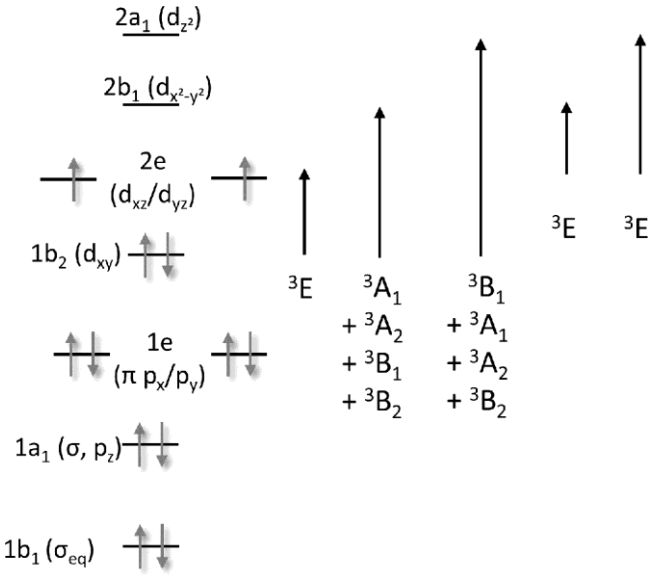

Scheme 6.2: Spin allowed dd-transitions for oxo-iron(IV)complexes ($^3A_2$ ground state) under C_{4v} symmetry.

There are three degenerate transitions of ^3E symmetry arising from the one electron excitations $^3E[1b_2(d_{xy})\rightarrow 2e(d_{xz}/d_{yz})]$, $^3E[2e(d_{xz}/d_{yz})\rightarrow 2b_1(d_{x^2-y^2})]$ and $^3E[3e(d_{xz}/d_{yz})\rightarrow 2a_1(d_{z^2})]$. A more complex situation is found for the excitations $1b_2(d_{xy})\rightarrow 2b_1(d_{x^2-y^2})$ and $1b_2(d_{xy})\rightarrow 2a_1(d_{z^2})$ that result in four unpaired electrons.[269-270] The transition of one electron from the $1b_2(d_{xy})$ into the $2b_1(d_{x^2-y^2})$ orbital results in excited states of A_1, A_2, B_1 and B_2 symmetry. Provided the electrons in the $2e(d_{xz}/d_{yz})$ sub-shell remain paired, this transition is of $^3A_1[1b_2(d_{xy})\rightarrow 2b_1(d_{x^2-y^2})]$ symmetry. Excited states of A_1, A_2, B_1 and B_2 symmetry result if one electron is transferred from the $1b_2(d_{xy})$ to the $2a_1(d_{z^2})$ orbital, the excited state is of $^3B_1[1b_2(d_{xy})\rightarrow 2a_1(d_{z^2})]$ if the electrons in the $2e(d_{xz}/d_{yz})$ sub shell remain coupled.

Excitation energies from a SA-CASSCF(12,9)/NEVPT2 calculation with 20 roots for the complex $[Fe^{IV}(O)(TMC)(MeCN)]^{2+}$ are provided in Table 6.3. Furthermore, the calculated oscillator strengths are provided that indicate significant intensity for the $^3E[2e(d_{yz}/d_{xz})\rightarrow 2b_1(d_{x^2-y^2})]$ transitions at 11272 cm^{-1} and 11630 cm^{-1} as well as for the $^3E[2e(d_{yz}/d_{xz})\rightarrow 2a_1(d_{z^2})]$ transitions at 16944 cm^{-1} and 17152 cm^{-1}, respectively. This is in reasonable agreement with the observed bands at 12100 cm^{-1} and 15600 cm^{-1} in the experimental absorption spectra.[75] In a more detailed MCD-study on the TMC-complex the $^3E[2e(d_{yz/xz})\rightarrow 2b_1(d_{x^2-y^2})]$ transition was assigned to bands observed at 12900 cm^{-1} in the MCD-spectrum, again in good agreement with the calculations presented here.[251] In this experimental study

further an MCD-band observed at 17600 cm^{-1} was assigned to the degenerated $^3E[2e(d_{xz}/d_{xz})\rightarrow 2a_1(d_{z^2})]$ transition which is again in very good agreement with the transitions calculated to be 16944 cm^{-1} and 17152 cm^{-1}.[251]

Table 6.3: Excitation energies and oscillator strengths from a SA-CASSCF(12,9)/NEVPT2 calculation with 20 roots for the $[Fe^{IV}(O)(TMC)(MeCN)]^{2+}$ complex in its triplet ground state ($^3A_2$, assuming C_{4v}).

Excitation Energy [cm^{-1}]	f_{osc} ($x10^4$)	Excited State
11272	3.3202	$^3E\ [2e(d_{yz})\rightarrow 2b_1(d_{x^2-y^2})]$
11630	3.0744	$^3E\ [2e(d_{xz})\rightarrow 2b_1(d_{x^2-y^2})]$
12216	0.4108	$^3E\ [1b_2(d_{xy})\rightarrow 2e(d_{yz})]$
12448	0.1253	$^3A_2\ [1b_2(d_{xy})\rightarrow 2e(d_{xz}) + 2e(d_{yz})\rightarrow 2b_1(d_{x^2-y^2})]$
12455	0.1576	$^3\Gamma\ [1b_2(d_{xy})\rightarrow 2b_1(d_{x^2-y^2})]$
13364	0.0105	$^3\Gamma\ [1b_2(d_{xy})\rightarrow 2b_1(d_{x^2-y^2})]$
13540	0.2422	$^3E\ [1b_2(d_{xy})\rightarrow 2e(d_{xz})]$
15397	0.0860	$^3A_2\ [1b_2(d_{xy})\rightarrow 2e(d_{yz}) + 2e(d_{xz})\rightarrow 2b_1(d_{x^2-y^2})]$
15662	0.2512	$^3\Gamma\ [1b_2(d_{xy})\rightarrow 2b_1(d_{x^2-y^2})]$
16944	0.6672	$^3E\ [2e(d_{yz})\rightarrow 2a_1(d_{z^2})]$
17152	0.8532	$^3E\ [2e(d_{xz})\rightarrow 2a_1(d_{z^2})]$
22085	0.0579	$^3\Gamma\ [1e(p_y)\rightarrow 2e(d_{xz})]$
22243	0.0034	$^3\Gamma\ [1e(p_x)\rightarrow 2e(d_{xz})]$
22535	0.0001	$^3\Gamma\ [1e(p_x)\rightarrow 2e(d_{yz})]$
26534	0.0021	$^2B_1\ \{2e(d_{xz})+2e(d_{yz})\}\rightarrow \{2b_1(d_{x^2-y^2})+2a_1(d_{z^2})\}$
26909	0.0775	$^2E\ [1b_2(d_{xy})\rightarrow 2b_1(d_{x^2-y^2})] + [2e(d_{yz}) \rightarrow 2b_1(d_{x^2-y^2})]$
26964	0.0251	$^2E\ [1b_2(d_{xy})\rightarrow 2b_1(d_{x^2-y^2})] + [2e(d_{xz}) \rightarrow 2b_1(d_{x^2-y^2})]$
30993	0.0001	$^2E\ \{1b_2(d_{xy}) + 2e(d_{yz})\} \rightarrow \{2b_1(d_{x^2-y^2}) + 2a_1(d_{z^2})\}$
31163	0.0156	$^2E\ \{1b_2(d_{xy}) + 2e(d_{xz})\} \rightarrow \{2b_1(d_{x^2-y^2}) + 2a_1(d_{z^2})\}$

$^3\Gamma=2A_1+A_2+B_1+B_2$ for $1b_2(d_{xy})\rightarrow 2b_1(d_{x^2-y^2})$ and $^3\Gamma=A_1+A_2+2B_1+B_2$ for $1b_2(d_{xy})\rightarrow 2a_1(d_{z^2})$

Results for the $[Fe^{IV}(O)(NHC)_4(EtCN)]^{2+}$ complex are summarized in Table 6.4. Large oscillator strengths were calculated for the $^3E[2e(d_{xz}/d_{yz})\rightarrow 2b_1(d_{x^2-y^2})]$ excitations at 24899 cm^{-1} / 24937 cm^{-1} which is again in good agreement with a band observed at 25000 cm^{-1} in the experimental absorption spectrum.[266]

Comparison of the excited states for the TMC- and NHC-systems highlight some remarkable differences in the electronic structure.

For the TMC-complex the $^3E[2e(d_{yz/xz})\rightarrow 2b_1(d_{x^2-y^2})]$ state is calculated to be the lowest excited state and the nearly degenerate transition energies are calculated to be 11272 cm^{-1} and 11630 cm^{-1}. Interestingly, these excitations appear at much higher energy for the NHC-complex. The $^3E[2e(d_{xz})\rightarrow 2b_1(d_{x^2-y^2})]$ excitations were calculated to be 24899 cm^{-1} and 24937 cm^{-1}, and therefore twice as high in energy than for the TMC-complex. Excitations calculated to appear for the NHC-system at 18559 cm^{-1} and 18602 cm^{-1} are corresponding to the $^3E[2e(d_{xz}/d_{xz})\rightarrow 2a_1(d_{z^2})]$ excited state, which is very similar to the TMC-complex (16944 cm^{-1} / 17152 cm^{-1}) but significantly lower in energy when compared with the $^3E[2e(d_{xz})\rightarrow 2b_1(d_{x^2-y^2})]$ excited state for the NHC-system. Taking these two excited states as a reference for the relative order of the $2b_1(d_{x^2-y^2})$ and $2a_1(d_{z^2})$ orbitals it can be concluded that in the TMC-system the $2b_1(d_{x^2-y^2})$ orbital is lower in energy than the $2a_1(d_{z^2})$ orbital (in agreement

with all previously studied non-heme tetragonal oxo-iron(IV) complexes[74,91,106,251,267,271-272]). For the NHC-system these orbitals are the other way around as indicated in Scheme 6.3.

Table 6.4: Excitation energies and oscillator strengths from a SA-CASSCF(12,9)/NEVPT2 calculation with 20 roots for the $[Fe^{IV}(O)(NHC)_4(EtCN)]^{2+}$ complex in its triplet ground state ($^3A_2$, assuming C_{4v}).

Excitation Energy [cm^{-1}]	f_{osc} ($x10^4$)	Excited State
12958	0.0018	^3E [$1b_2(d_{xy})\rightarrow 2e(d_{yz})$]
13074	0.0584	^3E [$1b_2(d_{xy})\rightarrow 2e(d_{xz})$]
18559	4.3264	^3E [$2e(d_{xz})\rightarrow 2a_1(d_{z^2})$]
18602	3.7493	^3E [$2e(d_{yz})\rightarrow 2a_1(d_{z^2})$]
23478	0.0064	$^3\Gamma$ [$1e(p_y)\rightarrow 2e(d_{xz})$]
23763	0.0807	$^3\Gamma$ [$1e(p_x)\rightarrow 2e(d_{xz})$]
24236	0.3176	$^3\Gamma$ [$1b_2(d_{xy})\rightarrow 2b_1(d_{x^2-y^2})$]
24899	9.2465	^3E [$2e(d_{xz})\rightarrow 2b_1(d_{x^2-y^2})$]
24937	7.3141	^3E [$2e(d_{yz})\rightarrow 2b_1(d_{x^2-y^2})$]
24987	2.7189	$^3A_2$ [$1b_2(d_{xy})\rightarrow 2e(d_{xz}) + 2e(d_{yz})\rightarrow 2b_1(d_{x^2-y^2})$]
25227	1.8630	$^3\Gamma$ [$1b_2(d_{xy})\rightarrow 2b_1(d_{x^2-y^2})$]
26827	0.0266	$^3\Gamma$ [$1b_2(d_{xy})\rightarrow 2b_1(d_{x^2-y^2})$]
27938	0.4291	$^3A_2$ [$1b_2(d_{xy})\rightarrow 2e(d_{xz}) + 2e(d_{yz})\rightarrow 2b_1(d_{x^2-y^2})$]
29258	0.8749	$^3\Gamma$ [$1b_2(d_{xy})\rightarrow 2b_1(d_{x^2-y^2})$]
30815	170.3311	$^3\Gamma$ [$1a_1(p_z)\rightarrow 2a_1(d_{z^2})$]
31313	0.5531	$^3\Gamma$ [$1b_2(d_{xy})\rightarrow 2b_1(d_{x^2-y^2})$]
31341	0.3196	$^3\Gamma$ [$1b_2(d_{xy})\rightarrow 2a_1(d_{z^2})$]
32467	2.4094	$^3\Gamma$ [$1b_2(d_{xy})\rightarrow 2a_1(d_{z^2})$]
34675	0.0013	$^2B_2$ [$1b_2(d_{xy}) \rightarrow 2e(d_{xz}) + 2e(d_{yz}) \rightarrow 2a_1(d_{z^2})$]

$^3\Gamma=2A_1+A_2+B_1+B_2$ for $1b_2(d_{xy})\rightarrow 2b_1(d_{x^2-y^2})$ and $^3\Gamma=A_1+A_2+2B_1+B_2$ for $1b_2(d_{xy})\rightarrow 2a_1(d_{z^2})$

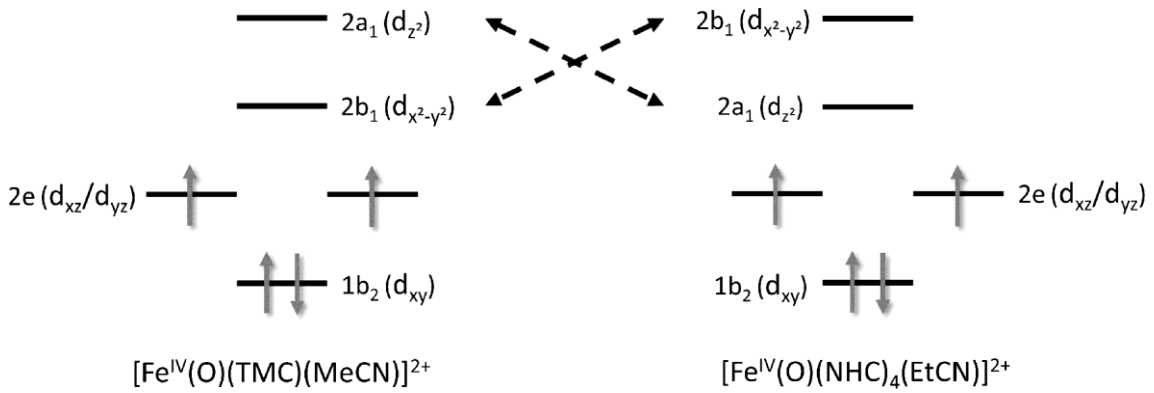

Scheme 6.3: Relative d-orbital arrangement for $[Fe^{IV}(O)(TMC)(MeCN)]^{2+}$ and $[Fe^{IV}(O)(NHC)_4(EtCN)]^{2+}$ complexes in their triplet ground state.

Therefore, the classical orbital splitting scheme can be applied for the complex $[Fe^{IV}(O)(TMC)(MeCN)]^{2+}$, as it was originally derived from the $[V(O)(H_2O)_5]^{2+}$ complex by Gray *et al.* for transition metal compounds with multiple bonded monoatomic ligands.[4,6,273] However, it cannot be applied to the novel NHC-system.

The reason for the distinctive relative order can be found in the equatorial ligand whose strength is reflected in transitions from the non-bonding $1b_2(d_{xy})$ orbital to the equatorial anti-bonding $2b_1(d_{x^2-y^2})$ orbital.[251] For the $[Fe^{IV}(O)(TMC)(MeCN)]^{2+}$ complex the lowest excitation of this type was calculated to be 12455 cm^{-1} while for the $[Fe^{IV}(O)(NHC)_4(EtCN)]^{2+}$ complex these transitions do not appear below 24236 cm^{-1}, i.e. at much higher energy, which shows that the NHC-ligand is a much stronger equatorial ligand than the TMC-ligand.

The energy of the $^3E[1b_2(d_{xy})\rightarrow 2e(d_{yz}/d_{xz})]$ excitation is a measure of the strength of the Fe-O π-bond.[251] Since the $2e(d_{yz}/d_{xz})$ orbitals are the anti-bonding π*-orbitals for the Fe-O bond, a higher $^3E[1b_2(d_{xy})\rightarrow 2e(d_{yz}/d_{xz})]$ excited state indicates a stronger Fe-O bond. However, for both systems studied here these excitations are of very similar energy (TMC:12216 cm^{-1}/13540 cm^{-1} NHC:12958 cm^{-1} / 13074 cm^{-1}) which indicates a very similar Fe-O bonding strength in the triplet ground state.

Prof. Mihail Atanasov recently proposed an *ab initio* based ligand field approach (*ab initio* parametric ligand field, AIPLF) that allows to connect results from the CASSCF/NEVPT2 calculations with ligand field theory and the angular overlap model (AOM).[204,274] On top of the above discussed calculations Prof. Mihail Atanasov applied the AIPLF approach and the derived relative energetic order for the d-orbitals is shown in Figure 6.3. In line with the calculated and discussed excitation energies (*vide supra*), in the TMC-system the mainly $d_{x^2-y^2}$ derived orbital is lower in energy than the d_{z^2}-orbital, while it is the other way around in the NHC complex. This is can be attributed to the much stronger equatorial carbene ligand, rising the energy of the $d_{x^2-y^2}$-orbital above the d_{z^2}-orbital, resulting in e_σ^{eq} values of 4309 cm^{-1} for the TMC-complex and 7718 cm^{-1} for the NHC-complex. Therefore, the AIPLF approach confirms quantitatively (Figure 6.3) the qualitative picture shown in Scheme 6.3.

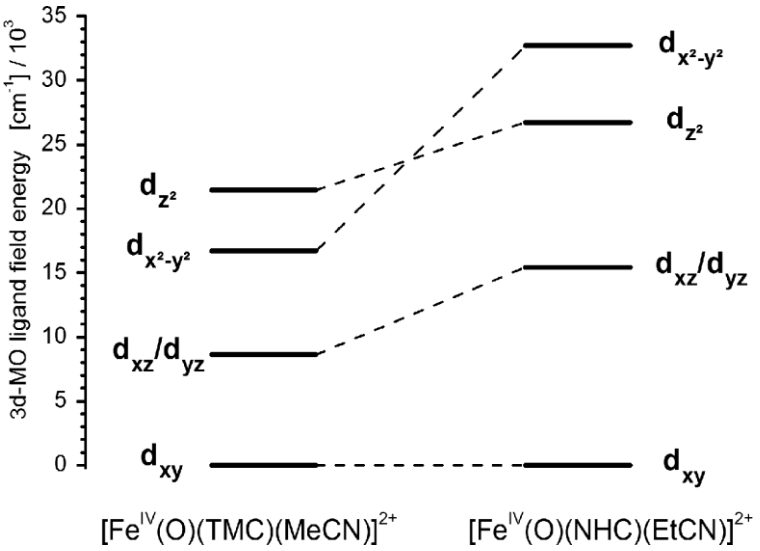

Figure 6.3: Ligand field splitting diagrams for $[Fe^{IV}O(TMC)(MeCN)]^{2+}$ and $[Fe^{IV}O(NHC)_4(EtCN)]^{2+}$ derived from the AIPLF approach.[These results were obtained by Prof. Mihail Atanasov, based on the CASSCF(12,9)/NEVPT2 calculations discussed above that were performed by the author of the present thesis.]

How the unequal energetic order of the $d_{x^2-y^2}$ and d_{z^2}-orbitals in the studied systems affects their reactivity will be explored in the following chapter.

6.2. Reactivity of Oxo-Iron(IV) Complexes

In the antecedent chapter the electronic structures of the complexes $[Fe^{IV}(O)(TMC)(MeCN)]^{2+}$ and $[Fe^{IV}(O)(NHC)_4(EtCN)]^{2+}$ were elucidated with a focus on differences between the two systems. While the TMC-system shows a d-orbital splitting identical to all previously studied tetragonal oxo-iron(IV) complexes, in the novel NHC-systems the vacant (triplet ground state) $d_{x^2-y^2}$- and d_{z^2}-orbitals are in reverse energetic order. In the quintet state this results in a singly occupied $d_{x^2-y^2}$-orbital while the d_{z^2}-orbital is vacant for the "classical" TMC system, the reverse situation being observed for the NHC-complex. Given that these orbitals are involved in C-H activation reactions, the well-established two-state-reactivity concept is not applicable anymore without modification. As outlined in the introduction (Chapter 1.3.1, page 9) the four possible reaction channels can be illustrated with electron shift diagrams (ESD).[86,89,91,93,98,101] This is shown in Scheme 6.4 (left) for the TMC-complex, but is applicable to all tetragonal oxo-iron(IV) complexes. Further shown in Scheme 6.4 (right) is the putative electron shift process for the NHC-complex.

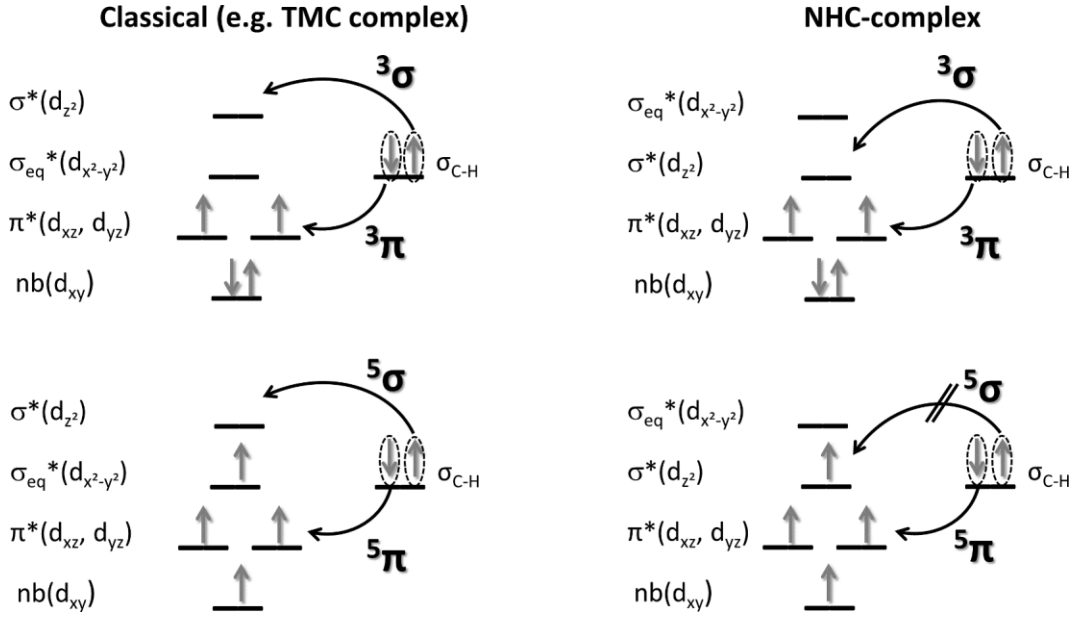

Scheme 6.4: Electron shift diagram (ESD) for the TMC- (left) and the NHC-system (right).

As discussed in Chapter 1.3.1, in the triplet state a spin-down electron is transferred from the C-H-bond to one of the singly occupied d_{xz}/d_{yz}-orbitals ($^3\pi$-pathway). Alternatively, a spin-up electron can be transferred to the vacant d_{z^2}-orbital ($^3\sigma$-pathway). Both options are possible for the TMC- and the NHC-system. However, for the systems studied so far[86,89,91,93,101] the quintet transition state was found to be lowest in energy, hence, the reaction is expected to proceed via the quintet state, even the initial $Fe^{IV}O$-complex shows a triplet ground state. In the quintet state σ- and a π-pathways represent possible reaction channels and the lowest barrier is usually found for the former. A spin-down electron is transferred from the C-H-bond into one of the singly occupied d_{xz}/d_{yz}-orbitals on the $^5\pi$-pathway, which is possible for both complexes (TMC and NHC). Within the $^5\sigma$-pathway a spin-up electron is shifted from the C-H-bond into the d_{z^2}-orbital which is vacant in the "classical" TMC-system. However, due to the specific electronic structure in the novel NHC-complex this orbital is occupied and cannot act as an accepting orbital for another spin-up electron. Hence, the $^5\sigma$-pathway which is the preferred pathway for all other oxo-iron(IV)-complexes studied before is now blocked for the NHC-complex.

Herein, the effect of these changes are studied in detail employing computational methods. All possible C-H-abstraction pathways on the triplet and quintet surface are computed for the complexes $[Fe^{IV}(O)(TMC)(MeCN)]^{2+}$ and $[Fe^{IV}(O)(NHC)_4(EtCN)]^{2+}$ with identical methods which allows for a comparison of the resulting barriers for the different complexes. As evident from the calculated singlet-triplet gaps (see Table 6.1 and Table 6.2) the singlet state for the $Fe^{IV}O$-complexes is well separated from the triplet and quintet states and is therefore not considered in the reactions. It will be shown that the calculated singlet-triplet gaps are already of the same order of magnitude and correlate with barriers for the corresponding triplet and quintet state. Reactions in the singlet state are therefore unlikely. Ethane was chosen as a model substrate since the main focus will lie on the comparison between the two $Fe^{IV}O$-complexes and ethane has proven to be a useful model substrate previously.[93]

Structures were optimized with the def2-SVP basis set on the ligand, while for iron, all atoms bond to iron as well as the hydrogen and carbon atoms participating in the reaction the larger def2-TZVP basis set was used. The B3LYP functional was used in combination with the RIJCOSX approximation to speed up the calculations. Solvent effects were taken into account within the COSMO model and Grimme's D3 (zero damping) dispersion correction was applied. Thermal corrections (for ΔG) and zero point energy corrections (for ΔH) were also obtained from the frequency calculation. Total energies were obtained from single-point calculations on these structures using the same methodological setup but employing the def2-TZVPP basis set for all atoms. The electronic structure is discussed in terms of orbital plots for which quasi restricted orbitals were used and corresponding orbitals for the magnetic orbitals that result from antiferromagnetic coupling.

Reported energies are relative to the reaction complex in the triplet ground state (^{3}**RC**) which is the oxo-iron(IV) complex and ethane weakly-bound via van der Waals interaction. Using ^{3}**RC** instead of two infinitely separated iron and substrate fragments as the reference will reduce the errors in the entropy term. Structures for the transition states of the $^3\sigma$-, $^3\pi$-, $^5\sigma$- and $^5\pi$-pathways (^{3}**TS**$_\sigma$, ^{3}**TS**$_\pi$, ^{5}**TS**$_\sigma$, ^{5}**TS**$_\pi$), respectively, are displaced along their imaginary mode to obtain guess structures for optimization to the intermediates of the C-H-oxidation reaction (^{3}**I**$_\sigma$, ^{3}**I**$_\pi$, ^{5}**I**$_\sigma$, ^{5}**I**$_\pi$). These hydroxo-iron(III) complexes are weakly coordinated to the resulting ethane-radical.

6.2.1. Hydrogen Abstraction by the Complex $[Fe^{IV}(O)(TMC)(MeCN)]^{2+}$

Calculations on hydrogen abstraction reactions by the complex $[Fe^{IV}(O)(TMC)(MeCN)]^{2+}$ were performed previously,[86,101,106-107] however, in these studies not all conceivable σ- and π-pathways were explored. Instead, these studies only considered one triplet and one quintet pathway. The ^{3}σ-, ^{5}σ-, ^{3}π and ^{5}π-pathways were only calculated for a series of smaller model complexes[93] as well as for some analogue compounds with different ligand systems.[87,275]

First, the energetics of the reaction shown in Scheme 6.5 will be examined before details of the electronic structure and the geometry will be discussed. Free Gibbs energies (Δ*G*) will be used in the following discussion, however, reaction enthalpies (Δ*H*) are very similar for the calculated reactions and lead to the same conclusions.

In agreement with the calculations in the previous section the reaction complex (Fe^{IV}O-complex + ethane) in the triplet state (**^{3}RC**) is calculated to be slightly lower in energy than in the quintet state (**^{5}RC** , Scheme 6.5).

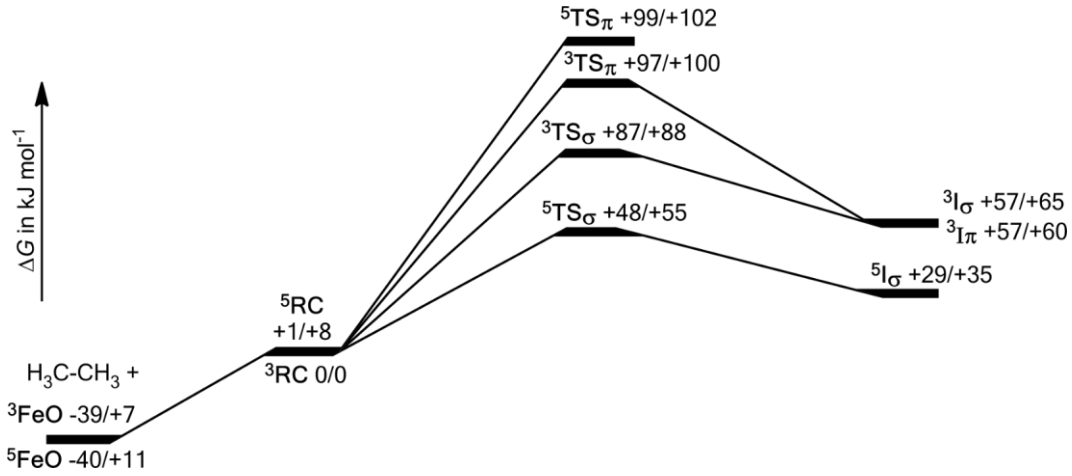

Scheme 6.5: Reaction profile for the hydrogen abstraction from ethane by $[Fe^{IV}(O)(TMC)(MeCN)]^{2+}$. Given energies for Δ*G*/Δ*H* in kJ mol^{-1} relative to ^{3}RC, upper left superscripts denote the multiplicity of the iron center.

The lowest barrier for hydrogen atom abstraction was calculated for the **$^5TS_\sigma$** transition state (48 kJ mol^{-1}), which agrees well with previous studies.[86,101,106-107] In these studies only the π-pathway on the triplet surface via **$^3TS_\pi$** was considered, which was calculated here to be 97 kJ mol^{-1} high, hence, 10 kJ mol^{-1} higher in energy than the **$^3TS_\sigma$** transition state (87 kJ mol^{-1}). The **$^5TS_\pi$** transition state (99 kJ mol^{-1}) was calculated to be nearly at the same energy as the **$^3TS_\pi$** transition state. From the calculated barriers the following reactivity can be derived for the hydroxylation reaction:

$$^5\sigma > {}^3\sigma > {}^3\pi \approx {}^5\pi$$

In a study on the model complex $[Fe^{IV}(O)(NH_3)_5]^{2+}$ with the same substrate (ethane) the ^{5}σ-pathway was also calculated to be lowest in energy and well separated from the other transition states.[93] In contrast to the TMC-system, the ^{3}σ-transition state was found to be highest in energy and above the π-pathways and the same was found in a study on the $[Fe^{IV}(O)(N4Py)]^{2+}$ complex.[87] However, it should be noted that the energy differences between the ^{3}σ-, ^{3}π- and ^{5}π-transition states is rather small in the present study as well as in those studies that were published previously.[87,93,276]

The resulting hydroxo-iron(III) complexes $^5\mathbf{I}_\sigma$, $^3\mathbf{I}_\pi$ and $^3\mathbf{I}_\sigma$ are in a similar energetic order as the transition states. Lowest in energy is the $^5\mathbf{I}_\sigma$ species, even the reaction is still calculated to be endergonic by about 29 kJ mol^{-1}. Identical energies were calculated for the $^3\mathbf{I}_\pi$ and $^3\mathbf{I}_\sigma$ complexes (57 kJ mol^{-1}). All attempts to locate a structure for the Fe^{III}(OH) intermediate $^3\mathbf{I}_\pi$ proved to be unsuccessful. Starting from the $^3\mathbf{TS}_\pi$ transition state, optimizations always result in barrier free rebound of the ethyl-radical resulting in ethanol and the corresponding iron(II)-complex.

Selected geometric parameters are provided in Table 6.5, Loewdin spin-populations for the transition states can be found in Table 6.6 and spin density plots are shown in Figure 6.4.

Table 6.5: Selected bond distances and angles for the [Fe^{IV}(O)(TMC)(MeCN)]$^{2+}$ complex, transition states and Fe^{III}(OH) intermediates.

	Fe-O [Å]	O-H [Å]	H-C [Å]	Fe-N$_{Ac}$ [Å]	Fe-O-H [°]	O-H-C [°]	O-Fe-N$_{Ac}$ [°]	Fe-N$_{Ac}$-C$_{Ac}$ [°]
Fe^{IV}O, *S*=1	1.623			2.049			179.13	175.64
Fe^{IV}O, *S*=2	1.619			2.028			178.86	175.03
^{5}TS$_\sigma$	1.736	1.223	1.301	2.177	175.33	176.11	176.09	173.03
^{3}TS$_\sigma$	1.762	1.154	1.355	2.305	168.58	177.20	178.47	171.96
^{5}TS$_\pi$	1.742	1.176	1.351	2.018	136.95	160.45	173.45	176.20
^{3}TS$_\pi$	1.749	1.187	1.352	2.032	136.45	162.99	173.65	177.44
^{5}I$_\sigma$	1.815	0.974	2.051	2.174	145.02	177.91	175.42	172.17
^{3}I$_\sigma$	1.868	0.969	2.106	2.329	138.78	161.35	178.00	178.78
^{3}I$_\pi$	1.800	0.964	2.324	1.998	119.44	136.25	175.70	178.73

B3LYP/COSMO(Acetonitril)/D3ZERO/def2-SVP, Fe bond atoms, C+H:def2-TZVP optmization

Table 6.6: Loewdin spin-population for selected atoms of transition states from the [Fe^{IV}(O)(TMC)(MeCN)]$^{2+}$ complex.

	Loewdin spin-population			
	^{5}TS$_\sigma$	**^{3}TS$_\sigma$**	**^{5}TS$_\pi$**	**^{3}TS$_\pi$**
Fe	3.90	2.55	2.91	1.04
O	0.18	0.14	0.34	0.47
H	-0.10	-0.09	0.10	0.11
C	-0.31	-0.34	0.31	0.33

B3LYP/def2-TZVPP/RIJCOSX/D3ZERO/COSMO single point calculations

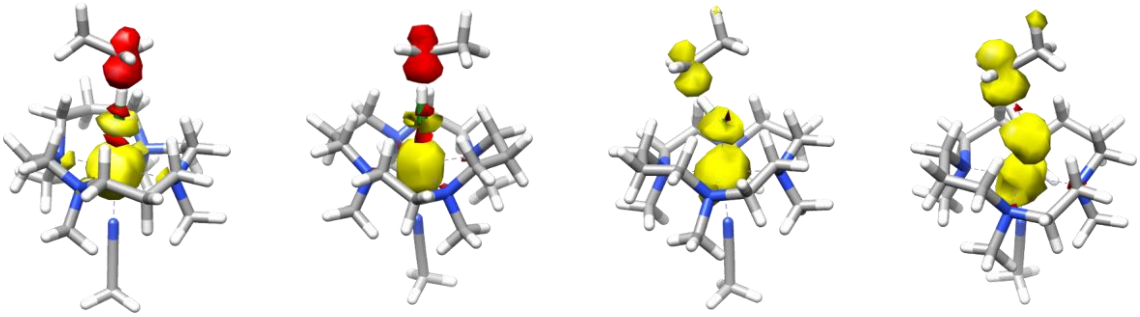

^{5}TS$_\sigma$ **^{3}TS$_\sigma$** **^{5}TS$_\pi$** **^{3}TS$_\pi$**

Figure 6.4: Spin density plots for the transition states of the [Fe^{IV}(O)(TMC)(MeCN)]$^{2+}$ complex (red: negative, yellow: positive).

For both σ-transition states the Fe-O-H bond is found to be nearly linear (^{5}**TS$_\sigma$**: 175°, ^{3}**TS$_\sigma$**: 169°), which can be explained by the overlap of the iron centered d_{z^2}-orbital with the C-H σ-bond of the substrate which is largest for a linear arrangement (see Scheme 1.12, page 9).[91,93] For the transition state lowest in energy (^{5}**TS$_\sigma$**) the shortest C-H distance and longest O-H-distance is found when compared to the alternative transition states. This can be described as an early transition state with a relatively low barrier where the structure still strongly resemble the geometry of the starting compound. As evidenced by the spin density plots for ^{5}**TS$_\sigma$** and ^{3}**TS$_\sigma$** (Figure 6.4) and the calculated spin-population (Table 6.6), negative spin density is located on the carbon-atom of the substrate. As already outlined in Scheme 6.4, the reason for this is the transfer of a spin-up electron from the substrate C-H-bond to the iron d_{z^2}-orbital while the spin-down electron remains on the carbon atom. Population of the d_{z^2}-orbital further explains the significant elongation of the bond between iron and the coordinated acetonitrile molecule (~0.1-0.2 Å) since the d_{z^2}-orbital is anti-bonding with respect to the axial iron ligands.

The electronic structure for the ^{5}**TS$_\sigma$** transition state and the resulting Fe^{III}(OH) complex ^{5}**I$_\sigma$** is shown in Figure 6.5. The d_{xy}-, d_{xz}-, d_{yz}- and $d_{x^2-y^2}$-orbitals remain singly occupied with one spin-up electron as was the case for the initial Fe^{IV}O-complex in the quintet state. Since one electron is transferred from the substrate to the metal, the d_{z^2}-orbital becomes occupied with one spin-up electron, and a singly occupied orbital that exhibits a spin-down electron is found at the substrate carbon atom. As can be seen in the orbital plot (Figure 6.5), a σ-bonding orbital (doubly occupied) is found between the carbon and hydrogen atom, slightly delocalized onto the oxygen atom (σ_{CHO}). The anti-bonding combination of this orbital is the σ^*_{CHO} bond that is occupied by a spin-down electron. Further, the spin-up electron centered on iron in the d_{z^2}-orbital and the spin-down electron on the carbon atom (σ^*_{CHO}) are antiferromagnetically coupled with an overlap of *S*=0.61. The three orbitals σ_{CHO}, σ^*_{CHO}, d_{z^2} are formed in course of the reaction from the vacant iron d_{z^2}-orbital, the doubly occupied oxygen p_z-orbital and the doubly occupied C-H σ-bond of the substrate.

Only minor differences in the electronic structure are observed when proceeding to the resulting Fe^{III}OH complex ^{5}**I$_\sigma$** (see Figure 6.5, right). The orbital occupation remains the same, however, the overlap between the antiferromagnetically coupled d_{z^2}- and σ^*_{CHO}- orbitals is reduced to *S*=0.19 which can be easily explained by elongation of the distance between the iron center and the substrate. While the C-H bond is elongated from 1.30 Å in ^{5}**TS$_\sigma$** to 2.05 Å in ^{5}**I$_\sigma$** the O-H bond is shortened from 1.22 Å to 0.97 Å. The nearly linear Fe-O-H angle in the ^{5}**TS$_\sigma$** transition state (175°) is more acute (145°) in the intermediate ^{5}**I$_\sigma$**.

In Figure 6.6 the electronic structure of the ^{3}**TS$_\sigma$** transition state and the ^{3}**I$_\sigma$** intermediate are shown. Overall, these closely resemble the electronic structure for the ^{5}**TS$_\sigma$** and ^{5}**I$_\sigma$** species just discussed, with the difference that the $d_{x^2-y^2}$-orbital is vacant now and the d_{xy}-orbital is doubly occupied. This is also reflected in the reduced positive spin population for ^{3}**TS$_\sigma$** on iron when compared to the analogue transition state in the quintet spin state ^{5}**TS$_\sigma$** (see Table 6.6).

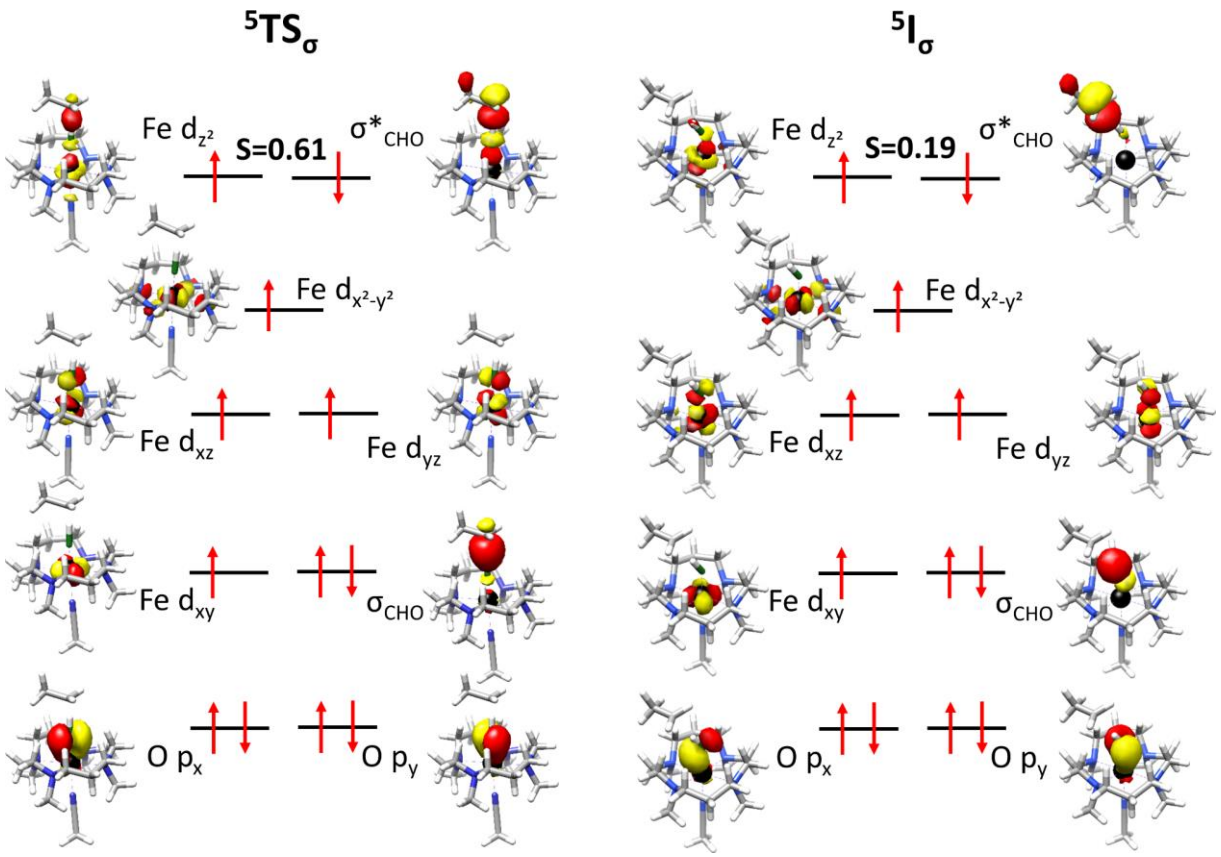

Figure 6.5: Electronic structure of $^5TS_\sigma$ (left) and $^5I_\sigma$ (right) for the $[Fe^{IV}(O)(TMC)(MeCN)]^{2+}$ complex.

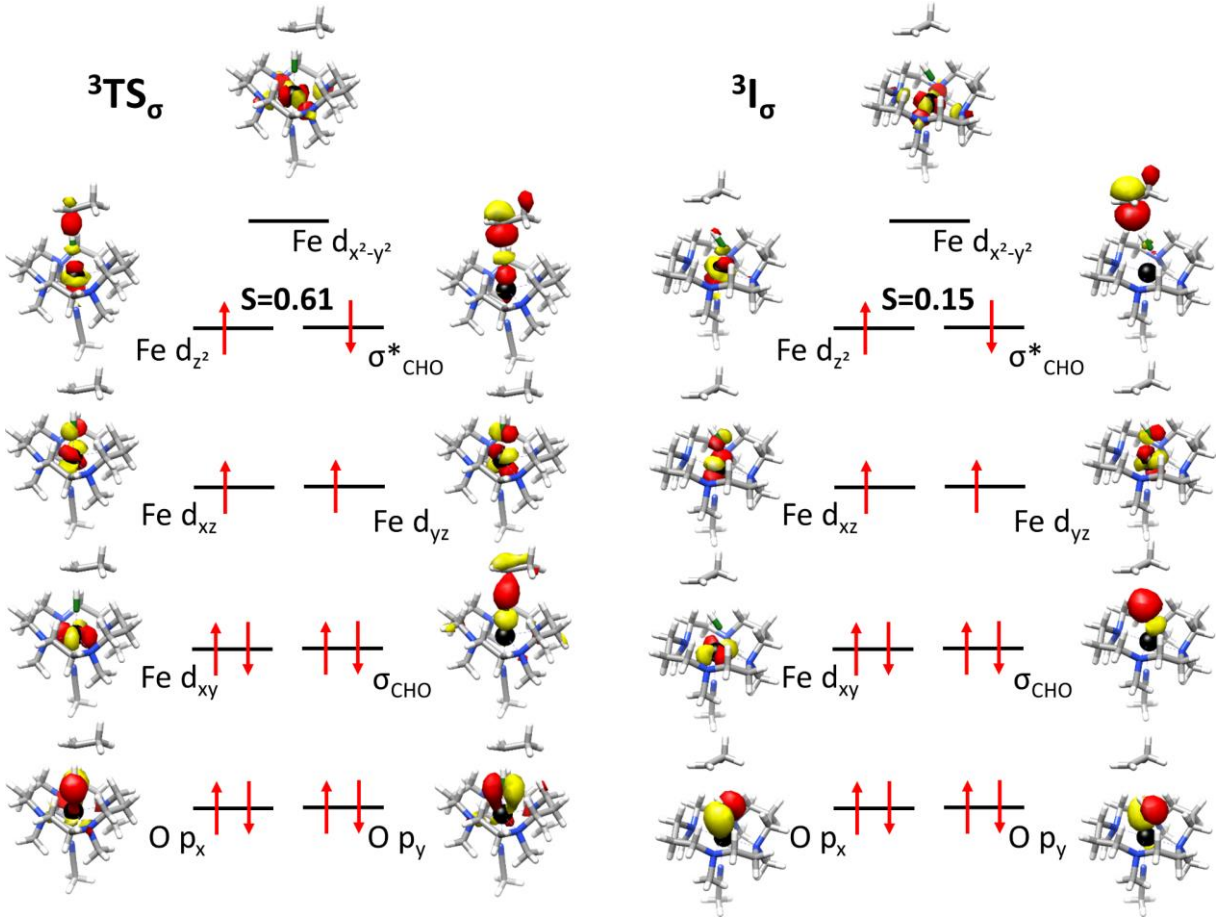

Figure 6.6: Electronic structure of $^3TS_\sigma$ (left) and $^3I_\sigma$ (right) for the $[Fe^{IV}(O)(TMC)(MeCN)]^{2+}$ complex.

Substantial differences are found when the σ-pathways are compared with the π-pathways. Most obviously, the Fe-O-H angle for $^5\mathbf{TS}_\pi$ (137°) and $^5\mathbf{TS}_\pi$ (137°) is much smaller when compared to the σ-transition states $^5\mathbf{TS}_\sigma$ (175°) and $^3\mathbf{TS}_\sigma$ (169°), respectively. This can be explained by the overlap of the involved orbitals. In the π-pathway a spin-down electron is transferred from the C-H σ-orbital to the singly occupied d_{xz}-orbital (or d_{yz}) at iron. Best overlap between these orbitals would be found in a rectangular fashion (Fe-O-H 90°, see Scheme 1.12, page 9), however, due to steric repulsion with the equatorial ligand the angle is increased but still significantly smaller than for the σ-pathway. The calculated spin population and spin densities bear out the described electron shift on the π-pathway. A spin population of 2.91 for iron was calculated for the $^5\mathbf{TS}_\sigma$ transition state which very well correlates with three singly occupied iron d-orbitals (d_{xy}, d_{yz}, $d_{x^2-y^2}$). While the d_{xz}-orbital is singly occupied in the initial $Fe^{IV}O$ complex in the quintet state, it is filled by two electrons now, due to the transfer of a spin-down electron from the substrate to the metal (see Figure 6.7). The doubly occupied oxygen p_x-orbital in the initial $Fe^{IV}O$-complex overlaps with the C-H σ-bond of the substrate forming a σ_{CHO}-bond. Because of the electron transfer from the substrate to the metal, the corresponding anti-bonding σ^*_{CHO}-orbital is singly occupied in the transition state. The transfer of one electron into the d_{xz}-orbital and not into the d_{z^2}-orbital that is antibonding with respect to the axial ligands is also indicated by the bond lengths. While for the σ-transition states the distance between iron and the coordinate acetonitrile molecule is strongly elongated, this is not the case for the π-transition states.

Unfortunately it was not possible to calculate the structure of intermediate $^5\mathbf{I}_\pi$, owing to the fact that all optimizations resulted directly in the formation of ethanol and the Fe^{II}-complex.

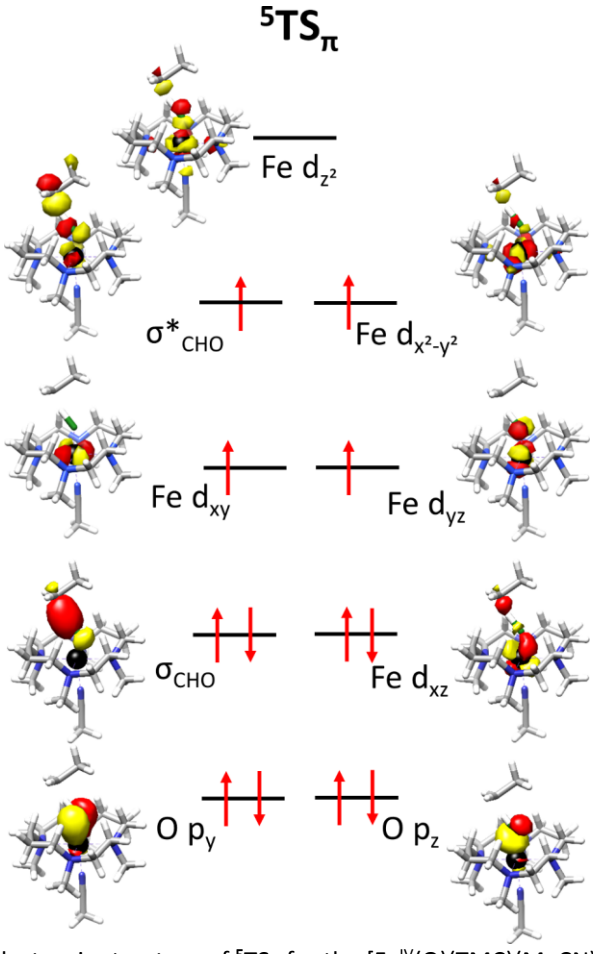

Figure 6.7: Electronic structure of $^5\mathbf{TS}_\pi$ for the $[Fe^{IV}(O)(TMC)(MeCN)]^{2+}$ complex.

On the π-pathway in the triplet state again one electron is transferred from the C-H bond of the substrate to the metal d_{xz}-orbital. Therefore the d_{xy}- and d_{xz}-orbitals are doubly occupied while the d_{yz}-orbital remains singly occupied. Due to the transfer of one electron to the metal center, there remains one unpaired electron on the substrate. As evident from the calculated spin population (O: 0.47; H:0.11; C:0.33) the unpaired electron is delocalized over the substrate and the oxo-atom. This is in good agreement with the shape of the singly occupied σ^*_{CHO}-orbital shown in Figure 6.8.

In the resulting $Fe^{III}(OH)$ species $^3\mathbf{I}_\pi$ the unpaired substrate electron is completely located on the carbon atom which can be explained by the elongation of the C-H-bond by ~1 Å from 1.35 Å in $^3\mathbf{TS}_\pi$ to 2.32 Å in $^3\mathbf{I}_\pi$. The σ_{HO}-bond is finally formed and the d_{yz}-orbital is singly occupied in the resulting low-spin iron(III) complex.

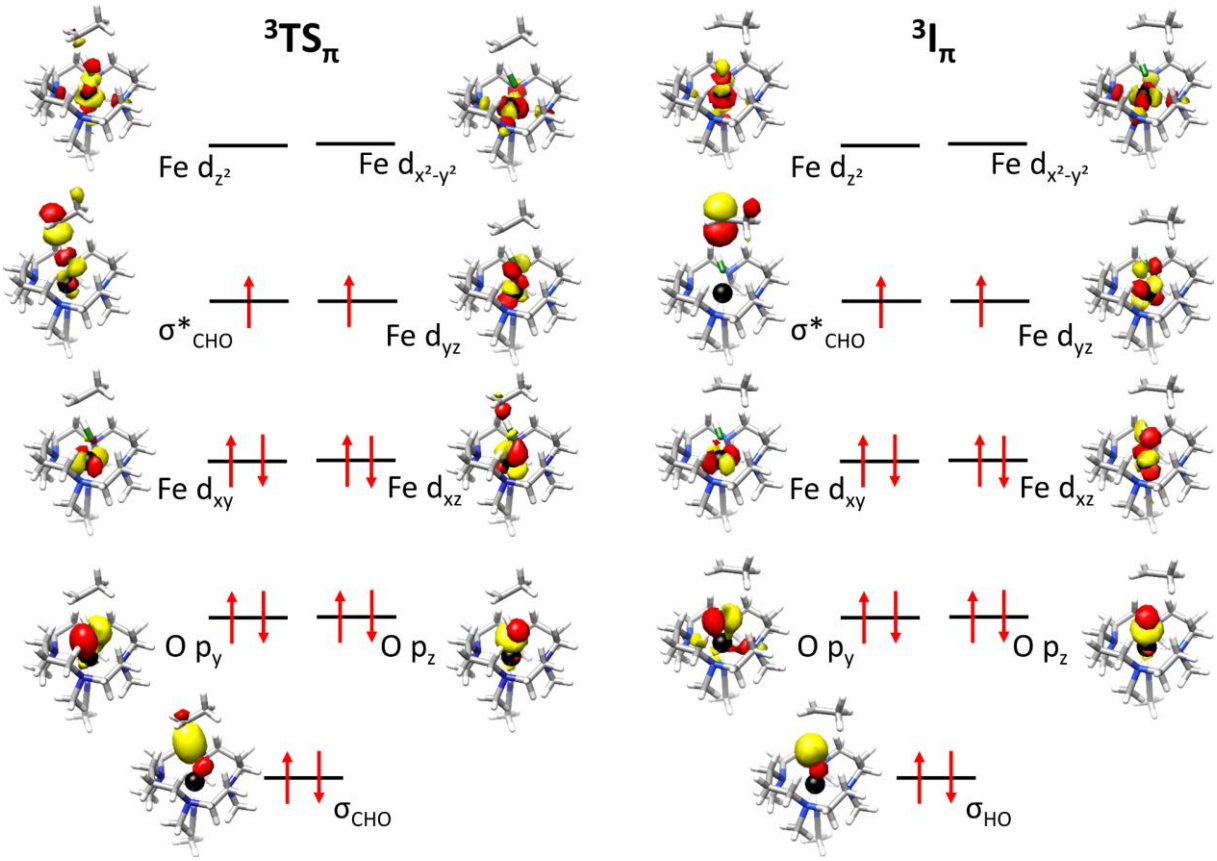

Figure 6.8: Electronic structure of $^3\mathbf{TS}_\pi$ (left) and $^3\mathbf{I}_\pi$ (right) for the $[Fe^{IV}(O)(TMC)(MeCN)]^{2+}$ complex.

The results are in line with previous studies on C-H abstraction reactions by the $[Fe^{IV}(O)(TMC)(MeCN)]^{2+}$ complex.[86,101,106-107] However, in these earlier studies only the $^5\sigma$- and $^3\pi$-pathways were explored. The present study reveals that the $^3\sigma$- and $^5\pi$-pathways are competitive alternatives when compared to the $^3\pi$-pathway. Still, the $^5\sigma$-transition state is found to be lowest in energy and well separated from the other alternatives.

The results discussed above will provide a reference for studying the C-H activation by the new complex $[Fe^{IV}(O)(NHC)_4(EtCN)]^{2+}$. Calculations will be performed to investigate in detail the consequences of the distinct electronic structures (see Chapter 6.1 and 6.1.3) in the $[Fe^{IV}(O)(NHC)_4(EtCN)]^{2+}$ and $[Fe^{IV}(O)(TMC)(MeCN)]^{2+}$ complexes in the following chapter.

6.2.2. Hydrogen Abstraction by the Complex $[Fe^{IV}(O)(NHC)_4(EtCN)]^{2+}$

In a similar vein to the TMC-complex, all possible reaction channels will be explored for the hydrogen abstraction from ethane by the oxo-iron(IV) NHC-complex. The energetics of the reaction shown in Scheme 6.6 will be examined first, before details of the electronic structure and the geometry will be discussed. During the following discussion energies will be reported as Gibbs free energies (Δ*G*), however, the reaction enthalpies (Δ*H*) are nearly identical for the calculated reactions and would result in the same conclusions.

It was demonstrated by the group of Prof. Franc Meyer in Göttingen (unpublished results) that the $[Fe^{IV}(O)(NHC)_4(EtCN)]^{2+}$ complex undergoes hydrogen abstraction reactions with alkanes such as dihydroanthracene. Currently, detailed kinetic measurements are underway in order to compare the reactivity of the TMC- and NHC-systems experimentally.

In agreement with the calculations in the previous section (Table 6.2, page 175) the reaction complex in the triplet state (**^{3}RC**) is calculated to be significantly lower in energy than in the quintet state, **^{5}RC** (see Scheme 6.6).

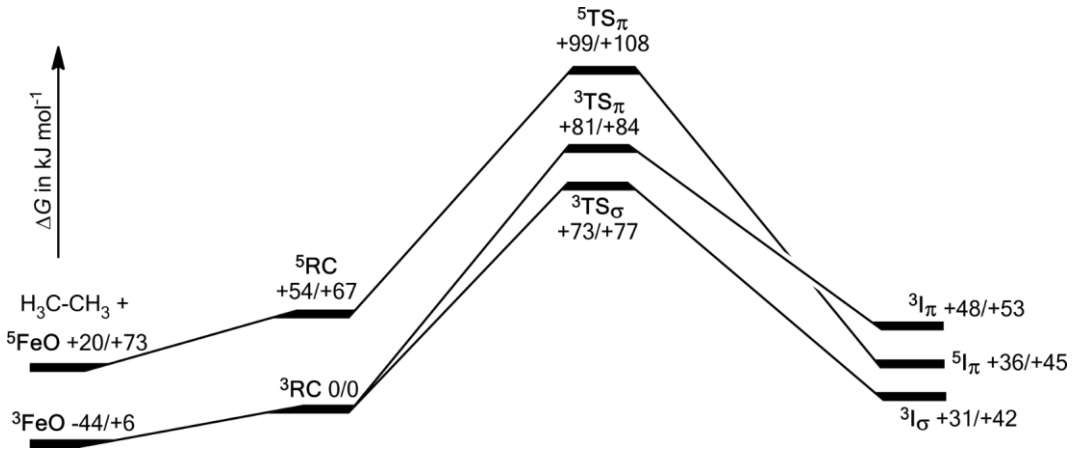

Scheme 6.6: Reaction profile for the hydrogen abstraction from ethane by $[Fe^{IV}(O)(NHC)_4(EtCN)]^{2+}$. Given energies for Δ*G*/Δ*H* in kJ mol^{-1} relative to **^{3}RC**, upper left superscripts denote the multiplicity of the iron center.

Calculated barriers and free reaction energies are summarized in Table 6.7 for both complexes $[Fe^{IV}(O)(TMC)(MeCN)]^{2+}$ and $[Fe^{IV}O(NHC)_4(EtCN)]^{2+}$, which will allow for a comparison between the two complexes in terms of their activation barriers and reaction energies.

Table 6.7: Calculated barriers and free reaction energies (Δ*G*) for the TMC- and NHC-complexes.

	$^5TS_\sigma$ [kJ mol^{-1}]	$^3TS_\sigma$ [kJ mol^{-1}]	$^5TS_\pi$ [kJ mol^{-1}]	$^3TS_\pi$ [kJ mol^{-1}]	$^5I_\sigma$ [kJ mol^{-1}]	$^3I_\sigma$ [kJ mol^{-1}]	$^5I_\pi$ [kJ mol^{-1}]	$^3I_\pi$ [kJ mol^{-1}]
$[Fe^{IV}(O)(TMC)(MeCN)]^{2+}$	48	87	99	97	29	57	-	57
$[Fe^{IV}(O)(NHC)_4(EtCN)]^{2+}$	-	73	99	81	-	31	36	48

As illustrated by the electron shift diagram in Scheme 6.4 (page 181), the classical $^5\sigma$-pathway is not accessible for the NHC-system since the d_{z^2}-orbital is already occupied in the quintet state and cannot serve as an accepting orbital for an additional spin-up electron. Attempts were made to locate a transition state featuring a (near) linear Fe-O-H angle that allows best overlap of the iron d_{z^2}- and

substrate σ_{CH}-orbital which might result in transfer of a spin-down electron from the substrate to the metal. However, no such transition state was found.

For the oxo-iron(IV) tetracarbene complex transition state $^{3}\mathbf{TS}_{\sigma}$ was calculated to be lowest in energy (73 kJ mol^{-1}). However, this barrier is still significantly higher in energy than the transition state $^{5}\mathbf{TS}_{\sigma}$ for the TMC-system (48 kJ mol^{-1}) which turned out to be the lowest energy pathway for the TMC-system (*vide supra*). The transition state $^{3}\mathbf{TS}_{\sigma}$ results in the $Fe^{III}(OH)$ intermediate $^{3}\mathbf{I}_{\sigma}$ that is calculated to be lowest in energy (31 kJ mol^{-1}) for the NHC system. Interestingly, the $^{3}\mathbf{TS}_{\sigma}$ transition state for the NHC-system (73 kJ mol^{-1}) is lower in energy when compared to the TMC-system (87 kJ mol^{-1}). Moreover, the $^{3}\mathbf{TS}_{\pi}$ transition state for the NHC-system (81 kJ mol^{-1}) is slightly lower in energy than the barrier calculated for $^{3}\mathbf{TS}_{\sigma}$ of the TMC-system (87 kJ mol^{-1}). Identical barriers were calculated for the $^{5}\mathbf{TS}_{\pi}$ transition states (+99 kJ mol^{-1}) for hydrogen abstraction by the complexes $[Fe^{IV}(O)(TMC)(MeCN)]^{2+}$ and $[Fe^{IV}(O)(NHC)_4(EtCN)]^{2+}$, respectively, and in both cases this is the highest energy pathway. From these calculations the following reactivity can be derived for hydrogen abstraction by the NHC-complex:

$$^{3}\sigma > {}^{3}\pi > {}^{5}\pi$$

Likewise, the order was $^{5}\sigma > {}^{3}\sigma > {}^{3}\pi \approx {}^{5}\pi$ for the classical TMC-system. Hence, the relative order for the different pathways is the same, despite the absence of a $^{5}\sigma$-pathway for the novel NHC-system for the aforementioned reasons. It should be further noticed, that for the NHC-system the transition state lowest in energy ($^{3}\mathbf{TS}_{\sigma}$) is not energetically well separated from the other pathways which was the case for the lowest energy pathway of the TMC-system ($^{5}\mathbf{TS}_{\sigma}$).

Selected key geometric parameters are summarized in Table 6.8, Loewdin spin populations and spin density plots for the transition states are provided in Table 6.9 and Figure 6.9, respectively.

Table 6.8: Selected geometric parameters for transition states and intermediates of $[Fe^{IV}(O)(NHC)_4(EtCN)]^{2+}$.

	Fe-O [Å]	O-H [Å]	H-C [Å]	Fe-N_{Pr} [Å]	Fe-O-H [°]	O-H-C [°]	O-Fe-N_{Pr} [°]	Fe-N_{Pr}-C_{Pr} [°]
$Fe^{IV}O$, *S*=1	1.645			2.107			176.55	167.40
$Fe^{IV}O$, *S*=2	1.734			3.826			153.16	123.59
$^{3}\mathbf{TS}_{\sigma}$	1.794	1.249	1.273	3.478	123.67	178.13	172.84	113.01
$^{3}\mathbf{TS}_{\pi}$	1.783	1.173	1.369	2.041	116.82	171.79	176.85	168.45
$^{5}\mathbf{TS}_{\pi}$	1.905	1.351	1.215	3.867	105.75	177.27	150.01	111.80
$^{3}\mathbf{I}_{\sigma}$	1.882	0.971	2.200	3.557	114.84	164.45	174.62	113.31
$^{3}\mathbf{I}_{\pi}$	1.846	0.971	2.198	2.012	109.54	165.66	176.88	169.62
$^{5}\mathbf{I}_{\pi}$	1.881	0.970	2.239	3.881	114.67	163.30	149.81	111.17

B3LYP/COSMO(Acetonitril)/D3ZERO/def2-SVP, Fe and bond atoms, C+H:def2-TZVP optimization.

Table 6.9: Loewdin spin-population for selected atoms of the transition states from the $[Fe^{IV}(O)(NHC)_4(EtCN)]^{2+}$-complex.

	Loewdin spin-population		
	$^{3}\mathbf{TS}_{\sigma}$	$^{3}\mathbf{TS}_{\pi}$	$^{5}\mathbf{TS}_{\pi}$
Fe	2.48	1.00	2.69
O	-0.02	0.47	0.82
H	-0.06	0.11	0.11
C	-0.36	0.35	0.24

B3LYP/def2-TZVPP/RIJCOSX/D3ZERO/COSMO single point calculations

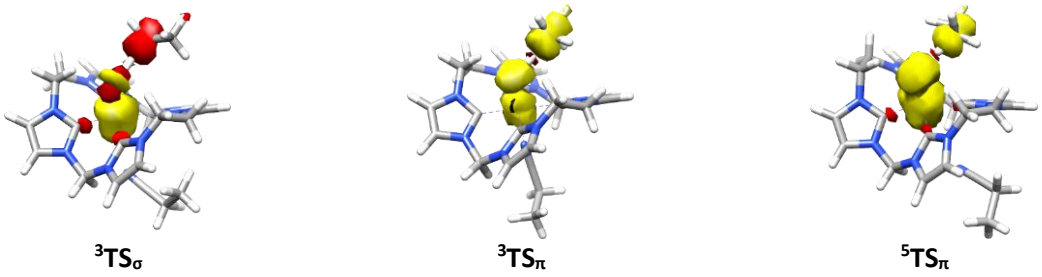

$^3TS_\sigma$ $^3TS_\pi$ $^5TS_\pi$

Figure 6.9: Spin density plots for the transition states of $[Fe^{IV}(O)(NHC)_4(EtCN)]^{2+}$. red: negative, yellow: positive

The calculated spin population and the spin density plot for $^3\mathbf{TS}_\sigma$ show that as expected a spin-down electron is located on the substrate since on this pathway a spin-up electron is transferred from the C-H bond of the substrate (ethane) to iron. However, the situation is less clear cut as it was the case for the TMC-system. The Fe-O-H angel (124°) in the σ-transition state $^3\mathbf{TS}_\sigma$ is far off from being linear and therefore differs from what is usually found for transition states on the σ-pathway.[91] This might suggest that the reaction passes through a rather late transition state where it resembles more the geometry of the product than the geometry of the starting molecule. In the hydroxo-iron(III) complex $^3\mathbf{I}_\sigma$, whose electronic structure is shown in Figure 6.10 (right) the Fe-O-H angle is 115°, hence even more bent than in the transition state. The MO-diagram for $^3\mathbf{TS}_\sigma$ and $^3\mathbf{I}_\sigma$ in Figure 6.10 reveals what the differences compared to the TMC-system are (compare Figure 6.6). Clearly, for $^3\mathbf{TS}_\sigma$ there are three unpaired spin-up electrons on iron and one spin-down electron on the substrate which is antiferromagnetically coupled with one of the electrons on iron (overlap S=0.54). However, due to mixing between the d_{xz} and d_{z^2}-orbitals it is difficult to distinguish the d_{z^2}- and d_{xz}-orbitals in the surface plot (inspection of the Kohn Sham orbitals instead of the corresponding and quasi restricted orbitals shown in Figure 6.6 gave the same result). While for the classical σ-transition state antiferromagnetic coupling between the metal d_{z^2}- and substrate σ^*_{CHO}-orbitals would be expected, from the orbitals in Figure 6.10 coupling between the unpaired-electron in a d_{xz}-orbital with an unpaired electron on the substrate could be concluded, too. Further, the orientation of the doubly occupied mainly oxygen derived orbitals is less well-defined as in the TMC-system. The orbital depicted as O p_x in Figure 6.10 (left) is bent in a way that it could be also described as oxygen p_z-orbital, even in a σ-transition state the p_z-orbital should have formed the σ_{CHO}-bond (see Figure 6.6 for the TMC-system).

The orbital picture (Figure 6.10) gives therefore rise to an alternative formulation for the electronic structure: The d_{z^2}- and d_{yz}-orbitals are singly occupied, the d_{xz}-orbital is singly occupied and antiferromagnetically coupled to the unpaired electron residing on the substrate. Then, overlap of the oxygen p_x-, the substrate σ_{CH}- and the d_{xz}-orbital in the transition state results in the formation of an σ_{CHO}-orbital that is doubly occupied as well as a singly occupied d_{xz}-orbital that is antiferromagnetically coupled to the electron in the mainly substrate derived σ^*_{CHO}-orbital. Overlap of the d_{xz}-orbital with the substrate σ_{CH}-bond is largest when the Fe-O-H angle is 90° which would explain the relatively small angle in the transition state (123.7°). Presumably, the electron from the substrate is directly transferred to the d_{z^2}-orbital (as it is usually the case on the σ-pathway) on an early stage of the reaction and in the structure that is localized as the transition state the Fe-O-H angle is already bent (indicative for a late transition state) which results in antiferromagnetic coupling between the spin-up electron in the iron d_{xz}-orbital with the spin-down electron on the substrate. Hence, while in the "classical" TMC-system the underlying electron transfer process is well-defined, the situation is less clear cut for the novel NHC-system.

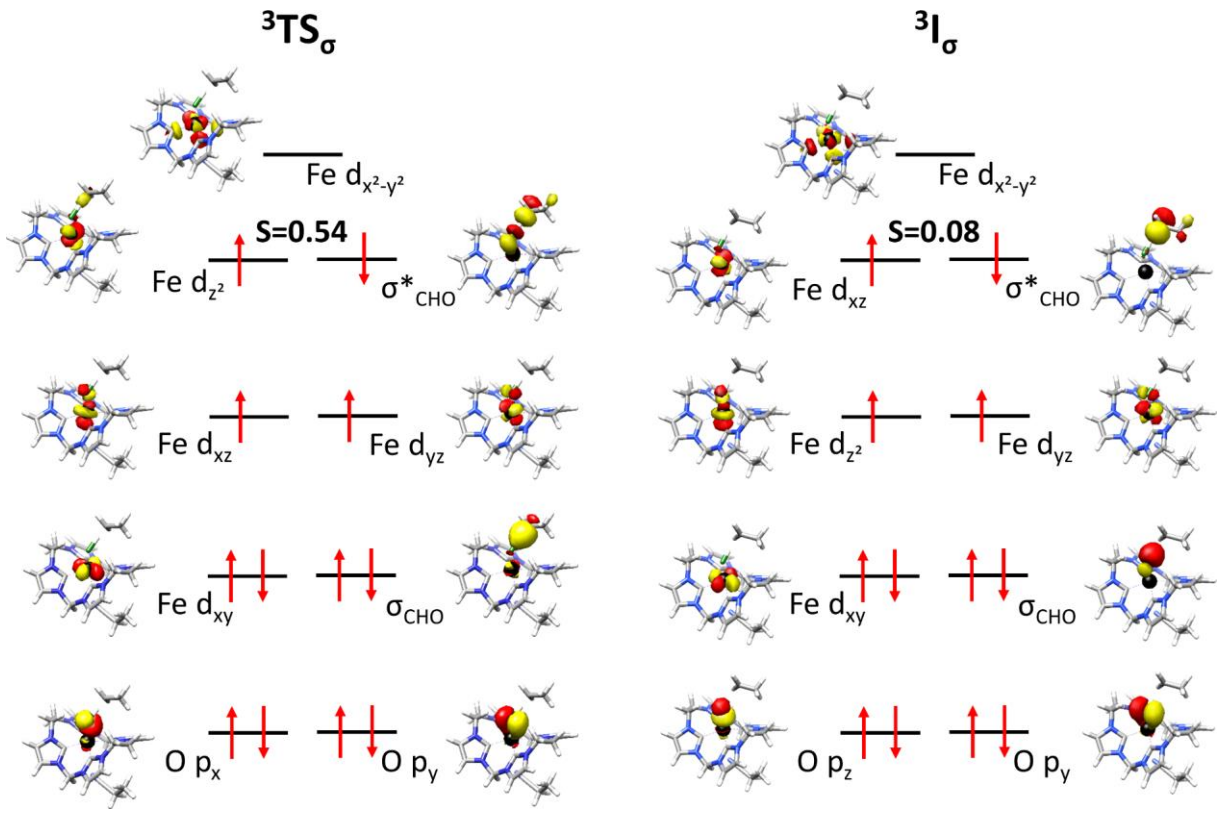

Figure 6.10: Electronic structure of $^3\mathbf{TS}_\sigma$ (left) and $^3\mathbf{I}_\sigma$ (right) for the $[Fe^{IV}(O)(NHC)_4(EtCN)]^{2+}$-complex.

Inspection of the electronic structure of the intermediate $^3\mathbf{I}_\sigma$ (Figure 6.10, right) indeed reveals differences when compared to the $^3\sigma$-pathway for the TMC-system (Figure 6.6, right). Antiferromagnetic coupling occurs between a spin-down electron on the substrate and a spin-up electron in the iron d_{xz}-orbital, however, the overlap *S*=0.08 is very small. Hence, what was indicated already in $^3\mathbf{TS}_\sigma$ due to the mixing of the d_{xz}- and d_{z^2}-orbitals is here completed. This explains why the Fe-O-H angle in the transition state $^3\mathbf{TS}_\sigma$ (124°) is nearly as small as for $^3\mathbf{TS}_\pi$ (117°) given that overlap between a substrate σ-orbital and a d_{xz}-orbital is best in a bent geometry. In a pointedly formulation, one could describe this transition state as a $^3\pi$-type transition state but in the present case a spin-up electron is transferred from the substrate to the metal center and not a spin-down electron, as it is usually the case for the π-pathway.

The electronic structure of the $^3\mathbf{TS}_\pi$ transition state and the resulting $^3\mathbf{I}_\pi$ intermediate is shown in Figure 6.11. On this pathway a spin-down electron is transferred from the substrate C-H bond to the d_{xz}-orbital on iron, resulting in an unpaired spin-up electron on iron (d_{yz}-orbital) and one unpaired spin-up electron distributed over the O-, H- and C-atoms of the substrate (see spin-population Table 6.9 and spin density plot Figure 6.9). The Fe-O-H angle with 117° is strongly bend as it is expected to allow best overlap between the substrate σ_{CH}-bond and the iron d_{xz}-orbital for the electron transfer. In contrast to $^3\mathbf{TS}_\sigma$ and $^5\mathbf{TS}_\pi$ the distance between iron and the coordinated solvent molecule is not significantly changed when the initial $Fe^{IV}O$-complex ($^3\mathbf{RC}$) is compared to $^3\mathbf{TS}_\pi$. This can be explained by the fact that only in the $^3\mathbf{TS}_\pi$ transition state the d_{z^2}-orbital is left unoccupied. Transition from $^3\mathbf{TS}_\pi$ to $^3\mathbf{I}_\pi$ is accompanied by relatively minor changes in the electronic structure. The σ_{HO}-bond is finally formed and the unpaired electron on the substrate is now completely located on the carbon atom. Interestingly, when the electronic structure of the transition states for the NHC- and TMC-systems are compared, most similarities are found for the pathway via $^3\mathbf{TS}_\pi$.

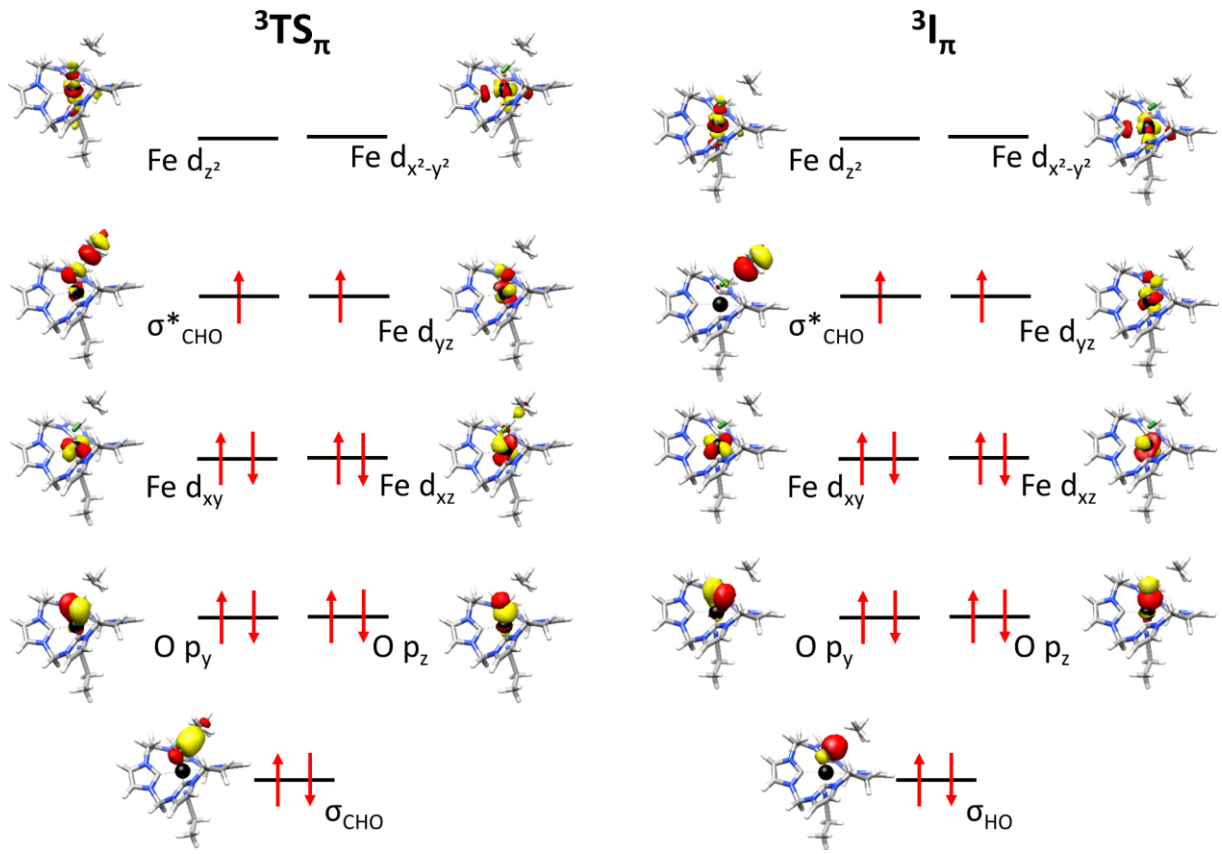

Figure 6.11: Electronic structure of ^{3}**TS$_\pi$** (left) and ^{3}**I$_\pi$** (right) for the $[Fe^{IV}(O)(NHC)_4(EtCN)]^{2+}$-complex.

The only pathway accessible on the quintet surface for the NHC-system is via transition state ^{5}**TS$_\pi$** whose electronic structure is shown in Figure 6.12 (left). Transfer of a spin-down electron from the substrate σ_{CH}-bond to the d_{yz}-orbital is expected which would result in the electron configuration $(d_{yz})^2(d_{xy})^1(d_{xz})^1(d_{z^2})^1$ on iron and a spin-up electron mainly located on the substrate. However, as is bone out in the schematic MO diagram for ^{5}**TS$_\pi$**, in the transition state the d_{xy}-orbital is doubly occupied while the d_{yz}-orbital is only occupied by one spin-up orbital. Given that efficient overlap is not possible between the substrate σ_{CH}-bond (the electron donating orbital in this pathway) and the iron centered d_{xy}-orbital required for a direct electron transfer, it seems to be more plausible that a redistribution of d-electrons took already place after the electron was transferred. Presumably, transfer of a spin-down electron from the substrate to the d_{yz}-orbital is followed directly by the transfer of this spin-down electron to the d_{xy}-orbital. This results in the electronic structure shown in Figure 6.12 (left). The strongly bent Fe-O-H angle of 106° is typical for a π-transition state where the d_{yz}-orbital (or d_{xz}) acts as the accepting orbital.

The $Fe^{III}(OH)$ species ^{5}**I$_\pi$** reveals the (local) electron configuration $(d_{xy})^2(d_{yz})^1(d_{xz})^1(d_{z^2})^1$ for iron and one unpaired electron on the substrate carbon atom (see Figure 6.12, right), similar to ^{5}**TS$_\pi$**.

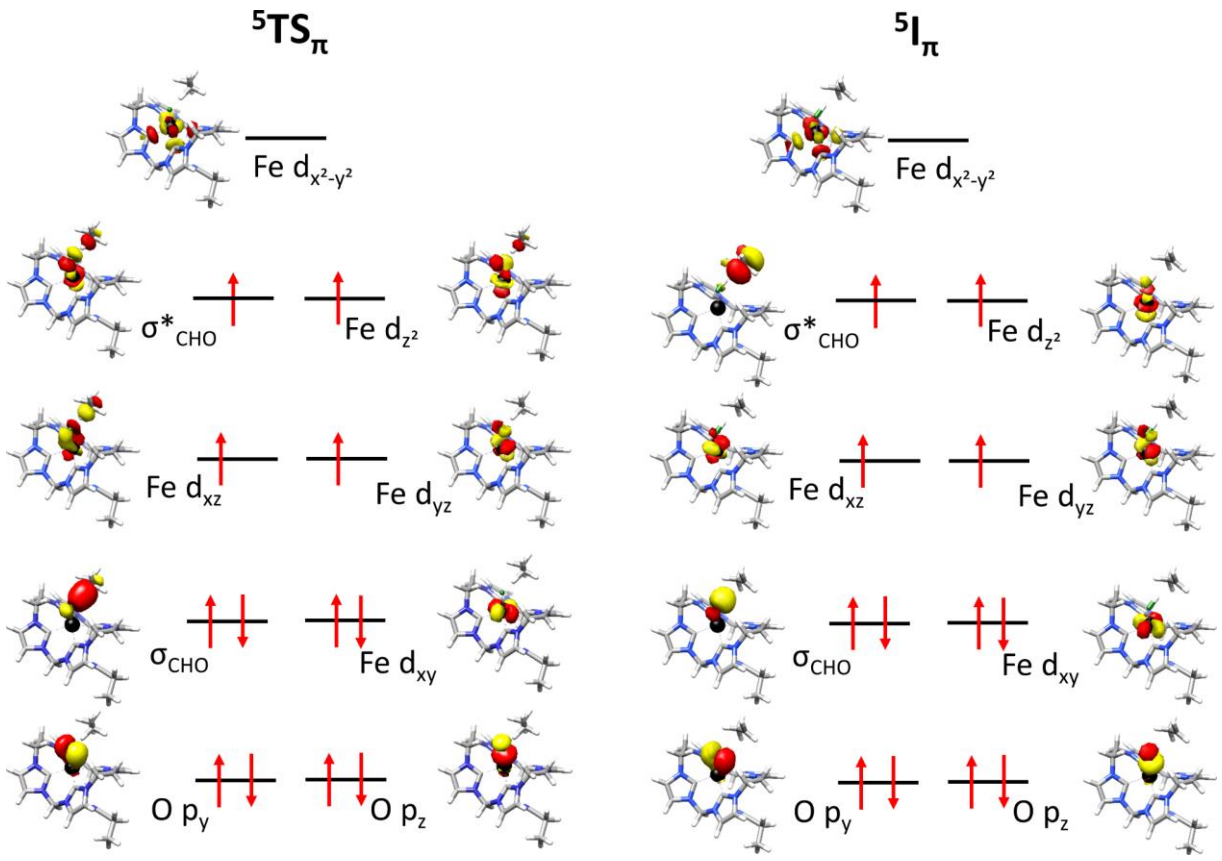

Figure 6.12: Electronic structure of $^5TS_\pi$ (left) and $^5I_\pi$ (right) for the $[Fe^{IV}(O)(NHC)_4(EtCN)]^{2+}$-complex.

Calculations on the hydrogen abstraction reaction by the oxo-iron(IV) complexes $[Fe^{IV}(O)(TMC)(MeCN)]^{2+}$ and $[Fe^{IV}(O)(NHC)_4(EtCN)]^{2+}$ have revealed major differences. While for the previously studied complex $[Fe^{IV}(O)(TMC)(MeCN)]^{2+}$ the $^5\sigma$ pathway was found to be lowest in energy, this reaction channel is blocked for the novel $[Fe^{IV}(O)(NHC)_4(MeCN)]^{2+}$ complex due to a distinct electronic structure that deviates from all previously described tetragonal oxo-iron(IV) complexes. For the complex $[Fe^{IV}(O)(NHC)_4(MeCN)]^{2+}$ the $^3\sigma$ pathway was found to be lowest in energy, but also significantly higher in energy than the $^5\sigma$ pathway for the "classical" complex $[Fe^{IV}(O)(TMC)(MeCN)]^{2+}$.

6.3. Electronic Structure of the Complex $[Fe_2O(NHC_4)_2]^{4+}$ [1]

As a decay product of the $[Fe^{IV}(O)(NHC)_4(EtCN)]^{2+}$ complex the oxo-bridged iron(III) dimer $[Fe_2O(NHC_4)_2]^{4+}$ was isolated and characterized in the group of Prof. Franc Meyer (see Scheme 6.7).[266]

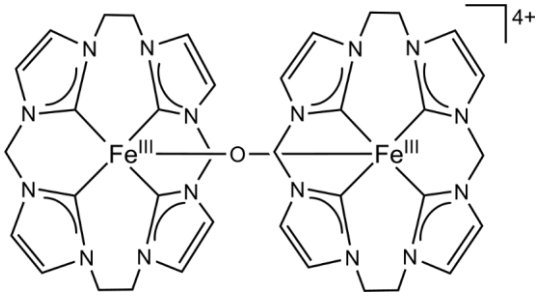

Scheme 6.7: Molecular structure of the iron dimer $[Fe_2O(NHC_4)_2]^{4+}$.

Commonly, μ-oxo Iron(III) dimers are considered to be high-spin (local spin S_{Fe}=5/2), as evidenced by a number of examples of this type[277] and only few low-spin complexes are known.[278-280] However, the Mössbauer isomer shift of δ=0.04 mm s^{-1} falls notably below the range of values (0.15-0.50 mm s^{-1}) observed for other μ-oxo bridged iron(III) dimers and already indicates differences in the electronic structure of this novel μ-oxo dimer containing macrocyclic carbene ligands.[277] Furthermore, the antiferromagnetic coupling of previously studied complexes (J usually between -10 and -200 cm^{-1}) is one order of magnitude smaller than it was measured for the present species.[277-280]

The complex was structurally characterized by X-ray crystallography, and further characterized by magnetic Mössbauer spectroscopy and SQUID measurements.[266] The data pointed to an S_{total}=0 ground state with a strong antiferromagnetic coupling of J=-606 cm^{-1}. However, it was not possible to determine the local spin due to the infinitesimal population of the first excited state even at 295 K. The obtained data is, therefore, consistent with local spins on iron of S_i=1/2, 3/2 and 5/2.

To reveal the spin state and provide detailed insight in the electronic structure of the complex, spectroscopic parameters were calculated by DFT. All possible spin states were considered for this purpose and the antiferromagnetic coupling was calculated within the broken symmetry approach. The notation BS(*m*,*n*) corresponds to *m* electrons on site *A* coupled with *n* electrons on site *B* (in the present case *A* and *B* are the iron centers).[17] Two coupled low-spin iron(III) centers are then denoted by BS(1,1), intermediate-spin iron(III) by BS(3,3) and high-spin iron(III) by BS(5,5). Additionally, the closed shell case is also considered, however, this seems to be an unlikely scenario since it would imply a superoxo (O_2^{2-}) bridged iron(IV) dimer or an iron(II) dimer bridged by an O_2^{2+} cation.

Calculations were performed on the crystal structure with the B3LYP functional, the def2-TZVP basis set and the corresponding def2-TZV/J auxiliary basis set for the RIJCOSX approximation. Solvent effects were considered by the COSMO model assuming acetonitrile as solvent. For the calculations of the Mössbauer parameters the CP(PPP) basis set was used for iron and calculations were performed without the RIJCOSX approximation.

[1] All experimental data given in the present Chapter 6.3 were obtained by the group of Franc Meyer and can be found in Ref.[266]

The structure was optimized in the spin state that yielded the energetically most stable ground state based on calculations on the X-ray structure. A def2-TZV basis set was used for optimizing the structure in combination with the BP86 functional, the RI approximation and COSMO to include solvent effects. Results from the calculations and experimental data are summarized in Table 6.10.

Table 6.10: Calculated and experimental parameters for the $[Fe_2O(NHC_4)_2]^{4+}$ complex.

	relative energy[a]	J[a]	Mössbauer parameters[b]		selected bond distances/angles			Loewdin spin population		
			δ	ΔE_Q	Fe-O	Fe-O	Fe-O-Fe	Fe	O	Fe
	[kJ mol^{-1}]	[cm^{-1}]	[mm s^{-1}]	[mm s^{-1}]	[Å]	[Å]	[°]			
S=0	279		0.14	+2.55						
BS(1,1)	110	1962	-0.04	+2.50				0.95	0.01	-0.95
BS(3,3)	0	-538	-0.03	+2.33				2.64	0.01	-2.64
BS(5,5)	332	-183	-0.02	+1.91				3.86	0.01	-3.84
optimized[c] BS(3,3)		-551	-0.04	+2.37	1.743	1.744	179.83	2.65	0.00	-2.65
Experimental[266]		-606	0.04	+2.56	1.752	1.752	178.79			

a: B3LYP/def2-TZVP/RIJCOSX/COSMO(Acetonitrile) single point calculation on X-ray structure.
b: B3LYP/def2-TZVP Fe: CP(PPP)/COSMO(Acetonitrile)
c: BP86/def2-TZVP/RI/COSMO(Acetonitrile) optimization

The calculated relative energies reveal that two antiferromagnetically coupled intermediate-spin iron centres (each S_{Fe}=3/2) are lowest in energy, corresponding to the BS(3,3) solution. As expected, the closed-shell solution is very high in energy. Low-spin iron(III) (BS(1,1)) results in strong ferromagnetic coupling (J=1962 cm^{-1}) and this solution is 110 kJ mol^{-1} higher in energy than the BS(3,3) solution. Highest in energy is the solution with two coupled high-spin centres (BS(5,5)). The Loewdin spin populations for iron reveal that the calculations converged to the desired solutions with +/- 0.95 for iron(III) low-spin, +/- 2.64 for intermediate-spin and +/- 3.86 for high-spin, even the spin population is slightly below the idealized number of unpaired electrons on each centre (1, 3, 5). Best agreement between the experimental and calculated coupling constant (J) is also found for the BS(3,3) solution and calculated Mössbauer parameters are in reasonable agreement with the experimental results. Subsequent optimization of the structure by DFT assuming the coupling of two intermediate-spin iron(III) centres result in excellent agreement between the calculated and experimental (XRD) iron-oxygen bond distances and the Fe-O-Fe angle.

From the calculations a detailed picture of the electronic structure was obtained and a MO scheme is shown in Figure 6.13. This demonstrates that the non-bonding d_{xy}-orbital is doubly occupied and the $d_{x^2-y^2}$-orbital is vacant. It was discussed in Chapter 6.1.3 that the strong NHC-ligand pushes the $d_{x^2-y^2}$-orbital high in energy and presumably the same effect is observed here. The population of the $d_{x^2-y^2}$-orbital with electrons is therefore precluded. Magnetic orbitals are the singly occupied d_{z^2}-, d_{xz}- and d_{yz}-orbitals with an overlap of S=0.36, S=0.33 and S=0.33, respectively, resulting in strong antiferromagnetic coupling with J=-551 cm^{-1} (for the optimized structure).

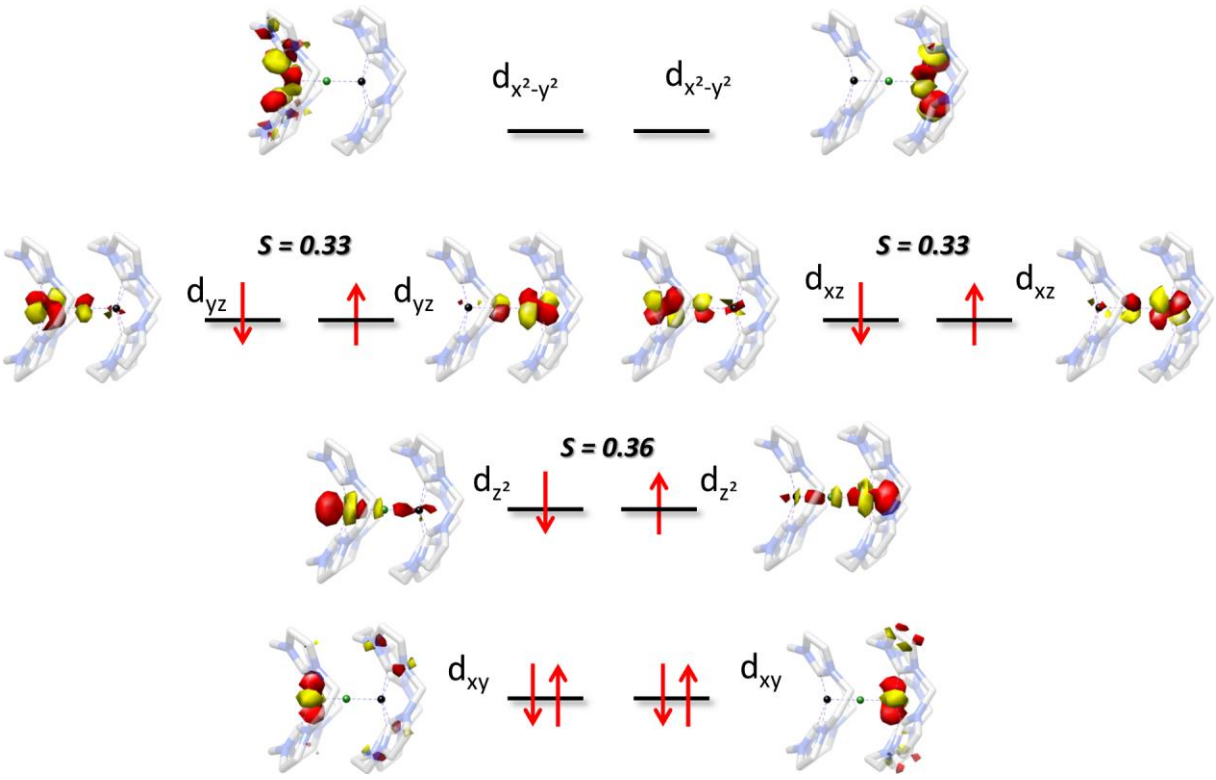

Figure 6.13: MO scheme from BS(3,3) calculations on the $[Fe_2O(NHC_4)_2]^{4+}$ complex. Quasi restricted orbitals (doubly occupied / vacant) and corresponding orbitals (SOMOs) are shown. Hydrogen atoms omitted for clarity.

The combination of experimental and computational results clearly show that the oxo-bridged dimer $[Fe_2O(NHC_4)_2]^{4+}$ is a rare case[277-280] of an intermediate-spin (local spin S_{Fe}=3/2) complex, with strong antiferromagnetic coupling. This is rather unexpected and in contrast to the low-spin state (S_{Fe}=1/2) that was initially assumed for the present complex based on the experimental results.[266]

For five coordinate, tetragonal iron(III) complexes the high-spin state is actually the most common spin state (e.g. in porphyrins[244]). However, as mentioned before, occupation of the $d_{x^2-y^2}$-orbital with electrons to form high-spin centers on iron in the present species is presumably precluded due to the strong equatorial NHC-ligand. This results in an intermediate-spin ground state.

6.4. Electronic Structure of the Complex $[Fe_2S_2(NHC_4)_2]^{4+}$ [2]

[2Fe-2S] clusters are common cofactors in various metalloproteins.[282] A large number of low molecular weight model complexes for these systems have been synthesized with different terminal ligands.[283-285] In contrast, only few examples are known of trans-1,2-disulfide-bridged [Fe-S-S-Fe] complexes with identical ligands.[286-287]

In the group of Prof. Franc Meyer a new species of this type was synthesized with the macrocyclic tetracarbene ligand that was used as well for the synthesis of the oxo-iron(IV) complex discussed in Chapter 6.1.[281] The resulting μ-η^1-η^1-disulfide bridged binuclear iron complex (see Scheme 6.8) is the S_2 analog of the μ-oxo bridged iron dimer that was discussed in the previous section.

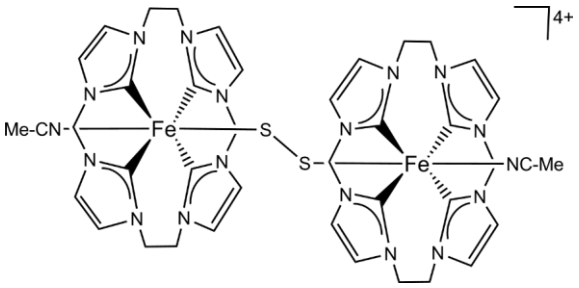

Scheme 6.8: Molecular structure of the disulfide bridged iron dimer $[Fe_2S_2(NHC_4)_2(MeCN)_2]^{4+}$.

It was possible to solve the crystal structure of this complex and it was further characterized by Mössbauer-, IR-, resonance Raman- and UV-*vis*-spectroscopy as well as SQUID measurements. All experimental data presented in this chapter were obtained by the group of Prof. Franc Meyer and published recently.[281] They are not part of this thesis but are provided here for consistency.

The magnetic measurements show a total spin of S=0, however, it was not possible to determine the local spins from the experimental data and even both oxidation states +III and +II on iron are compatible with the experimental results. Therefore, a closed shell Fe^{II}-SS-Fe^{II} structure, or strong antiferromagnetic coupling that is not measurable anymore in a conventional temperature range (J<-800 cm^{-1}) with local spins of S_i=1/2, 3/2 or 5/2 for two ferric sites or S_i=1 or 2 for two ferrous sites are conceivable.

Binuclear disulfide bridged dimers can be formally described by three resonance structures, depicted in Scheme 6.9.[288]

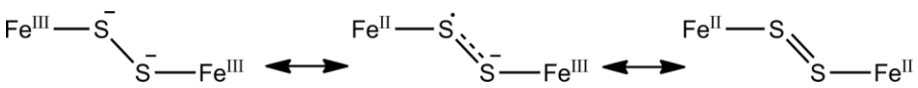

Scheme 6.9: Possible resonance structures of the Fe-SS-Fe core.

The mixed-valence structure (center of Scheme 6.9) is rather unlikely, since the single-crystal analysis reveals a symmetric structure with equivalent Fe-S bonds. Further, the experimental Fe-S and S-S bond

[2] This section is reprinted/adapted with permission from S. Meyer, O. Krahe, C. Kupper, I. Klawitter, S. Demeshko, E. Bill, F. Neese, F. Meyer *Inorg*. *Chem*. 2015, *54*, 9770. Copyright 2015 American Chemical Society.
All experimental data given in the present chapter 6.4 were obtained by the Meyer group and can be found in Ref.[281]

distances (2.148 Å, 2.023 Å) are similar to a previously published *trans*-$Fe_2(\mu\text{-}S_2)$ (2.191 Å, 2.046 Å) complex for which an antiferromagnetically coupled iron(III) low-spin structure was postulated.[286]

DFT calculations were performed on the crystal structure assuming both, a closed-shell *S*=0 spin state as well as all possible open-shell coupling schemes that result in a total spin *S*=0. Using once more the broken symmetry approach, the possible couplings between the iron centers are BS(1,1) for low-spin iron(III), BS(3,3) for intermediate-spin iron(III), BS(5,5) for high-spin iron(III), BS(2,2) for intermediate-spin iron(II) and BS(4,4) for high-spin iron(II). The B3LYP functional was used, the def2-TZVP basis set and the corresponding def2-TZV/J auxiliary basis set for the RIJCOSX approximation. Solvent effects were taken into account within the COSMO model, assuming acetonitrile as the solvent. Results from single point calculations on the X-ray structure are summarized in Table 6.11 together with the experimental data.

Table 6.11: Calculated and experimental[281] parameters for the $[Fe_2S_2(NHC_4)_2(MeCN)_2]^{4+}$ complex.

	relative energy[a] [kJ mol^{-1}]	J[a] [cm^{-1}]	Mössbauer parameters[b] δ [mm s^{-1}]	ΔE_Q [mm s^{-1}]	η	Loewdin spin population Fe	S	S	Fe
S=0	46	0	0.15	2.55	0.72	0.00	0.00	0.00	0.00
BS(1,1)	0	-912	0.10	-2.93	0.94	0.75	0.14	-0.14	-0.75
BS(2,2)	0	-2291	0.10	-2.93	0.94	0.75	0.14	-0.14	-0.75
BS(3,3)	0	-2167	0.10	-2.93	0.94	0.75	0.14	-0.14	-0.75
BS(4,4)	0	-1869	0.10	-2.94	0.94	0.75	0.14	-0.14	-0.75
BS(5,5)	548	-81	0.16	-0.97	0.68	3.80	0.25	-0.25	-3.80
optimized[c] BS(1,1)		-836	0.07	-2.78	0.97	0.76	0.14	-0.14	-0.75
experimental[281]		< -800	0.13	2.80	0.72				

a: B3LYP/def2-TZVP/RIJCOSX/COSMO(Acetonitrile) single point calculation on X-ray structure.
b: B3LYP/deft-TZVP Fe: CP(PPP)/COSMO(Acetonitrile)
c: BP86/deft-TZVP/RI/COSMO(Acetonitrile) optimization

As evident from the calculated Loewdin spin population on iron and sulfur (Table 6.11), the BS(2,2), BS(3,3) and BS(4,4) calculations all converge to the BS(1,1) solution for antiferromagnetically coupled low-spin iron(III) centers. The calculated coupling J=-912 cm^{-1} from the BS(1,1) calculation is consistent with the experimental finding, that the complex must be closed shell (*S*=0) or the antiferromagnetic coupling must be very strong (J<-800 cm^{-1}) that it is not measurable anymore in a conventional temperature range. Calculated Mössbauer parameters for the low-spin iron(III) case (δ=0.10 mm s^{-1}, ΔE_Q=-2.93 mm s^{-1}) are in good agreement with the experimental results (δ=0.13 mm s^{-1}, ΔE_Q=2.80 mm s^{-1}), even the sign for the quadrupole splitting is different when compared to the experiment. It should be noted, that the sign of the quadrupole splitting loses its meaning when η approaches unity,[139] like seen in the present case (calculated η=0.94).

The high-spin iron(III) case is calculated to be very high in energy, which again can be explained by population of the $d_{x^2-y^2}$-orbitals. As discussed for the oxo-iron(IV)-complex this is unfavorable due to the strongly donating tetracarbene ligand. Furthermore, the calculated antiferromagnetic coupling of J=-81 cm^{-1} for the high-spin case is completely at odds with the experiment.

Mössbauer parameters calculated for the closed-shell case, which would result in a local [Fe^{II}-S_2-Fe^{II}] electronic structure, are in reasonable agreement with the experimental values, and as mentioned before, the SQUID measurements would also be consistent with this electronic structure. However, this electronic structure was calculated to be 46 kJ mol^{-1} higher in energy than the antiferromagnetically coupled low-spin iron(III) case, and can therefore be confidently ruled out.

The calculations on the crystal structure point towards an antiferromagnetically coupled low-spin iron(III) system in this compound. The structure was optimized by DFT ((BS(1,1)/def2-TZVP/BP86/RI/COSMO) within the broken symmetry approach. Results for selected geometric parameters in comparison to the experimental results are provided in Table 6.12, calculated spectroscopic parameters and spin populations can be found in Table 6.11. Only minor changes in the calculated coupling and Mössbauer parameters are obtained, in line with the fact that the bonding parameters remain close to the ones in the crystal structure. This further confirms that the present complex should be considered as a strongly antiferromagnetically coupled iron(III) dimer bridged by an S_2^{2-} -anion. For an [Fe^{II}-S=S-Fe^{II}] species the S-S-bond would be expected to be significantly shorter.

Table 6.12: Selected experimental and calculated geometric parameters for the $[Fe_2S_2(NHC_4)_2]^{4+}$ complex

	Fe-S [Å]	S-S [Å]	Fe-S [Å]	Fe-S-S [°]	Fe-S-S [°]	Fe-S-S-Fe [°]
exp	2.148	2.023	2.148	112.59	112.59	180.00
calc	2.152	2.042	2.152	111.91	111.77	178.10

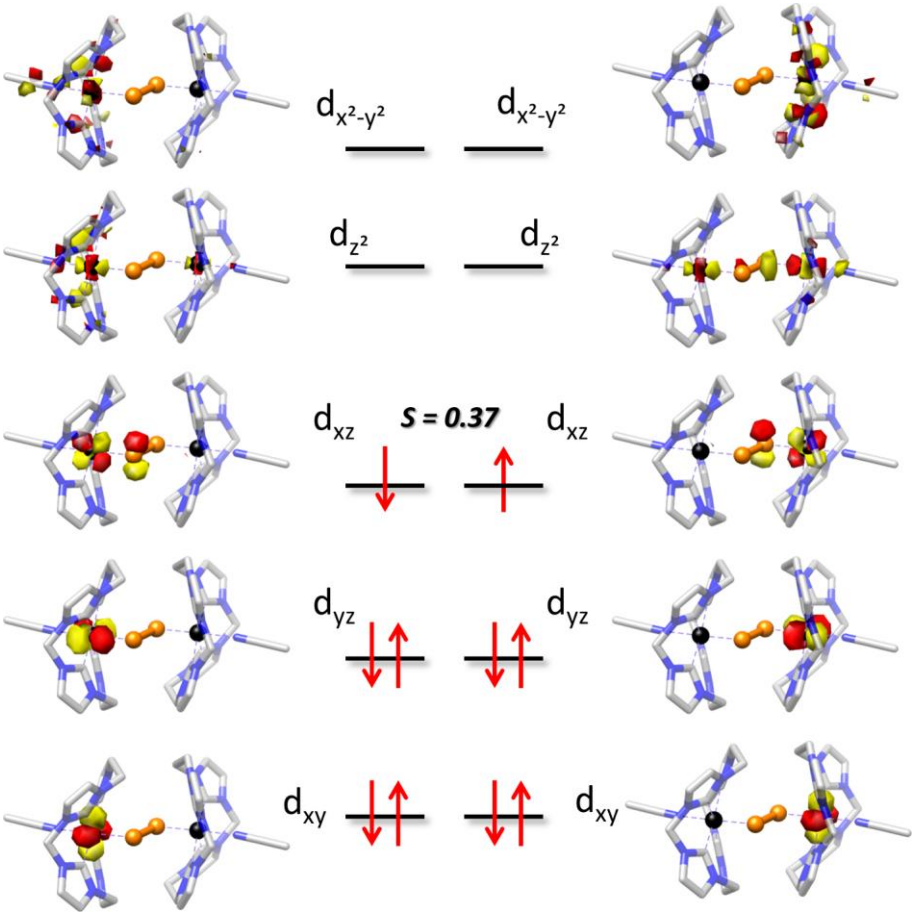

Figure 6.14: MO scheme from BS(1,1) calculations on the $[Fe_2S_2(NHC_4)_2]^{4+}$ complex. Quasi restricted orbitals (doubly occupied / vacant) and corresponding orbitals (SOMOs) are shown. Hydrogen atoms omitted for clarity.

An MO-scheme obtained from the BS(1,1) calculations is provided in Figure 6.14. As expected for an low-spin iron(III) complex in pseudo octahedral coordination the d_{xy}-orbital and d_{yz}-orbitals are doubly occupied. The singly occupied d_{xz}-orbitals correspond to the magnetic orbitals with an overlap of *S*=0.37. As can be seen inferred from the plot, the d_{xz}-orbitals are slightly delocalized over the S_2^{2-}-bridge. Interestingly, even throughout the $[Fe_2S_2(NHC_4)_2(MeCN)_2]^{4+}$ complex and the $[Fe_2O_2(NHC_4)_2]^{4+}$ complex discussed in the previous section are both iron(III), they show different electronic structures. While the oxo-bridged dimer is intermediate-spin, the S_2^{2-}-bridged dimer is low-spin. This might be due to the additional solvent molecule that is coordinated in the complex $[Fe_2S_2(NHC_4)_2(MeCN)_2]^{4+}$ which results in a preference of the low-spin state in contrast to the five-coordinate oxo-bridged complex that is intermediate-spin.

The $[Fe_2S_2(NHC_4)_2(MeCN)_2]^{4+}$ complex was further characterized spectroscopically in the group of Prof. Franc Meyer by IR-, resonance Raman- and UV-*vis*/NIR-spectroscopy (experimental data is not shown here in detail but can be found in Ref[281]).

In the experimental absorption spectrum a very intense band was observed at 9852 cm^{-1}, and additional bands at 14663 cm^{-1} and 27778 cm^{-1}. TD-DFT calculations were performed to explore the origin of these bands. The calculated spectrum is shown in Figure 6.15 and selected difference density plots are provided in Figure 6.16. At 11473 cm^{-1} an intense band was calculated which is in reasonable agreement with the experimentally observed intense band at 9852 cm^{-1}. The difference density plot in Figure 6.16 (root 5, 11473 cm^{-1}) reveals that this signal results from a LMCT-transition from the π_x-system of the $[S\text{-}S]^{2-}$unit into the singly occupied d-orbitals. This is in agreement with comparable bands of *trans*-1,2-disulfide ruthenium and iron complexes that Sellmann and coworkers assigned to $\pi \rightarrow \pi^*$ transitions of the delocalized [M-S-S-M]-core.[289-291]

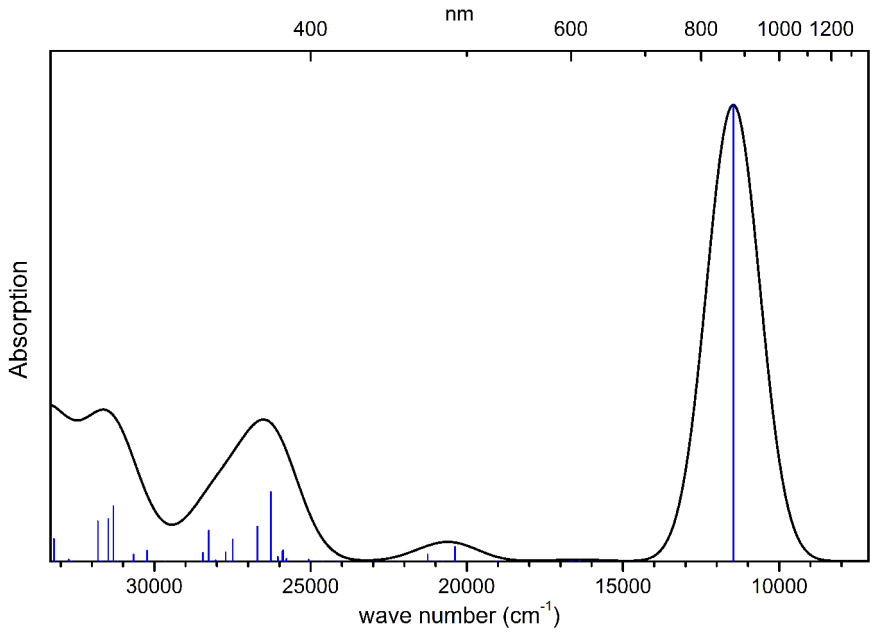

Figure 6.15: TD-DFT calculated absorption spectrum for the $[Fe_2S_2(NHC_4)_2(MeCN)_2]^{4+}$ complex. Blue bars represent the calculated oscillator strengths and the black curve was obtained by simulating the spectrum with Gaussian functions assuming a FWHM of 2000 cm^{-1}.

A band of lower intensity was calculated to appear at 20379 cm^{-1} which mainly results from a $\pi_y(S) \rightarrow d_{z^2}$ LMCT-transition. Experimentally, the closest band to this calculated one was observed at 14663 cm^{-1}, hence, with a significant deviation from the computational result.

In agreement with the experimental results where additional signals were observed at higher energy (~28000 cm^{-1}), several bands were calculated in this region by TD-DFT. As shown in the difference density plots in Figure 6.16, these do mainly draw their intensities from transitions from the NHC-ligand to the metal centers.

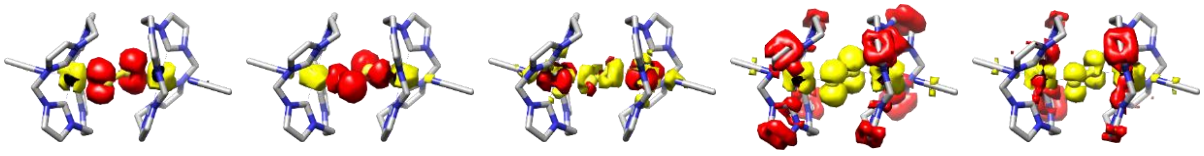

root 5	root 12	root 15	root 31	root 32
11473 cm^{-1}	20379 cm^{-1}	21255 cm^{-1}	26277 cm^{-1}	26700 cm^{-1}
$\pi_x(S_2) \rightarrow d_{xz}$	$\pi_y(S_2) \rightarrow d_{z^2}$	$d_{yz} \rightarrow d_{z^2}$	NHC$\rightarrow d_{xz}$ (SOMO)	NHC$\rightarrow d_{xz}$ (SOMO)

Figure 6.16: Difference density plots for selected transitions in the $[Fe_2S_2(NHC_4)_2(MeCN)_2]^{4+}$ complex. red: negative; yellow: positive, hydrogen atoms omitted for clarity.

The nature of the visible band in the absorption spectrum was further investigated by resonance Raman measurements with an excitation wavelength of 633 nm (15798 cm^{-1}) that hits the band at 14663 cm^{-1}. This results in intense signals at 389 cm^{-1} and 501 cm^{-1} which can be assigned to the total symmetric (A_g) stretching vibrations ν(S-S) and ν(Fe-SS-Fe), respectively. Further evidence for this assignment is found in the calculations where the ν(S-S) and ν(Fe-SS-Fe) vibrations were predicted to appear at 379 cm^{-1} and 483 cm^{-1}, respectively. Hence, even the transition calculated to appear at 20379 cm^{-1} significantly deviates from the observed band at 14663 cm^{-1}, the calculated nature of this transition ($\pi_y(S) \rightarrow d_{z^2}$) is compatible with the results from the resonance Raman measurements. A transition from the S_2 π-system to the metal d_{z^2}-orbitals will strongly affect the S-S and Fe-S bonds and therefore enhancement is expected for modes that resemble these deformations.

It can be summarized, that based on the experimental results it was not possible to assign the a spin state or even an oxidation state to the μ-η^1-η^1-disulfide bridged binuclear iron complex $[Fe_2S_2(NHC_4)_2(MeCN)_2]^{4+}$. By calculating the spectroscopic parameters with DFT it was possible to show that the complex should be described as iron(III) low-spin (S_{Fe}=1/2) with very strong antiferromagnetic coupling. Hence, the S_2^{2-}bridged iron(III) dimer is low-spin (S_{Fe}=1/2) in contrast to the intermediate-spin (S_{Fe}=3/2) oxo-bridged iron(III) dimer discussed in the antecedent chapter.

6.5. Discussion and Conclusions

In the present chapter the novel oxo-iron(IV) complex $[Fe^{IV}(O)(NHC)_4(EtCN)]^{2+}$ was studied computationally in conjunction with experimental results obtained in the group of Prof. Franc Meyer. The hydrogen abstraction reaction was compared to the previously studied complex $[Fe^{IV}(O)(TMC)(MeCN)]^{2+}$. Further, the electronic structures of the dimeric iron complexes $[Fe_2O(NHC_4)_2]^{4+}$ and $[Fe_2S_2(NHC_4)_2(MeCN)_2]^{4+}$ were revealed, again, by combining computational and experimental approaches.

It was shown that the electronic structure of the complex $[Fe^{IV}(O)(TMC)(EtCN)]^{2+}$ is in line with the classical $d_{xy}<d_{xz},d_{yz}<d_{x^2-y^2}<d_{z^2}$ orbital splitting,[4,6] found for all tetragonal oxo-iron(IV) complexes so far and for most mononuclear tetragonal transition metal oxo-complexes. In contrast, the d-orbital splitting for the novel complex $[Fe^{IV}(O)(NHC)_4(MeCN)]^{2+}$ is $d_{xy}<d_{xz},d_{yz}<d_{z^2}<d_{x^2-y^2}$ and differs from all previously described tetragonal oxo-iron(IV) complexes.[86,101,106-107] Both complexes exhibit a $^3A_2[(d_{xy})^2(d_{xz})^1(d_{yz})^1]$ ground state, however, due to the distinct d-orbital splitting the TMC-system shows a $^5A_1[(d_{xy})^1(d_{xz})^1(d_{yz})^1(d_{x^2-y^2})^1]$ lowest energy quintet state (that was shown to be involved in hydrogen abstraction reactions previously[86,101,106-107]) while the NHC-system shows a $^5B_1[(d_{xy})^1(d_{xz})^1(d_{yz})^1(d_{z^2})^1]$ quintet state.

As anticipated from the differences in their electronic structures, transition states differ significantly for the lowest energy pathways of hydrogen abstraction from model substrate ethane by the two oxo-iron(IV) complexes. The $[Fe^{IV}(O)(TMC)(MeCN)]^{2+}$ complex is expected to follow the established *S*=2, $^5\sigma$-pathway (activation barrier 48 kJ mol^{-1}) which is in agreement with previous studies.[86,101,106-107] It was further shown for the TMC-system that the barriers for the $^3\sigma$-, $^5\pi$- and $^3\pi$-pathway are of comparable height, 87 kJ mol^{-1}, 97 kJ mol^{-1}, and 99 kJ mol^{-1}, respectively, and well separated from the $^5\sigma$-transition state. It should be noted here, that the $^3\sigma$- and $^5\pi$-pathways have not been considered for the present TMC-system in previous studies and therefore it is interesting to see that the barrier for the $^3\sigma$-pathway is even 10 kJ mol^{-1} lower than for the $^3\pi$-pathway.[86,101,106-107]

For the novel NHC complex the lowest barrier was found for the $^3\sigma$-pathway (73 kJ mol^{-1}), however, lying significantly higher in energy than the lowest barrier for the TMC-complex ($^5\sigma$, 48 kJ mol^{-1}). Given the overall higher energy span of the profile, the $[Fe^{IV}(O)(NHC)_4(EtCN)]^{2+}$ complex is expected to be less reactive towards CH-bond oxidation than the $[Fe^{IV}(O)(TMC)(MeCN)]^{2+}$ complex.

Comparison of the TMC- and NHC-systems leads to some remarkable conclusions. While for all previously studied oxo-iron(IV) complexes the CH-activation was found to proceed via the quintet state,[85-89,93,99,104,107,265,275-276] this so called "two-state-reactivity" cannot be found for the novel NHC-complex. Hence, the well-established concepts are not applicable to the present NHC-system. Reactions via the high-spin state are generally explained by the gain of exchange energy due to the largest number of unpaired electrons on the $^5\sigma$-pathway when compared to the other conceivable reaction channels. However, the $d_{x^2-y^2}$-orbital is pushed up in energy due to the strong NHC-ligand which results in the population of the d_{z^2}-orbital instead of the $d_{x^2-y^2}$-orbital in the quintet state for the complex $[Fe^{IV}(O)(NHC)_4(EtCN)]^{2+}$. Therefore the d_{z^2}-orbital cannot act as the accepting orbital, blocking the classical $^5\sigma$-pathway.

The dimeric complexes $[Fe_2O(NHC_4)_2]^{4+}$ and $[Fe_2S_2(NHC_4)_2(MeCN)_2]^{4+}$ were also isolated in the Meyer group, both featuring the strong equatorial tetra carbene ligand (NHC_4). While the former was obtained as a decay product of the parent monomeric $Fe^{IV}O$ species, the latter was obtained by reacting the $Fe^{IV}O$ precursor $[Fe^{II}(NHC_4)(MeCN)]^{2+}$ with sulfur. Both complexes were characterized by Mössbauer, UV-*vis* spectroscopy and SQUID measurements revealing a total spin of S=0. However, it was not possible to elucidate from the experimental data if the complexes are closed-shell, or if strong antiferromagnetic coupling results in a total spin of S=0. DFT calculations on both complexes have demonstrated that the spectroscopic parameters of the complex $[Fe_2O(NHC_4)_2]^{4+}$ are in best agreement with the experimental results for a local iron spin of S_{Fe}=3/2 and for the $[Fe_2S_2(NHC_4)_2(MeCN)_2]^{4+}$ complex for S_{Fe}=1/2. Hence the oxo-bridged dimer is best describes as two intermediate-spin iron(III) centers while the iron centers in the disulfide bridged dimer are best described as low-spin S_{Fe}=1/2 iron(III) sites. Antiferromagnetic coupling in both cases is very strong.

The results of the present chapter are highly relevant for the understanding of hydrogen abstraction by oxo-iron(IV) complexes that was studied previously for various systems and was shown to be an important reaction in metalloenzymes. It is demonstrated here that the novel complex $[Fe^{IV}(O)(NHC)_4(EtCN)]^{2+}$ cannot undergo this reaction following the well-established two-states reactivity mechanism that is applicable to all tetragonal oxo-iron(IV) complexes reported so far. Since the d-orbital ordering established in the present study appears as the only viable alternative to the established pattern, it is suspected that the present conclusions have a broader range of validity and should hold in similar fashion for other systems in which the d_{z^2}-based orbital is found below the $d_{x^2-y^2}$-orbital.

7. Appendices

7.1. Appendices to Chapter 5.6

Additional results are provided here, relevant for deriving the discussed spin-Hamiltonian equations.

7.1.1. Calculation of Orbital Zeeman Matrix Elements

Throughout the process the Hermitian property of the angular momentum operator is used, which significantly reduces the number of terms that have to be calculated. The coordinate system is defined in Figure 2.2, page18 and superscripts in parenthesis denote the ligand atoms. MOs were defined in Equation 5.1a-5.1e on page 139.

Some terms include the derivative of wave functions resulting from replacement of the angular momentum operator from the metal to the ligand (nitrido or oxo) as described on page 17. This results in the contributions $< p_a | \frac{\partial}{\partial b} | p_c >$ (a=x,y,z; b=x,y,z; c=x,y,z≠b) and $< d_n | \frac{\partial}{\partial b} | p_c >$ (n=xz,yz,xy,x^2-z^2,z^2), hence, the overlap of a p- or d-orbital with the derivative of a p-orbital. It can be shown, that the derivative of a p-orbital with respect to x, y or z results in an orbital with the radial properties of the p-orbital and the angular properties of a d-orbital multiplied by an additional constant factor.[109] These "orbitals" are abbreviated in the following as $\frac{\partial}{\partial b} | p_c >= | \delta_{bc} >$. Inspection of the coordinate system (Figure 2.2, page 18) reveals that several overlap integrals vanish. Further, overlap integrals between different ligand atoms as well as between metal and ligand orbitals will be neglected here. These overlap integrals are expected to be small (S<<1, for example see ref.[296-298]) and the derived formulas are still accurate enough for a near quantitative interpretation of the g-values.

matrix elements: $< \psi_{yz}|l_x^{Fe}|\psi_{x^2-y^2} >$ and $< \psi_{x^2-y^2}|l_x^{Fe}|\psi_{yz} >$

$$< \psi_{yz}|l_x^{Fe}|\psi_{x^2-y^2} > = +\alpha_\pi\alpha_{x^2-y^2} < d_{yz}|\, l_x^{Fe}|d_{x^2-y^2} >$$
$$-\beta_\sigma\beta_\pi < p_y^{(6)}|l_x^{Fe}|p_x^{(3)} - p_x^{(1)} + p_y^{(2)} - p_y^{(4)} >$$
$$-\alpha_\pi\beta_\sigma < d_{yz}|l_x^{Fe}|p_x^{(3)} - p_x^{(1)} + p_y^{(2)} - p_y^{(4)} >$$
$$-\alpha_{x^2-y^2}\beta_\pi < p_y^{(6)}|l_x^{Fe}|d_{x^2-y^2} >$$

with Equation 2.26b and since $R_z^{(1,2,3,4)} = 0$

$$= -i\,\alpha_\pi\alpha_{x^2-y^2} + \mathrm{i}\alpha_{x^2-y^2}\beta_\pi < p_y^{(6)}||d_{yz} >$$
$$+\,\mathrm{i}\,\beta_\sigma\beta_\pi\left[< p_y^{(6)}|\,|p_z^{(2)} > - < p_y^{(6)}|\,|p_z^{(4)} > -\hbar R_y^{(2)} < p_y^{(6)}|\,|\delta_{yz}^{(2)} > +\hbar R_y^{(4)} < p_y^{(6)}|\,|\delta_{yz}^{(4)} >\right]$$
$$-\,\mathrm{i}\,\beta_\sigma\alpha_\pi\left[< d_{yz}|\,|p_z^{(2)} > - < d_{yz}|\,|p_z^{(4)} > -\hbar R_y^{(2)} < d_{yz}|\,|\delta_{yz}^{(2)} > +\hbar R_y^{(4)} < d_{yz}|\,|\delta_{yz}^{(4)} >\right]$$

Here, several ligand-ligand as well as ligand-metal overlap integrals are neglected. This is a plausible approximation, since the overlap integrals are expected to be much smaller than the remaining term. Further, the last two lines are of opposite sign and expected to be at the same order of magnitude.

$$< \psi_{yz}|l_x^{Fe}|\psi_{x^2-y^2} > = -< \psi_{x^2-y^2}|l_x^{Fe}|\psi_{yz} > \approx -i\,\alpha_\pi\alpha_{x^2-y^2}$$

matrix elements: $< \psi_{yz}|l_x^{Fe}|\psi_{z^2} >$ and $< \psi_{z^2}|l_x^{Fe}|\psi_{yz} >$

$$< \psi_{yz}|l_x^{Fe}|\psi_{z^2} > = -< \psi_{z^2}|l_x^{Fe}|\psi_{yz} >$$
$$= \alpha_\pi\alpha_{z^2} < d_{yz}|l_x^{Fe}|d_{z^2} > + \beta_\pi\beta_z < p_y^{(6)}|l_x^{Fe}|p_z^{(6)} >$$
$$-\beta_\pi\alpha_{z^2} < p_y^{(6)}|l_x^{Fe}|d_{z^2} > -\beta_z\alpha_\pi < d_{yz}|l_x^{Fe}|p_z^{(6)} >$$

$$= -i\,\alpha_\pi\alpha_{z^2}\sqrt{3} + i\,\beta_\pi\alpha_{z^2}\sqrt{3} < p_y^{(6)}||d_{yz} > + \beta_\pi\beta_z\left[< p_y^{(6)}\left|l_x^{(6)}\right|p_z^{(6)} > + i\hbar R_z^{(6)}\underbrace{< p_y^{(6)}||\delta_{yz}^{(6)} >}_{=0}\right]$$
$$-\alpha_\pi\beta_z\left[< d_{yz}\left|l_x^{(6)}\right|p_z^{(6)} > + i\hbar R_z^{(6)} < d_{yz}||\delta_{yz}^{(6)} >\right]$$

$$= -i\,\alpha_\pi\alpha_{z^2}\sqrt{3} - i\,\beta_\pi\beta_z$$
$$+i\,\beta_\pi\alpha_{z^2}\sqrt{3} < p_y^{(6)}||d_{yz} > -i\alpha_\pi\beta_z\left[< d_{yz}||p_y^{(6)} > +\hbar R_z^{(6)} < d_{yz}||\delta_{yz}^{(6)} >\right]$$

$$< \psi_{yz}|l_x^{Fe}|\psi_{z^2} > = -< \psi_{z^2}|l_x^{Fe}|\psi_{yz} > \approx -i\,\alpha_\pi\alpha_{z^2}\sqrt{3} - i\,\beta_\pi\beta_z$$

matrix elements: $< \psi_{xz}|l_x^{Fe}|\psi_{xy} >$ and $< \psi_{xy}|l_x^{Fe}|\psi_{xz} >$

$$< \psi_{xz}|l_x^{Fe}|\psi_{xy} > = -< \psi_{xy}|l_x^{Fe}|\psi_{xz} > = \alpha_\pi < d_{xz}|l_x^{Fe}|d_{xy} > - \beta_\pi < p_x^{(6)}|l_x^{Fe}|d_{xy} >$$
$$= i\,\alpha_\pi - i\,\beta_\pi < p_x^{(6)}||d_{xz} >$$

$$< \psi_{xz}|l_x^{Fe}|\psi_{xy} > = -< \psi_{xy}|l_x^{Fe}|\psi_{xz} > \approx i\,\alpha_\pi$$

matrix elements: $< \psi_{yz}|l_y^{Fe}|\psi_{xy} >$ and $< \psi_{xy}|l_y^{Fe}|\psi_{yz} >$

$$< \psi_{yz}|l_y^{Fe}|\psi_{xy} > = -< \psi_{xy}|l_y^{Fe}|\psi_{yz} > = \alpha_\pi < d_{yz}|l_y^{Fe}|d_{xy} > -\beta_\pi < p_y^{(6)}|l_y^{Fe}|d_{xy} >$$
$$= -i\,\alpha_\pi + i\,\beta_\pi < p_y^{(6)}||d_{yz} >$$

$$< \psi_{yz}|l_y^{Fe}|\psi_{xy} > = -< \psi_{xy}|l_y^{Fe}|\psi_{yz} > \approx -i\,\alpha_\pi$$

matrix elements: $< \psi_{xz}|l_y^{Fe}|\psi_{x^2-y^2} >$ and $< \psi_{x^2-y^2}|l_y^{Fe}|\psi_{xz} >$

$$< \psi_{xz}|l_y^{Fe}|\psi_{x^2-y^2} > = -< \psi_{x^2-y^2}|l_y^{Fe}|\psi_{xz} >$$
$$= \alpha_\pi\alpha_{x^2-y^2} < d_{xz}|l_y^{Fe}|d_{x^2-y^2} > -\beta_\pi\alpha_{x^2-y^2} < p_x^{(6)}|l_y^{Fe}|d_{x^2-y^2} >$$

$$-\beta_\pi\beta_\sigma < p_x^{(6)}|l_y^{Fe}|p_x^{(3)} - p_x^{(1)} + p_y^{(2)} - p_y^{(4)} > -\alpha_\pi\beta_\sigma < d_{xz}|l_y^{Fe}|p_x^{(3)} - p_x^{(1)} + p_y^{(2)} - p_y^{(4)} >$$

since $R_z^{(1,2,3,4)} = 0$ and $R_x^{(2,4)} = 0$ and $l_y|p_y >= 0$

$$= -i\alpha_\pi\alpha_{x^2-y^2} - i\beta_\pi\alpha_{x^2-y^2} < p_x^{(6)}||d_{xz} >$$

$$-\beta_\pi\beta_\sigma[< p_x^{(6)}|l_y^{(3)}|p_x^{(3)} > -< p_x^{(6)}|l_y^{(1)}|p_x^{(1)} > + i\hbar R_x^{(3)}\underbrace{< p_x^{(6)}||\delta_{xy}^{(3)} >}_{=0} - i\hbar R_x^{(1)}\underbrace{< p_x^{(6)}||\delta_{xy}^{(1)} >}_{=0}]$$
$$-\alpha_\pi\beta_\sigma[< d_{xz}|l_y^{(3)}|p_x^{(3)} > -< d_{xz}|l_y^{(1)}|p_x^{(1)} > + i\hbar R_x^{(3)}\underbrace{< d_{xz}||\delta_{xy}^{(3)} >}_{=0} - i\hbar R_x^{(1)}\underbrace{< d_{xz}||\delta_{xy}^{(1)} >}_{=0}]$$

$$= -i\alpha_\pi\alpha_{x^2-y^2} - i\beta_\pi\alpha_{x^2-y^2} < p_x^{(6)}||d_{xz} >$$
$$+i\beta_\pi\beta_\sigma\left[< p_x^{(6)}||p_z^{(3)} > -< p_x^{(6)}||p_z^{(1)} >\right] + i\alpha_\pi\beta_\sigma[< d_{xz}||p_y^{(3)} > -< d_{xz}||p_y^{(1)} >]$$

$$< \psi_{xz}|l_y^{Fe}|\psi_{x^2-y^2} > = -< \psi_{x^2-y^2}|l_y^{Fe}|\psi_{xz} > \approx -i\,\alpha_{xz}\alpha_{x^2-y^2}$$

matrix elements: $< \psi_{xz}|l_y^{Fe}|\psi_{z^2} >$ and $< \psi_{z^2}|l_y^{Fe}|\psi_{xz} >$

$$< \psi_{xz}|l_y^{Fe}|\psi_{z^2} > = -< \psi_{z^2}|l_y^{Fe}|\psi_{xz} >$$
$$= \alpha_\pi\alpha_{z^2} < d_{xz}|l_y^{Fe}|d_{z^2} > + \beta_\pi\beta_z < p_x^{(6)}|l_y^{Fe}|p_z^{(6)} > -\alpha_\pi\beta_z < d_{xz}|l_y^{Fe}|p_z^{(6)} >$$
$$-\beta_\pi\alpha_{z^2} < p_x^{(6)}|l_y^{Fe}|d_{z^2} >$$

$$= i\sqrt{3}\alpha_\pi\alpha_{z^2} + i\sqrt{3}\beta_\pi\alpha_{z^2} < p_x^{(6)}||d_{yz} > + \beta_\pi\beta_z < p_x^{(6)}|l_y^{Fe}|p_z^{(6)} > - \alpha_\pi\beta_z < d_{xz}|l_y^{Fe}|p_z^{(6)} >$$

$$= i\sqrt{3}\alpha_\pi\alpha_{z^2} + i\sqrt{3}\beta_\pi\alpha_{z^2} < p_x^{(6)}||d_{yz} > + i\,\beta_\pi\beta_z[< p_x^{(6)}||p_x^{(6)} > -\hbar R_z^{(6)}\underbrace{< p_x^{(6)}||\delta_{xz}^{(6)} >}_{=0}]$$
$$- i\alpha_\pi\beta_z[< d_{xz}||p_x^{(6)} > -\hbar R_z^{(6)} < d_{xz}||\delta_{xz}^{(6)} >]$$

$$= i\sqrt{3}\alpha_\pi\alpha_{z^2} + i\,\beta_\pi\beta_z + i\sqrt{3}\beta_\pi\alpha_{z^2} < p_x^{(6)}||d_{yz} >$$
$$- i\alpha_\pi\beta_z[< d_{xz}||p_x^{(6)} > -\hbar R_z^{(6)} < d_{xz}||\delta_{xz}^{(6)} >]$$

$$< \psi_{xz}|l_y^{Fe}|\psi_{z^2} > = -< \psi_{z^2}|l_y^{Fe}|\psi_{xz} > \approx i\,\alpha_{xz}\alpha_{z^2}\sqrt{3} + i\,\beta_x\beta_z$$

7.1.2. The Zeeman Matrix

The resulting Zeeman matrix with the Zeeman operator 5.12 in the basis $\widetilde{\Psi}_0^{\frac{1}{2},\pm\frac{1}{2}}$ is written as:

$$\beta_e \begin{pmatrix} \langle\widetilde{\Psi}_0^{\frac{1}{2},+\frac{1}{2}}|\mu_x B_x|\widetilde{\Psi}_0^{\frac{1}{2},+\frac{1}{2}}\rangle + \langle\widetilde{\Psi}_0^{\frac{1}{2},+\frac{1}{2}}|\mu_y B_y|\widetilde{\Psi}_0^{\frac{1}{2},+\frac{1}{2}}\rangle + \langle\widetilde{\Psi}_0^{\frac{1}{2},+\frac{1}{2}}|\mu_z B_z|\widetilde{\Psi}_0^{\frac{1}{2},+\frac{1}{2}}\rangle & \langle\widetilde{\Psi}_0^{\frac{1}{2},+\frac{1}{2}}|\mu_x B_x|\widetilde{\Psi}_0^{\frac{1}{2},-\frac{1}{2}}\rangle + \langle\widetilde{\Psi}_0^{\frac{1}{2},+\frac{1}{2}}|\mu_y B_y|\widetilde{\Psi}_0^{\frac{1}{2},-\frac{1}{2}}\rangle + \langle\widetilde{\Psi}_0^{\frac{1}{2},+\frac{1}{2}}|\mu_z B_z|\widetilde{\Psi}_0^{\frac{1}{2},-\frac{1}{2}}\rangle \\ \langle\widetilde{\Psi}_0^{\frac{1}{2},-\frac{1}{2}}|\mu_x B_x|\widetilde{\Psi}_0^{\frac{1}{2},+\frac{1}{2}}\rangle + \langle\widetilde{\Psi}_0^{\frac{1}{2},-\frac{1}{2}}|\mu_y B_y|\widetilde{\Psi}_0^{\frac{1}{2},+\frac{1}{2}}\rangle + \langle\widetilde{\Psi}_0^{\frac{1}{2},-\frac{1}{2}}|\mu_z B_z|\widetilde{\Psi}_0^{\frac{1}{2},+\frac{1}{2}}\rangle & \langle\widetilde{\Psi}_0^{\frac{1}{2},-\frac{1}{2}}|\mu_x B_x|\widetilde{\Psi}_0^{\frac{1}{2},-\frac{1}{2}}\rangle + \langle\widetilde{\Psi}_0^{\frac{1}{2},-\frac{1}{2}}|\mu_y B_y|\widetilde{\Psi}_0^{\frac{1}{2},-\frac{1}{2}}\rangle + \langle\widetilde{\Psi}_0^{\frac{1}{2},-\frac{1}{2}}|\mu_z B_z|\widetilde{\Psi}_0^{\frac{1}{2},-\frac{1}{2}}\rangle \end{pmatrix}$$

The matrix elements are calculated with the given orbital Zeeman matrix elements and as (omitting B_n and β_e and only those are given here that do not vanish):

$$\langle\widetilde{\Psi}_0^{\frac{1}{2},+\frac{1}{2}}|\boldsymbol{l_z}+g_e\boldsymbol{s_z}|\widetilde{\Psi}_0^{\frac{1}{2},+\frac{1}{2}}\rangle = -\sin 2\theta - \frac{\alpha_\pi^2\alpha_{x^2-y^2}^2\zeta_{Fe}^2[\cos\theta-\sin\theta]^2}{2\Delta_{xy}\Delta_{x^2-y^2}} + g_e\left[\frac{1}{2} - \frac{\alpha_\pi^2\alpha_{x^2-y^2}^2\zeta_{Fe}^2[\cos\theta-\sin\theta]^2}{8\left(\Delta_{x^2-y^2}\right)^2} + \frac{\alpha_\pi^2\zeta_{Fe}^2[\cos\theta-\sin\theta]^2}{8\left(\Delta_{xy}\right)^2} - \frac{3\alpha_\pi^2\alpha_{z^2}^2\zeta_{Fe}^2[\cos\theta+\sin\theta]^2}{8\left(\Delta_{z^2}\right)^2}\right]$$

$$\langle\widetilde{\Psi}_0^{\frac{1}{2},-\frac{1}{2}}|\boldsymbol{l_z}+g_e\boldsymbol{s_z}|\widetilde{\Psi}_0^{\frac{1}{2},-\frac{1}{2}}\rangle = +\sin 2\theta + \frac{\alpha_\pi^2\alpha_{x^2-y^2}^2\zeta_{Fe}^2[\cos\theta-\sin\theta]^2}{\Delta_{xy}\Delta_{x^2-y^2}} + g_e\left[-\frac{1}{2} + \frac{\alpha_\pi^2\alpha_{x^2-y^2}^2\zeta_{Fe}^2[\cos\theta-\sin\theta]^2}{8\left(\Delta_{x^2-y^2}\right)^2} - \frac{\alpha_\pi^2\zeta_{Fe}^2[\cos\theta-\sin\theta]^2}{8\left(\Delta_{xy}\right)^2} + \frac{3\alpha_\pi^2\alpha_{z^2}^2\zeta_{Fe}^2[\cos\theta+\sin\theta]^2}{8\left(\Delta_{z^2}\right)^2}\right]$$

$$\langle\widetilde{\Psi}_0^{\frac{1}{2},+\frac{1}{2}}|\boldsymbol{l_x}+g_e\boldsymbol{s_x}|\widetilde{\Psi}_0^{\frac{1}{2},-\frac{1}{2}}\rangle = \frac{g_e\cos 2\theta}{2} + \frac{g_e\alpha_\pi^2\zeta_{Fe}^2}{8}\left[\frac{\alpha_{x^2-y^2}^2(\cos\theta-\sin\theta)^2}{\left(\Delta_{x^2-y^2}\right)^2} - \frac{(\cos\theta-\sin\theta)^2}{\left(\Delta_{xy}\right)^2} + \frac{3\alpha_{z^2}^2(\cos\theta+\sin\theta)^2}{\left(\Delta_{z^2}\right)^2}\right] - \frac{\alpha_\pi^2\alpha_{x^2-y^2}^2\zeta_{Fe}(\cos^2\theta-\sin\theta\cos\theta)}{\Delta_{x^2-y^2}} - \frac{\left[3\alpha_\pi^2\alpha_{z^2}^2+\sqrt{3}\alpha_\pi\alpha_{z^2}\beta_\pi\beta_z\right]\zeta_{Fe}(\cos^2\theta+\sin\theta\cos\theta)}{\Delta_{z^2}} - \frac{\alpha_\pi^2\zeta_{Fe}(\sin^2\theta-\sin\theta\cos\theta)}{\Delta_{xy}}$$

$$\langle \widetilde{\Psi}_0^{\frac{1}{2},+\frac{1}{2}} \left| \boldsymbol{l_y} + g_e \boldsymbol{s_y} \right| \widetilde{\Psi}_0^{\frac{1}{2},-\frac{1}{2}} \rangle = \frac{i\, g_e \cos 2\theta}{2}$$

$$+ \frac{i\, g_e \alpha_\pi^2 \zeta_{Fe}^2}{8} \left[\frac{\alpha_{x^2-y^2}^2 (\cos\theta - \sin\theta)^2}{\left(\Delta_{x^2-y^2}\right)^2} - \frac{(\cos\theta - \sin\theta)^2}{\left(\Delta_{xy}\right)^2} + \frac{3\alpha_{z^2}^2 (\cos\theta + \sin\theta)^2}{\left(\Delta_{z^2}\right)^2} \right] - \frac{i\, \alpha_\pi^2\, \zeta_{Fe} (\cos^2\theta - \cos\theta \sin\theta)}{\Delta_{xy}}$$

$$- \frac{i\, \alpha_\pi^2 \alpha_{x^2-y^2}^2\, \zeta_{Fe} (\sin^2\theta - \cos\theta \sin\theta)}{\Delta_{x^2-y^2}} - \frac{i\, [3\alpha_\pi^2 \alpha_{z^2}^2 + \sqrt{3}\alpha_\pi\, \alpha_{z^2} \beta_\pi \beta_z]\, \zeta_{Fe} (\sin^2\theta + \cos\theta \sin\theta)}{\Delta_{z^2}}$$

$$\langle \widetilde{\Psi}_0^{\frac{1}{2},-\frac{1}{2}} \left| \boldsymbol{l_x} + g_e \boldsymbol{s_x} \right| \widetilde{\Psi}_0^{\frac{1}{2},+\frac{1}{2}} \rangle = \frac{g_e \cos 2\theta}{2}$$

$$+ \frac{g_e \alpha_\pi^2 \zeta_{Fe}^2}{8} \left[\frac{\alpha_{x^2-y^2}^2 (\cos\theta - \sin\theta)^2}{\left(\Delta_{x^2-y^2}\right)^2} - \frac{(\cos\theta - \sin\theta)^2}{\left(\Delta_{xy}\right)^2} + \frac{3\alpha_{z^2}^2 (\cos\theta + \sin\theta)^2}{\left(\Delta_{z^2}\right)^2} \right] - \frac{\alpha_\pi^2 \alpha_{x^2-y^2}^2 \zeta_{Fe} (\cos^2\theta - \sin\theta \cos\theta)}{\Delta_{x^2-y^2}}$$

$$- \frac{\left[3\alpha_\pi^2 \alpha_{z^2}^2 + \sqrt{3}\alpha_\pi\, \alpha_{z^2} \beta_\pi \beta_z\right] \zeta_{Fe} (\cos^2\theta + \sin\theta \cos\theta)}{\Delta_{z^2}} - \frac{\alpha_\pi^2 \zeta_{Fe} (\sin^2\theta - \sin\theta \cos\theta)}{\Delta_{xy}}$$

$$\langle \widetilde{\Psi}_0^{\frac{1}{2},-\frac{1}{2}} \left| \boldsymbol{l_y} + g_e \boldsymbol{s_y} \right| \widetilde{\Psi}_0^{\frac{1}{2},+\frac{1}{2}} \rangle = \frac{i\, g_e \cos 2\theta}{2}$$

$$- \frac{i\, g_e \alpha_\pi^2 \zeta_{Fe}^2}{8} \left[\frac{\alpha_{x^2-y^2}^2 (\cos\theta - \sin\theta)^2}{\left(\Delta_{x^2-y^2}\right)^2} - \frac{(\cos\theta - \sin\theta)^2}{\left(\Delta_{xy}\right)^2} + \frac{3\alpha_{z^2}^2 (\cos\theta + \sin\theta)^2}{\left(\Delta_{z^2}\right)^2} \right] + \frac{i\, \alpha_\pi^2\, \zeta_{Fe} (\cos^2\theta - \cos\theta \sin\theta)}{\Delta_{xy}}$$

$$+ \frac{i\, \alpha_{x^2-y^2}^2 \alpha_\pi^2\, \zeta_{Fe} (\sin^2\theta - \cos\theta \sin\theta)}{\Delta_{x^2-y^2}} + \frac{i\, [3\alpha_\pi^2 \alpha_{z^2}^2 + \sqrt{3}\alpha_\pi\, \alpha_{z^2} \beta_\pi \beta_z]\, \zeta_{Fe} (\sin^2\theta + \cos\theta \sin\theta)}{\Delta_{z^2}}$$

7.1.3. Contributions to the g-values by quadratic terms Δ_n^2

It should be noted that these terms are identical for g_{xx}, g_{yy} and g_{zz} , only the signs are different (see Equations 5.14- 5.16). Here, the absolute values for the individual terms are given for calculations with θ_{calc} (Table 7.1) and calculations with θ_{exp} derived from the experimental g_{zz}-value (Table 7.2).

Table 7.1: Contributions to the g-values by terms of the order Δ_n^2, calculations performed with θ_{calc}.

	$\left(\Delta_{x^2-y^2}\right)^2$	$\left(\Delta_{xy}\right)^2$	$(\Delta_{z^2})^2$	$\Delta_{xy} \cdot \Delta_{x^2-y^2}$ (g_{zz})
$[Fe^{V}(N)cyc\text{-}ac]^{+}$	0.007	0.000	0.000	0.001
$[Fe^{V}(N)(N_3)cyc]^{+}$	0.002	0.000	0.000	0.001
$[Fe^{V}(N)TMC\text{-}ac]+$	0.014	0.000	0.000	0.002
$[Fe^{V}(N)TPP]$	0.004	0.000	0.001	0.001
$[Fe^{V}(O)TAML]^{-}$	0.000	0.001	0.002	0.000
$[Fe^{V}(O)cyc\text{-}ac]^{2+}$	0.000	0.001	0.000	0.000

Table 7.2: Contributions to the g-values by terms of the order Δ_n^2, calculations performed with θ_{exp}.

	$\left(\Delta_{x^2-y^2}\right)^2$	$\left(\Delta_{xy}\right)^2$	$(\Delta_{z^2})^2$	$\Delta_{xy} \cdot \Delta_{x^2-y^2}$ (g_{zz})
$[Fe^{V}(N)cyc\text{-}ac]^{+}$	0.009	0.000	0.000	-0.001
$[Fe^{V}(N)(N_3)cyc]^{+}$	0.002	0.000	0.000	-0.001
$[Fe^{V}(N)TMC\text{-}ac]+$	0.012	0.000	0.000	-0.001
$[Fe^{V}(O)TAML]^{-}$	0.000	0.001	0.002	0.000

7.2. Additional Mass Spectrometry Data for Chapter 5.9.2

The gas-chromatography electron ionization mass spectrometry measurements were performed on a Finnigan SSQ 7000 spectrometer. The resulting data is provided in Table 7.3. Furthermore the background data is provided that was recorded just before the injection of the gaseous sample.

Table 7.3: Raw data from EI-MS measurements of the gas phase over the photolyzed samples.

m/z	$[Fe(^{15}NN_2)cyc\text{-}ac]PF_6$	$[Fe(^{15}NN_2)cyc\text{-}ac]PF_6$ background	$[Fe(^{15}NN_2)_2cyc]ClO_4$	$[Fe(^{15}NN_2)_2cyc]ClO_4$ background
25	0.00	0.01	0.00	0.00
26	0.00	0.07	0.00	0.00
27	0.14	0.13	0.11	0.01
28 ($^{14}N^{14}N$)	100.00	100.00	100.00	100.00
29 ($^{15}N^{14}N$)	30.04	1.32	18.70	0.71
30 ($^{15}N^{15}N$)	5.31	0.53	2.99	0.02
31	0.00	0.05	0.00	0.00
32 (O_2)	4.68	25.51	7.05	14.98
33	0.00	0.01	0.00	0.01
34	0.02	0.11	0.03	0.06
35	0.00	0.02	0.00	0.00
36	0.06	0.26	0.07	0.14
37	0.00	0.02	0.00	0.00
38	0.01	0.10	0.01	0.03
39	0.00	0.09	0.00	0.02
40 (Ar)	14.36	1.63	20.73	48.10
41	0.01	0.21	0.01	0.01
42	0.01	0.15	0.00	0.00
43	0.01	0.05	0.01	0.01
44	0.18	2.42	0.18	0.24
45	0.00	0.04	0.00	0.00

8. References

[1] A. F. Holleman, E. Wiberg, N. Wiberg, *Lehrbuch der anorganischen Chemie*, de Gruyter, **1995**.
[2] R. R. Crichton, in *Practical Approaches to Biological Inorganic Chemistry* (Eds.: R. R. Crichton, R. O. Louro), Elsevier, Oxford, **2013**.
[3] J. F. Berry, *Comments Inorg. Chem.* **2009**, *30*, 28-66.
[4] W. A. Nugent, J. M. Mayer, *Metal-ligand multiple bonds: the chemistry of transition metal complexes containing oxo, nitrido, imido, alkylidene, or alkylidyne ligands*, Wiley, **1988**.
[5] F. A. Cotton, G. Wilkinson, *Advanced inorganic chemistry: a comprehensive text*, Interscience Publishers, **1966**.
[6] C. J. Ballhausen, H. B. Gray, *Inorg. Chem.* **1962**, *1*, 111-122.
[7] J. F. Berry, S. DeBeer George, F. Neese, *Phys. Chem. Chem. Phys.* **2008**, *10*, 4361-4374.
[8] J. Bendix, R. J. Deeth, T. Weyhermüller, E. Bill, K. Wieghardt, *Inorg. Chem.* **2000**, *39*, 930-938.
[9] K. Meyer, J. Bendix, E. Bill, T. Weyhermüller, K. Wieghardt, *Inorg. Chem.* **1998**, *37*, 5180-5188.
[10] K. Meyer, J. Bendix, N. Metzler-Nolte, T. Weyhermüller, K. Wieghardt, *J. Am. Chem. Soc.* **1998**, *120*, 7260-7270.
[11] J. Bendix, *J. Am. Chem. Soc.* **2003**, *125*, 13348-13349.
[12] J. Bendix, T. Birk, T. Weyhermuller, *Dalt. Trans.* **2005**, 2737-2741.
[13] T. Birk, J. Bendix, *Inorg. Chem.* **2003**, *42*, 7608-7615.
[14] C. D. Garner, I. H. Hillier, F. E. Mabbs, C. Taylor, M. F. Guest, *J. Chem. Soc. Dalton Trans.* **1976**, 2258-2261.
[15] C. D. Garner, J. Kendrick, P. Lambert, F. E. Mabbs, I. H. Hillier, *Inorg. Chem.* **1976**, *15*, 1287-1291.
[16] J. Hohenberger, K. Ray, K. Meyer, *Nat Commun* **2012**, *3*, 720.
[17] S. C. Bart, K. Chłopek, E. Bill, M. W. Bouwkamp, E. Lobkovsky, F. Neese, K. Wieghardt, P. J. Chirik, *J. Am. Chem. Soc.* **2006**, *128*, 13901-13912.
[18] E. W. Svastits, J. H. Dawson, R. Breslow, S. H. Gellman, *J. Am. Chem. Soc.* **1985**, *107*, 6427-6428.
[19] R. N. Thorneley, D. J. Lowe, *Biochem. J* **1984**, *224*, 903-909.
[20] R. N. Thorneley, D. J. Lowe, *Biochem. J* **1984**, *224*, 887-894.
[21] D. J. Lowe, R. N. Thorneley, *Biochem. J* **1984**, *224*, 877-886.
[22] K. M. Lancaster, M. Roemelt, P. Ettenhuber, Y. Hu, M. W. Ribbe, F. Neese, U. Bergmann, S. DeBeer, *Science* **2011**, *334*, 974-977.
[23] G. Ertl, *Angew. Chem. Int. Ed.* **1990**, *29*, 1219-1227.
[24] G. Ertl, *The Chemical Record* **2001**, *1*, 33-45.
[25] J. M. Smith, D. Subedi, *Dalt. Trans.* **2012**, *41*, 1423-1429.
[26] J. M. Smith, in *Progress in Inorganic Chemistry Volume 58*, John Wiley & Sons, Inc., **2014**, pp. 417-470.
[27] M. P. Mehn, J. C. Peters, *J. Inorg. Biochem.* **2006**, *100*, 634-643.
[28] R. A. Eikey, M. M. Abu-Omar, *Coord. Chem. Rev.* **2003**, *243*, 83-124.
[29] K. Meyer, E. Bill, B. Mienert, T. Weyhermüller, K. Wieghardt, *J. Am. Chem. Soc.* **1999**, *121*, 4859-4876.
[30] D. A. Summerville, I. A. Cohen, *J. Am. Chem. Soc.* **1976**, *98*, 1747-1752.
[31] T. Jüstel, T. Weyhermüller, K. Wieghardt, E. Bill, M. Lengen, A. X. Trautwein, P. Hildebrandt, *Angew. Chem. Int. Ed.* **1995**, *34*, 669-672.
[32] M. M. Rodriguez, E. Bill, W. W. Brennessel, P. L. Holland, *Science* **2011**, *334*, 780-783.
[33] M. V. Bennett, R. H. Holm, *Angew. Chem. Int. Ed.* **2006**, *45*, 5613-5616.
[34] T. M. Powers, A. R. Fout, S.-L. Zheng, T. A. Betley, *J. Am. Chem. Soc.* **2011**, *133*, 3336-3338.

[35] J. J. Scepaniak, C. S. Vogel, M. M. Khusniyarov, F. W. Heinemann, K. Meyer, J. M. Smith, *Science* **2011**, *331*, 1049-1052.
[36] C. Vogel, F. W. Heinemann, J. Sutter, C. Anthon, K. Meyer, *Angew. Chem. Int. Ed.* **2008**, *47*, 2681-2684.
[37] T. A. Betley, J. C. Peters, *J. Am. Chem. Soc.* **2004**, *126*, 6252-6254.
[38] J. J. Scepaniak, J. A. Young, R. P. Bontchev, J. M. Smith, *Angew. Chem. Int. Ed.* **2009**, *48*, 3158-3160.
[39] J. J. Scepaniak, M. D. Fulton, R. P. Bontchev, E. N. Duesler, M. L. Kirk, J. M. Smith, *J. Am. Chem. Soc.* **2008**, *130*, 10515-10517.
[40] W. D. Wagner, K. Nakamoto, *J. Am. Chem. Soc.* **1989**, *111*, 1590-1598.
[41] N. Aliaga-Alcalde, S. DeBeer George, B. Mienert, E. Bill, K. Wieghardt, F. Neese, *Angew. Chem. Int. Ed.* **2005**, *44*, 2908-2912.
[42] J. F. Berry, E. Bill, E. Bothe, T. Weyhermüller, K. Wieghardt, *J. Am. Chem. Soc.* **2005**, *127*, 11550-11551.
[43] C. A. Grapperhaus, B. Mienert, E. Bill, T. Weyhermüller, K. Wieghardt, *Inorg. Chem.* **2000**, *39*, 5306-5317.
[44] O. Krahe, E. Bill, F. Neese, *Angew. Chem. Int. Ed.* **2014**, *53*, 8727-8731.
[45] T. Petrenko, S. DeBeer George, N. Aliaga-Alcalde, E. Bill, B. Mienert, Y. Xiao, Y. Guo, W. Sturhahn, S. P. Cramer, K. Wieghardt, F. Neese, *J. Am. Chem. Soc.* **2007**, *129*, 11053-11060.
[46] W. D. Wagner, K. Nakamoto, *J. Am. Chem. Soc.* **1988**, *110*, 4044-4045.
[47] J. F. Berry, E. Bill, E. Bothe, S. D. George, B. Mienert, F. Neese, K. Wieghardt, *Science* **2006**, *312*, 1937-1941.
[48] J. F. Berry, E. Bill, E. Bothe, F. Neese, K. Wieghardt, *J. Am. Chem. Soc.* **2006**, *128*, 13515-13528.
[49] R. J. Audette, J. W. Quail, *Inorg. Chem.* **1972**, *11*, 1904-1908.
[50] J.-U. Rohde, T. A. Betley, T. A. Jackson, C. T. Saouma, J. C. Peters, L. Que, *Inorg. Chem.* **2007**, *46*, 5720-5726.
[51] J. J. Scepaniak, R. P. Bontchev, D. L. Johnson, J. M. Smith, *Angew. Chem. Int. Ed.* **2011**, *50*, 6630-6633.
[52] M. P. Hendrich, W. Gunderson, R. K. Behan, M. T. Green, M. P. Mehn, T. a. Betley, C. C. Lu, J. C. Peters, *Proc. Natl. Acad. Sci. U.S.A.* **2006**, *103*, 17107-17112.
[53] D. Schröder, H. Schwarz, N. Aliaga-Alcalde, F. Neese, *Eur. J. Inorg. Chem.* **2007**, *2007*, 816-821.
[54] J. Torres-Alacan, U. Das, A. C. Filippou, P. Vöhringer, *Angew. Chem. Int. Ed.* **2013**, *52*, 12833-12837.
[55] J. Torres-Alacan, P. Vöhringer, *Int. Rev. Phys. Chem.* **2014**, *33*, 521-553.
[56] H. Vennekate, D. Schwarzer, J. Torres-Alacan, P. Vöhringer, *J. Am. Chem. Soc.* **2014**, *136*, 10095-10103.
[57] C. Krebs, D. Galonić Fujimori, C. T. Walsh, J. M. Bollinger, *Acc. Chem. Res.* **2007**, *40*, 484-492.
[58] M. Costas, M. P. Mehn, M. P. Jensen, L. Que, *Chem. Rev.* **2004**, *104*, 939-986.
[59] W. Nam, *Acc. Chem. Res.* **2007**, *40*, 465-465.
[60] S. Chakrabarty, R. N. Austin, D. Deng, J. T. Groves, J. D. Lipscomb, *J. Am. Chem. Soc.* **2007**, *129*, 3514-3515.
[61] S. Friedle, E. Reisner, S. J. Lippard, *Chem. Soc. Rev.* **2010**, *39*, 2768-2779.
[62] H. Fujii, *Coord. Chem. Rev.* **2002**, *226*, 51-60.
[63] J. T. Groves, *J. Inorg. Biochem.* **2006**, *100*, 434-447.
[64] J. T. Groves, R. C. Haushalter, M. Nakamura, T. E. Nemo, B. J. Evans, *J. Am. Chem. Soc.* **1981**, *103*, 2884-2886.
[65] C. E. Tinberg, S. J. Lippard, *Acc. Chem. Res.* **2011**, *44*, 280-288.
[66] C. Jung, *Biochim. Biophys. Acta* **2011**, *1814*, 46-57.
[67] S. Shaik, D. Kumar, S. P. de Visser, A. Altun, W. Thiel, *Chem. Rev.* **2005**, *105*, 2279-2328.
[68] S. Shaik, S. Cohen, Y. Wang, H. Chen, D. Kumar, W. Thiel, *Chem. Rev.* **2010**, *110*, 949-1017.
[69] M. Costas, K. Chen, L. Que Jr, *Coord. Chem. Rev.* **2000**, *200–202*, 517-544.
[70] E. I. Solomon, T. C. Brunold, M. I. Davis, J. N. Kemsley, S.-K. Lee, N. Lehnert, F. Neese, A. J. Skulan, Y.-S. Yang, J. Zhou, *Chem. Rev.* **2000**, *100*, 235-350.

[71] J. C. Price, E. W. Barr, T. E. Glass, C. Krebs, J. M. Bollinger, *J. Am. Chem. Soc.* **2003**, *125*, 13008-13009.
[72] J. C. Price, E. W. Barr, B. Tirupati, J. M. Bollinger, C. Krebs, *Biochemistry* **2003**, *42*, 7497-7508.
[73] D. A. Proshlyakov, T. F. Henshaw, G. R. Monterosso, M. J. Ryle, R. P. Hausinger, *J. Am. Chem. Soc.* **2004**, *126*, 1022-1023.
[74] A. R. McDonald, L. Que Jr, *Coord. Chem. Rev.* **2013**, *257*, 414-428.
[75] J.-U. Rohde, J.-H. In, M. H. Lim, W. W. Brennessel, M. R. Bukowski, A. Stubna, E. Münck, W. Nam, L. Que, *Science* **2003**, *299*, 1037-1039.
[76] F. T. de Oliveira, A. Chanda, D. Banerjee, X. Shan, S. Mondal, L. Que, E. L. Bominaar, E. Münck, T. J. Collins, *Science* **2007**, *315*, 835-838.
[77] K. M. Van Heuvelen, A. T. Fiedler, X. Shan, R. F. De Hont, K. K. Meier, E. L. Bominaar, E. Münck, L. Que, *Proc. Natl. Acad. Sci. USA* **2012**, *109*, 11933-11938.
[78] W. Nam, *Acc. Chem. Res.* **2007**, *40*, 522-531.
[79] P. Ortiz de Montellano, J. De Voss, in *Cytochrome P450* (Ed.: P. Ortiz de Montellano), Springer US, **2005**, pp. 183-245.
[80] P. R. Ortiz de Montellano, *Chem. Rev.* **2010**, *110*, 932-948.
[81] J. Rittle, M. T. Green, *Science* **2010**, *330*, 933-937.
[82] L. Que, *Acc. Chem. Res.* **2007**, *40*, 493-500.
[83] J. Kaizer, E. J. Klinker, N. Y. Oh, J.-U. Rohde, W. J. Song, A. Stubna, J. Kim, E. Münck, W. Nam, L. Que, *J. Am. Chem. Soc.* **2004**, *126*, 472-473.
[84] M. S. Seo, N. H. Kim, K.-B. Cho, J. E. So, S. K. Park, M. Clemancey, R. Garcia-Serres, J.-M. Latour, S. Shaik, W. Nam, *Chemical Science* **2011**, *2*, 1039-1045.
[85] H. Chen, W. Lai, S. Shaik, *J. Phys. Chem. Lett.* **2010**, *1*, 1533-1540.
[86] H. Hirao, D. Kumar, L. Que, S. Shaik, *J. Am. Chem. Soc.* **2006**, *128*, 8590-8606.
[87] D. Janardanan, D. Usharani, H. Chen, S. Shaik, *J. Phys. Chem. Lett.* **2011**, *2*, 2610-2617.
[88] D. Kumar, H. Hirao, L. Que, S. Shaik, *J. Am. Chem. Soc.* **2005**, *127*, 8026-8027.
[89] S. Shaik, H. Hirao, D. Kumar, *Acc. Chem. Res.* **2007**, *40*, 532-542.
[90] S. Shaik, S. Visser, D. Kumar, *JBIC J. Biol. Inorg. Chem.* **2004**, *9*, 661-668.
[91] S. Ye, C.-Y. Geng, S. Shaik, F. Neese, *Phys. Chem. Chem. Phys.* **2013**, *15*, 8017-8030.
[92] A. Decker, E. I. Solomon, *Angew. Chem. Int. Ed.* **2005**, *44*, 2252-2255.
[93] C. Geng, S. Ye, F. Neese, *Angew. Chem. Int. Ed.* **2010**, *49*, 5717-5720.
[94] S. P. de Visser, *J. Am. Chem. Soc.* **2006**, *128*, 9813-9824.
[95] P. Comba, M. Maurer, P. Vadivelu, *J. Phys. Chem. A* **2008**, *112*, 13028-13036.
[96] D. Danovich, S. Shaik, *J. Am. Chem. Soc.* **1997**, *119*, 1773-1786.
[97] N. Harris, S. Shaik, D. Schröder, H. Schwarz, *Helv. Chim. Acta* **1999**, *82*, 1784-1797.
[98] L. Bernasconi, E. J. Baerends, *Eur. J. Inorg. Chem.* **2008**, *2008*, 1672-1681.
[99] S. Ye, F. Neese, *Proc. Natl. Acad. Sci. USA* **2011**, *108*, 1228-1233.
[100] H. Hirao, D. Kumar, W. Thiel, S. Shaik, *J. Am. Chem. Soc.* **2005**, *127*, 13007-13018.
[101] D. Usharani, D. Janardanan, C. Li, S. Shaik, *Acc. Chem. Res.* **2013**, *46*, 471-482.
[102] E. I. Solomon, S. D. Wong, L. V. Liu, A. Decker, M. S. Chow, *Curr. Op. Chem. Biol.* **2009**, *13*, 99-113.
[103] C. Michel, E. J. Baerends, *Inorg. Chem.* **2009**, *48*, 3628-3638.
[104] S. Shaik, H. Chen, D. Janardanan, *Nat. Chem.* **2011**, *3*, 19-27.
[105] G. Herzberg, J. W. T. Spinks, *Atomic Spectra and Atomic Structure*, Dover publications, **1944**.
[106] S. A. Wilson, J. Chen, S. Hong, Y.-M. Lee, M. Clémancey, R. Garcia-Serres, T. Nomura, T. Ogura, J.-M. Latour, B. Hedman, K. O. Hodgson, W. Nam, E. I. Solomon, *J. Am. Chem. Soc.* **2012**, *134*, 11791-11806.
[107] A. J. Johansson, M. R. A. Blomberg, P. E. M. Siegbahn, *J. Phys. Chem. C* **2007**, *111*, 12397-12406.
[108] N. M. Atherton, *Principles of Electron Spin Resonance*, Ellis Horwood Limited, Chichester, West Sussex, England, **1993**.
[109] F. E. Mabbs, D. Collison, in *Studies in Inorganic Chemistry, Vol. Volume 16* (Eds.: F. E. Mabbs, D. Collison), Elsevier, **1992**, pp. xvii-xix.

[110] J. A. Weil, J. R. Bolton, *Electron Paramagnetic Resonance - Elementary Theory and Practical Applications*, John Wiley & Sons, Inc, Hoboken, New Jersey, **2007**.
[111] A. Carrington, A. D. McLachlan, *Introduction to Magnetic Resonance*, Harper & Row John Weatherhill, New York / Tokyo, **1969**.
[112] A. X. Trautwein, E. Bill, E. L. Bominaar, H. Winkler, *Struct. Bonding* **1991**, *78*, 95.
[113] R. S. Drago, *Physical methods for chemists*, Saunders College Pub., **1992**.
[114] L. Que, *Physical Methods in Bioinorganic Chemistry: Spectroscopy and Magnetism*, University Science Books, **2000**.
[115] M. Wächtler, J. Guthmuller, L. González, B. Dietzek, *Coord. Chem. Rev.* **2012**, *256*, 1479-1508.
[116] R. J. H. Clark, T. J. Dines, *Angew. Chem. Int. Ed.* **1986**, *25*, 131-158.
[117] M. H. L. Pryce, *Proceedings of the Physical Society. Section A* **1950**, *63*, 25.
[118] A. Abragam, M. H. L. Pryce, *Theory of the Nuclear Hyperfine Structure of Paramagnetic Resonance Spectra in Crystals, Vol. 205*, **1951**.
[119] F. Neese, E. I. Solomon, in *Magnetism: Molecules to Materials IV*, Wiley-VCH Verlag GmbH & Co. KGaA, **2003**, pp. 345-466.
[120] F. Neese, E. I. Solomon, *Inorg. Chem.* **1998**, *37*, 6568-6582.
[121] J. E. Harriman, *Theoretical foundations of electron spin resonance*, Academic Press, **1978**.
[122] R. Boča, *Theoretical Foundations of Molecular Magnetism*, Elsevier Science, **1999**.
[123] F. E. Mabbs, D. Collison, *Electron Paramagnetic Resonance of d Transition Metal Compounds*, **1992**.
[124] F. E. Mabbs, D. J. Machin, *Magnetism and Transition Metal Complexes*, Dover Publications, **2008**.
[125] R. McWeeny, *Quantum Systems in Chemistry and Physics. Trends in Methods and Applications: Trends in Methods and Applications*, Springer, **1998**.
[126] R. McWeeny, *Spins in Chemistry*, Dover Publications, **2004**.
[127] R. McWeeny, *J. Chem. Phys.* **1965**, *42*, 1717-1725.
[128] M. E. Rose, *Elementary theory of angular momentum*, Wiley, **1957**.
[129] J. C. Slater, *Phys. Rev.* **1929**, *34*, 1293-1322.
[130] J. C. Slater, *Phys. Rev.* **1931**, *38*, 1109-1144.
[131] J. Bendix, M. Brorson, C. E. Schaffer, *Inorg. Chem.* **1993**, *32*, 2838-2849.
[132] McGarvey, *Transition Met. Chem.* **1966**, *3*.
[133] M. Gerloch, J. R. Miller, in *Progress in Inorganic Chemistry*, John Wiley & Sons, Inc., **2007**, pp. 1-47.
[134] J. Ammeter, *Chimia* **1968**, *22*.
[135] P. W. Atkins, R. S. Friedman, *Molecular Quantum Mechanics*, OUP Oxford, **2011**.
[136] R. Mössbauer, *Z. Physik* **1958**, *151*, 124-143.
[137] R. Mössbauer, *Naturwissenschaften* **1958**, *45*, 538-539.
[138] R. Mössbauer, *Z. Naturforsch.* **1959**, *14*, 211-216.
[139] P. Gütlich, E. Bill, A. X. Trautwein, *Mössbauer Spectroscopy and Transition Metal Chemistry: Fundamentals and Applications*, Springer, **2010**.
[140] R. R. Crichton, *Practical Approaches to Biological Inorganic Chemistry*, Elsevier Science, **2012**.
[141] A. Bakac, *Physical Inorganic Chemistry: Principles, Methods, and Models*, Wiley, **2010**.
[142] E. I. Solomon, A. B. P. Lever, *Inorganic Electronic Structure and Spectroscopy, Methodology*, Wiley, **1999**.
[143] F. Neese, *Inorg. Chim. Act.* **2002**, *337*, 181-192.
[144] M. Römelt, S. Ye, F. Neese, *Inorg. Chem.* **2009**, *48*, 784-785.
[145] A. C. Albrecht, *J. Chem. Phys.* **1961**, *34*, 1476-1484.
[146] F. A. Savin, *Opti. i. Spektr.* **1965**, *19*, 555.
[147] F. A. Savin, *Opti. i. Spektr.* **1965**, *19*, 743.
[148] F. A. Savin, *Opti. i. Spektr.* **1966**, *20*, 989.
[149] F. Neese, T. Petrenko, D. Ganyushin, G. Olbrich, *Coord. Chem. Rev.* **2007**, *251*, 288-327.
[150] T. Petrenko, F. Neese, *J. Chem. Phys.* **2007**, *127*, 164319.
[151] T. Petrenko, F. Neese, *J. Chem. Phys.* **2012**, *137*, 234107.

[152] B. Kirchner, F. Wennmohs, S. Ye, F. Neese, *Curr. Op. Chem. Biol.* **2007**, *11*, 134-141.
[153] M. Orio, D. A. Pantazis, F. Neese, *Photosynth. Res.* **2009**, *102*, 443-453.
[154] F. Jensen, *Introduction to Computational Chemistry*, Wiley, **2007**.
[155] A. Szabo, N. S. Ostlund, *Modern Quantum Chemistry: Introduction to Advanced Electronic Structure Theory*, Dover Publications, **1989**.
[156] C. J. Cramer, *Essentials of Computational Chemistry: Theories and Models*, Wiley, **2005**.
[157] F. Neese, *Coord. Chem. Rev.* **2009**, *253*, 526-563.
[158] B. O. Roos, in *Advances in Chemical Physics*, John Wiley & Sons, Inc., **2007**, pp. 399-445.
[159] B. O. Roos, K. Andersson, M. P. Fülscher, P.-â. Malmqvist, L. Serrano-Andrés, K. Pierloot, M. Merchán, in *Advances in Chemical Physics*, John Wiley & Sons, Inc., **2007**, pp. 219-331.
[160] W. Koch, M. C. Holthausen, *A chemist's guide to density functional theory*, Wiley-VCH, **2000**.
[161] C. J. Cramer, D. G. Truhlar, *Phys. Chem. Chem. Phys.* **2009**, *11*, 10757-10816.
[162] R. Deeth, in *Principles and Applications of Density Functional Theory in Inorganic Chemistry II, Vol. 113*, Springer Berlin Heidelberg, **2004**, pp. 37-70.
[163] W. Kohn, *Rev. Mod. Phys.* **1999**, *71*, 1253-1266.
[164] J. A. Pople, *Rev. Mod. Phys.* **1999**, *71*, 1267-1274.
[165] P. Hohenberg, W. Kohn, *Phys. Rev.* **1964**, *136*, B864-B871.
[166] W. Kohn, L. J. Sham, *Phys. Rev.* **1965**, *140*, A1133-A1138.
[167] S. H. Vosko, L. Wilk, M. Nusair, *Can. J. Phys.* **1980**, *58*, 1200-1211.
[168] Y. Wang, J. P. Perdew, *Physical Review B* **1991**, *44*, 13298-13307.
[169] J. P. Perdew, *Physical Review B* **1986**, *34*, 7406-7406.
[170] J. P. Perdew, *Physical Review B* **1986**, *33*, 8822-8824.
[171] A. D. Becke, *Phys. Rev. A* **1988**, *38*, 3098-3100.
[172] J. P. Perdew, K. Burke, M. Ernzerhof, *Phys. Rev. Lett.* **1996**, *77*, 3865-3868.
[173] J. P. Perdew, K. Burke, M. Ernzerhof, *Phys. Rev. Lett.* **1997**, *78*, 1396-1396.
[174] A. D. Becke, *J Chem Phys* **1993**, *98*, 5648-5652.
[175] F. Neese, *Wiley Interdisciplinary Reviews: Computational Molecular Science* **2012**, *2*, 73-78.
[176] M. Bühl, H. Kabrede, *J. Chem. Theory Comput.* **2006**, *2*, 1282-1290.
[177] M. Bühl, C. Reimann, D. A. Pantazis, T. Bredow, F. Neese, *J. Chem. Theory Comput.* **2008**, *4*, 1449-1459.
[178] O. Vahtras, J. Almlöf, M. W. Feyereisen, *Chem. Phys. Lett.* **1993**, *213*, 514-518.
[179] A. Schafer, H. Horn, R. Ahlrichs, *J. Chem. Phys.* **1992**, *97*, 2571-2577.
[180] F. Weigend, R. Ahlrichs, *Phys. Chem. Chem. Phys.* **2005**, *7*, 3297-3305.
[181] A. Klamt, *J. Phys. Chem.* **1995**, *99*, 2224-2235.
[182] A. Klamt, G. Schuurmann, *Journal of the Chemical Society-Perkin Transactions 2* **1993**, 799-805.
[183] S. Grimme, *Wiley Interdisciplinary Reviews: Computational Molecular Science* **2011**, *1*, 211-228.
[184] S. Grimme, J. Antony, S. Ehrlich, H. Krieg, *J. Chem. Phys.* **2010**, *132*, 154104.
[185] S. Grimme, S. Ehrlich, L. Goerigk, *J. Comput. Chem.* **2011**, *32*, 1456-1465.
[186] A. P. Scott, L. Radom, *J. Phys. Chem.* **1996**, *100*, 16502-16513.
[187] F. Neese, F. Wennmohs, A. Hansen, U. Becker, *Chem. Phys.* **2009**, *356*, 98-109.
[188] T. Petrenko, K. Ray, K. E. Wieghardt, F. Neese, *J. Am. Chem. Soc.* **2006**, *128*, 4422-4436.
[189] K. Ray, T. Petrenko, K. Wieghardt, F. Neese, *Dalt. Trans.* **2007**, 1552-1566.
[190] F. Furche, *J. Chem. Phys.* **2001**, *114*, 5982-5992.
[191] F. Neese, G. Olbrich, *Chem. Phys. Lett.* **2002**, *362*, 170-178.
[192] T. Petrenko, S. Kossmann, F. Neese, *J. Chem. Phys.* **2011**, *134*, 054116.
[193] L. Noodleman, *J. Chem. Phys.* **1981**, *74*, 5737-5743.
[194] R. Caballol, O. Castell, F. Illas, I. de P. R. Moreira, J. P. Malrieu, *J. Phys. Chem. A* **1997**, *101*, 7860-7866.
[195] K. Pierloot, in *Computational Organometallic Chemistry* (Ed.: T. R. Cundari), Taylor & Francis, **2001**, pp. 123-158.
[196] C. Angeli, S. Borini, M. Cestari, R. Cimiraglia, *J. Chem. Phys.* **2004**, *121*, 4043-4049.
[197] C. Angeli, R. Cimiraglia, S. Evangelisti, T. Leininger, J.-P. Malrieu, *J. Chem. Phys.* **2001**, *114*, 10252-10264.

[198] C. Angeli, R. Cimiraglia, J.-P. Malrieu, *Chem. Phys. Lett.* **2001**, *350*, 297-305.
[199] C. Angeli, R. Cimiraglia, J.-P. Malrieu, *J. Chem. Phys.* **2002**, *117*, 9138-9153.
[200] D. Ganyushin, F. Neese, *J. Chem. Phys.* **2006**, *125*, 024103.
[201] F. Neese, *J. Chem. Phys.* **2005**, *122*, 034107.
[202] M. Atanasov, D. Aravena, E. Suturina, E. Bill, D. Maganas, F. Neese, *Coord. Chem. Rev.* **2015**, *289–290*, 177-214.
[203] M. Atanasov, D. Ganyushin, D. A. Pantazis, K. Sivalingam, F. Neese, *Inorg. Chem.* **2011**, *50*, 7460-7477.
[204] M. Atanasov, D. Ganyushin, K. Sivalingam, F. Neese, *Struct. Bond.* **2012**, *143*, 149-220.
[205] N. Gilka, J. Tatchen, C. M. Marian, *Chem. Phys.* **2008**, *343*, 258-269.
[206] B. O. Roos, in *Lecture Notes in Quantum Chemistry, Vol. 58* (Ed.: B. Roos), Springer Berlin Heidelberg, **1992**, pp. 177-254.
[207] D. Ganyushin, F. Neese, *J. Chem. Phys.* **2013**, *138*, 104113.
[208] D. A. Skoog, J. J. Leary, *Principles of instrumental analysis*, Saunders College Pub., **1992**.
[209] R. S. Czernuszewicz, W.-D. Wagner, G. B. Ray, K. Nakamoto, *J. Mol. Struct.* **1991**, *242*, 99-117.
[210] A. M. Heyns, *Spectrochim. Acta, Pt. A: Mol. Spectrosc.* **1977**, *33*, 315-322.
[211] M. Hesse, H. Meier, B. Zeeh, *Spektroskopische Methoden in der organischen Chemie*, 6 ed., Georg Thieme Verlag, Stuttgart, **2002**.
[212] C. T. Gutman, I. A. Guzei, T. C. Brunold, *Inorg. Chem.* **2013**, *52*, 8909-8918.
[213] S. Y. Lee, E. J. Heller, *J. Chem. Phys.* **1979**, *71*, 4777-4788.
[214] Myers, Mathies, in *Biological Applications of Raman Spectroscopy, Vol. Vol 2* (Ed.: Spiro), John Wiley and Sons, New York, **1987**.
[215] K. Nakamoto, *Infrared and Raman Spectra of Inorganic and Coordination Compounds, Part B*, John Wiley & Sons Inc, New York, **1997**.
[216] C. K. Poon, *Inorg. Chim. Act.* **1971**, *5*, 322-324.
[217] H. Vennekate, D. Schwarzer, J. Torres-Alacan, O. Krahe, A. C. Filippou, F. Neese, P. Vohringer, *Phys. Chem. Chem. Phys.* **2012**, *14*, 6165-6172.
[218] J. Torres-Alacan, O. Krahe, A. C. Filippou, F. Neese, D. Schwarzer, P. Vöhringer, *Chem. Eur. J.* **2012**, *18*, 3043-3055.
[219] J. D. Simon, K. S. Peters, *Chem. Phys. Lett.* **1983**, *98*, 53-56.
[220] J. D. Simon, X. Xie, *J. Phys. Chem.* **1986**, *90*, 6751-6753.
[221] B. Li, T. Liu, C. V. Popescu, A. Bilko, M. Y. Darensbourg, *Inorg. Chem.* **2009**, *48*, 11283-11289.
[222] S. D. Brown, J. C. Peters, *J. Am. Chem. Soc.* **2005**, *127*, 1913-1923.
[223] B. Askevold, J. T. Nieto, S. Tussupbayev, M. Diefenbach, E. Herdtweck, M. C. Holthausen, S. Schneider, *Nat. Chem.* **2011**, *3*, 532-537.
[224] R. Tian, J. C. Facelli, J. Michl, *J. Phys. Chem.* **1988**, *92*, 4073-4079.
[225] M. Zhou, L. Andrews, *J. Phys. Chem. A* **2000**, *104*, 1648-1655.
[226] M. S. Workentin, B. D. Wagner, F. Negri, M. Z. Zgierski, J. Lusztyk, W. Siebrand, D. D. M. Wayner, *J. Phys. Chem.* **1995**, *99*, 94-101.
[227] M. Bittererová, H. Östmark, T. Brinck, *J. Chem. Phys.* **2002**, *116*, 9740-9748.
[228] P. Zhang, K. Morokuma, A. M. Wodtke, *J. Chem. Phys.* **2005**, *122*, 014106.
[229] J. Wasilewski, *J Chem Phys* **1996**, *105*, 10969-10982.
[230] P. C. Samartzis, A. M. Wodtke, *Phys. Chem. Chem. Phys.* **2007**, *9*, 3054-3066.
[231] O. Krahe, F. Neese, M. Engeser, *ChemPlusChem* **2013**, *78*, 1053-1057.
[232] M. Schlangen, J. Neugebauer, M. Reiher, D. Schröder, J. P. López, M. Haryono, F. W. Heinemann, A. Grohmann, H. Schwarz, *J. Am. Chem. Soc.* **2008**, *130*, 4285-4294.
[233] M. R. DeFelippis, M. Faraggi, M. H. Klapper, *J. Phys. Chem.* **1990**, *94*, 2420-2424.
[234] S. Ye, F. Neese, *Inorg. Chem.* **2010**, *49*, 772-774.
[235] M. Olivucci, *Computational Photochemistry*, Elsevier Science, **2005**.
[236] J. M. Zurek, M. J. Paterson, *Current Inorganic Chemistry* **2013**, *3*, 196-212.
[237] N. S. Almeida, R. McKinlay, M. Paterson, *Struct. Bond.* **2014**, 1-32.
[238] F. Bernardi, M. Olivucci, M. A. Robb, *Chem. Soc. Rev.* **1996**, *25*, 321-328.
[239] B. G. Levine, C. Ko, J. Quenneville, T. J. MartÍnez, *Mol. Phys.* **2006**, *104*, 1039-1051.

[240] B. G. Levine, T. J. Martínez, *An. Rev. Phys. Chem.* **2007**, *58*, 613-634.
[241] G. J. Kavarnos, *Fundamentals of photoinduced electron transfer*, VCH Publishers, **1993**.
[242] K. Meyer, J. Bendix, N. Metzler-Nolte, T. Weyhermüller, K. Wieghardt, *J. Am. Chem. Soc.* **1998**, *120*, 7260.
[243] A. Dey, A. Ghosh, *J. Am. Chem. Soc.* **2002**, *124*, 3206-3207.
[244] K. M. Kadish, K. M. Smith, R. Guilard, *The Porphyrin Handbook*, Academic Press, **1999**.
[245] K. M. Kadish, K. M. Smith, R. Guilard, *The Porphyrin Handbook: Applications of phthalocyanines*, Academic Press, **2003**.
[246] M. Radoń, E. Broclawik, K. Pierloot, *J. Chem. Theory Comput.* **2011**, *7*, 898-908.
[247] G. E. Cutsail Iii, B. W. Stein, D. Subedi, J. M. Smith, M. L. Kirk, B. M. Hoffman, *J. Am. Chem. Soc.* **2014**, *136*, 12323-12336.
[248] H. Kropp, A. E. King, M. M. Khusniyarov, F. W. Heinemann, K. M. Lancaster, S. DeBeer, E. Bill, K. Meyer, *J. Am. Chem. Soc.* **2012**, *134*, 15538-15544.
[249] H. Kropp, A. Scheurer, F. W. Heinemann, J. Bendix, K. Meyer, *Inorg. Chem.* **2015**, *54*, 3562-3572.
[250] C. Geng, S. Ye, F. Neese, *Dalt. Trans.* **2014**, *43*, 6079-6086.
[251] A. Decker, J.-U. Rohde, E. J. Klinker, S. D. Wong, L. Que, E. I. Solomon, *J. Am. Chem. Soc.* **2007**, *129*, 15983-15996.
[252] P. Chandrasekaran, S. C. E. Stieber, T. J. Collins, J. L. Que, F. Neese, S. DeBeer, *Dalt. Trans.* **2011**, *40*, 11070-11079.
[253] J. H. Ammeter, *J. Magn. Reson.* **1978**, *30*, 299-325.
[254] J. H. Ammeter, J. D. Swalen, *J. Chem. Phys.* **1972**, *57*, 678-698.
[255] M. Nussbaum, J. Voitländer, *Z. Naturforsch.* **1965**, *20a*, 1417.
[256] H. E. Zimmerman, *Quantum mechanics for organic chemists*, Academic Press, **1975**.
[257] E. U. Condon, *Phys. Rev.* **1930**, *36*, 1121-1133.
[258] J. Owen, J. H. M. Thornley, *Rep. Prog. Phys.* **1966**, *29*, 675.
[259] J. H. Ammeter, R. Bucher, N. Oswald, *J. Am. Chem. Soc.* **1974**, *96*, 7833-7835.
[260] J. H. Ammeter, N. Oswald, R. Bucher, *Helv. Chim. Acta* **1975**, *58*, 671-682.
[261] J. J. Scepaniak, C. G. Margarit, J. N. Harvey, J. M. Smith, *Inorg. Chem.* **2011**, *50*, 9508-9517.
[262] H. Vennekate, D. Schwarzer, J. Torres-Alacan, P. Vöhringer, *J. Am. Chem. Soc.* **2014**, *136*, 10095-10103.
[263] M. G. Scheibel, B. Askevold, F. W. Heinemann, E. J. Reijerse, B. de Bruin, S. Schneider, *Nat. Chem.* **2012**, *4*, 552-558.
[264] R. G. Serres, C. A. Grapperhaus, E. Bothe, E. Bill, T. Weyhermüller, F. Neese, K. Wieghardt, *J. Am. Chem. Soc.* **2004**, *126*, 5138-5153.
[265] S. Ye, F. Neese, *Curr. Op. Chem. Biol.* **2009**, *13*, 89-98.
[266] S. Meyer, I. Klawitter, S. Demeshko, E. Bill, F. Meyer, *Angew. Chem. Int. Ed.* **2013**, *52*, 901-905.
[267] A. Decker, J.-U. Rohde, L. Que, E. I. Solomon, *J. Am. Chem. Soc.* **2004**, *126*, 5378-5379.
[268] A. Decker, M. D. Clay, E. I. Solomon, *J. Inorg. Biochem.* **2006**, *100*, 697-706.
[269] J. C. Schöneboom, F. Neese, W. Thiel, *J. Am. Chem. Soc.* **2005**, *127*, 5840-5853.
[270] F. Neese, *J. Inorg. Biochem.* **2006**, *100*, 716-726.
[271] T. A. Jackson, J.-U. Rohde, M. S. Seo, C. V. Sastri, R. DeHont, A. Stubna, T. Ohta, T. Kitagawa, E. Münck, W. Nam, L. Que, *J. Am. Chem. Soc.* **2008**, *130*, 12394-12407.
[272] C. V. Sastri, M. J. Park, T. Ohta, T. A. Jackson, A. Stubna, M. S. Seo, J. Lee, J. Kim, T. Kitagawa, E. Münck, L. Que, W. Nam, *J. Am. Chem. Soc.* **2005**, *127*, 12494-12495.
[273] D. J. Robbins, M. J. Stillman, A. J. Thomson, *J. Chem. Soc. Dalton Trans.* **1974**, 813-820.
[274] D. Schweinfurth, J. Krzystek, I. Schapiro, S. Demeshko, J. Klein, J. Telser, A. Ozarowski, C.-Y. Su, F. Meyer, M. Atanasov, F. Neese, B. Sarkar, *Inorg. Chem.* **2013**, *52*, 6880-6892.
[275] H. Tang, J. Guan, H. Liu, X. Huang, *Inorg. Chem.* **2013**, *52*, 2684-2696.
[276] H. Tang, J. Guan, H. Liu, X. Huang, *Dalt. Trans.* **2013**, *42*, 10260-10270.
[277] D. M. Kurtz, *Chem. Rev.* **1990**, *90*, 585-606.
[278] C. Ercolani, M. Gardini, K. S. Murray, G. Pennesi, G. Rossi, P. R. Zwack, *Inorg. Chem.* **1987**, *26*, 3539-3543.

[279] S. Sievertsen, K. S. Murray, B. Moubaraki, K. J. Berry, Y. Korbatieh, J. D. Cashion, L. J. Brown, H. Homborg, *Z. Anorg. Allg. Chem.* **1994**, *620*, 1203-1212.
[280] I. Vernik, D. V. Stynes, *Inorg. Chem.* **1996**, *35*, 2011-2018.
[281] S. Meyer, O. Krahe, C. Kupper, I. Klawitter, S. Demeshko, E. Bill, F. Neese, F. Meyer, *Inorg. Chem.* **2015**, *54*, 9770-9776.
[282] A. Messerschmidt, W. Bode, M. Cygler, *Handbook of Metalloproteins, Handbook of Metalloproteins*, Wiley, **2004**.
[283] P. Venkateswara Rao, R. H. Holm, *Chem. Rev.* **2004**, *104*, 527-560.
[284] A. Albers, S. Demeshko, S. Dechert, C. T. Saouma, J. M. Mayer, F. Meyer, *J. Am. Chem. Soc.* **2014**, *136*, 3946-3954.
[285] J. Ballmann, A. Albers, S. Demeshko, S. Dechert, E. Bill, E. Bothe, U. Ryde, F. Meyer, *Angew. Chem. Int. Ed.* **2008**, *47*, 9537-9541.
[286] J. D. Franolic, M. Millar, S. A. Koch, *Inorg. Chem.* **1995**, *34*, 1981-1982.
[287] H. Kämpf, D. Daunke, F. Heinemann, A. Grohmann, *Appl. Phys. A* **2008**, *93*, 303-311.
[288] G. T. Kubas, T. G. Spiro, A. Terzis, *J. Am. Chem. Soc.* **1973**, *95*, 273-274.
[289] D. Sellmann, I. Barth, *Inorg. Chim. Act.* **1989**, *164*, 171-177.
[290] D. Sellmann, P. Lechner, F. Knoch, M. Moll, *J. Am. Chem. Soc.* **1992**, *114*, 922-930.
[291] D. Sellmann, G. Mahr, F. Knoch, *Angew. Chem. Int. Ed.* **1991**, *30*, 1477-1479.
[292] W. S. Szulbinski, *Polish. J. Chem.* **2000**, *74*, 1163-1175.
[293] W. S. Szulbinski, D. H. Busch, *Inorg. Chim. Act.* **1995**, *234*, 143-148.
[294] M. Studer, T. A. Kaden, *Helv. Chim. Acta* **1986**, *69*, 2081-2086.
[295] E. K. Barefield, F. Wagner, A. W. Herlinger, A. R. Dahl, S. Holt, in *Inorganic Syntheses*, John Wiley & Sons, Inc., **2007**, pp. 220-225.
[296] H. H. Jaffé, *J. Chem. Phys.* **1953**, *21*, 258-263.
[297] H. H. Jaffé, G. O. Doak, *J. Chem. Phys.* **1953**, *21*, 196-200.
[298] R. S. Mulliken, C. A. Rieke, D. Orloff, H. Orloff, *J. Chem. Phys.* **1949**, *17*, 1248-1267.